



HAL
open science

Reactivity at aqueous interfaces by DFT-MD simulations

Flavio Siro Brigiano

► **To cite this version:**

Flavio Siro Brigiano. Reactivity at aqueous interfaces by DFT-MD simulations. Organic chemistry. Université Paris-Saclay, 2020. English. NNT : 2020UPASF025 . tel-03283670

HAL Id: tel-03283670

<https://theses.hal.science/tel-03283670v1>

Submitted on 12 Jul 2021

HAL is a multi-disciplinary open access archive for the deposit and dissemination of scientific research documents, whether they are published or not. The documents may come from teaching and research institutions in France or abroad, or from public or private research centers.

L'archive ouverte pluridisciplinaire **HAL**, est destinée au dépôt et à la diffusion de documents scientifiques de niveau recherche, publiés ou non, émanant des établissements d'enseignement et de recherche français ou étrangers, des laboratoires publics ou privés.

Reactivity at aqueous interfaces by DFT-MD simulations

Thèse de doctorat de l'université Paris-Saclay

École doctorale n°571 Sciences Chimiques : Molécules, Matériaux,
Instrumentation et Biosystèmes (2MIB)
Spécialité de doctorat: Chimie

Unité de recherche : Université Paris-Saclay, Univ Evry, CNRS, LAMBE, 91025, Evry-
Courcouronnes, France
Référent : Université d'Evry Val D'Essonne

Thèse présentée et soutenue à Evry le 14/12/2020 par

Flavio Siro Brigiano

Composition du Jury

Piero UGLIENGO

Professeur, Università degli Studi di Torino, Italie Président du jury

Barbara KIRCHNER

Professeure, University of Bonn, Germany Rapporteuse

Fabio PIETRUCCI

Maître de Conférences, Sorbonne
Université, France Rapporteur

Weitao LIU

Professeure, Fudan University, China Examinatrice

Marie-Anne HERVÉ DU PENHOAT

Maître de Conférences, Sorbonne
Université, France Examinatrice

Daniel PELÁEZ RUIZ

Professeur, Université Paris Saclay, France Examineur

Marie-Pierre GAIGEOT

Professeure, Université d'Evry Val
D'Essonne, Université Paris Saclay,
France Directrice de thèse

Contents

1	Chemical reactions at aqueous interfaces	3
1.1	General Introduction	3
1.2	Condensation reactions at aqueous interfaces in prebiotic chemistry	7
1.3	The amorphous silica-water interface, an elusive chemical environment	14
1.4	Outlines of this manuscript	17
2	Theoretical Methods	21
2.1	Molecular dynamics (MD)	21
2.1.1	Numerical integration of the Newton's equations of motion	22
2.1.2	Temperature control	23
2.1.3	Initial conditions and time step	24
2.1.4	Periodic boundary conditions	24
2.2	Born-Oppenheimer BOMD in the DFT electronic framework (DFT-MD)	25
2.2.1	Density Functional Theory	26
2.3	The CP2K software and the computational set-up chosen for the DFT-MD simulations in this thesis	30
2.4	Metadynamics	31
2.4.1	Set up for metadynamics	33
2.5	Thermodynamic integration	35
2.6	SFG spectra calculations in DFT-MD	36
3	Peptide bond formation at the air-water interface	41
3.1	Factors governing reactions at the air-water interface	42
3.2	In situ observation of the peptide bond formation	47
3.3	The catalytic roles of the air-water interface in the prebiotic peptide bond formation	51
3.3.1	Peptide bond formation at the air-water interface: mechanisms and energetics	51
3.3.2	Stabilization of the reactive complex (R) at the air-water interface	53
3.3.3	The Catalytic Role of the Cl ⁻ anion	55
3.3.4	The peptide condensation in bulk liquid water	55

4	Stability of neutral and zwitterionic forms of amino acids at the air-water interface	107
4.1	Introduction	107
4.2	Neutral-zwitterion interconversion: air-water vs bulk water	109
4.3	Concerted mechanism in bulk water <i>vs</i> two step mechanism at the air-water interface	112
4.4	The alanine dance at the air-water interface makes the difference	115
5	Structural and spectroscopic characterization of the amorphous silica-water interface	121
5.1	Generalities on amorphous silica-water interfaces	123
5.2	Effects of the surface degree of hydroxylation on silica-water interfaces	125
5.3	Effects of ions on silica-water interfaces	127
5.4	SFG spectroscopy, a useful tool to interrogate silica-water interfaces	129
5.5	DFT-MD allows the deconvolution of SFG spectra. Test case on the most common amorphous silica-water interface (4.5 OH-/nm ² hydroxylation)	132
5.6	Tuning the silica surface hydrophilicity and the silica-water interactions	135
5.7	Tuning the silica surface hydrophilicity and consequence on the BIL-water network	161
5.8	An aspect of the surface morphology effects: how silanol nests can affect interfacial properties	189
5.9	Effects of Electrolytes on the structure, dynamics and spectroscopy of amorphous silica-water interfaces	196
5.10	Summary of the chapter	240
6	The amorphous silica aqueous surface as a function of pH conditions	243
6.1	Generalities	243
6.2	Experimental data and opened questions (from Y.R.Shen, W.Liu <i>et al.</i> , Fudan University)	248
6.3	DFT-MD at aqueous silica and pKa values of silanols. Appearance of Si5 motifs at the surface.	250
6.4	DFT-MD and SFG bands at increasing pH	254
6.5	Si5 structures stability as a function of the pH conditions	257
6.6	Conclusions	260
6.7	Experimental and computational details	262
6.7.1	SSP and PPP SFG spectra of the amorphous silica-water interface	262
6.7.2	DFT-MD and metadynamics set up	262
6.7.3	Details for the DFT-MD metadynamics	263
6.7.4	Validation of the pKa values	265
6.7.5	Structural Characterization of Si5 species	267
6.7.6	Velocity Density of States calculations	272

7	Conclusions and perspectives	289
	Bibliography	295
	Appendix A The formation of urea in space	311
	Appendix B Influence of argon and D ₂ tagging on the hydrogen bond network in Cs ⁺ (H ₂ O) ₃ ; kinetic trapping below 40 K	327

List of Publications

1. Ions Control Interfacial Water Structure and Dynamics at Silica Surfaces.
A Tuladhar, S Dewan, S Pezzotti, F Siro Brigiano, MP Gaijeot, E Borguet.
J. Am. Chem. Soc., **142**, 6991, (2020).
2. Molecular hydrophobicity at a macroscopically hydrophilic surface.
JD Cyran, MA Donovan, D Vollmer, F Siro Brigiano, S Pezzotti, DR Galimberti, MP Gaijeot, M Bonn, EHG Backus.
Proc. Natl. Acad. Sci., **116**, 1520, (2019).
3. Influence of argon and D₂ tagging on the hydrogen bond network in Cs⁺(H₂O)₃; kinetic trapping below 40 K.
TK Esser, H Knorke, F Siro Brigiano, DR Galimberti, KR Asmis, MP Gaijeot, JM Lisy *Phys. Chem. Chem. Phys.*, **20**, 28476, (2018).
4. The formation of urea in space-I. Ion-molecule, neutral-neutral, and radical gas-phase reactions
F Siro Brigiano, Y Jeanvoine, A Largo, R Spezia *A&A*, **610**, A26, (2018).
5. The catalytic roles of the air/water interface in the prebiotic peptide bond formation.
F Siro Brigiano, S Pezzotti, DR Galimberti, V.Vaida, MP Gaijeot
To be submitted soon
6. From hydrophilic to hydrophobic aqueous silica, from a vertical to a horizontal order of interfacial water.
F Siro Brigiano, S Pezzotti, DR Galimberti, MP Gaijeot
In final preparation
7. New species identified at the silica water interfaces.
X Li, F Siro Brigiano, S Pezzotti, H Chen, Y Li, YR Shen, MP Gaijeot, WT Liu
To be submitted soon

8. Stability of neutral and zwitterionic forms of amino acids at the air-water interface.

F Siro Brigiano, DR Galimberti, S Pezzotti, MP Gaigeot
In preparation.

9. Molecular fingerprints of hydrophobicity at interfaces from theory and vibrational spectroscopies.

S Pezzotti, A Serva, F Sebastiani, F Siro Brigiano, DR Galimberti, L Potier, S Alfani, G Schwaab, M Havenith, MP Gaigeot.
To be submitted soon.

Chapter 1

Chemical reactions at aqueous interfaces

1.1 General Introduction

The microscopic comprehension of chemical reactions that occur at the boundary between water and other media represents an essential step in chemical science for the development and conception of high yield reactions. Recently, striking findings in the field of mass spectrometry showed reactions on water aerosols[1, 2, 3, 4, 5, 6] to be accelerated by around six orders of magnitude with respect to the corresponding ones in bulk water. This has moved the attention of the scientific community on the catalytic roles played by aqueous interfaces. The possibility to reproduce such reaction rates on a larger industrial scale represents one promising pathway toward the chemistry of the future. Chemical reactions at the boundary with liquid water and other media have indeed huge applications in heterogeneous catalysis, in industrial applications, geochemistry, chemical nanoscience, atmospheric chemistry as well as prebiotic chemistry.

Beyond the acceleration of chemical reactions, the water interface has been found to modulate each aspect of the chemistry by typically changing the reaction mechanisms, the product selectivity and by altering the ionization state of reactive species. This is especially the case in atmospheric chemistry where the specific interfacial water hydrogen bond (H-Bond) network at the surface of cloud aerosols has been shown to modulate the chemistry in the troposphere. Hence, many reactions are found at interfaces with mechanisms that are different from the ones in the gas phase, significantly impacting the fate of the polluting agents in the atmosphere and on the atmosphere composition[7, 8, 9, 10, 11, 12, 13].

Reactions at the surface of aqueous aerosols have been also envisaged in prebiotic chemistry for which chemical environments in partially dehydrated conditions are needed in order to rationalize the origin of biopolymers on the primordial Earth. The formation of these polymers is strongly unfavoured in bulk water[14]. For instance, Vaida *et al.*[15] have observed the formation of

polypeptides at the air-water interface, suggesting the surface of oceans and water aerosols as suitable environments for the birth of life on the prebiotic Earth.

As discussed more in detail in section 1.2, also mineral clay-water interfaces have been found relevant in catalysing condensation reactions in prebiotic chemistry and in protecting the biopolymers from water hydrolysis. In this context a wide range of heterogeneous catalytic reactions (e.g. Fischer-Tropsch, alkene epoxydation, glucose isomerization, peptides cycles, Bayer-Villegier oxydation) at mineral[16, 17, 18, 19, 20, 21, 22, 23, 23] and at metal[24, 25, 26, 27, 28, 29] surfaces have been found to be either significantly promoted or inhibited by the presence of water either in the vapour-phase or in the liquid-phase form. Stabilization of intermediates and/or transition states, proton hopping mediation and promotion of the reactants adsorption are the main roles attributed to the water along the reaction mechanisms.

The case of zeolites is really interesting. They are employed in the biomass degradation, where the influence of the water is of paramount importance because of its production in stoichiometric quantities in the catalyst active site during the bio-degradation cycles[17, 19, 30, 21, 22]. Recent works have also shown that the use of zeolites as catalysts in liquid water is a viable route for conversion of some biomass molecules on hydrophobic zeolite crystallites[17, 18]. A transition state stabilization in the proton transfer process along the zeolite-catalysed reactions has been ascribed to the water molecules, however a molecular description of the effect associated to the specific water hydrogen bond network on the sub-nanometer pores of zeolites is still lacking.

Computational works based on quantum static calculations and molecular dynamics simulations (MD) (both classical and *ab initio*) are extremely important in the field because they provide a description of the chemical environment at a microscopic level that is not often accessible by experiments. For instance computational models for mesoporous silica materials[31, 32] now allow MD and quantum static calculations on the role and behaviour of water inside silica nanopores[33].

The astonishing development in the conception and fabrication of inorganic [34, 35, 36] and bio-inspired[37] nano reactors have led many works exploring the organization and properties of water in nano-confined environments in order to rationalize their effect on chemical reactions[38, 39, 40, 41, 42].

The work of Muñoz-Santiburcio *et al.*[43] has shown the effect of water nano solvation in mackinawite (FeS) sheets on a prebiotic peptide cycle. Their results highlight how the specific structure and properties of the water under nano confinement stabilize much more the charged chemical species with respect to bulk water, at the same temperature and pressure conditions. Such effect has an impact on the energetic and mechanisms of the reaction in the water confined environment.

The specific structural organization and properties (thermodynamic and electrochemical) of water at various interfaces can induce enormous changes in the mechanisms and energetics of chemical and physical processes. However the experimental difficulty in discerning the specific catalytic effect originating from the specific interfacial water environment, especially at the boundaries with a solid surface, makes the role of the interfacial water along the reaction pathways still far to be understood. Such detailed molecular information can only be provided by computational chemistry.

In the last decade, with the advance of the computational power and the development of enhanced sampling techniques, molecular calculations have shown to be ‘more than useful’ tools to characterize chemical reactions at interfaces. For example computational studies of peptide bond reactions assisted by mineral clays[44] have shed light on the unexplored catalytic role of the substrates, while recent *ab initio* molecular dynamics simulations (AIMD) on relevant atmospheric reactions find different reaction mechanisms at the air-water interface with respect to the gas phase[45].

In this PhD thesis we have therefore investigated the reactivity of/at aqueous interfaces by coupling DFT-MD (Density Functional Theory based Molecular Dynamics) simulations (naturally taking into account chemical reactions) with the enhanced sampling of biased DFT-molecular dynamics techniques[46, 47]. The structural and spectroscopic properties of the interfaces considered in this work, have been investigated by coupling DFT-MD simulations and theoretical SFG (Sum Frequency Generation) spectroscopy.

The first part of this manuscript is dedicated to the study of the chemical reactions that lead to the peptide bond formation at the air-water interface (chapters 3 and 4).

In particular the recent experimental findings by Vaida *and coll.*[15] on the polypeptide formation at the air-water interface from amino acid esters and Cu(II)-chloride salt have attracted our attention. In chapter 3 we provide a full microscopical insight into this chemical route in order to understand the interfacial factors that promote such reaction at the air-water interface.

In chapter 4 we consider another chemical route for the formation of polypeptides on the primordial Earth: the condensation of amino acids at the air-water interface in absence of an inorganic catalyst. In particular we have characterized the reactivity of two amino acids at the air-water interface, i.e. the alanine and the leucine.

The principal findings in these works are: 1) the identification of the interfacial factors that modulate the substrate’s reactivity at the air-water interface, 2) the assessment of the plausibility of such chemical routes as sources of polypeptides on the primordial Earth.

Our general approach consists in providing a description at the molecular level of the reaction processes at the air-water interface and compare

them with the ones occurring in bulk water. The comparison of the reaction energetics and mechanisms at the interface and in bulk water, coupled with a full characterization of the air-water interface previously achieved by our group in recent works[48, 49] allow us to unveil the relationships between reactivity and water structure at the hydrophobic air-water interface. For an introduction on the peptide bond condensation reaction in prebiotic chemistry see section 1.2.

The study of reactions at aqueous interfaces continues in chapter 6 where we investigate the chemistry of silica aqueous interfaces as a function of pH. We have decided to focus on the reactivity of the amorphous silica-water interface due to its relevance in geochemistry, biomedicine and many industrial applications. Before being able to fully understand the reactivity of this interface, chapter 5 provides a characterization of the molecular organization at the boundary between amorphous silica and liquid water. For an introduction on amorphous/silica water interfaces see section 1.3.

Part of my thesis work has also been dedicated to gas phase chemistry. In the first part of my PhD I have indeed focused on the gas phase reactivity of small organic and inorganic compounds of astrochemical interest. The principal objective of this project was to explore the possible chemical routes leading to the formation of Urea in the interstellar medium (ISM). This work has been done under the supervision of Dr. Riccardo Spezia (now at Sorbonne University, Paris), my thesis advisor during the first 8 months of my PhD. At page 311 in the Appendix A the published paper[50] associated to this project is reported.

After the departure of Dr. Riccardo Spezia from the LAMBE laboratory (Laboratory of Analyses and Modelling for Biology and Environment) at the University of Evry, I have made the choice to change thesis advisor, starting a new PhD topic on the reactivity of aqueous interfaces, under the supervision of Prof. Marie-Pierre Gageot (this topic is therefore the central goal of this manuscript).

Beyond the work on the reactivity at aqueous interfaces, I have also contributed to a research project which main objective has been the structural characterization of Cesium water clusters by theory and spectroscopy in the gas phase. This work has been performed under the supervision of Prof. M.P. Gageot, in collaboration with the experimental group of Prof. J.M. Lisy (University of Illinois at Urbana-Champaign, USA). The associated published paper[51] is reported in the Appendix B at page 327.

1.2 Condensation reactions at aqueous interfaces in prebiotic chemistry

The emergence of proteins in the early ages of the Earth originating from the condensation of small organic compounds in the "primordial soup" is a fascinating unresolved question in prebiotic chemistry. The transition from small organic compounds to complex self-replicating organisms represents a mysterious time-laps in the origin of life science whose sophisticated chemistry in abiotic conditions (i.e. in absence of enzymes) is still not clear.

The issue in prebiotic chemistry arises from the uncertainty on the Earth conditions more than 3.5 billion years ago (the first fossil remainder of a cell-like structure[52] dates back to ~ 3.5 billion years ago). The temperature of the primitive Earth is unknown. Cold and hot scenarios are thus both considered plausible for the origin of life together with fluctuating temperature conditions around the boiling point of water during the hydrosphere formation[53, 54]. Also the composition of the primordial atmosphere is debated: a wide spectrum of gas mixtures, ranging from reducing (i.e. which contain actively reducing gases), e.g. $\text{CH}_4 + \text{N}_2 + \text{NH}_3$ or $\text{CO}_2 + \text{H}_2 + \text{N}_2$ [55], to neutral (i.e. which contain mainly inert gases) e.g. $\text{CO}_2 + \text{N}_2 + \text{H}_2\text{O}$ ones, have been proposed. Both reducing and neutral atmospheres, when exposed to electrical discharges mimicking those occurring in thunderstorms, have been shown to produce amino acids and simple organic molecules[55].

Conversely, there is a general consensus on the presence of water as well as on the large abundance of amino acids and other small bio-organic compounds. These latter were being either delivered by meteorites (Murchison meteorite for instance[56, 57, 58, 59]) or formed directly on the primitive Earth[55, 60]. All the ingredients of life were thus present on the early Earth.

However, the condensation of amino acids into oligopeptides (Fig. 1.1) in absence of enzymes is known to be hindered by both thermodynamic and kinetic reasons in bulk water at ambient conditions[14]. The condensation

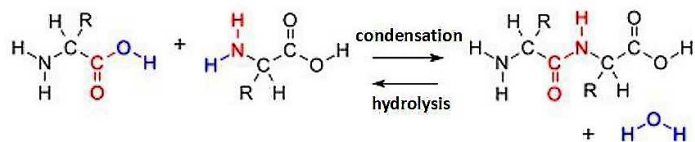


Figure 1.1: Scheme of the peptide bond condensation reaction from two amino acids. In the scheme 'R' stands for the residue of the amino acid. The reaction leads to the formation of a dipeptide and one water molecule. The OH from the C-terminal of one amino acid reacts with one hydrogen atom from the N-terminal of the other amino acid, to produce one dipeptide and one water molecule (blue).

reaction between two amino acids indeed requires a water removal that is strongly unfavoured in bulk water by chemical equilibrium. The large excess of water and the positive free reaction energy difference ΔG_r ($G_{products}$ -

$G_{\text{reactants}}$) of ~ 17 kJ/mol per peptide bond keeps the reaction far on the side of the hydrolysis[14], i.e. the reaction in Fig. 1.1 is energetically favoured to go from the right to the left side, hence favouring the hydrolysis reaction.

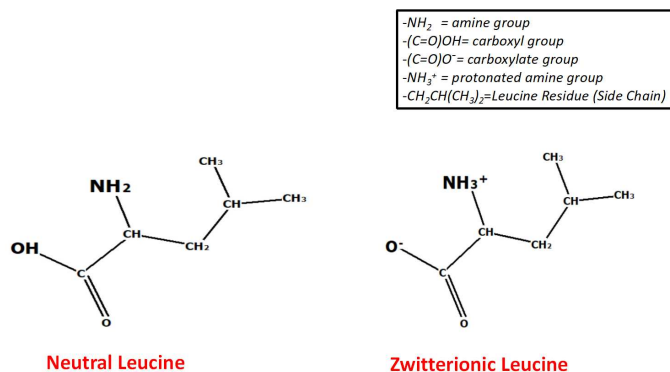


Figure 1.2: On the left and on the right sides are depicted the amino acid leucine structures respectively in the neutral and zwitterionic form. The amine and carboxyl groups, which protonation states distinguish the amino acid neutral form from the zwitterionic one, are highlighted in bold. A legend with chemical nomenclatures is reported on the top-right.

Furthermore the predominance of the amino acid zwitterionic form over the neutral one (see Fig. 1.2) in liquid water kinetically disfavours the formation of the peptide bond (i.e. high activation energy). For instance, during the peptide bond formation reaction, the amine (-NH₂) nitrogen of one amino acid approaches with its lone pair (pair of valence electrons) the carboxyl carbon (COOH) of the other amino acid (this is a nucleophilic attack) leading to the formation of a new covalent N-C bond. When in the zwitterionic form, the protonation states of both the protonated amine and of the carboxylate group (-NH₃⁺ and -COO⁻ on the right side of Fig. 1.2) respectively reduce the nucleophilicity (the capacity of a chemical species to donate electrons) and the electrophilicity (the capacity of a chemical species to receive electrons) of the nitrogen and of the carbon atoms involved in the nucleophilic attack. This factor leads to a high energetic barrier for the nucleophilic attack, hindering the peptide bond condensation reaction to occur in bulk water at ambient conditions.

In order to overcome such thermodynamic and kinetic issues, it is necessary to move away from bulk water. "Plausible" prebiotic scenarios for the peptide bond condensation thus take into account "partially dehydrated" conditions. Many chemical routes in partially dehydrated conditions have been proposed by the scientific community, including wet and dry cycles[53, 61] (i.e. wet and dry conditions are alternated during the reaction), reaction on mineral clays[62, 63, 20], heating with an inorganic catalyst[64, 65], reactions at the air-water interface[15].

Mineral-water interfaces have gained importance in prebiotic chemistry for

their possible catalytic roles in the biopolymer formation on the early Earth. Recent and past works in the literature[66, 67, 68, 69] have highlighted the mineral/water interfaces capacities in favouring the condensation reaction by : 1) concentrating and "crowding" the species in space, simply by offering a confined environment, 2) stabilizing the reaction species and substrates in molecular proximity and in favourable orientations, 3) preventing biomolecular degradation, e.g. hydrolysis of ribose[70, 71, 72] and oligopeptides[54, 62].

Mineral-water interfaces have been envisaged in many plausible prebiotic scenarios, varying the chemical physical conditions from hydrothermal vents (fissure on the seafloor from which geothermally heated water issues) at extreme temperatures and pressures to coastal volcanic environment, where the oligopeptide formation is supposed to start in the high temperature conditions of hot lava to then terminate in the cooler volcanic-hosted rock pools (where water and basaltic rocks are present)[73, 74, 75, 76].

In particular Marx *et al.*[20] in their theoretical work have investigated the peptide formation at the pyrite-water interface in extreme thermodynamic conditions in order to reproduce the chemistry that would exist at the deep see hydrothermal vents, proposed as a suitable environment for the peptide synthesis[77, 78]. This work pointed out the capability of a pyrite surface in decreasing many of the energy barriers of reactions by especially reducing the entropy of the reactants when adsorbed on the surface and by stabilizing transition states. Furthermore, the pyrite surface was found to protect the oligopeptide from hydrolysis thanks to its ability to screen the adsorbed products from water. When the peptide is anchored to the pyrite surface the water molecules can perform a nucleophilic attack on the carbon that will be involved in the peptide bond (CO-NH in Fig. 1.1) only from certain angles, while in bulk the water is free to approach the peptide from all the sides.

Silica SiO₂ is the most abundant mineral on the Earth crust and many attention has been put on its possible catalytic role in relevant prebiotic reactions[79, 44, 80, 81, 63]. In particular Rimola *et al.*[81, 82] have focused on the silica surface catalytic role in the peptide bond formation, by coupling IR spectroscopy on different heat-treated silica surfaces and static quantum chemistry calculations. By their synergistic approach they managed to reveal the catalytic role of the Si-O strained rings and of the weakly interacting isolated silanols in the peptide bond formation.

In this context Saladino *et al.*[83] have shown how formamide, a simple organic molecule which existence is highly plausible on the primordial Earth, is at the origin of the formation of nucleobases, amino acids and condensing agents when reacting at the interface of a SiO₂ based material in water at high temperature (80°). Following such interesting results, Signorile *et al.*[84] have provided a microscopic picture of the formamide adsorption on a dry amorphous silica surface with a low degree of hydroxylation by combining FTIR spectroscopy and computer modelling techniques.

Generally speaking, the formation of polypeptides has been obtained by

reactions at the boundary between liquid water and mineral clay surfaces (silica, alumina, montmorillonite, pyrite) in various pressure and temperature conditions, but only in low yields[63, 85, 68, 86, 87, 88]. However the capacity of mineral clays in favouring the chain elongation and in stabilizing oligopeptides against hydrolysis (see Fig.1.1), reported in many computational and experimental studies, could have played a fundamental role in the polypeptides evolution.

One of the simplest way to get high yields of production of polypeptides in liquid water under plausible prebiotic conditions is given by the "salt-induced peptide bond formation" (SIPF)[64, 65, 89, 90]. In this reaction, done at high temperature, a pivotal role is played by the formation of a monochloride copper(II)-amino acid reaction complex (see Fig .1.3 left). In this complex two amino acids, two water molecules and one Cl^- counter ion are coordinated to Cu^{2+} in an octahedral geometry. The specific geometry of the complex (Fig .1.3 right) has been predicted by gas phase *ab initio* calculations[64]. A high concentration of NaCl is used as dehydrating agent in liquid water in order to reduce the thermodynamic barriers of the peptide bond condensation reaction (i.e. decrease of the ΔG of reaction). It is important to mention here that an essential component of the reaction is the coordination of the Cl^- to the Cu^{2+} in the complex[89]. The presence of the Cl^- within the reaction complex is indicated by the color of the active solution, i.e. green color instead of blue color if the solution contained only copper-amino acid complexes[91]. In absence of such coordination (other anions than Cl^- are used in the experiments) a dramatic decrease in the polypeptide production is obtained. However a mechanistic insight into this reaction, able to disentangle all the complex microscopic factors governing the rate of reaction, was lacking at the time and only a dehydration effect has been ascribed to the Cl^- .

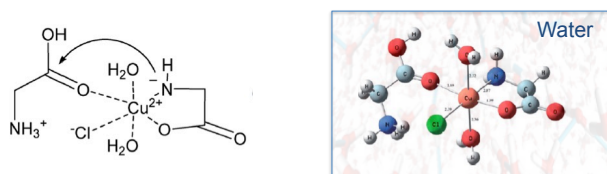


Figure 1.3: *Supposed pre-reaction complex of the SIPF (salt induced peptide bond formation)[65, 54, 89]. Figure reproduced with permission from ref.[88]*

The SIPF reaction has been combined experimentally with wet-dry cycles, in order to reproduce the possible fluctuating conditions of the primordial Earth. This was leading to higher reaction efficiency[92]. It is interesting to

know that in presence of mineral clays the SIPF reaction brings to the formation of longer oligopeptides[54], presumably thanks to the mineral capacity in preventing the hydrolysis of the formed peptides. In particular, Rode *et al.*[54] experimentally combined the SIPF reaction with wet and dry cycles at the surface of many mineral clays in order to discern which solid surfaces could have catalysed best the peptide bond formation in temperature fluctuating conditions. The rates of the reaction reveal silica and alumina to be the only surfaces to play a catalytic role in the peptides oligomerization under these conditions. Other important features of the SIPF reaction are its applicability to all amino acids and its low racemization rate (i.e. L-amino acids lead to reaction yields around 6.5 times higher than the D-amino acids). As a drawback, high temperatures and high concentrations of reactants are needed to make such reaction occur, doubtful conditions in a cold prebiotic scenario.

Vaida *et al.*[15] have recently experimentally observed the formation of polypeptides at room temperature in dilute conditions from amino acid esters and Copper- chloride salt at the air-water interface, suggesting the surface of oceans and marine aerosols as suitable environments for the birth of life on the prebiotic Earth[93, 94, 95, 96, 97].

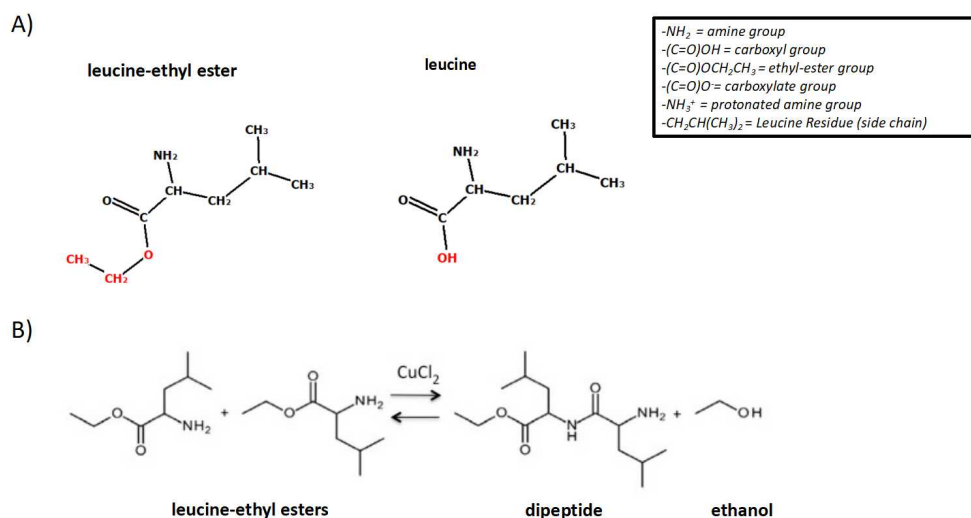


Figure 1.4: Panel A: Chemical structures of the leucine-ethyl-ester (left) and of the leucine (right) amino acids. In red we have highlighted the atoms that distinguish the ester group from the carboxylic one. On the top right of the figure is reported a legend with chemical nomenclatures. Panel B: Scheme of the peptide bond condensation reaction observed experimentally at the air-water interface for leucine ethyl ester amino acids.

In such reaction, two leucine ethyl ester amino acids (the structure is reported in Panel A of Fig. 1.4) condense and lead to the production of one leucine-leucine dipeptide plus one ethanol molecule (see Panel B of Fig. 1.4

for the reaction). The CuCl_2 salt is used as a catalyst for the reaction in the experiment since the well-known ability of the Copper cation Cu^{2+} in forming coordination complexes with amino acids and peptides[90, 65]. For instance, spectroscopic evidences[15] indicate the formation of a reaction complex between the Cu^{2+} cation and the amino acid esters, that promote the peptide bond condensation reaction at the air-water interface. From these experiments, it is not known whether the Cl^- ion stays bonded to the Cu^{2+} in the reaction complex at the air-water interface and whether it has a catalytic role along the reaction. Leucine-ethyl ester, a short amino acid ester plausibly present on the primordial Earth, is used as reactant in order to prevent the zwitterionic form of the amino acid that is known to kinetically unfavour the peptide bond formation in liquid water (see discussion page 8). Moreover this condensation reaction produces ethanol, that is a better leaving group than water, and shifts the chemical equilibrium of the reaction toward the side of the products. This reaction, done at the air/water interface, is compatible with geochemical conditions of the primitive Earth where air-water interfaces were ubiquitous during and after the hydrosphere formation in early oceans and salty water droplets. The presence of copper ions in the early ocean is also indicated by the presence of green pre-cambrian zones (rocks rich in copper that date back to 4.5 billion years ago)[98, 68].

Among the chemical routes leading to the formation of polypeptides in plausible prebiotic scenarios described above, we have decided to provide a microscopical insight into the peptide bond formation reaction at the air-water interface in order to shed light on the interfacial factors that make the reaction performed by Vaida's group[15] possible at the air-water interface.

Many capabilities have been ascribed to the air-water interface in accelerating organic reactions, among which the ability to concentrate reactants, the alignment of biochemical precursors, the shift of pKas, and the partial dehydration of the reactants[99, 100, 101].

However the specific role of the air-water interface during the peptide bond condensation reaction and the reasons for which this reaction occurs at the interface and not in bulk water are still unclear. In particular, experiments have been performed on the same condensation reaction from leucine-ethyl esters catalyzed by copper-chloride salt in aqueous solution, yielding no polypeptides production[102].

The formation of a chelated complex in bulk water, where one of the two leucine-ethyl esters is bonded with both the ester and the amine groups to the Copper Cu^{2+} cation (see Panel B of Fig. 1.5), leads experimentally to a high degree of hydrolysis of the ester group, thus hampering the peptide condensation reaction in bulk water[102]. With the coordination of the ester group to the Cu^{2+} , in bulk water, there is a flux of positive charge ($\delta+$) to the ester carbon that in turn becomes more prone to the nucleophilic attack from water (see Fig. 1.6 for the reaction scheme). The nucleophilic attack of the water on the ester carbon leads to the loss of the ester group with the production of a carboxyl group in the amino acid and a leaving ethanol molecule. With the loss of the ester activating group the peptide bond con-

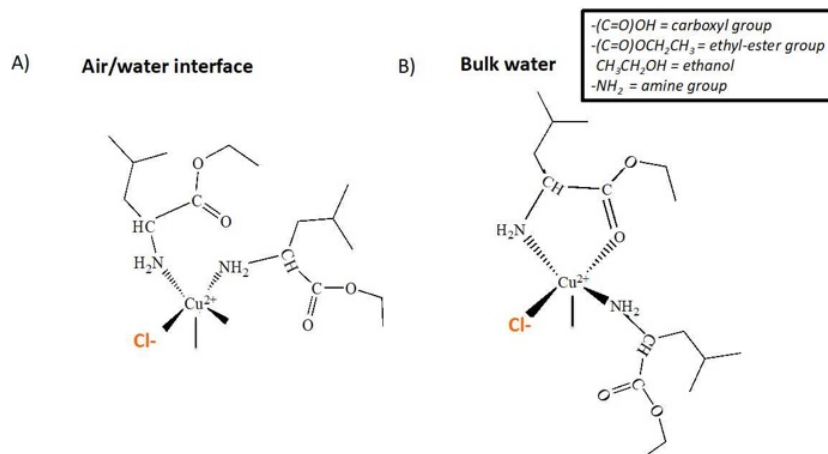


Figure 1.5: Panel A: Structure of the Cu(II)-Cl bis-leucine-ethyl esters complex observed by spectroscopy techniques at the air-water interface[15]. Panel B: Cu(II)-Cl -bis-leucine-ethyl ester complex observed experimentally in bulk water[102]. Beware, for both complexes, there are not direct evidences whether the Cl^- counter ion (depicted in orange in the figure) is covalently bonded to the Cu^{2+} (air-water interface and bulk water alike).

denation reaction cannot occur in bulk water.

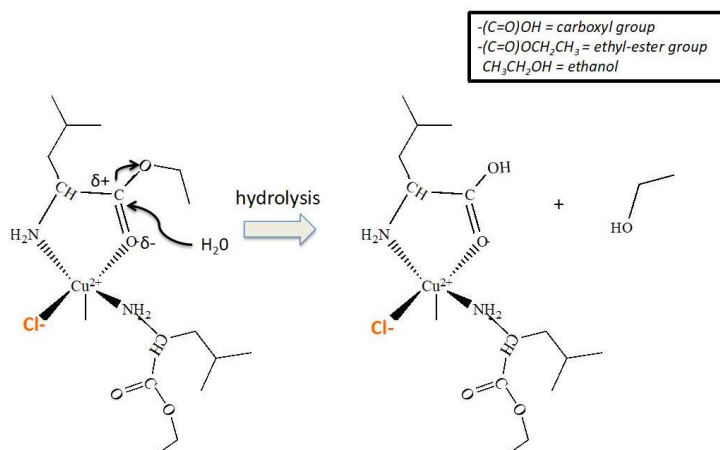


Figure 1.6: Bulk water: Reaction scheme of the hydrolysis of the ester group belonging to the amino acid leucine ethyl ester observed in the Cu(II)-Cl -bis-leucine-ethyl ester complex[102].

Differently, IRRAS spectroscopic experiments[15] find a reactive complex at the air-water interface (see Panel A Fig. 1.5), conformationally different from the non-reactive one observed in bulk water. In this reactive complex the two leucine ethyl esters are coordinated to the Cu^{2+} cation by the two amine groups, there is no coordination of any ester group ($-\text{COOCH}_2\text{CH}_3$) to the Cu^{2+} . The absence of the ester direct coordination to the Cu^{2+} in the complex at the air-water interface thus prevents the ester hydrolysis and now allows the peptide bond condensation reaction to proceed. The experimental evidence of two different complex structures at the air-water interface versus

bulk water highlights a direct role of the interface in the peptide condensation chemistry that goes beyond already well-known catalytic interfacial factors (e.g. concentration of reactants, aligning bio-molecules, pK_a shifts, partial desolvation of reactants).

It is therefore obvious that a microscopic characterization of the air-water interface structure together with a deep insight into the mechanisms and energetics of the reaction at the interface versus in bulk water is needed, in order to rationalize the success of the polypeptide formation at the air-water interface. To achieve this objective we provide in chapter 3 a deep molecular insight into the peptide bond condensation reaction at the air-water interface by means of DFT-MD and biased DFT-MD techniques. The characterization of the interfacial water network[103, 104, 105], coupled with the comparison between energetics and reaction mechanisms observed at the air-water interface versus bulk water allows us to reveal the key factors that promote the reaction in heterogeneous conditions.

Our data point to novel catalytic roles of the air-water interface which are essential in making the reaction occur (see chapter 3). We especially identify why the solvation properties of the reactive species at the interface are of utmost importance in catalyzing the peptide bond condensation reaction.

1.3 The amorphous silica-water interface, an elusive chemical environment

In the previous section we have mentioned the importance of mineral clay-water interfaces in prebiotic chemistry. We have seen some reasons why these interfaces offer a unique chemical environment to the reaction species, being able at the same time to catalyse condensation reactions and to protect the resulting products from hydrolysis (see again Figs. 1.1 and 1.6). A particular emphasis has been put on the role of SiO_2 since its high abundance on Earth. The amorphous silica-water interface has especially been shown capable in catalysing many relevant prebiotic reactions under various physical-chemical conditions[63, 71, 54, 83, 44].

Beyond the importance in prebiotic chemistry, the understanding of reactions at the boundary between silica and water represents a fundamental step toward the development of new technologies in many domains ranging from liquid chromatography to biomedicine. Hydrophobic and hydrophilic interactions between silica surfaces and aqueous solutions at the molecular level are typically of particular importance in order to rationalize the water-mediated catalysis[106] of organic reactions and phase separation processes in applications ranging from liquid chromatography to mineral froth partitioning of hydrophobic and hydrophilic particles[107]. Amorphous silica-water interfaces have also attracted an increased recent attention by the scientific community since the possible employment of silica based materials as drug delivery systems in the body[108, 109, 110, 111, 110].

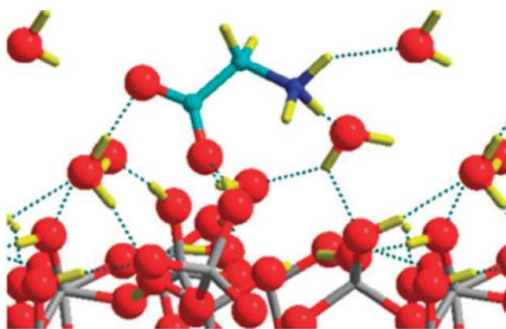


Figure 1.7: Snapshot of the most stable glycine adsorption configuration on a silica surface at the interface with liquid water from DFT-MD simulations. The oxygen atoms are coloured in red, the nitrogen atom in dark blue, the carbon atoms in cyan and the hydrogen atoms in yellow. Figure adapted with permission from ref.[112]

Costa *et al.*[112] for instance have studied the adsorption of glycine on a hydrophilic amorphous silica surface in presence of liquid water molecules by means of DFT-MD simulations. The competition between water and glycine for the adsorption on the exposed silanols induces the emergence of stable adsorption configurations where the amine group of the glycine does not interact directly with the silica surface (see Fig.1.7). In particular, the most stable configuration is characterized by the glycine oriented parallel to the silica surface with the carboxyl group H-Bonded to the silica surface, while the amine group interacts with water molecules that are then in turn H-Bonded to the silica surface (see Fig.1.7).

Similar results are obtained by Delle Piane *et al.*[109] who studied the adsorption of ibuprofen on a hydrophobic amorphous silica surface in a microsolvated environment by means of DFT-MD simulations. They found that the most stable adsorption configuration of ibuprofen on silica is through the ibuprofen's polar group which interacts with two water molecules (W1 and W3 in Fig. 1.8) that are then in turn H-Bonded to the silica surface (see Fig. 1.8). Such water mediation in the biomolecule interaction with the silica surface is found to strongly alter the thermodynamics of the adsorption with respect to the one observed in absence of water molecules.

Folliet *et al.*[113] investigated the adsorption of liposils (liposome) on silica in presence of water molecules by means of solid state NMR experiments combined with classical MD and quantum static calculations. Such synergistic approach revealed that the presence of interfacial H-Bonded water molecules located in between the head groups of the phospholipid and the silica surface play an essential role in the stabilization of the liposils at the silica surface.

All the above mentioned works highlight how the water, mediating the interactions between the adsorbate and the silica surface, strongly affects the nature of the adsorption processes and alters in turn the adsorbate reactivity at the interface.

However another fundamental aspect is how the specific water restricted environment offered by the silica-water interface could affect the structure

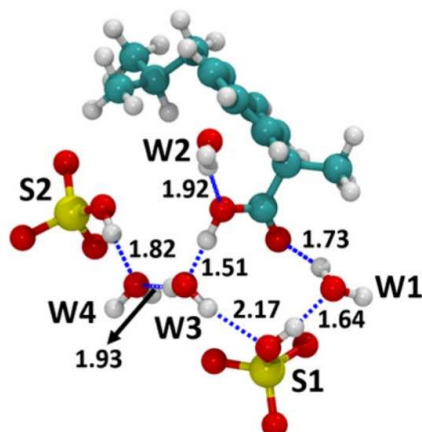


Figure 1.8: *Optimized local view for the most stable microsolvated ibuprofen–silica configuration. The water molecules located in between the ibuprofen polar groups and the silanol groups are labelled W1 and W3. The silicon atoms are coloured in yellow and labelled S1 and S2, the oxygen atoms of the ibuprofen polar group and of the water molecules are coloured in red, the carbon atoms are coloured in blue and the hydrogen atoms in white. Figure reproduced with permission from ref.[109]*

and ionization states of the reactive species. It is fair to think that also this effect will impact the thermodynamic and kinetic properties of chemical reactions. Such crucial aspect is highlighted in chapter 3 of this PhD thesis, where we show the specific interfacial water organization to strongly affect the compositions, structures and stabilities of the reaction complexes at the aqueous air-water interface with respect to bulk liquid water, thereby changing the energetics of the peptide bond formation reaction.

Since the proven sensibility of chemical reactions toward the water specific H-Bond network organization[16, 62, 43, 42], there is a need in the characterization of the water structure at aqueous interfaces.

Therefore following the global works done in the Gaigeot group for revealing solid-water and air-water interfacial structures, one objective in my PhD work has also been to characterize the silica-water interface as a prerequisite knowledge for chemistry occurring at this interface. We have thus studied the interfacial water organization as a function of the silica surface degree of hydroxylation, morphology and electrolytes concentration. This is presented in chapter 5.

In a second step we have moved our attention to the silica surface in itself. After characterizing the surface groups structure and organization in contact with liquid water as a function of the surface degree of hydroxylation we have considered the silica surface reconstruction and reorganization when exposed to increasing pH conditions, see chapter 6.

1.4 Outlines of this manuscript

Chapter 2 of this manuscript is dedicated to a general introduction on the principles of molecular dynamics simulations (MD), biased molecular dynamics and Sum Frequency Generation (SFG) spectroscopy (which will be an experimental probe used in this work). A more detailed discussion will be dedicated to Density Functional Theory (DFT) based MD simulations as they represent the principal theoretical method used to characterize reactivity, structural and spectroscopic properties of the interfaces in this work. Regarding SFG spectroscopy, a general introduction on the technique will be provided, with a brief description of the method developed and used in the Gageot Group to calculate theoretical SFG spectra from MD simulations.

In chapter 3, we present the full computational characterization of the formation of polypeptides at the air-water interface. The first section 3.1 introduces the reader into the chemistry at air-water interfaces by an overview on recent works. Special emphasis will be put on the interfacial factors, known up to now, to catalyse reactions at the air-water interface.

The second section 3.2 reports a detailed description of the *in situ* peptide bond formation reaction at the air-water interface performed experimentally by Vaida's group[15] in the USA. We will focus on the main pending questions regarding the catalytic roles of the interface in the peptide bond formation, to which we will provide answers by our computational approach in the next section 3.3.

Our theoretical work starts in section 3.3. After assessing the location, structure and composition of the reaction complexes formed at the air-water interface, we will simulate the peptide bond formation reaction at the air-water interface by various DFT-based biased molecular dynamics simulations. In each biased DFT-MD simulation we will take into account a different condition, in terms of structure composition and solvation state, to which is exposed the pre-reaction complex at the air-water interface in order to quantify one by one the effect of the interfacial factors on the chemical reaction.

The study of the prebiotic peptide bond condensation continues in chapter 4 where we envisage another chemical route for the synthesis of polypeptides: the peptide bond condensation reaction now starts at the air-water interface in absence of any inorganic catalyst. Our main interest is to evaluate the capability of the air-water interface in shifting the ionization state of the amino acids toward their neutral form, an effect that would strongly reduce the kinetic limit on the peptide bond formation at the interface. We will consider the stability and reactivity of two amino acids, i.e. the alanine and the leucine at the air-water interface. We will simulate the interconversion between the neutral and zwitterionic forms of these two amino acids at the air-water interface versus in bulk water, by biased DFT-MD. We will compare the results obtained by the metadynamics scheme in the light of a detailed analysis of the water environment of the amino acids in the two media.

In chapter 5 we move our attention to the structural characterization of the

amorphous silica-water interface. Section 5.1 is a state-of-the-art presentation of computational and experimental works on silica-water interfaces where the main controversies and results are reported. The recent improvements in the knowledge of the water organization at the boundary with silica as a function of the surface degree of hydroxylation and electrolytes concentration from experimental and computational works are described and commented.

We put the basis of our spectroscopic and structural investigations in section 5.5 by theoretically deconvolving the theoretical SFG spectrum of the most common amorphous silica surface, with a density of surface silanols of 4.5 OH/nm², in contact with liquid water, into solid-water and water-water SFG signatures. Such approach allows us to obtain useful SFG marker bands of the solid-water and water-water interactions that govern the organization of the amorphous silica-water interface.

In section 5.6 we identify the presence of two interface water populations for this amorphous aqueous silica interface, respectively located above the hydrophobic (silanols poor) and hydrophilic (silanols rich) microscopic patches of the amorphous silica surface. We find that the hydrophobic and hydrophilic patches template the water's organization in the BIL (Binding Interfacial Layer[114]). We have characterized the specific water organization above the hydrophilic and hydrophobic patches, and we have identified the SFG spectroscopic marker bands for the hydrophobicity of water by monitoring the evolution of the SFG water-solid marker bands as a function of the spatial extension of hydrophobic and hydrophilic patches over the silica surface.

In section 5.7 we characterize the structural organization of water at the interface with silica as a function of the silica surface degree of hydroxylation. By tuning the degree of hydroxylation of the amorphous model surface we play with the patches's size and we observe the outcome on the interfacial water organization, and provide explanations in terms of solid-water and water-water interactions.

After gaining the information on the local water organization above the amorphous surface, we analyse the chemical properties and reorganization of the surface silanols when exposed to water at different pH conditions in chapter 6. The combination between simulations and SFG experiments allows us to detect the microscopic reorganization and reconstruction processes at the silica-water interface as a function of pH conditions and to make the relationships with the spectroscopic marker bands.

The most relevant results from this PhD work are summarized in chapter 7 and put in perspective with possible future directions in the research field dedicated to the characterization of aqueous interfaces.

The list of publications related to this PhD work is provided in page 1 of this manuscript. These papers include published works as well as papers submitted or in preparation. They are also reported in the various chapters, at the exception of two papers. These latter publications are not described in the manuscript and are reported in the appendix, starting at page 311.

Chapter 2

Theoretical Methods

I have decided to write in this chapter only the basic elements of Density Functional Theory based Molecular Dynamics (DFT-MD) simulations and of the SFG (sum frequency generation) spectroscopy, employed in this thesis work. More detailed information are reported in other PhD manuscripts from the Gaigeot group (see for instance the thesis of Dr. Jerome Mahé, NNT: 2017SACLE043 and Dr. Simone Pezzotti NNT:2019SACLE008).

2.1 Molecular dynamics (MD)

Molecular Dynamics (MD) simulations are a powerful tool in order to provide microscopical insights into the organization of inhomogeneous and complex systems, like the ones investigated in this work.

MD simulations provide the theoretical prediction of the nuclei/atomic motions of a target molecular system over a given interval of time (from ps to ns and beyond depending on the level of representation of the forces). Most of the *ab initio* MD simulations are based on the Born-Oppenheimer approximation where the motion of the nuclei and electrons are treated separately. In the works presented here the motion of the nuclei will be described classically. The motions of the nuclei can then be predicted by solving the Newton's equations of motions, step-by-step at discrete intervals of time (time-step), for each nuclei i of the system:

$$m_i \frac{\partial^2 \vec{r}_i}{\partial t^2} = \vec{F}_i \quad \forall i \quad (2.1)$$

where \vec{r}_i is the position vector (in cartesian coordinates) of each nucleus i of the system and m_i is its mass. \vec{F}_i is the total force acting on nucleus i , calculated as the negative of the potential energy gradient:

$$\vec{F}_i = -\frac{\partial V}{\partial \vec{r}_i} \quad \forall i \quad (2.2)$$

where V is the potential energy of the system.

The way V is modelled is different between *ab initio* and classical MD simulations. In Born-Oppenheimer *ab initio* MD simulations the electrons are treated explicitly and V is obtained by solving the time-independent electronic Schrödinger equation (see eq. 2.10). This approach represents the most computationally costly but also the most accurate one. It follows that *ab initio* simulations are limited in time-scale and size, to usually systems containing hundreds, thousands of atoms for tens of picoseconds trajectories. When dealing with larger systems and/or longer time-scales *ab initio* simulations cannot be used anymore. Classical MD simulations using an approximate estimation of the potential V are then used. The electrons are not explicitly treated anymore and V is approximated via parametrized analytical functions called force fields. This allows reduce the computational cost and afford the sizes and time-scales needed.

2.1.1 Numerical integration of the Newton's equations of motion

The dynamical behaviour of the simulated system is obtained by integrating numerically the Newton's equations of motions. In order to propagate both the positions and velocities of the atoms of the system a discretization of the time in small time intervals is needed: this is the time-step δt in any MD simulation. Many propagation algorithms based on the Taylor expansion of the nuclei positions around the positions and velocities at a certain instant t (i.e. at each MD step) have been developed. The most commonly used propagation method derives from the seminal work of Verlet[115]: this is the Verlet algorithm based on two Taylor expansions one for positive and one for negative times respectively:

$$\vec{r}(t + \delta t) = \vec{r}(t) + \vec{v}(t)\delta t + \frac{\vec{F}(t)}{2m}\delta t^2 + O(\delta t^3) + \dots \quad (2.3)$$

$$\vec{r}(t - \delta t) = \vec{r}(t) - \vec{v}(t)\delta t + \frac{\vec{F}(t)}{2m}\delta t^2 - O(\delta t^3) + \dots \quad (2.4)$$

Summing these two equations, we obtain:

$$\vec{r}(t + \delta t) = 2\vec{r}(t) - \vec{r}(t - \delta t) + \frac{\vec{F}(t)}{m}\delta t^2 + O(\delta t^4) \quad (2.5)$$

which provides the estimate of the new position of any atom at time $t + \delta t$, based on positions and forces only. It contains an error of the order of δt^4 , where δt is the time step. Note that this algorithm does not use the velocity to compute the new position. However, one can derive the velocity at time t from the knowledge of the positions at times $t - \delta t$ and $t + \delta t$:

$$\vec{v}(t) = \frac{\vec{r}(t + \delta t) - \vec{r}(t - \delta t)}{2\delta t} \quad (2.6)$$

It is also possible to compute positions and velocities at the same time $t + \delta t$, by making use of the velocity Verlet algorithm:

$$\vec{r}(t + \delta t) = \vec{r}(t) + \vec{v}(t)\delta t + \frac{\vec{F}(t)}{2m}\delta t^2 \quad (2.7)$$

$$\vec{v}(t + \delta t) = \vec{v}(t) + \frac{\delta t}{2} \left(\frac{\vec{F}(t)}{2m}\delta t + \frac{\vec{F}(t + \delta t)}{2m}\delta t \right) \quad (2.8)$$

Note that all Verlet algorithms are symplectic, meaning that they are capable to conserve the total energy of the system. Therefore an MD simulation performed with symplectic algorithms will naturally provide the time evolution of the simulated system in the NVE (microcanonical) ensemble. However, other ensembles can be exploited (like the NVT, and NPT ensembles), by making use of specific algorithms accounting for a thermostat/barostat in order to fix temperature/pressure in the MD simulations. Such algorithms are briefly discussed in the following section.

2.1.2 Temperature control

In the NVT ensemble, the temperature is fixed while the total energy of the system is free to fluctuate. In the NPT ensemble the pressure is fixed while the volume V of the system is free to fluctuate. One intensive quantity (T or P) has thus to be kept constant along the simulation time when performing a MD simulation in another ensemble than the microcanonical one (NVE). The thermostat/barostat algorithms modify the Newtonian MD scheme in order to generate a thermodynamical ensemble at constant temperature/pressure. Several algorithms have been developed in the literature to that end.

Temperature can be controlled by the use of a thermostat. This implies the definition of an instantaneous temperature at each time-step of the MD, that will be systematically compared to the reference temperature T_0 of the heat bath coupled to the system. Following the equipartition theorem, the kinetic energy of a system at any time is related to its macroscopic temperature T through the following equation:

$$E_{kin}(t) = \sum_{i=1}^N \frac{1}{2} m_i \vec{v}_i^2(t) = \frac{1}{2} (3N - 6) k_B T(t) \quad (2.9)$$

where k_B is the Boltzmann's constant and $(3N - 6)$ is the number of internal degrees of freedom of the system with N the number of nuclei/atoms of the system. $T(t)$ is the instantaneous temperature, i.e. the temperature of the system at time t . Since the instantaneous temperature is related to the atomic velocities, a control on the rate of change of velocities is required in order to maintain the temperature constant in MD simulations. The thermostat keeps the average temperature of the system constant by typically rescaling the atomic velocities in a way that maintains the NVT ensemble defined. The same principle is true for a barostat.

It is important to mention here that if the average distribution of velocities obtained from NVT MD simulations is correct with respect to the target temperature, the time evolution of the atomic velocities is not, as it is affected by the coupling with the thermostat. Therefore, when MD simulations are employed to investigate properties that are dependent on the time evolution of velocities, as vibrational spectroscopic properties of interest to us in these works, the microcanonical NVE ensemble has to be chosen. For these reasons when calculating Sum Frequency Generation (SFG) spectra of silica-water interfaces in chapters 5 and 6 of this thesis, all simulations have been conducted in the NVE ensemble.

2.1.3 Initial conditions and time step

When starting an MD simulation, initial coordinates and velocities have to be assigned to each particle of the system. Even if a MD trajectory is independent on the initial configuration (after proper equilibration), the initial set of atomic positions and velocities is important, especially for DFT-MD, where the equilibration time-scale is limited. The initial velocities of the system are generated by a Maxwell-Boltzmann distribution of velocities at the targeted simulation average temperature. This distribution is generated from random numbers, according to the following equation:

$$p(\vec{v}_i) = \sqrt{\frac{m_i}{2\pi k_B T}} \exp\left(-\frac{m_i v_i^2}{2k_B T}\right)$$

where $p(\vec{v}_i)$ is the probability of the i particle to have the \vec{v}_i velocity, m_i is the mass of this particle, T is the temperature of the system.

Another important choice for a simulation is the time step δt that we saw in Verlet algorithms (eqs 2.5-2.8). The maximum value of the time step that can be chosen is dictated by the fastest process in the system, i.e. typically an order of magnitude smaller than the fastest process. Since the molecular rotations and vibrations occur with frequencies in the range 10^{11} - 10^{14} s⁻¹, the time step has to be chosen in the order of fs (10^{-15} s) or less in order to model such motions with sufficient accuracy. In our molecular systems, the fast vibrational motion is the OH-stretching vibration that requires a time step between 0.1-0.5 fs to be correctly modelled. Beyond that, *ab initio* MD requires δt of this order of magnitude in the NVE ensemble for a proper conservation of the total energy. As a correct description of the OH-stretching motion and vibration is mandatory in order to reproduce the properties investigated along this thesis, a time step of 0.4 fs is systematically chosen for all the MD simulations discussed in the manuscript.

2.1.4 Periodic boundary conditions

The modelling of continuous systems, like solids and liquids, requires the use of periodic boundary conditions (PBC). The atoms of the system are

placed in a box, generally cubic or parallelepipedic, that is replicated in the three directions of space. If an atom leaves the central box through the right wall for instance, its image will enter the box through the left wall from the neighbouring box. The result is a quasi-periodic model, with a periodicity equal to the box dimensions. It is important to keep in mind that the imposed artificial periodicity could cause errors for properties that are affected by long-range correlations, such as for charged and dipolar systems. Corrections for the finite size of MD simulations are also necessary when evaluating long-range collective properties.

2.2 Born-Oppenheimer BOMD in the DFT electronic framework (DFT-MD)

In Born-Oppenheimer BOMD simulations, the motions of the nuclei and electrons are treated separately and the time independent electronic Schrödinger equation is solved at each time step of the dynamics in order to obtain the electronic energy of the system E_e :

$$H_e \Psi_e(\{\vec{r}\}) = E_e \Psi_e(\{\vec{r}\}) \quad (2.10)$$

where $\Psi_e(\{\vec{r}\})$ is the electronic wavefunction of the system, a function of the $3N$ cartesian coordinates of the N electrons in the system (labelled here $\{\vec{r}\} = \{\vec{r}_i, \vec{r}_j, \dots, \vec{r}_N\}$), and H_e is the electronic Hamiltonian, which for a system composed of M nuclei and N electrons is defined as:

$$H_e(\{\vec{r}\}, \{\vec{R}\}) = T_e + V_{ee} + V_{Ne} \quad (2.11)$$

where T_e is the operator that describes the electronic kinetic energy of the system, V_{ee} and V_{Ne} are respectively the potential energies for the electron-electron and nuclei-electron interactions. In this equation $\{\vec{R}\} = \{\vec{R}_1, \dots, \vec{R}_M\}$ is the ensemble of positions of the nuclei. The H_e hamiltonian is thus indirectly dependent on these positions, and directly dependent on the positions of electrons.

Once solving the time independent electronic Schrödinger equation, the electronic energy of the system E_e is obtained and the total potential energy of the system E_{pot} can be calculated by adding the potential energy of the nuclei-nuclei interaction to E_e ($V_{NN} = \frac{1}{2} \sum_A^M \sum_{B \neq A}^M \frac{Z_A Z_B e^2}{|R_{AB}|}$, where R_{AB} is the distance between nuclei A and B and $Z_{A/B}$ their atomic number).

However, an analytic solution to eq. 2.10 is solely obtained for mono-electronic species, like the hydrogen atom and any hydrogenoid atom as well as for the H_2^+ molecule. The reason for that lies in the V_{ee} complex term, not present when dealing with only one electron, which is a N -body term, preventing an easy solution of eq. 2.10. Also, the kinetic energy of one given electron system depends on all other electrons, which increases the complexity in the

evaluation of the T_e term. In practice, the introduction of approximations is needed in order to estimate the electronic wavefunction and energy. Several approximations have been proposed, starting from the seminal Hartree and Hartree-Fock approaches. The methods differ in the level of accuracy in the estimation of E_e , which is inversely proportional to the computational cost. The challenge thus becomes to find the better compromise between accuracy and computer cost for a given system. Despite the differences between the various approaches, most of them are based on the writing of the electronic wavefunction of the system in terms of mono-electronic wavefunctions, via one Slater determinant (needed to antisymmetrize the electronic wavefunction, as invoked by the Pauli principle), so that:

$$\Psi(\{\vec{r}\}) = \frac{1}{\sqrt{N!}} \begin{bmatrix} \psi_1(\vec{r}_1) & \psi_2(\vec{r}_1) & \dots & \psi_j(\vec{r}_1) & \dots & \psi_N(\vec{r}_1) \\ \psi_1(\vec{r}_2) & \psi_2(\vec{r}_2) & \dots & \psi_j(\vec{r}_2) & \dots & \psi_N(\vec{r}_2) \\ \dots & \dots & \dots & \dots & \dots & \dots \\ \psi_1(\vec{r}_i) & \psi_2(\vec{r}_i) & \dots & \psi_j(\vec{r}_i) & \dots & \psi_N(\vec{r}_i) \\ \dots & \dots & \dots & \dots & \dots & \dots \\ \psi_1(\vec{r}_N) & \psi_2(\vec{r}_N) & \dots & \psi_j(\vec{r}_N) & \dots & \psi_N(\vec{r}_N) \end{bmatrix} \quad (2.12)$$

where $\psi_i(\vec{r}_j)$ is the i -th spinorbital (mono-electronic wavefunction) populated by the j -th electron. We do not report the notations related to spins for simplicity of writing. The spinorbitals are then expressed on a basis set, which can be either based on plane-waves or gaussian functions.

Among the different approximated solutions existing for the time-independent Schrödinger equation, the Density Functional Theory (DFT) approach is certainly the most used methodology adopted in the literature especially for *ab initio* MD simulations. It usually represents the best level of accuracy affordable at a reasonable computational cost for complex molecular systems. The computational cost is "low enough" to perform MD simulations typically for 100-1000 atoms over 10-100 ps. These are the typical size- and time-scales of DFT-MD simulations. Note here that multi-determinant methods exist, but they are still not affordable for MD simulations.

2.2.1 Density Functional Theory

Let us now describe the DFT method. The Density Functional Theory (DFT) was introduced in Hohenberg and Kohn's work published in 1964, with the original objective to remove the N-body electronic wave function that depends on 3N spatial coordinates and replace it by a density function that depends only on three spatial coordinates \vec{r} :

$$\rho(\vec{r}) = N \int \dots \int |\psi(\vec{r}_1, \dots, \vec{r}_N)|^2 d\vec{r}_2 \dots d\vec{r}_N \quad (2.13)$$

Such approach reduces the dimensionality of the problem (i.e. eq. 2.10) from the 3N electronic degrees of freedom to 3 degrees of freedom (x,y,z) of

the electronic density $\rho(\vec{r})$.

Two Hohenberg and Kohn theorems[116] are at the basis of the Density Functional Theory.

1st. For any interacting many-body electronic system immersed in an external potential $V_{ext}(\mathbf{r})$ (which is the potential arising from the nuclei and from any other force applied on the system), $V_{ext}(\mathbf{r})$ is uniquely determined, upon the addition of a constant, by the electronic density $\rho(\vec{r})$ of the system in its ground state.

The most important consequence of the 1st HK theorem is that all the properties of the system can be calculated as soon as the electronic density $\rho(\vec{r})$ is known.

2nd. There is a universal energy called $E^{HK}[\rho]$, functional of the density (thus the $[\rho]$ notation), whatever the external potential $V_{ext}(\mathbf{r})$. For each $V_{ext}(\mathbf{r})$, the ground-state energy of the electronic system is obtained via the variational principle applied to the energy functional: the obtained density corresponds to the exact ground-state density.

The 2nd HK theorem introduces the notion of energy functional and establishes the validity of the variational principle applied to the energy functional in order to obtain the ground state density $\rho_0(\vec{r})$.

The total electronic energy is thus a functional of the density, written as:

$$\begin{aligned} E[\rho] &= E^{HK}[\rho] + E_{ext}[\rho] \\ E[\rho] &= T[\rho] + V_{ee}[\rho] + E_{ext}[\rho] \end{aligned} \tag{2.14}$$

with $E^{HK}[\rho] = T[\rho] + V_{ee}[\rho]$, where $T[\rho]$ is the kinetic energy functional and $V_{ee}[\rho]$ is the electron-electron interaction energy functional. $E_{ext}[\rho]$ is the energy functional related to the external potential, i.e. arising from the nuclei, so that $E_{ext}[\rho] = \int \rho(\vec{r})V_{ext}(\vec{r})d\vec{r}$.

Following the 2nd HK theorem, the ground-state density $\rho_0(\vec{r})$ could be in principle obtained with a variational approach as the density that minimizes $E^{HK}[\rho]$.

However, the exact analytical expression of the kinetic energy $T[\rho]$ and electron-electron energy $V_{ee}[\rho]$ functional is not known for interacting electronic systems. However, it is exactly known for non-interacting electronic systems. The modern theory of Kohn-Sham thus makes use of such knowledge by associating to the real system (i.e. with interacting electrons) a model system made of free non-interacting electrons, stating that there is always a non interacting system that has the exact same density as the one of the interacting system.

The fictitious non-interacting system has an electronic density equal to the one generated by the real interacting system.

By reintroducing the mono-electronic wave-functions $\psi_i(\vec{r}_i)$ we can now calculate the kinetic energy term $T[\rho]$ for the system. The density of the non-interacting system is simply expressed as $\rho(\vec{r}) = \sum_i^N |\psi_i(\vec{r})|^2$, and the total kinetic energy of the non interacting system $T_s[\rho]$ can thus be written as:

$$T_s[\rho] = -\frac{1}{2} \sum_i^N \langle \psi_i(\vec{r}) | \nabla^2 | \psi_i(\vec{r}) \rangle \quad (2.15)$$

However, the correlation between the electrons (i.e. the fact that they in reality are not independent) will have to be reintroduced at some point in eq. 2.15. If the electrons were classical particles instead of quantum particles, then the coulomb electron-electron interaction energy functional is known simply as the Hartree energy $E_H[\rho]$:

$$E_H[\rho] = \frac{1}{2} \int \int \frac{\rho(\vec{r})\rho(\vec{r}')}{|\vec{r} - \vec{r}'|} d\vec{r}d\vec{r}' \quad (2.16)$$

However, $E_H[\rho]$ represents only a part of the total electron-electron interaction energy ($V_{ee}[\rho]$) of the real system, as this latter also includes the contribution from electronic correlations (i.e. interactions) and quantum effects known as exchange interactions between electrons.

The total electronic energy of the real interacting system (eq. 2.14) can be written in terms of the known energy terms for the non-interacting electronic system and of unknown terms that take into account the fact that electrons do interact:

$$\begin{aligned} E[\rho] &= T[\rho] + V_{ee}[\rho] + E_{ext}[\rho] \\ E[\rho] &= T[\rho] - T_s[\rho] + T_s[\rho] + V_{ee}[\rho] - E_H[\rho] + E_H[\rho] + E_{ext}[\rho] \\ E[\rho] &= T_s[\rho] + E_{ext}[\rho] + E_H[\rho] + (T[\rho] - T_s[\rho]) + (V_{ee}[\rho] - E_H[\rho]) \end{aligned} \quad (2.17)$$

$$E[\rho] = T_s[\rho] + E_{ext}[\rho] + E_H[\rho] + E_{XC}^{HK}[\rho]$$

where $T_s[\rho]$, $E_{ext}[\rho]$ and $E_H[\rho]$ are the known terms for the non interacting electrons and the unknown terms for the correlation interaction between electrons is put in a term $E_{XC}^{HK}[\rho]$ for the exchange (quantum nature of electrons) and correlation (interactions) between electrons. All is now in $E_{XC}^{HK}[\rho]$, which is called the DFT functional.

The $E_{XC}^{HK}[\rho]$ term can be generally expressed as:

$$E_{XC}^{HK}[\rho] = \int d\vec{r} F(\rho(\vec{r}), \nabla\rho(\vec{r}), \nabla^2\rho(\vec{r}), \dots) \quad (2.18)$$

where F is a functional written as a Taylor expansion of the electronic density $\rho(\vec{r})$, its first gradient $\nabla\rho(\vec{r})$, its second gradient $\nabla^2\rho(\vec{r})$ and etc.

Many DFT functionals have been proposed by the scientific community in order to describe the $E_{XC}^{HK}[\rho]$ term. Four main families of DFT-functionals have been developed up-to-now: the Local Density Approximation (LDA), the Generalized Gradient Approximation (GGA), the Hybrids and the meta-GGA. They differ by the order term of the Taylor expansion (see eq. 2.18) in which the electron density $\rho(\vec{r})$ is expanded: LDA ($\rho(\vec{r})$), GGA ($\rho(\vec{r})$ and $\nabla\rho(\vec{r})$), meta-GGA ($\rho(\vec{r})$, $\nabla\rho(\vec{r})$ and $\nabla^2\rho(\vec{r})$), and by the inclusion of a part of the Hartree exchange in the case of Hybrid functionals.

Local Density Approximation (LDA)

The Local Density Approximation (LDA) is the first and simplest class of approximations of the exchange and correlation functionals. This class of functionals is generally based on the homogeneous electron gas (HEG) model where the electron density is uniformly distributed over the space. $E_{XC}^{HK}[\rho]$ is thus a simple functional of the density that depends solely upon the value of the electronic density at each point in space (i.e. independent on the density gradient). Since the HEG approximation is appropriate for metals but not for molecules, where the electron density has maxima between covalently bonded atoms and the density gradient is non negligible, LDA functionals generally provide good energy estimations for metals but not for molecular systems. They are thus non appropriate in order to describe the aqueous interfaces investigated in this thesis work.

Generalized Gradient Approximation (GGA)

Generalized Gradient Approximation (GGA) functionals were developed from LDA functionals in order to provide a less local approximation of the exchange-correlation energy $E_{XC}^{HK}[\rho]$. For instance GGA functionals take into account the dependence of $E_{XC}^{HK}[\rho]$ not only on the density but also on its gradient. Generally GGA functionals provide a good balance between computational cost and accuracy of covalent bonds description. It makes this second generation of functionals a more suitable choice for the modelling of molecular systems with respect to LDA functionals. Therefore, we have chosen GGA functionals to perform the DFT-MD simulations reported in this PhD manuscript.

A weak point of GGA functionals, and of other DFT approaches based on a local description of the exchange-correlation energy, is the poor description of van der Waals (vdW) interactions. For instance, DFT neglects long-range dispersion because the exchange-correlation term is a functional of the local electron density (LDA), or of the electron density gradient (GGA). This means that only local contributions to the electron correlation are included. Therefore LDA and GGA functionals neglect the long-range dispersion. Many

corrections have been thus developed to overcome such issue, as for example the Grimme D2 correction[117] employed in our simulations, which is a semi-empirical vdW correction to DFT functionals where the dispersion energy is included as an additive term to the Kohn-Sham energy. The van der Waals interactions are described via a simple pair-wise force field, that does not depend on the electron density but only on the atomic coordinates.

Hybrid Functionals

Hybrid functionals have been developed because of the failure of GGA functionals in correctly describing the exchange interaction term. In the Hybrid functional scheme, elements of the exchange-correlation from LDA or GGA functionals are combined with a fraction of exact exchange from the Hartree-Fock theory. Despite the improved accuracy reached on average with this third generation of functionals, the higher computational cost of such hybrid functionals makes them often too computationally expensive for DFT-MD simulations. Using hybrid functionals, roughly costs 40 times more computational time than GGA functionals.

2.3 The CP2K software and the computational set-up chosen for the DFT-MD simulations in this thesis

All the DFT-MD simulations in this thesis have been carried out using the CP2K package[118, 119] where the system wave-function is described as a combination of dual Plane Wave and Gaussian basis sets. In particular, the DVZP-MOLOPT-SR basis set, augmented with a 400 Ry plane wave basis set has been used (possible different choices for the plane-wave cut-off are indicated in the manuscript). The nuclei displacements have been predicted using the classical Newton's equations of motion integrated through the velocity verlet algorithm (see eq. 2.5). The BLYP[120][121] functional augmented with the Grimme D2[122] correction for van der Waals interactions have been adopted for the electronic representation. GTH pseudo-potentials[123] have been adopted for all atoms.

Box-sizes, ranging from $13 \times 13 \times 35 \text{ \AA}^3$ for the smallest simulated systems to $24.2 \times 24.2 \times 45 \text{ \AA}^3$ for the biggest ones, have been chosen in our DFT-MD simulations in order to reproduce the density of bulk water (liquid water composed by 120 to 512 water molecules) and periodic boundary conditions have been applied in all three directions of space.

2.4 Metadynamics

As already reported in the introduction of the manuscript one objective of this PhD thesis is to understand the reactivity of/at aqueous interfaces. The characterization of reactions by MD requires an efficient sampling of the phase space of the molecular system over the simulation time. The fluctuations in the system during the MD simulations can in principle lead the system to escape from one local minimum on the free energy surface (FES) to another, allowing for instance the sampling of chemical events. In practice, the rather too small time scale accessible in DFT-MD simulations (of the order of tens of ps) prevents rare events such as chemical reactions to occur, which time scale can actually range from few fs to hours and days. The free energy surface (FES) is characterized by minima often separated by high energy barriers that are rarely crossed at room temperature over the affordable time of the dynamics, especially in DFT-MD dynamics.

DFT-MD enhanced sampling techniques, that can promote the exit of the system from one minimum of the FES to another minimum, are thus mandatory to apply in order to model chemical reactions. In these techniques, an "a priori" choice of the coordinates over which the FES exploration is done, is needed, *i.e* variables whose fluctuations are critical in order to cross the free-energy barriers underlying the chemical reaction of interest. These critical coordinates are called "reaction coordinates". The reaction coordinates S_i are usually functions of the atomic coordinates of the system \mathbf{R} :

$$\{S_1(\mathbf{R}), S_2(\mathbf{R}) \dots S_N(\mathbf{R})\} \quad (2.19)$$

where N is the number of reaction coordinates adopted to describe the reaction event. Examples of reaction coordinates are inter-atomic distances, angles, coordination numbers and combinations of these variables.

The metadynamics is an enhanced sampling technique introduced for the first time by Alessandro Laio and Michele Parrinello 20 years ago[46]. In metadynamics the sampling is accelerated by introducing in the hamiltonian of the system a history-dependent bias potential $V_G(\mathbf{S}, t)$ constructed in the space of the reaction coordinates $\{S_1(\mathbf{R}), S_2(\mathbf{R}) \dots S_N(\mathbf{R})\}$. The history dependent potential $V_G(\mathbf{S}, t)$ can be expressed as the sum of Gaussian hills deposited along the time of the simulation on the space of the reaction coordinates. In particular, at time t for a certain disposition in space of the nuclei \mathbf{R} the history dependent potential $V_G(\mathbf{S}, t)$ acting on the system is written:

$$V_G(\mathbf{S}, t) = \int_0^t dt' \frac{W}{\tau_g} \exp \left(- \sum_{i=1}^N \frac{(S_i(\mathbf{R}) - S_i(\mathbf{R}(t')))^2}{2\sigma_i^2} \right) \quad (2.20)$$

where W is the height of the Gaussian hills (kJ/mol), τ_g the Gaussian deposition stride (fs), S_i is the i_{th} reaction coordinate and σ_i is the half width of the deposited Gaussian hill along the i_{th} reaction coordinate.

At the top of Fig. 2.1 is reported the evolution with time of the history dependent bias potential $V(\mathbf{x})$ as a function of the reaction coordinate x ,

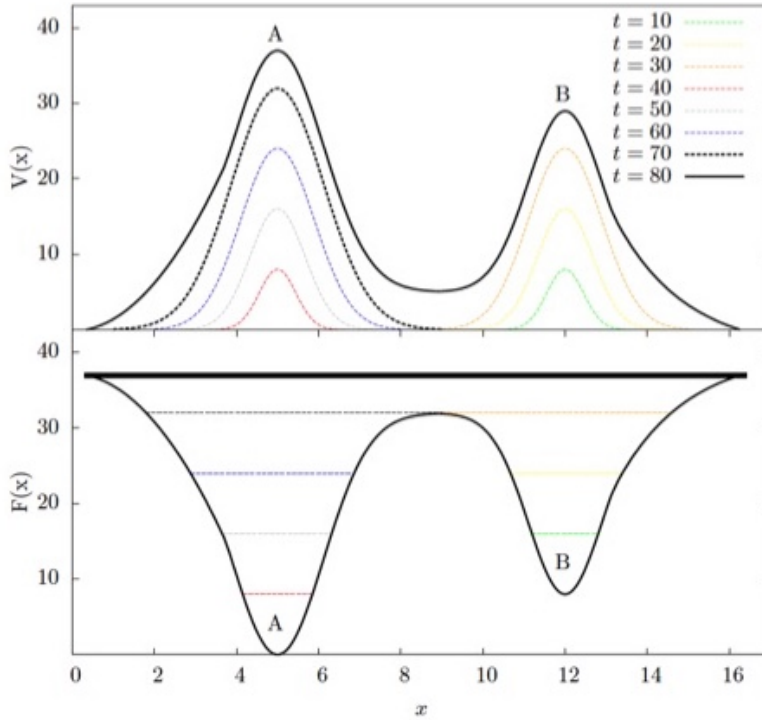


Figure 2.1: *On the top: Bias potential accumulated along a metadynamics simulation. At the bottom: Free energy profile filled by the bias potential. Figure reproduced with permission from ref.[124]*

while at the bottom we show the corresponding free energy profile $F(x)$, for a model made of one dimensional free energy profile characterized by two wells. The simulation starts with the system trapped in the local minimum B and intermittently along the dynamics a Gaussian hill is added at the instantaneous position x . As the bias potential increases, the probability of visiting configurations already explored (history dependent potential) decreases and the system is ultimately promoted to explore another local minimum. When $t = 30$ the bias potential completely fills the well B (Panel at the bottom of Fig. 2.1) inducing the system to explore the new accessible well A. The Gaussian hills deposition continues until the local minimum A is completely filled at $t=70$. After that, the metadynamics is at convergence, the free energy surface is flattened and the system will walk randomly between the two minima A and B, without exploring any other potentials.

To summarize, in metadynamics the exploration of the FES is reached by discouraging the system to visit the configurations already sampled along the dynamics. This is achieved by the introduction of a history dependent bias potential expressed as a sum of cumulative Gaussian hills that are deposited along the reaction coordinates. When the metadynamics reaches convergence, the free energy surface is fully filled by the bias potential. It follows that at convergence the free energy $F(\mathbf{S})$ is equal to $-V_G(\mathbf{S})$. Indeed, a central as-

sumption of metadynamics is:

$$\lim_{t \rightarrow \infty} V_g(\mathbf{S}, t) \simeq -F(\mathbf{S}) + \text{const.} \quad (2.21)$$

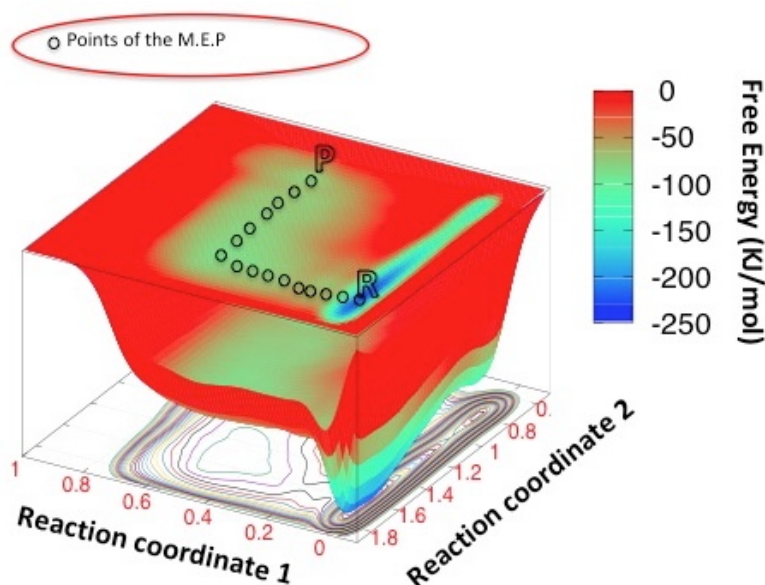


Figure 2.2: Free energy landscape with the minimum energy path (MEP in black circles) obtained for a reaction described by two coordinates of reaction.

Another advantage of metadynamics is that in the case of multidimensional reactions it does not require an "a priori" knowledge of the free energy surface with respect to other enhanced sampling techniques such as Umbrella Sampling and thermodynamic integration. See for example in Fig. 2.2 the free energy landscape associated to a chemical reaction described by two reaction coordinates. As one can see, different reaction pathways can be thought in order to convert the reactants (R) into the products (P). Given a meaningful choice of the coordinates of reaction and a slow addition of energy to the system (in terms of Gaussian hills), metadynamics explores first the low free energy zones and then explores the interconversion/transition state zones. The use of algorithms known as chain of states methods (e.g. nudged elastic band [125]) allows to identify the minimum energy path (MEP) connecting the two wells (R and P) on this free energy landscape and to obtain the energetics of reaction. That is what we have done in this work.

2.4.1 Set up for metadynamics

In order to obtain the free energy curves underlying the reactions of interest in my work (see chapters 3, 4 and 6) the metadynamics technique has been used. We use the CP2K software package[118] to that end.

Our computational approach for the metadynamics is similar to the one successfully adopted in previous works[62, 20, 126]. The adopted reaction coordinate $c(A-B)$ is the coordination number[127] between an atom A with respect to a set of atoms B, defined as:

$$c(A - B) = \sum_{I \in B} \frac{1 - (R_{AI}/R_{AB}^0)^6}{1 - (R_{AI}/R_{AB}^0)^{12}} \quad (2.22)$$

where R_{AI} is the distance between the atom A and atom I belonging to the set of B atoms and R_{AB}^0 is a fixed cutoff parameter based on the bond distance between A and B.

The height of the Gaussian hills added along the biased dynamics has been chosen to be systematically 0.8 kJ/mol. The width of the Gaussian hills (δ_s) is chosen to be 0.05.

In order to avoid the "hill-surfing", as discussed in ref.[43, 62, 20, 126], a Gaussian hill is added every time the dynamics explores a spot on the reaction coordinate at a distance $3/2\delta_s$ from the spot where the previous Gaussian Hill was deposited, which means:

$$|s(t) - s(ti)| = \frac{3}{2}\delta_s \quad (2.23)$$

where $s(t)$ is the position along the reaction coordinate considered and $s(ti)$ is the position on the reaction coordinate where the previous Gaussian Hill was deposited.

In chapter 3 we have used multiple interacting metadynamics simulations, called walkers, for exploring and reconstructing the free energy surface for the peptide bond condensation reaction. This is the multiple walker scheme[128]. We have systematically located the walkers in different minima of the free energy surface, e.g. the reactant and intermediate/product minima, in order to speed up the free energy sampling. For the peptide bond condensation reaction, the structures of the reactant/intermediate/product are known from the literature [129, 15], which allows us to easily apply the multiple walker scheme.

In order to show the free-energy convergence criterion used in this work we report in Fig. 2.3 the time evolution of the free energy profile for the chemical reaction of interest. Once the two energy basins along the reaction coordinate have been explored, the free energy surface is flattened and we reach convergence (purple curve in Fig. 2.3).

In order to further assess the convergence of our metadynamics we continue sampling the flat free energy surface till we recover the converged free energy surface (after 7 ps).

The same principle is applied to the 2D FES with the exception that once observing the double crossing of the energetic barrier backward and forward along the same reaction coordinate we report directly the free energy associated to the barrier.

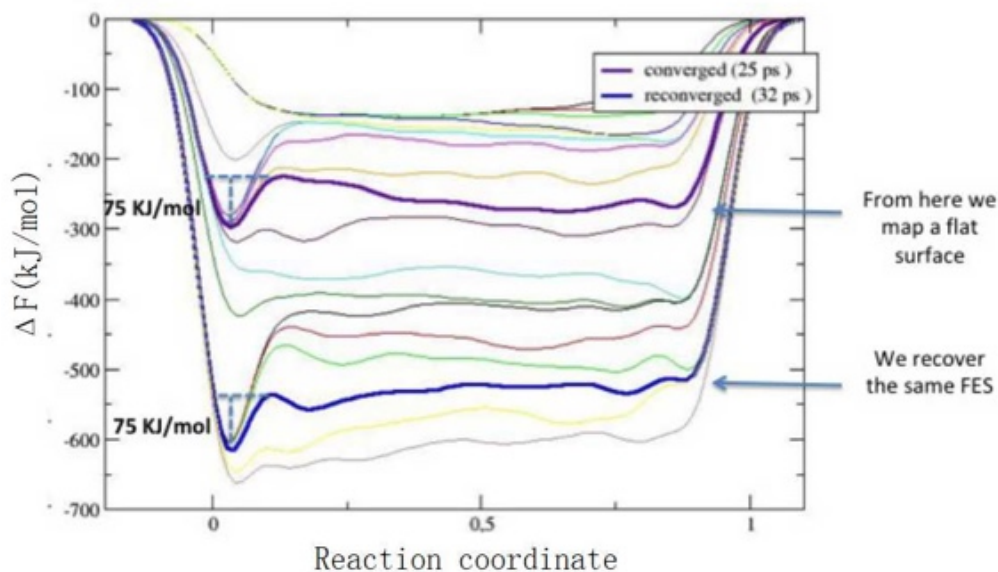


Figure 2.3: *Time evolution of the free energy profile during a metadynamics simulation. Once the two basins have been mapped, we continue sampling the flat free energy surface till we recover the converged free energy surface.*

2.5 Thermodynamic integration

A fast sampling of the reaction space during the metadynamics can possibly lead to inaccurate estimations of the energetics of reaction. For this reason in chapter 3 we make use of thermodynamic integration in order to refine the energetics along the MEP (minimum energy path) of the reactions revealed by the metadynamics.

The thermodynamic integration is a method that allows evaluate the free energy differences between two states with different spatial coordinates and potential energies (U_A and U_B). The free energy difference is calculated by integrating the derivative of the potential energy along a thermodynamic path linking the two states. The thermodynamic path can be either a chemical process or an alchemical one (as in the case of the "reversible proton-insertion" method[130]).

The free energy F depends on the partition function Q of the system and the free energy difference between two states ΔF cannot be calculated directly from the system potential energy U . The following formulations show how differences in the free energy ΔF can be calculated by integrating the average derivative of the potential energy $U \langle \frac{dU_x}{dx} \rangle$ along a chosen reaction coordinate.

We consider two systems with potential energy U_A and U_B connected by a reaction coordinate x varying from 0 to 1 (it takes the value of zero for $U=U_A$ and 1 for $U=U_B$). We can express the potential energy U of the system as a

function of x .

$$U(x) = (1 - x)U_A - xU_B \quad (2.24)$$

The partition function of the system Q in the canonical ensemble can be expressed as:

$$Q(N, V, T, x) = \sum_s \exp -\frac{U_s(x)}{k_B T} \quad (2.25)$$

where s are the states of the thermodynamic ensemble with a specific value of the reaction coordinate x , k_B is the Boltzmann constant and T the temperature of the system.

The free energy depends on the partition function as follows:

$$F = -k_B T \ln Q(N, V, T, x) \quad (2.26)$$

We now consider the difference in free energy between states A and B:

$$\begin{aligned} \Delta F &= \int_0^1 \frac{dF(x)}{dx} dx = - \int_0^1 \frac{k_B T}{Q} \frac{dQ(x)}{dx} dx \\ &= \int_0^1 \frac{k_B T}{Q} \sum_s \frac{\exp\langle -\frac{U_s(x)}{k_B T} \rangle}{k_B T} \frac{dU_s(x)}{dx} dx = \int_0^1 \langle \frac{dU(x)}{dx} \rangle dx \end{aligned} \quad (2.27)$$

One can thus compute the free energy difference between states A and B from the integral of the ensemble averaged derivative of the potential energy over the reaction coordinate x .

In practice, a constrained MD simulation for each point along the thermodynamic path connecting A and B is performed, with the reaction coordinate x kept constant along the simulation time. Such approach allows evaluate the ensemble averaged derivative of the potential energy $\frac{dU(x)}{dx}$ with respect to the reaction coordinate x at each point of the thermodynamic pathway. This is done by the Lagrangian multiplier method.

Finally, computing the integral over the potential energy ensemble averaged derivatives (either by trapezoidal or Simpson's Rule integration) one obtains the free energy difference ΔF between states A and B.

2.6 SFG spectra calculations in DFT-MD

Sum Frequency Generation (SFG) spectroscopy is of great interest for our work because of its capability to probe non centro-symmetric media such as aqueous interfaces, which properties are investigated along this PhD manuscript (see chapters 5 and 6). SFG is a second-order nonlinear optical process, where two incident beams of frequencies ω_1 and ω_2 generate an emit-

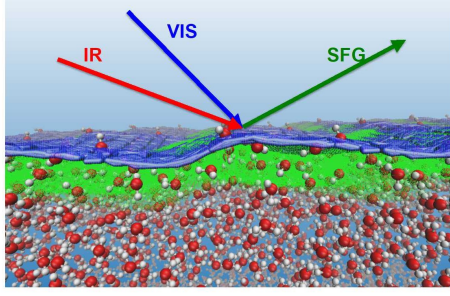


Figure 2.4: Schematic illustration of a standard SFG experimental geometry, where the two incoming IR (red) and visible (blue) beams, as well as the outgoing SFG beam (green) are shown at the air-water interface. The interfacial water layer probed in SFG experiments is also highlighted in green and the instantaneous water surface is marked in blue. Figure reproduced with permission from ref.[131]

ted field at the sum of the two input frequencies $\omega_{SFG} = \omega_1 + \omega_2$ (see Fig. 2.4). The SFG beam is recorded and reveals the vibrational response of the interfacial molecules. We will focus in the frequency range of resonance of the O-H stretching motions between 2800-4000 cm^{-1} (see chapter 5), where the vibrational response of the H-Bond network can be probed at non centrosymmetric solid/liquid interfaces. The recorded SFG intensity (I_{SFG}) is proportional to the square of the second order dipole susceptibility $|\chi^{(2),res}(\omega)|^2$ that can be theoretically calculated from MD simulations by the Fourier transform of the correlation function of the total dipole moment (\overline{M}) and polarizability tensor (\overline{A}) of the system, following the time-dependent method introduced by Morita *et al.*[132, 133]:

$$\chi_{PQR}^{(2)}(\omega) = \frac{i\omega}{k_B T} \int_0^\infty dt \exp(i\omega t) \langle A_{PQ}(t) M_R(0) \rangle \quad (2.28)$$

where (P,Q,R) are any x, y, z direction in the laboratory frame, and k_B and T are the Boltzmann constant and temperature of the system. $\langle \dots \rangle$ is a time-correlation function, ω is the frequency, $A_{PQ}(t)$ and $M_R(0)$ are respectively the PQ component of the total polarizability tensor \overline{A} and the R component of the total dipole moment \overline{M} of the system. However, to unveil the molecular contribution to the SFG spectra eq. 2.28 is rewritten as the sum of the contributions from each molecular species:

$$\chi_{PQR}^{(2)}(\omega) = \frac{i\omega}{k_B T} \sum_{i=1}^N \int_0^\infty dt \exp(i\omega t) \langle \alpha_{PQ}^i(t) \mu_z^i(0) \rangle \quad (2.29)$$

where N is the number of molecules that belongs to the interfacial layer, $\alpha_{PQ}^i(t)$ and $\mu_z^i(0)$ now refer to the PQ and R components of the individual polarizability and dipole of the i -th molecule. We do not consider in this equation the cross correlation terms $\langle \alpha_{PQ}^j(t) \mu_z^i(0) \rangle$ arising from the vibra-

tional intermolecular couplings.

The high computational cost of extracting *ab initio* dipole moments and polarizability tensors for each atom/molecule of the system at each time-step and the slow convergence of the dipole-polarizability correlation function makes the use of equation 2.29 for the calculation of theoretical SFG spectra from DFT-MD unsuccessful. In order to overcome such limitations we rewrite eq. 2.29 in terms of the velocity-velocity correlation function, which is trivial to calculate and fast to converge (few ps typically). As presented in refs.[114, 48], $\chi_{PQR}^{(2)}(\omega)$ arising from the water is thus calculated by the following equation:

$$\chi_{PQR}^{(2)}(\omega) = \sum_{mol=l}^M \sum_{OH1=1}^2 \sum_{OH2=1}^2 \frac{i}{k_b T \omega} \int dt \exp^{-i\omega t} \left\langle \left(\sum_i^3 \sum_j^3 D_{Pl}^{mol}(t) D_{Qm}^{mol}(t) \frac{d\alpha_{ij}^{mol}}{dr_{OH1}} \right) v_{OH1}^{mol}(t) v_{OH2}^{mol}(0) \left(\sum_k^3 D_{Rn}^{mol}(0) \frac{d\mu_k}{dr_{OH2}} \right) \right\rangle \quad (2.30)$$

where (P,Q,R) are any x, y, z direction in the laboratory frame, and k_B and T are respectively the Boltzmann constant and temperature of the simulated system. $\langle \dots \rangle$ is a time-correlation function, $\frac{d\alpha_{ij}}{dr_{OH}}$ and $\frac{d\mu_k}{dr_{OH}}$ are respectively the individual O-H bond contributions to the Raman tensor and Atomic Polar Tensor of the water molecules or (silanol groups if surface silanols are included in the calculation). M is the number of water molecules and OH1,2 are the two O-H oscillators/water. D is the matrix that projects the molecular frame onto the laboratory frame. The D matrix and the projection of the velocities on the O-H bond axis are obtained from DFT-MD trajectories while $\frac{d\alpha_{ij}}{dr_{OH}}$ and $\frac{d\mu_k}{dr_{OH}}$ terms have been parameterized. Parameterization for water is taken from ref.[134]. A similar equation can be obtained for hydroxyl (O-H) surface groups (see S.I. of ref.[135]).

A more detailed description of the mathematical procedures to go from equation 2.29 to equation 2.30 can be found in the PhD manuscript of Dr. Simone Pezzotti[131].

The $|\chi^{(2)}(\omega)|^2$ spectra measured by the SFG experimental set-up as well as calculated via theoretical SFG spectroscopy through eqs. 2.30 and 2.29, provide direct information on the vibrational motions of interfacial water.

The first $|\chi^{(2)}(\omega)|^2$ experimental spectrum was recorded by Shen and coworkers more than 20 years ago[136], while the first heterodyne detected HD-SFG spectrum, i.e. that allows a separation of the real and imaginary components of $\chi^{(2)}(\omega)$, was published by the same group 12 years ago[137], leading to the direct knowledge of the average orientation of the water molecules and surface groups at the interface [138, 139].

The Imaginary $\Im(\chi^{(2)}(\omega))$ component is the relevant one for the interpretation of HD-SFG spectra.

Theoretically, $\Im(\chi^{(2)}(\omega))$ and $\Re(\chi^{(2)}(\omega))$ are readily calculated considering the cosine and sine parts in eqs. 2.28 and 2.30. The M_z component of the dipole moment determines the sign of the $\Im(\chi^{(2)}(\omega))$ spectra. The $\Im(\chi^{(2)}(\omega))$ signal can thus be either positive or negative depending on the orientation of the interfacial species. By convention in the SFG community, if the interface molecular species has a net "up" orientation (i.e. dipole pointing along the normal to the surface which is directed from the aqueous phase to the other phase), then M_z is positive and $\Im(\chi^{(2)}(\omega))$ is also positive, while if the molecular species has the opposite "down" orientation, M_z and hence $\Im(\chi^{(2)}(\omega))$ have negative sign.

Chapter 3

Peptide bond formation at the air-water interface

In this chapter are presented the results for the peptide bond formation at the air-water interface. As already discussed, one of the main objective of this PhD thesis is to provide a microscopical insight into the interfacial factors governing the polypeptides formation at the air-water interface.

In the first section of this chapter we propose a general introduction on the reactions at the air-water interface, focusing in particular on the interfacial factors shown in the literature to affect the mechanisms and the energetics of reaction processes.

We then move the attention in section 3.2 to the targeted reaction of our computational study: the peptide bond condensation at the air-water interface. At this stage our objectives are to provide to the reader the knowledge on the peptide bond condensation reaction at the air-water interface gained in Prof. Vaida's experiments[15] and to present the main pending questions arising from such pioneering work.

We then proceed to a general presentation of our computational results on the peptide bond formation reaction at the air/interface by a top-down approach in section 3.3. We first characterize the mechanisms and energetics of the peptide bond formation at the air-water interface by DFT-MD metadynamics and thermodynamic integration DFT-MD techniques. In a second step we focus on the interfacial factors that govern the reaction at the air-water interface, which are absent in bulk water.

Our results point to two specific catalytic roles of the air-water interface, that are able to affect the structure and the composition of the reaction complexes thereby decreasing the reaction barriers with respect to bulk water conditions.

3.1 Factors governing reactions at the air-water interface

Many works in the literature have shown how the air-water interface provides a unique chemical environment to organic and inorganic reactions, inducing changes in the mechanisms and energetics observed in bulk water and in the gas phase[7, 9, 8, 10, 12, 140, 141, 142, 143, 144, 145, 100, 146, 147]. In this respect many efforts have been spent in studying relevant atmospheric reactions at the surface of aerosols in order to understand how air-water interfaces can modify the chemical composition of the atmosphere.

In particular, computational studies have focused on the reactivity of the Criegee intermediates at the air-water interface, a class of oxidizing agents (e.g. CH_2OO , syn- and anti- CH_3CHOO in Fig. 3.1) recently proposed to play a relevant role in atmospheric chemistry[7, 9].

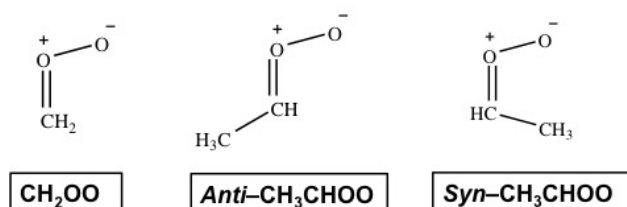
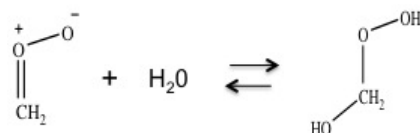
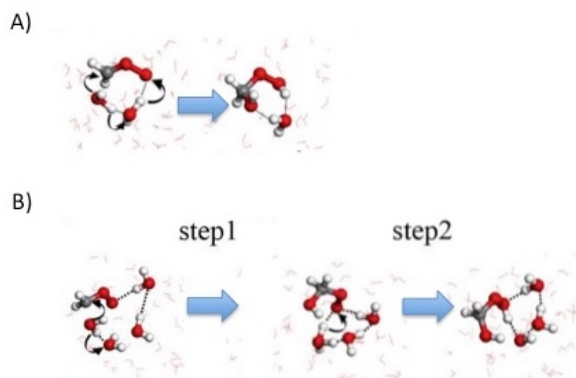


Figure 3.1: Criegee intermediates with varying degree of hydrophilicity whose reactivity on cloud surface aerosols have been studied in ref.[12]



Figure 3.2: Snapshot of the CH_2OO Criegee intermediate on the surface of an aerosol. Figures reproduced with permission from ref.[8]

One example is the work of Zhu *et al.*[8] that explored by quantum mechanics/molecular mechanics (QM/MM) dynamics simulations the chemistry of the simplest Criegee intermediate CH_2OO on the surface of a water droplet, comparing its reactivity to the one in the gas phase (Fig. 3.2). As schematically reported in Fig. 3.3 the hydration reaction of the CH_2OO Criegee

Figure 3.3: Scheme of the Criegee intermediate CH_2OO^- hydration reactionFigure 3.4: Panel A: Snapshot of the structures obtained from the simulations of the concerted mechanism reaction of CH_2OO with water. Panel B: Snapshots of the structures obtained from the simulations of the two-step reaction of CH_2OO with water. Figure reproduced with permission from ref.[8]

intermediate is characterized by the hydrolysis of a water molecule and the formation of C–OH and O–H bonds that lead to the production of the $HOCH_2OOH$ species.

In the gas phase, the CH_2OO reaction with water is driven by a concerted mechanism mediated by a water dimer[10]. In this mechanism of reaction (see Panel A of Fig. 3.4) the OH fragment of one water molecule binds to the carbon of the Criegee intermediate, while the remnant hydrogen atom of the same water molecule is simultaneously donated to the terminal Criegee oxygen through a proton transfer mediated by a water. Interestingly, at the air-water interface more channels of reaction become possible for the CH_2OO hydration reaction. For instance, different concerted mechanisms mediated by a variable number of water molecules (2-4) and a two-step reaction mechanism have been identified[8]. As one can see in Panel B of Fig. 3.4 the first stage of the two-step reaction mechanism is characterized by the nucleophilic attack of the water oxygen on the Criegee carbon with the simultaneous formation of a H_3O^+ species and of a C–OH bond. The second stage is characterized by the proton transfer from the H_3O^+ to the terminal Criegee oxygen with the consequent formation of $HOCH_2OOH$.

The reaction at the air-water interface is also found to be 2-3 orders of magnitude faster than in the gas phase. Such acceleration is ascribed to the capability of interfacial water molecules in stabilizing the intermediates of reaction and in inducing the presence of more reaction channels with respect to the gas phase.

Another interesting aspect is how the affinity of molecular species with the air-water interface can modulate the reaction rates. In their work, Zhong *et al.*[12] have simulated Criegee intermediates (see Fig. 3.1) that differ by their degree of hydrophilicity for the surface of cloud aerosols. They find interesting trends in the hydration reactivity. As mentioned above the simplest Criegee intermediate, CH_2OO (Fig. 3.1), is reactive at the interfacial water; conversely more hydrophobic Criegee intermediates, carrying non-polar substitutes (syn- and anti- CH_3CHOO in Fig. 3.1) are found to be chemically inert at interfacial water. The observed phenomena is explained by Zhong *et al.*[12] with the presence of the CH_3 hydrophobic group in larger Criegee intermediates that perturbs the interconnectivity of the solvation shell of the Criegee intermediate, thereby reducing the interfacial water proton-transfer ability that is necessary for the hydration reaction to occur.

Such results point to the water capability in modulating the reactivity of substrates at the air-water interface as a function of their affinity with interfacial water.

In chapter 4 we will investigate more in details such aspect, by comparing the changes between bulk and the air-water interface in substrates' reactivity as a function of their degree of hydrophilicity. We will especially study the interconversion reaction from the zwitterionic to the neutral form of different hydrophobic amino acids at the air-water interface that we will compare to bulk water. We find an enhanced reaction sensitivity to the substrates chemical nature at the air-water interface with respect to bulk water that we will try to put into the light of shifts in pKa values at the interface.

The pKa shift of polar groups represents an essential feature of the species reactivity at the air-water interface. Many works have indeed highlighted the capability of the air-water interface in shifting the pKa values of polar groups with respect to bulk water[140, 141, 142, 143, 144, 145, 100, 146, 147]. However there is not a general consensus on the intensity and on the direction of such shift. For example, Vibrational Sum Frequency Generation Spectroscopy (SFG) has shown a significant shift toward the neutral form of long chain acids at the air-water interface (increase of the pKa of COOH groups) when compared to bulk solutions[140, 141, 147]. A recent work[143], combining SFG and Attenuated Total Reflection (ATR) spectroscopies, has revealed the cationic L-proline and L-alanine residues to be favoured over the zwitterionic species at the air-water interface in certain pH ranges (3-7).

A different conclusion has been reached by the group of Prof. Vaida, investigating the ionization state of phenylalanine at the air-water interface by Infra-Red Reflection Adsorption Spectroscopy (IRRAS)[146]. They indeed found that the air-water interface increases the acidity of both the phenylalanine polar groups (decrease of both NH_2 and COOH pKa values) with respect to bulk water. As can be seen in Table 3.1, where the ionization states of the phenylalanine at the air-water interface as a function of the pH conditions are compared with the ones found in bulk water, the polar groups of the molecules residing at the interface get deprotonated at lower pH than in the

bulk. For instance the COOH function starts to get deprotonated in the pH range 1–2 at the interface *vs* 2–6 in the bulk, while the NH_3^+ function gets deprotonated in the pH range 6–11 at the interface *vs* 11–13 in the bulk (see Table 3.1). These results indicate a shift of the chemical equilibrium toward the phenylalanine anion species at the air-water interface.

Table 3.1: Ionization states of L-phenylalanine molecules at an aqueous surface and in bulk water from IRRAS and solid-state infrared spectra. Table reproduced with permission from ref.[146]

pH	surface ionization state	bulk ionization state
1	cation	cation
2	cation and zwitterion	cation
6	zwitterion	zwitterion
11	anion	zwitterion
13	anion	zwitterion

The interfacial factors proposed to be responsible for the shifts in the observed ionization states are: 1) the pH of the bare air-water interface, known to differ from the one of bulk water[148, 149, 150, 151, 152, 153, 154, 155, 156] and 2) the different water environment experienced by the chemical species at the air-water interface with respect to bulk water[143, 140, 141, 147]. The latter effect is related to the connectivity and properties of the water in the solvation shell of the species that can be strongly influenced by the presence and location of the hydrophilic/hydrophobic species groups at the interface. Such effect could represent a possible explanation for the discrepancies in the direction of the pKa’s shifts observed for different amino acids at the air-water interface[143, 142]. In chapter 4 we will analyse in details such possibility.

Many experimental works in the field of Mass Spectrometry have shown how organic reactions occurring in aereosols produced by Electron Spray Ionization Processes (ESI) are accelerated as compared to the corresponding reactions in bulk water[157, 158, 159, 160, 161]. The partial droplet evaporation between the ionization source and the mass inlet, which leads to the increase in concentration of the reactants in the droplet and the significant solution pH decrease induced by the ESI process have been ascribed as possibly explaining the accelerations in the reactions.

However, for small droplets, the air-water interface has been demonstrated to be an important catalytic factor for the acceleration of the reaction[1, 2]. An aspect to consider when dealing with reactions at the air-water surface is the transition from a 3D distribution of reagents into a 2D distribution, that increases the reagent concentration and proximity. It has been proposed in the literature that such effect can result in a favourable orientation of the molecules residing at the interface, thereby increasing the reaction rate[5, 97, 4]. In section 3.3 we will observe such effect along the peptide bond formation at the air-water interface, surprisingly induced by the enrich-

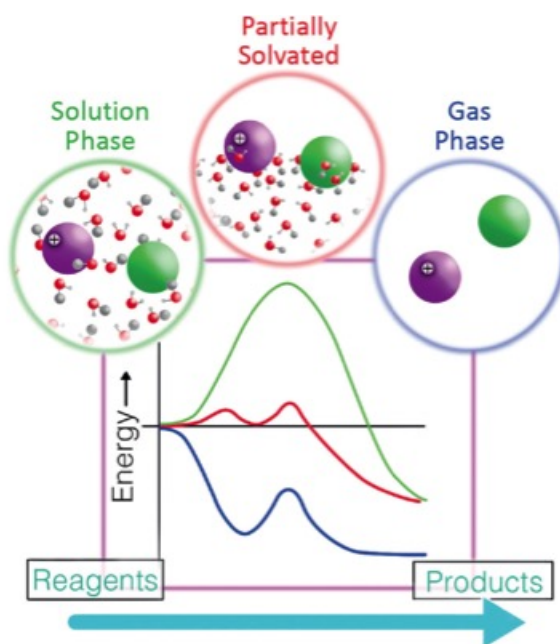


Figure 3.5: *Energetics associated with incomplete solvation that highlight acceleration of reactions at the air-water interface. The bulk solution (green line) reaction has a substantial energy barrier; droplet occurs (red line) at an accelerated rate compared to bulk. The reaction in the gas phase (blue line) occurs at every collision, thereby increasing the rate of reaction.*

ment in the counter-ion Cl^- concentration within the reaction complex at the air-water interface.

Another interfacial factor that has been proposed as an explanation in the acceleration of reactions at the surface of small droplets is the partial desolvation of species at the interface as compared to bulk water[6]. Chemical species residing at the interface indeed present smaller or incomplete solvation shells as compared to the ones in bulk water, implying a reduced desolvation energy[6]. It follows that, if a desolvation process occurs along a reaction, the activation energy of the reaction at the interface will benefit from a lower desolvation energy with respect to bulk water, thus leading to an acceleration of the reaction as schematically presented in Figure 3.5. Despite the partial dehydration of all the polar and non polar groups of the chemical species at the air-water interface studied along my PhD work, such effect did not seem to impact the energetics and mechanisms of the reactions explored.

3.2 In situ observation of the peptide bond formation

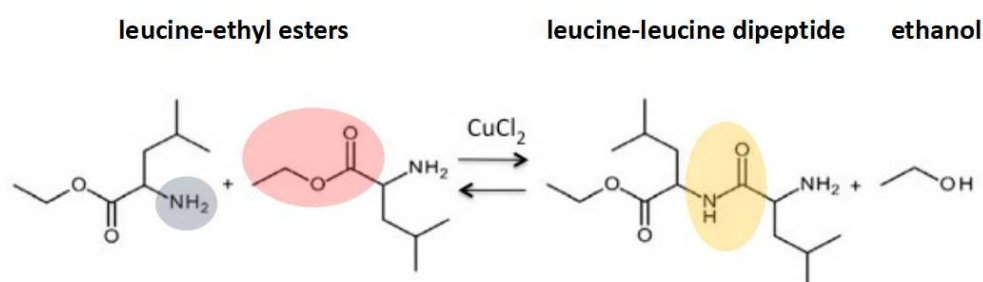


Figure 3.6: Scheme of the peptide bond condensation reaction observed experimentally at the air-water interface^[15]. The chemical groups involved in the reaction are highlighted by coloured circles, respectively: blue for the amine, red for the ester group and yellow for the peptide bond.

In this section we provide a short summary of the published paper " *In situ* observation of peptide bond formation at the water-air interface" ^[15] where the condensation of leucine-ethyl ester amino acids catalyzed by Cu²⁺ at the air-water interface has been experimentally characterized. In particular, we will focus on the mechanistic insights into the reaction at the interface obtained by IRRAS spectroscopy. For a detailed description of the peptide bond condensation reaction, which is the main subject of study in this chapter, see pages 11-14 of this manuscript. The experimental findings of this work^[15] are the starting points of our theoretical investigation, reported in section 3.3 of this chapter.

As already mentioned in the previous sections, Prof. Vaida's group^[15] has proposed a new prebiotic route for the formation of polypeptides at the air-water interface, capable of circumventing the thermodynamic and kinetic limits of the peptide bond formation as they exist in bulk water at neutral pH. In this experiment the amino acid leucine-ethyl ester is used as reactant (see Fig. 3.6) because it prevents the formation of the zwitterion and provides a better leaving group than water (see section 1.2 for more details).

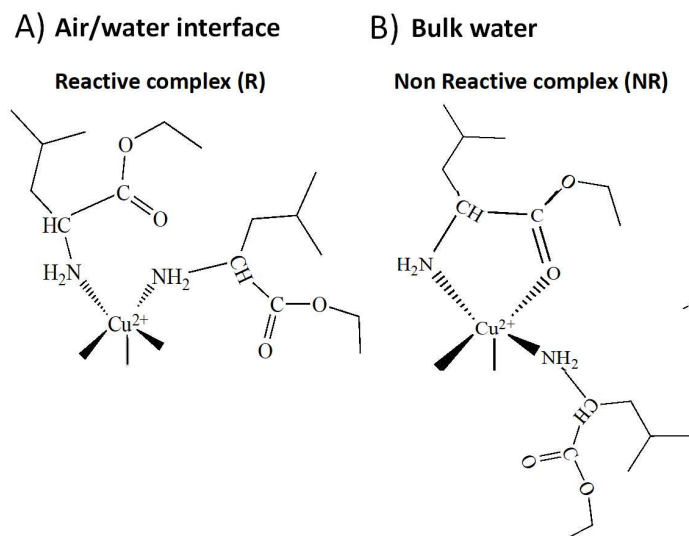


Figure 3.7: Proposed structure of the reactive complex (R) characterized at the air-water interface (see ref.[15]). The structure of the non reactive complex (NR) observed in bulk water is from ref.[102].

The CuCl_2 salt, which presence in the early oceans is indicated by green pre-cambrian zones[68], is used as a catalyst for the reaction at the air-water interface. The Cu^{2+} cation is found to form complexes with the amino acid esters (see the structures of the complexes in Fig. 3.7 as inferred from the experimental data in ref.[15]) in solution, that depending on their specific conformations can either promote or hinder the peptide bond condensation reaction. For instance, the formation of a non reactive chelated complex (NR complex in Fig. 3.7) characterized by the coordination of both the ester and amine groups of one leucine ethyl ester to the Cu^{2+} hinders the reaction in bulk water[102]. The coordination of the ester group to the Cu^{2+} leads to the hydrolysis of the ester group. The loss of the ester activating group leads to the formation of the carboxylate anion that hinders the reaction in bulk water (see Fig. 1.6 in section 1.2).

Therefore the structure of the reaction complex formed between the Cu^{2+} and the leucine-ethyl esters at the air-water interface is of crucial importance. In this regard, Vaida's group has followed *in situ*, the formation of the reaction complex at the air-water interface by coupling IRRAS spectroscopy and Langmuir-film trough techniques. In Fig. 3.8A the black line represents the IRRAS spectrum of the leucine-ethyl ester at the air-water interface in absence of copper Cu^{2+} in solution. The most prominent band in the spectrum at 1726 cm^{-1} is assigned to the leucine ester $\text{C}=\text{O}$ stretching mode. The red, blue and green curves in Fig. 3.8A report the time evolution of the IRRAS spectra of the leucine-ethyl ester solution in presence of CuCl_2 salt with compression of the surface film by the Langmuir-trough technique. The evolution of the spectra as a function of time is characterized by the enhancement of the IRRAS band at 1200 cm^{-1} associated to amine group ($-\text{NH}_2$) modes.

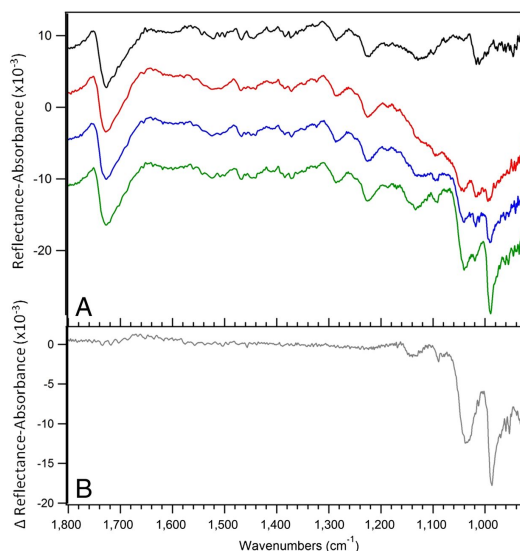


Figure 3.8: IRRAS spectra showing Cu^{2+} coordinated to the amine group of leucine ethyl ester over time, with compression. Extracted with permission from ref.[15]. (A) Leucine ethyl ester: (black) in the absence of Cu^{2+} ions in the solution; (red) in the presence of Cu^{2+} ions immediately after beginning constant pressure of 15 mN/m; (blue) after 30 min of constant pressure; and (green) after 60 min of constant pressure. (B) Subtraction spectrum (gray) of uncoordinated leucine ethyl ester (black) from the Cu^{2+} coordinated leucine ethyl ester IRRAS spectrum (green) showing the peaks enhanced through coordination to Cu^{2+} only.

The amine band enhancement indicates the formation of a complex at the air-water interface in which there is the coordination of the amine side of the leucine-ethyl ester to Cu^{2+} (see R structure in Fig. 3.7). The band associated to the C=O stretching at 1726 cm^{-1} remains over the compression, hence excluding a coordination of the ester side of the leucine-ethyl ester to the Cu^{2+} as would be observed for the non reactive complex (NR) in bulk water. This can be easily appreciated by the difference spectrum in Fig. 3.8B where the IRRAS spectrum of leucine-ethyl ester in absence of Cu^{2+} (black line in Fig. 3.8A) is subtracted from the leucine ester/ Cu^{2+} spectrum (green line in Fig. 3.8A).

Such results unveil the formation of a reactive complex at the air-water interface characterized by the coordination of the amine side of the leucine-ethyl ester to the Cu^{2+} . The supposed structure of the reactive complex (R) is reported in Fig. 3.7. The formation of the R complex at the air-water interface avoids the ester hydrolysis and thus prevents the protonation of the amine group (NH_2) by water, therefore allowing the peptide bond formation to occur.

Subsequent to the formation of the R complex, the reaction at the air-water interface proceeds over time and shows the appearance of a band at 1625 cm^{-1} in the IRRAS spectrum (Fig. 3.9A-B). Such band is assigned to the amide group of the peptide product. The position of the amide band provides useful information on the coordination of the oligopeptide products to the copper Cu^{2+} . In particular the amide band position at 1625 cm^{-1} indi-

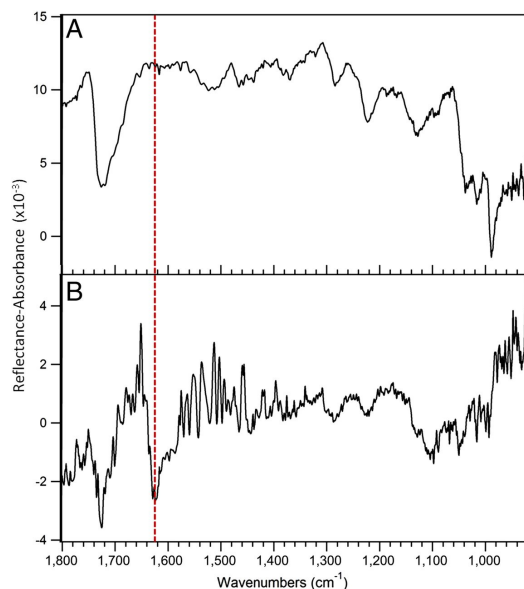


Figure 3.9: IRRAS spectra of (A) leucine-ethyl ester complexed with Cu^{2+} ions, and (B) the peptide product formed at the air-water interface (red dotted line indicates a new Amide I band due to the peptide bond formed). Extracted with permission from ref.[15]

icates that the oligopeptide product is still covalently coordinated to the Cu^{2+} (it means that the R complex is not broken after the oligopeptide production), because the non coordinated oligopeptide amide band would be located at the higher frequency of 1675 cm^{-1} .

The microscopical reasons for the presence of a reactive complex (R) at the air-water interface structurally different from the non reactive one (NR) observed in bulk water are still missing in ref.[15]. In section 3.3.2 we will shed light on a novel interfacial factor governing the stabilization of the R complex at the air-water interface with respect to bulk water.

3.3 The catalytic roles of the air-water interface in the prebiotic peptide bond formation

The results presented hereafter refer to the computational side of the work reported at the end of this section, that is planned to be submitted soon to *Nature Chemistry*.

3.3.1 Peptide bond formation at the air-water interface: mechanisms and energetics

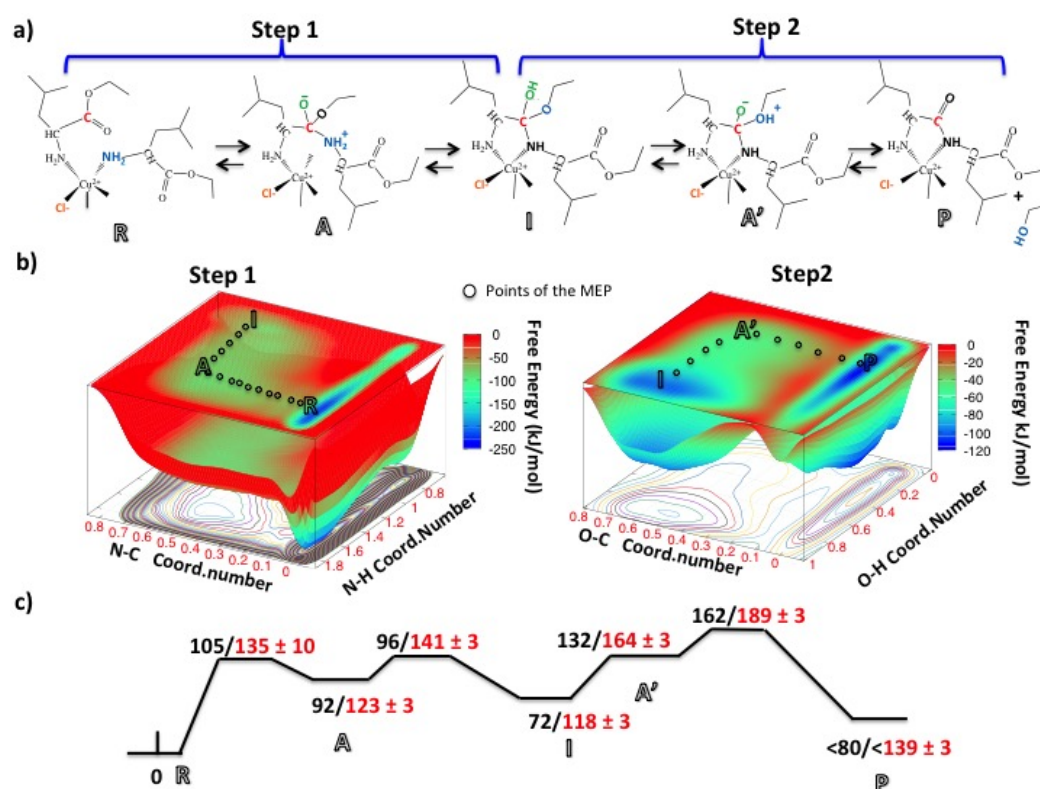


Figure 3.10: a) Scheme of the mechanisms of the reactions obtained by DFT-MD metadynamics for the peptide bond condensation at the air/water interface. The reactive groups are reported in color for both reactions steps. b) Free-energy landscapes and the MEP associated to respectively the tetrahedral intermediate formation (Step 1) and the dipeptide production (Step 2). c) Scheme of the energetics of the reactions along the MEP obtained from the metadynamics (red) and from thermodynamic integration (in black). The error bars are relative to the metadynamics energetics calculated by using the method of ref.[162]

We have dissected the condensation reaction between two leucine ethyl esters catalysed by the CuCl₂ salt at the air/water interface by means of DFT based enhanced sampling metadynamics. The reactive complex at the

air/water interface (R in Fig. 3.7) experimentally inferred by IRRAS spectroscopy [15] has two leucine ethyl esters covalently bonded by their amine groups ($-\text{NH}_2$) to one copper Cu^{2+} . The choice on the coordinates of reaction for the metadynamics has been based on the following considerations. From the literature the peptide bond condensation in solution is expected to be a nucleophilic acyl substitution reaction characterized by a two step mechanism[129]. The first step (Step 1 in Fig. 3.10a) is the nucleophilic attack of the amine group nitrogen (blue $-\text{NH}_2$ in structure R of Fig. 3.10a) of one amino acid ester onto the ester carbon ($-\text{COOCH}_2\text{CH}_3$, red carbon in structure R of Fig. 3.10a) of the other amino acid ester, with the formation of a tetrahedral intermediate (I in Fig. 3.10a). The tetrahedral intermediate (I) is characterized by one carbon atom (red carbon in structure I of Fig. 3.10) tetrahedrally coordinated to the nitrogen of a amine group (black), the oxygen of a OH group (green), the oxygen of a ethoxy group (blue) and one carbon atom. The second step (Step 2 in Fig. 3.10a) is the release of one ethanol molecule ($\text{CH}_3\text{CH}_2\text{OH}$) from the carbon at the center of the tetrahedral intermediate (red carbon in structure I), giving rise to the dipeptide production (P). We have thus performed two separate metadynamics, for respectively the tetrahedral intermediate formation (Step 1) and for the dipeptide (P) production with ethanol release (Step 2).

Since CuCl_2 salt is used in the experiment, we have included the Cl^- counter ion within the reaction complex (R) in our calculations (Cl^- in orange in all structures of Fig. 3.10a). In section 3.3.3 we will justify such choice by revealing the higher affinity between the Cl^- and the Cu^{2+} ions at the air-water interface than in bulk water.

In Fig. 3.10b the free energy landscapes for steps 1 and 2 obtained from the metadynamics are depicted together with their relative minimum free energy paths (MEP). The energetics obtained by the metadynamics are reported in red in Fig. 3.10c. The energetics of the reactions at the air/water interface have been refined by thermodynamic integration [47] (blue moon ensemble black values in Fig. 3.10c) by selecting the MEP points revealed by the metadynamics. This is similar to the strategy adopted in refs.[163, 16]

Our metadynamics reveal both the formation of the tetrahedral intermediate (Step 1) and the dipetide production with ethanol release (Step 2) to be characterized by double step mechanisms. The energetics of the reactions either calculated from the metadynamics or from thermodynamic integration (see Fig.3.10c) show good agreements and both indicate that the intermolecular nucleophilic attack of the nitrogen onto the carbon site ($\text{R}\rightarrow\text{A}$ in Fig. 3.10b) is the energetically bottleneck step of the reaction. For this $\text{R}\rightarrow\text{A}$ step, the free energy barrier is respectively 105 kJ/mol from thermodynamic integration and 135 kJ/mol from metadynamics.

As discussed more in details in the S.I. of the paper reported at the end of this section, the convergence of the metadynamics is assessed by observing the double crossing of the energetic barriers backward and forward along the same reaction coordinate. Since the large size of the system (256 water molecules), the high dimensionality of the reaction and the small height

(0.8 kJ/mol) of the Gaussian Hills used to accurately sample the reaction space of interest (see S.I. and method section for the computational details), only one recrossing event for free energy barrier has been simulated in the case of the peptide bond condensation reaction. This could have led to an overestimation of the free energy barriers. However the strong reduction in the free energy barriers due to the catalytic effects of the air-water interface (presented in the next sections), the refining of the reaction energetics along the MEP by thermodynamic integration and the small sizes of the gaussian Hills deposited along the metadynamics simulations (see the Computational details of the paper for more details) ensure the good quality of our results. The estimation of the error in the metadynamics free energies (reported in Fig. 5.10c) have been calculated by the formula in ref.[162] where the error is expressed as a function of the gaussian hills parameters (deposition time, height and width) and few parameters characterizing the physical system. It is important to mention here that such formula is meant to work in ideal cases (fast transverse degrees of freedom, parallel growth with many recrossings etc.).

Now that the mechanisms and energetics of the peptide bond condensation reaction at the air/water interface have been revealed, we now focus on the molecular factors that promote the reaction at the air/water interface. As described in details in the next sections, we have identified two catalytic roles of the air/water interface: (i) a net stabilization of the reactive complex conformation (R) directly modulated by the air/water interface, and (ii) a strong catalytic role of the Cl^- ion, which presence in the reaction complex is enhanced at the air/water interface.

The details on the mechanisms of reaction and the choice of the reaction coordinates for the metadynamics are found in the first section of the paper included at the end of this section.

3.3.2 Stabilization of the reactive complex (R) at the air-water interface

We start by considering the structure of the aqueous Cu(II)-Cl^- bis-leucine-ethyl esters complex at the air/water interface (R in Fig. 3.11a), which structure has been found to differ from the one observed in bulk water. As already mentioned in the previous sections, IRRAS spectroscopy at the air/water interface indicates the formation of a reactive complex (R in Fig. 3.11a) characterized by the two leucine ethyl esters being simultaneously covalently bonded to the copper by the amine groups only. Conversely, in bulk water the formation of a non reactive chelated complex is observed [102] (denoted hereafter NR, see Fig. 3.11a) where one of the two leucine ethyl esters is covalently bonded to the Cu^{2+} by both its amine and its ester groups, while the second leucine ester is covalently bonded to the Cu^{2+} via its amine group.

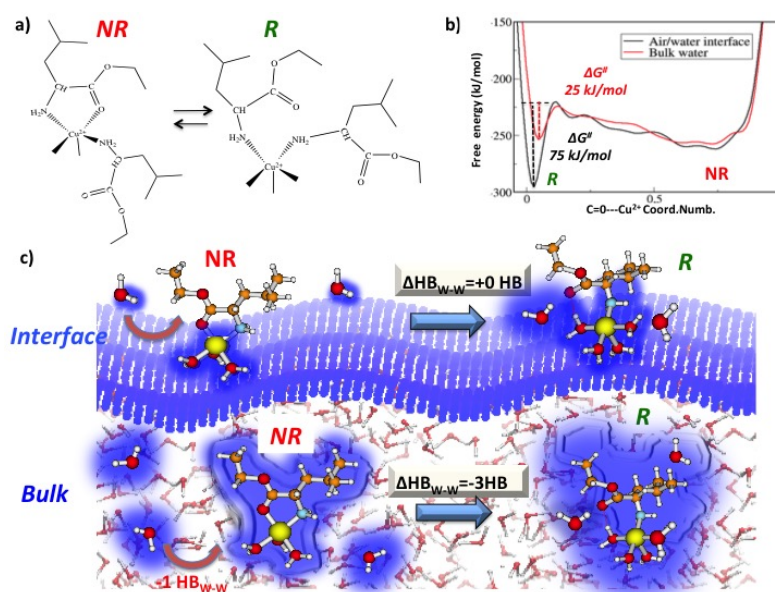


Figure 3.11: a) Schemes of the reactive complex (R) / non reactive complex (NR) respectively at the air/water interface and in liquid water. b) Free energy profile for the inter-conversion between R and NR complexes in bulk water (red line) and at the air/water interface (black line), choosing the $C=O \cdots Cu^{2+}$ coordination number as reaction coordinate. c) Scheme for the variation in water-water H-bonds during the inter-conversion between the R/NR complexes, comparing the air/water interface and bulk liquid water environments.

In order to shed light on these experimental evidences the relative free energy between the two complexes R and NR along the $C=O \cdots Cu^{2+}$ coordination number, chosen as reaction coordinate for the DFT-MD metadynamics, has been quantified for the two aqueous environments. Our metadynamics unveil (Fig. 3.11b) a roughly 50 kJ/mol higher free energy barrier for the inter-conversion from R towards NR at the air/water interface (black line in Fig. 3.11b) with respect to bulk water (red line in Fig. 3.11b): the R complex is thus three times more stable at the air/water interface than in bulk water.

The stabilization of the R complex is one (however not the only one) of the necessary ingredients to make the peptide bond condensation reaction possible at the air/water interface. For instance, experiments [102] have revealed the coordination of the ester group to the copper Cu^{2+} ion in the NR complex to induce a high degree of hydrolysis of the ester group in bulk water (enhanced by 10^6 by the metal). The loss of the ester activating group (following the ester group hydrolysis) hinders the peptide bond formation in liquid water. Conversely the stabilization of the R complex at the air/water interface, in which ester groups are not coordinated to the Cu^{2+} , prevents the ester hydrolysis at the interface, thus allowing the peptide bond condensation to proceed.

Coupling our simulations with previous published *in situ* experiments from Vaida's group [15], we have hence unambiguously characterized the for-

mation of a complex at the air/water interface (R) that is structurally and chemically different in structure from the one observed in bulk water (NR).

We have then investigated the microscopic reasons behind the R complex stabilization at the air/water interface. As described in detail in the second section of the paper reported at the end of this section, the reason for the reactive complex (R) stabilization is in the under-coordinated nature of the interfacial water molecules that enhances the water affinity to the solute, thus altering the chemical equilibrium between the reactive (R) /non reactive (NR) complexes at the interface when compared to bulk water.

3.3.3 The Catalytic Role of the Cl^- anion

A second issue that needs to be considered is the possible modulation of the affinity between the Cu^{2+} cation and the counter anion Cl^- in the reaction complex R induced by the air/water interface, when compared to bulk water. Many works have indeed pointed to an enhanced ion pairing as well as enrichment of Cl^- at the air/water interface. Therefore the presence of the counter-ion within the R complex at the air/water interface cannot be excluded. We have therefore analyzed the CuCl^- dissociation curve at the air-water interface and in bulk water, by the thermodynamic integration technique. The resulting potential of mean force (PMF) reports a stabilization by 15 kJ/mol for the Contact Ion Pair (CIP) at the air/water interface with respect to bulk water. Therefore the probability to find the Cl^- bonded to the Cu^{2+} within the reactive complex (R) is larger at the air-water than in the bulk.

In the light of this result, corroborated by several experimental and theoretical observations in the literature [164, 165], [166] we have decided to study the peptide bond condensation reaction with and without Cl^- in the reactive complex (R). When the Cl^- is replaced by one water molecule in the reactive complex R, a more than two-times increase in the free energy barrier of the bottleneck step (Step 1, $\text{R} \rightarrow \text{A}$) is obtained. Such finding thus reveals a strong catalytic effect of the Cl^- anion in the rate-determining step of the condensation reaction during the nucleophilic attack of the amine nitrogen onto the ester carbon ($\text{R} \rightarrow \text{A}$ in Fig. 3.10a).

We have identified two microscopic reasons for such Cl^- catalytic effect: 1) the proximity of the amino acid esters reactive groups, and the energetic stabilization of the transition state (TS) structure associated to the bottleneck step.

3.3.4 The peptide condensation in bulk liquid water

In order to investigate if the two effects revealed in the previous sections (stabilization of the R complex and Cl^- catalytic role) are the major fac-

tors for the peptide bond condensation formation at the air/water interface, or if a prominent role is also played e.g. by the ‘reactants dehydration’ at the interface, we now turn our attention to bulk water. We have performed metadynamics simulations of the peptide bond condensation reaction in bulk water, imposing the same conditions that we now know to promote the reaction at the air/water interface. For instance, we have used the R complex (which is not the most stable one in bulk water, see again Fig. 3.11), we have included the Cl^- within it (despite the CIP is more easily broken in the bulk than at the interface). We remind the reader that such conditions are unrealistic in bulk water, but such theoretical approach allows us to directly compare the effects of the two aqueous environments on the mechanisms and energetics of the condensation reaction.

Under these conditions, we find that the reaction occurs in bulk water with the same mechanisms and similar energetics as the reaction occurring at the air/water interface. Such result confirms the stabilization of the R complex and the counter ion Cl^- as the two most relevant ingredients that indeed the air-water interface can provide.

The details of this investigation have been presented in the paper that can be found in the next pages. This paper is planned to be submitted soon to Nature Chemistry.

The catalytic roles of the air/water interface in the prebiotic peptide bond formation

Flavio Siro Brigiano,^{*,†} Simone Pezzotti,[†] Daria Ruth Galimberti,[†] Veronica
Vaida,[‡] and Marie-Pierre Gaigeot^{*,†}

[†]*LAMBE CNRS UMR8587, Université d'Evry val d'Essonne, Evry, France & Université
Paris-Saclay, France*

[‡]*Department of Chemistry and Biochemistry and Cooperative Institute for Research in
Environmental Sciences, University of Colorado at Boulder, UCB 215, Boulder, CO 80309*

E-mail: flavio.sirobrigiano@univ-evry.fr; mgaigeot@univ-evry.fr

Abstract

Introduction

The understanding of the formation of biopolymers in the early ages of the Earth is crucial to fully rationalize the origin of life on our planet. In which conditions and how organic compounds polymerized in the primordial soup, before the emergence of the enzymes, remains a fascinating unresolved question in prebiotic chemistry. In particular, the first peptide bond condensation reaction is a highly debated and controversial topic. The peptide bond formation is known to be unfavoured in bulk water for both thermodynamic and kinetic reasons,¹ and many chemical routes in partially dehydrated conditions have been proposed by the scientific community, including wet and dry cycles^{2,3} reaction on mineral clays^{4,5,6}, heating with an inorganic catalyst.^{7,8}

These works shed light on the specific catalytic effects offered by partially dehydrated environments, e.g. "crowding" of the reactive species, pK_as shift, stabilization of the oligopeptides against hydrolysis. As a drawback, high temperatures and high concentrations of reactants were required in order to make the reaction occur. Griffith et al.⁹ have recently experimentally observed the formation of polypeptides at room temperature in dilute conditions from amino acid esters and CuCl₂ salt at the air-water interface (Fig. 1a), suggesting the surface of oceans and marine aerosols as suitable environments for the birth of life on the prebiotic Earth.^{10,11,12,13,14}

CuCl₂ salt is used as a catalyst because of the well known ability of the copper cation Cu²⁺ in forming coordination complexes with amino acids and peptides.^{8,15} The presence of copper in the early oceans is plausible, as indicated by green pre-cambrian zones^{16,17} (rocks rich in copper that date back to 4.5 billion years ago). Leucine ethyl ester, a short

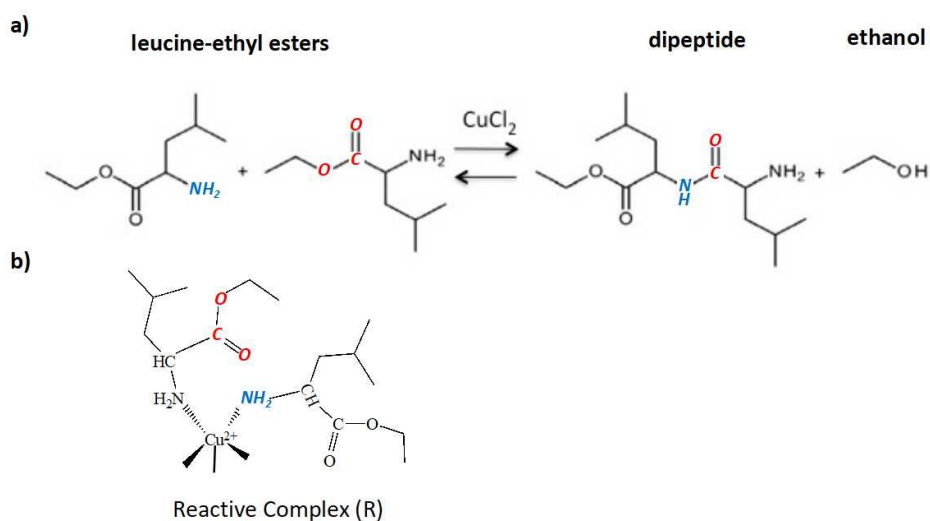


Figure 1: *Panel a) Scheme of the peptide bond condensation reaction at the air/water. Experimentally CuCl_2 salt is used as catalyst. Panel b) Structure of the Reactive complex (R) at the air/water interface inferred experimentally by IRRAS spectroscopy.⁹ The atoms of the reactive groups are depicted respectively in blue for the amine group and in red for the carboxyl ester group.*

amino-acido ester, plausibly present on the primordial Earth, was used as reactant in order to prevent the formation of the zwitterionic form that is known to kinetically unfavour the peptide bond formation in water.¹

In particular, the ester group ($-\text{COOCH}_2\text{CH}_3$) protects the carboxyl side of the leucine-ethyl ester preventing the formation of a carboxylate anion (COO^-) and shifts the pKa of the amine group by two units toward the neutral form,^{18,19} thus hampering the formation of the non-reactive protonated amine (R-NH_3^+). Moreover the reaction produces ethanol that is a better leaving group than water and thus shifts the chemical equilibrium of the reaction toward the side of the products. This reaction, done at the air/water interface, is compatible with geochemical conditions of the primitive Earth where air-water interfaces were ubiquitous during and after the hydrosphere formation in early oceans and salty water droplets. More generally, the role of the air/water interface in catalysing reactions is crucial in understanding phenomena in various domains, ranging e.g. from atmospheric chemistry^{20 21 22 23 24 25} to mass spectrometry.^{26 27 28} The air-water interface has been found able to accelerate organic

reactions, and reasons for that have been ascribed to its ability to concentrate reagents, to align the biochemical precursors, to shift pK_as, and to partially dehydrate the reactants.^{29–32} However the specific role of the air-water interface during the peptide bond condensation reaction and the reasons for which this reaction occurs at the interface and not in bulk water are still unclear. In particular, experiments have also been performed for the same condensation reaction from leucine-ethyl esters, also catalyzed by CuCl₂ salt, in aqueous solution, yielding no production of polypeptides.³³ The formation of a chelated complex between two amino acid esters and the copper Cu²⁺ cation has been found to lead to a high degree of hydrolysis of the ester group, thus hampering the peptide condensation reaction in bulk water. On the contrary, IRRAS spectroscopic experiments⁹ find a reactive complex at the air-water interface (R in Fig. 1b), conformationally different from the non-reactive (NR) one that is observed in bulk water. The experimental evidence for two different complex structures with two distinct reactivities at the air-water interface and in bulk liquid water highlights the direct role of the interface in the peptide condensation chemistry that goes beyond already well-known catalytic interfacial factors (e.g. concentration of reactants, aligning bio-molecules, pK_a shifts, partial desolvation of reactants).

In the last decade, with the advance of the computational power and the development of enhanced MD sampling techniques, molecular simulations have shown to be more than useful tools to characterize chemical reactions at interfaces. For example computational studies of peptide bond reactions assisted by mineral clays³⁴ have shed light on the unexplored catalytic role of the substrates, while recent *ab initio* molecular dynamics simulations (AIMD) on relevant atmospheric reactions reveal different reaction mechanisms at the air-water interface with respect to the gas phase.³⁵

Herein we provide a deep molecular insight into the peptide bond condensation reaction at the air/water interface by coupling DFT-MD (Density Functional Theory based Molecular Dynamics) simulations (naturally taking into account chemical reactions) with the enhanced sampling of biased DFT-MD techniques.^{36,37} The comparison of the reaction ener-

getics and mechanisms at the air/water interface *versus* in bulk water coupled with a full structural characterization of the air-water interface previously achieved by our group in recent works^{38,39} allows us weight the possible factors that modulate the reaction.

Our data point to novel catalytic roles of the air/water interface in the reaction mechanisms. We specifically find the presence of the salt counter ion Cl^- within the reactive complex (R) at the air/water interface to be a necessary ingredient for the peptide bond formation reaction to occur, as well as the special 2D-H-Bond network of the air-water interface³⁸ to be an essential element in the reactivity.

Results

Peptide bond formation at the air/water interface

We have dissected the condensation reaction between two leucine ethyl esters catalysed by the CuCl_2 salt at the air/water interface by means of DFT based enhanced sampling metadynamics. The reactive complex at the air/water interface (R in Fig. 1b) experimentally inferred by IRRAS spectroscopy⁹ has two leucine ethyl esters covalently bonded by their amine groups ($-\text{NH}_2$ depicted in blue in Fig. 1b) to one copper Cu^{2+} . The choice for the coordinates of reaction for the metadynamics method has been based on the following considerations. From the literature, the peptide bond condensation in solution is expected to be a nucleophilic acyl substitution reaction characterized by a two-step mechanism.⁴⁰ The first step (Step 1 in Fig. 2a) is the nucleophilic attack of the amine group nitrogen (blue $-\text{NH}_2$ in structure R of Fig. 2a) of one amino acid ester onto the ester carbon ($-\text{COOCH}_2\text{CH}_3$, red carbon in structure R) of the other amino acid ester, with the formation of a tetrahedral intermediate (I in Fig. 2a). The tetrahedral intermediate (I) is characterized by one carbon atom (red carbon in structure I of Fig. 2) tetrahedrally coordinated respectively to the nitrogen of a amine group (black), the oxygen of a OH group (green), the oxygen of a ethoxy group (blue) and one carbon atom. The second step (Step 2 in Fig. 2a) is the release

of one ethanol molecule ($\text{CH}_3\text{CH}_2\text{OH}$) from the carbon at the center of the tetrahedral intermediate (red carbon in structure I) giving rise to the dipeptide production (P). We have thus performed two separate metadynamics, for respectively the tetrahedral intermediate formation (Step 1) and for the dipeptide production with ethanol release (Step 2).

In order to span the relevant phase space, the following choices of reaction coordinates have been made. For Step 1: the coordination number of the nitrogen atom of one leucine ethyl ester amino acid (blue nitrogen atom in structure R of Fig. 2a) with respect to all non aliphatic hydrogen atoms in the system (it is called N-H coordinate in the rest of the text), and the coordination number of the same nitrogen with respect to the ester carbon (red carbon in structure R of Fig. 2a) of the other leucine ethyl ester (it is called N-C coordinate in the rest of the text). Since CuCl_2 salt is used in the experiment, we have included the Cl^- counter ion within the reaction complex (R) in our calculations.

In section "The Catalytic Role of the Cl^- " we will justify such choice by revealing the affinity between the Cl^- and the Cu^{2+} ions at the air/water interface. For Step 2, choice is made to use both the coordination number of the alcohol group oxygen atom (-OH depicted in green in structure I of Fig. 2a) that belongs to the tetrahedral intermediate with respect to all water hydrogen atoms in the system (O-H coordinate in the rest of the text) and the coordination number of the carbon at the center of the tetrahedral intermediate (red carbon in structure I of Fig. 2a) with respect to the oxygen of the alkoxy group ($-\text{OCH}_2\text{CH}_3$, blue oxygen in structure I of Fig. 2a).

In Fig. 2b the free energy landscapes for steps 1 and 2 obtained from the metadynamics are depicted together with their relative minimum free energy paths (MEP). The energetics obtained by the metadynamics are reported in red in Fig. 2c. The energetics of the reactions at the air/water interface have been refined by thermodynamic integration (blue moon ensemble approach, black values in Fig. 2c) by selecting the MEP points revealed by the

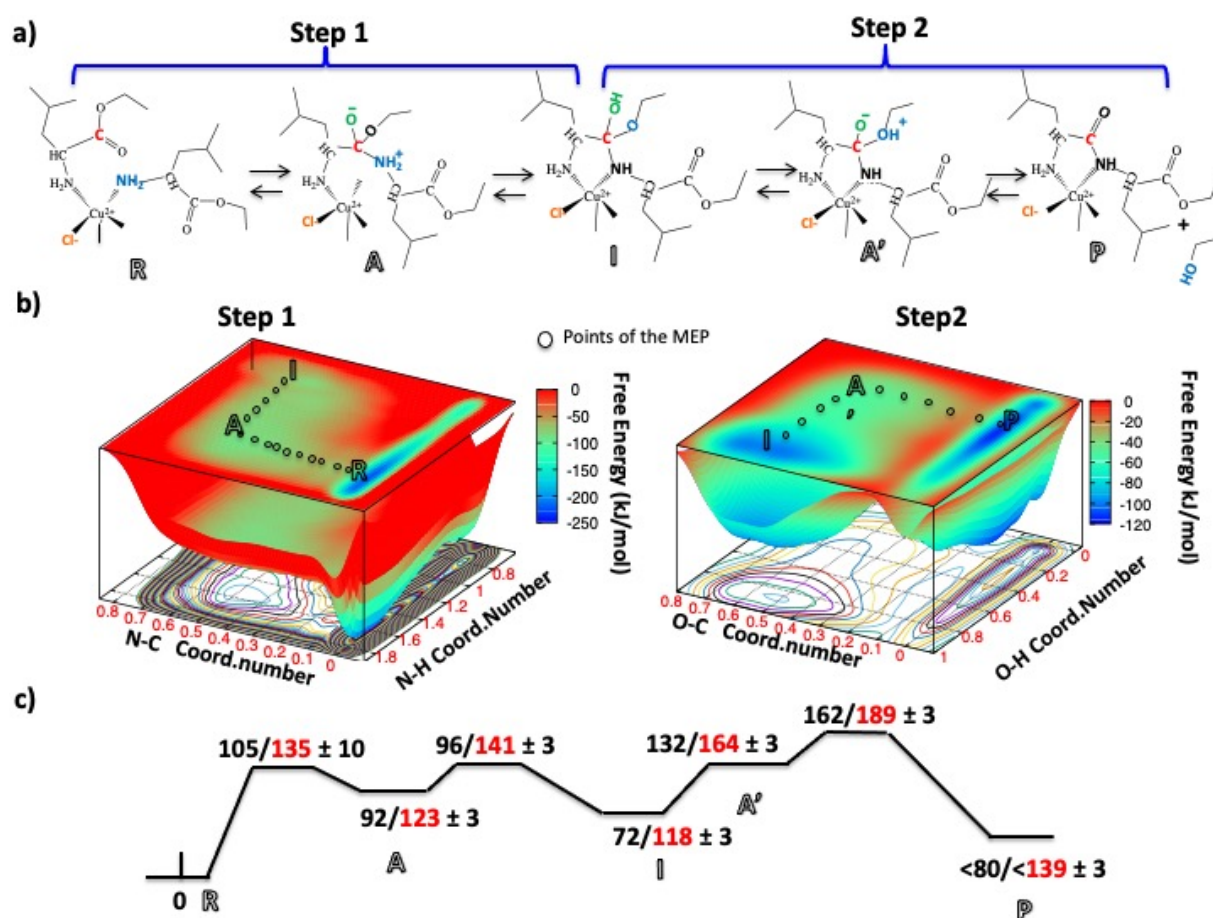


Figure 2: a) Scheme of the mechanisms of the reactions obtained by DFT-MD metadynamics for the peptide bond condensation at the air/water interface. The reactive groups are reported in color for both reactions steps. b) Free-energy landscapes and the MEP associated to respectively the tetrahedral intermediate formation (Step 1) and the dipeptide production (Step 2). c) Scheme of the energetics of the reactions along the MEP obtained from the metadynamics (red) and from thermodynamic integration (in black). The error bars are relative to the metadynamics energetics calculated by using the method of ref.⁴¹

metadynamics. This is similar to the strategy adopted in refs.^{42,43}

The formation of the tetrahedral intermediate (Step 1 in Fig. 2a) starts with the intermolecular nucleophilic attack ($R \rightarrow A$) of the amine nitrogen onto the ester carbon atom (the reactive groups are reported in color in Fig. 2a). The formation of the metastable tetrahedral adduct (A) has a high free energy barrier of 135 kJ/mol (red values Fig. 2c).

The reaction then proceeds perpendicularly along the N-H coordinate (A→I) with a proton transfer from the amine (NH_2^+ , blue) to the alcoxyde group (C-O^- , green) mediated by surrounding hydrogen bonded water chains. Such process leads to the formation of the tetrahedral intermediate (I) with a small free energy barrier of 18 kJ/mol. This first metadynamics shows a MEP characterized by a double step mechanism for the tetrahedral intermediate formation (I), where the two chosen coordinates of reaction are independent (orthogonal) from each other.

As shown from the free energy landscape in Fig. 2b, the formation of the dipeptide from the tetrahedral intermediate (I) also proceeds through a two-step mechanism. It starts (I→A') with the deprotonation of the oxygen atom (blue) of the alcohol group (C-OH) and the spontaneous protonation of the alcoxy group (that now becomes a good "leaving group") by water. This leads to the formation of the metastable intermediate A'. The process has an energy barrier of 46 kJ/mol. In a second step (A'→P), the molecular rearrangement of A' causes the expulsion of ethanol and the formation of the dipeptide (P) with an energy barrier of 25 kJ/mol. The dipeptide (P) remains coordinated to the copper along all the simulation time in agreement with the IR band Amide shift observed experimentally.⁹ We have not assessed the exothermic/endothermic character of the reaction because that would require a much longer time-scale for a full exploration of the free energy basin of the product P, i.e. we have not carried out the metadynamics of step 2 until full convergence (the final value of the free energy of 139 kJ/mol for the products P is not the ultimate one, convergence would decrease this value).

The energetics of all the reactions either calculated from the metadynamics or from thermodynamic integration (see Fig.2b) show good agreements (for details see S.I.) and both indicate that the intermolecular nucleophilic attack of the nitrogen onto the carbon site (R→A in Fig. 2b) is the energetically bottleneck step of the reaction. For this R→A step, the free energy barrier is respectively 105 kJ/mol from thermodynamic integration and 135 kJ/mol from metadynamics.

As discussed more in details in the S.I. the convergence of the metadynamics is assessed by observing the double crossing of the energetic barriers backward and forward along the same reaction coordinate. Since the large size of the system (256 water molecules), the high dimensionality of the reaction and the small height (0.8 kJ/mol) of the Gaussian Hills used to accurately sample the reaction space of interest (see S.I. and method section for the computational details), only one recrossing event for free energy barrier has been simulated in the case of the peptide bond condensation reaction. This could have lead to an overestimation of the free energy barriers. However the strong reduction in the free energy barriers due to the catalytic effects of the air-water interface (presented in the next sections), the refining of the reaction energetics along the MEP by thermodynamic integration and the small sizes of the gaussian Hills deposited along the metadynamics simulations ensure the good quality of our results. The estimation of the error in the metadynamics free energies (reported in Fig. 2c) have been calculated by the formula in ref.⁴¹ where the error is expressed as a function of the gaussian hills parameters (deposition time, height and width) and few parameters characterizing the physical system. It is important to mention here that such formula is meant to work in ideal cases (fast transverse degrees of freedom, parallel growth with many recrossings etc.).

Now that the mechanisms and energetics of the peptide bond condensation reaction at the air/water interface have been revealed, we now focus on the molecular factors that promote the reaction at the air/water interface. To that end, we have compared the structures and solvation properties of the reactants and of all the reaction intermediates when they are formed at the air/water interface versus when they are formed in bulk liquid water. We have quantified their impact on the energetics and reaction mechanisms in the two aqueous media. As described in details in the next section, we have identified two catalytic roles of the air/water interface: (i) a net stabilization of the reactive complex conformation (R) directly modulated by the air/water interface, and (ii) a strong catalytic role of the Cl^- ion,

which presence in the reaction complex is enhanced at the air/water interface.

The direct role of the air/water interface

We start by considering the structure of the aqueous Cu(II)-Cl⁻ bis-leucine-ethyl esters complex at the air/water interface, which structure has been found to differ from the one in bulk water. As already mentioned in the previous sections, IRRAS spectroscopy at the air/water interface indicates the formation of a reactive complex (R in Fig. 3a) characterized by the two leucine ethyl esters being simultaneously covalently bonded to the copper by the amine groups only. Conversely, in bulk water the formation of a non reactive chelated complex is observed³³ (denoted hereafter NR, see Fig. 3a) where one of the two leucine ethyl esters is covalently bonded to the Cu²⁺ by both its amine and its ester groups, while the second leucine ester is covalently bonded to the Cu²⁺ via its amino group.

In order to shed light on these experimental evidences the relative free energy between the two complexes R and NR along the C=O...Cu²⁺ coordination number, chosen as reaction coordinate for the DFT-MD metadynamics, has been quantified for the two aqueous environments. Our metadynamics unveil (Fig. 3b) a roughly 50 kJ/mol higher free energy barrier for the inter-conversion from R towards NR at the air/water interface (black line in Fig. 3b) with respect to bulk water (red line in Fig. 3b): the R complex is thus three times more stable at the air/water interface than in bulk water. Note also that the free energy profiles in Fig. 3 show a slightly broader well for the R complex at the air/water interface. This indicates that also entropic effects play a role in the stabilization of the R complex at the air/water interface.

The stabilization of the R complex is one (however not the only one) of the necessary ingredients to make the peptide bond condensation reaction possible at the air/water interface. For instance, experiments^{33,44} have revealed the coordination of the ester group to the copper Cu²⁺ ion in the NR complex to induce a high degree of hydrolysis of the ester group in

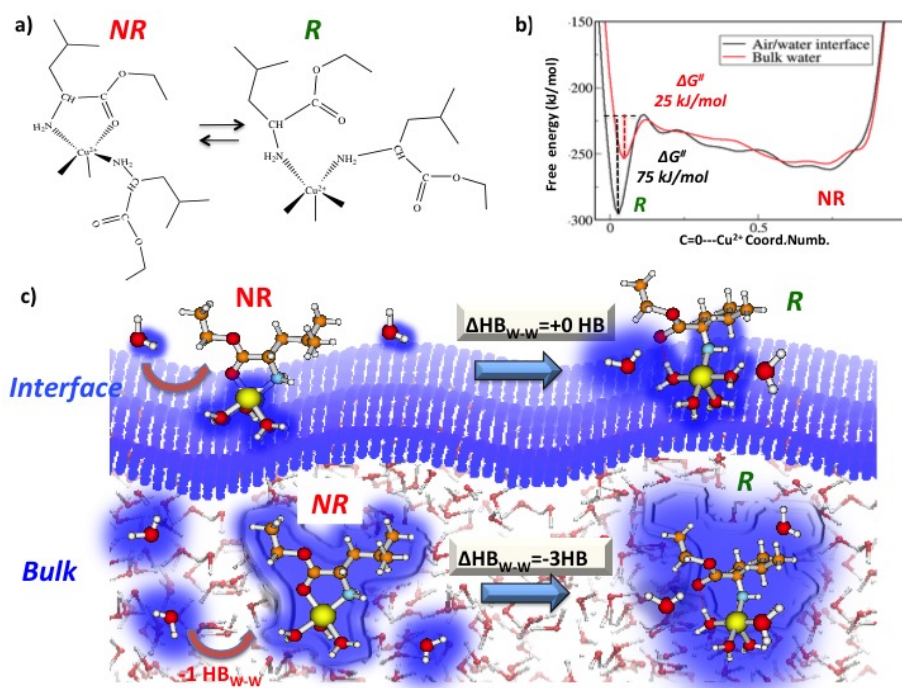


Figure 3: a) Schemes of the reactive complex (R) / non reactive complex (NR) respectively at the air/water interface and in liquid water. b) Free energy profile for the inter-conversion between R and NR complexes in bulk water (red line) and at the air/water interface (black line), choosing the $C=O \cdots Cu^{2+}$ coordination number as reaction coordinate. c) Scheme for the variation in water-water H-bonds during the inter-conversion between the R/NR complexes, comparing the air/water interface and liquid water environments.

bulk water (enhanced by 10^6 by the metal). The loss of the ester activating group (following the ester group hydrolysis) hinders the peptide bond formation in liquid water. Conversely the stabilization of the R complex at the air/water interface, in which ester groups are not coordinated to the Cu^{2+} , prevents the ester hydrolysis at the interface, thus allowing the peptide bond condensation to proceed.

Coupling our simulations with previous published *in situ* experiments from Vaida's group,⁹ we have hence unambiguously characterized the formation of a complex at the air/water interface (R) that is structurally and chemically different in structure from the one observed in bulk water (NR).

We have then investigated the microscopic reasons behind the R complex stabilization at the air/water interface. We have first investigated if the structures of the two complexes (R

and NR) with respect to the copper cation differ in the two aqueous media. When simulated at the air/water interface, both R and NR complexes keep their 5-fold coordinated square pyramidal geometry around the copper cation, as it is observed along our DFT-MD simulations in bulk water. We thus exclude this factor to play a role on the R stabilization at the aqueous interface.

Two other possible explanations can be thought: difference in the number of solute-water interactions and/or water-water hydrogen-bonds between the R and NR complexes at the air/water interface and in the bulk.

We observe a partial depletion of the first solvation shell (Table 1) of the R and NR complexes when they are located at the air/water interface, caused not only by the amino acid esters non polar tails facing the vacuum but also by a partial dehydration of the polar groups that are found ‘surfing’ over the under-coordinated 2D interfacial water network (2D-HB-network characterized in our previous works^{38,45,46}). The "surfing" of a series of amphiphile organic compounds at the air-water interface has been previously identified and characterized by biased classical molecular dynamics simulations⁴⁷ (see S.I. for details). Despite the partial dehydration of the polar groups at the interface, the same variations in the number of solute-water H-Bonds have been detected when going from the NR to the R complexes, whether these complexes are located in bulk water or at the air/water interface (ΔN_{W-S} in Table 1). Therefore the variation of solute-water interactions is not responsible for the higher stability of the R complex at the air/water interface.

If we now consider the variations in water-water interactions within the systems when going

Table 1: Number of Water-Solute interactions

Media	NR complex N_{W-S}	R complex N_{W-S}	R-NR ΔN_{W-S}	R-NR ΔN_{W-W}
Bulk water	7.0	8.6	1.6	-3.0
Air/water interface	6.3	7.9	1.6	0.0

from NR to R complex, no change in water-water H-Bonds are detected at the air/water interface, while a decrease by three water-water H-Bonds is systematically observed in the

bulk (ΔN_{w-w} in Table 1). As shown in Fig. 3c the evolution from the NR complex to the R complex in bulk water involves at least three ‘bulky’ water molecules to enter into the larger first solvation shell of the R complex, resulting in the cleavage of one existing water-water H-bond for each entering water molecule. This causes in total the loss of three H-Bonds in bulk water when the R complex is formed. On the contrary water molecules are under-coordinated (on average 2.7 water-water H-Bonds per molecule at the interface *vs* 3.4 in bulk water) at the air/water interface. As a consequence, when an interfacial water molecule gets into the first solvation shell of the R complex, it can now complete its coordination sphere without requiring any breaking of water-water H-bonds. The cleavage of the three H-Bonds, needed to form the R complex in the bulk liquid water, are thus not required at the air/water interface.

These findings reveal water-water interactions as the driving force for the R complex stabilisation at the air/water interface. Such water under coordination effect of the air/water interface is a novel factor in chemistry that can be possibly extended to other reactions occurring in water restricted environments.

The Catalytic Role of the Cl^- anion.

A second issue that needs to be considered is the possible modulation of the affinity between the Cu^{2+} cation and the counter anion Cl^- in the reaction complex R induced by the air/water interface, when compared to bulk water. Many works have indeed pointed to an enhanced ion pairing as well as enrichment of Cl^- at the air/water interface, therefore the presence of the counter-ion within the R complex at the air/water interface cannot be excluded.

We have analyzed the CuCl^- dissociation curve in the two environments by thermodynamic integration and the resulting potential of mean force (PMF) reports a stabilization by 15 kJ/mol for the contact ion pair (CIP) at the air/water interface with respect to bulk wa-

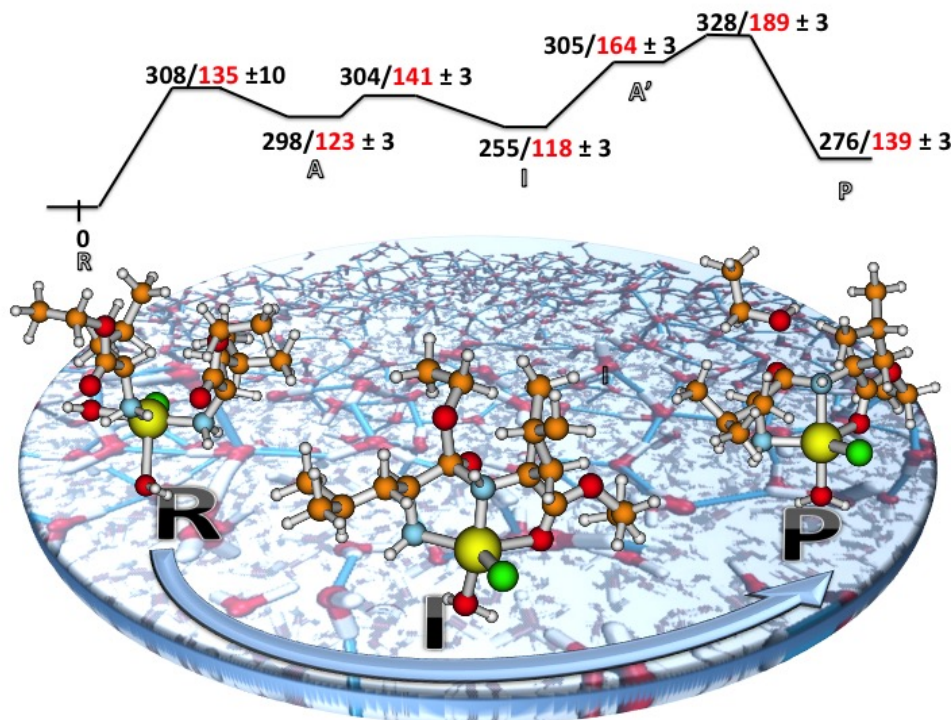


Figure 4: *Peptide bond formation pathway and energetics along the MEP found by biased metadynamics DFT-MD simulations at the air/water interface. Energies are given for the simulation without Cl^- (black) and with Cl^- (red, same values as in Fig. 2c) for the R (reactive) complex at the air/water interface.*

ter. Furthermore a solvent separated ion pair (SSIP) configuration exists at the interface ($\Delta G (G_{SSIP} - G_{CIP}) = 30 \text{ kJ/mol}$) while it is absent in bulk. The presence of the SSIP increases the probability that the dissociated ionic couple forms back at the interface (see S.I. for PMF curves). Such results, together with several experimental and theoretical observations in the literature,^{48,49 50} made us consider that the Cl^- anion is a partner within the reaction complex R at the air/water interface, and made us consider its possible role during the peptide bond formation. Interestingly the presence of the Cl^- in the reactive complex does not affect the stabilization of the R complex conformation at the air/water interface as demonstrated by the free energy curves that are presented in the S.I.

We have therefore studied the role of the Cl^- along the peptide bond condensation reaction at the air/water interface. When the Cl^- is replaced by one water molecule in the reactive

complex R, a more than two-times increase in the free energy barrier of the bottleneck step (Step 1, R→A) is obtained (Fig. 4: see the scheme of the free energy path respectively reporting in black and in red the energetics from the metadynamics without and with the Cl⁻ included in the complex). Such finding thus reveals a strong catalytic effect of the Cl⁻ anion in the rate-determining step of the condensation reaction during the nucleophilic attack of the amine nitrogen onto the ester carbon (R→A in Fig. 2a). We have identified two microscopic reasons for such Cl⁻ catalytic effect: 1) the proximity of the amino acid esters reactive groups, and the energetic stabilization of the transition state (TS) structure associated to the bottleneck step.

As regard proximity, the presence of the Cl⁻ stabilizes a conformation of the R complex where the leucine ethyl esters amine and carboxyl ester groups are in proximity to each other and are optimally oriented for the nucleophilic attack (R→A). When replacing the Cl⁻ by a water molecule in the equilibrium geometry of the R complex, we observe a drastic conformational change (after few ps in all the 6 dynamics performed) that leads the amine and ester groups to be located at a long distance (~ 6 Å) and with a wrong orientation for the nucleophilic attack. In the top of Fig. 5a are shown the two stable R complex conformations observed along our simulations with (left) and without (right) the Cl⁻. The amine nitrogen and the ester oxygen are depicted in pale blue and red balls in the Figure.

In order to show the stability of the two complex conformations we report at the bottom of Fig. 5 their associated free energy profiles along the amine nitrogen-ester carbon intermolecular distance (N-C) and along the C=O \cdots Cu²⁺ coordination number. The two complex conformations differ for the N-C intermolecular distance, i.e. a shift in the minima position along the N-C distance when the Cl⁻ is included (4 Å) or not (6 Å) in the complex is observed in the free energy landscapes. This result is also confirmed by gas-phase optimizations of the reaction complexes at higher levels of theory (B3LYP^{51,52}, PBE0⁵³ and MP2,⁵⁴ see S.I. for details).

A charge population analysis (CHELP,⁵⁵ CHELPG,⁵⁶ MK⁵⁷ see S.I.) sheds light on the ori-

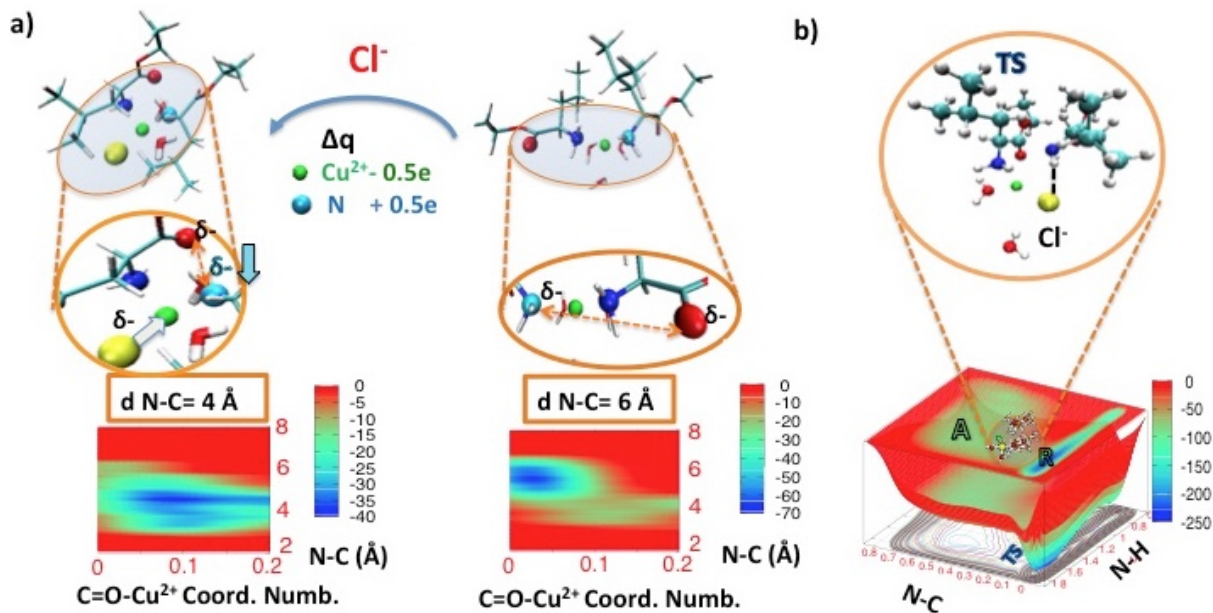


Figure 5: *Panel a) The R complex conformations predicted at the air/water interface by DFT-MD simulations in presence of Cl^- (on the left) and without Cl^- (on the right). Cu^{2+} in green, Cl^- in yellow, oxygen in red, nitrogen in pale blue. Variations in the charge values obtained by CHELPG analysis between the two complexes and the related flux of charge induced by the Cl^- are depicted. At the bottom of the panel, free energy minima along the N-C intermolecular distance (N-C) obtained by metadynamics for the two R complexes with and without the Cl^- in the complex. Panel b) TS structure of the rate determining step of the reaction captured by enhanced sampling DFT based MD simulations. The hydrogen bond between the Cl^- and the nitrogen stabilizes the TS.*

gin of such effect: the amine nitrogen (pale blue ball in Fig. 5a) and the oxygen of the ester group (red ball in Fig. 5a), both strongly negatively charged (δ^-), repel each other, leading to the increase in the N-C distance when the Cl^- is not included in the R complex. Conversely, when the Cl^- (yellow ball in Fig. 5a) is within the R complex, it induces a strong flux of negative charge (grey arrow in Fig. 5 a) to the Cu^{2+} ion (green ball), which in turn causes a decrease on the bonded nitrogen negative charge (pale blue arrow). The charge drop ($-0.5 e$) on the nitrogen hence allows the ester and the amine groups to be in close proximity (4 \AA) and with the optimal orientation for the nucleophilic attack. Such proximity effect driven by the presence of Cl^- leads to a strong decrease of the barrier in the bottleneck step of the condensation reaction ($\text{R} \rightarrow \text{A}$ in Fig. 2) favouring the peptide bond formation.

The second identified catalytic effect is the energetic stabilization of the TS for the bottleneck step of reaction (Fig. 5b). We observe that the amine, during the nucleophilic attack on the ester carbon (R→A), points its N-H (nitrogen in blue) to the Cl⁻ (yellow ball), forming an H-Bond along our enhanced sampling DFT-MD simulations. The strong H-Bond between the amine and the Cl⁻ (Fig. 5b), absent in the reactive complex, stabilizes the TS. Such H-Bond is not replaced by a water H-Bond when the Cl⁻ is not in the reactive complex (R) along our simulations.

It is important to mention here that past experimental works⁵⁸ using copper and amino acids in partially dehydrated conditions with high concentration of sodium chloride (5M) have found the coordination of the Cl⁻ to the Cu(II) in the reaction complex to be an essential feature to make the peptide bond condensation occur. However a mechanistic insight on the reaction was lacking at that time and only a dehydration effect was ascribed to the Cl⁻ to play a role in such reaction.

In the light of our findings it could be an intriguing hypothesis to test a similar role of the Cl⁻ in the bulk of anhydrous solvent where the same peptide bond reaction as studied in this work leads to high yields of polypeptides⁴⁴. In such reactions, the Cl⁻ is assumed to be bonded to the copper ion in the reaction complex, due to the higher stability of CIP in anhydrous solvents with respect to bulk water (lower capacity of anhydrous solvents in separating the ions when they are in a CIP conformation).

The peptide condensation in bulk liquid water

In order to investigate if the two effects revealed in the previous sections (stabilization of the R complex and Cl⁻ catalytic role) are the major factors for the peptide bond condensation formation at the air/water interface, or if a prominent role is also played e.g. by the ‘reactants dehydration’ at the interface, we now turn our attention to bulk water. We have performed metadynamics simulations of the peptide bond condensation reaction in bulk water, imposing the same conditions that we now know to promote the reaction at the air/water interface

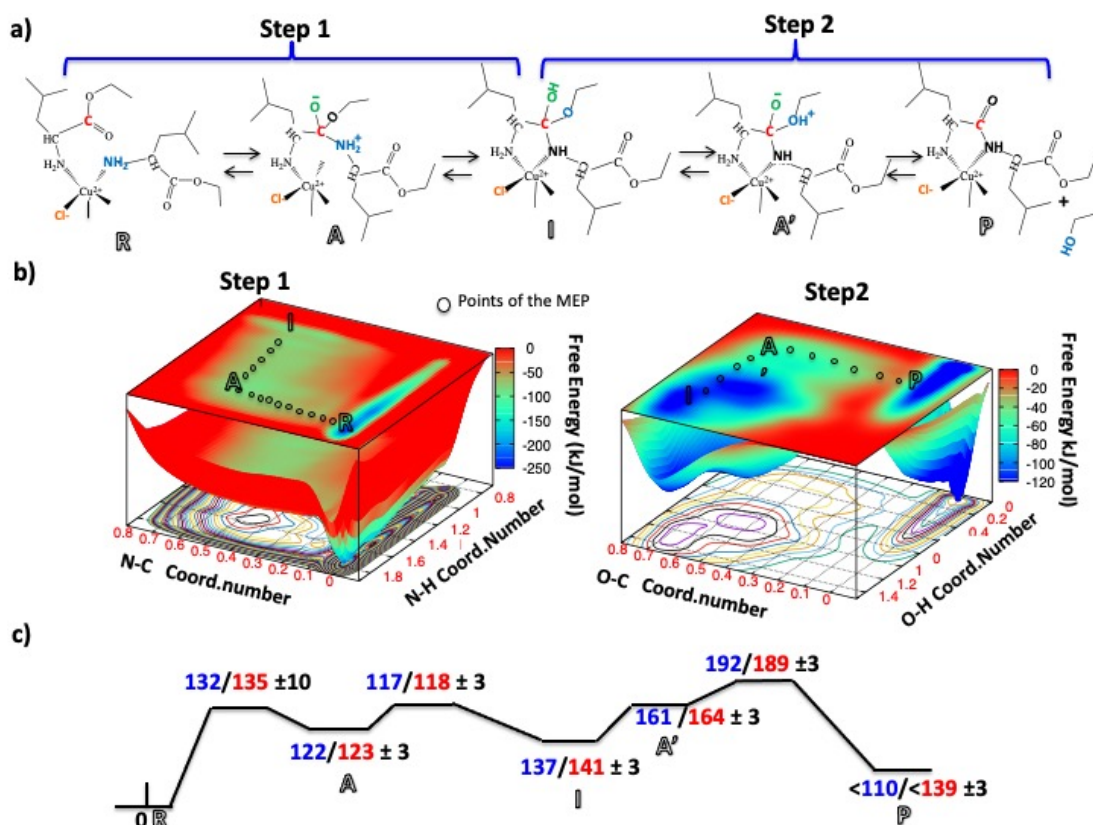


Figure 6: a) Scheme of the mechanisms of reactions obtained by metadynamics for the peptide bond condensation in liquid water. The reactive groups are reported in color for both reactions steps. b) Free energy landscapes and MEPs associated to respectively the tetrahedral intermediate formation (Step 1) and the dipeptide production (Step 2) in bulk water. c) Schemes of the energetics of the reactions obtained by metadynamics for the peptide bond condensation at the air/water interface (red) and in bulk water (blue). The error bars are relative to the metadynamics energetics calculated by using the method of ref.⁴¹.

(Fig. 6). For instance, we have used the R complex (which is not the most stable one in bulk water, see again Fig. 3), we have included the Cl⁻ within it (despite the CIP is more easily broken in the bulk than at the interface). We remind the reader that such conditions are unrealistic in bulk water, but such theoretical approach allows us to directly compare the effects of the two aqueous environments on the mechanisms and energetics of the condensation reaction. In bulk water, a clear positive shift of the position of the minimum for the reactants along the N-H coordination number (Fig. 6a) with respect to the minimum position at the air/interface is observed (Fig. 2a), indicating a larger first solvation shell of

the amine group in bulk water. Nevertheless, we find that the reaction occurs in bulk water with the same mechanisms and similar energetics as the reaction occurring at the air/water interface (the energetics obtained for the reaction in bulk water and at the air/water interface are reported respectively in blue and in red in Fig. 6c). Such result confirms the stabilization of the R complex and the counter ion Cl^- as the two most relevant ingredients provided that the specific interfacial environment provides to synthesize polypeptides.

Conclusions and outlooks

We have provided mechanistic views of the peptide bond condensation reaction at the air/water interface by means of DFT-MD and enhanced sampling DFT-MD simulations, and hence shed light on the interfacial factors that govern the synthesis of polypeptides in a water restricted environment. Comparing the energetics, mechanisms of the reaction, compositions and structures of the reactants at the air/water interface when compared to bulk water, we have identified novel catalytic effects at the interface which are essential in making the reaction occur. We especially find that the air/water interface is stabilizing by a factor of three a reactive complex (R) conformation over a non reactive one (NR), known to be the more stable in bulk water. The reason of the reactive complex stabilization is in the under-coordinated nature of the interfacial water molecules, that enhances the water affinity for the solute, and thus alters the chemical equilibrium between the reactive/non reactive complex at the interface with respect to bulk water.

We have further shown that the catalytic role of the Cl^- counter ion catalytic role is at the heart of the peptide bond condensation reaction at the air/water interface. The presence of the Cl^- in the R complex reduces by a factor of two the barrier of the bottleneck step, hence speeding up the peptide bond condensation reaction. This is achieved in two ways, (I) proximity and good orientation of the substrates for the nucleophilic attack that is in play in the rate determining step, (II) energetic stabilization of the transition state in the slow

step of the reaction because of the formation of a strong H-Bond between the Cl^- and the substrate.

The results presented here highlight the microscopic reasons for the production of polypeptides at the air/water interface and confirm the high feasibility of such reaction at the surface of salty water droplets in oceans in the primitive Earth. The air/water interface provides a unique chemical under-coordinated environment where the peptide bond formation can take place.

An aspect not to be under-evaluated is the possible bridge that the catalytic role of the Cl^- could establish between the peptide bond condensation at the air/water interface, presented in this work, and the "salt induced peptide formation" (SIPF)¹⁵ reaction known in the literature. The SIPF is a chemical route that produces high yields of polypeptides in simple prebiotic-compatible conditions using copper Cu^{2+} and amino acids in a partially dehydrated aqueous environment with high concentrations of NaCl (5M). In this high temperature reaction, a pivotal role is played by the formation of a monochloride copper(II)-amino acid complex, where two amino acids, two water molecules and one Cl^- counter ion are found coordinated in an octahedral geometry around Cu^{2+} . For instance, an essential component of the reaction is the coordination of the Cl^- to the Cu^{2+} in the complex⁵⁸. The presence of the Cl^- within the reactive complex is experimentally indicated by the color of the active solution, i.e. green instead of blue if it contained only copper-amino acid complexes.⁵⁹ In absence of such coordination (other anions than Cl^- were used in the experiments) a dramatic decrease in the polypeptide production is obtained experimentally. However a mechanistic insight into this reaction, able to disentangle all the complex microscopic factors governing the rate of the reaction, was lacking at the time and only a dehydration effect was ascribed to Cl^- .

Our findings can possibly be extended to other water restricted environment chemical processes. For instance, the stabilization of the transition state and the proximity of reactants observed along the peptide formation reaction at the air/water interface in our work, are

two main catalytic effects that have been hypothesized to play a crucial role in the synthesis of polypeptide in the Ribosome Active site⁶⁰.

Methods

All the DFT-MD and the enhanced sampling DFT-MD simulations have been carried out using the CP2K package⁶¹ at the BLYP^{51,62} electronic level of representation and including Grimme D2⁶³ corrections for van der Waals interactions. A combination of GTH pseudo-potentials⁶⁴ and Gaussian Plane Waves basis sets⁶⁵ are used. The DVZP-MOLOPT-SR basis set, augmented with a 400 Ry plane wave basis set are used. The nuclei displacements have been predicted using the classical Newton's equations of motion integrated through the velocity verlet algorithm. The DFT-MD simulations of the reactants, intermediates and product of the peptide bond condensation reaction are done in the NVE ensemble for 25 ps, after a proper equilibration in the NVT ensemble. The liquid Phase is modelled with 554 water molecules and the box dimensions are 24.2 x 24.2 x 45.0 Å³. In order to calculate free energy curves, DFT-MD metadynamics and thermodynamic integration (blue moon ensemble approach)³⁷ methods have been used as implemented in CP2K. The enhanced sampling DFT-MD simulations have been run in the NVT ensemble with a CSVR thermostat⁶⁶ at the target temperature of 300 K. The height (W) and the width of the gaussian hills added along the biased metadynamics are respectively 0.8 kJ/mol and 0.05 (δ_s). The ratio between the gaussian width δ_s and the size S of the reaction space explored δ_s/S is systematically lower than 0.1 for all the metadynamics, as recommended by ref.⁴¹ in order to provide an accurate description of the FES features. In order to avoid the "hill-surfing", as discussed in ref.,⁶⁷ a Gaussian hill is added every time the dynamics explores a spot on the reaction coordinate at a distance $3/2\delta_s$ from the spot where the previous

Gaussian hill was deposited, which means:

$$|s(t) - s(t_i)| = \frac{3}{2}\delta_s \quad (1)$$

where $s(t)$ is the position along the reaction coordinate considered and $s(t_i)$ is the position on the reaction coordinate where the previous Gaussian hill was deposited. It is important to mention that in ref.⁶⁷ the free energy profiles obtained by metadynamics with different protocols against hill surfing are compared with the results obtained by Umbrella Sampling. The best agreement is obtained when using a spatial criteria of $3/2\delta_s$ for the hills deposition, the same criteria adopted in this work. For all the reactive systems (in bulk water and at the interface) we have used multiple interacting metadynamics simulations, called walkers, for exploring and reconstructing the free energy surface for the peptide bond condensation reaction. This is the multiple walker scheme.⁶⁹ See the S.I. for all details.

Our set-up is similar to the one successfully adopted in refs.^{4,6} for the study of peptide bond formation reactions in aqueous solutions under various physical and chemical conditions.

The convergence of the metadynamics was tested with two different methods, respectively for the 1D and 2D free energy profiles (see S.I. for details). The metadynamics were applied on a model system where one leucine ethyl ester is replaced by a methylamine in the reaction complex, so that a smaller box is used (256 water molecules) and thus reduce the computational cost (see S.I. for details). Thermodynamic integration on the "real system" was performed using the points obtained and identified along the minimum energy path (MEP) in the metadynamics in order to refine the energetics of the reaction. The minimum energy path (MEP) on the free energy surface obtained from the metadynamics was identified by the nudged elastic band method.⁶⁸ Seventeen points along the MEP were used for the reaction path discretization in the thermodynamic integration. Ensemble averages were performed at $T = 300$ K from production runs of 15 ps subsequent to 5 ps of equilibration.

The gas phase calculations made on the complexes and on the substrates to obtain ge-

ometries, energies and atomic charges have been performed with the Gaussian 16 software package.⁷⁰

References

- (1) Brack, A. From interstellar amino acids to prebiotic catalytic peptides: a review. *Chemistry & biodiversity* **2007**, *4*, 665–679.
- (2) Forsythe, J. G.; Yu, S.-S.; Mamajanov, I.; Grover, M. A.; Krishnamurthy, R.; Fernández, F. M.; Hud, N. V. Ester-mediated amide bond formation driven by wet–dry cycles: a possible path to polypeptides on the prebiotic Earth. *Angewandte Chemie International Edition* **2015**, *54*, 9871–9875.
- (3) Mamajanov, I.; MacDonald, P. J.; Ying, J.; Duncanson, D. M.; Dowdy, G. R.; Walker, C. A.; Engelhart, A. E.; Fernández, F. M.; Grover, M. A.; Hud, N. V. et al. Ester formation and hydrolysis during wet–dry cycles: generation of far-from-equilibrium polymers in a model prebiotic reaction. *Macromolecules* **2014**, *47*, 1334–1343.
- (4) Schreiner, E.; Nair, N. N.; Marx, D. Influence of extreme thermodynamic conditions and pyrite surfaces on peptide synthesis in aqueous media. *Journal of the American Chemical Society* **2008**, *130*, 2768–2770.
- (5) Lambert, J.-F. Adsorption and polymerization of amino acids on mineral surfaces: a review. *Origins of Life and Evolution of Biospheres* **2008**, *38*, 211–242.
- (6) Schreiner, E.; Nair, N. N.; Wittekindt, C.; Marx, D. Peptide synthesis in aqueous environments: the role of extreme conditions and pyrite mineral surfaces on formation and hydrolysis of peptides. *Journal of the American Chemical Society* **2011**, *133*, 8216–8226.

- (7) Schwendinger, M. G.; Rode, B. M. Salt-induced formation of mixed peptides under possible prebiotic conditions. *Inorganica chimica acta* **1991**, *186*, 247–251.
- (8) Rode, B. M.; Schwendinger, M. G. Copper-catalyzed amino acid condensation in water? a simple possible way of prebiotic peptide formation. *Origins of Life and Evolution of the Biosphere* **1990**, *20*, 401–410.
- (9) Griffith, E. C.; Vaida, V. In situ observation of peptide bond formation at the water–air interface. *Proceedings of the National Academy of Sciences* **2012**, *109*, 15697–15701.
- (10) Griffith, E. C.; Tuck, A. F.; Vaida, V. Ocean–Atmosphere interactions in the emergence of complexity in simple chemical systems. *Accounts of chemical research* **2012**, *45*, 2106–2113.
- (11) Anbar, A. D. Elements and evolution. *Science* **2008**, *322*, 1481–1483.
- (12) Tuck, A. The role of atmospheric aerosols in the origin of life. *Surveys in Geophysics* **2002**, *23*, 379–409.
- (13) Dobson, C. M.; Ellison, G. B.; Tuck, A. F.; Vaida, V. Atmospheric aerosols as prebiotic chemical reactors. *Proceedings of the National Academy of Sciences* **2000**, *97*, 11864–11868.
- (14) Donaldson, D.; Tervahattu, H.; Tuck, A.; Vaida, V. Organic aerosols and the origin of life: An hypothesis. *Origins of Life and Evolution of the Biosphere* **2004**, *34*, 57–67.
- (15) Rode, B. M. Peptides and the origin of life¹. *Peptides* **1999**, *20*, 773–786.
- (16) Cairns-Smith, A. Precambrian solution photochemistry, inverse segregation, and banded iron formations. *Nature* **1978**, *276*, 807.
- (17) CAIRNS-SMITH, A.; Hartman, H. Clay minerals and the origin of life((Book)). *Cambridge and New York, Cambridge University Press, 1986, 204* **1986**,

- (18) Martin, R. B. Free energies and equilibria of peptide bond hydrolysis and formation. *Biopolymers: Original Research on Biomolecules* **1998**, *45*, 351–353.
- (19) Hay, R.; Porter, L.; Morris, P. The basic hydrolysis of amino acid esters. *Aust. J. Chem.* **1966**, *19*, 1197–1205.
- (20) Finlayson-Pitts, B. J. Chlorine chronicles. *Nat. Chem.* **2013**, *5*, 724–724.
- (21) Wingen, L. M.; Moskun, A. C.; Johnson, S. N.; Thomas, J. L.; Roeselova, M.; Tobias, D. J.; Kleinman, M. T.; Finlayson-Pitts, B. J. Enhanced surface photochemistry in chloride-nitrate ion mixtures. *Phys.Chem.Chem.Phys.* **2008**, *10*, 5668–5677.
- (22) Dawson, M.; Varner, M. E.; Perraud, V.; Ezell, M. J.; Gerber, R. B.; Finlayson-Pitts, B. J. Simplified Mechanism for New Particle Formation from Methane Sulfonic Acid, Amines, and Water via Experiments and Ab Initio Calculations. *Proc. Nat. Acad. Sciences* **2012**, *109*, 18719–18724.
- (23) Finlayson-Pitts, B. J. Atmospheric Chemistry. *Proc. Nat. Acad. Sciences* **2012**, *107*, 6566–6567.
- (24) Finlayson-Pitts, B. J.; Pitts, J. N. *Chemistry of the Upper and Lower Atmosphere*; Academic Press, 2000.
- (25) Clifford, D.; Donaldson, D. J. Direct Experimental Evidence for a Heterogeneous Reaction of Ozone with Bromide at the Air- Aqueous Interface. *J. Phys. Chem. A.* **2007**, *111*, 9809–9814.
- (26) Yan, X.; Bain, R. M.; Cooks, R. G. Organic reactions in microdroplets: Reaction acceleration revealed by mass spectrometry. *Angewandte Chemie International Edition* **2016**, *55*, 12960–12972.
- (27) Lee, J. K.; Banerjee, S.; Nam, H. G.; Zare, R. N. Acceleration of reaction in charged microdroplets. *Quarterly reviews of biophysics* **2015**, *48*, 437–444.

- (28) Banerjee, S.; Gnanamani, E.; Yan, X.; Zare, R. N. Can all bulk-phase reactions be accelerated in microdroplets? *Analyst* **2017**, *142*, 1399–1402.
- (29) Zhao, X.; Subrahmanyam, S.; Eisenthal, K. B. Determination of pKa at the air/water interface by second harmonic generation. *Chemical physics letters* **1990**, *171*, 558–562.
- (30) Bianco, R.; Wang, S.; Hynes, J. T. Infrared Signatures of HNO₃ and NO₃ at a Model Aqueous Surface. A Theoretical Study. *J. Phys. Chem. A* **2008**, *112*, 9467–9476.
- (31) Liao, K.; Du, X. In Situ IRRAS Studies of NH Stretching Bands and Molecular Structures of the Monolayers of Amphiphiles Containing Amide and Amine Units at the Air-Water Interface. *The Journal of Physical Chemistry B* **2009**, *113*, 1396–1403.
- (32) Ruiz-Lopez, M. F.; Francisco, J. S.; Martins-Costa, M. T.; Anglada, J. M. Molecular reactions at aqueous interfaces. *Nature Reviews Chemistry* **2020**, 1–17.
- (33) Sutton, P. A.; Buckingham, D. A. Cobalt (III)-promoted hydrolysis of amino acid esters and peptides and the synthesis of small peptides. *Accounts of Chemical Research* **1987**, *20*, 357–364.
- (34) Pantaleone, S.; Ugliengo, P.; Sodupe, M.; Rimola, A. When the Surface Matters: Prebiotic Peptide-Bond Formation on the TiO₂ (101) Anatase Surface through Periodic DFT-D2 Simulations. *Chemistry—A European Journal* **2018**, *24*, 16292–16301.
- (35) Kumar, M.; Zhong, J.; Zeng, X. C.; Francisco, J. S. Reaction of Criegee intermediate with nitric acid at the air–water interface. *Journal of the American Chemical Society* **2018**, *140*, 4913–4921.
- (36) Laio, A.; Parrinello, M. Escaping free-energy minima. *Proceedings of the National Academy of Sciences* **2002**, *99*, 12562–12566.
- (37) Sprik, M.; Ciccotti, G. Free energy from constrained molecular dynamics. *The Journal of chemical physics* **1998**, *109*, 7737–7744.

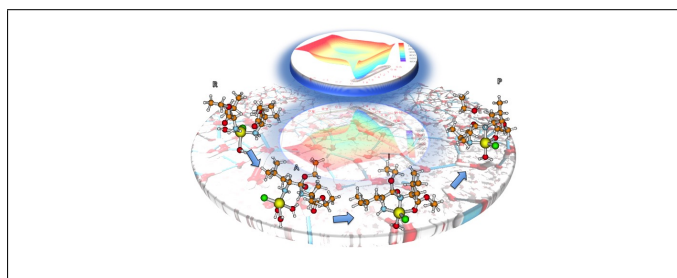
- (38) Pezzotti, S.; Galimberti, D. R.; Gageot, M.-P. 2D H-bond network as the topmost skin to the air–water interface. *The journal of physical chemistry letters* **2017**, *8*, 3133–3141.
- (39) Pezzotti, S.; Galimberti, D. R.; Gageot, M.-P. Deconvolution of BIL-SFG and DL-SFG spectroscopic signals reveals order/disorder of water at the elusive aqueous silica interface. *Phys. Chem. Chem. Phys.* **2019**, *21*, 22188–22202.
- (40) McMurry, J., Susan.McMurry *Study guide and solutions manual, Fundamentals of organic chemistry, seventh edition*; Thomson, 2011.
- (41) Laio, A.; Rodriguez-Forteza, A.; Gervasio, F. L.; Ceccarelli, M.; Parrinello, M. Assessing the accuracy of metadynamics. *The journal of physical chemistry B* **2005**, *109*, 6714–6721.
- (42) Ferus, M.; Pietrucci, F.; Saitta, A. M.; Knížek, A.; Kubelík, P.; Ivanek, O.; Sheshtivska, V.; Civiš, S. Formation of nucleobases in a Miller–Urey reducing atmosphere. *Proceedings of the National Academy of Sciences* **2017**, *114*, 4306–4311.
- (43) Laporte, S.; Pietrucci, F.; Guyot, F.; Saitta, A. M. Formic Acid Synthesis in a Water–Mineral System: Major Role of the Interface. *The Journal of Physical Chemistry C* **2020**, *124*, 5125–5131.
- (44) Wagatsuma, M.; Terashima, S.; Yamada, S. Amino acids and peptides?V: Novel peptide bond formation catalyzed by metal ions?III Elucidation of the formation mechanism. *Tetrahedron* **1973**, *29*, 1497–1502.
- (45) Pezzotti, S.; Galimberti, D. R.; Shen, Y. R.; Gageot, M.-P. Structural definition of the BIL and DL: a new universal methodology to rationalize non-linear $\chi(2)(\omega)$ SFG signals at charged interfaces, including $\chi(3)(\omega)$ contributions. *Phys. Chem. Chem. Phys.* **2018**, *20*, 5190–5199.
- (46) Pezzotti, S.; Serva, A.; Gageot, M.-P. *J. Chem. Phys.* **2018**,

- (47) Hub, J. S.; Caleman, C.; van der Spoel, D. Organic molecules on the surface of water droplets—an energetic perspective. *Phys. Chem. Chem. Phys.* **2012**, *14*, 9537–9545.
- (48) Venkateshwaran, V.; Vembanur, S.; Garde, S. Water-mediated ion–ion interactions are enhanced at the water vapor–liquid interface. *Proceedings of the National Academy of Sciences* **2014**, *111*, 8729–8734.
- (49) Knipping, E.; Lakin, M.; Foster, K.; Jungwirth, P.; Tobias, D.; Gerber, R.; Dabdub, D.; Finlayson-Pitts, B. Experiments and simulations of ion-enhanced interfacial chemistry on aqueous NaCl aerosols. *Science* **2000**, *288*, 301–306.
- (50) Knipping, E. M.; Lakin, M. J.; Foster, K. L.; Jungwirth, P.; Tobias, D. J.; Gerber, R. B.; Dabdub, D.; Finlayson-Pitts, B. J. Experiments and Simulations of Ion-Enhanced Interfacial Chemistry on Aqueous NaCl Aerosols. *Science* **2000**, *288*, 301–306.
- (51) Becke, A. D. Density-Functional Exchange-Energy Approximation with Correct Asymptotic Behavior. *Phys. Rev. A* **1988**, *38*, 3098–3100.
- (52) Stephens, P.; Devlin, F.; Chabalowski, C.; Frisch, M. J. Ab initio calculation of vibrational absorption and circular dichroism spectra using density functional force fields. *The Journal of Physical Chemistry* **1994**, *98*, 11623–11627.
- (53) Adamo, C.; Barone, V. Toward reliable density functional methods without adjustable parameters: The PBE0 model. *The Journal of chemical physics* **1999**, *110*, 6158–6170.
- (54) Møller, C.; Plesset, M. S. Note on an Approximation Treatment for Many-Electron Systems. *Phys. Rev.* **1934**, *46*, 618–622.
- (55) Chirlian, L. E.; Francl, M. M. Atomic charges derived from electrostatic potentials: A detailed study. *Journal of Computational Chemistry* **1987**, *8*, 894–905.

- (56) Breneman, C. M.; Wiberg, K. B. Determining atom-centered monopoles from molecular electrostatic potentials. The need for high sampling density in formamide conformational analysis. *Journal of Computational Chemistry* **1990**, *11*, 361–373.
- (57) Besler, B. H.; Merz Jr, K. M.; Kollman, P. A. Atomic charges derived from semiempirical methods. *Journal of Computational Chemistry* **1990**, *11*, 431–439.
- (58) Rode, B. M.; Suwannachot, Y. The possible role of Cu (II) for the origin of life. *Coordination Chemistry Reviews* **1999**, *190*, 1085–1099.
- (59) Eder, A. H.; Rode, B. M. Influence of alkali-and alkaline-earth-metal cations on the ‘salt-induced peptide formation’ reaction. *Journal of the Chemical Society, Dalton Transactions* **1994**, 1125–1130.
- (60) Nissen, P.; Hansen, J.; Ban, N.; Moore, P. B.; Steitz, T. A. The structural basis of ribosome activity in peptide bond synthesis. *Science* **2000**, *289*, 920–930.
- (61) Hutter, J.; Iannuzzi, M.; Schiffmann, F.; VandeVondele, J. CP2K: Atomistic Simulations of Condensed Matter Systems. *WIREs Comput Mol Sci* **2014**, *4*, 15–25.
- (62) Lee, C.; Yang, W.; Parr, R. G. Development of the Colle-Salvetti Correlation-Energy Formula into a Functional of the Electron Density. *Phys. Rev. B* **1988**, *37*, 785–789.
- (63) Grimme, S.; Antony, J.; Ehrlich, S.; Krieg, H. A consistent and accurate ab initio parametrization of density functional dispersion correction (DFT-D) for the 94 elements H-Pu. *The Journal of chemical physics* **2010**, *132*, 154104.
- (64) Goedecker, S.; Teter, M.; Hutter, J. Separable Dual-Space Gaussian Pseudopotentials. *Phys. Rev. B* **1996**, *54*, 1703–1710.
- (65) VandeVondele, J.; Krack, M.; Mohamed, F.; Parrinello, M.; Chassaing, T.; Hutter, J. Quickstep: Fast and Accurate Density Functional Calculations Using a Mixed Gaussian and Plane Waves Approach. *Comp. Phys. Comm.* **2005**, *167*, 103–128.

- (66) Bussi, G.; Donadio, D.; Parrinello, M. Canonical sampling through velocity rescaling. *J. Chem. Phys.* **2007**, *126*, 014101.
- (67) Ensing, B.; Laio, A.; Parrinello, M.; Klein, M. L. A recipe for the computation of the free energy barrier and the lowest free energy path of concerted reactions. *The journal of physical chemistry B* **2005**, *109*, 6676–6687.
- (68) Jónsson, H.; Mills, G.; Jacobsen, K. W. Nudged elastic band method for finding minimum energy paths of transitions. **1998**,
- (69) Raiteri, P.; Laio, A.; Gervasio, F. L.; Micheletti, C.; Parrinello, M. Efficient reconstruction of complex free energy landscapes by multiple walkers metadynamics. *The journal of physical chemistry B* **2006**, *110*, 3533–3539.
- (70) Frisch, M. J.; Trucks, G. W.; Schlegel, H. B.; Scuseria, G. E.; Robb, M. A.; Cheeseman, J. R.; Scalmani, G.; Barone, V.; Petersson, G. A.; Nakatsuji, H. et al. Gaussian~16 Revision B.01. **2016**, Gaussian Inc. Wallingford CT.

Graphical TOC Entry



Supporting information

Flavio Siro Brigiano,^{*,†} Simone Pezzotti,[†] Daria Ruth Galimberti,[†] Veronica
Vaida,[‡] and Marie-Pierre Gaijeot^{*,†}

[†]*LAMBE CNRS UMR8587, Université d'Evry val d'Essonne, Evry, France & Université
Paris-Saclay, France*

[‡]*Department of Chemistry and Biochemistry and Cooperative Institute for Research in
Environmental Sciences, University of Colorado at Boulder, UCB 215, Boulder, CO 80309*

E-mail: flavio.sirobrigiano@univ-evry.fr; mgaigeot@univ-evry.fr

Computational approach

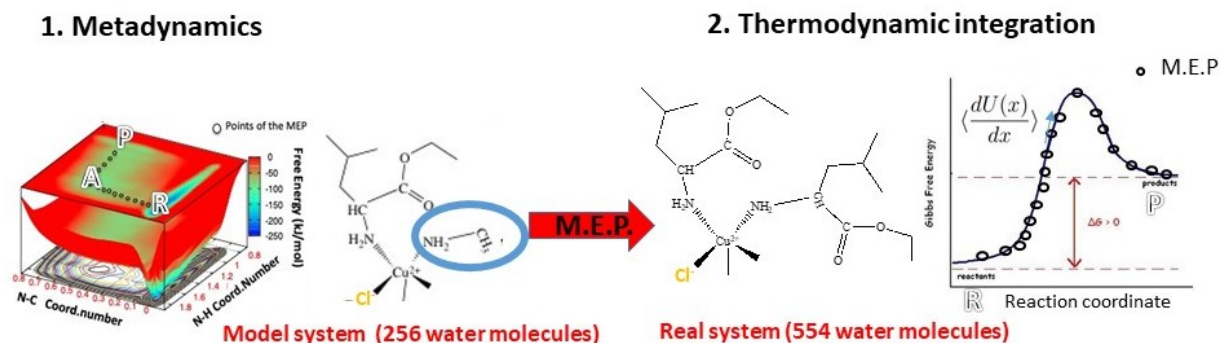


Figure 1: Top: the model reaction with the relative free energy profiles and the minimum energy path (MEP) extrapolated by the free energy surfaces obtained by metadynamics technique. Bottom: of the figure the peptide bond reaction mechanism of the real system simulated by thermodynamic integration (blue moon ensemble¹) technique using the points of the MEP (minimum energy path) extrapolated by the metadynamics on the model system reaction.

All the reactions studied in this work have been simulated by metadynamics on model systems, where one of the two leucine-ethyl esters bounded to the Cu^{2+} have been replaced by a methylamine, CH_3NH_2 . The metadynamics at the air/water interface were performed in a simulation box of dimensions $19.735 \times 19.735 \times 35.0 \text{ \AA}^3$ composed of 256 water molecules where the air is approximated by 10 \AA vacuum. The reactions in bulk water were simulated in a simulation box of dimensions $19.735 \times 19.735 \times 19.735 \text{ \AA}^3$ with 256 water molecules, without vacuum. The PMF (Potential of Mean Force) of the peptide bond condensation reaction at the air/water interface was calculated on the real system (composed by two leucine-ethyl esters coordinated to the Cu^{2+} in an aqueous complex) by thermodynamic integration (blue moon ensemble¹) along the minimum energy path (MEP) extrapolated by the free energy surfaces obtained by metadynamics on the model system reaction, as schematically represented in Fig. 1. For these latter simulations a big simulation box ($24.2 \times 24.2 \times 45 \text{ \AA}^3$) composed by 554 water molecules plus 15 \AA of vacuum has been used.

All the reactants and intermedia of the reactions considered in this work, have been previously equilibrated in the canonical ensemble NVT for 10 ps with a CSVR thermostat² with

a time constant of 50 fs.

All the DFT-MD and enhanced sampling DFT-MD simulations have been carried out using the CP2K package³ at the BLYP⁴⁵ electronic level of representation and including Grimme D2⁶ corrections for van der Waals interactions. A combination of GTH pseudo-potentials⁷ and Gaussian Plane Waves basis sets⁸ are used. The DVZP-MOLOPT-SR basis set, augmented with a 400 Ry plane wave basis set are used. The nuclei displacements have been predicted using the classical Newton’s equations of motion integrated through the velocity verlet algorithm.

Metadynamics

In order to obtain the free energy surfaces underlying the reactions of interest, in solution and at the air/water interface, metadynamics technique has been used as implemented on CP2K software package.³

Our computational approach for the metadynamics is similar to the one successfully adopted in previous works on the study of the peptide bond formation in aqueous media.⁹⁻¹¹ The adopted reaction coordinate $c(A-B)$ is the coordination number¹² between an atom A with respect to a set of atoms B, defined as:

$$c(A - B) = \sum_{I \in B} \frac{1 - (R_{AI}/R_{AB}^0)^6}{1 - (R_{AI}/R_{AB}^0)^{12}} \quad (1)$$

where R_{AI} is the distance between the atom A and atom I belonging to the set of B atoms and R_{AB}^0 is a fixed cutoff parameter based on the bond distance between A and B.

The height of the Gaussian hills added along the biased dynamics has been chosen to be systematically 0.8 kJ/mol. The width of the Gaussian Hills (δ_s) is chosen to be 0.05.

In order to avoid the "hill-surfing", as discussed in ref.,^{9-11,13,14} a Gaussian hill is added every time the dynamics explores a spot on the reaction coordinate at a distance $3/2\delta_s$ from the

spot where the previous Gaussian hill was deposited, which means:

$$|s(t) - s(ti)| = \frac{3}{2}\delta_s \quad (2)$$

where $s(t)$ is the position along the reaction coordinate considered and $s(ti)$ is the position on the reaction coordinate where the previous Gaussian hill was deposited. It is important to mention that in ref.¹³ the free energy profiles obtained by metadynamics with different protocols against hill surfing are compared with the results obtained by Umbrella Sampling. The best agreement is obtained when using a spatial criteria of $3/2\delta_s$ for the hills deposition, the same criteria adopted in this work.

For all the reactive systems (in bulk water and at the interface) we have used multiple interacting metadynamics simulations, called walkers, for exploring and reconstructing the free energy surface for the peptide bond condensation reaction. This is the multiple walker scheme,¹⁵ which scaling is linear with the number of walkers. This allows to use many processors in a massively parallel fashion in order to speed up the free energy sampling. We have systematically located the walkers in different minima of the free energy surface, e.g. the reactant and intermediate/product minima. The walkers were not allowed to sample contemporary the same regions of the free energy surface, once a crossing of the free barrier was observed along the simulation, the metadynamics associated to the walker was stopped. The walkers were allowed to share the biasing potential in each time step of the dynamics. In the case of the tetrahedral intermediate formation (Step 1, Fig.2 in the main text) three multiple walkers have been used, each one located in a minimum of the free energy surface. In the case of the dipeptide and ethanol production (Step 2, Fig.2 in the main text) two multiple walkers, located respectively in the reactant and product minima have been used. The multiple walker scheme was not adopted in the Reactive-Non Reactive complex interconversion reaction (Fig.3 in the main text).

Moreover one wall potential was used in the metadynamics for the first step of the peptide

bond formation reaction (tetrahedral intermediate formation $R \rightarrow A$ in Fig. 2-A of the main text): the wall potential acts for $c(N_{\text{methylamine}} - H) > 1.9$ in order to prevent the formation of the CH_3NH_3^+ species.

In order to show the free-energy convergence criteria adopted in this work, in Fig. 2 we report the time evolution of the free energy profile underlying the interconversion reaction at the air/water interface between the reactive (R) and the non reactive (NR) complex. Once the two energy basins along the reaction coordinates have been explored, the free energy surface is flattened and we reach convergence (purple curve in Fig. 2). In order to further assess the convergence of our metadynamics we continue sampling the flat free energy surface till we recover after 7 ps the converged free energy surface, i.e. the same energy free energy barrier of the converged FES are obtained (75 kJ/mol, see blue curve in Fig. 2).

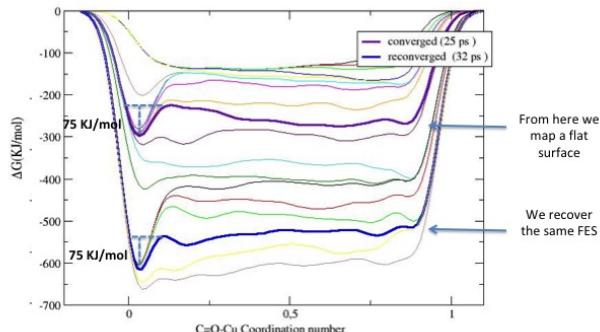
Because of the higher dimensionality of the system the same principle is applied to the 2D FES with the exception that once observing the double crossing of the energetic barrier backward and forward along the same reaction coordinate we report directly the free-energy associated to the barrier.

PMF sampling

In order to refine the energetics of the peptide bond condensation reaction at the air/water interface a thermodynamic integration technique on the real system have been performed. We have used the points along the MEP revealed by metadynamics. Seventeen points along the MEP have been simulated in the NVT ensemble for 15 ps plus 5 ps of equilibration.

The resulting PMF of reaction on the real system shows a good agreement with respect to the energetic obtained by the metadynamics on the model system (see Fig. 2C in the Main Text).

The PMF for the dissociation of the CuCl^- at the air/water interface (blue curve) and in bulk water (red curve) is reported Fig. 3. The dissociation curves were obtained by 15 points



15

Figure 2: *Time evolution of the free energy profile underlying the interconversion reaction between the reactive (R) and non reactive (NR) complex at the air/water interface. After having explored the two basins we map the flat free energy surface until we recover the converged free energy profile.*

each simulated for 15 ps plus 5 ps of equilibration, both in the NVT ensemble.

CuCl⁻ dissociation curve

We have analysed the CuCl⁻ dissociation curve (Fig. 3) in the two aqueous media (air/water interface and bulk water). The resulting potential of mean force (PMF) reports a stabilization by 15 kJ/mol for the contact ion pair (CIP) at the air/water interface with respect to bulk water. Furthermore a solvent separated ion pair (SSIP) configuration exists at the interface ($\Delta G (G_{SSIP} - G_{CIP}) = 30 \text{ kJ/mol}$) while it is absent in bulk. The presence of the SSIP increases the probability that the dissociated ionic couple forms back at the interface (see S.I. for PMF curves).

The CuCl⁻ ion pair has been simulated with boxes composed by 256 water molecules respectively of dimensions 19.735 x 19.735 x 19.735 Å³ for the simulations in bulk water and of 19.735 x 19.735 x 35.0 Å³ at the air/water interface. To ensure the charge neutrality of

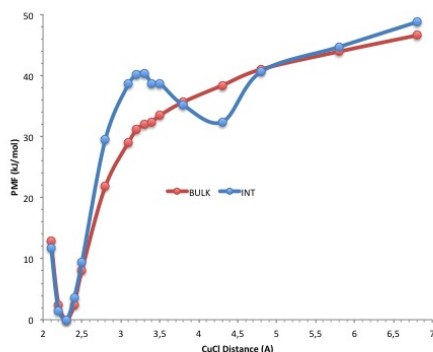


Figure 3: CuCl^- dissociation curves respectively at the air/water interface (blue) and in bulk water (red). The PMF shows a stabilization of 15 kJ/mol for the contact ion pair (CIP) at the air/water interface with respect to bulk water together with the presence of solvent separated ion pair (SSIP) minimum (around 4.4 Å along the $\text{Cu}^{2+} \cdots \text{Cl}^-$ distance) at the interface absent in bulk water

the box a second Cl^- has been placed in the simulation box at least at 7Å from the CuCl^- ion pair for all the simulation time.

Role of the Cl^- in the stabilization of reactive complexes

As reported in the main text when studying the interconversion between the R (reactive) and the NR (non reactive) complexes at the air/water interface and in bulk water, the presence of the Cl^- in the reaction complex doesn't affect the relative stability of the two complexes at the air/water interface. There are not relevant differences in the two converged free energy profiles, as you can observe from the comparison of the free energy curves (Fig. 4) underlying the interconversion reaction between the R to the NR complex at the air/water interface respectively with (red curve) and without (black curve) the Cl^- within the complexes.

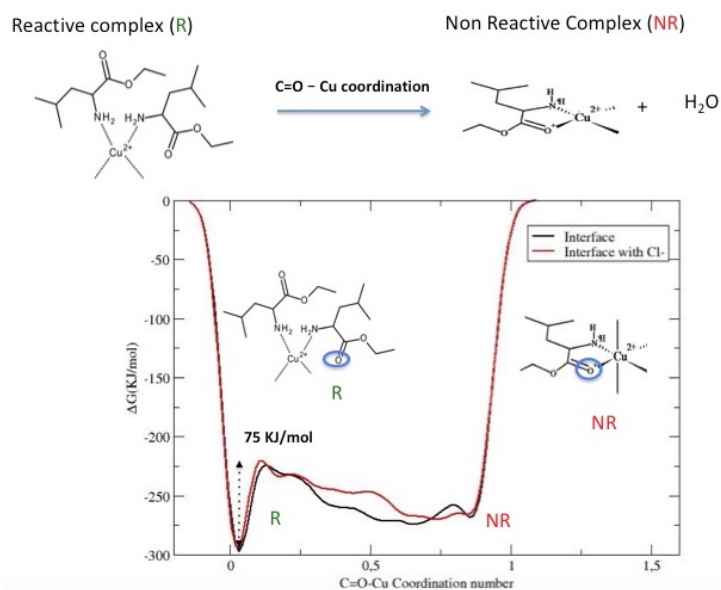


Figure 4: Free energy profiles for the inter-conversion between the R (reactive) and NR (non reactive) complexes at the air/water interface respectively with the Cl^- bonded to the Cu^{2+} (red line) and without (black line), choosing the $\text{C}=\text{O} \cdots \text{Cu}^{2+}$ coordination number as reaction coordinate.

Gas Phase calculations

As reported in the main text the presence of the Cl^- stabilizes a conformation of the R complex where the leucine ethyl ester amine and carboxyl ester groups are in proximity to each other and are optimally oriented for the nucleophilic attack, hence strongly reducing the free energy barrier in the rate determining step of the peptide bond condensation. In Fig. 5 are shown the two stable R complex conformations observed along our simulations with (left) and without (right) the Cl^- . The amine nitrogen and the ester oxygen are depicted in pale blue and red balls in the Figure. The two complexes differ for the amine nitrogen-ester carbon intermolecular distance (N-C distance, the relevant reaction coordinate during the rate determining step in Fig. 2 of the main text). When the Cl^- is replaced by a water molecule in the R complex, the N-C distance increases from 4 Å (Cl^- within the reaction complex) to 6 Å (no Cl^- within the reaction complex).

In order to test the reliability of the results obtained by our dynamics, we have performed

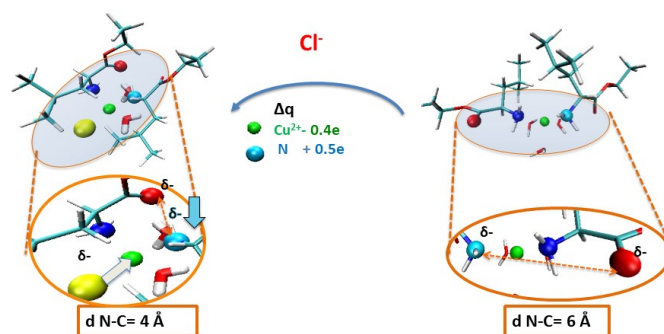


Figure 5: *The conformations obtained at the air/water interface by DFT-MD simulations in presence of Cl^- on the left and without on the right. Cu^{2+} in green, Cl^- in yellow, oxygen in red, nitrogen in pale blue. Variations in charge values obtained by CHELPG analysis between the two complexes and related flux of charge induced by the Cl^- are depicted.*

gas phase geometry optimizations at higher levels of theory for the reactive R (reactive) complexes in presence and in absence of the Cl^- . The DFT gas phase optimizations using BLYP, B3LYP, PBE0 and m06-2x functionals plus GD2 corrections with the 6-311++G(d,p) basis set confirms the results of our dynamics: The conformation that puts in proximity and orients the leu-ethyl esters substrates optimally for the nucleophilic attack (represented in the left of Fig. 5) is found as a stable minima only when the Cl^- is within the R complex. Conversely when the Cl^- is replaced by a water molecule in the complex, the geometry optimization leads to a non-reactive complex structure characterized by a long N-C distance ($\sim 6 \text{ \AA}$).

Charge population analysis (CHELP,¹⁶CHELPG,¹⁷MK¹⁸ adding the constraint of reproducing the overall molecular dipole moment) have been performed on the optimized R complexes structure at the level of theory used for the geometry optimizations plus one MP2 calculation with the 6-311+G(d,p) basis set. All the charge population analysis find the amine nitrogen (pale blue ball in Fig.5) and the oxygen of the ester group (red ball), both strongly

negatively charged (δ^-), repel each other, leading to the strong increase of the N-C distance when the Cl^- is not included in the R complex. On the contrary when the Cl^- (yellow ball Fig.5) is within the R complex, it induces a strong flux of negative charge to the Cu^{2+} ion (green ball), which in turns causes a decrease on the bounded nitrogen negative charge (see table 1 for the comparison of the delta charges obtained by various charge analysis at the DFT and MP2 levels of theory). The charge drop (-0.5 e) on the nitrogen allows the ester and the amine groups to be in close proximity (4 Å) and with the optimal orientation for the nucleophilic attack.

Table 1: Cl^- flux of negative charge calculated by the CHELPG population analysis

	BLYP/6-311++G**	m06-2x/6-311++G**	PBE0/6-311++G**	MP2/6-311+G**
$\Delta Q_{\text{Cu}^{2+}}$	+0.39	+0.33	+0.46	+0.44
ΔQ_N	-0.48	-0.21	-0.56	-0.57

All the gas phase calculations presented in this section were systematically applied on the model and real system finding the same trends. Similar results in terms of structure and atomic charges were obtained including two Cl^- bounded to the Cu^{2+} . All the gas phase calculations were performed by Gaussian09 Software Package.¹⁹

Reaction complexes at the air/water interface

We have characterized the air/water interfaces in the presence of the reaction complexes (R and NR), using our methodology already shown in recent articles^{20,21} that defines binding interfacial layer (BIL) trough three structural descriptors: water density profile, water coordination number and OH orientation analysis.

The interface has been modelled using the instantaneous Willard and Chandler interface.²² The same results in terms of location and water structure at the air/water interface are obtained for the R and NR complexes.

At the bottom of Fig. 6 the water (black curve) and the complexes non polar (light blue) and polar (red, blue, green) groups densities are plotted as a function of the distance from the surface. The distance is defined as positive in the liquid phase and negative in the vapour phase. The first peak in the water density represents the BIL (binding interfacial layer), the first water layer in contact with the air, that is found systematically for all the interfaces analysed to be composed by under-coordinated water molecules with a water-water coordination number (N_{w-w}) of 2.7, as compared to the water-water coordination number of 3.4 in bulk water.

We find the presence of a water 2D-H-Bond-Network structure in the BIL (orange dashed

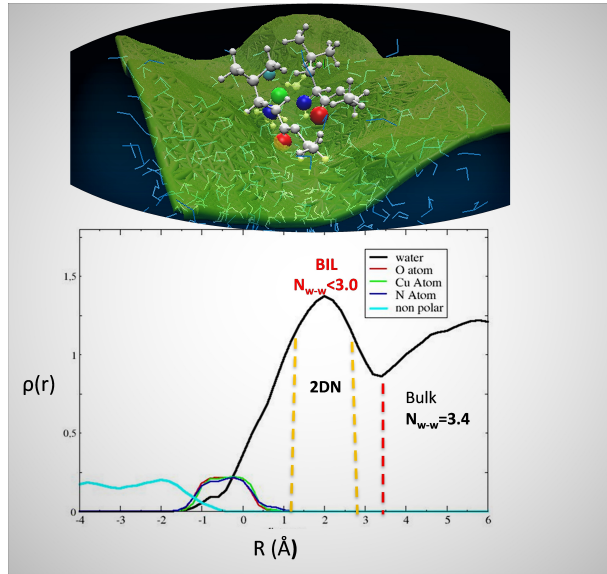


Figure 6: *Top: snapshot of the MD simulation of the R complex surfing on the air/water interface. The non polar groups are in white, the Cu^{2+} in green, the oxygens in red and the nitrogens in blue. The instantaneous interface is depicted in hunter green.*

Bottom: The water (black curve) and the complexes non polar (light blue) and polar groups (Cu^{2+} is in green, the oxygens in red and the nitrogens in blue) densities are plotted as a function of the distance from the instantaneous surface. The water-water coordination number (N_{w-w}) for both the BIL (binding interfacial layer) and the bulk water is reported. The location of the 2D-H-BOND-Network in the BIL is defined by the orange dashed lines

lines in Fig. 6), previously identified and characterized at the neat air/water interface.^{20,21}

At the neat air/water interface, the 2D-H-Bond-Network is composed by under-coordinated

water molecules ($N_{w-w}=3.0$) that maximize the water-water HBs parallel to the surface ($N_{w-w//}=1.7$).

We find the water 2D-H-Bond-Network to be maintained when the reaction complexes are located at the air/water interface. The 2D-H-Bond-Network is located at a distance between 1.2 and 2.8 Å from the instantaneous surface (orange dashed lines in Fig. 6). As in the case of the neat air/water interface the 2D-H-Bond-Network is composed by water molecules with a total water water coordination number $N_{w-w}=3.0$ while a slightly lower number of water-water HBs parallel to the instantaneous surface $N_{w-w//}=1.4$ is registered. Such results point to a weakening of the 2D-H-Bond-Network at the air/water interface when the reaction complexes are located at the interface.

This is also confirmed by the 3D-plots in Fig. 7 where the probability for the water molecules to form HBs with a given O-O distance and given orientation with respect to the normal to the surface is evaluated in the 2D-H-Bond layer respectively in presence (on the left) and in absence of the reaction complex (on the right) at the interface. The results obtained for bulk water are depicted at the bottom of Fig. 7. Comparing the 3D plots of the two 2D-H-Bond Layers we can clearly notice the presence of a maximum at cosine values 0 for both interfaces that indicates a preferential orientation of the water-water HBs parallel to the surface. However we find a maximum centred at a cosine value of -1 when the complex is located at the interface (on the right). This indicates a second preferential orientation of the water OH-O HBs in the 2D-H-Bond Layer, perpendicular to the surface and pointing toward bulk water. The presence of the reaction complexes at the air/water interface induces the re-orientation of a part of the water molecules composing the 2D-H-Bond-Network from a parallel to a perpendicular orientation. This in turn cause a consequent weakening of the interfacial water network. This is coherent with the lowering of $N_{w-w//}$ HBs observed when the reaction complexes are located at the interface.

At the bottom of Fig. 7 we can observe how the water in the bulk differently from the interface forms a homogeneous HB network with 2.7-2.9 Å distances and isotropic orientations in

space (cosines homogeneously distributed from -1 to +1).

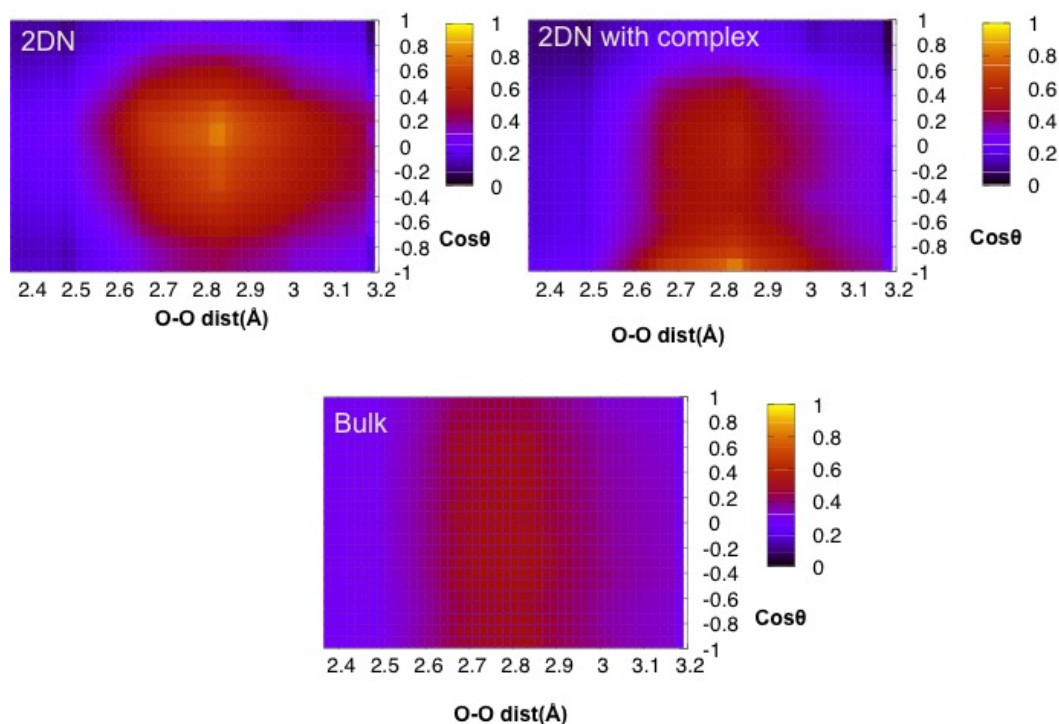


Figure 7: 3D plots of the HB patterns formed between the water molecules located in the 2D-H-Bond-Network (2DN) layers with and without the presence of the reaction complex and in bulk water. The horizontal axis represents the O-O distance (\AA) between two H-bonded water molecules, and the vertical axis provides the angle (cosine value) between the O-O vector (from donor to acceptor) and the normal to the surface (oriented from the liquid to vapor phase). The colors represent the probability to find one O-H group forming one HB with a given distance and orientation. The probability increases from blue to yellow.

The density of polar and non polar groups of the R reaction complex, reported at the bottom of Fig. 6, shows how not only the non polar tails are facing the vacuum but also the polar groups are literally surfing all the time of the dynamics above the 2D-H-Bond-Network. On the top of Fig. 6 is reported a snapshot of the reaction complex R surfing on the air/water interface along the dynamics. The surfing of the polar groups above the air/water interface cause the reaction complexes first solvation shell to be only composed by under coordinated water molecules of the BIL (average N_{w-w} of 2.7).

Table 2: Polar groups first solvation shell

Media	amine	ester	Total(ester+Amine)
Bulk water	4.1	5.8	8.4
Air/water interface	3.3	4.4	5.9

It is important to mention here that the complexes have been introduced in the simulation box with different starting positions from the air/water interface (4.5-6 Å distance from the instantaneous interface, in the bulk). Systematically (8 simulations) we observe the spontaneous diffusion of the species from the bulk to the air/water interface after few ps of equilibration. The complexes stay stables at the air/water interface along all the time of the biased and unbiased simulations (in total 650 ps).

The "surfing" of a series of amphiphile organic compounds at the air-water interface have been previously identified and characterized by biased classical molecular dynamic simulations.²³ The free energy analysis of Hub et al.,²³ based on potential of mean force (PMF) calculations, has revealed an enthalpic effect due to the preservation of water-water interactions at the air-water interface as the main driving force.

The specific location of the reaction complexes at the air/water interface induces a partial dehydration of the polar groups as can be observed comparing the number of water molecules in the polar groups first solvation shell at the air/water interface and in bulk water (table 2). The leucine-ethyl esters and the cation Cu^{2+} have been simulated alone at the air/water interface in order to rationalize how they affect the water structure and the location of the reaction complex at the interface.

When the leucine-ethyl ester amino-acid is simulated alone at the air/water interface, it surfs above the 2D-H-Bond network how can be easily observed by the density of the polar groups with respect to the air/water interface in Fig. 8. Coherently with what seen in the previous sections, the polar groups of the leucine-ethyl ester at the air/water interface result are dehydrated with respect to bulk water.

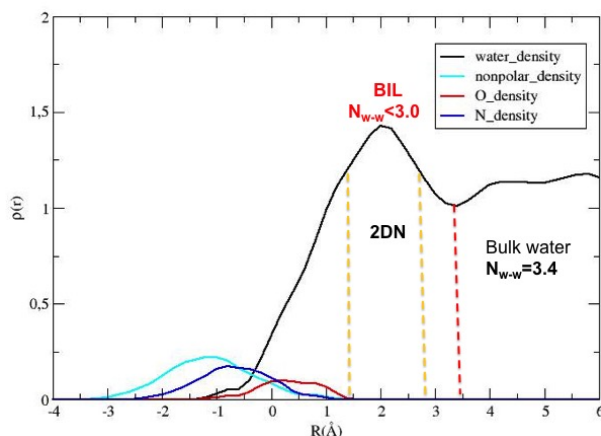


Figure 8: The water (black curve) and the leucine-ethyl ester non polar (light blue) and polar groups (the oxygen in red and the nitrogen in blue) densities are plotted as a function of the distance from the instantaneous surface. The water-water coordination number (N_{w-w}) for both the BIL (binding interfacial layer) and the bulk water is reported respectively in red and in black. The location of the 2D-H-BOND-network in the BIL is defined by the orange dashed lines

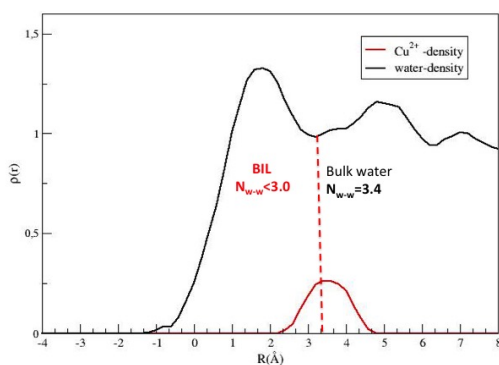


Figure 9: The water (black curve) and Cu^{2+} (red curve) densities are plotted as a function of the distance from the instantaneous surface. The water-water coordination number (N_{w-w}) for both the BIL (binding interfacial layer) and the bulk water is reported.

Contrary the location of the Cu^{2+} at the air/water interface strongly differs from the one observed when within the reaction complexes. As the reader can appreciate from the Cu^{2+} density profile (Fig. 9) its preferential location is at the border between the BIL layer and

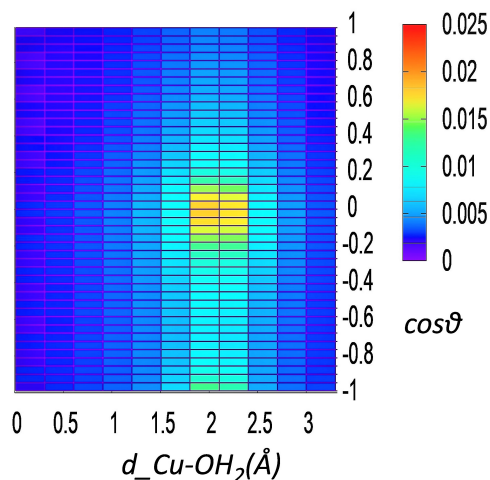


Figure 10: *Combinatorial distribution function (cdf) of the water Cu^{2+} - OH_2 distance (x-axis) and H_2O - Cu^{2+} - OH_2 angle cosine (y-axis) at the air/water interface. You can observe the formation of a square pyramidal copper aqueous complex*

the bulk water. Three different simulations from different starting points lead after few ps of equilibration to the same Cu^{2+} location with respect to the air/water interface. When the Cu^{2+} is simulated within the reaction complexes (R and NR) the location between the BIL and bulk water results to be not stable and it diffuses above the air/water interface after few ps of equilibration.

The Cu^{2+} is found at the air/water interface to form an aqueous complex characterized by a 5-fold coordinated square base pyramidal geometry. In Fig. 10 is mapped the probability for the Cu^{2+} at the air/water interface to be coordinated by a water molecule with a given Cu-O distance and given O-Cu-O angle. The same 5-fold coordinated base square pyramidal geometry is observed when simulating the Cu^{2+} in bulk water. This is in agreement with previous computational and experimental works.^{24,25}

References

- (1) Sprik, M.; Ciccotti, G. Free energy from constrained molecular dynamics. *The Journal of chemical physics* **1998**, *109*, 7737–7744.

- (2) Bussi, G.; Donadio, D.; Parrinello, M. Canonical sampling through velocity rescaling. *The Journal of chemical physics* **2007**, *126*, 014101.
- (3) Hutter, J.; Iannuzzi, M.; Schiffmann, F.; VandeVondele, J. CP2K: Atomistic Simulations of Condensed Matter Systems. *WIREs Comput Mol Sci* **2014**, *4*, 15–25.
- (4) Becke, A. D. Density-Functional Exchange-Energy Approximation with Correct Asymptotic Behavior. *Phys. Rev. A* **1988**, *38*, 3098–3100.
- (5) Lee, C.; Yang, W.; Parr, R. G. Development of the Colle-Salvetti Correlation-Energy Formula into a Functional of the Electron Density. *Phys. Rev. B* **1988**, *37*, 785–789.
- (6) Grimme, S.; Antony, J.; Ehrlich, S.; Krieg, H. A consistent and accurate ab initio parametrization of density functional dispersion correction (DFT-D) for the 94 elements H-Pu. *The Journal of chemical physics* **2010**, *132*, 154104.
- (7) Goedecker, S.; Teter, M.; Hutter, J. Separable Dual-Space Gaussian Pseudopotentials. *Phys. Rev. B* **1996**, *54*, 1703–1710.
- (8) VandeVondele, J.; Krack, M.; Mohamed, F.; Parrinello, M.; Chassaing, T.; Hutter, J. Quickstep: Fast and Accurate Density Functional Calculations Using a Mixed Gaussian and Plane Waves Approach. *Comp. Phys. Comm.* **2005**, *167*, 103–128.
- (9) Schreiner, E.; Nair, N. N.; Marx, D. Influence of extreme thermodynamic conditions and pyrite surfaces on peptide synthesis in aqueous media. *Journal of the American Chemical Society* **2008**, *130*, 2768–2770.
- (10) Schreiner, E.; Nair, N. N.; Wittekindt, C.; Marx, D. Peptide synthesis in aqueous environments: the role of extreme conditions and pyrite mineral surfaces on formation and hydrolysis of peptides. *Journal of the American Chemical Society* **2011**, *133*, 8216–8226.

- (11) Nair, N. N.; Schreiner, E.; Marx, D. Peptide synthesis in aqueous environments: The role of extreme conditions on amino acid activation. *Journal of the American Chemical Society* **2008**, *130*, 14148–14160.
- (12) Sprik, M. Computation of the pK of liquid water using coordination constraints. *Chemical Physics* **2000**, *258*, 139–150.
- (13) Ensing, B.; Laio, A.; Parrinello, M.; Klein, M. L. A recipe for the computation of the free energy barrier and the lowest free energy path of concerted reactions. *The journal of physical chemistry B* **2005**, *109*, 6676–6687.
- (14) Munoz-Santiburcio, D.; Marx, D. Chemistry in nanoconfined water. *Chemical science* **2017**, *8*, 3444–3452.
- (15) Raiteri, P.; Laio, A.; Gervasio, F. L.; Micheletti, C.; Parrinello, M. Efficient reconstruction of complex free energy landscapes by multiple walkers metadynamics. *The journal of physical chemistry B* **2006**, *110*, 3533–3539.
- (16) Chirlian, L. E.; Francl, M. M. Atomic charges derived from electrostatic potentials: A detailed study. *Journal of Computational Chemistry* **1987**, *8*, 894–905.
- (17) Breneman, C. M.; Wiberg, K. B. Determining atom-centered monopoles from molecular electrostatic potentials. The need for high sampling density in formamide conformational analysis. *Journal of Computational Chemistry* **1990**, *11*, 361–373.
- (18) Besler, B. H.; Merz Jr, K. M.; Kollman, P. A. Atomic charges derived from semiempirical methods. *Journal of Computational Chemistry* **1990**, *11*, 431–439.
- (19) Frisch, M. J.; Hratchian, H. P.; Nielsen, A. B. *Gaussian 09: Programmer's Reference*; gaussian, 2009.
- (20) Pezzotti, S.; Galimberti, D. R.; Shen, Y. R.; Gageot, M.-P. Structural definition of the BIL and DL: a new universal methodology to rationalize non-linear $\chi(2)(\omega)$

- SFG signals at charged interfaces, including $\chi^{(3)}$ contributions. *Phys. Chem. Chem. Phys.* **2018**, *20*, 5190–5199.
- (21) Pezzotti, S.; Galimberti, D. R.; Gaigeot, M.-P. 2D H-Bond Network as the Topmost Skin to the Air-Water Interface. *J. Phys. Chem. Lett.* **2017**, *8*, 3133–3141.
- (22) Willard, A.; Chandler, D. Instantaneous Liquid Interfaces. *J. Phys. Chem. B.* **2010**, *114*, 1954–1958.
- (23) Hub, J. S.; Caleman, C.; van der Spoel, D. Organic molecules on the surface of water droplets—an energetic perspective. *Phys. Chem. Chem. Phys.* **2012**, *14*, 9537–9545.
- (24) Pasquarello, A.; Petri, I.; Salmon, P. S.; Parisel, O.; Car, R.; Tóth, É.; Powell, D. H.; Fischer, H. E.; Helm, L.; Merbach, A. E. First solvation shell of the Cu (II) aqua ion: evidence for fivefold coordination. *Science* **2001**, *291*, 856–859.
- (25) Bryantsev, V. S.; Diallo, M. S.; Goddard III, W. A. Computational study of copper (II) complexation and hydrolysis in aqueous solutions using mixed cluster/continuum models. *The Journal of Physical Chemistry A* **2009**, *113*, 9559–9567.

Chapter 4

Stability of neutral and zwitterionic forms of amino acids at the air-water interface

The results reported in this section are preliminary data. Further investigations are needed for complete conclusions.

4.1 Introduction

We have observed in the previous chapter how the peptide bond condensation reaction from amino acid esters catalysed by the CuCl_2 salt at the air-water interface represents a plausible chemical route for the formation of polypeptides on the primordial Earth. Here we move a step further by investigating the possibility that the formation of polypeptides in prebiotic ages has proceeded from amino acids in absence of an inorganic catalyst at the air-water interface.

As already mentioned in chapter 1 the peptide bond condensation reaction is strongly unfavoured in bulk liquid water for both thermodynamic and kinetic reasons. In particular the zwitterionic form of the amino acid in bulk water prevents the nucleophilic attack of the amine group ($-\text{NH}_2$) on the carboxylic carbon ($-\text{COOH}$), thus hindering the peptide bond formation. It follows that a chemical environment able to stabilize the amino acid neutral form instead of the zwitterionic one has to be envisaged in order to rationalize the formation of polypeptides from amino acids in absence of any biological machinery (enzymes).

We have shown in the previous chapter that the air-water interface can offer such a suitable structural environment for the prebiotic synthesis of polypeptides. The next question is whether this is also a chemically favourable environment capable to alter the ionization states of the amino acids. It is known for many other chemical species[[140](#), [141](#), [142](#), [143](#), [144](#), [145](#), [100](#), [146](#), [147](#)] .

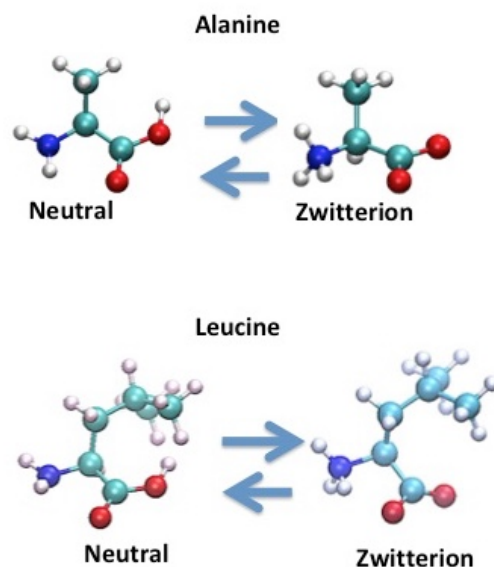


Figure 4.1: Schematic representations of the interconversion from the neutral form to the zwitterionic form for alanine (on the top) and leucine (at the bottom). In red are depicted the oxygen atoms, in blue the nitrogen atoms, in pale blue the carbon atoms, and in white the hydrogen atoms.

Recent works have reported shifts of amino acid ionization states at the air-water interface with respect to bulk water[146, 143, 142]. The direction and intensity of such shifts depend on the nature of the amino acid side chain (as discussed in detail in section 3.1). The interfacial factors proposed to be responsible for these shifts are: 1) the pH condition of the bare air-water interface, known to differ from the one of bulk water [148, 149, 150, 151, 152, 153, 154, 155, 156] and 2) the different water environment experienced by chemical species at the air-water interface[143, 140, 141, 147]. The latter is related to solvation shells at the air-water interface that can strongly differ from the ones in bulk water.

The main goal of this chapter is to understand if the specific chemical environment offered by the air-water interface to amino acids can shift their ionization states toward the neutral form, allowing possibly the peptide bond condensation reaction to occur.

Another point of interest is how the nature of the amino acid side chain modulates the amino acid reactivity at the interface with respect to the bulk. As reported in section 3.1 the stability and reactivity of chemical compounds is modulated by the air-water interface and strongly depends on the solute hydrophilicity. Here, we want to understand if the H-Bond network (water-water H-Bonds) organization at the interface can be affected by the amino acid hydrophobicity and if this effect has a role in the shifts of the amino acid ionization state and reactivity that have been observed experimentally at the air-water interface [146, 143, 142].

To that end, we consider the alanine and the leucine amino acids and

we simulate the reaction of interconversion between their neutral and zwitterionic forms (see Fig. 4.1) either at the air-water interface or in bulk liquid water by biased DFT-MD simulations. The comparison between the reaction mechanisms and energetics at the air-water interface and in bulk water coupled with a detailed analysis of the solvation shell of the species allows us identify and rationalize the stabilities of the neutral and zwitterionic forms of the two considered amino acids at the air-water interface and assess the feasibility of the peptide bond condensation reaction at the interface.

Furthermore the comparison between the reactions for the alanine on the one side and for the leucine on the other side allows us evaluate how the amino acid stability and reactivity are modulated by the air-water interface as a function of the amino acid side chain degree of hydrophobicity (the degree of hydrophobicity increases from alanine to leucine [129]).

4.2 Neutral-zwitterion interconversion: air-water vs bulk water

We have investigated the interconversion between the neutral and zwitterionic forms for leucine and alanine in bulk water as well as at the air-water interface, by means of enhanced sampling DFT-MD metadynamics. We have chosen two coordinates of reaction for the metadynamics: 1) the coordination number of the amino acid nitrogen (there is only one nitrogen per amino acid), with respect to all non-aliphatic hydrogen atoms of the system in order to sample the amine group protonation state. This is denoted N-H coordination number hereafter. 2) the coordination number of the oxygen atom of the amino acid terminal OH group with respect to all the non-aliphatic hydrogen atoms of the system in order to sample the terminal carboxylic group (-COOH) protonation state. This is denoted O-H coordination number hereafter.

The same mechanisms and energetics for the interconversion are obtained for alanine and leucine in bulk water. As reported by the reaction scheme and the associated free energy landscape at the top of Fig. 4.2 the reactions in bulk water proceed from the neutral form (N) to the zwitterionic one (ZW) through a concerted mechanism where there is a simultaneous deprotonation of the carboxylic oxygen and protonation of the amine group mediated by a surrounding water-chain structure (see illustration in Fig. 4.2).

The free energy profile in Fig. 4.2 reveals the zwitterionic form (ZW) to be more stable by about ~ 40 kJ/mol with respect to the neutral form for both the alanine (red values) and the leucine (black values). A free energy barrier of ~ 20 kJ/mol is required for both amino acids in order to convert the neutral form into the zwitterionic form. By contrast, a higher barrier of ~ 65 kJ/mol is obtained for the interconversion of the zwitterionic form into the neutral form of the amino acid.

In agreement with previous theoretical and experimental works [167, 168,

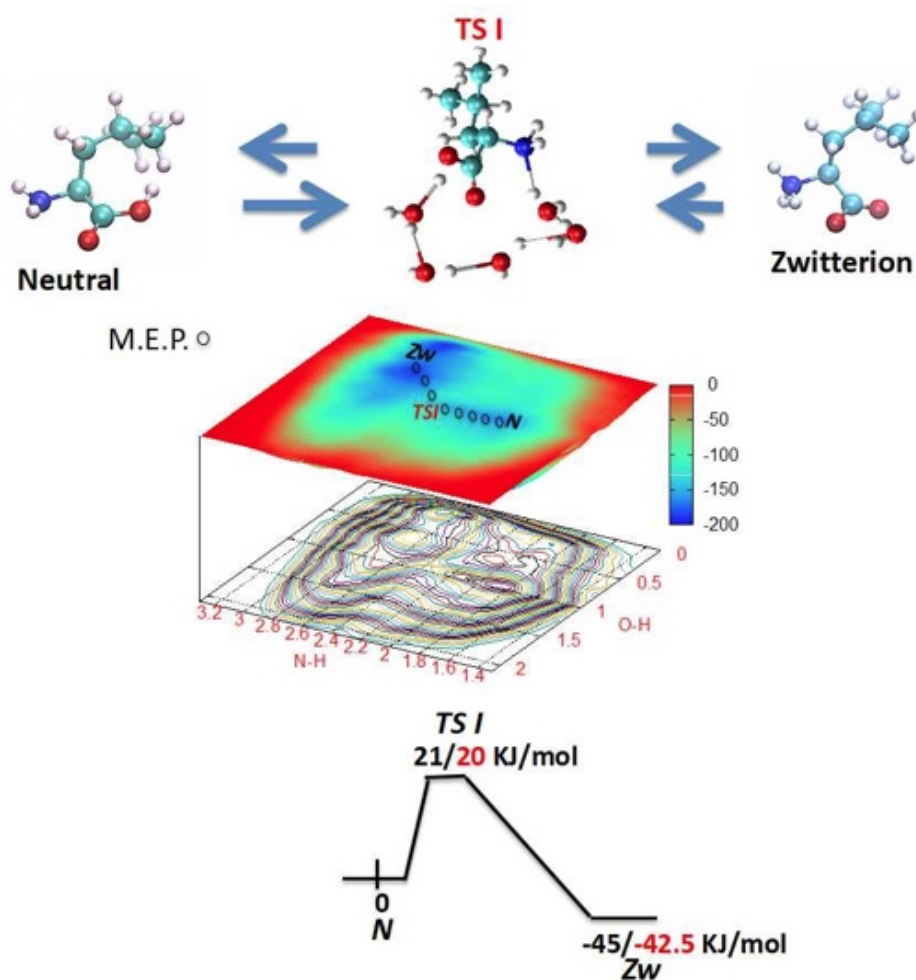


Figure 4.2: *Top: reaction mechanisms observed for the alanine and leucine neutral-zwitterion interconversion in bulk water. Middle: the free-energy landscape and the MEP (minimum energy path) associated with the reaction. Bottom: scheme of the energetics along the MEP for alanine (red) and leucine (black).*

169, 170, 171, 172] our findings reveal a higher thermodynamic and kinetic stability of the zwitterionic form for both alanine and leucine in bulk water.

New reaction pathways, i.e. differing in energetics and mechanisms from the pathway observed in bulk water, emerge when we instead simulate the same interconversion at the air-water interface. As shown from the free energy landscape in Fig. 4.3-A, the alanine neutral-zwitterionic interconversion is characterized by a double stepwise mechanism at the air-water interface. It starts with the deprotonation of the carboxylic oxygen of the neutral alanine (N), leading to the formation of the anion species A^- with a barrier of 21 kJ/mol (see the free energy profile at the bottom of panel A). The reaction then proceeds perpendicularly along the N-H coordination number, with the protonation of the amine group and consequent formation of the zwitterion (ZW) with an energetic cost of 11.8 kJ/mol. The zwitterionic alanine is more stable by 10 kJ/mol than the neutral form at the air-water interface. There-

fore a 32.5 kJ/mol destabilization of the zwitterionic alanine is obtained at the air-water interface with respect to bulk water.

When considering the free energy cost required in order to convert the zwitterion into the neutral form, a lower free energy barrier than the one observed in bulk water is now obtained at the air-water interface: 38.8 kJ/mol at the air-water interface *vs* 65 kJ/mol in bulk water.

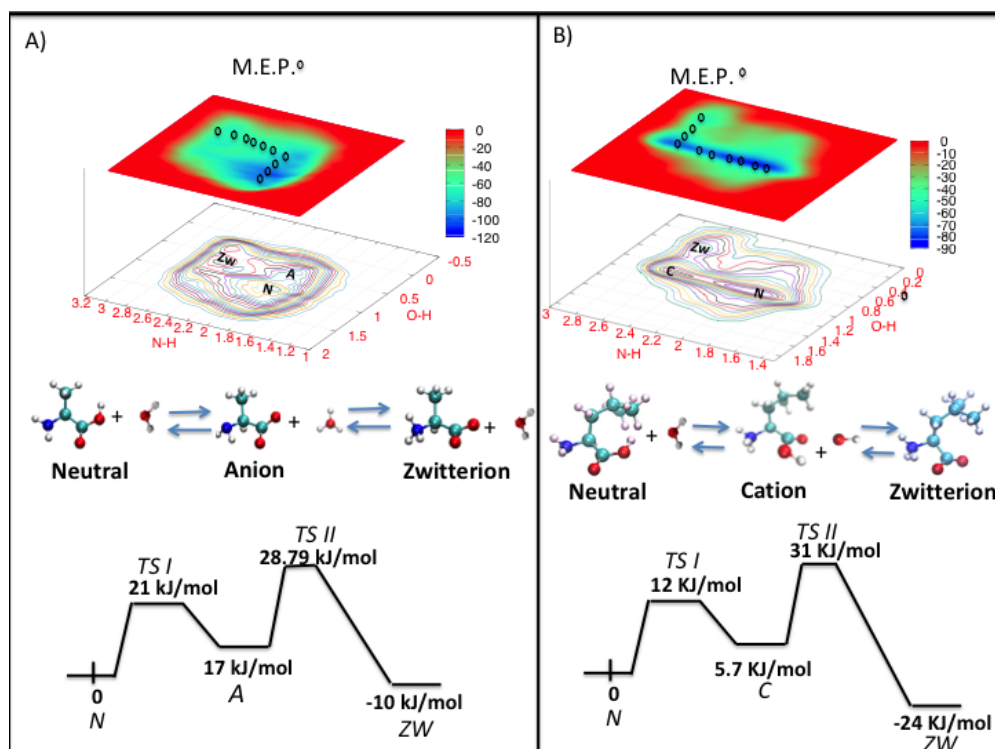


Figure 4.3: A: free-energy landscape and MEP (minimum energy path) associated with the neutral-zwitterion interconversion of alanine at the air-water interface (top). The observed reaction mechanism (middle) and the energetics along the MEP (bottom) are also shown. B: free-energy landscape and MEP associated with the neutral-zwitterion interconversion of leucine at the air-water interface (top). The observed reaction mechanism (middle) and the energetics along the MEP (bottom) are also shown below.

Such findings point to a shift in the ionization state of the alanine at the air-water interface in going from the zwitterionic form to the neutral form of alanine.

Similar trends in terms of energetics, are obtained for leucine at the air-water interface. However the mechanisms are not found identical. The free energy landscape and the reaction scheme (Fig. 4.3-B) reveal the neutral-zwitterion interconversion of leucine to proceed through a double step-wise mechanism at the air-water interface. The formation of the zwitterion starts with the protonation of the neutral leucine (N) amine group and the consequent formation of the leucine cation C^+ , with a free energy barrier of 12 kJ/mol (see the free energy profile at the bottom of Fig. 4.3-B). In a

second step, the deprotonation of the amine leads to the formation of the leucine zwitterion (ZW) with a free energy barrier of 25.3 kJ/mol. The zwitterion leucine at the air-water interface is more stable by 24 kJ/mol than the neutral leucine. As for the alanine, a 20 kJ/mol destabilization of the leucine zwitterionic form is obtained at the air-water interface with respect to bulk water.

When considering the free energy cost required in order to convert the zwitterionic form into the neutral one, a lower free energy barrier is obtained at the air-water interface than in bulk water, i.e. 55 kJ/mol at the air-water interface *vs* 65 kJ/mol in bulk liquid water.

The energetics obtained from our metadynamics reveal a shift of the alanine and leucine amino acids ionization states at the air-water interface toward the neutral form. However for both amino acids, the zwitterionic form remains the most stable at the air-water interface, from both thermodynamic and kinetic points of view.

Despite the capacity of the chemical environment at the air-water interface in shifting the two amino acid ionization states toward their neutral form, such effect cannot explain alone the possible formation of polypeptides from simple amino acids at the air-water interface. Our work allows to discern the effect of the air-water interface environment on the amino acid ionization states from the one due to the specific pH conditions of the air-water interface, known to differ from the one of bulk water [148, 149, 150, 151, 152, 153, 154, 155, 156]. Further studies treating explicitly the effect of the specific air-water interface pH conditions on the stability of neutral/zwitterionic forms of alanine and leucine amino acids are needed in order to gain a full view on the feasibility of the prebiotic amino acid condensation reaction to occur at the air-water interface.

4.3 Concerted mechanism in bulk water *vs* two step mechanism at the air-water interface

Our metadynamics reveal the neutral-zwitterion interconversion for both the alanine and the leucine amino acids in bulk water to be achieved through a concerted mechanism, while a two-step mechanism is obtained for the reaction at the air-water interface.

In order to gain a deeper insight into these behaviours we have calculated the probability to form water wires connecting the amino acid carboxyl and amine groups (panel A of Fig. 4.4) in bulk water and at the air-water interface along our molecular dynamics simulations (for a total of four trajectories composed of 10 ps of equilibration in the NVT ensemble + 15 ps in the NVE ensemble, two trajectories in liquid water, two at the air-water interface).

Panel B of Fig. 4.4 reports the probability to find the amine and the

4.3 Concerted mechanism in bulk water vs two step mechanism at the air-water interface

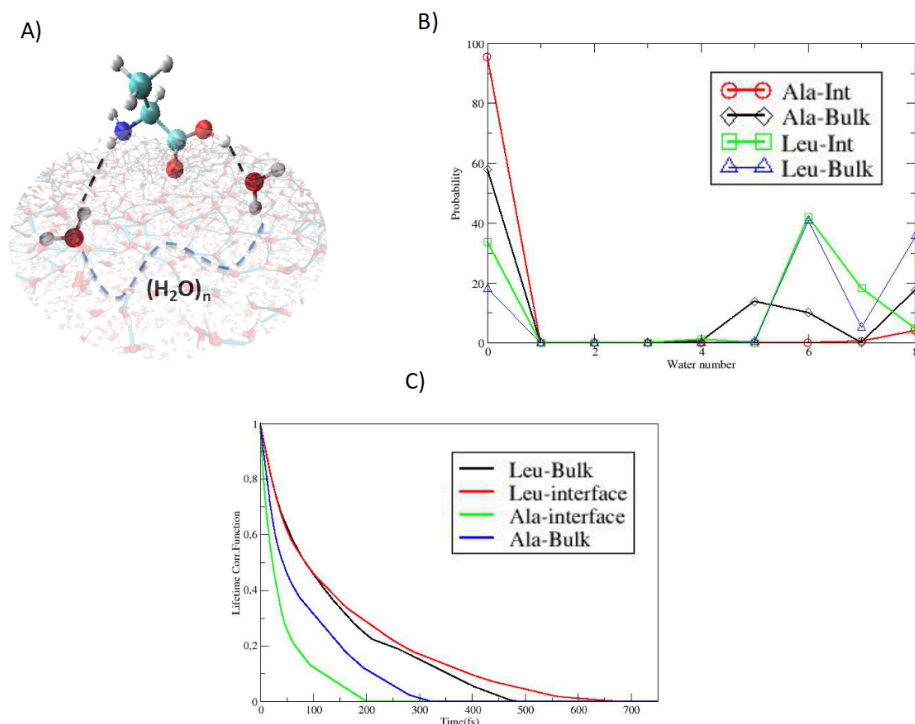


Figure 4.4: *Panel A: Schematic representation of a wire structure formed between polar groups of the amino acid and the water molecules at the air-water interface. Panel B: The probability of existence of wires as a function of the number of water molecules in the wire. The probability for the alanine is reported respectively in red at the air-water interface (circles) and in black in the bulk liquid water (diamonds). The probability for the leucine is reported respectively in green at the air-water interface (square) and in blue in the bulk (triangles). Panel C: The correlation functions of the wires observed along the molecular dynamics (MD). The wires for alanine are depicted respectively in green at the air-water interface and in blue in the bulk. The ones for leucine are depicted respectively in red at the air-water interface and in black in the bulk.*

carboxylic amino acid groups involved in a amino acid-water chain structure with a variable number of water molecules, comparing the air-water interface with bulk water. The probability is determined by the percentage of time along the dynamics that a water wire composed by a given number of water molecules ($(\text{H}_2\text{O})_n$ in Fig. 4.4) can connect the amino acid carboxylic group to the amine group. Only the water wires that connect the two functions with the lowest number of water molecules are taken into account, at each time step. At the air-water interface, the alanine (red line) is less involved in wires than when it is located in bulk water (black line). The percentage of time the two amino acid functions are not connected by any water wire along the dynamics is given by the probability to find a water chain with zero water molecules in Fig. 4.4-B. Wires with 5, 6 and 8 water molecules are identified in bulk water while, at the air-water interface, they are hardly seen (i.e. wires with 8 water molecules are observed for solely 5 % of the dynamics at the interface). The alanine is found never involved in any wire over 95 % of the dynamics at the air-water, while it is observed for 59% of the time when the

amino acid is located in bulk water (see the probability for water number=0 reported in Fig. 4.4-B).

Interestingly, the leucine at the air-water interface is less involved in wires when it is located at the air-water interface than when it is located in bulk water, see the probability for water number=0 reported in Fig. 4.4-B (values are: ~ 40 for green (Leu interface) and ~ 20 for blue (Leu bulk)). For instance the leucine is not involved in wire structures for 33 % of the time at the air-water interface while it is for 18% in bulk water. When wires exist for Leu, they are of larger size at the air-water interface (centred on $N_w=8$) than in the bulk (N_w centred at ~ 7). However the integration of the two peaks shows a larger value for Leu at the air-water interface.

The low probability for both amino acids to form wires with water at the air-water interface induces a lower connectivity between the amine and carboxylic amino acid functions, that in turn prevents a systematic concerted mechanism for the neutral-zwitterion interconversion at the interface. Our calculations reveal a lower capability of the polar groups of both amino acids at the air-water interface in being connected by water wires with respect to the situation in bulk liquid water.

We have then investigated the dynamics of the most probable wires (maxima in Panel B) for both amino acids in both aqueous environments by computing the correlation function $C(\Delta t)$ that measures the life time of the wires over time (over the trajectory). The correlation function $C(\Delta t)$ of wires is defined by:

$$\langle C(\Delta t) \rangle = \frac{\langle [h(t)h(t + \Delta t)] \rangle}{\langle h(t)h(t) \rangle} \quad (4.1)$$

where $[h(t)h(t+\Delta t)]$ is 1 if the loop is continuously formed between t and $t+\Delta t$, and 0 otherwise.

In panel C of Fig. 4.4, we report these correlation functions for the wire structures of the alanine at the interface (blue) and in bulk water (green), for leucine at the interface (red) and in bulk water (black). The life-time of these wires is found on the order of few hundreds of femto seconds. The decay rates for leucine is roughly identical whether the amino acid is located at the air-water interface (red) or in bulk water (black). Conversely the alanine is found to form far less stable wires at the air-water interface than in bulk water.

Interestingly, our structural and dynamical analyses thus reveal a different connectivity with surrounding water for leucine and alanine at the air-water interface. In particular higher numbers of stable wires (panels B + C) are preferentially found for leucine at the air-water interface. Those findings reveal a distinct water wire connectivity of the two amino acids at the air-water interface, that in the next section we will try to put in relation with the two different mechanisms of reactions observed for the alanine and the leucine at the air-water interface.

4.4 The alanine dance at the air-water interface makes the difference

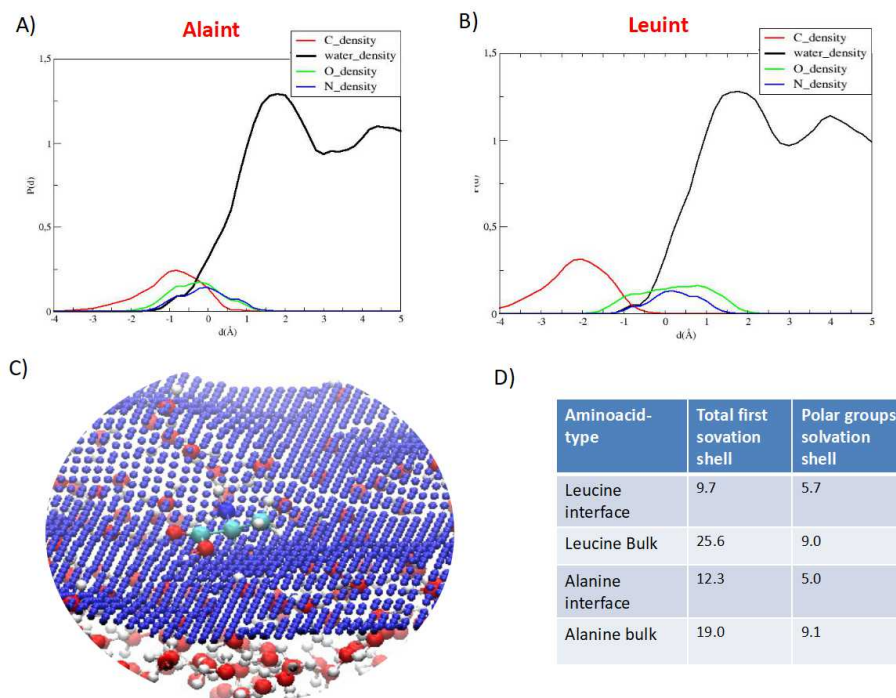


Figure 4.5: *Panel A: Density profiles for water (black curve), alanine non polar (red) and polar groups (the oxygens in green and the nitrogen in blue) plotted as a function of the distance from the surface. Panel B: Density profiles for water (black curve), leucine non polar (red) and polar groups (the oxygens in green and the nitrogen in blue) plotted as a function of the distance from the surface. Panel C: Snapshot of the alanine surfing on top of the air-water interface (surface defined by the blue points). The oxygen atoms are depicted in red, the nitrogens in blue, the hydrogens in white and the carbons in light blue. Panel D: Number of water molecules in the solvation shells of the amino acids and in the ones of their polar groups only. Liquid water and air-water are compared.*

As already discussed, our metadynamics show two distinct reactivities for the alanine and leucine at the air-water interface in terms of neutral-zwitterion conversion. In particular the neutral alanine (N) converts into the zwitterion (ZW) through the formation of an anionic intermediate (A^-) (anion reaction channel) while the reaction for the leucine proceeds through a cation intermediate (C^+) (cation reaction channel).

In order to rationalize these two behaviours we have investigated the location and solvation properties of the two amino acids at the air-water interface. In Fig. 4.5 the density profile of the water molecules (black curve) and the amino acid non polar (light blue) and polar groups (red, blue, green) are plotted as a function of the distance from the instantaneous surface of Willard and Chandler [173] (that serves to define the air-water interface, see ref.[48]) for respectively the alanine (panel A) and the leucine (panel B).

As one can see from the density profiles, not only the non-polar tails of

both amino acids are facing the vacuum but also the polar groups are literally ‘surfing’ on top of the water surface (see snapshot in panel C of Fig. 4.5 for an illustration). Such behaviour is reflected by the number of water molecules in the polar groups solvation shell (panel D) found systematically lower for both amino acids at the air-water interface than in bulk liquid water.

The “surfing” of a series of amphiphile organic compounds at the air-water interface has been previously identified and characterized by biased classical molecular dynamics simulations [174]. The free energy analysis of Hub *et al.*[174], based on potential of mean force (PMF) calculations, has typically revealed an enthalpic effect, due to the preservation of water-water interactions at the air-water interface as the main driving force. Coherently, we find the same averaged water-water coordination number (3.0) at the air-water interface in presence and in absence of the amino acids. Such result indicates the “surfing” of both leucine and alanine amino acids to not alter the “pristine” air-water interface structure, previously characterized by our group in ref.[48] as a special 2D-HBond-Network organization.

An interesting aspect that could be useful in order to understand the observed difference in the wires connectivity and N-ZW conversion between the two amino acids investigated here at the interface is the degree of hydration of the non-polar tails. Comparing the number of water molecules in the amino acid first solvation shells (Fig. 4.5 panel D), one can see that the alanine apolar tail is now found immersed in water with a higher probability with respect to the leucine one. Also the density profiles (panels A and B) show the alanine non-polar group to penetrate deeper (panel A, red curve) into the aqueous phase when compared to the leucine one (panel B, red curve).

Such differences are easily rationalized considering the orientation of the two amino acids non-polar tails at the air-water interface: the neutral leucine non-polar tail is oriented out of the liquid phase for all the time of the dynamics, while the alanine tail is found to continuously oscillate between the air and the water phases.

In order to explore the orientation of the non-polar groups at the air-water interface in more details, we report in panel A of Fig. 4.6 the distribution of the angle between the interface normal (z-axis) and the molecular vector $C1 \rightarrow C2$ pointing from the C1 atom to the carbon atom C2 of the terminal alkyl group, for both amino acids.

The orientation analysis reports the leucine non-polar tail (black curve) to point all the time out of the water phase with an orientation of 30° with respect to the z-axis. Conversely the alanine non polar tail is found without a preferential orientation, with the -CH₃ group continuously pointing in and out of the liquid phase all along the dynamics. Our simulations predict a clear effect of the chain length on the dynamics of the amino acids at the air-water interface.

Those findings are in agreement with a previous theoretical work based on classical molecular dynamics simulations of a class of amphiphile compounds (n-alkyl halides) [175] at the air-water interface. Habartova *et al.*

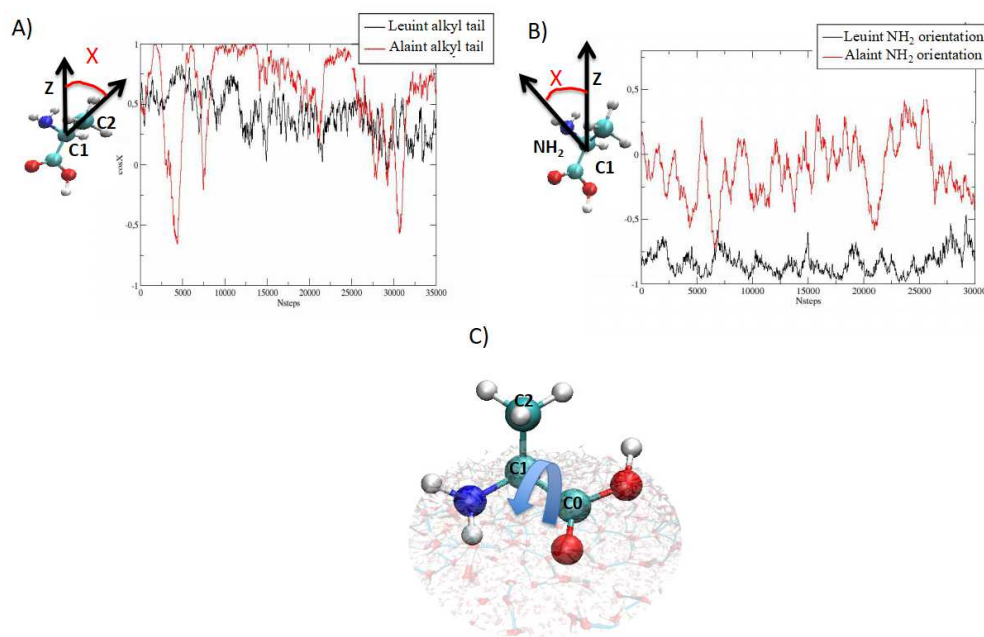


Figure 4.6: *Panel A: We consider the alanine (red curve) and the leucine (black curve) non polar groups orientations with respect to the air-water interface by reporting the distribution of $\cos(X)$ where X is the angle between the interface normal (z -axis, oriented toward the air phase) and the molecular vector $C1 \rightarrow C2$ pointing from the $C1$ atom to the carbon atom $C2$ of the terminal alkyl group (last $-CH_3$ group of the non polar tail). Panel B: We consider the alanine (red curve) and the leucine (black curve) amine groups orientations with respect to the air-water interface by reporting the distribution of $\cos(X)$, where X is the angle between the interface normal (z -axis) and the molecular vector $C1 \rightarrow NH_2$ pointing from the $C1$ atom to the nitrogen atom of the terminal amine group (NH_2). Panel C: Schematic representation of the Alanine "dance" at the air-water interface. The alanine is found to rotate with its $-CH_3$ and $-NH_2$ groups around the $C1-C0$ covalent bond along all the time of the dynamics. The data reported in this figure are obtained by the analysis of the DFT-MD metadynamics trajectories of respectively the neutral alanine and the neutral leucine at the air-water interface.*

[175] have shown how the amphiphiles orientations at the air-water interface is modulated by the non-polar tail chain length: 1) Amphiphile species with short chain lengths (as the alanine) are systematically found to "dance" on the air-water interface, pointing their non polar tails in and out of the water phase (as found here in the case of alanine). 2) Amphiphile species with long chain lengths (as leucine) are found aligned perpendicularly to the air-water interface, facing away from water into the gas phase.

We have then investigated if the alanine "dance" on the water surface is at the origin of the distinct reaction channels of interconversion observed for the two amino acids at the air-water interface, by considering its effect on the polar groups orientation and solvation properties. In panel B of Fig. 4.6 are

reported the alanine and leucine amine groups orientations at the air-water interface. The leucine amine group (black curve) is found steadily pointing toward the water phase along all the time of the dynamics ($\cos(X)=-1$), while the alanine amine group (red curve) does not present any preferential location and is found to oscillate between the water and the vapor phase for all the length of the trajectory.

Our orientation analyses and the observations from the dynamics reveal the neutral alanine "dance" at the air-water interface to be characterized by a continuous rotation of the -CH₃ and -NH₂ groups around the C0-C1 covalent bond (see panel C of Fig. 4.6), leading to variations in the water exposition of the two groups at the air-water interface.

The neutral alanine "dance" on the water surface explains the lower capability of the alanine at the interface in forming less stable wires with water than leucine (panel C of Fig. 4.4).

The amine groups dynamical behaviours induce two distinct H-Bond connectivity with water for alanine and leucine. Along the metadynamic simulations the leucine amine group is found two times more H-Bonded to water molecules with respect to the alanine one (1.0 HB for the leucine *vs* 0.5 HB for the alanine). Such effect can also be appreciated by the comparison of the neutral amino acid free energy profiles reported along the N-H coordination number with water in panel A of Fig. 4.7. The neutral alanine free energy well is characterized by a sharp peak with the minimum located between 1.8 and 1.9 along the N-H coordination number while the leucine amine group is more hydrated with a broader free energy well with a minimum located between 1.8 and 2.2.

The minima positions, the free energy wells' shapes and the H-Bond connectivities reveal a smaller and weaker solvation shell of the alanine amine groups with respect to the leucine one at the air-water interface.

Following such findings, we have studied the interconversion between the neutral and the cation amino acid forms at the air-water interface for both amino acids. Our intent is to understand if the lower H-Bond connectivity of the alanine amine group destabilizes the formation of the NH₃⁺ group at the interface, favouring the "anion" reaction channel over the "cation" one in the zwitterionic formation (see free energy landscapes in Fig. 4.3). We report in panel B of Fig. 4.7 the energy profiles along the N-H coordination number for the interconversion reaction between the neutral and cation forms of both amino acids. The free energy profiles report a barrier of ~ 24 kJ/mol in order to convert the neutral alanine (N) into the cation intermediate (C⁺) while a ~ 12 kJ/mol barrier is obtained for leucine. The lower hydrogen bond connectivity experienced by the alanine amine group seems to hinder its protonation at the air-water interface, inducing the presence of a high energetic barrier. Furthermore the alanine cation intermediate (C⁺) is less stable than at the air-water interface than for leucine (i.e. 5.7 kJ/mol for leucine *vs* 19 kJ/mol for alanine). Also in this case the perturbation of the ammonium group (NH₃⁺) solvation shell induced by the alanine dance leads to a destabi-

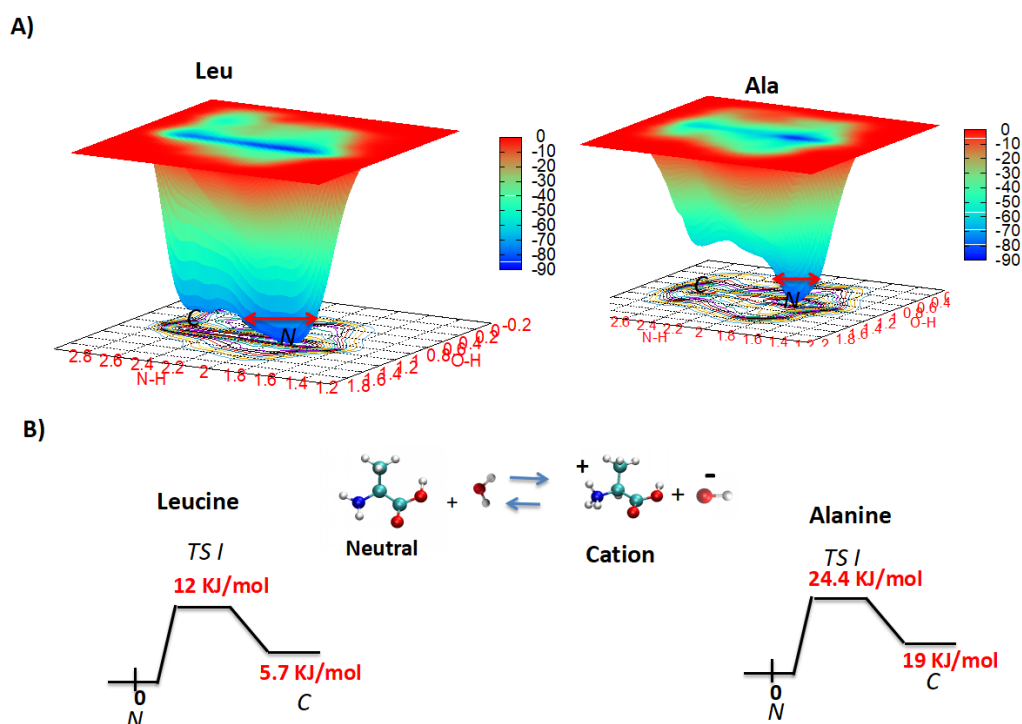


Figure 4.7: Panel A: Free energy profiles of the leucine and alanine depicted along the N-H coordination number (defined as the coordination of the amino acid nitrogen with respect to all non-aliphatic hydrogen atoms of the system) and the O-H coordination number (defined as the coordination number of the oxygen atom of the amino acid terminal OH group with respect to all the non-aliphatic hydrogen atoms of the system). Panel B: Free energy profiles with their associated reaction schemes for the neutral-cation interconversion of leucine and alanine at the air-water interface.

lization of the alanine cation intermediate (C^+).

Beyond that, our metadynamics calculations show an enormous barrier in order to convert the alanine cation intermediate into the zwitterionic form of the amino acid (>50 kJ/mol, cation channel) while a lower barrier (11.8 kJ/mol) is required in order to convert the anionic form of alanine into its zwitterionic form (anion channel). The origin of the lower energy barrier in the alanine anion-zwitterion interconversion is possibly explained by considering the alanine orientation at the air-water interface when it evolves into the anion form along the metadynamics: the alanine "stops dancing", the $-CH_3$ group is found steadily pointing into the vacuum while the amine group is immersed in water with both its hydrogens pointing toward water molecules. Such change in orientation for the anionic alanine induces an increase in the number of water-amine H-Bonds along the dynamics, that goes up from 0.5 to 1.0. The increase in the water H-Bond connectivity leads the anion amine group to be easily protonated by water, with a consequent lowering of the free energy barrier for its conversion into the zwitterionic form. It follows that for the alanine at the air-water interface, the "anion channel" is more

favourable with respect to the "cation" one.

Our data suggest the different H-Bond connectivity of alanine and leucine with water at the air-water interface, that result from the different dynamical behaviours of the non-polar and polar groups of the two amino acids at the boundary between the water and the air, to be at the origin of the two distinct mechanisms of interconversion.

Chapter 5

Structural and spectroscopic characterization of the amorphous silica-water interface

The main goal of this chapter is to provide a global understanding of the silica-water interface organization under various solution and surface conditions. The first sections (sections 5.1, 5.2, 5.3 and 5.4) are a state-of-the-art report where the recent improvements in the knowledge of silica-water interfaces from experimental and computational works are presented. These works show how the dynamics, the structure and the reactivity of the interface species (both from the liquid and the solid sides) are strongly modulated by the silica surface hydrophilic character and morphology (see section 5.2) and the electrolytes concentration (see section 5.3). However the inhomogeneous degree of hydroxylation and the heterogeneous chemistry of the amorphous silica surface in contact with water make the interfacial organization both on the water and solid sides far to be understood.

The second part of the chapter reports my DFT-MD works that provide a microscopical characterization of the amorphous silica-water interface in response to the variations in the hydrophilic character of the silica surface at the interface with liquid water (see sections 5.6 and 5.7), in response to the variations in the surface morphology (see section 5.8) and in response to the electrolytes concentration (see section 5.9).

We report in section 5.1 a general description of the silica surface species (silanols, silanolates, siloxane bridges), known from the literature to be present at the amorphous silica-water interfaces. The experimental knowledge in the composition (i.e. the nature of the surface species), the degree of hydroxylation and the protonation states of the silica surface as a function of the temperature used for the pretreatment of the surface or the solution pH conditions is reported[176, 177, 178]. This knowledge is essential in order to mimic in our simulations the "right" surface composition, degree of hydroxylation

and protonation states for a given pH condition.

Sections 5.2 and 5.3 are a state-of-the-art presentation of computational and experimental works that reveal the effects of the surface degree of hydroxylation, morphology and ionic concentration on the structural, dynamical and chemical properties of silica-water interfaces. A particular emphasis is put on the computational finding[179] regarding the existence of hydrophilic (silanols rich) and hydrophobic (silanols poor) patches over the amorphous silica surface.

In section 5.4 we report the recent advancements in the comprehension of silica-water interfaces obtained by SFG spectroscopy, that represents the major technique employed by the Gageot group for the characterization of mineral-water interfaces[180, 114, 181, 182]. We present our approach based on a combination of theoretical spectroscopy and DFT-MD simulations, that is systematically adopted for the study of silica-water interfaces in the next sections.

The presentation of our results starts in section 5.5 where we put the basis of our spectroscopic and structural investigations by theoretically deconvolving the theoretical SFG spectrum of the most common amorphous silica surface (i.e. made of a density of surface silanols of 4.5 SiOH/nm^2) in contact with liquid water, into solid-water and water-water SFG signatures. Such approach allows us to obtain useful SFG marker bands of the solid-water and water-water interactions that govern the organization of the amorphous silica-water interface. In the next sections, the evolution of the SFG marker bands are monitored spectroscopically and reveal the evolution of the silica-water interface organization as a function of the surface hydrophilic character.

In section 5.6 we identify the presence of two interfacial water populations for the 4.5 OH/nm^2 amorphous aqueous silica interface, respectively located above the hydrophobic (silanols poor) and hydrophilic (silanols rich) microscopic patches of the amorphous silica surface. We have characterized the specific interactions of water with the hydrophilic and hydrophobic patches of the silica surface. We have identified the SFG spectroscopic marker bands for the hydrophobicity of water by monitoring the evolution of the SFG water-solid marker bands as a function of the spatial extension of hydrophobic and hydrophilic patches over the silica surface.

We consider in section 5.7 the evolution of the structural arrangements of the interfacial water molecules in response to variations in the silica surface degree of hydroxylation. By tuning the degree of hydroxylation of the amorphous surface model we can play with the patches's size, and hence observe the outcome on the interfacial water organization, and provide explanations in terms of solid-water and water-water interactions.

In section 5.8 we have considered one specific aspect of the morphology of highly hydroxylated silica surfaces: the silanol nest, a concave zone of the surface characterized by a high density of silanols. We especially focus on how the presence of silanol nests at the silica surface modulates the specific coordination environment and the SFG response of interfacial water molecules.

We conclude in section 5.9 by investigating the effect of electrolytes on the

structure, the dynamics and the spectroscopy of amorphous silica-water interfaces. We reveal that ions adsorbed as inner sphere tune the hydrophobicity of the silica-water interface by inducing an interfacial water that is highly interconnected into a 2D-H-Bond network, reminiscent of the one observed and characterized at the hydrophobic air-water interface[48]. The formation of this extended 2D-HB network is put in relation with the experimental findings of our collaborator Prof. Borguet (USA) of a decrease in the vibrational life time of vibrationally excited water OH stretching modes when increasing the solution electrolytes concentration.

5.1 Generalities on amorphous silica-water interfaces

The characterization of the amorphous silica-water interface faces the complexity of the surface composed by an irregular (not periodic) and inhomogeneous distribution of various kinds of surface groups that can each interact differently with water molecules. Spectroscopic evidence by NMR and IR spectroscopies [183, 184] have shown that near neutral pH condition (pH=7) the surface is mainly composed by siloxane bridges (Si-O-Si, see Fig.5.1-A), silanols (Si-OH, see Fig.5.1 B-C-D) and negatively charged silanolates (SiO⁻).

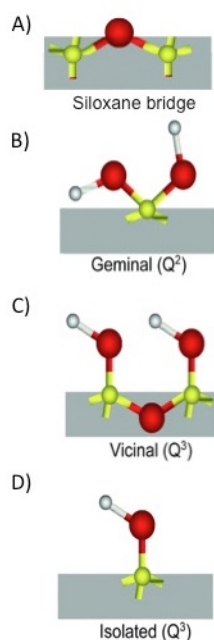


Figure 5.1: Schematic representations of siloxane bridge (A) and of geminal (B), vicinal (C) and isolated (D) silanols encountered at silica surfaces. Extracted from ref.[185]

The heterogeneous nature of the surface is also seen through the presence

of several kinds of silanols Si-OH groups with a variable number of Si-(O-Si)_n bonds involving the considered central Si atom (labelled Qⁿ where n is the number of bonded siloxane bridges). Three kinds of surface silanols have been detected by NMR[186]: geminals (Q²) where two OH groups are linked to the same Si atom (B in Fig. 5.1), vicinals (Q³) characterized by one OH linked to a Si atom that shares an oxygen with another silanol group (C in Fig. 5.1), isolated (Q³) characterized by one OH linked to a silicon atom that is not sharing any oxygen with another silanol group (D in Fig. 5.1).

The degree of deprotonation of the silanol groups is strictly dependent on the pH of the solution in contact with the silica, e.g. when increasing the pH over the point of zero charge (PZC) (\sim pH 2-4[178]) part of the silanol groups starts to get deprotonated with the consequent formation of silanolates (SiO⁻) on the surface.

The ratio between siloxane bridges (hydrophobic) and silanol groups (hydrophilic) monitors the macroscopic hydrophilicity of the silica surface. The balance between the two species can be tuned by changing the conditions of the surface preparation, typically by outgassing (i.e. gaseous emission from the surface) the silica surface at high temperature. Pairs of neighbour silanols located over the high hydroxylated zones of the silica surface, start to condensate and thus lead to the formation of siloxane bridges at high temperature.

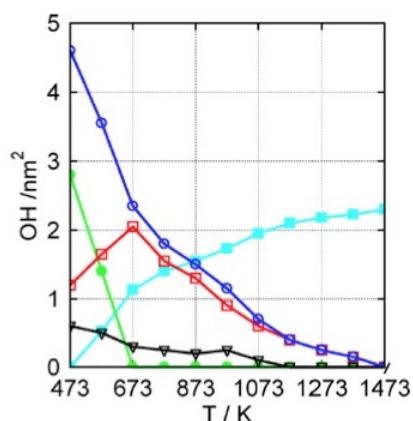


Figure 5.2: Distribution of the Si-OH groups as a function of the temperature of the surface: (blue open circles) average concentration of total OH/nm²; (cyan solid squares) average concentration of Si-O-Si; (red open squares) average concentration of free OH groups; (green solid circles) average concentration of H-bonded OH groups; (black open triangles) average concentration of geminal groups. Reproduced with permission from ref.[184]

Such process of reconstruction of the silica surface is easily rationalized by the distribution of OH groups as a function of the temperature of the pretreatment of silica, as can be seen in Fig. 5.2: at \sim 700 K all the H-Bonded silanols (green curve, the H-Bond connectivity of the silanols can be obtained by IR spectroscopy[177]) disappear in favour of siloxane bridges (cyan curve), while no H-Bonded silanols (now free OH silanols) are still present and reach their maximum concentration at the temperature of \sim 1000 K. The higher the temperature of the surface pretreatment, the more hydrophobic is the resulting

silica surface. See for example the wettability angle measurements of Lamb *et al.*[187] on flat silica surfaces pretreated at various temperatures (between 800-1000 °C).

In absence of high temperature pre-treatment the average silanol density on amorphous silica surfaces in presence of water vapour is ~ 5.0 SiOH/nm²-[177]. The average degree of hydroxylation of the silica surface in contact with liquid water is however unknown.

In our paper reported at the end of section 5.7 we have tested the stability of various hydroxylated amorphous silica model surfaces put in contact with liquid water.

An aspect to consider when dealing with amorphous surfaces is their inhomogeneous character: zones with high and low degree of hydroxylations coexist, each one with its local chemistry and thus specific interactions with water and varying from one amorphous surface to the next one. In order to describe at the molecular level such inhomogeneous character different nano-models of amorphous silica surfaces with various degrees of hydroxylation have been proposed in the literature[31, 188, 189]. The results obtained in the nano-scale by computational techniques on the different hydroxylated model silica surfaces are averaged in order to accurately mimic the complex behaviour of amorphous silica surfaces in the macro-scale. Such approach has revealed to be successful for the reproduction of the experimental IR spectra of amorphous silica surfaces[31].

5.2 Effects of the surface degree of hydroxylation on silica-water interfaces

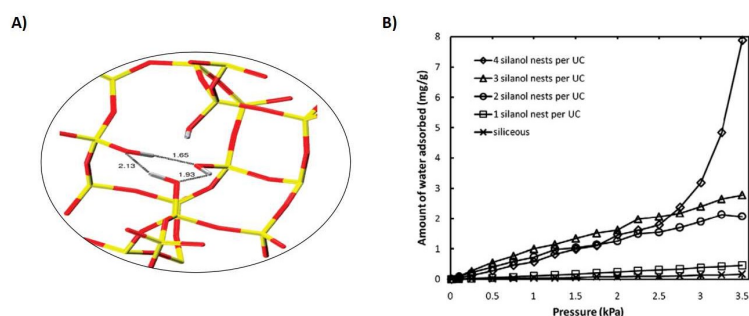


Figure 5.3: Panel A: Schematic representation of a silanol nest. Yellow: silicon atoms; red: oxygen atoms; white: hydrogen atoms. Panel B: Simulated water adsorption isotherms in silicalite with various numbers of silanol nests per unit cell. Figure reproduced with permission from ref.[190]

The heterogeneous surface composition of silica makes its interactions with water notoriously complicated to identify experimentally, where only average information both on the silica and the water are usually obtained. In this regard modelling techniques based on molecular dynamics simulations have

been successful approaches in order to get a microscopical insight into the "local" properties of water in contact with different hydroxylated zones of an amorphous silica surface.

Experimental and computational works have for instance focused on how the presence of silanol nests, i.e. highly hydroxylated zones at the silica surface composed by groups of silanols mutually interacting together (Fig. 5.3-A), can modulate the adsorption of water and bio-molecules on silica-based materials (fused silica, silicalite and zeolites)[190, 191, 192, 112, 193]. The silanol nests represent the most hydroxylated regions of amorphous silica surfaces and can also be seen as defects on crystalline silica surfaces (e.g. silicalite).

Yazaydin *et al.*[190] simulated the isotherms of water adsorption on silicalite samples as a function of the number of silanol nests present at the surface, by classical MD dynamics (see Fig. 5.3-B). Silicalite without silanol nests adsorb an insignificant amount of water, as deduced also by experimental data[194]. Progressively increasing the number of silanol nests at the surface leads to a significantly higher water adsorption with respect to the "defect-free" structure. Such result points to the higher hydroxylated zones of silica surfaces as favored sites of (vapour) water adsorption.

Also when considering bulk water in contact with amorphous silica surfaces, similar results are obtained. Hassanali *et al.*[179] simulated liquid water in contact with an amorphous silica surface by classical MD simulations. They showed the existence of surface regions characterized by high and low water affinity. As one can appreciate by the comparison of the two panels in Fig. 5.4, the water is found with a high affinity for the silica surface regions that are rich in silanol groups (hydrophilic patches) while it is found with a low affinity for the regions poor in silanol groups (hydrophobic patches).

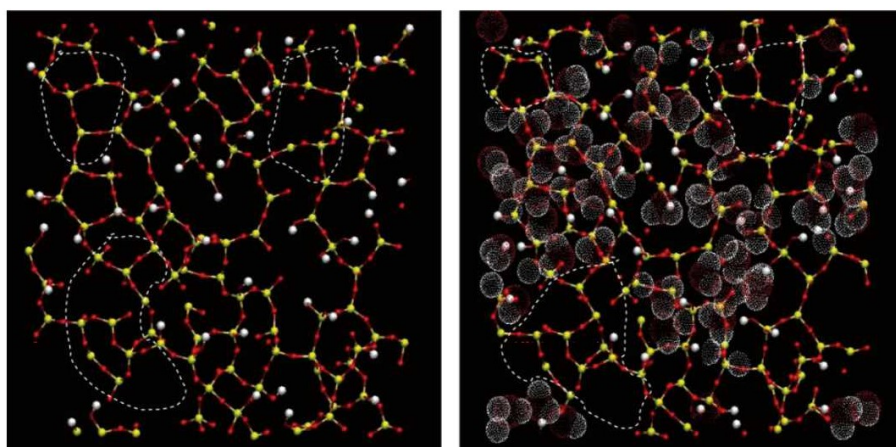


Figure 5.4: Figure showing the affinity of water for hydrophilic patches on an amorphous silica surface. The hydrophobic patches are delineated with white dashed lines. Figure reproduced with permission from ref.[179]

In Section 5.6 we will also identify the presence of hydrophilic and hydropho-

bic patches on differently hydroxylated amorphous silica surfaces in contact with water. By tuning the degree of hydroxylation of the silica surface we will play with the patches size and we will study the outcome on the interfacial water organization.

Another example on how the surface degree of hydroxylation can template the interfacial water properties is given by the work of Schrader *et al.*[195]. The diffusion of water in contact with amorphous silica surfaces of varying degrees of hydroxylation, morphologies and kinds of surface silanol sites (geminal, isolated, vicinal) is studied by combining Overhauser dynamic nuclear polarization (ODNP) experiments and classical molecular dynamics simulations. Their findings reveal the water diffusivity to correlate with the average silica surface degree of hydroxylation; in particular diffusivity strongly depends on the silica surface degree of hydroxylation and corrugation rather than on the nature of the silanol sites at the surface (geminal, isolated, vicinal).

5.3 Effects of ions on silica-water interfaces

Beyond the surface degree of hydroxylation, the presence of ions is another factor that can tune both the surface and water organization at silica-water interfaces. Ions at the boundary between water and silica are of particular interest in the domains of geochemistry and environmental sciences because of the high abundance of water, ions and silica in/on the Earth crust. The most abundant cations in natural water are Na^+ , K^+ , Ca^{2+} , Mg^{2+} ; the ones present in polluting emissions Cs^+ , Rb^{2+} , Sr^{2+} , Ba^{2+} have been shown to have an enormous impact on the silica-water interface properties. For instance, each of these cations have been shown to promote the accumulation of surface negative charges on the silica surface by cation-anion specific electrostatic interactions[196, 197]. The promotion of negative charges at the silica surface induced by ions is of particular interest for our work since it can modulate the water organization at the interface. In this regard the computational work of Pezzotti *et al.*[49] by MD and theoretical spectroscopy has extensively characterized the water organization as a function of an increasing negative charge on crystalline and amorphous silica surfaces.

Many works[198, 199, 200, 197], mostly based on potentiometric titrations, have tried to unveil the origin of the ions induced silica surface charge, by correlating the cationic hydration radius with the surface charge generated at the silica surface. Two opposite trends for the alkali metal (IA, group 1 in the periodic table) and alkali earth cations (IIA, group 2 in the periodic table) are obtained (Fig. 5.5). For the alkali metal monovalent cations (IA, solid circles) the surface charge increases proportionally with respect to the hydration radius (positive lyotropic trend), while the opposite trend (negative lyotropic trend) is obtained for the alkaly earth divalent cations (IIA,

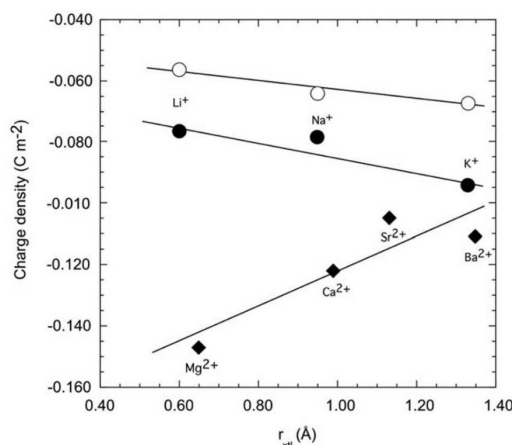


Figure 5.5: Relationship between the crystallographic radius of alkali and alkaline earth cations and the silica surface charge density. The surface charge is measured at pH=8. Figure reproduced with permission from ref.[197]

diamonds). Dove *et al.*[197] found the same lyotropic trends in the magnitude that the ions affect the water structure (i.e. structure-breaker for IA cations and structure-maker for IIA cations). These authors invoke the specific interfacial water organization in the cation solvation shell as the origin of such phenomenon. In agreement, the theoretical work of Lyklema *et al.*[201] points to changes in the configurational entropy of the interfacial water in response to ions adsorption on the silica surface as the origin of the ion specific behaviour. Instead, the phenomenon has been rationalized by Severjensky[202, 203] by following the trends in the hydration energy in the case of alkali metals (IA) and hydrated radii size for the alkaline earths (IIA).

Recently, works have focused on how adsorbed ions directly modulate the water interfacial organization. Dello Stritto *et al.*[204] have provided a microscopical insight into the monovalent and divalent ions adsorption at the quartz (101)/water interface under different pH conditions by DFT-MD. They nicely find that both cations and anions adsorb at the surface and perturb the interfacial H-Bond network by inducing an O-H in plane orientation of both the silanol groups and of the water molecules residing at the interface. Both cations and anions have a stronger effect on the interfacial water structure when compared to the structure of liquid water, especially when a contact ion pair (CIP) is formed. Similarly the previous computational work of Pfeiffer *et al.*[205] reported the inner sphere adsorption of K⁺ and Na⁺ at the α -(0001) quartz-water interface to induce an O-H in plane ordering of the silanol groups at the surface.

Notice at last that the dissolution of quartz is also promoted by the presence of ions at the interface. Several experimental works have shown that the presence of ions, even at low concentrations, can increase the quartz rate of dissolution at neutral pH condition by more than one order of magnitude[206, 207, 208, 209, 210, 211]. Interestingly the quartz dissolution is found to be dependent on the specific ionic species and shows different trends with respect

to different electrolytes.

5.4 SFG spectroscopy, a useful tool to interrogate silica-water interfaces

All the aforementioned works point to a strong modulation of the interfacial water properties by the silica surface degree of hydroxylation and solution ionic strength. However in order to fully rationalize the effect of the degree of hydroxylation and electrolytes on the silica-water interface, an experimental technique able to probe "in situ" the heterogeneous chemistry governing the interface structural and dynamical properties is mandatory.

In this regard optical second harmonic generation spectroscopy (SHG)[212, 213] and sum frequency generation spectroscopy (SFG)[214, 215, 216, 217, 218, 219, 220, 221, 222, 223, 224] offer the required surface specificity, as they specifically probe non centro-symmetric media, like the interfaces. In SFG experiments, in particular, the heterogeneous chemical interactions occurring at the boundary between the water and other media are probed and resolved on the frequency domain, allowing to directly unveil the specific interface structure.

More in details, SFG experiments are based on one tunable IR beam and one fixed visible beam that overlap at an interface. The second order susceptibility $\chi^{(2)}(\omega)$ of the interface is measured as a function of the frequency ω , which is the sum of the two laser input frequencies. The outgoing SFG beam intensity is in fact proportional to the square of $\chi^{(2)}(\omega)$, while its frequency is equal to the sum of the frequencies of the two incoming IR and VIS beams. Thanks to Heterodyne (HD) SFG experiments providing direct measurements of the imaginary $\Im(\chi^{(2)}(\omega))$ and the real $\Re(\chi^{(2)}(\omega))$ parts of the susceptibility, the direct knowledge of the water molecules and surface groups averaged orientations at the interface can be obtained[138, 139]. More recently, time resolved (TR-SFG) and 2D-SFG (the surface specific equivalent of 2D-IR) experimental set-ups have been developed, providing direct time dependent information on the interfacial vibrational relaxation processes[225, 226, 227, 228, 229, 230, 231].

Because of its sensitivity to non centro-symmetric media, SFG is considered as one of the most powerful technique to interrogate mineral/water interfaces. Several works based on vibrational sum frequency generation (SFG) non-linear spectroscopy in the OH stretching region have for instance unravelled the puzzling water and solid organizations at silica-water interfaces[232, 233, 185, 234, 235, 236, 237].

There are mainly two bands recorded, one at 3200 and one at 3400 cm^{-1} (see the conventional $|\chi^2(\omega)|^2$ spectra in Fig. 5.6-A). They have been early on assigned respectively to "liquid like" (3400 cm^{-1}) and "ice like" (3200 cm^{-1})

water populations[232]. Recently the advent of phase resolved HD-SFG technique[238], sensitive to the O–H orientations with respect to the surface normal, has allowed to reveal the orientation of the water populations at the origin of the two SFG bands (see the $\Im(\chi^{(2)}(\omega))$ spectrum in Fig. 5.6-B [234]). A new assignment based on water donor/acceptor H-Bonds to the amorphous surface groups has been proposed. In particular, the positive maximum in the $\Im(\chi^{(2)}(\omega))$ spectrum (Fig. 5.6-B) has been associated to water molecules donating H-Bonds to silanols while the negative band has been assigned to water molecules accepting H-Bonds from silanol groups[234].

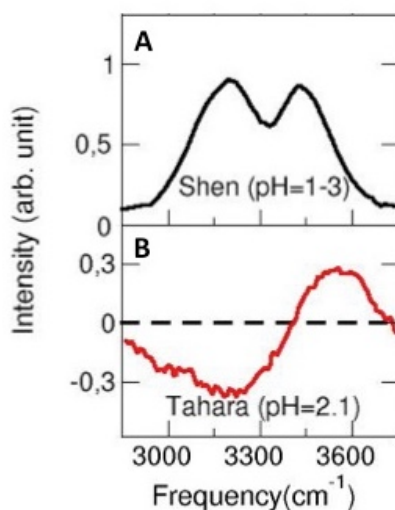


Figure 5.6: *Panel A: Shen's group $|\chi^2(\omega)|^2$ SFG signal of silica-water interfaces at PZC (pH=2–4). Panel B: Tahara's group $\Im(\chi^{(2)}(\omega))$ SFG signal of silica-water interfaces at PZC. Figure reproduced with permission from ref.[234][239]*

The origin of the signal at $\sim 3600 \text{ cm}^{-1}$, present at the amorphous silica-water interface spectrum and absent in the quartz/water interface SFG spectrum, has been source of controversies in the literature. In particular it has been long debated whether it arises from unbonded silanol groups[185] or water quasi-free OH groups[135, 234, 237, 236]. The SFG spectra reported and discussed here above have been conducted at pH=PZC where the silica surface is fully protonated, and thus neutral. In these isoelectric conditions, SFG spectroscopy probes solely the Binding Interfacial Layer (BIL[49, 239]), i.e. the first water layer in contact with the silica surface where centrosymmetry is broken by the chemical and physical interactions of the water molecules with the silica surface[114, 240]. Conversely when the silica surface is charged (pH>PZC) or charged chemical species (e.g. ions) are residing at the interface, a long-range electrostatic perturbation comes into play and both the BIL and the Diffuse Layer (DL)[114, 240] are probed by SFG. The Diffuse Layer is the water layer, subsequent to the BIL, composed by water molecules possessing the bulk H-Bonding structure but oriented by the long-range static field arising from the screening of charged chemical species

at surfaces. This is in a nutshell liquid water oriented by an electric field.

It follows that the interpretation of SFG spectra of silica water interfaces at pH higher than the PZC, where the silica surface is negatively charged and/or in presence of ions, requires the deconvolution of the signal arising from the DL layer from the one arising from the "true BIL interface". Recently, both experimental[240] and theoretical[114] communities have developed the required tools to achieve such deconvolution and hence be able to reveal the BIL structure and dynamics at charged interfaces. Thanks to this it becomes possible to study and rationalize how pH and ions change the spectroscopic and structural properties of the BIL-water in contact with silica[49, 241, 237, 242, 243]

Both steady-state-SFG (static SFG) and TR-SFG (time resolved SFG) spectroscopy in combination with molecular dynamics[232, 224, 244, 245, 234, 241, 231, 135, 230, 243, 246, 247, 248, 249, 250, 232, 234, 236, 251, 252, 253] have strongly improved our knowledge of the effects of pH, surface degree of hydroxylation and ions concentration on the silica-water interface organization. However, controversies arising from the molecular assignments of the SFG bands, the SFG probing depth and the complexity of the system make the question on how water behaves in contact with amorphous silica surfaces still far to be solved.

This is the starting point of this thesis work for the structural characterization of the water in contact with amorphous silica surfaces by means of DFT-MD simulations and theoretical and experimental SFG spectroscopy. The use of theoretical spectroscopy offers a direct link between the microscopic knowledge given by DFT-MD simulations and the macroscopic one probed by SFG experiments. This is the expertise of the Gaigeot group. In particular we extract from simulations useful SFG marker bands describing the chemistry at the interface arising from the OH interfacial water and OH silica surface groups, and we compare them with SFG experiments in the OH stretching frequency region. In this way the relationships between structure and spectroscopy can be unveiled and the interfacial water organization at the amorphous silica-water interface and its evolution in response to changes in the surface degree of hydroxylation and solution ionic strength can be rationalized. Moreover the interfacial vibrational relaxation mechanisms can be directly probed in time resolved SFG experiments, providing further complementary information on the aqueous interface. Our synergistic approach puts us in the position to reveal the molecular interactions that govern the microscopic and macroscopic organization of the water at the interface with silica and to unveil the microscopic origin of the detected experimental SFG spectra.

5.5 DFT-MD allows the deconvolution of SFG spectra. Test case on the most common amorphous silica-water interface (4.5 OH/nm² hydroxylation)

The results presented in this chapter have been obtained in collaboration with my colleagues Dr. Simone Pezzotti (PhD thesis[131] NNT:2019SACLE008) and Dr. Daria Ruth Galimberti (Post-Doc in the group). The SFG deconvolution scheme reported in this section is related to the one used for the characterization of other water-silica interfaces by the Gageot group in ref.[49].

In this section we identify and classify the interactions that finely govern the silica-water interface structural organization by deconvolving the theoretical SFG spectrum of the 4.5 SiOH/nm² silica model surface in contact with liquid water into specific OH groups populations, that are the markers of the water-water and solid-water interactions. In the next sections, by studying the evolution of the SFG marker bands of the OH-groups, identified hereafter on the 4.5 SiOH/nm² silica surface, we investigate the evolution of the silica-water (section 5.6) and water-water (section 5.7) interactions as a function of varying solution ionic strength and surface degree of hydroxylation.

Our investigation starts by comparing the theoretical SFG spectrum of a hydroxylated 4.5 SiOH/nm² silica model surface in contact with liquid water with an experimental SFG spectrum of the fused/silica water interface. The choice to use a silica model surface with 4.5 SiOH/nm² degree of hydroxylation is dictated by the following considerations:

1) It is by far the most representative model silica surface to reproduce correctly the spectroscopic properties of a "macroscopic" non treated amorphous silica surface in the OH frequency region as shown by ref.[31]

2) The value of 4.5 SiOH/nm² is close to the 5.0 SiOH/nm² averaged degree of hydroxylation found by Zhuravlev for a set of about 100 different silica aerogel samples.[254, 176, 177]

The experimental and theoretical spectra have been obtained at pH=PZC (pH~2-4), without including electrolytes in the case of the DFT-MD simulations. This is the isoelectric point, where only the first water layer in contact with the solid (i.e. BIL) is probed by SFG.

We have applied the deconvolution scheme developed in the Gageot group [131] in order to separate BIL/DL SFG contributions. We find the SFG-signal arising solely by the BIL (3.0 Å thickness), while centrosymmetry is recovered in the water layer located just after the BIL and composed by non SFG-active bulk water molecules (centrosymmetry of liquid water).

All the computational details regarding the DFT-MD simulations of silica-water interfaces presented in this chapter, using the model silica surfaces developed by Ugliengo and Bernasconi[31, 188], are found in the method sections of the papers reported at the end of each section.

Within these conditions, we compare the results of the theoretical $\Im(\chi^{(2)}(\omega))$

5.5 DFT-MD allows the deconvolution of SFG spectra. Test case on the most common amorphous silica-water interface (4.5 OH/nm² hydroxylation)

spectrum, obtained by DFT-MD, to the experimental $\Im(\chi^{(2)}(\omega))$ spectrum of ref.[234] in order to test the reliability of our model in reproducing the spectroscopic and structural properties of the considered silica-water interface. Once validated to experiment, the simulated spectrum can be deconvolved into elemental contributions. The comparison in Fig. 5.7-A shows an excellent agreement between the theoretical and experimental $\Im(\chi^{(2)}(\omega))$ spectra.

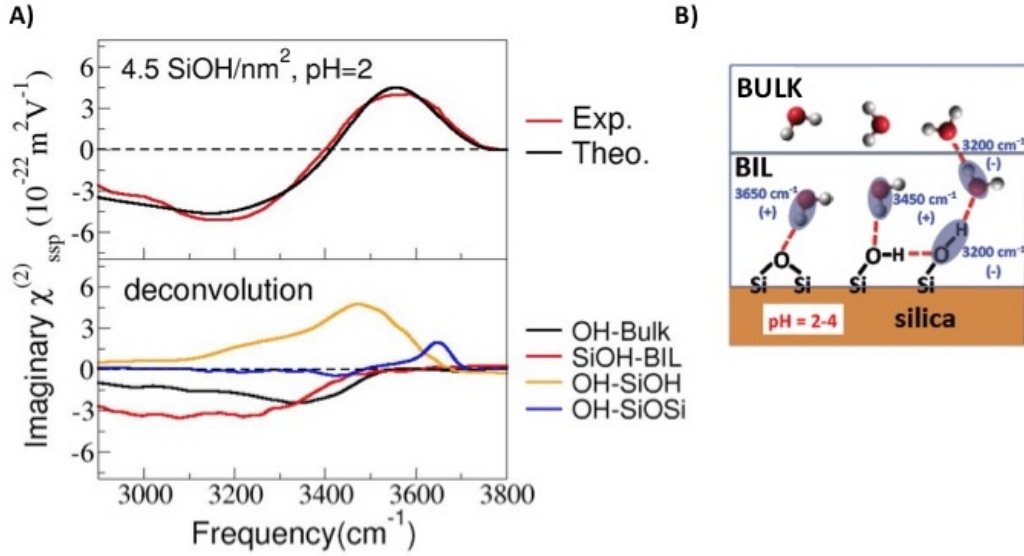


Figure 5.7: (A): comparison between theoretical (black) and experimental[234] (red) $\Im(\chi^{(2)}(\omega))$ spectra of the fused/amorphous silica-water interface in absence of high temperature surface pre-treatment (estimated 4.5–5.0 SiOH/nm² surface hydroxylation). Theoretical deconvolution of the SFG spectrum into the individual contributions of the four SFG-active OH-populations in the BIL (bottom) for silica-water interfaces at the iso-electric point. The notation is organized in the way that the first part of the name refers to the OH-oscillator considered, i.e. BIL water OH, while the second part (after the –) refers to the H-Bonded partner, i.e. siloxane bridge Si-O-Si, in-plane silanol. (B): scheme of the four SFG-active OH-populations found here.

Now that the reliability of our model is assessed, we provide a deconvolution of the theoretical SFG spectrum into the OH populations that are present in the BIL. The OH populations have been classified by chemical nature, respectively of the OH donor of hydrogen bonds (silanol or water) and of the H-Bond acceptors (siloxane bridge, silanols, BIL-water, bulk-water).

Four OH populations, schematically presented in Fig. 5.7-B, have hence been found to be SFG active. One of them arises from the Si-OH groups donating HBs to BIL-water, while the rest are various OH groups of the BIL water molecules. Looking at the SFG spectrum deconvolved into these four OH populations, we find (Fig. 5.7-A):

1) The OH groups of the BIL water molecules that donate H-Bonds to surface silanols (OH-SiOH, orange curve in the figure) provide a positive $\Im(\chi^{(2)}(\omega))$ band, centred at ~ 3450 cm⁻¹. The positive sign of the band

arises from the OH orientation, i.e. pointing from the liquid to the solid phase (along the normal to the surface as defined by convention in SFG). Among the four populations, this population is the one with the most intense signal in the high frequency region, i.e. $\geq 3400 \text{ cm}^{-1}$.

2) The OH groups of the BIL water molecules weakly interact with the surface siloxane bridges (OH-SiOSi, blue curve in the figure) and provide a positive $\Im(\chi^{(2)}(\omega))$ signature blue shifted in position with respect to the OH-SiOH one ($\sim 3660 \text{ cm}^{-1}$ vs $\sim 3450 \text{ cm}^{-1}$). This is due to the exposed Si-O-Si groups[135, 236, 255] being hydrophobic sites with a weaker Lewis basicity with respect to the hydrophilic silanol groups[256]. The high frequency ($\sim 3660 \text{ cm}^{-1}$) of this feature indicates the quasi-free nature of the water OH groups, weakly interacting with Si-O-Si sites. The lower intensity of the OH-SiOSi band with respect to the OH-SiOH band (Fig. 5.7-A) is due to the lower number of BIL-water molecules interacting with Si-O-Si groups compared to the number of BIL-water interacting with SiOH groups at the 4.5 SiOH/nm^2 silica-water interface (all details can be found in ref.[135]). The balance between these two water OH populations can be monitored by the intensity ratio of their relative SFG signatures that, as will be elucidated in the next section 5.6, depends on the surface degree of hydroxylation.

3) OH groups of silanols donate strong HBs to water molecules in the BIL (denoted SiOH-BIL, red curve in the figure) and provide a negative $\Im(\chi^{(2)}(\omega))$ band because of their opposite orientation with respect to the previous two populations. The red-shifted position of their SFG signature as compared to the one arising from OH-SiOH groups (~ 3150 vs $\sim 3450 \text{ cm}^{-1}$) is the spectroscopic evidence of the asymmetric H-Bonding properties of surface silanols, with the SiOH sites being able to donate stronger HBs than the ones they accept, coherently with previous calculated pK_a values for SiOH and $\text{Si}(\text{OH}_2)^+$ species[257, 258]. Such OH population is the major contributors to the SFG spectrum below 3400 cm^{-1} .

4) OH groups of the BIL water molecules donate HBs to the subsequent water molecules that are located in the bulk liquid (denoted OH-Bulk, black curve in the figure). The water molecules that receive HBs from surface silanols (population 3) in turn donate HBs preferentially to water molecules located in the subsequent bulk layer, which are thus predominantly oriented toward the bulk of water and consequently provide a negative $\Im(\chi^{(2)}(\omega))$ signature, here centred at $\sim 3350 \text{ cm}^{-1}$. None of the BIL-water molecules is found with both its O-H groups simultaneously H-Bonded to surface SiOH groups (OH-SiOH population in our nomenclature) or simultaneously H-bonded to bulk water molecules (OH-Bulk population).

The microscopic picture emerging from the theoretical deconvolution of the $\Im(\chi^{(2)}(\omega))$ spectrum is consistent with the experimental investigations

and interpretations by Tahara’s group[234], concluding that the positive intensity in the $\Im(\chi^{(2)}(\omega))$ spectrum (reported in black in the upper panel of Fig. 5.7-A) arises from water molecules donating HBs either to SiOH or to Si-O-Si surface terminations, while the negative intensity arises from water molecules receiving HBs from surface silanols and simultaneously donating HBs to water molecules located farther from the surface[234, 241]. Additional isotopic dilution ($\text{H}_2\text{O}/\text{D}_2\text{O}$) experiments performed by this experimental group, also showed that the SFG spectrum in the $2600\text{-}4000\text{ cm}^{-1}$ is not strongly modified upon an increase in the percentage of deuterated water, suggesting that intra- and inter- molecular couplings do not play a relevant role in the SFG response of silica-water interfaces at low pH (isoelectric) conditions. This leads to the conclusions that interfacial water molecules in the BIL statistically have both its O-H groups neither simultaneously H-Bonded to surface SiOH groups (OH-SiOH population in our nomenclature) nor simultaneously H-bonded to bulk water molecules (OH-Bulk population).

With the gained knowledge on the specific SFG signatures of the silica-water and water-water interactions at the origin of the SFG spectrum we are now in the position to follow and characterize their evolution as a function of changes in the silica surface degree of hydroxylation (see sections 5.6 and 5.7) and as a function of changes in the surface morphology (see section 5.8).

5.6 Tuning the silica surface hydrophilicity and the silica-water interactions

The results presented hereafter refer to the computational side of our [PNAS, 116, 1520-1525 (2019)] published work included at the end of this section. They have been obtained in collaboration with one of our experimental partners: the Bonn and Backus’s group at the Max Planck Institute for Polymers in Mainz, Germany.

In this section we investigate the evolution of silica-water interactions by tuning the degree of hydroxylation of the silica surface and monitoring the outcome on the solid-water SFG signatures assigned to specific OH (water and surface silanols) populations. In order to achieve that by means of DFT-MD and theoretical SFG spectroscopy, we will use two model silica surfaces in contact with liquid water, differing by the degree of hydroxylation, i.e. 4.5 (hydrophilic) and 3.5 (less hydrophilic) SiOH/nm^2 . Both model surfaces were obtained[31] from the same highly hydroxylated silica surface ($7.2\text{ SiOH}/\text{nm}^2$) by simulating the dehydration process occurring when outgassing the silica at high temperature[31] plus further reconstruction when in contact with water. More details on the computational set up and on the model surfaces can be found in the method section and in the S.I. of our paper [PNAS, 116, 1520-1525 (2019)] reported at the end of this section.

We first focus on the surface morphologies of the two model surfaces. Fig. 5.8-A reports the distribution of silanols (hydrophilic sites, grey balls in the figure) and of the exposed siloxane bridges (hydrophobic sites, red balls in the figure) for the 4.5 and 3.5 SiOH/nm² model surfaces. We observe for both surfaces a non-uniform distribution of silanols and siloxane bridges, with coexisting silanol rich and silanol poor domains over the surface. The dashed red lines in Fig. 5.8-A indicate the most hydrophobic surface areas where the local silanol density is ≤ 1.5 SiOH/nm². We can clearly notice how the silica surface is organized in hydrophilic (silanol rich) and hydrophobic (silanol poor) patches which size is strictly dependent on the degree of hydroxylation of the amorphous silica surface.

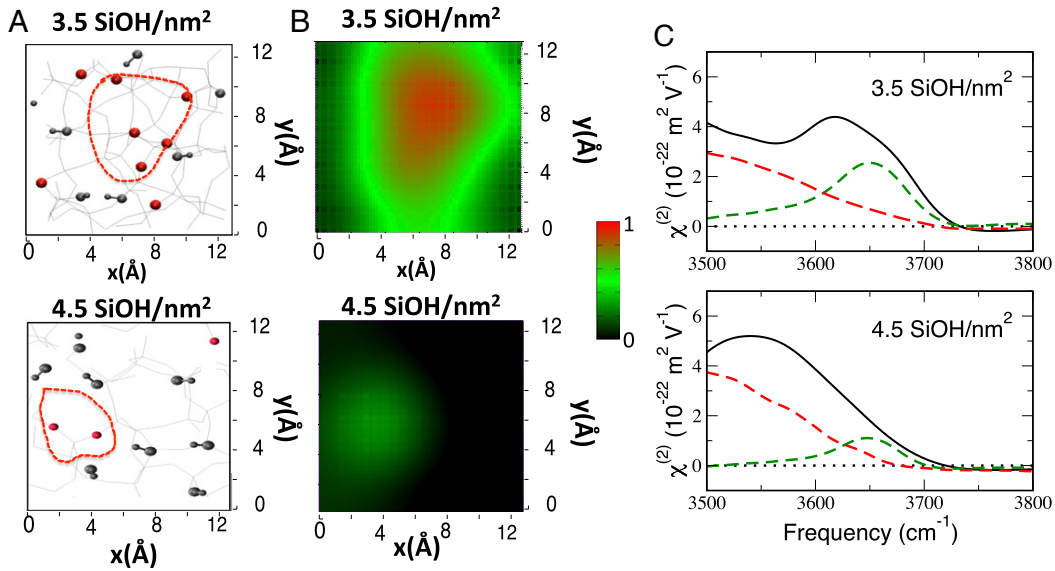


Figure 5.8: Surface hydrophilic/hydrophobic patches and associated SFG markers as a function of the silica surface hydroxylation. (A): top view of the two silica surfaces used in the DFT-MD simulations, respectively with silanol density of 3.5 SiOH/nm² and 4.5 SiOH/nm². The red lines indicate the hydrophobic patches (i.e. areas of the surface with the lowest silanol densities). The surface SiOH groups are highlighted with gray balls for oxygens and hydrogens, while the Si-O-Si siloxanes are highlighted by the oxygens only in red. (B): density of water OH groups involved in OH-SiOSi interactions (giving rise to the 3660 cm⁻¹ SFG marker band of the hydrophobic patches) spatially resolved above the surface x - y plane. (C): theoretical SFG $\Im(\chi^{(2)}(\omega))$ signal in the 3500-3800 cm⁻¹ region for the two silica-water interfaces. The black line is the total SFG signal, the green dashed line is the signal of water OH groups involved in the OH-SiOSi interactions (see Fig. 5.7 for OH-groups definition), markers of hydrophobic patches, while the red dashed line is the signal of water OH groups involved in OH-SiOH interactions, markers of hydrophilic patches.

The organization of the hydrophilic and hydrophobic surface sites in patches is totally coherent with the chemistry behind the reconstruction of the silica surface when outgassed at high temperature. The condensation of two SiOH-SiOH groups located in proximity from each other leads to the formation of a siloxane bridge at the surface and one desorbed water molecule.

Without those silanols, all the siloxanes in the proximity of the newly formed siloxane bridge become exposed, which results in the formation of an extended hydrophobic patch. They are now free to interact with water.

The density of water interacting with the siloxane bridges (Fig. 5.8-B) is calculated along our MD simulations for the two differently hydroxylated amorphous silica aqueous surfaces and reported in Fig. 5.8-B. One can immediately see that the density of water is correlated with the one of the siloxane bridges, i.e. directly correlated with the patch of hydrophobicity. The presence of a more extended hydrophobic patch (and less extended hydrophilic one) at the 3.5 SiOH/nm² compared to the 4.5 SiOH/nm² leads to an increase in the water-siloxane bridge interactions (see the red spot in Fig. 5.8-B).

As a consequence, the SFG peak at $\sim 3660\text{ cm}^{-1}$, marker of the hydrophobic patches, gains intensity over the $\sim 3450\text{ cm}^{-1}$ band (marker of hydrophilic patches). This is shown in Fig. 5.8-C, where the contributions of OH-SiOH and OH-SiOSi water OH groups to the total SFG spectrum are deconvolved (red and green lines respectively). The 3660 cm^{-1} band arising from the OH-SiOSi population hence increases with decreasing hydroxylation of the silica surface from 4.5 SiOH/nm² to 3.5 SiOH/nm².

In the next section, by playing further with the surface patches, i.e. tuning the degree of hydroxylation of the model silica surface, we will study the evolution of the water structure organization at the boundary with the silica surface.

All details on the hydrophilic/hydrophobic patches at silica-water interfaces and their SFG markers as a function of silica surface hydroxylation can be found in our attached paper [PNAS, 116, 1520-1525 (2019): "Molecular hydrophobicity at a macroscopically hydrophilic surface"].



Molecular hydrophobicity at a macroscopically hydrophilic surface

Jenée D. Cyran^{a,1}, Michael A. Donovan^{a,1}, Doris Vollmer^a, Flavio Siro Brigiano^b, Simone Pezzotti^b, Daria R. Galimberti^b, Marie-Pierre Gaigeot^b, Mischa Bonn^{a,2}, and Ellen H. G. Backus^{a,c,2}

^aMax Planck Institute for Polymer Research, 55128 Mainz, Germany; ^bLaboratoire Analyse et Modélisation pour la Biologie et l'Environnement (LAMBE), Univ Evry, Université Paris-Saclay, CNRS UMR8587, 91025 Evry, France; and ^cDepartment of Physical Chemistry, University of Vienna, 1090 Vienna, Austria

Edited by B. Montgomery Pettitt, University of Texas Medical Branch, Galveston, TX, and accepted by Editorial Board Member Peter J. Rosky December 16, 2018 (received for review November 6, 2018)

Interfaces between water and silicates are ubiquitous and relevant for, among others, geochemistry, atmospheric chemistry, and chromatography. The molecular-level details of water organization at silica surfaces are important for a fundamental understanding of this interface. While silica is hydrophilic, weakly hydrogen-bonded OH groups have been identified at the surface of silica, characterized by a high O-H stretch vibrational frequency. Here, through a combination of experimental and theoretical surface-selective vibrational spectroscopy, we demonstrate that these OH groups originate from very weakly hydrogen-bonded water molecules at the nominally hydrophilic silica interface. The properties of these OH groups are very similar to those typically observed at hydrophobic surfaces. Molecular dynamics simulations illustrate that these weakly hydrogen-bonded water OH groups are pointing with their hydrogen atom toward local hydrophobic sites consisting of oxygen bridges of the silica. An increased density of these molecular hydrophobic sites, evident from an increase in weakly hydrogen-bonded water OH groups, correlates with an increased macroscopic contact angle.

hydrophobicity | sum frequency generation spectroscopy | surface science | water | silica

Molecular-level insights into the structure and dynamics of minerals in contact with aqueous solutions contribute not only to a fundamental understanding of dissolution and sorption processes on mineral surfaces, but also to potential new avenues for their synthetic design (1, 2). Hydrophobic and hydrophilic interactions between mineral oxide surfaces and aqueous solutions are in particular relevant for water-mediated catalysis (3, 4) of organic reactions and phase separation processes used in applications ranging from liquid chromatography to mineral froth partitioning of hydrophobic and hydrophilic particles (5, 6). The surfaces of minerals, in particular, silica, have been previously characterized at the molecular level with NMR spectroscopy and mass spectrometry to determine the surface density of hydroxyl groups (7, 8). Spectroscopic evidence from NMR and IR spectroscopies have shown that, near neutral pH, the surface consists of siloxane (Si-O-Si), silanol (Si-OH), and negatively charged silanolate (Si-O⁻) groups (7, 9–11). The presence of surface OH groups is not limited to silica: on CaF₂ interfaces in contact with NaOH solution at pH 12, Ca-OH groups have been identified (12, 13). Similarly at alumina oxide/water interfaces Al-OH groups have been shown to terminate the Al₂O₃ surface (14–16).

For silica, much work on silanol groups has focused on either dry silica surfaces in ultrahigh vacuum environments or under exposure to water vapor (17–21). Isolated silanol groups in air typically display a vibrational resonance around 3,750 cm⁻¹ with ~100 ps vibrational lifetimes (18, 19). However, typically silica surfaces are in contact with aqueous solutions. This raises the question of how the water affects the silica surface.

Surface-sensitive nonlinear optical techniques, like second harmonic generation (SHG) and sum frequency generation (SFG) spectroscopy have been used to elucidate the structure of interfacial water at the silica/water interface (10, 20–26). SHG and

SFG are second-order nonlinear optical processes, where two incident beams generate an emitted field at the sum of the two input frequencies. In particular, vibrational SFG (vSFG) utilizes a mid-infrared pulse resonant with a molecular vibration and reveals the vibrational response of the interfacial molecules. The primary focus of vSFG studies on the silica/water interface is on the hydrogen-bonded O-H stretch modes, centered at 3,200 and 3,400 cm⁻¹. However, several studies have, in addition, revealed a peak centered at 3,680 cm⁻¹, which corresponds to O-H vibrations that are weakly hydrogen bonded, the free O-H (10, 21, 22, 27). At the silica/water interface, the free O-H can originate from the silica surface as a silanol group or an O-H group at the surface of water terminating the hydrogen bond network. The origin of the peak is difficult to ascertain with conventional (homodyne detected) vSFG spectroscopy since information on molecular orientation is contained in the sign of the response, which is lost because the intensity signal is proportional to the square of the response. Owing to the recent developments in phase-resolved vSFG spectroscopy, it is possible to probe buried solid/liquid interfaces and to determine the sign of the response and thereby the absolute orientation of the interfacial O-H groups (12, 23–25). Moreover, the vibrational and reorientational

Significance

Silica, the most abundant mineral on Earth, is exploited in many technologies and naturally occurring geological and atmospheric processes. The physical and chemical interactions between silica and water are the fundamental driving forces for water purification systems, oil extraction, and coatings. Characterizing the silica/water interface is therefore important to improve existing technologies, in particular for silica coatings, which rely on wettability and thermal-resistant properties to remain effective. We investigated the silica/water interface using a mixture of macroscopic and microscopic techniques, including experimental and theoretical surface-specific sum frequency generation spectroscopy and contact angle measurements. Strikingly, we observed the presence of water molecules non-hydrogen bonded to the nominally hydrophilic silica surface.

Author contributions: J.D.C., M.A.D., F.S.B., S.P., D.R.G., M.-P.G., M.B., and E.H.G.B. designed research; J.D.C., M.A.D., D.V., F.S.B., S.P., D.R.G., M.-P.G., and E.H.G.B. performed research; J.D.C., M.A.D., D.V., F.S.B., S.P., D.R.G., M.-P.G., M.B., and E.H.G.B. analyzed data; and J.D.C., M.A.D., D.V., F.S.B., S.P., D.R.G., M.-P.G., M.B., and E.H.G.B. wrote the paper.

The authors declare no conflict of interest.

This article is a PNAS Direct Submission. B.M.P. is a guest editor invited by the Editorial Board.

This open access article is distributed under [Creative Commons Attribution-NonCommercial-NoDerivatives License 4.0 \(CC BY-NC-ND\)](https://creativecommons.org/licenses/by-nc-nd/4.0/).

¹J.D.C. and M.A.D. contributed equally to this work.

²To whom correspondence may be addressed. Email: bonn@mpip-mainz.mpg.de or backus@mpip-mainz.mpg.de.

This article contains supporting information online at www.pnas.org/lookup/suppl/doi:10.1073/pnas.1819000116/-DCSupplemental.

Published online January 17, 2019.

dynamics of interfacial molecules with this high vibrational frequency have been reported (28, 29). Here, we show that a combination of the phase-resolved vSFG and molecular dynamics (MD) simulations provides evidence for very weakly hydrogen-bonded water at the silica/water interface, which correlates with the macroscopic wetting properties of the surface. Furthermore, time-resolved vSFG reveals that these weakly hydrogen-bonded water molecules have similar properties as water at the water–air interface. This behavior of water is normally seen for water at hydrophobic interfaces, but not for hydrophilic interfaces. Thus, we define these water molecules as hydrophobic water, following the terminology in ref. 30.

Results

The static vSFG spectrum of water at the buried interface of an Infrasil 302 (fused) silica window in *ssp* polarization combination (*s*-polarized SFG, *s*-polarized visible, and *p*-polarized infrared) is depicted in Fig. 1A (blue line). The experiments are conducted with pure Millipore water (pH ~ 6). Three Lorentzian-shaped resonances in the spectral region from 3,300 to 3,800 cm^{-1} adequately describe the data (red line). The two peaks at low frequencies (~3,200 and 3,400 cm^{-1}) represent hydrogen-bonded O-H stretch vibrational modes, and the peak at ~3,660 cm^{-1} indicates the presence of weakly hydrogen-bonded OH groups. Although the bandwidth in Fig. 1A does not extend to 3,200 cm^{-1} , the resonance has been well documented previously (24, 31). A detailed description of the experimental setups can be found in the *SI Appendix*.

The high-frequency peak was not as pronounced in all previous studies with a planar window due to different sample preparation. The peak at ~3,660 cm^{-1} is more prominent following heat

treatment (950 °C for 4 h) of the silica (10). This peak was observed by Dalstein et al. (10), and assigned to silanol groups. However, previous studies have contended that the density of silanol groups decreases upon heating the silica substrate, with a sharp decrease above 800 °C (8, 32). Furthermore, the full rehydroxylation of the silica substrate in contact with water has previously been found to proceed exceedingly slow (8, 9).

The origin of the ~3,660 cm^{-1} peak is ambiguous; both water and silica could have free OH groups, and both are viable options to contribute to the resonance at ~3,660 cm^{-1} . One key difference between the free OH from water and the silanol (Si-OH) group is the molecular orientation: the free OH from water would orient with the hydrogen pointing toward the silica surface, whereas the silanol groups would be pointing toward the bulk water. It should be noted that there are different types of surface silanol groups; however, the net orientation of the OH is similar (8, 9, 33–35). One technique to address the orientation of the free OH resonance is phase-resolved vSFG spectroscopy, which measures the complex vSFG spectrum. Depending on the net orientation of the vibrational transition dipole, the response is positive or negative. Thus, phase-resolved vSFG spectroscopy can differentiate between a free OH from water pointing toward the silica surface and a silanol group with the OH directed away from the silica.

The imaginary spectrum from the phase-resolved vSFG experiments of the silica/water interface reveals two positive peaks, as illustrated in Fig. 1B. The peak centered around 3,400 cm^{-1} corresponds to hydrogen-bonded water at the silica/water interface. The positive sign of this peak indicates that these hydrogen-bonded water molecules are oriented with their hydrogen atoms toward the negatively charged surface, in agreement with previous results (23, 24). The peak at ~3,660 cm^{-1} is also positive (Fig. 1B) and indicates the net orientation of the hydrogen atom of the OH groups contributing to this vibrational resonance are likewise oriented toward the silica surface. Therefore, the data indicate that the free OH signal originates from water molecules with the hydrogen atom of their OH groups oriented toward the silica surface, rather than from silanol groups. Further spectroscopic evidence utilizing H_2^{18}O is included in the *SI Appendix*. Isotopic substitution of ^{16}O to ^{18}O shifts the high-frequency O-H stretch vibration to lower frequencies; this is not expected for silanol groups, which are not expected to exchange oxygens with nearby water. The free OH groups from water oriented toward the silica substrate dominate the spectrum, yet silanol groups, pointing toward the water may still be present at the surface.

To further characterize these hydrophobic OH groups at the silica/water interface, we employ time-resolved vSFG spectroscopy and compare their behavior with water in contact with other hydrophobic interfaces. We measure both the population lifetime and reorientation dynamics of the weakly hydrogen bonded –OH species at the silica/ H_2O interface. Time- and polarization-resolved measurements have previously been reported for the air/water, octadecylsilane (ODS)/water, and aqueous peptide solution/air interfaces, and we use these results as a comparison for the silica/water interface (28, 29, 36, 37).

In the time-resolved vSFG experiments, a subset of OH groups was excited with a 150-fs mid-IR excitation pulse spectrally centered at 3,640 cm^{-1} (green line in Fig. 1C), and the time-dependent vSFG intensity spectrum was detected with *ppp* polarization configuration at various times after the pump pulse excitation (Fig. 1D). The pump polarization was alternated between *p*- and *s*-polarization, which are parallel and perpendicular to the probe pulse, respectively, to probe the reorientation dynamics. The excitation pulse breaks the azimuthal symmetry at the interface, and the decay of the induced anisotropy can be followed in real time. In the absence of molecular reorientation, the bleach lifetime should not display any polarization dependence (28, 38).

Fig. 1C shows the static spectrum obtained from negative time delays from the time-resolved vSFG experiments, which clearly

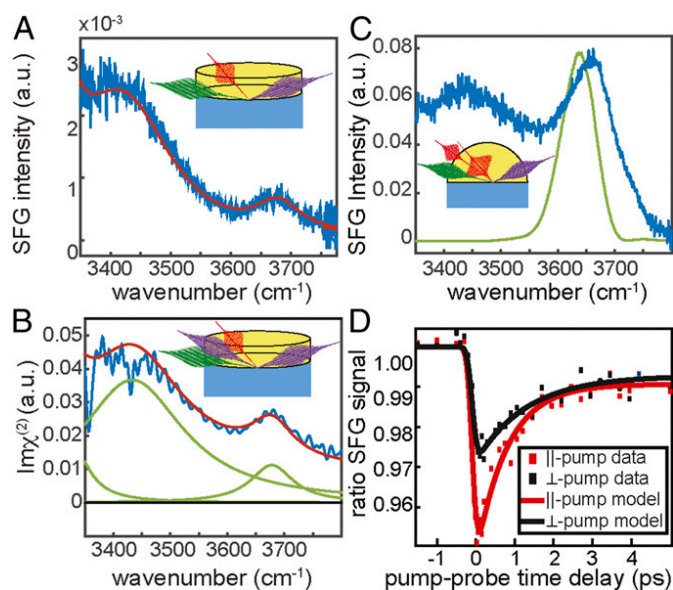


Fig. 1. Intensity and phase- and time-resolved surface-specific spectroscopy of the silica–water interface; vSFG (A) intensity spectrum and (B) phase-resolved (imaginary) spectrum of the silica/water interface collected in *ssp* polarization combination (blue traces). The red lines are a description of both datasets with one set of Lorentzian line shapes with a small non-resonant signal shown as green lines. The vSFG (C) static intensity spectrum (blue) and (D) time-resolved vSFG data of the silica/water (10 mM NaCl) interface. The excitation pulse spectrum used in the time-resolved experiments is illustrated in green (C). The data were collected in *ppp* polarization combination. The time-resolved traces were collected for parallel-pump (red) and perpendicular-pump (black) polarizations. The solid lines through the time-resolved data originate from the model described in the text. The sample geometries are illustrated in the *Insets* for the (A) intensity, (B) phase-resolved, and (C) time-resolved setups.

differs from the spectrum in Fig. 1A. For the time-resolved measurements, the polarization combination, salt concentration, and optical geometry were chosen to enhance the free OH signal. To this end, an IR-grade fused hemispherical silica substrate (Infrasil 302) is heated similarly to the previously described silica windows before being put in contact with a 10-mM salt solution. The 10-mM NaCl solution has been previously shown to reduce the intensity of hydrogen-bonded water peaks, thereby increasing the relative intensity of the free OH. The angles of incidence in the vSFG setup were set to take advantage of total internal reflection (TIR) conditions to further boost the signal (39). The employed *ppp* (rather than *ssp*) polarization combination yields higher signal-to-noise for the TIR geometry (39). Combined, these measures result in the high-frequency peak being more enhanced using the hemisphere (Fig. 1C) than the window (Fig. 1A).

The time-resolved results are shown in Fig. 1D, where the ratio of the SFG signals in presence and absence of the pump pulse is plotted as a function of pump-probe delay. The decrease in the ratio around 0 fs is the bleach of the ground state population. The offset at long delay times is due to slight heating (about a few degrees) (40) of the sample after vibrational relaxation. The time-resolved data were fit with a single exponential described by a three-level model, where a population of molecules in the ground state is excited to a vibrationally excited state and relaxes further to a heated ground state (41). The excitation pulse was modeled by a Gaussian with an FWHM of 150 fs. A single time constant, e.g., the bleach lifetime (τ_1), is extracted from the fits. The bleach lifetimes were 0.8 ± 0.08 ps and 1.3 ± 0.2 ps for parallel-polarized (τ_{\parallel}) and perpendicular-polarized (τ_{\perp}) excitation pulses, respectively.

Indeed, the bleach lifetimes of the “free” O-H at the silica/water interface are very comparable to that of ~ 1 ps reported for the free O-H of water at the water/air interface and 1.3 ± 0.1 ps for the extended hydrophobic interfaces (28, 36, 42). In contrast, the observed dynamics are an order of magnitude faster than the ~ 56 ps bleach lifetime measured for rigid surface silanol groups in contact with water (43). It should be noted, that Heilweil et al. (43) measured silica powder with physisorbed water in CCl_4 , but not fully in contact with water and relied on infrared transmission pump-probe measurements, rather than time-resolved SFG, each with distinct selection rules. Therefore, the time-resolved data indicates that the high-frequency peak from water pointing to the silica surface behaves similarly to water at hydrophobic interfaces.

Beyond the vibrational bleach relaxation lifetime, the dynamics contain information on the reorientation of the free OH groups at the silica/water interface. Specifically, the time-dependent difference in the parallel and perpendicularly pumped traces reflects a reorientation of excited OH groups. (28, 36) We semiquantitatively compare the results obtained here $\tau_{\parallel} = 0.80 \pm 0.08$ ps and $\tau_{\perp} = 1.3 \pm 0.2$ ps, with results from experiments on free OH groups at the water/air interface ($\tau_{\parallel} = 0.64 \pm 0.04$; $\tau_{\perp} = 0.80 \pm 0.07$ ps) and the extended hydrophobic ODS/water surface ($\tau_{\parallel} = 1.34 \pm 0.03$; $\tau_{\perp} = 1.55 \pm 0.04$ ps) (28, 36). The difference between the lifetimes observed for different polarizations shows that reorientation contributes significantly to the bleach dynamics, consistent with the OH groups originating from water. It is further evident that the reorientation dynamics of the OH groups studied here at the water-silica interface are very comparable to the reorientational dynamics of free OH groups of water at the hydrophobic water/air and water/ODS interfaces.

Summarizing the dynamic studies, it is evident that both the vibrational and reorientational dynamics of the free OH feature occurs on a ~ 1 ps timescale. This timescale is typical for interfacial water and therefore consistent with the OH group being part of a water molecule, rather than being a surface-bound silanol group.

Although the SFG results show there is microscopically water present that behaves like water at a hydrophobic surface, it is well known that macroscopically the silica surface is hydrophilic,

as can be seen from the contact angle measurements for a nonheated and heated silica sample, illustrated in Fig. 2A and B. The contact angles were measured to be $8.9^\circ \pm 1.0^\circ$ and $20.0^\circ \pm 1.5^\circ$ for the non-heat-treated and heat-treated silica window, respectively. These contact angles are in agreement with previous studies (44). The larger contact angle for the heated sample indicates a macroscopically less hydrophilic surface. Remarkably, the SFG spectra reveal that this surface, as opposed to the non-heated surface, exhibits an enhanced $3,660 \text{ cm}^{-1}$ intensity in the SFG spectra (Fig. 2C and D). This points to a clear correlation between the $3,660 \text{ cm}^{-1}$ intensity, reflecting microscopic hydrophobicity, and the macroscopic contact angle. Apparently, water with very weakly hydrogen-bonded OH groups, i.e., hydrophobic water, is present at a hydrophilic surface.

The molecular origin of this very weakly hydrogen-bonded water is not a priori evident: it could originate from a saturation of the hydrogen bond acceptors from the silica, rendering unpaired free OH groups from water. Another explanation could be steric hindrance at the surface, resulting from, e.g., a spatial mismatch between the typical distance between hydrogen bond donors of the interfacial water network, and that of the hydrogen-bonded acceptors at the silica surface.

To unravel the origin of this very weakly hydrogen-bonded water, we performed density functional theory (DFT) MD simulations. Silica surfaces are composed of Si-OH silanols, which have various pK_a activity (11, 45, 46) and Si-O-Si siloxane bridges, known as hydrophilic and hydrophobic sites, respectively (11, 47). The surface density of silanols reveals the hydrophilic/hydrophobic character of the surface, with 4–5 SiOH/nm², which is representative of hydrophilic surfaces and 1–2 SiOH/nm², which is representative of hydrophobic ones (11). SFG phonons (48) do show the existence of hydrophobic surface siloxanes at hydrophilic silica surfaces. Two silica models are used in the DFT-MD simulations, differing by the degree of surface hydroxylation (11), i.e., 4.5 (hydrophilic) and 3.5 (less hydrophilic) SiOH/nm². The 3.5 SiOH/nm² surface is chosen as a qualitative model for the effect of the heating treatment in the experiment (11). The simulations are performed at the point of zero charge, which also corresponds to the isoelectric point. Further discussion regarding the effect of surface charge on both the experimental and theoretical spectra can be found in the *SI Appendix*.

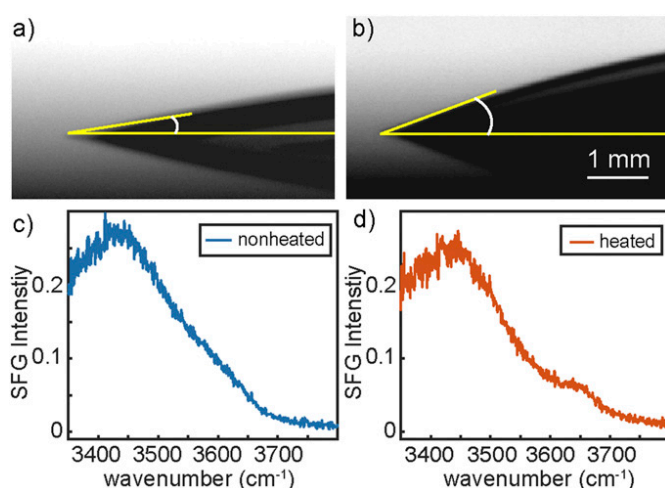


Fig. 2. Correlation between molecular and macroscopic hydrophobicity. Contact angle of water in contact with a nonheated (A) and heat-treated (B) silica window. The representative tangent line fits (yellow) were used to extract the contact angle. (C and D) The corresponding vSFG intensity spectra reveal a correlation between the contact angle and the $3,660 \text{ cm}^{-1}$ quasi-free OH intensity.

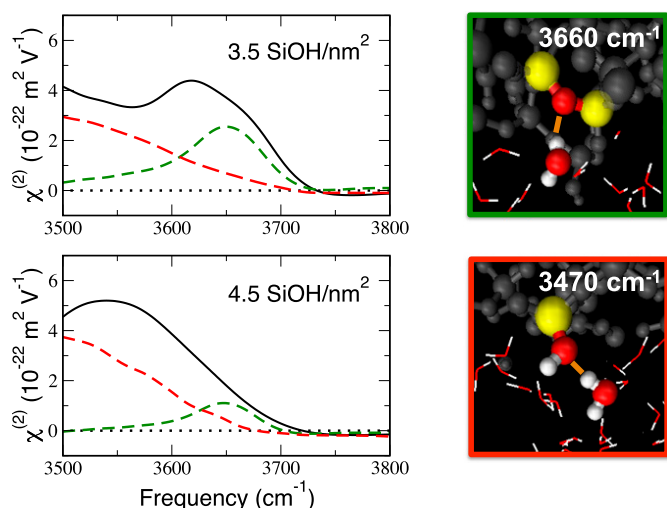


Fig. 3. DFT-MD simulations reveal the origin of hydrophobic sites on the fused silica surface. (Left) Theoretical vSFG signal ($\text{Im}\chi^{(2)}$) in the 3,500–3,800 cm^{-1} region for two silica surfaces with various degrees of surface hydroxylation (3.5 and 4.5 SiOH/nm^2). The black line is the total vSFG signal and the dotted lines are the microscopic assignments (deconvolved signatures, see text and *SI Appendix*). Green dashed line: vSFG due to the water molecules that have one O-H oscillator pointing toward a siloxane bridge. Red dashed line: vSFG due to the water molecules with one O-H oscillator pointing toward an in-plane silanol group. (Right) Snapshots from DFT-MD simulations illustrating the microscopic origin of the observed spectral contributions (see text for details).

The vSFG spectrum ($\text{Im}\chi^{(2)}$) of interfacial water has been extracted from the DFT-MD simulations, following our recent works (49–51) (black lines in Fig. 3, details in the *SI Appendix*) for the 3,500–3,800 cm^{-1} spectral region for each silica–water interface. The vSFG spectral intensity in this range can be traced to the 3-Å-thickness water monolayer at the direct interface with the silica surface (binding interfacial layer [BIL], see *SI Appendix* and refs. 49 and 50) and more specifically to contributions from two distinct water OH groups (dashed red and green lines in Fig. 3; details in the *SI Appendix*). Within the BIL, water molecules with one OH group pointing toward a siloxane bridging oxygen atom solely produce the positive band at 3,660 cm^{-1} (green line in Fig. 3). The high frequency of these features indicates the quasi-free nature of the OH groups. The water molecules with one OH group pointing toward an in-plane surface silanol site give rise to the broad positive vSFG band, centered at 3,470 cm^{-1} , illustrated as red lines in Fig. 3 and showing only the tail of the band in the 3,500–3,800 cm^{-1} range of interest here. On average, the latter water population has no dangling O-H, while the O-H pointing toward the siloxane bridge in the former water population is the only dangling O-H. The surface silanol sites do not contribute to the vSFG spectral features in the 3,500–3,800 cm^{-1} range (see *SI Appendix* where we show that only the in-plane silanols have vibrational signatures in the 3,500–3,800 cm^{-1} range, however not vSFG active because of their in-plane orientation). Note that although the DFT-MD-vSFG is obtained at the isoelectric point ($\text{pH} \sim 2$) the experiment is measured at $\text{pH} \sim 7$, where the surface is slightly negatively charged, hence providing an overlapping diffuse layer vSFG positive contribution at 3,200–3,400 cm^{-1} (51, 52). This does not affect the 3,660 cm^{-1} band of interest in this work.

The number of water molecules that belong to these two populations depends on the degree of hydroxylation of the surface. We find that the water population with one OH group pointing toward a siloxane bridge increases from 0.8 to 3.0 water molecules/ nm^2 when going from 4.5 to 3.5 SiOH/nm^2 surface silica

hydroxylation. With increased silanol density, fewer water molecules interact with siloxane bridges due to steric hindrance by adjacent silanol groups. Removing one SiOH/nm^2 from the silica surface leads to the reconstruction of the surface, creating one siloxane bridge and one desorbed water starting from two surface silanols. Without these silanols, the siloxanes are now free to interact with water and hence give rise to the observed roughly 4 times increase in water interacting with siloxanes.

There is spectroscopic evidence from experiments and simulations of water dangling/quasi-free OH groups at the direct interface with nominal hydrophilic silica surfaces. This counterintuitive result stems from the coexistence of hydrophilic and hydrophobic patches on the silica surface. This is derived from the DFT-MD simulations and illustrated in Fig. 4 by correlating the spatial distribution of surface silanol/siloxane (exposed) sites with the spatial distribution of BIL-water molecules that have one dangling O-H group with the 3,660 cm^{-1} vSFG signature for two surfaces with a different silanol density. The lateral (x - y directions along the solid surface) spatial distribution of silanol groups (represented by gray balls) and siloxane sites (Si-O-Si represented by red O atoms) at the two silica surfaces are presented in Fig. 4 *A* and *C*, Left. The corresponding density of BIL water with one 3,660 cm^{-1} O-H group is presented in Fig. 4 *B* and *D*, Right, over the same lateral dimensions and same orientation of the silica surfaces. The maximum density is in red in these plots. A one-to-one correspondence between siloxane sites and quasi-free OH density is clearly observed.

Fig. 4 *A* and *C* nicely show that there is a nonuniform distribution of silanols and siloxanes at the two silica surfaces, with coexisting silanol-rich (hydrophilic) and siloxane-rich (hydrophobic) domains at the surfaces. The red line in the figures indicates the most hydrophobic surface areas where the silanol density is ≤ 1.5 SiOH/nm^2 . Clearly, hydrophobic patches are

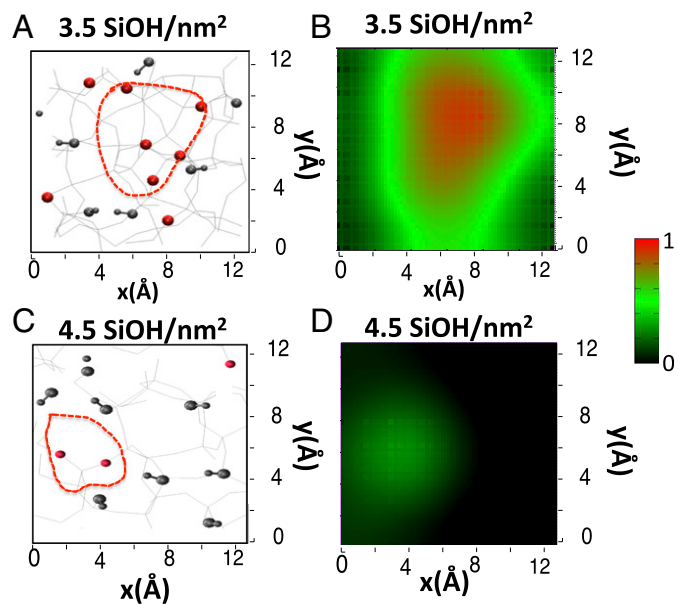


Fig. 4. Correlation between the spatial distributions of surface silanol/siloxane exposed sites (Left) and water molecules with a quasi-free OH group (Right). (Left) Top view of the two silica surfaces modeled in the DFT-MD: silanol density of 3.5 SiOH/nm^2 (A) and 4.5 SiOH/nm^2 (C). The red lines indicate the hydrophobic patches (i.e., areas of the surface with the lowest silanol densities). The surface SiOH groups are highlighted with gray balls for oxygens and hydrogens, while the Si-O-Si siloxanes are highlighted by the oxygens only (in red). (Right) Density of water quasi-free OH groups spatially resolved above the surface (x - y plane, same dimension and same orientation as in A and C) for the 3.5 SiOH/nm^2 (B) and 4.5 SiOH/nm^2 (D) silica–water interfaces modeled in the DFT-MD. The red/green colors refer to the maximum probability to find a water quasi-free OH group, indicated by the scale bar.

present at a nominally hydrophilic silica surface, in agreement with ref. 47. Such hydrophobic patches have also been identified at model solid surfaces (53) and self-assembled monolayers (54). Not surprisingly, the dimension of these patches is dependent on the surface degree of hydroxylation. We find one large hydrophobic patch made of five siloxane bridges at the 3.5 SiOH/nm² silica surface, while the hydrophobic patch consists only of two adjacent O-Si-O sites at the 4.5 SiOH/nm² surface. Thus, the latter surface can be seen as more hydrophilic, which is in agreement with the experimental results showing a smaller contact angle in combination with the absence of a high frequency vSFG signal. Based on the DFT-MD results, we thus conclude that surface hydrophobic patches induce areas in the water layer in direct contact with silica, which are composed of water molecules with one quasi-free O-H group interacting with the siloxane bridges of the hydrophobic patches. These molecular groups are responsible for the 3,660 cm⁻¹ vSFG feature.

The relationship between macroscopic contact angle measurements and microscopic vSFG spectroscopy can furthermore be rationalized as follows: the decrease in surface silanols, macroscopically probed with the increase in contact angle, results in an increase of exposed O-Si-O siloxane bridges at the surface that consequently result in water quasi-free O-H groups at the direct interface with silica, solely contributing to the vSFG intensity at 3,660 cm⁻¹.

Molecular-level insights into the structure and dynamics of minerals in contact with aqueous solutions contribute not only to a fundamental understanding of dissolution and sorption processes on mineral surfaces but also to potential new avenues for their synthetic design. This study explores the tunable hydrophobicity of silica surface chemistry in contact with water, both on a macroscopic and molecular scale. The spectroscopic results and MD simulations unambiguously show that the free OH peak observed at the water-fused silica interface is due to water. The OH groups are oriented toward the surface of silica, specifically toward siloxane bridges, and the dynamics of the free OH groups at the silica/water interface are quantitatively comparable to the free OH at the air-water interface, both regarding its reorientational and vibrational dynamics (28, 29). Our study reveals water interacting with hydrophobic patches at the nominally hydrophilic silica/water interface.

Methods and Materials

Samples. Sodium chloride (NaCl) was purchased from Sigma-Aldrich (99%) and H₂¹⁸O (97%) was purchased from Euriso-top. The NaCl was heated to 550 °C for 3 h to remove impurities. The Infrasil 302 silica samples were in two different geometries, 10-mm diameter hemispheres (CVI Melles Griot) and 25 mm × 2 mm windows (Korth Kristalle). The hemispheres and the windows (both heated and nonheated) were sonicated in ethanol, water, and then immersed in 3:1 Piranha solution for 10 min. The “heated” samples were subsequently heated at 950°C for 4 h and after cooling down, the

samples were placed in 3:1 acidic Piranha solution for 10 min. All glassware was sonicated in Deconex, ethanol, and Millipore water for 15 min and finally rinsed thoroughly with Millipore water.

Phase-Resolved SFG Spectrometer. The phase-resolved SFG spectrometer utilizes pulses centered at 800 nm and ~40 fs in duration, which are generated from a Ti:Sapphire regenerative amplifier (Spitfire Ace; Spectra-Physics). A portion of the output is directed to an optical parametric amplifier (Light Conversion TOPAS-Prime) with a noncollinear difference frequency generation stage to produce pulses centered around 3,600 cm⁻¹ (IR). Another portion of the regen output (~1 mJ) is passed through an etalon to provide a 25 cm⁻¹ visible pulse (VIS) and sets the spectral resolution of the SFG experiments. The IR and VIS pulses are focused with 5- and 100-cm lenses, respectively, and overlapped in time and space on a gold mirror to generate the local oscillator (LO). The IR, VIS, and LO are directed to a 5-cm focal length curved mirror and focused at the sample, an Infrasil 302 silica window in contact with water. The angles of incidence with respect to the surface normal of the silica-air interface are ~45° for the IR and 40° for the VIS. The LO is delayed relative to the IR and VIS pulses with a 1-mm-thick fused silica plate. The LO and the SFG signal are directed to a spectrometer (Acton SP-2300; Princeton Instruments) and measured on an electron-multiplying charge-coupled device camera (Newton 970; Andor). The phase-resolved SFG spectra were collected for 5 min in the ssp polarization combination. An intensity spectrum can also be measured with the phase-resolved SFG spectrometer by blocking the LO signal. Further details on the phase-resolved measurements, and data analysis can be found in the [SI Appendix](#).

MD Simulations. Born-Oppenheimer DFT-MD simulations have been carried out on amorphous silica/liquid water interfaces, consisting in the Becke Lee Yang Parr (BLYP) (55, 56) representation including the Grimme D2 correction for dispersion (57, 58). Two hydrophobic silica models have been chosen, displaying a surface degree of hydroxylation of 4.5 SiOH/nm² (i.e., eight SiOH groups in the simulation box) and 3.5 SiOH/nm² (six SiOH in our simulation box), respectively. The amorphous silica models are taken from Ugliengo et al. (59). The surfaces in contact with air have a 4.5 and 2.4 SiOH/nm² coverage in silanols that become 4.5 and 3.5 SiOH/nm², respectively, once the surfaces are put in contact with water (see [SI Appendix](#) for more details). Theoretical vibrational sum frequency generation spectra of the silica/water interfaces (including both water and solid contributions) are calculated using the formalism presented in refs. 51, 60. We refer to [SI Appendix](#) for more details about the computational setup and theoretical spectra calculations and their microscopic assignments.

ACKNOWLEDGMENTS. We thank Azadeh Sharifi for assistance with the contact angle measurements; Eric Tyrode, Jonathan Liljebald, and Shumei Sun for helpful discussions; Malte Deiseroth for the analytical solution for the fit function for the time-resolved data; and Hansjörg Menges and Marc-Jan van Zadel for excellent technical support. We thank Wybren-Jan Buma for suggesting the H₂¹⁸O experiments and P. Ugliengo for sharing amorphous silica models. High-performance computing resources from Grand équipement national de calcul intensif (GENCI)-France Grant 072484 (CINES/IDRIS/TGCC) are acknowledged. J.D.C. acknowledges the Alexander von Humboldt Foundation for financial support. This work was funded by a European Research Council Starting Grant (Grant 336679) and the bilateral France-Germany ANR-DFG DYNAMIN Grant 14-CE35-0011-01 and BA 5008/3.

- Putnis A (2014) Materials science. Why mineral interfaces matter. *Science* 343:1441–1442.
- Brown GE, Jr (2001) Surface science. How minerals react with water. *Science* 294: 67–69.
- Minakata S, Komatsu M (2009) Organic reactions on silica in water. *Chem Rev* 109: 711–724.
- Kubicki JD, ed (2016) *Molecular Modeling of Geochemical Reactions* (John Wiley & Sons, West Sussex, United Kingdom).
- El Hage K, Gupta PK, Bemish R, Meuwly M (2017) Molecular mechanisms underlying solute retention at heterogeneous interfaces. *J Phys Chem Lett* 8:4600–4607.
- Farrokhpay S (2011) The significance of froth stability in mineral flotation—A review. *Adv Colloid Interface Sci* 166:1–7.
- Leonardelli S, Facchini L, Fretigny C, Toungne P, Legrand AP (1992) Silicon-29 NMR study of silica. *J Am Chem Soc* 114:6412–6418.
- Zhuravlev LT (1987) Concentration of hydroxyl groups on the surface of amorphous silicas. *Langmuir* 3:316–318.
- Zhuravlev LT (2000) The surface chemistry of amorphous silica. Zhuravlev model. *Colloids Surf Physicochem Eng Asp* 173:1–38.
- Dalstein L, Potapova E, Tyrode E (2017) The elusive silica/water interface: Isolated silanols under water as revealed by vibrational sum frequency spectroscopy. *Phys Chem Chem Phys* 19:10343–10349.
- Rimola A, Costa D, Sodupe M, Lambert J-F, Ugliengo P (2013) Silica surface features and their role in the adsorption of biomolecules: Computational modeling and experiments. *Chem Rev* 113:4216–4313.
- Khatib R, et al. (2016) Water orientation and hydrogen-bond structure at the fluorite/water interface. *Sci Rep* 6:24287.
- Becraft KA, Richmond GL (2001) In situ vibrational spectroscopic studies of the CaF₂/H₂O interface. *Langmuir* 17:7721–7724.
- Zhang L, Tian C, Waychunas GA, Shen YR (2008) Structures and charging of α-alumina (001)/water interfaces studied by sum-frequency vibrational spectroscopy. *J Am Chem Soc* 130:7686–7694.
- Tong Y, et al. (2015) Optically probing Al-O and O-H vibrations to characterize water adsorption and surface reconstruction on α-alumina: An experimental and theoretical study. *J Chem Phys* 142:054704-12.
- Tuladhar A, Dewan S, Kubicki JD, Borguet E (2016) Spectroscopy and ultrafast vibrational dynamics of strongly hydrogen bonded OH species at the α-Al₂O₃(1120)/H₂O interface. *J Phys Chem C* 120:16153–16161.
- Casassa MP, Heilweil EJ, Stephenson JC, Cavanagh RR (1986) Time-resolved measurements of OH(v=1) vibrational relaxation on SiO₂ surfaces: Isotope and temperature dependence. *J Chem Phys* 84:2361–2364.

18. Heilweil EJ, Casassa MP, Cavanagh RR, Stephenson JC (1985) Temperature dependence of the vibrational population lifetime of OH($\nu = 1$) in fused silica. *Chem Phys Lett* 117:185–190.
19. Zhdanov SP, Kosheleva LS, Titova TI (1987) IR study of hydroxylated silica. *Langmuir* 3: 960–967.
20. Casillas-Iltuarte NN, Allen HC (2009) Water, chloroform, acetonitrile, and atrazine adsorption to the amorphous silica surface studied by vibrational sum frequency generation spectroscopy. *Chem Phys Lett* 483:84–89.
21. Isaienko O, Borguet E (2013) Hydrophobicity of hydroxylated amorphous fused silica surfaces. *Langmuir* 29:7885–7895.
22. Yang Z, Li Q, Gray MR, Chou KC (2010) Structures of water molecules at solvent/silica interfaces. *Langmuir* 26:16397–16400.
23. Ostroverkhov V, Waychunas GA, Shen YR (2005) New information on water interfacial structure revealed by phase-sensitive surface spectroscopy. *Phys Rev Lett* 94: 046102.
24. Myalitsin A, Urashima S, Nihonyanagi S, Yamaguchi S, Tahara T (2016) Water structure at the buried silica/aqueous interface studied by heterodyne-detected vibrational sum-frequency generation. *J Phys Chem C* 120:9357–9363.
25. Vanselow H, Petersen PB (2016) Extending the capabilities of heterodyne-detected sum-frequency generation spectroscopy: Probing any interface in any polarization combination. *J Phys Chem C* 120:8175–8184.
26. Jena KC, Hore DK (2009) Variation of ionic strength reveals the interfacial water structure at a charged mineral surface. *J Phys Chem C* 113:15364–15372.
27. Tyrode E, Liljeblad JFD (2013) Water structure next to ordered and disordered hydrophobic silane monolayers: A vibrational sum frequency spectroscopy study. *J Phys Chem C* 117:1780–1790.
28. Hsieh C-S, et al. (2011) Ultrafast reorientation of dangling OH groups at the air-water interface using femtosecond vibrational spectroscopy. *Phys Rev Lett* 107:116102.
29. Hsieh C-S, et al. (2013) Mechanism of vibrational energy dissipation of free OH groups at the air-water interface. *Proc Natl Acad Sci USA* 110:18780–18785.
30. Tong Y, Lapointe F, Thämer M, Wolf M, Campen RK (2017) Hydrophobic water probed experimentally at the gold electrode/aqueous interface. *Angew Chem Int Ed Engl* 56:4211–4214.
31. Ostroverkhov V, Waychunas GA, Shen YR (2004) Vibrational spectra of water at water/ α -quartz (0 0 0 1) interface. *Chem Phys Lett* 386:144–148.
32. Schrader AM, et al. (2018) Surface chemical heterogeneity modulates silica surface hydration. *Proc Natl Acad Sci USA* 115:2890–2895.
33. Ong S, Zhao X, Eisenthal KB (1992) Polarization of water molecules at a charged interface: Second harmonic studies of the silica/water interface. *Chem Phys Lett* 191: 327–335.
34. Sulpizi M, Gaigeot M-P, Sprk M (2012) The silica-water interface: How the silanols determine the surface acidity and modulate the water properties. *J Chem Theory Comput* 8:1037–1047.
35. Liu X, Cheng J, Lu X, Wang R (2014) Surface acidity of quartz: Understanding the crystallographic control. *Phys Chem Chem Phys* 16:26909–26916.
36. Xiao S, Figge F, Stirnemann G, Laage D, McGuire JA (2016) Orientational dynamics of water at an extended hydrophobic interface. *J Am Chem Soc* 138:5551–5560.
37. Donovan MA, et al. (2016) Ultrafast reorientational dynamics of leucine at the air-water interface. *J Am Chem Soc* 138:5226–5229.
38. Nienhuys H-K, Bonn M (2009) Measuring molecular reorientation at liquid surfaces with time-resolved sum-frequency spectroscopy: A theoretical framework. *J Phys Chem B* 113:7564–7573.
39. Liljeblad JFD, Tyrode E (2012) Vibrational sum frequency spectroscopy studies at solid/liquid interfaces: Influence of the experimental geometry in the spectral shape and enhancement. *J Phys Chem C* 116:22893–22903.
40. Ramasesha K, De Marco L, Mandal A, Tokmakoff A (2013) Water vibrations have strongly mixed intra- and intermolecular character. *Nat Chem* 5:935–940.
41. van der Post ST, et al. (2015) Strong frequency dependence of vibrational relaxation in bulk and surface water reveals sub-picosecond structural heterogeneity. *Nat Commun* 6:8384.
42. McGuire JA, Shen YR (2006) Ultrafast vibrational dynamics at water interfaces. *Science* 313:1945–1948.
43. Heilweil EJ, Casassa MP, Cavanagh RR, Stephenson JC (1985) Vibrational deactivation of surface OH chemisorbed on SiO₂: Solvent effects. *J Chem Phys* 82:5216–5231.
44. Lamb RN, Furlong DN (1982) Controlled wettability of quartz surfaces. *J Chem Soc Faraday Trans 1 Phys Chem Condens Phases* 78:61–73.
45. Pfeiffer-Laplaud M, Gaigeot M-P, Sulpizi M (2016) pKa at quartz/electrolyte interfaces. *J Phys Chem Lett* 7:3229–3234.
46. Cimas Á, Tielens F, Sulpizi M, Gaigeot M-P, Costa D (2014) The amorphous silica-liquid water interface studied by ab initio molecular dynamics (AIMD): Local organization in global disorder. *J Phys Condens Matter* 26:244106–244115.
47. Hassanali AA, Singer SJ (2007) Model for the water-amorphous silica interface: The undissociated surface. *J Phys Chem B* 111:11181–11193.
48. Liu W-T, Shen YR (2008) Surface vibrational modes of α -quartz(0001) probed by sum-frequency spectroscopy. *Phys Rev Lett* 101:016101-4.
49. Pezzotti S, Galimberti DR, Shen YR, Gaigeot M-P (2018) What the diffuse layer (DL) reveals in non-linear SFG spectroscopy. *Minerals (Basel)* 8:305–315.
50. Pezzotti S, Gaigeot M-P (2018) Spectroscopic BIL-SFG invariance hides the chaotropic effect of protons at the air-water interface. *Atmosphere* 9:396–411.
51. Pezzotti S, Galimberti DR, Shen YR, Gaigeot M-P (2018) Structural definition of the BIL and DL: A new universal methodology to rationalize non-linear $\chi^{(2)}(\omega)$ SFG signals at charged interfaces, including $\chi^{(3)}(\omega)$ contributions. *Phys Chem Chem Phys* 20: 5190–5199.
52. Urashima SH, Myalitsin A, Nihonyanagi S, Tahara T (2018) The topmost water structure at a charged silica/aqueous interface revealed by heterodyne-detected vibrational sum frequency generation spectroscopy. *J Phys Chem Lett* 9:4109–4114.
53. Shin S, Willard AP (2018) Water's interfacial hydrogen bonding structure reveals the effective strength of surface-water interactions. *J Phys Chem B* 122:6781–6789.
54. Xi E, et al. (2017) Hydrophobicity of proteins and nanostructured solutes is governed by topographical and chemical context. *Proc Natl Acad Sci USA* 114:13345–13350.
55. Becke AD (1988) Density-functional exchange-energy approximation with correct asymptotic behavior. *Phys Rev A Gen Phys* 38:3098–3100.
56. Lee C, Yang W, Parr RG (1988) Development of the Colle-Salvetti correlation-energy formula into a functional of the electron density. *Phys Rev B Condens Matter* 37: 785–789.
57. Grimme S (2004) Accurate description of van der Waals complexes by density functional theory including empirical corrections. *J Comput Chem* 25:1463–1473.
58. Grimme S (2006) Semiempirical GGA-type density functional constructed with a long-range dispersion correction. *J Comput Chem* 27:1787–1799.
59. Ugliengo P, et al. (2008) Realistic models of hydroxylated amorphous silica surfaces and MCM-41 mesoporous material simulated by large-scale periodic B3LYP calculations. *Adv Mater* 20:4579–4583.
60. Pezzotti S, Galimberti DR, Gaigeot M-P (2017) 2D H-bond network as the topmost skin to the air-water interface. *J Phys Chem Lett* 8:3133–3141.

Molecular Hydrophobicity at a Macroscopically Hydrophilic Surface

Jenée D. Cyran,^{a,†} Michael A. Donovan,^{a,†} Doris Vollmer,^a Flavio Siro Brigiano,^b Simone Pezzotti,^b Daria R. Galimberti,^b Marie-Pierre Gageot,^b Mischa Bonn^a and Ellen H.G. Backus^{a,c*}

^aMax Planck Institute for Polymer Research, Ackermannweg 10, 55128 Mainz, Germany

^bLAMBE, Univ Evry, Université Paris-Saclay, CNRS UMR8587, 91025 Evry, France

^cDepartment of Physical Chemistry, University of Vienna, Währinger Strasse 42, 1090 Vienna, Austria

[†]These authors contributed equally to this work.

*email: bonn@mpip-mainz.mpg.de; backus@mpip-mainz.mpg.de

Section S1. Phase-Resolved SFG Details

To extract the real and imaginary spectra, a gold-coated silica window was used for referencing and alignment purposes. The gold reference and the aqueous samples utilized the exact same Infrasil 302 silica window. The silica/water experiments were completed and then the silica window was coated with 100 nm gold with no chromium layer. The gold reference and aqueous samples were placed at the same height and position using an alignment laser and measuring the SFG signal at the same height on the CCD camera. Careful alignment is critical to ensure no phase ambiguities in the data. Following previously described methods for data analysis,^(1, 2) the raw spectra are inversed Fourier transformed into the time domain, filtered for specific terms, and Fourier transformed into the frequency domain. Subsequently, the sample was divided by the reference, rendering the real and imaginary spectra. Similar to

the CaF₂/water phase-resolved results,(3) a phase correction of -170° was applied to account for differences in the Fresnel factors and reflectivity between the silica/gold reference and the silica/water samples. Previous work used the silica/D₂O interface to rephase the silica/water SFG data.(4) However, the nonresonant SFG signal from the interference fringes were too weak in the high frequency region in our phase-resolved SFG spectrometer. Thus, the gold/silica interface was used for the reference. Knowing that the phase of quartz is ±90 degrees,(5) we compare the phase of quartz and gold to find that gold has a real nonresonant signal. The IR Fresnel factors (L_{zz}) were calculated following a procedure outlined by Zhuang, et al.,(6) where the index of refraction for interface 1 was set equal to water.(7) The refractive indices of water and silica were taken from literature.(8, 9)

To check for impurities at the interface, the output of the TOPAS was shifted to the C-H stretch region (around 2900 cm⁻¹). No signal was observed in the C-H region, indicating the samples were clean.

Section S2. Time-Resolved SFG Spectrometer

For the time resolved SFG spectrometer, a 1 kHz Ti:Sapphire amplified laser (Spectra-Physics Spitfire Pro) produces pulses centered at 800 nm, ~5 mJ in energy, and 40 fs in duration. A portion of the 800 nm output is used to pump two OPAs (Light Conversion TOPAS-C). One OPA collinearly mixes the signal and idler in a DFG generation stage with a AgGaS₂ crystal centered at roughly 3600 cm⁻¹. The Idler field from the other OPA is doubled in a BBO crystal and mixed in a KTP crystal with 2 mJ of the 800 nm beam. The output pulses, referred to as the pump, are centered around 3650 cm⁻¹. The remaining 800 nm pulse output is used as the visible upconversion pulse and is narrowed to 20 cm⁻¹ by a Fabry Perot etalon. The visible, probe and excitation pulses have incident angles of 71°, 55° and 42° with

respect to the surface normal and energies of 12, 0.5, and 10 μJ per pulse at the sample, respectively. The SFG signal is divided into two signals; a signal with excitation pulse and without excitation pulse, via a vibrating galvano-mirror set to 500 Hz and synchronized to a mechanical chopper to block every other excitation pulse. The excited and not excited signals are dispersed in a spectrometer (Acton SP-300i, Princeton Instruments) and measured simultaneously on a CCD detector (Newton 971, Andor). The spectra were measured at 55 time delays ranging from -5 to 100 ps. The SFG signals are acquired for 20 s for *p*- and *s*-pump polarizations at each time delay. The results are an average of 25 scans. The visible and the probe pulses are set to *p*-polarized.

A gold coated hemisphere was used for referencing and alignment purposes. The laser beams were overlapped spatially in the center of the hemisphere, which was confirmed using a white light microscope (InfiniTube). The sample cell consisted of a custom-made glass cell sealed with a Kalrez O-ring and the Infrasil silica hemisphere placed on top.

Section S3. Contact Angle Measurements

Contact angles were measured using a DataPhysics OCA35 contact angle goniometer. Initially, 1 μL drop were deposited on the Infrasil silica windows. To reduce evaporation the silica window was placed inside a homemade transparent humidity chamber, containing a small hole for the syringe. The humidity was adjusted by placing water near the window in the chamber. Afterwards, 2 μL of water were added to the drop at a velocity of 1 $\mu\text{L}/\text{s}$ and the shape of the contact line was monitored during spreading. After about 20 s, the drop reached its maximum diameter. The contact angle was determined by aligning a tangent to the drop shape by hand, as illustrated in the insets in Figure S1. For comparison, the angles were determined using the supplied software as a function of time. As evaporation cannot be

completely prevented, the contact angle slowly decreased over the course of time. After about 30s, the angle decreased by 1-2°. The measurement was consecutively repeated on four spots for the nonheat-treated and the heat-treated windows. The error of the contact angle measurements was estimated to be $\pm 2^\circ$.

Section S4. H₂¹⁸O Measurements

Experiments were completed to compare H₂O with H₂¹⁸O. If the free OH signal originates from water, one would expect a shift in the spectrum, as illustrated in Figure S1. The spectra were not corrected for Fresnel factors and the change from ¹⁶O to ¹⁸O could change the refractive index.

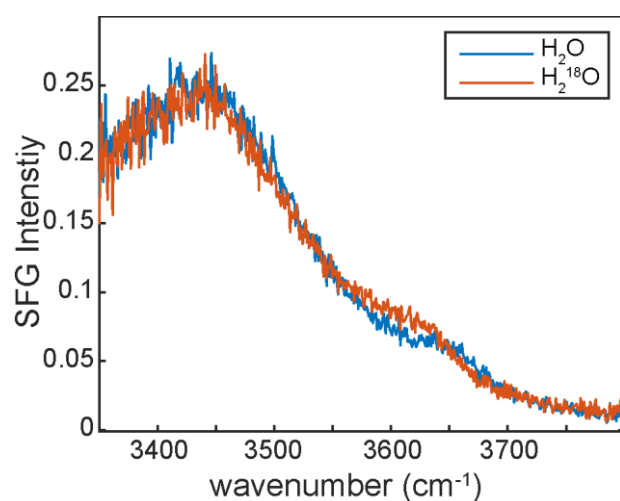


Figure S1. vSFG intensity spectra for comparison between the silica/water interface with H₂O (blue) and H₂¹⁸O (red).

Section S5. Effect of Surface Charge

The effect of surface charge was explored with a combination of intensity and phase-resolved vSFG. The intensity spectra in Figure S2a illustrate that while the hydrogen bonded water at lower frequencies changes based on pH, the high frequency peak remains constant.

The 10 mM NaCl solution has the same ionic strength as the pH 2 solution (i.e. 10^{-2} mM HCl) and was tested to verify that the ions were not contributing to the differences between the pH 2 and pH 6 spectra.

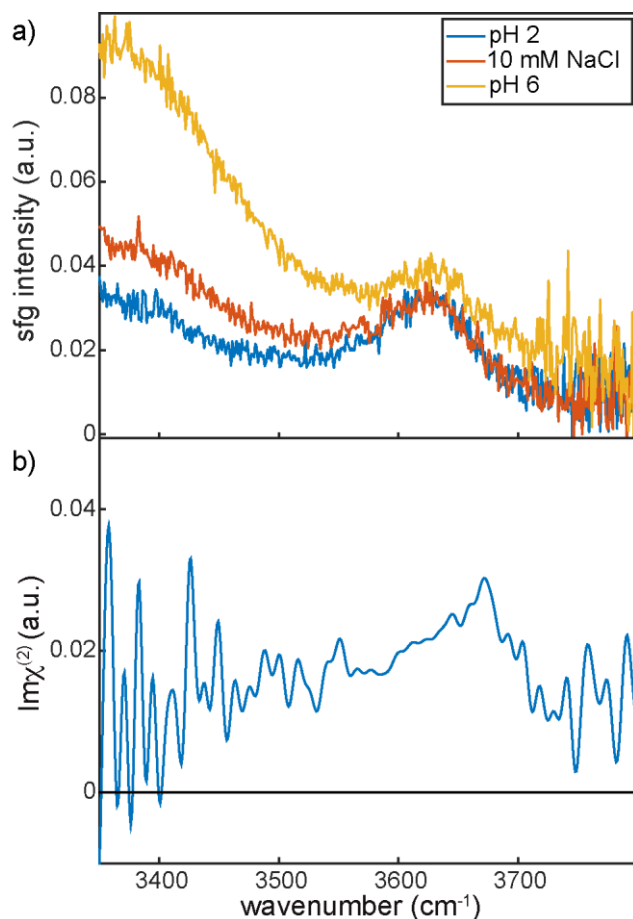


Figure S2. vSFG a) intensity spectra for pH 2, 10 mM NaCl, and \sim pH 6 (MilliQ water) in contact with a silica window. b) Imaginary vSFG spectrum of pH 2 in contact with a silica window.

Figure S2b depicts the imaginary spectrum for a pH 2 solution in contact with silica. The high frequency peak is positive, which is similar to the spectral feature for a pH 6 solution in contact with silica (see Figure 1b in manuscript).

Section S6. Amorphous models and computational methods.

DFT-MD (Density Functional Theory-based Molecular Dynamics) simulations have been carried out on amorphous silica/liquid water interfaces. Two hydrophobic silica models have been chosen, displaying a surface degree of hydroxylation respectively of 4.5 SiOH/nm² (i.e. eight SiOH groups in our simulation box) and 3.5 SiOH/nm² (six SiOH in our simulation box). These models are taken from Ugliengo *et al.*,⁽¹²⁾ respectively with a 4.5 SiOH/nm² and 2.4 SiOH/nm² silanol coverage of the surface in contact with air. Once put in contact with water, the 4.5 SiOH/nm² surface is found stable, while the 2.4 SiOH/nm² initial surface coverage evolves to 3.5 SiOH/nm². There is indeed a very fast adsorption of one water molecule, leading to the breaking of an adjacent siloxane bridge and subsequent dissociation of the adsorbed water molecule. This results into the creation of two new silanol groups upon local reconstruction of the silica surface, hence increasing the hydroxylation coverage of the aqueous surface from 2.4 to 3.5 SiOH/nm². The protonation state of these silica surfaces is around the potential of zero charge PZC (pH=2-4 conditions), and as will be seen in the next sections corresponds to isoelectric conditions (no surface electric field).

The DFT-MD simulations have been conducted with the CP2K software package,^(13, 14) consisting in Born-Oppenheimer MD, BLYP^(15, 16) electronic representation including Grimme D2 correction for dispersion,^(17, 18) GTH pseudopotentials⁽¹⁹⁾ and a combined plane waves (400 Ry energy cut-off) and SR-DZVP-MOLOPT gaussian basis set for all atoms. Dimensions of the simulation boxes are 13.386 Å X 13.286 Å X 37.0 Å (4.5 SiOH/nm² model) and 12.670 Å X 13.270 Å X 37.0 Å (3.5 SiOH/nm² model), and are periodically repeated in all directions of space. The silica slabs are 12 Å thick, composed of 204 and 198 atoms (4.5 & 3.5 SiOH/nm² models, respectively). Liquid water is modeled with 120 and 116 water molecules in these boxes, providing the required 1 g/cm³ liquid density. The amorphous silica slabs were reoptimized in the gas phase at the level of theory adopted

for the dynamics, and then put in contact with bulk water. After an equilibration run of 10 ps (5 ps with possible rescaling of velocities plus 5 ps in the pure NVE ensemble) the dynamics were run in the NVE ensemble for 20 ps with a time step of 0.4 fs. All analyzed data are taken from these 20 ps thermalized trajectories.

The vSFG (vibrational Sum Frequency Generation) spectra presented in this work measure the $\chi^{(2)}(\omega)$ response in the O-H stretching region, which could arise from both the water molecules (eq 1) and from the solid surface silanols (eq 2). Surface silanols can indeed contribute to the O-H stretching signal, as shown at the quartz/water interface.⁽²⁰⁾ See next sections and main text for a description of the water layers that indeed contribute to the vSFG signals at the amorphous/water interfaces investigated here. The imaginary (and real, not presented here) parts of the resonant electric dipole nonlinear susceptibility $\chi^{(2)}(\omega)$ are calculated.

As presented in refs (21, 22), $\chi^{(2)}(\omega)$ arising from water is calculated through equation 1:

$$\chi_{PQR}^{(2)}(\omega) = \sum_{mol=1}^M \sum_{OH1=1}^2 \sum_{OH2=1}^2 \frac{i}{k_b T \omega} \int dt e^{-i\omega t} \left\langle \left(\sum_{i=1}^3 \sum_{j=1}^3 D_{Pi}^{mol}(t) D_{Qj}^{mol}(t) \frac{d\alpha_{ij}}{dr_{OH1}} \right) v_{OH1}^{mol}(t) \left(\sum_k D_{Rk}^{mol}(0) \frac{d\mu_k}{dr_{OH2}} \right) v_{OH2}^{mol}(0) \right\rangle \quad (1)$$

Similarly, the surface silanols contribution to vSFG is calculated as:

$$\chi_{PQR}^{(2)}(\omega) = \sum_{SiOH=1}^N \frac{i}{k_b T \omega} \int dt e^{-i\omega t} \left\langle \left(\sum_{i=1}^3 \sum_{j=1}^3 D_{Pi}^{SiOH}(t) D_{Qj}^{SiOH}(t) \frac{d\alpha_{ij}}{dr_{OH}} \right) v_{OH}^{SiOH}(t) \left(\sum_k D_{Rk}^{SiOH}(0) \frac{d\mu_k}{dr_{OH}} \right) v_{OH}^{SiOH}(0) \right\rangle \quad (2)$$

where (P,Q,R) are any x, y, z directions in the laboratory frame (here PQR=xxz & yyz for the *ssp* signal), and k_b and T are respectively the Boltzmann constant and temperature of the simulated system. $\langle \dots \rangle$ is a time-correlation function, $d\alpha_{ij}/dr_{OH}$ and $d\mu_k/dr_{OH}$ are respectively the individual O-H bond contributions to the Raman tensor and Atomic Polar Tensor of water molecules or silanol groups. M is the number of water molecules and OH_{1,2} are the two O-H oscillators/water, N is the number of silanol groups. D is the matrix that

projects the molecular frame onto the laboratory frame.

The D matrix and the projection of the velocities on the O-H bond axis ($v_{OH1,2}^{mol}$, v_{OH}^{SiOH}) are readily obtained from DFT-MD trajectories while $d\alpha_{ij}/dr_{OH}$ and $d\mu_k/dr_{OH}$ terms have been parameterized. Parameterization for water is taken from ref (3, 23) as successfully applied in refs (3, 21, 22). Parameterization for silanol groups has been achieved in this work on the basis of a silicic acid building block model. Four possible Si-OH configurations have been observed along the DFT-MD trajectories of the 2 amorphous silica/water interfaces and they have thus been solely taken into account for the parameterization. The four configurations are illustrated in Figure S3: a Si-OH group donating an H-Bond to a water molecule (1), a Si-OH group accepting an H-Bond from a water molecule (2), a free Si-OH group (3) and a Si-OH group being simultaneously H-Bond acceptor and donor with water (4). Importantly, DFT-MD trajectories revealed that intra-solid H-Bonds are statistically negligible at the amorphous silica aqueous surfaces (0.2 SiOH...SiOH HBs/nm² for both 4.5 & 3.5 SiOH/nm² silanol surface coverage). Such configurations are therefore not included in the parameterization (also justifies our choice of the silicic acid building block model for parameterization).

Structures 1-4 in Figure S3 have been optimized with Gaussian09 code(24) and the computed Raman and Atomic Polar Tensor components for each of them are reported in Table S1. The final tensor elements used for the calculation of the silanols vSFG spectra in eq 2 are average weighted (w_{1-4} in Table S2) according to the probability of occurrence of each of the 1-4 model configurations in the DFT-MD simulations of the amorphous silica/water interfaces.

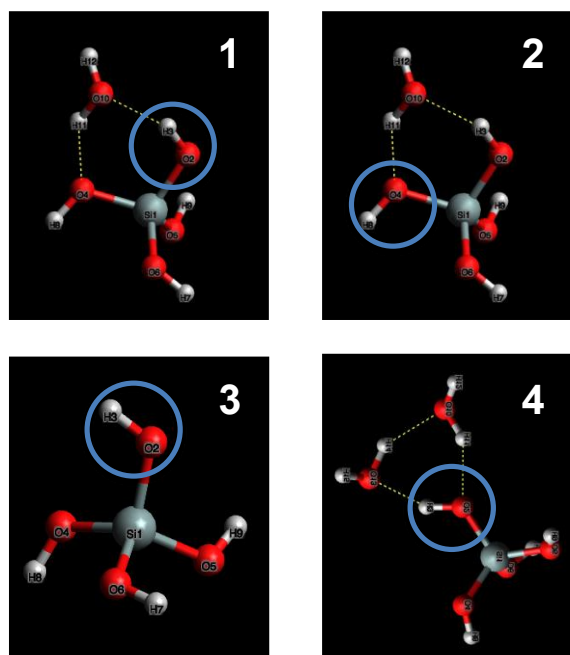


Figure S3. Illustration of the four reference model configurations used for the parameterization of the $d\mu_k/dr_{OH}$ and $d\alpha_{ij}/dr_{OH}$ terms needed in eq 2 for the vSFG theoretical spectrum of Si-OH silanol groups at aqueous amorphous silica surfaces.

Table S1. Calculated $d\mu_k/dr_{OH}$ and $d\alpha_{ij}/dr_{OH}$ terms for each of the 1-4 reference configurations presented in figure S1.

	$d\mu_x/dr_{OH}$ (D/Å)	$d\mu_y/dr_{OH}$ (D/Å)	$d\mu_z/dr_{OH}$ (D/Å)	$d\alpha_{xx}/dr_{OH}$ (Å ²)	$d\alpha_{xy}/dr_{OH}$ (Å ²)	$d\alpha_{xz}/dr_{OH}$ (Å ²)	$d\alpha_{yy}/dr_{OH}$ (Å ²)	$d\alpha_{yz}/dr_{OH}$ (Å ²)	$d\alpha_{zz}/dr_{OH}$ (Å ²)
1	0.005	0.402	3.589	0.630	-0.105	0.118	0.388	0.296	3.351
2	0.267	-0.047	1.054	0.650	-0.054	0.499	0.338	0.222	2.694
3	-0.315	-0.0469	1.028	0.616	-0.0142	-0.669	0.302	0.118	2.643
4	-1.676	0.389	4.309	1.168	-0.247	-1.331	0.319	0.281	3.444

Table S2. Weights (w_{1-4}) used to average the $d\mu_k/dr_{OH}$ and $d\alpha_{ij}/dr_{OH}$ parameterized terms from Table S1 ($\sum_i \omega_i = 1$). The weights correspond to the probability of occurrence of each model configuration in the DFT-MD trajectories of the two amorphous silica/water interfaces performed here.

	w1	w2	w3	w4
4.5 SiOH/nm ²	0.63	0.02	0.00	0.35
3.5 SiOH/nm ²	0.59	0.01	0.00	0.40

Section S7. Definition of interfacial layers at silica/water interfaces from DFT-MD simulations.

A critical issue in calculating and interpreting vSFG non-linear spectra is a clear and unambiguous definition of the water participating to the non-centrosymmetric spectral activity. The pioneering work of Tian and Shen(25) has laid out the principles of three universal water layers, respectively named BIL (Binding Interfacial Layer), DL (Diffuse Layer) and Bulk, that have to be considered in vSFG spectroscopy. In refs (21, 22), we have laid out and applied the formal definitions of these layers based solely on structural properties of water. This methodology has been applied here for the two investigated amorphous silica/water interfaces. Because these interfaces are at the isoelectric point, there is no DL (no surface electric field creating a DL), such that the interfacial layer is composed of the BIL only, which is therefore the only layer being vSFG active at these aqueous silica interfaces. The vSFG spectra calculated at the aqueous amorphous silica/water interfaces investigated here thus measure the O-H stretching $\chi_{ssp}^{(2)}(\omega)$ response of the solid surface silanols and of the water molecules belonging to the BIL within a rather small 3Å thickness (extracted from the definition of the water layers). Beyond the 3Å thickness of the non-centrosymmetric BIL, centrosymmetric non-SFG active bulk water is recovered. See Figure S4 for a schematic representation of the water layers at the two amorphous silica/water interfaces investigated here.

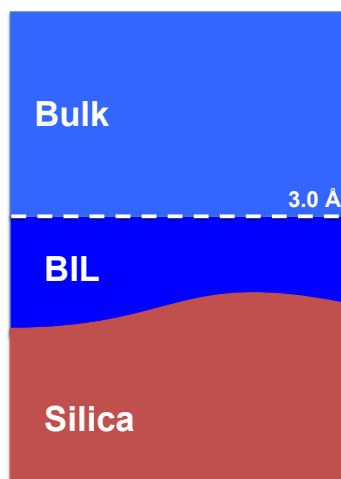


Figure S4. Schematic representations of the different water layers (BIL and Bulk) identified for the two amorphous silica/water interfaces investigated here. The 3Å thickness of the interfacial region, consisting of the BIL only, is highlighted in dark blue.

Section S8. Deconvolution of the water vSFG signal into identified water population contributions.

Water populations can be further identified in the BIL and their individual contribution to the vSFG spectra can be calculated by selecting the cartesian coordinates of the atoms belonging to a specific water population into the summation in eq. 1. To assign the BIL interfacial water molecules into one of these populations, the 20 ps trajectories have been cut into four pieces of 5 ps each over which vSFG spectra have been calculated, and then averaged in order to give the total signal. In each portion of the trajectory, a water molecule is assigned to one given population if it is found to be in that specific configuration over 80% of the simulation time (i.e. 4 ps over 5 ps). Four different water populations in the BIL have been identified with these criteria: **(a)** water molecules with one O-H oscillator pointing towards an in-plane silanol group (i.e. donor of H-Bond to the oxide surface), **(b)** water molecules with one O-H oscillator pointing towards a siloxane bridge (water donor to the surface), **(c)** water molecules rocking their pointing O-H in between a siloxane bridge and a silanol group, **(d)** water molecules not pointing any O-H towards the solid.

Only populations (a), (b) & (c) participate to the 3500-3800 cm^{-1} signatures. The contribution of populations a) and b) to the total $\text{Im } \chi_{ssp}^{(2)}(\omega)$ vSFG signal is presented in Figure 3 of the main text, respectively with the red and green lines (the total spectrum is in black lines). See the main text for all comments.

In Figure S5, we now also include the contribution of the rocking water molecules (dashed black lines). Not surprisingly, the rocking waters give a vSFG signature inbetween the signatures from the (a) and (b) populations (red and green dashed lines in fig S5), with a maximum around 3600 cm^{-1} .

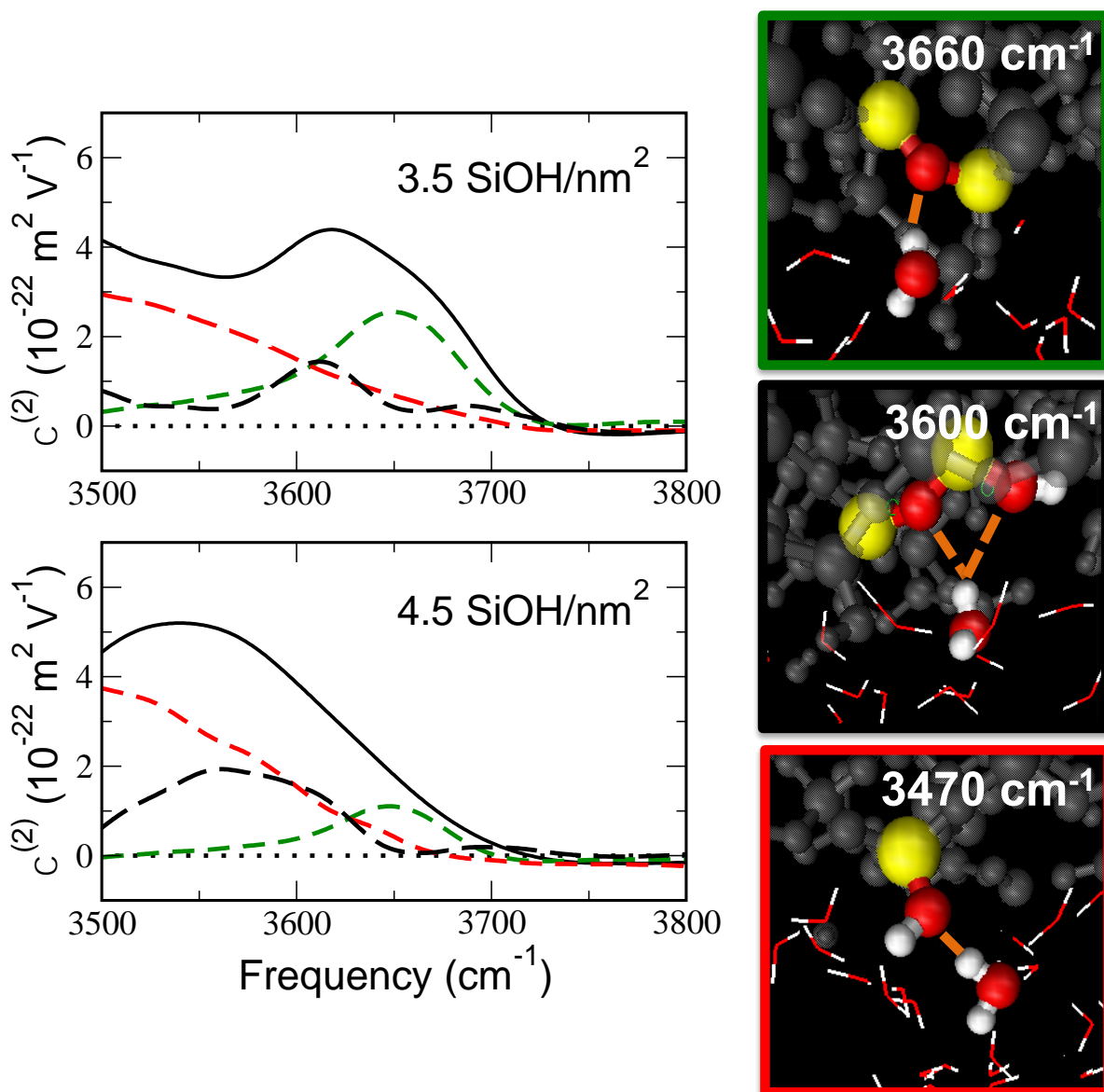


Figure S5. Left: Theoretical vSFG signal ($\text{Im } \chi_{ssp}^{(2)}$) in the 3500-3800 cm^{-1} region for two amorphous silica aqueous surfaces with various degrees of surface hydroxylation (3.5 SiOH/nm^2 and 4.5 SiOH/nm^2). The solid black line is the total vSFG signal while the dashed lines are the microscopic assignments (deconvolved signatures). Green dashed lines: water molecules that have one O-H oscillator pointing towards a siloxane bridge. Red dashed lines: water molecules with one O-H oscillator pointing towards a silanol group. Black dashed lines: rocking water molecules. **Right:** Snapshots from DFT-MD simulations illustrating the microscopic origin of the observed spectral contributions.

Section S9. Surface silanols contribution to vSFG

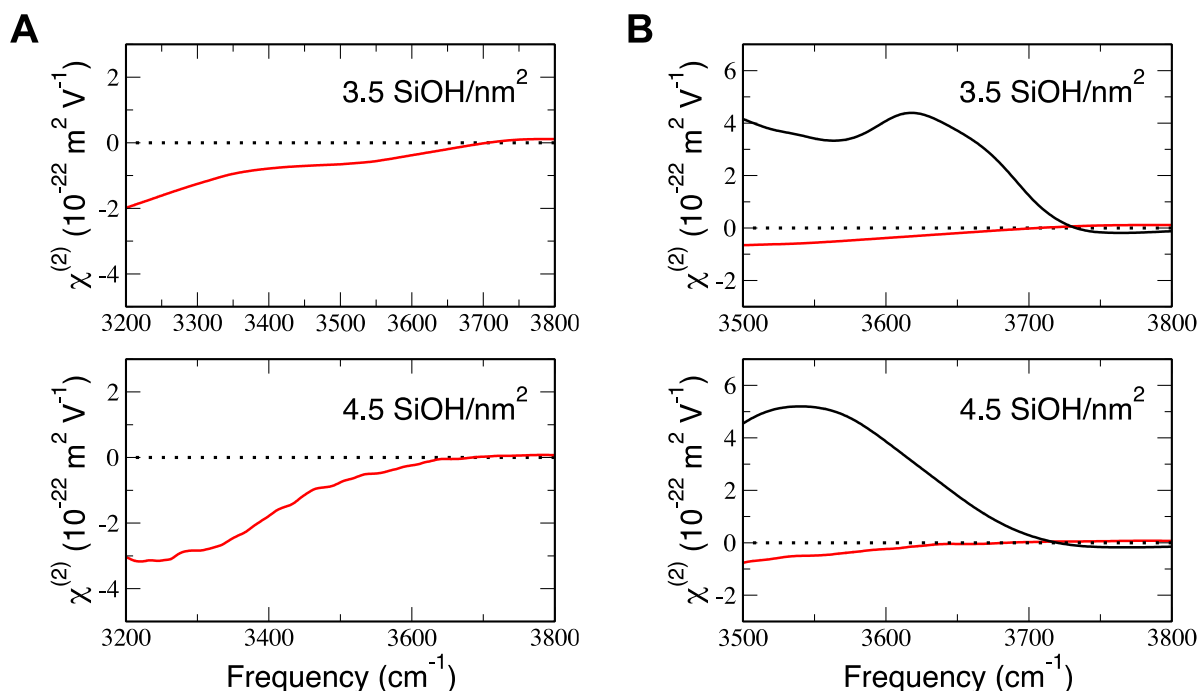


Figure S6. A: Theoretical vSFG spectral contributions ($Im\chi_{ssp}^{(2)}(\omega)$) of the surface silanol groups in the OH stretching region calculated from DFT-MD simulations for amorphous silica/water interfaces with two degrees of hydroxylation of the silica surface: 3.5 SiOH/nm² (left) and 4.5 SiOH/nm² (right). **B:** zoom in the 3500-3800 cm⁻¹ spectral region of interest in the present work, where the solid contribution to vSFG (red line) is reported together with the water contribution (black line).

There are two populations of surface silanols at the amorphous surface: ‘in-plane’ silanols oriented parallel to the surface (13%/17% of silanols at the 4.5/3.5 SiOH/nm² surface coverage) and ‘out-of-plane’ silanols pointing out of the surface towards water (87%/83% at the 4.5/3.5 SiOH/nm² surface). The ‘in-plane’ silanols are not vSFG active due to their orientation while the ‘out-of-plane’ silanols donate strong H-Bonds to water, thus providing a negative band at $\omega < 3400 \text{ cm}^{-1}$ in the $Im\chi_{ssp}^{(2)}(\omega)$ spectra. As a consequence, the silica surface does not provide any vSFG activity in the 3500-3800 cm⁻¹ spectral region of interest here.

Figure S6 presents the $Im\chi_{ssp}^{(2)}(\omega)$ vSFG contribution arising from the surface silanol groups for the two amorphous silica/water interfaces investigated here (3.5 SiOH/nm² vs 4.5

SiOH/nm² surface silanol coverage). The spectra clearly show that the solid does not contribute to the SFG intensity in the 3500-3800 cm⁻¹ region, and instead vSFG solely arises from the interfacial water molecules identified in the 3Å thickness BIL (Binding Interfacial Layer).

Section S10. Effect of surface charge on theoretical vSFG spectra

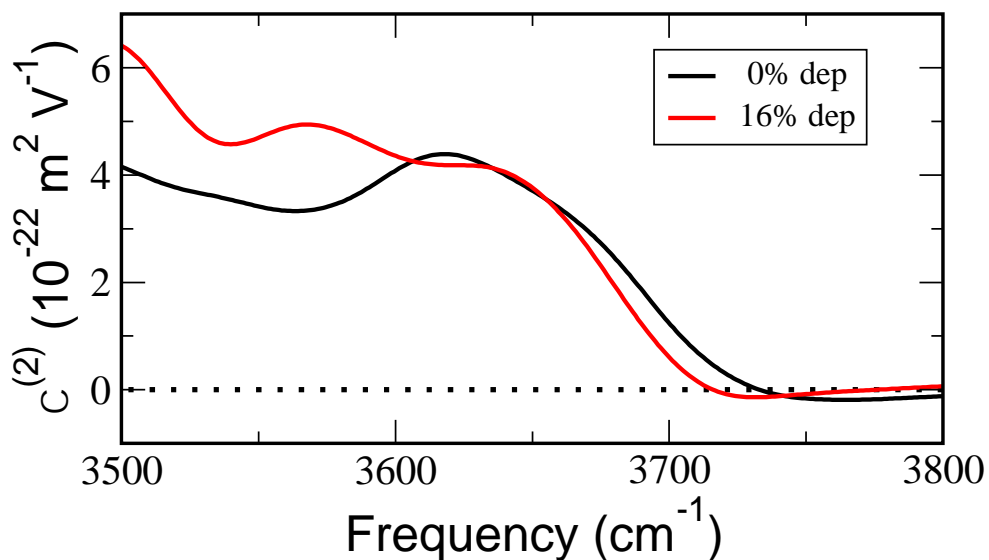


Figure S7. Theoretical vSFG signal ($\text{Im } \chi_{ssp}^{(2)}$) in the 3500-3800 cm⁻¹ region for the 3.5 SiOH/nm² amorphous silica/water interface with 2 degrees of silica surface protonation state: fully hydroxylated surface (0% dep) and 16 % of surface sites being deprotonated (16% dep).

The effect of surface charge was explored by calculating theoretical vSFG spectra from DFT-MD simulations of the 3.5 SiOH/nm² amorphous silica/water interface, with the surface either fully hydroxylated or with 16 % of surface silanols being deprotonated (figure S7). The 3650 cm⁻¹ band, marker of the water O-H groups pointing to siloxane bridges is observed with the same position and same intensity independently of the protonation state of the surface.

References

1. Pool RE, Versluis J, Backus EHG, Bonn M (2011) Comparative Study of Direct and Phase-Specific Vibrational Sum-Frequency Generation Spectroscopy: Advantages and Limitations. *J Phys Chem B* 115(51):15362–15369.
2. Nihonyanagi S, Yamaguchi S, Tahara T (2009) Direct evidence for orientational flip-flop of water molecules at charged interfaces: A heterodyne-detected vibrational sum frequency generation study. *J Chem Phys* 130(20):204704.
3. Khatib R, et al. (2016) Water orientation and hydrogen-bond structure at the fluorite/water interface. *Sci Rep* 6:24287.
4. Myalitsin A, Urashima S, Nihonyanagi S, Yamaguchi S, Tahara T (2016) Water Structure at the Buried Silica/Aqueous Interface Studied by Heterodyne-Detected Vibrational Sum-Frequency Generation. *J Phys Chem C* 120(17):9357–9363.
5. Sun S, et al. (2016) Phase reference in phase-sensitive sum-frequency vibrational spectroscopy. *J Chem Phys* 144(24):244711.
6. Zhuang X, Miranda PB, Kim D, Shen YR (1999) Mapping molecular orientation and conformation at interfaces by surface nonlinear optics. *Phys Rev B* 59(19):12632–12640.
7. Backus EHG, Garcia-Araez N, Bonn M, Bakker HJ (2012) On the Role of Fresnel Factors in Sum-Frequency Generation Spectroscopy of Metal–Water and Metal–Oxide–Water Interfaces. *J Phys Chem C* 116(44):23351–23361.
8. Hale GM, Query MR (1973) Optical Constants of Water in the 200-nm to 200- μ m Wavelength Region. *Appl Opt* 12(3):555–563.
9. Malitson IH (1965) Interspecimen Comparison of the Refractive Index of Fused Silica*,†. *JOSA* 55(10):1205–1209.
10. Hsieh C-S, et al. (2011) Ultrafast Reorientation of Dangling OH Groups at the Air–Water Interface Using Femtosecond Vibrational Spectroscopy. *Phys Rev Lett* 107(11):116102.
11. Xiao S, Figge F, Stirnemann G, Laage D, McGuire JA (2016) Orientational Dynamics of Water at an Extended Hydrophobic Interface. *J Am Chem Soc* 138(17):5551–5560.
12. Ugliengo P, et al. (2008) Realistic Models of Hydroxylated Amorphous Silica Surfaces and MCM-41 Mesoporous Material Simulated by Large-scale Periodic B3LYP Calculations. *Adv Mater* 20(23):4579–4583.
13. Hutter J, Iannuzzi M, Schiffmann F, VandeVondele J (2014) cp2k: atomistic simulations of condensed matter systems. *Wiley Interdiscip Rev Comput Mol Sci* 4(1):15–25.
14. VandeVondele J, et al. (2005) Quickstep: Fast and accurate density functional calculations using a mixed Gaussian and plane waves approach. *Comput Phys Commun* 167(2):103–128.
15. Becke AD (1988) Density-functional exchange-energy approximation with correct asymptotic behavior. *Phys Rev A* 38(6):3098–3100.

16. Lee C, Yang W, Parr RG (1988) Development of the Colle-Salvetti correlation-energy formula into a functional of the electron density. *Phys Rev B* 37(2):785–789.
17. Grimme S (2004) Accurate description of van der Waals complexes by density functional theory including empirical corrections. *J Comput Chem* 25(12):1463–1473.
18. Grimme S (2006) Semiempirical GGA-type density functional constructed with a long-range dispersion correction. *J Comput Chem* 27(15):1787–1799.
19. Goedecker S, Teter M, Hutter J (1996) Separable dual-space Gaussian pseudopotentials. *Phys Rev B* 54(3):1703–1710.
20. Gageot M-P, Sprik M, Sulpizi M (2012) Oxide/water interfaces: how the surface chemistry modifies interfacial water properties. *J Phys Condens Matter* 24(12):124106.
21. Pezzotti S, Galimberti DR, Shen YR, Gageot M-P (2018) Structural definition of the BIL and DL: a new universal methodology to rationalize non-linear $\chi^{(2)}$ (ω) SFG signals at charged interfaces, including $\chi^{(3)}$ (ω) contributions. *Phys Chem Chem Phys* 20(7):5190–5199.
22. Pezzotti S, Galimberti DR, Gageot M-P (2017) 2D H-Bond Network as the Topmost Skin to the Air–Water Interface. *J Phys Chem Lett* 8(13):3133–3141.
23. Corcelli SA, Skinner JL (2005) Infrared and Raman Line Shapes of Dilute HOD in Liquid H₂O and D₂O from 10 to 90 °C. *J Phys Chem A* 109(28):6154–6165.
24. Frisch MJ *Gaussian 09. Revision D.01*.
25. Wen Y-C, et al. (2016) Unveiling Microscopic Structures of Charged Water Interfaces by Surface-Specific Vibrational Spectroscopy. *Phys Rev Lett* 116(1):016101.

5.7 Tuning the silica surface hydrophilicity and consequence on the BIL-water network

Hereafter are presented the main results of the paper to be submitted "From hydrophilic to hydrophobic aqueous silica, from a vertical to a horizontal order of interfacial water" reported at the end of this section. This is a preliminary version of the paper.

In the previous section we have reported the existence of two water populations at macroscopic amorphous silica surfaces respectively interacting with hydrophobic (silanols poors) and hydrophilic (silanols rich) patches, showing specific water SFG-marker band signatures[135]. In this section we now provide the information on how the water network is organized above such patches and how its structure evolves as a function of the patches area by tuning the degree of hydroxylation of the silica surfaces.

Three DFT-MD simulations have been carried out on amorphous silica-water interfaces with increasing degrees of hydroxylation of the solid surface models: 3.5 SiOH/nm², 4.5 SiOH/nm² (both are Ugliengo's models[31]) and 7.6 SiOH/nm² (Bernasconi's model[259]). The three amorphous silica surfaces have been preliminarily re-optimized in the gas phase at the level of theory adopted for the DFT-MD dynamics without observing any relevant changes in the structure. More details on the surface preparation can be found in the method section of the paper reported at the end of this section.

We have started by characterizing the amorphous/water interfaces using our methodology already shown in refs.[114, 103] that defines water BIL/DL/Bulk layers through three structural descriptors: the water density profile perpendicular to the silica surface, the water coordination number in each layer, and the water OH orientation in each layer. The BIL, the first water layer in contact with the solid, is found for all interfaces to have a thickness between 2.5 and 3.0 Å, and to be systematically composed by water molecules with an average coordination of 2.8, much lower than the coordination of 3.4 in bulk liquid water.

We have then characterized the BIL-water organization above the hydrophilic and hydrophobic patches by spatially resolving the interfacial water properties (water density and coordination) along the lateral dimensions of the simulation boxes in order to understand how the inhomogeneous silica surface can template the water-water network.

In Fig. 5.9 are presented the maps of the silanol density (Panel-A), of the water density (Panel-B) and of the water coordination number (Panel-C) for the three hydroxylated silica-water interfaces of interest here. The comparison of the surface silanol density maps in Fig. 5.9-A shows a distribution of silanols more and more uniform when decreasing the degree of hydroxylation of the amorphous surface. The reader can appreciate how the hydrophilic patch becomes less and less extended in space when moving from the 7.6 to the 3.5 SiOH/nm² silica surface.

The water density and coordination number (Fig. 5.9-B) above the hy-

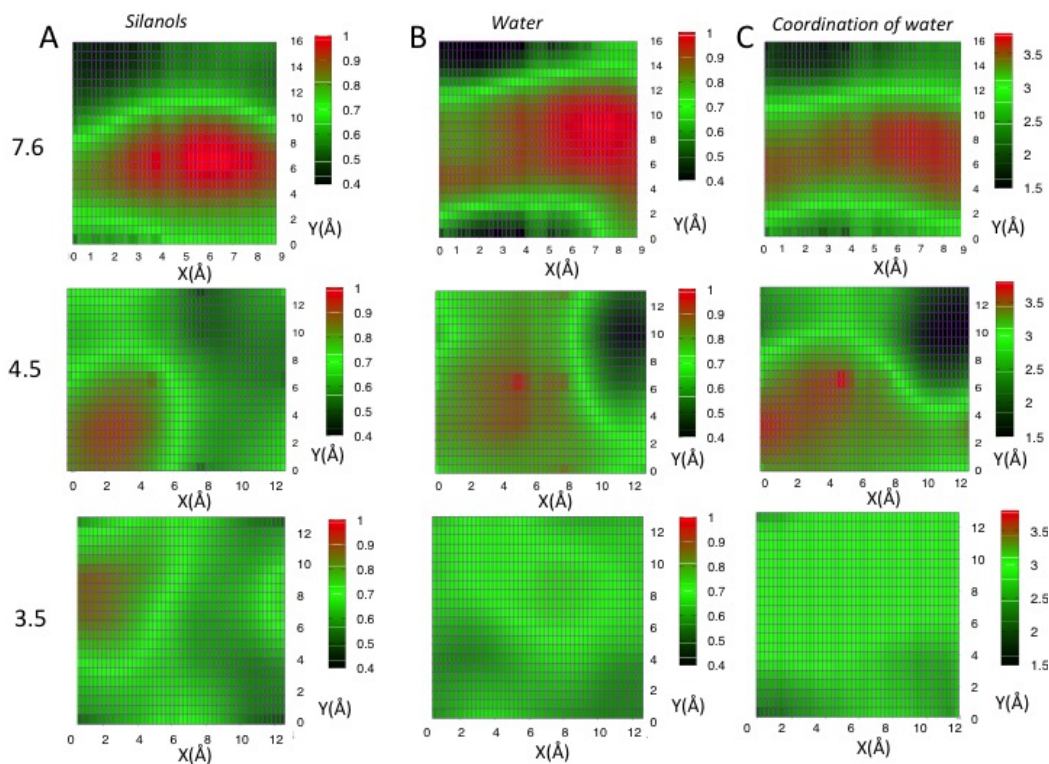


Figure 5.9: From the top to the bottom we consider the 7.6, 4.5 and 3.5 OH/nm^2 hydroxylated amorphous silica surfaces. Density maps (A): the density of silanols over the amorphous silica surface. (B): the density of BIL-water molecules over the xy plane along the lateral dimensions of the simulation box. (C): the coordination of the BIL-water molecules (water-water + water-solid H-Bonds). The color coding of each map is reported next to it.

drophilic and hydrophobic patches at the 7.6 and 4.5 SiOH/nm^2 surfaces reveal the presence of two distinct water populations at the boundary with the two most hydroxylated silica surfaces: 1) In correspondence with the surface hydrophilic patches we find a high density of water (red spots in Fig. 5.9-B) where water molecules present a coordination of ~ 3.5 (red spots in Fig. 5.9-C). 2) In correspondence with the hydrophobic patches, there is a low density of water molecules (green and black zones in Fig. 5.9-B) with a strong undercoordinated character, i.e. water molecules with a coordination ranging between 2.8 and 1.5 (Fig. 5.9-C).

Investigating in details the possible specific structural arrangements of the water population at the 7.6 and 4.5 SiOH/nm^2 silica surfaces, we have identified and characterized in the water dense zones (red spots in Fig. 5.9-B) the presence of interconnected 5-membered ring motifs composed by a chain of three water molecules in the BIL interacting with two surface silanols (Fig. 5.10) that belong to the surface hydrophilic patches.

The same highly interconnected water motifs have been previously identified at the (0001) α -quartz/water interface[49], uniformly and periodically

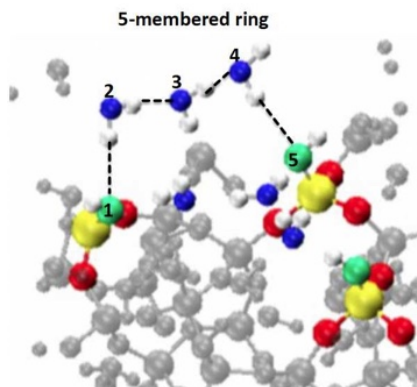


Figure 5.10: *Illustration of the 5-membered ring structure locally found above the higher hydroxylated parts of the amorphous silica surfaces. The chain of three water molecules and the two silanols involved in the 5-membered ring are coloured respectively in blue and green.*

repeated all over the crystalline surface. We have now identified the same organization over the 7.6 and 4.5 SiOH/nm² amorphous surface (Fig. 5.10) but only locally present over the hydrophilic patches of the silica surface. A locally ordered "quartz-like" water structure is thus found in the BIL of the 7.6 and 4.5 SiOH/nm² amorphous silica-water interfaces.

The rather high water interconnectivity in the five-membered ring structure is reflected by the coordination value of 3.5 (red zones in Fig. 5.9-C) above the hydrophilic patches. Conversely we find a less ordered and connected water environment above the hydrophobic patches, now characterized by water molecules poorly coordinated (coordination between 2.8 and 1.5).

Moving now our attention to the low 3.5 SiOH/nm² hydroxylated silica surface at the interface with water, the density maps provide a very different picture from the two other hydroxylated aqueous surfaces: the density of water above the solid is now fully homogeneous (no red zones anymore) and is totally decorrelated from the silanols density distribution over the amorphous surface, i.e. there is no red zone in Fig. 5.9-B above the small red zone in the SiOH map. The local water organization above the hydrophilic patch observed at the two more hydrophilic silica surfaces (7.6 and 4.5 SiOH/nm²), is replaced by a homogeneous water structural organization at the 3.5 SiOH/nm² surface characterized by water molecules with a homogeneous coordination number around ~ 2.8 .

We have hence investigated the nature of the transition in the water structure when water is in contact with high to low hydroxylated amorphous silica surfaces, by plotting in Fig. 5.11-A the orientational distributions of the H-bonds (water-water and water-solid H-Bonds are considered) for interfacial BIL-water molecules. We consider parallel H-Bonds (histogram in blue) and perpendicular H-Bonds (histogram in red) with respect to the silica surface. In these definitions the water-water H-Bonds formed between the water

molecules of the BIL (OH-BIL in Fig.5.11-B) are the parallel H-Bonds (we will see that they are indeed oriented parallel to the silica surface), while the H-Bonds formed between the water molecules and the silanol groups (OH-SiOH in Fig.5.11-B) and the H-Bonds formed between the water molecules located in the BIL and the ones located in the subsequent Bulk layer (OH-Bulk in Fig.5.11-B) are both perpendicular H-Bonds. The results are reported for each aqueous amorphous silica model surface investigated in this work and compared to the air-water interface taken as the reference for hydrophobic interfaces (where the water forms a 2D-HB-Network with water-water H-Bonds oriented parallel to the air).

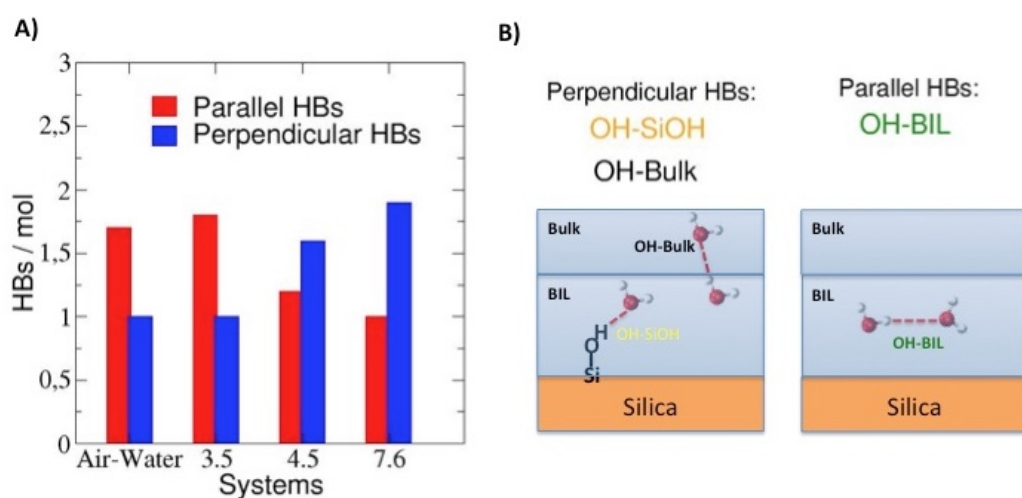


Figure 5.11: **(A)**: distributions of the water H-bonds formed parallel or perpendicular to the silica surface for the three amorphous silica-water interfaces analysed in this work. See the definition of parallel and perpendicular H-Bonds in the text and in panel B. The air-water interface is used as reference. **(B)**: the perpendicular HBs include the H-Bonds between the water and the silanol groups (OH-SiOH) and the H-Bonds between the water molecules in the BIL and the water molecules in the Bulk (OH-Bulk). The parallel H-Bonds include only the water-water interactions occurring between the water molecules in the BIL (OH-BIL).

As one can see in Fig. 5.11-A, by reducing the degree of hydrophilicity of the silica surface (i.e. going from the 7.6 to the 3.5 SiOH/nm²) there is a diminution of the number of water-SiOH perpendicular H-bonds formed (from a value of 1.8 to 1.0), while the number of parallel H-bonds between the water molecules in the BIL (OH-BIL) increases from a value of 1.0 and 1.2 respectively for the 7.6 SiOH/nm² and 4.5 SiOH/nm² surfaces to a value of 1.8 for the 3.5 SiOH/nm² surface.

We can conclude that the lowering of the surface degree of hydroxylation down to the value of 3.5 SiOH/nm² causes a drastic change in the water organization at the interface with the silica. We hence find that the water molecules maximize water-water interactions formed parallel to the surface (that we call horizontal order) to compensate for the lack of solid-water interactions (that we call vertical order).

In particular, we find that interfacial water at the 3.5 SiOH/nm² silica

surface forms an extended homogeneous 2D H-Bond network parallel to the surface. This is the same organization that we revealed and fully characterized at the prototypic hydrophobic air-water interface in ref.[103].

All the details on the 5-membered ring structures, on the horizontal and vertical water orders and on the SFG spectra of the three interfaces of interest here are reported hereafter in the paper to be soon submitted. Beware that only the Results and Methods sections of the paper are reported. The Introduction and Conclusions sections are in preparation.

1.

From hydrophilic to hydrophobic aqueous
silica, from a vertical to a horizontal order of
interfacial water

Flavio Siro Brigiano,* Simone Pezzotti, Daria Ruth Galimberti, and Marie-Pierre
Gaigneot*

*LAMBE CNRS UMR8587, Université d'Evry val d'Essonne, Evry, France & Université
Paris-Saclay, France*

E-mail: flavio.sirobrigiano@univ-evry.fr; mgaigeot@univ-evry.fr

Results

Amorphous silica/water interface structure

DFT-MD simulations have been carried out on amorphous silica/water interfaces where several degrees of hydroxylation of the solid surface have been modelled: 3.5 SiOH/nm², 4.5 SiOH/nm² (both models from Ugliengo *et al.*³²) and 7.6 SiOH/nm² (model from Bernasconi *et al.*³³). The three amorphous silica surfaces were preliminarily re-optimized in the gas phase at the level of theory adopted for the dynamics without observing any relevant modification of the structure. We start by characterizing the amorphous-water interfaces from

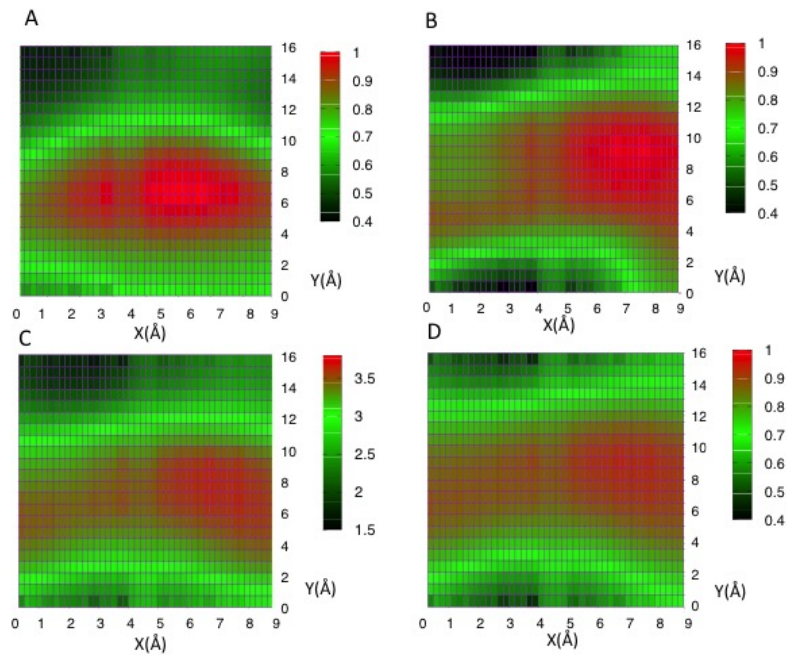


Figure 1: 7.6 OH/nm² hydroxylation of the amorphous silica surface, density maps (A): the density of silanols over the amorphous silica surface. (B): the density of BIL-water molecules over the *xy* plane along the lateral dimensions of the simulation box. (C): the coordination of the BIL-water molecules. (D): the density of water involved in 5-membered-ring structures. The color coding for each map is reported next to it.

the point of view of the water, by using our methodology from refs.^{34,35} where the water is

decomposed into three layers, i.e. BIL (Binding Interfacial Layer), DL (Diffuse Layer), Bulk through three structural descriptors: the water density profile perpendicular to the surface, the water coordination number, and the OH orientation of the water molecules. The BIL is the first water layer in direct contact with the silica solid. It is found to have a thickness between 2.5 and 3.0 Å for all three interfaces investigated here and to be systematically composed by water with an average coordination number of 2.8, to be compared to the 3.4 coordination number in liquid water. In order to investigate if the inhomogeneous distribution of silanol SiOH groups over the amorphous silica surface induces a non-homogeneous structural organization of the BIL-water at the nanoscale, we characterize the BIL with a spatial resolution along the (x,y) lateral dimensions of the simulation box. We first detail the data for the 7.6 SiOH/nm² hydroxylated silica surface in contact with water. See Fig. 1 for density maps extracted as averages over the DFT-MD trajectories of the aqueous surface (see method section for all details). As can be observed from the density map of silanols (Fig. 1 A) this surface is characterized by an inhomogeneous distribution of hydroxylated sites over the (x,y) coordinates of the surface. In particular, two maxima (red spots in Fig. 1A) can be identified on the silanol density map. They are "silanol nests", as reported in ref.³⁶ at the same surface in presence of few water molecules. Silanol nests are concave zones at the surface characterized by high concentration of silanols mutually interacting. Their presence in zeolites as defects and their capacity in tuning the properties of adsorption of water and biomolecules on silica-based materials^{20,37} has already been emphasized.

Panels B, C and D of Fig. 1 report maps of various properties of BIL-water over the same (x,y) lateral grid. Fig. 1B clearly shows that the two maxima in the water density mirror the two maxima for the silanol density. There is thus a preferential water adsorption over the silanol nests, as already seen by experimental and theoretical works analysing the adsorption of water clusters on highly hydroxylated silica surfaces.^{20,37}

The map that reports the coordination of the water molecules (i.e. water-water + water-solid H-Bonds) in Fig. 1C has a similar shape to the density map in Fig. 1B, with a maximum

value of ~ 3.4 - 3.5 reached above the silanol nests on the amorphous silica surface. The map in Fig. 1C shows two water populations. One population with a high coordination number of ~ 3.4 , located above the silanol rich areas of the silica surface (hydrophilic patches, see Fig. 1). The 3.4 coordination is identical to the value in liquid water or to coordination numbers obtained at the highly hydroxylated ($9.6 \text{ SiOH}/\text{nm}^2$) crystalline (0001) α -quartz aqueous surface.³⁸ The second population has a coordination number between 1.5 and 2.8 , and is located over poor silanol surface areas (hydrophobic patches). These data suggest a local organization of the water above the hydrophilic and hydrophobic patches of the surface where the water somehow templates the silica surface. We systematically observed the formation of "5-membered ring" structures characterized by a chain of three water molecules that interact with two surface silanols (Fig. 2). We have mapped the density of five membered ring structures over the (x,y) coordinates of the surface (Panel D of Fig. 2). The map indicates the five membered rings to be preferentially located above the hydrophilic patches of the surface. In a previous work, we have already found interfacial BIL-water in contact with the (0001) α -quartz surface to be organized in interconnected 5-membered rings, uniformly and periodically repeated all over the 2D crystalline surface.³⁸ We have hereby identified the same organization over the rather highly hydroxylated $7.6 \text{ SiOH}/\text{nm}^2$ amorphous surface (Fig. 2), but only locally present on the most hydrophilic patches of the surface. It is however not a repeated motif over the surface anymore, it is only a local motif that adapts to the local hydroxylation of the surface. We thus conclude that a locally "quartz-like" BIL-water structure can be found at the $7.6 \text{ SiOH}/\text{nm}^2$ amorphous silica/water interface.

Previous observations by Cimas *et al.*¹⁵ from DFT-MD simulations of an amorphous silica/water interface ($5.8 \text{ SiOH}/\text{nm}^2$) also identified 5-membered ring structures made by water, using the geminal silanol sites as the template. The presence of Q2 geminal silanols induces a local increase of silanol density at the surface that, in agreement with the present results, leads to the local formation of 5-membered ring structures.

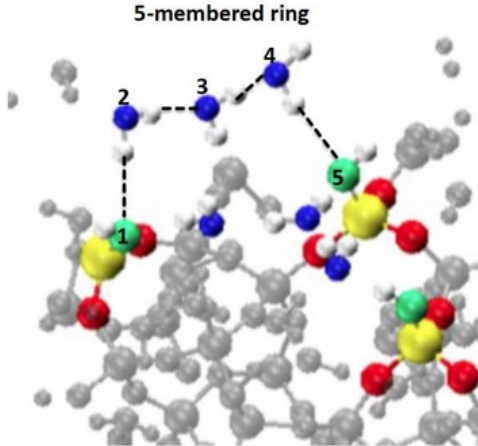


Figure 2: A 5-membered ring structure locally found above the higher hydroxylated part of the amorphous silica surface. The three chain water molecules and the two silanols involved in the 5-membered ring structure are coloured respectively in blue and green

We now compare in Fig. 3 the silanol density maps, water density maps and water coordination maps for the three aqueous silica interfaces of interest here, respectively of hydroxylation 7.6, 4.5 and 3.5 SiOH/nm². The silanol density maps (Fig. 3-A) nicely show that the hydrophilic patches (rich in silanol groups) over the surface are reduced to a small spatial spot (red in Fig. 3-A) for the lower 3.5 SiOH/nm² hydroxylation. One direct consequence of the reduction in the number of SiOH sites and of the spatial shrinking of the associated hydrophilic surface patches is the density of SiOH-SiOH hydrogen bonds that can be formed. Table 1 shows a huge reduction in the density of solid-solid H-Bonds for the lower surface hydroxylation rates.

Table 1: *First column: silica surfaces degrees of hydroxylation. Second column: density of solid-solid H-Bonds (number of H-Bonds/nm²). Both the silanol-silanol (OH-OH) and silanol-syloxane bridge (SiOH-SiOSi) H-Bonds are included in the solid-solid interactions. Third column: density of silica-water H-Bonds (number of H-Bonds/nm²).*

Degree of hydroxylation (SiOH/nm ²)	solid-solid (SiOH-SiOH + SiOH-OSiO) (HBs/nm ²)	solid-water (SiOH-water) (HBs/nm ²)
7.6	4.2	7.0
4.5	0.9	6.5
3.5	0.2	4.6

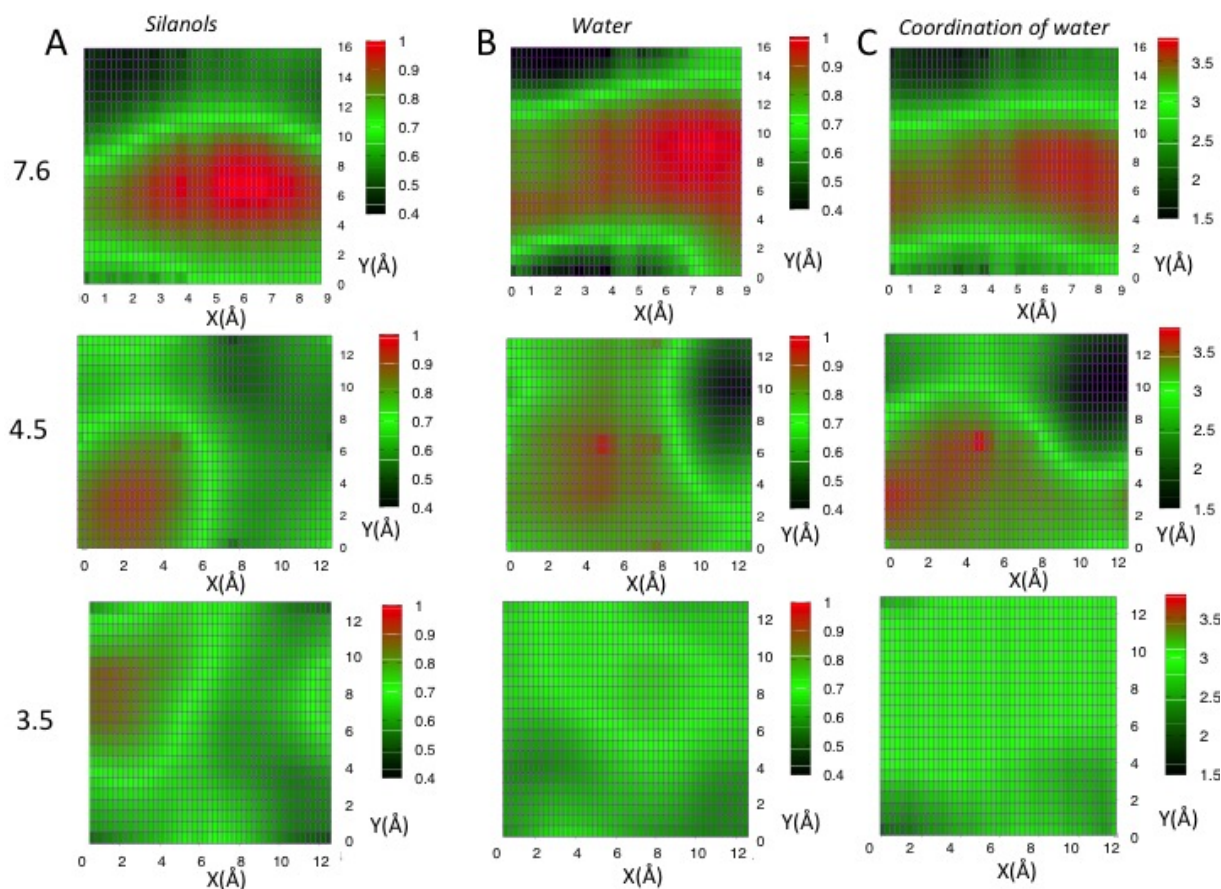


Figure 3: *From the top to the bottom we consider the 7.6, 4.5 and 3.5 OH/nm² hydroxylated amorphous silica surfaces. Density maps (A): the density of silanols over the amorphous silica surface. (B): the density of BIL-water molecules over the xy plane along the lateral dimensions of the simulation box. (C): the coordination of the BIL-water molecules. The color coding for each map is reported next to it.*

This is due to two effects: 1) The higher proximity between silanol SiOH groups on the high hydroxylated silica surface (7.6 SiOH/nm²) with respect to low hydroxylated ones (3.5 SiOH/nm² and 4.5 SiOH/nm²). 2) A greater energetic stability of solid-solid H-Bonds in presence of water at the high hydroxylated silica surface, i.e. solid-solid H-Bonds are found to be more difficult to be replaced by water-solid H-Bonds at the high hydroxylated silica surface (7.6 SiOH/nm²) compared to the low hydroxylated ones (3.5 SiOH/nm² and 4.5 SiOH/nm²). This is shown in the Supporting Information (S.I.) by comparing the percentages of solid-solid interactions that "survive" on the silica surfaces once they are put in

contact with water.

The phenomenon is in part ascribed to the presence of silanol nests on the 7.6 SiOH/nm² silica surface (see S.I. for the discussion).

The densities of solid-water H-Bonds (Table 1) mirror the different hydrophilic characters of the surfaces: a strong increase in solid-water interactions from the 3.5 to the 4.5 SiOH/nm² surface is observed. On the contrary only a slight increase is observed when going from the 4.5 to the 7.6 SiOH/nm² surface. The higher number of solid-solid H-Bonds present on the 7.6 SiOH/nm² surface with respect to the 4.5 SiOH/nm² one (4.2 vs 0.9 solid-solid H-Bonds/nm²) reduces the number of silanols available for H-Bonding with water, resulting in a decrease in the solid-water H-Bonds density. Our data show the 3.5 SiOH/nm² to be far less hydrophilic than the other two surfaces if hydrophilicity is measured by water-solid H-Bonds only.

The same BIL-water behaviour as observed over the 7.6 SiOH/nm² surface is found also above the 4.5 SiOH/nm² surface: water molecules in the BIL are found fully coordinated (coordination number of ~ 3.4) and organized in interconnected 5-membered ring structures above hydrophilic patches of the amorphous silica surface, while they are found under coordinated (coordination number between 1.5 and 2.8) and not organized in a specific arrangement above the hydrophobic patches (Panel A-B of Fig. 3). The local "quartz-like" BIL-water structure is hence found also above the hydrophilic patch of the 4.5 SiOH/nm² interface.

We consider now the 3.5 SiOH/nm² silica surface at the interface with water (Fig. 3 bottom). The water density maps provide a very different picture from the two other hydroxylated aqueous surfaces: the density of water above the solid is now homogeneous and is totally decorrelated from the silanols density distribution over the amorphous surface (there is no more correspondence between the maxima of the silanols and the water density). The local water organization above the hydrophilic patches observed at the two more hydrophilic silica surfaces (4.5 and 7.6 SiOH/nm²), is replaced at the 3.5 SiOH/nm² surface by a homogeneous

(homogeneous water density and coordination number) water structural organization composed by water molecules with a coordination number around ~ 2.8 .

In order to shed light on the nature of the transition in the BIL-water structure, in going from the high to low hydroxylated amorphous silica surfaces, we now show in Fig. 4 the orientational distributions of the H-bonds made by interfacial water molecules categorized into parallel H-Bonds (histograms in blue) and into perpendicular H-Bonds (histograms in red) to the surface.

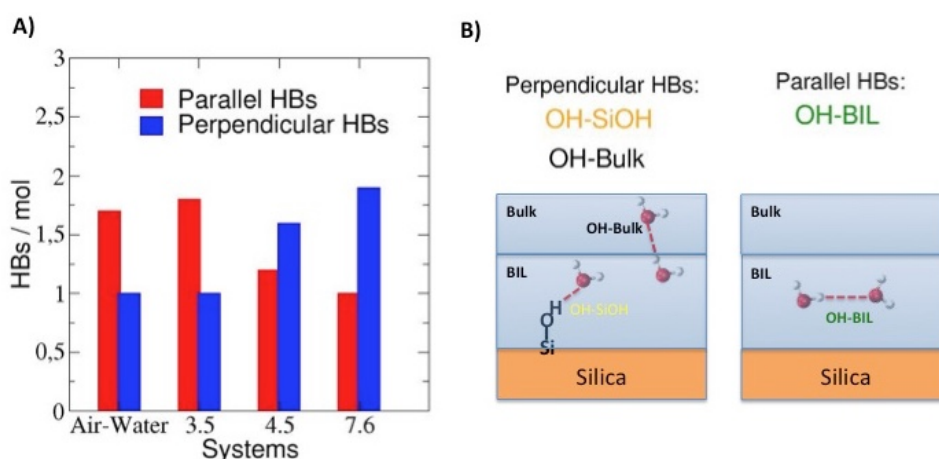


Figure 4: **(A)**: distributions of the water H-bonds formed parallel or perpendicular to the silica surface for the three amorphous silica-water interfaces analysed in this work. The air-water interface is used as reference for the prototypic hydrophobic interface. See the main text for definitions of parallel and perpendicular H-Bonds and illustrations in **(B)**. **(B)**: the perpendicular HBs include the H-Bonds between the water and the silanol groups (OH-SiOH) and the H-Bonds between the water molecules located in the BIL and the water molecules in the Bulk (OH-Bulk). The parallel H-Bonds include only the water-water interactions occurring between water molecules in the BIL (OH-BIL).

The water-water H-Bonds formed between the water molecules of the BIL (OH-BIL in Fig. 4B) are the parallel H-Bonds, while the H-Bonds formed between the water molecules and the silanol groups (OH-SiOH in Fig. 4B) and the H-Bonds formed between the water molecules in the BIL and the ones in the Bulk (OH-Bulk in Fig. 4 B) are all together accounting

for the perpendicular H-Bonds. The results are reported for each aqueous amorphous silica surface considered here and compared to the air/water interface taken as the reference for the prototypic hydrophobic interface.

Our results reveal a preferential perpendicular orientation of the BIL-water molecules at the 4.5 and 7.6 SiOH/nm² silica-water interfaces, while a preferential parallel orientation of the BIL-water molecules is observed at the 3.5 SiOH/nm² silica-water and at the air-water interfaces. By reducing the degree of hydrophilicity of the silica surface (i.e. going from the 7.6 to the 3.5 SiOH/nm²) there is a diminution of the number of water H-Bonds that can be formed perpendicular to the interface (thus a reduction in the solid-liquid H-Bonds). Conversely the number of water-water H-bonds parallel to the surface strongly increases from a value of 1.0 and 1.2 respectively for the 7.6 SiOH/nm² and 4.5 SiOH/nm² surfaces to a value of 1.8 for the 3.5 SiOH/nm² surface. We can conclude that the lowering of the degree of hydroxylation of the silica surface down to a value of 3.5 SiOH/nm² causes a drastic change in the water organization at the interface: water molecules now maximize water-water interactions in the BIL (horizontal order) at this low hydroxylated surface to compensate for the lack of solid-water interactions (vertical order). In particular, we find that interfacial water at the 3.5 SiOH/nm² silica surface forms an extended homogeneous 2D H-Bond network where the water-water H-Bonds are formed parallel to the surface. This is exactly the same organization as the one observed and characterized at the air/water interface in our refs.^{35,39,40}

To summarize, we find the organization of water above amorphous silica surfaces to be dictated by the relative dimensions of hydrophilic and hydrophobic silica surface patches. A disordered BIL structure, characterized by the simultaneous presence of low (above the hydrophobic patches) and high coordinated (above the hydrophilic patches) water molecules, is obtained when none of the hydrophobic and hydrophilic patches prevail, while the homogeneous "quartz like" five membered ring structure and the "air/water like" 2D-HB-network are respectively formed when the hydrophilic or the hydrophobic patches dominate.

SFG-marker bands

We turn our attention to SFG spectroscopy at the silica-water interface in order to establish marker bands and their assignments in relation with the hydrophilic and hydrophobic organizations discussed above. The heterodyne (phase resolved) SFG signal is calculated with our methodology.^{31,41} We focus on the marker bands in the OH-stretching region. Our goal is to establish markers in the change of the solvent structure as a result in the change in the hydroxylation state of the silica surface (i.e. change in hydrophilicity/hydrophobicity). In order to assess the reliability of our model we first compare in Fig. 5A the theoretical SFG signal calculated for the hydroxylated 4.5 SiOH/nm² aqueous silica and the experimental SFG spectrum of fused silica from Tahara *et al.*²³ obtained at the same pH=2 (near the isoelectric point). The comparison between the theoretical and experimental $\Im_m\chi^{(2)}(\omega)$ spectra shows an excellent agreement.

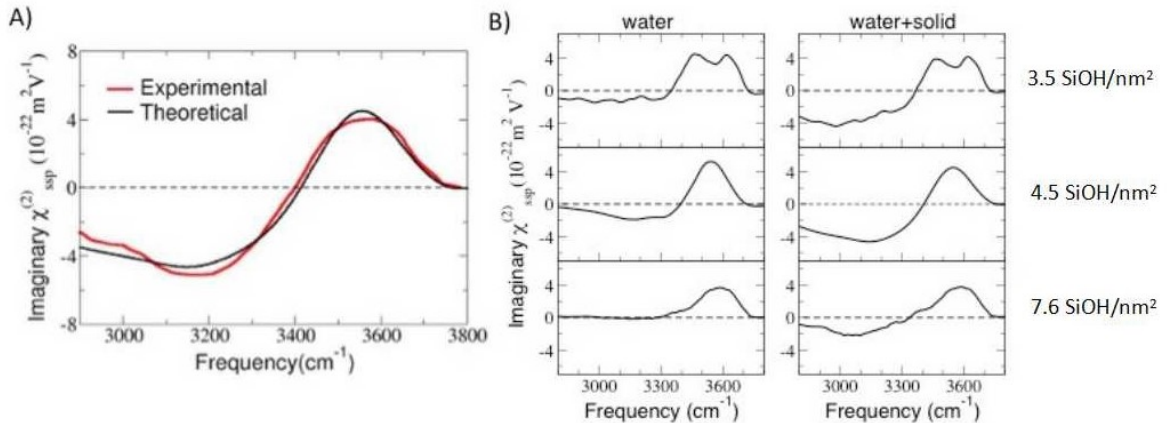


Figure 5: **(A)** theoretical (black line) $\Im_m\chi^{(2)}(\omega)$ SFG spectrum for the 4.5 SiOH/nm² amorphous silica surface and its comparison to the experimental SFG of Tahara *et al.*²³ **(B)** $\Im_m\chi^{(2)}(\omega)$ SFG spectra for three hydroxylated amorphous silica interfaces. Both the water and the surface contributions are taken into account in the SFG theoretical signals.

We now report in Fig. 5B the spectra of the three aqueous silica interfaces considered here,

including both the contribution from water (left side in Fig. 5B, note that only BIL water is SFG active at the isoelectric conditions for all the three systems), and summing the contributions from the water and the silica surface (right side in Fig. 5B). Independently of the degree of hydroxylation of the surface, the theoretical spectra are systematically characterized by a positive band at high frequencies (3430-3750 cm^{-1}) and a negative band at low frequencies (3000-3200 cm^{-1}). Deconvolving solid and water contributions to the SFG signals (Fig. 5-B, right side) demonstrate that the positive band arises solely from water. In our previous study³¹ we have shown that only two water OH group populations contribute to this positive band (3430-3750 cm^{-1}) at silica-water interfaces: the water OH either pointing toward a siloxane bridge (3650 cm^{-1} , hereafter denoted OH-SiOSi) or toward a silanol (3450 cm^{-1} , hereafter denoted OH-SiOH). Interestingly, when decreasing the degree of hydroxylation of the silica surface from 7.6 and 4.5 to the 3.5 SiOH/ nm^2 we observe an overall blue shift in the position of the water positive band associated to these two water populations (Fig. 5-B, left side). The breaking of the local BIL-water five-membered ring structures when decreasing the size of the hydrophilic patches over the silica surface (i.e. going from the 7.6 to the 3.5 SiOH/ nm^2) leads to a decrease in intensity of the OH-SiOH band at 3450 cm^{-1} (less SiOH-water H-Bonds) and to an increase of the quasi-free-OH OH-SiOSi band at 3650 cm^{-1} (more SiOSi-water H-bonds). This results in an overall blue shift of the positive band in the high frequency region of the 3.5 SiOH/ nm^2 water SFG spectra (Fig. 5B). The 3650 cm^{-1} and 3450 cm^{-1} marker bands are thus good descriptors for the evolution of the water-solid interactions (OH-SiOH and OH-SiOSi H-Bonds) occurring at the silica-water interfaces when tuning the surface degree of hydroxylation. They can for instance be used to monitor the breaking/formation of 5-membered ring structures over the silica surface. However, as previously discussed, breaking the 5-membered ring structures can bring to two different scenarios depending on the surface degree of hydroxylation: 1) under coordinated BIL-water above the surface hydrophobic patches at intermediate degree of hydroxylation (4.5 SiOH/ nm^2), 2) formation of the BIL-water 2D-HB-network above the least hydrophilic

silica surface (3.5 SiOH/nm²).

SFG technique cannot distinguish between these two scenarios since the in-plane water-water H-Bonds forming the 2D-HB-network are not SFG active. Therefore the 3650 cm⁻¹ and 3450 cm⁻¹ bands cannot directly probe the transition in the BIL-water structure from the 5-membered rings (7.6 and 4.5 SiOH/nm²) to the 2D-HB-network (3.5 SiOH/nm²) characterized by DFT-MD in the previous section.

The negative SFG signal in the lower frequency region below 3200 cm⁻¹ is due to both interfacial (BIL) water donating H-Bonds to the subsequent liquid layer (denoted hereafter OH-Bulk, See Fig. 4B) and to out-of-plane silanol groups donating strong H-Bonds to BIL-water (denoted hereafter SiOH-BIL, See Fig. 4B). It is important to stress here that all the silanol groups in all systems investigated here pointing toward water are found H-Bonded and there are no out-of-plane free OH groups reminiscent of the silica-air interface.³² Therefore the SiOH-BIL signature is the only solid contribution to the negative band at 3200 cm⁻¹ (see Fig.5) for the three surfaces considered. The SiOH-BIL signature is found with similar intensity for the 3.5 and 4.5 SiOH/nm² hydroxylated surfaces, while a lower intensity is obtained for the 7.6 SiOH/nm² one. This trend is in apparent contradiction with the density of solid-water H-Bonds reported for the three surfaces in Table 1, showing the 7.6 SiOH/nm² as the most hydrophilic surface (i.e. more solid-water interactions) followed by the 4.5 and 3.5 SiOH/nm² ones. In order to explain such apparently counter intuitive result we have evaluated the silanol groups SiOH SFG activity by calculating the silanol groups OH average orientations with respect to the surface normal for the three hydroxylated surfaces. We remind the reader that silanols with the OH group pointing parallel to the silica surface (in-plane silanols) are not SFG active. We find the silanol groups at the 7.6 SiOH/nm² to have on average a slightly more parallel orientation (77.5° orientation with respect to the surface normal) with respect to the silanol groups at the 4.5 and 3.5 SiOH/nm² surfaces (respectively 61.7 ° and 64.3°). The silanol groups more in-plane ordering at the 7.6 OH/nm² surface is the cause for most of the SiOH groups to be SFG inactive, with a consequent decrease in

the SiOH-BIL band intensity at 3200 cm^{-1} (see Fig. 5B). The result is in agreement with the high number of silanol-silanol Si-OH-Si-OH H-Bonds (by construction formed parallel to the surface) at the 7.6 SiOH/nm^2 reported in Table 1.

Methods

Amorphous silica/water interfaces with various degrees of hydroxylation of the silica surface have been modelled by DFT-MD (Density Functional Theory-based Molecular Dynamics) simulations. Three silica models have been selected, with a surface degree of hydroxylation respectively of 7.6 SiOH/nm² (thirteen SiOH groups at the surface in the simulation box), 4.5 SiOH/nm² (eight SiOH groups) and 2.4 SiOH/nm² (four SiOH). The 7.6 SiOH/nm² surface has been obtained by Bernasconi *et al.*,³³ the other two silica surfaces by Ugliengo *et al.*³², respectively with a 4.5 SiOH/nm² and 2.4 SiOH/nm² silanol coverage at the air interface. When in contact with water, the hydroxylation state of the 7.6 and the 4.5 SiOH/nm² surfaces are found stable, while the hydroxylation of the 2.4 SiOH/nm² surface increases to 3.5 SiOH/nm² silanol coverage. Indeed, the adsorption of one water molecule is observed in the first ps of dynamics, leading to the cleavage of a siloxane bridge and subsequent dissociation of the adsorbed water molecule. This brings to the formation of two new silanol groups at the silica surface, thus increasing the degree of hydroxylation of the amorphous surface from 2.4 to 3.5 SiOH/nm². The protonation state of all three silica surfaces is around the potential of zero charge (PZC, pH=2-4 conditions). The interfaces are at isoelectric conditions (no surface electric field) as shown in ref.³¹ The DFT-MD simulations have been generated with the CP2K software package⁴², that consists in Born-Oppenheimer MD, using the DFT-BLYP^{43,44} electronic representation, GTH pseudopotentials⁴⁵, and a combined plane waves (400 Ry energy cut-off) and SR-DZVP-MOLOPT gaussian basis set for all atoms. Dispersion interactions were included by the Grimme D2 correction⁴⁶. The box dimensions are the following: 9.117 X 16.342 X 32.000 Å³ (7.6 SiOH/nm² hydroxylated silica model), 13.386 X 13.286 X 37.000 Å³ (4.5 SiOH/nm² hydroxylated silica model) and 12.670 X 13.270 X 37.000 Å³ (3.5 SiOH/nm² hydroxylated silica model). The 7.6 SiOH/nm² silica slab is 6 Å thick and is composed by 102 atoms, while the 3.5 and 4.5 SiOH/nm² slabs are both 12 Å thick and are respectively composed of 198 and 204 atoms. Liquid water is simulated with 112, 120 and 116 water molecules, respectively for the 7.6, 4.5 and 3.5 SiOH/nm² silica models,

providing the expected experimental water density of 1 g/cm³. The amorphous silica slabs were reoptimized in the gas phase at the same level of theory adopted for the dynamics, and then put in contact with bulk water. After an equilibration of 10 ps (5 ps with velocities rescaling plus 5 ps in the pure NVE ensemble) the dynamics were generated in the NVE ensemble for 30 ps with a time step of 0.4 fs. All analyses were performed over these 30 ps trajectories.

The theoretical SFG spectra measure the $\Im_m \chi^{(2)}(\omega)$ non linear optical response of the solid-water interface in the O-H stretching region (3000-4000 cm⁻¹), including the contributions of both the water molecules and the solid surface silanols. The imaginary part of the resonant electric dipole non-linear susceptibility $\chi^{(2)}(\omega)$ is calculated, following our previous works^{34,41}.

For water:

$$\chi_{PQR}^{(2)}(\omega) = \sum_{mol=1}^M \sum_{OH1=1}^2 \sum_{OH2=1}^2 \frac{i}{k_B T \omega} \int dt \exp^{-i\omega t} \left\langle \left(\sum_i^3 \sum_j^3 D_{Pi}^{mol}(t) D_{Qj}^{mol}(t) \frac{d\alpha_{ij}^{mol}}{dr_{OH1}} \right) v_{OH1}^{mol}(t) v_{OH2}^{mol}(0) \left(\sum_k^3 D_{Rk}^{mol}(0) \frac{d\mu_k}{dr_{OH2}} \right) \right\rangle \quad (1)$$

where (P,Q,R) are any x, y, z direction in the laboratory frame (here PQR=xxz,yyz for the ssp signal), and k_B and T are respectively the Boltzmann constant and the temperature of the system. $\langle \dots \rangle$ is a time-correlation function, $\frac{d\alpha_{ij}}{dr_{OH}}$ and $\frac{d\mu_k}{dr_{OH}}$ are respectively the individual O-H bond contributions to the Raman tensor and Atomic Polar Tensor of water molecules. M is the number of water molecules and OH1,2 are the two O-H oscillators per water molecule. D is the matrix that projects the water molecular frame onto the laboratory frame. The D matrix and the projection of the velocities on each O-H bond axis are obtained from DFT-MD trajectories while $\frac{d\alpha_{ij}}{dr_{OH}}$ and $\frac{d\mu_k}{dr_{OH}}$ terms have been parametrized. Parametrization for water is taken from ref.⁴⁷

For silanols:

$$\chi_{PQR}^{(2)}(\omega) = \sum_{SiOH=l}^N \frac{i}{k_b T \omega} \int dt \exp^{-i\omega t} \left\langle \left(\sum_i^3 \sum_j^3 D_{Pl}^{SiOH}(t) D_{Qm}^{SiOH}(t) \frac{d\alpha_{ij}^{mol}}{dr_{OH}} \right) v_{OH}^{SiOH}(t) v_{OH}^{SiOH}(0) \left(\sum_k^3 D_{Rn}^{SiOH}(0) \frac{d\mu_k}{dr_{OH}} \right) \right\rangle \quad (2)$$

The parametrization of $\frac{d\alpha_{ij}}{dr_{OH}}$ and $\frac{d\mu_k}{dr_{OH}}$ for the silanols was performed using silicic acid unit block models. Four possible Si-OH configurations have been taken into account for the parametrization as reported in the Supporting Information (SI) of ref.³¹

We have characterized the three amorphous silica-water interfaces using our methodology shown in refs.^{34,35} where the water is decomposed into three layers, i.e. BIL, DL, Bulk through three structural descriptors: the water density profile perpendicular to the surface, the water coordination number, and the OH orientation of the water molecules. The BIL is the first water layer in direct contact with the silica solid. It is found to have a thickness between 2.5 and 3.0 Å for all three interfaces and to be systematically composed by water with an average coordination number of 2.8, to be compared to the 3.4 coordination number in liquid water.

Fig. 3 of the main text reports the time averaged spatial distribution of the silanol density, the water density and the coordination number of water at the interface with silica for the three aqueous interfaces of interest here. The silanol and water densities include all silanols of the silica surface and all water molecules belonging to the identified BIL-interface (identified by the structural analysis presented in refs.^{34,35}), at each time step of the dynamics and then averaged over the whole trajectory. The calculated water densities have been plotted with respect to the average position of the water molecules along the trajectory along the (x-y) lateral directions of the simulation box (parallel to the surface), resulting in the (x-y) spatial maps reported in Fig. 3A and Fig. 3D. The results are 3D maps where the color-coding (scale on the right-hand side of each figure) reports the average densities of water and silanol. Both the silanol and water densities are normalized to one.

The coordination maps in Fig. 3C of the main text, use the H-Bond criterion from ref⁴⁸

where two water molecules are considered H-Bonded if the O-O distance is less than 3.2 Å and the O(-H)-O angle is in the range 140-220°. The same criterion is applied for water-silanol hydrogen bonds. The coordination numbers in Fig. 3 report the sum of the water-water and water-silanol HBs. The coordination number per water molecule is calculated at each time-step of the dynamics and then averaged over the whole trajectory. These coordination numbers have been calculated for each water molecule that belongs to the BIL interfacial layer. The calculated water coordination numbers have been plotted with respect to the average position of the water molecules along the trajectory, along the (x-y) lateral directions of the simulation box. The resulting (x-y) spatial maps are reported in Fig. 3C of the main text.

The time averaged spatial distribution of water molecules belonging to the 5-membered ring structures (chain of three water molecules interacting with two silanols) is depicted in Fig. 1D. The H-Bond criterion used to identify the water molecules belonging to the 5-membered ring structure is the same as for the coordination maps and the methodology is the same as for the silanol and water density maps.

References

- (1) Aerts, C.; Verraedt, E.; Depla, A.; Follens, L.; Froyen, L.; Van Humbeeck, J.; Augustijns, P.; Van den Mooter, G.; Mellaerts, R.; Martens, J. Potential of amorphous microporous silica for ibuprofen controlled release. *International journal of pharmaceutics* **2010**, *397*, 84–91.
- (2) Delle Piane, M.; Vaccari, S.; Corno, M.; Ugliengo, P. Silica-based materials as drug adsorbents: first principle investigation on the role of water microsolvation on ibuprofen adsorption. *The Journal of Physical Chemistry A* **2014**, *118*, 5801–5807.
- (3) Delle Piane, M.; Corno, M.; Pedone, A.; Dovesi, R.; Ugliengo, P. Large-scale B3LYP

- simulations of ibuprofen adsorbed in MCM-41 mesoporous silica as drug delivery system. *The Journal of Physical Chemistry C* **2014**, *118*, 26737–26749.
- (4) Tielens, F.; Folliet, N.; Bondaz, L.; Etemovic, S.; Babonneau, F.; Gervais, C.; Azais, T. Molecular picture of the adsorption of ibuprofen and benzoic acid on hydrated amorphous silica through DFT-D calculations combined with solid-state NMR experiments. *The Journal of Physical Chemistry C* **2017**, *121*, 17339–17347.
- (5) Tielens, F.; Gierada, M.; Handzlik, J.; Calatayud, M. Characterization of Amorphous Silica Based Catalysts Using DFT Computational Methods. *Catalysis Today* **2019**,
- (6) Pantaleone, S.; Ugliengo, P.; Sodupe, M.; Rimola, A. When the Surface Matters: Prebiotic Peptide-Bond Formation on the TiO₂ (101) Anatase Surface through Periodic DFT-D2 Simulations. *Chemistry—A European Journal* **2018**, *24*, 16292–16301.
- (7) Lambert, J.-F. Adsorption and polymerization of amino acids on mineral surfaces: a review. *Origins of Life and Evolution of Biospheres* **2008**, *38*, 211–242.
- (8) Stievano, L.; Piao, L. Y.; Lopes, I.; Meng, M.; Costa, D.; Lambert, J.-F. Glycine and lysine adsorption and reactivity on the surface of amorphous silica. *European Journal of Mineralogy* **2007**, *19*, 321–331.
- (9) Rimola, A.; Fabbiani, M.; Sodupe, M.; Ugliengo, P.; Martra, G. How Does Silica Catalyze the Amide Bond Formation under Dry Conditions? Role of Specific Surface Silanol Pairs. *ACS Catalysis* **2018**, *8*, 4558–4568.
- (10) Shi, B.; Shin, Y. K.; Hassanali, A. A.; Singer, S. J. Biomolecules at the amorphous silica/water interface: Binding and fluorescence anisotropy of peptides. *Colloids and Surfaces B: Biointerfaces* **2017**, *157*, 83–92.
- (11) Casillas-Ituarte, N. N.; Allen, H. C. Water, chloroform, acetonitrile, and atrazine ad-

- sorption to the amorphous silica surface studied by vibrational sum frequency generation spectroscopy. *Chemical Physics Letters* **2009**, *483*, 84–89.
- (12) Rimola, A.; Costa, D.; Sodupe, M.; Lambert, J.-F.; Ugliengo, P. Silica Surface Features and Their Role in the Adsorption of Biomolecules: Computational Modeling and Experiments. *Chem. Rev.* **2013**, *113*, 4216–4313.
- (13) Hassanali, A. A.; Singer, S. J. Model for the water- amorphous silica interface: The undissociated surface. *The Journal of Physical Chemistry B* **2007**, *111*, 11181–11193.
- (14) Schrader, A. M.; Monroe, J. I.; Sheil, R.; Dobbs, H. A.; Keller, T. J.; Li, Y.; Jain, S.; Shell, M. S.; Israelachvili, J. N.; Han, S. Surface chemical heterogeneity modulates silica surface hydration. *Proceedings of the National Academy of Sciences* **2018**, *115*, 2890–2895.
- (15) Cimas, Á.; Tielens, F.; Sulpizi, M.; Gaigeot, M.-P.; Costa, D. The amorphous silica–liquid water interface studied by ab initio molecular dynamics (AIMD): local organization in global disorder. *Journal of Physics: Condensed Matter* **2014**, *26*, 244106.
- (16) Pfeiffer-Laplaud, M.; Costa, D.; Tielens, F.; Gaigeot, M.-P.; Sulpizi, M. Bimodal acidity at the amorphous silica/water interface. *The Journal of Physical Chemistry C* **2015**, *119*, 27354–27362.
- (17) Du, Q.; Freysz, E.; Shen, Y. R. Vibrational spectra of water molecules at quartz/water interfaces. *Phys. Rev. Lett.* **1994**, *72*, 238.
- (18) Bouhadja, M.; Skelton, A. Dynamical Properties of Water and Ions at the Quartz (101)–Water Interface at a Range of Solution Conditions: A Classical Molecular Dynamics Study. *The Journal of Physical Chemistry C* **2018**, *122*, 1535–1546.
- (19) Darlington, A. M.; Jarisz, T. A.; DeWalt-Kerian, E. L.; Roy, S.; Kim, S.; Azam, M. S.; Hore, D. K.; Gibbs, J. M. Separating the pH-dependent behavior of water in the Stern

- and diffuse layers with varying salt concentration. *The Journal of Physical Chemistry C* **2017**, *121*, 20229–20241.
- (20) Zhang, H.; Hassanali, A. A.; Shin, Y. K.; Knight, C.; Singer, S. J. The water–amorphous silica interface: Analysis of the Stern layer and surface conduction. *The Journal of chemical physics* **2011**, *134*, 024705.
- (21) Dewan, S.; Carnevale, V.; Bankura, A.; Eftekhari-Bafrooei, A.; Fiorin, G.; Klein, M. L.; Borguet, E. Structure of water at charged interfaces: A molecular dynamics study. *Langmuir* **2014**, *30*, 8056–8065.
- (22) Yates, D. E.; Healy, T. W. The structure of the silica/electrolyte interface. *Journal of Colloid and Interface Science* **1976**, *55*, 9–19.
- (23) Myalitsin, A.; Urashima, S.-h.; Nihonyanagi, S.; Yamaguchi, S.; Tahara, T. Water Structure at the Buried Silica/Aqueous Interface Studied by Heterodyne-Detected Vibrational Sum-Frequency Generation. *J. Phys. Chem. C* **2016**, *120*, 9357–9363.
- (24) Urashima, S.-h.; Myalitsin, A.; Nihonyanagi, S.; Tahara, T. The topmost water structure at a charged silica/aqueous interface revealed by heterodyne-detected vibrational sum frequency generation spectroscopy. *The journal of physical chemistry letters* **2018**, *9*, 4109–4114.
- (25) Isaienko, O.; Borguet, E. Hydrophobicity of Hydroxylated Amorphous Fused Silica Surfaces. *Langmuir* **2013**, *29*, 7885–7895.
- (26) Ohno, P. E.; Wang, H.-f.; Geiger, F. M. Second-order spectral lineshapes from charged interfaces. *Nat. Comm.* **2017**, *8*, 1032.
- (27) Darlington, A. M.; Gibbs-Davis, J. M. Bimodal or trimodal? The influence of starting pH on site identity and distribution at the low salt aqueous/silica interface. *The Journal of Physical Chemistry C* **2015**, *119*, 16560–16567.

- (28) Ohno, P. E.; Saslow, S. A.; Wang, H.-f.; Geiger, F. M.; Eienthal, K. B. Phase-referenced nonlinear spectroscopy of the α -quartz/water interface. *Nature communications* **2016**, *7*, 13587.
- (29) Ostroverkhov, V.; Waychunas, G. A.; Shen, Y. Vibrational spectra of water at water/ α -quartz (0 0 0 1) interface. *Chemical Physics Letters* **2004**, *386*, 144–148.
- (30) Laetitia Dalstein, E. P.; Tyrode, E. The Elusive Silica/Water Interface: Isolated Silanols Under Water as Revealed by Vibrational Sum Frequency Spectroscopy. *Phys.Chem.Chem.Phys.* **2017**, *19*, 10343–10349.
- (31) Cyran, J. D.; Donovan, M. A.; Vollmer, D.; Siro Brigiano, F.; Pezzotti, S.; Galimberti, D. R.; Gaigeot, M.-P.; Bonn, M.; Backus, E. H. G. Molecular hydrophobicity at a macroscopically hydrophilic surface. *Proc. Nat. Acad. Sciences* **2019**, *116*, 1520–1525.
- (32) Ugliengo, P.; Sodupe, M.; Musso, F.; Bush, I. J.; Orlando, R.; Dovesi, R. Realistic Models of Hydroxylated Amorphous Silica Surfaces and MCM-41 Mesoporous Material Simulated by Large-scale Periodic B3LYP Calculations. *Advanced Materials* **2008**, *20*, 4579–4583.
- (33) Masini, P.; Bernasconi, M. Ab initio simulations of hydroxylation and dehydroxylation reactions at surfaces: amorphous silica and brucite. *Journal of Physics: Condensed Matter* **2002**, *14*, 4133.
- (34) Pezzotti, S.; Galimberti, D. R.; Shen, Y. R.; Gaigeot, M.-P. Structural definition of the BIL and DL: a new universal methodology to rationalize non-linear $\chi^{(2)}$ (ω) SFG signals at charged interfaces, including $\chi^{(3)}$ (ω) contributions. *Phys. Chem. Chem. Phys.* **2018**, *20*, 5190–5199.
- (35) Pezzotti, S.; Galimberti, D. R.; Gaigeot, M.-P. 2D H-Bond Network as the Topmost Skin to the Air-Water Interface. *J. Phys. Chem. Lett.* **2017**, *8*, 3133–3141.

- (36) Tielens, F.; Gervais, C.; Lambert, J. F.; Mauri, F.; Costa, D. Ab Initio Study of the Hydroxylated Surface of Amorphous Silica: A Representative Model. *Chemistry of Materials* **2008**, *20*, 3336–3344.
- (37) Yazaydin, A. Ö.; Thompson, R. W. Molecular simulation of water adsorption in silicalite: Effect of silanol groups and different cations. *Microporous and Mesoporous Materials* **2009**, *123*, 169–176.
- (38) Pezzotti, S.; Galimberti, D. R.; Gaigeot, M.-P. Deconvolution of BIL-SFG and DL-SFG spectroscopic signals reveals order/disorder of water at the elusive aqueous silica interface. *Physical Chemistry Chemical Physics* **2019**, *21*, 22188–22202.
- (39) Serva, A.; Pezzotti, S.; Bougueroua, S.; Galimberti, D. R.; Gaigeot, M.-P. Combining ab-initio and classical molecular dynamics simulations to unravel the structure of the 2D-HB-network at the air-water interface. *Journal of Molecular Structure* **2018**, *1165*, 71 – 78.
- (40) Pezzotti, S.; Serva, A.; Gaigeot, M.-P. *J. Chem. Phys.* **2018**,
- (41) Pezzotti, S.; Galimberti, D. R.; Gaigeot, M.-P. 2D H-bond network as the topmost skin to the air–water interface. *The journal of physical chemistry letters* **2017**, *8*, 3133–3141.
- (42) Hutter, J.; Iannuzzi, M.; Schiffmann, F.; VandeVondele, J. CP2K: Atomistic Simulations of Condensed Matter Systems. *WIREs Comput Mol Sci* **2014**, *4*, 15–25.
- (43) Lee, C.; Yang, W.; Parr, R. G. Development of the Colle-Salvetti Correlation-Energy Formula into a Functional of the Electron Density. *Phys. Rev. B* **1988**, *37*, 785–789.
- (44) Becke, A. D. Density-Functional Exchange-Energy Approximation with Correct Asymptotic Behavior. *Phys. Rev. A* **1988**, *38*, 3098–3100.
- (45) Goedecker, S.; Teter, M.; Hutter, J. Separable Dual-Space Gaussian Pseudopotentials. *Phys. Rev. B.* **1996**, *54*, 1703–1710.

- (46) Grimme, S.; Antony, J.; Ehrlich, S.; Krieg, H. A consistent and accurate ab initio parametrization of density functional dispersion correction (DFT-D) for the 94 elements H-Pu. *The Journal of chemical physics* **2010**, *132*, 154104.
- (47) Khatib, R.; Backus, E. H. G.; Bonn, M.; Perez-Haro, M.-J.; Gaigeot, M.-P.; Sulpizi, M. Water Orientation and Hydrogen-Bond Structure at the Fluorite/Water Interface. *Sci. Reports* **2016**, *6*, 24287.
- (48) White, J. A.; Schwegler, E.; Galli, G.; Gygi, F. The Solvation of Na⁺ in Water: First-Principles Simulations. *J. Chem. Phys.* **2000**, *113*, 4668–4673.

5.8 An aspect of the surface morphology effects: how silanol nests can affect interfacial properties

The results reported in this section are preliminary data. Further investigations are needed.

We now investigate how the HB-network formed by water and surface groups at silica-water interfaces can be affected by a variation in the morphology of the silica surface. The hydroxylated $7.6 \text{ SiOH}/\text{nm}^2$ silica surface is interesting as it presents a specific morphology that the two other hydroxylated surfaces considered in this work (4.5 and $3.5 \text{ SiOH}/\text{nm}^2$) do not possess: two "silanol nests" [112, 260]. Silanol nests are defined as a concave zone on the silica surface with a high density of silanols mutually interacting [184, 112]. These concave zones are not only rich in SiOH sites, but they also maximize, by construction, the exposure of Si-O-Si siloxane groups to water. The presence of nests in zeolites as defects and their capacity in tuning the properties of adsorption of water and biomolecules on silica based materials have already been emphasized [248, 261, 262]. One of the silanol nest at the $7.6 \text{ SiOH}/\text{nm}^2$ model silica surface is illustrated in Fig. 5.12.

We now consider the effect of silanol nests present at the silica-water interface on the water molecular arrangements and on the SFG response. This allows to test the capability of SFG spectroscopy to identify the presence of silanol nests at silica surfaces as they can be key elements for adsorption processes.

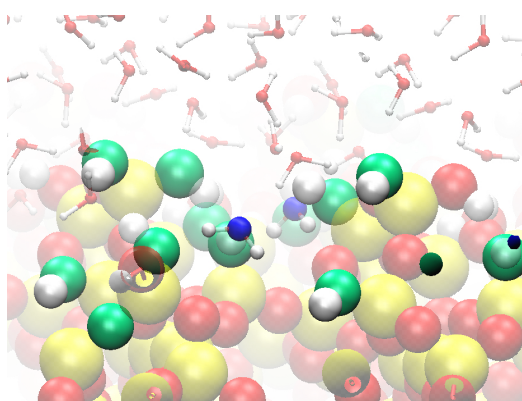


Figure 5.12: MD-snapshot illustrating one of the silanol nest in the DFT-MD simulation of the $7.6 \text{ SiOH}/\text{nm}^2$ hydroxylated silica surface at the interface with liquid water. The oxygen atoms of the SiOH groups forming the nest are coloured in green. Some of the water molecules entering the nest are colored with blue oxygens.

The interfacial properties induced by the presence of silanol nests are investigated by comparing both the structural and spectroscopic properties of

the interface in presence of nests with the results obtained for the two surfaces with a lower degree of hydroxylation (no silanol nests on these surface), i.e. 3.5 and 4.5 SiOH/nm² degree of hydroxylation.

A first aspect we have considered in our work is the effect of the silanol nests in the organization of the silanol groups in contact with liquid water. We have therefore compared the solid-solid interactions, expressed in terms of silanol-silanol SiOH–SiOH and silanol-siloxane bridge OH–SiOSi H-Bonds with the ones present at the silica-air interface. We thus report in Table 5.1 the ratio (reported as a percentage) between the solid-solid H-Bonds respectively found at the silica-water interface (denoted afterwards solid-solid^{SW}) and at the silica-air interface (denoted afterwards solid-solid^{SA}) for the three hydroxylated surfaces of interest here. We also report values for the crystalline (0001) α -quartz-water interface with a high degree of hydroxylation of 9.6 SiOH/nm². These ratio thus provide the percentage of solid-solid H-Bonds that are maintained on the silica surfaces once contact with liquid water has been made. The solid-solid H-Bonds that can be made are SiOH–SiOH (between silanols) and SiOH–SiOSi (between silanols and siloxane bridges).

The (0001) α -quartz-water interface represents the hydrophilic extreme of silica surfaces in the present investigations. It has a high degree of hydroxylation, close to the most hydroxylated (7.6 SiOH/nm²) amorphous silica surface considered. The crystalline surface does not present silanol nests. By using this crystalline silica surface we can directly deconvolve the effect of silanol nests on the interface organization. We refer to ref.[49] for all details about the quartz-water interface.

Table 5.1: The ratio between solid-solid H-Bonds respectively obtained at the silica-water (solid-solid^{SW}) and at the silica-air interfaces (solid-solid^{SA}) for the four silica surfaces considered in this work. Both the silanol-silanol (SiOH–SiOH) and silanol-siloxane bridge (SiOH–SiOSi) solid-solid H-Bonds are reported.

Degree of surface hydroxylation (SiOH/nm ²)	solid-solid ^{SW} /solid-solid ^{SA} SiOH–SiOH SiOH–OSiO
9.6 (0001) α -quartz	50 \emptyset *
7.6 amorphous silica	50 33
4.5 amorphous silica	33 18
3.5 amorphous silica	18 18

*There are no SiOH–OSiO H-Bonds on both the dry and aqueous (0001) α -quartz surfaces. For this reason the ratio solid-solid^{SW}/solid-solid^{SA} cannot be calculated for the (0001) α -quartz.

At the 3.5 and 4.5 SiOH/nm² low rates of surface hydroxylation, i.e. surfaces without silanol nests, the presence of water leads to a massive reorganization of the surface-surface interactions (only 18 and 33% of the silanol-silanol H-Bonds are maintained when going from the gas phase to the liquid phase, see table 5.1). As one can see in Table 5.1, a low percentage

of the silanol-silanol H-Bonds (SiOH-SiOH) originally present at the 3.5 and 4.5 SiOH/nm² dry surfaces is maintained once the two surfaces are put in contact with liquid water: few silanol-silanol (18% and 33%) and silanol-siloxane bridge H-Bonds (18%) are maintained once the surface is in contact with water. Higher percentages of solid-solid H-Bonds are however maintained for the 7.6 SiOH/nm² and the (0001)- α quartz surfaces once in contact with water (50%). It is important to mention here that the silanol-silanol H-Bonds at the 7.6 SiOH/nm² aqueous surface are in great part involved in the two silanol nests present on this surface.

Our findings indicate that solid-solid H-Bonds are more easily replaced by solid-water interactions at low hydroxylated silica aqueous surfaces (3.5 and 4.5 SiOH/nm²) than at the high hydroxylated ones (7.6 SiOH/nm² and the (0001) α quartz surfaces). This is illustrated in Fig. 5.13 and is discussed below in the text.

Before such discussion, we propose two possible explanations for this phenomenon:

1) The 7.6 SiOH/nm² and the (0001)- α quartz surfaces present higher numbers of SiOH surface groups with respect to the low hydroxylated surfaces, which implies that less solid-solid H-Bonds need to be broken in order to make the interfacial water molecules fully coordinated (coordination number of 3.5).

2) Strong intra-molecular H-Bonds are formed between silanols in "silanol" nests or over the surface of (0001)- α quartz, thus far less easy to break. Previous studies have indeed shown that silanols involved in complex H-Bonded structures[191, 263] as the ones present in "silanol nests" or at the surface of the neat (0001) α -quartz (see ref. [182]), form strong H-Bonds.

The high number of solid-solid interactions in silanol nests in turn affect the silica-water interface structure as one can see by the solid-solid and solid-water H-Bonds formed at the amorphous-water and quartz-water interfaces considered in this work and reported in Fig. 5.13.

The average number of both solid-solid (blue curve) and solid-water (red curve) HBs steadily increases when going respectively from the 3.5 SiOH/nm² to the 4.5 SiOH/nm² surfaces and from the 4.5 SiOH/nm² to the 9.6 SiOH/nm² surfaces, while the values calculated for the 7.6 SiOH/nm² surface are offsets. In particular, the number of solid-solid HBs (4.2 HBs/nm²) formed at the 7.6 SiOH/nm² interface is much larger than the numbers obtained for the 3.5 SiOH/nm² and 4.5 SiOH/nm² interfaces (0.2 and 0.9 HBs/nm² respectively), and it almost reaches the limit value of 4.8 HBs/nm² obtained for the highly hydrophilic quartz-water interface. This is due to the SiOH groups within the silanol nests, which are strongly inter-connected via solid-solid HBs.

A further consequence of the high number of SiOH-SiOH HBs formed within the silanol nests is that they do not allow to fully exploit the hydrophilic potential (i.e. the capacity to form H-Bonds with water) of the

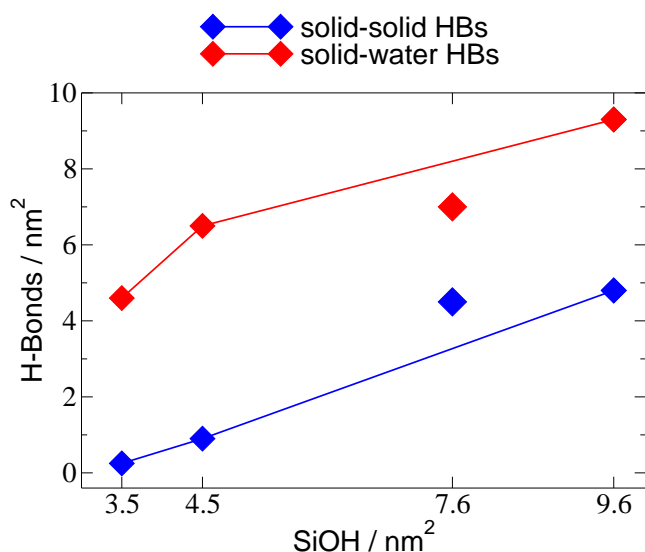


Figure 5.13: *DFT-MD simulations: time averaged numbers of H-Bonds formed per surface area (H-Bonds/nm²), either between two SiOH terminations of the silica surface (solid-solid HBs, blue diamonds) or between SiOH groups and BIL-water molecules (solid-water HBs, red diamonds), calculated for silica-water interfaces with a silica surface having an average silanol density of 3.5 SiOH/nm², 4.5 SiOH/nm² and 7.6 SiOH/nm², as well as for the crystalline (0001) α -quartz-water interface with 9.6 SiOH/nm² hydroxylation. The trend lines (blue and red lines) obtained from the values calculated only for the systems with 3.5 SiOH/nm², 4.5 SiOH/nm² and 9.6 SiOH/nm² hydroxylation numbers are also reported to better highlight the offset position of the values calculated for the 7.6 SiOH/nm² silica surface (that has silanol nests).*

7.6 SiOH/nm² silica surface. For instance only 0.5 more solid-water HBs/nm² (i.e. 7.0 solid-water HBs/nm² for the 7.6 SiOH/nm² surface vs 6.5 solid-water HBs/nm² for the 4.5 SiOH/nm² one) are formed at the 7.6 SiOH/nm² silica surface than at the 4.5 SiOH/nm² surface (see red curve in Fig. 5.13), despite an increase in the silanol density by 2.1 SiOH/nm² (i.e. 7.6 SiOH/nm² minus 4.5 SiOH/nm²). This is due to the competition between solid-solid and water-solid HBs: since SiOH groups within the nests form more solid-solid HBs, they interact less with water than the silanols located outside the nests. The sharp increase in silanol density within nests thus mostly results in the maximization of solid-solid HBs and does not provide an equivalent increase in the density of solid-water HBs. The intra-molecular H-Bond network formed between silanols in the "silanol nests" is only slightly affected by the presence of BIL-water molecules above or inside the nests.

A direct consequence of the special H-Bonding properties of the surface sites within a silanol nest can be already observed when looking at the coordination of BIL-water molecules located inside the nests. The MD simulations indeed show that BIL-water molecules entering the nest loose on average one water-water HB/molecule, because of the confined environment of the nest, which is not compensated by additional water-SiOH HBs. The dangling water OH-groups resulting from such missing water-water HBs are hence found

to mostly interact with Si-O-Si siloxane sites, which exposure to water is now maximized within the nest.

Water molecules within the nest are mostly found in two H-Bond arrangements:

- 1) pointing both O-H groups toward surface Si-O-Si siloxanes, while simultaneously accepting one HB from a BIL-water molecule located above the nest.
- 2) pointing one O-H group toward one surface Si-O-Si siloxane and the other one to one SiOH group, while simultaneously accepting one HB from a BIL-water molecule located above the nest.

These two water populations are observed only within the nests and are not found at the other silica-water interfaces considered in this work.

At this point, one naturally raising question is whether such water populations specifically found within the silanol nests can have a signature in SFG spectra. We hence present in Fig. 5.14 theoretical $\Im(\chi^{(2)}(\omega))$ spectra calculated for the silica-water interfaces with an average silanol density of 3.5 SiOH/nm², 4.5 SiOH/nm² and 7.6 SiOH/nm², including only the contributions from water (left panel, note that only BIL-water is SFG active at the isoelectric conditions for all the three systems), but also summing the contributions from water and the silica surface SiO-H groups (right panel).

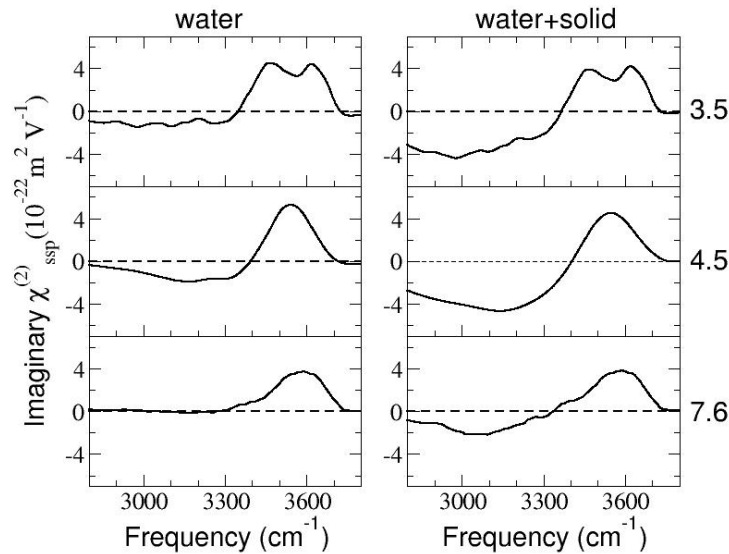


Figure 5.14: Comparison between theoretical $\Im(\chi^{(2)}(\omega))$ spectra calculated from DFT-MD simulations of water at the interface with fused/amorphous silica surfaces with an average silanol density of 3.5 SiOH/nm², 4.5 SiOH/nm² and 7.6 SiOH/nm² (including silanol nests). Left: $\Im(\chi^{(2)}(\omega))$ spectra obtained by including only the contribution from water (i.e. BIL-water). Right: $\Im(\chi^{(2)}(\omega))$ spectra obtained by including both the water and silica surface contributions.

As one can see in Fig. 5.14, the only change in the total SFG signal obtained by adding the solid contribution is in the negative $\Im(\chi^{(2)}(\omega))$ band, which systematically becomes more pronounced once the solid contribution

to SFG is added (right panels). From our previous discussion in section 5.5, we already know that this is due to out-of-plane SiOH groups donating HBs to BIL-water (i.e. SiOH-BIL groups, see Fig. 5.7 for OH-groups classification and their SFG signatures), as they are the only solid surface sites contributing to SFG in the OH-stretching region and providing a negative band at 3200 cm^{-1} in $\Im(\chi^{(2)}(\omega))$ spectra. Their signature is here found to be similar for all the three silica-water interfaces, while the major differences in the spectra are coming from the water contribution (left panels in Fig. 5.14).

Once again the 7.6 SiOH/nm^2 surface with the silanol nests shows an outsider behaviour, which is detected by the intensities of two bands: the 3200 cm^{-1} negative band and the 3660 cm^{-1} positive band. Starting from the negative band, we remind the readers that we have already shown it arises from O-H groups of BIL-water molecules donating HBs to bulk water molecules (i.e. OH-Bulk groups, see Fig. 5.7, section 5.5). The intensity of such band increases with the increase in the surface hydroxylation from 3.5 SiOH/nm^2 to 4.5 SiOH/nm^2 , while it decreases again (becoming almost zero) for the 7.6 SiOH/nm^2 surface. One of the possible causes are the water molecules that reside in the silanol-nests, that systematically accept HBs from BIL-water above the nests. These newly formed HBs have opposite orientation with respect to the HBs formed by OH-Bulk groups. This leads to a partial compensation between the positive $\Im(\chi^{(2)}(\omega))$ intensity and the negative intensity from OH-Bulk groups at 3200 cm^{-1} . Another possible explanation could be given by a higher basicity of the SiOH groups involved in the silanol nest H-Bond structure (see e.g.[191, 263]) with respect to the ones at less hydroxylated amorphous surfaces: this leads to a red shift of the band associated with the OH-SiOH groups (see Fig. 5.7) with a consequent enhancement of the positive band at 3200 cm^{-1} . Such enhancement would lead to a compensation between the positive $\Im(\chi^{(2)}(\omega))$ intensity and the negative intensity from OH-Bulk groups at 3200 cm^{-1} .

We now move to the 3660 cm^{-1} positive band which arises from OH-SiOSi water groups and which represents the major change between the SFG spectra of the three silica-water interfaces reported in Fig. 5.14. In order to better show the trend for its intensity, the integrated area of the 3660 cm^{-1} positive band is plotted in Fig. 5.15 for the three interfaces, as well as for the fully hydroxylated (0001) α -quartz-water interface for comparison. The band intensity decreases by a factor of four from the silica hydroxylation state of 3.5 SiOH/nm^2 to 4.5 SiOH/nm^2 and becomes zero for the quartz-water interface with 9.6 SiOH/nm^2 (which has no Si-O-Si groups exposed at the surface). On the basis of this trend, one would expect a 3660 cm^{-1} positive band with almost zero intensity also for the 7.6 SiOH/nm^2 surface. On the contrary, what is revealed by Fig. 5.15 is that the 3660 cm^{-1} positive band gains again intensity for the surface containing silanol nests, becoming almost twice more intense than the band obtained for the 4.5 SiOH/nm^2 surface. This is due to the BIL-water molecules within the nests which we have shown to interact more with Si-O-Si groups than with the water molecules located outside the nests.

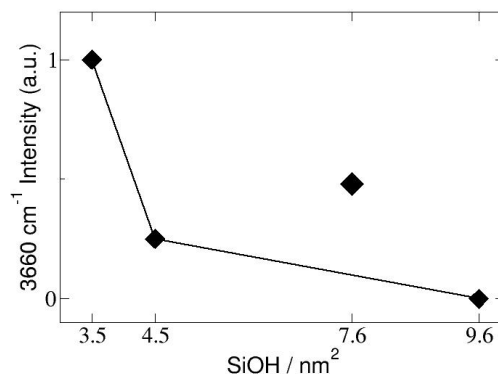


Figure 5.15: $\Im(\chi^{(2)}(\omega))$ intensity (integrated area of the peaks in Fig. 5.14) of the 3660 cm^{-1} band in the theoretical SFG spectra of silica-water interfaces as a function of the degree of hydroxylation of the silica surface. The fused silica surfaces with 3.5 SiOH/nm^2 , 4.5 SiOH/nm^2 and 7.6 SiOH/nm^2 have been considered, as well as the crystalline (0001) α -quartz-water interface with 9.6 SiOH/nm^2 . The 3660 cm^{-1} band intensity for each interface (black diamonds) has been calculated as the integral of the $\Im(\chi^{(2)}(\omega))$ signal arising from the OH-SiOSi population (solely contributing to the 3660 cm^{-1} band, see Fig. 5.7), normalized with respect to the most intense 3660 cm^{-1} band (obtained for the fused silica with 3.5 SiOH/nm^2). The trend line (black line) obtained from the values calculated only for the systems with 3.5 SiOH/nm^2 , 4.5 SiOH/nm^2 and 9.6 SiOH/nm^2 is reported to better highlight the offset position of the value calculated for the 7.6 SiOH/nm^2 silica surface.

We thus can suggest that silanol nests could be detected by SFG spectroscopy, thanks to their impact on the intensity of the 3660 cm^{-1} $\Im(\chi^{(2)}(\omega))$ positive band. Given two silica-water interfaces with increasing hydroxylation states, if the surface with higher silanol density exhibits a more prominent 3660 cm^{-1} band compared to the surface with lower silanol density, then our investigation shows that one of the possible reasons could be the presence of silanol nest(s) at the more hydroxylated silica-water interface.

Despite the SFG response of silica-water interfaces is modulated by the specific coordination environment experienced by water molecules entering the nests, silanol nests are however found to not have detectable effects on the balance between hydrophilic/hydrophobic patches at silica surfaces, neither on the microscopic water arrangement above them. Water molecules above the silanol nests, which are by construction part of the hydrophilic domain of water in the BIL, are in fact found to maintain the characteristic 5-membered HB-rings structures already observed at the 4.5 SiOH/nm^2 surface (see scheme in Fig. 5.10). As a consequence, the transition from the hydrophobic "horizontal ordering" (characterized by the air-water hydrophobic interface 2D-HB-Network[103]) typical of the least hydrophilic 3.5 SiOH/nm^2 silica-water interface toward the "vertical ordering" (characterized by the 5-membered HB-rings structure) typical of the more hydrophilic silica-water interfaces, is not affected by the presence of silanol nests on the surface.

5.9 Effects of Electrolytes on the structure, dynamics and spectroscopy of amorphous silica-water interfaces

The results presented hereafter are extracted from our paper [JACS, 142, 6991-7000 (2020)] [243] included at the end of this section. They have been obtained in collaboration with one of our experimental partners: the Borguet's group at Temple University in Philadelphia (USA).

In this section we investigate how the structure and the SFG response of electrolytic silica-water interfaces is affected by changes in the solution ionic strength, by combining theoretical modelling from DFT-MD simulations with TR-SFG spectroscopy experiments.

TR-SFG (time resolved sum frequency generation) [230, 233] spectroscopy has been used to interrogate silica-electrolyte aqueous interfaces, especially focusing on amorphous silica-water interfaces, with an average surface degree of hydroxylation of 4.5 SiOH/nm². Ions have been shown experimentally to modulate the structure, SFG response and vibrational relaxation processes at the interface in two ways: (1) by screening the surface charge and thus reducing the SFG probing depth, and (2) by inducing changes in the local water organization and thus by inducing modifications in the BIL water SFG signal. However, a clear microscopic interpretation of these two effects is still missing. These can be reconsidered in the light of the two distinct water interfacial regions at charged interfaces, i.e. the Binding Interfacial Layer (BIL) and the Diffuse Layer (DL): (1) is due to the ions affecting the thickness of the DL, while (2) is due to the ions modifying the water H-Bond network in the BIL. Both effects are being simultaneously included in the spectroscopic TR-SFG measurements. It is thus essential to disentangle the relaxation time of the truly interfacial BIL-water from the subsequent “bulk like” reoriented DL-water in TR-SFG measurements. All the following rationalizations will hence make use of the BIL/DL deconvolution scheme we have developed in ref. [114]. See ref.[243] reported at the end of this section for details.

The solution pH has further been shown to alter ion's adsorption, with expected consequences on interfacial structure and spectroscopy[264, 49]. As we have shown in ref.[243] (reported at the end of this section), both theory and experiments provide evidences that cations are preferentially accumulated at the interface for negatively charged silica surfaces (pH>PZC) so that they screen the surface charge, while both cations and anions populate the interfacial layer with the same probability for neutral silica aqueous interfaces at PZC (pH≈2-4). The effect of ions on the structural/spectroscopic properties thus need to be evaluated at different pH conditions. This is indeed what has been done in ref.[243], which results will be now discussed in the following. We focused on the ions effect at the fused 4.5 SiOH/nm² silica-water interface.

Both the concentration of the NaCl electrolyte (in the 0-0.5 M range) and the pH conditions (in the 2-12 range) are varied in the experiments. Only one DFT-MD is used for theory, i.e. one concentration (0.5 M) of the electrolyte.

The vibrational lifetime T_1 is experimentally measured at NaCl concentrations of 0 M, 0.1 M and 0.5 M and at pH values of 2, 6, 12. The values are reported in Fig. 5.16-A. They clearly show that the vibrational dynamics at silica-water interfaces is a function of both bulk pH and ionic strength.

Focusing firstly on the electrolytes effect at the neutral pH \sim 2, which

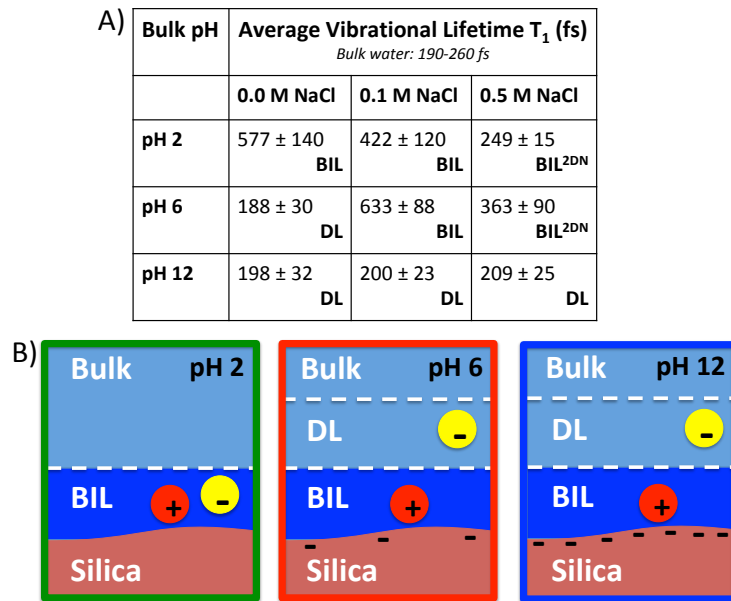


Figure 5.16: Electrolytes alter the vibrational relaxation of interfacial water in both BIL/DL regions. A: average vibrational lifetime T_1 at different bulk pH and NaCl concentrations, obtained from 4 level model fits to the measured TR-SFG traces. The T_1 values reported are the average T_1 from separate measurements repeated 3-5 times. The error bars indicate the standard deviation for all the individual T_1 values obtained on different days. The labels “BIL” (Binding Interfacial Layer), “BIL^{2DN}” (2DN is a short notation for the 2D-HBond-Network formed by the BIL-water at electrolytes concentrations \geq 0.5 M), and “DL” (Diffuse Layer) refer to the interfacial region that dominates the SFG response in each aqueous environment, as demonstrated in the text. B: schemes of the structural organization of water and ions at 1 M electrolytic silica-water interfaces (pH=2, 6, 12) extracted from the DFT-MD simulations. Red/yellow balls with +/- signs represent the cations/anions and their distribution at the interface. See ref.[243] for all details.

corresponds to the point of zero charge (PZC) conditions, the measured T_1 lifetimes show that the vibrational relaxation of water next to the silica surface at pH \sim 2 is accelerated by increasing the bulk ionic concentration. In the absence of salt, the surface potential calculated using the silica deprotonation ratio and the Gouy-Chapman model (see ref.[243]) is close to zero, so that the DL contribution to SFG is negligible and the water T_1 lifetime consequently reflects the true interfacial water structure, i.e. the BIL. When ions are added

in the solution, the T1 lifetime decreases from 577 fs, for the neat interface, to 422 fs for 0.1 M NaCl concentration and to 249 fs for 0.5 M NaCl concentration. As we demonstrate in ref.[243], there is not a preferential adsorption of cations over anions or vice-versa at pH 2 conditions, i.e. both ionic species have the same probability to populate the BIL layer at such low pH, so that the surface potential remains close to zero in all the explored concentration range. The changes in the measured T1 lifetimes at pH~2 conditions are consequently due to ions that are altering the water structure in the BIL.

As revealed by the DFT-MD simulations reported in ref.[243], the ions induced acceleration of the interfacial relaxation process are due to the capability of electrolytes like KCl and NaCl to induce in-plane ordering of the water H-Bond network at the fused silica-water interface. The microscopic mechanism we have identified to be at the heart of the observed ions kosmotropic effect in the BIL is summarized hereafter. When the ions concentration is lower than 0.1 M, the microscopic arrangement of water in the BIL at the 4.5 SiOH/nm² silica-water interface is inhomogeneous, made of very distinct water HB-structures formed above the surface hydrophilic/hydrophobic patches. As characterized in section 5.6, the hydrophobic patches of the 4.5 SiOH/nm² silica surface are too small to allow water above them be arranged similar to the air-water-like 2D-HB-Network [103, 105, 104] which we have seen to allow maximize the water coordination above the silica surface with a lower silanol density of 3.5 SiOH/nm². The water molecules located above the hydrophobic patches at the 4.5 SiOH/nm² hydroxylated silica surface are hence found strongly undercoordinated. This is shown in Fig. 5.17-A, where the water coordination is spatially resolved above the silica surface and shown to be lower than 2.2 HBs/molecule above the surface areas with a low silanol density (i.e. the hydrophobic patches, rich in Si-O-Si siloxane sites), while water is as much coordinated as in the bulk (3.4 HBs/molecule) above the hydrophilic patches, where the quartz-like "vertical order" made of the 5-membered HB-ring structures is recovered (see sections 5.7).

The substantial density of under-coordinated water molecules in the hydrophobic patches (40% of all water in the BIL) and weak H-bond interconnectivity between the water molecules in the BIL, resulting in less intermolecular couplings, have been hence identified as the microscopic reasons for the slow T1 lifetime of 577 fs measured at pH 2 without excess salt.

As soon as salt is added (in the 0.1-1.0 M range), the HB-network in the BIL is dramatically changed by both cations and anions starting to populate the BIL and forming inner-sphere complexes, i.e. completing their solvation shell using both silanols and BIL-water molecules (as illustrated at the top of Fig. 5.17). The newly formed ion-silanol interactions replace previously existing HBs between BIL-water and SiOH sites, which are a mandatory brick for the 5-membered HB-ring structures in the hydrophilic domains. As

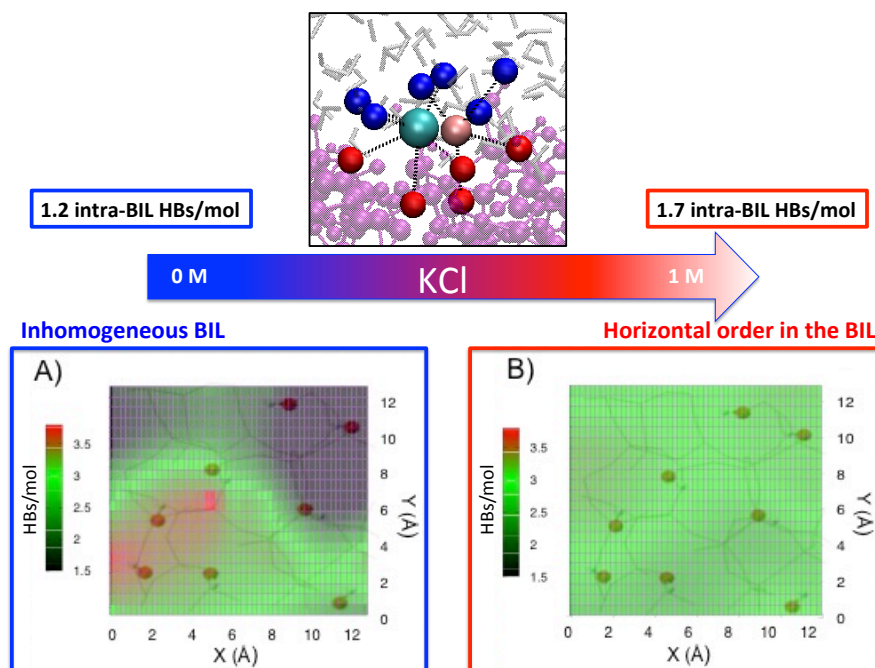


Figure 5.17: *KCl induced in-plane ordering in the BIL. The time averaged coordination number of the water molecules in the BIL, spatially resolved along the lateral x - y directions of the silica surface, is reported for (A): Neat (0 M KCl) aqueous silica interface and B: electrolytic (1 M KCl) aqueous silica interface. The water coordination is expressed in terms of the number of HBs (sum of water-water and water-silanol HBs) per water molecule. The color coding (vertical scale in the plots) goes from dark blue (1.5 HBs/molecule) to red (3.7 HBs/molecule). For each of the two extreme situations with 0 M and 1 M KCl concentration, the number of intra-BIL HBs formed is also reported as it is a structural marker of the formation of the "horizontal order" in the BIL (at 1 M KCl concentration). A MD-snapshot illustrating the inner-sphere adsorption of the KCl ion-pair at the silica-water interface, responsible for the in-plane ordering of the water HB-Network in the BIL, is also shown. The ions use silanols (red balls for the oxygens) and water in the BIL (blue balls for the oxygens) in order to achieve an inner-sphere adsorption.*

shown by the DFT-MD simulations, water above the hydrophilic patches is consequently not able anymore to maintain the vertical order. The dangling water O-H groups resulting from the breaking of water-silanol HBs hence re-orient in-plane in order to maximize water-water intra-BIL HBs. The ions induced increase in intra-BIL HBs ultimately leads to the formation of an air-water-like interface made of a 2D-HB-Network[103, 105, 104], at electrolytes concentrations equal to 0.5 M or greater. This is shown in Fig. 5.17-B by reporting the number of intra-BIL HBs formed in the BIL, which increases from 1.2 HBs/molecule for the neat interface to 1.7 HBs/molecule when 1 M KCl is added (same value as for the air-water interface [103]).

The addition of electrolytes at the 4.5 SiOH/nm^2 hydroxylated silica-water interface thus produces the same effect as decreasing the surface hydroxylation, inducing the transition from the inhomogeneous water BIL structure obtained at the 4.5 SiOH/nm^2 silica-water interface toward the "hori-

zontal order” typical of the least hydroxylated silica-water interfaces (i.e. 3.5 SiOH/nm^2 , see section 5.7). In agreement, the T1 lifetime of the silica-water interface is experimentally found to change in response to such variation in the microscopic arrangement in the BIL. The value of $T1=249\pm 15 \text{ fs}$ is indeed measured for $[\text{NaCl}]=0.5 \text{ M}$ (Fig. 5.16-A), similar to the T1 lifetime of $\sim 250 \text{ fs}$ measured by the TR-SFG and 2D-SFG experiments reported in the literature for the air-water interface [265, 266, 225].

When more basic conditions of the silica-water interfaces are concerned, the BIL is not solely responsible anymore for the relaxation T1 times measured by TR-SFG, which are now averages over the distinct BIL/DL relaxation processes. Making use of the deconvolution scheme to separate BIL/DL contributions conceived in our group [49] (see ref.[243] reported at the end of this section for all details), we have shown that TR-SFG spectroscopy solely probes the relaxation T1 time of bulk-like water in the DL at $\text{pH}=12$ conditions in the $0.0\text{-}0.5 \text{ M}$ ions concentration range. At such conditions the preferential adsorption of cations in the BIL, due to the negative surface charge, has been found to be not sufficient to screen the DL contribution to SFG, and the fast $T1\approx 200 \text{ fs}$ relaxation time of DL-water is systematically measured. On the contrary, 0.1 M of NaCl has been found sufficient to completely screen the DL contribution to SFG at $\text{pH}=6$ conditions, with consequent increase of the measured T1 time from 188 fs for 0 M NaCl (when DL dominates the SFG signal) to 633 fs for 0.1 M NaCl (when only the BIL is probed). At higher ionic concentrations, the T1 time has been finally shown to decrease again down to 363 fs , due to the same water-water in-plane ordering by ions as the one revealed at $\text{pH}=2$ conditions.

More details on the impact of KCl and NaCl electrolytes at the 4.5 SiOH/nm^2 amorphous silica-water interface at various pH conditions, and on the ions effect inducing ”horizontal ordering” of water in the BIL can be found in the work reported hereafter [243].

Ions Tune Interfacial Water Structure and Modulate Hydrophobic Interactions at Silica Surfaces

Aashish Tuladhar,^{||} Shalaka Dewan,^{||} Simone Pezzotti,^{||} Flavio Siro Brigiano, Fabrizio Creazzo, Marie-Pierre Gaigeot,^{*} and Eric Borguet^{*}

Cite This: *J. Am. Chem. Soc.* 2020, 142, 6991–7000

Read Online

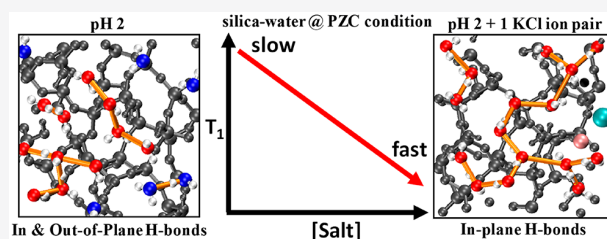
ACCESS |

Metrics & More

Article Recommendations

Supporting Information

ABSTRACT: The structure and ultrafast dynamics of the electric double layer (EDL) are central to chemical reactivity and physical properties at solid/aqueous interfaces. While the Gouy–Chapman–Stern model is widely used to describe EDLs, it is solely based on the macroscopic electrostatic attraction of electrolytes for the charged surfaces. Structure and dynamics in the Stern layer are, however, more complex because of competing effects due to the localized surface charge distribution, surface–solvent–ion correlations, and the interfacial hydrogen bonding environment. Here, we report combined time-resolved vibrational sum frequency generation (TR-vSFG) spectroscopy with ab initio DFT-based molecular dynamics simulations (AIMD/DFT-MD) to get direct access to the molecular-level understanding of how ions change the structure and dynamics of the EDL. We show that innersphere adsorbed ions tune the hydrophobicity of the silica–aqueous interface by shifting the structural makeup in the Stern layer from dominant water–surface interactions to water–water interactions. This drives an initially inhomogeneous interfacial water coordination landscape observed at the neat interface toward a homogeneous, highly interconnected in-plane 2D hydrogen bonding (2D-HB) network at the ionic interface, reminiscent of the canonical, hydrophobic air–water interface. This ion-induced transformation results in a characteristic decrease of the vibrational lifetime (T_1) of excited interfacial O–H stretching modes from $T_1 \sim 600$ fs to $T_1 \sim 250$ fs. Hence, we propose that the T_1 determined by TR-vSFG in combination with DFT-MD simulations can be widely used for a quantitative spectroscopic probe of the ion kosmotropic/chaotropic effect at aqueous interfaces as well as of the ion-induced surface hydrophobicity.



INTRODUCTION

Water is critical to sustaining life on Earth, and knowledge about its chemistry and physics is central to a vast range of subjects.^{1–11} However, the organization of water in inhomogeneous environments remains controversial, owing to water’s many anomalous properties.¹² A simple question such as how far away ions can affect the physical and the chemical properties of water is still rigorously debated.^{13–20} To make matters worse, understanding the behavior of water and solvated ions at an interface is an even more arduous task. Intuitively, it is fairly obvious that when ions approach an interface, they screen the surface charge (if present) and also (most likely) reorganize the interfacial environment by restructuring the original surface–solvent and solvent–solvent interactions since competing ion–solvent, ion–surface, and ion–ion interactions are introduced. Therefore, a quantitative and molecular-level understanding of these interactions is essential to understand and predict ion activity at interfaces and their influence on chemical reactivity.

The mineral oxide–electrolyte aqueous interface provides an excellent platform to investigate surface–ion–solvent interactions as a function of surface charge by manipulating the pH

of the bulk aqueous solution across the point of zero charge (PZC) of the mineral, hence tuning the electrostatic attraction between the surface and the ions. The silica–water interface represents the most widely studied mineral–aqueous interface. Therefore, many spectroscopic and imaging techniques have been used extensively to study the electric double layer (EDL) at the silica–electrolyte interface.^{21–26} The EDL can be broadly subdivided into a Stern layer located within the first one/two aqueous monolayers from the solid surface where ions accumulate, followed by a diffuse layer consisting of solvated ions that screen the remaining surface charge.^{27,28} While the energetics of the diffuse layer is reasonably well approximated by the Gouy–Chapman (GC) model, the understanding of the Stern layer is still limited. This is largely because the structure and dynamics of the Stern layer are

Received: December 10, 2019

Published: April 1, 2020



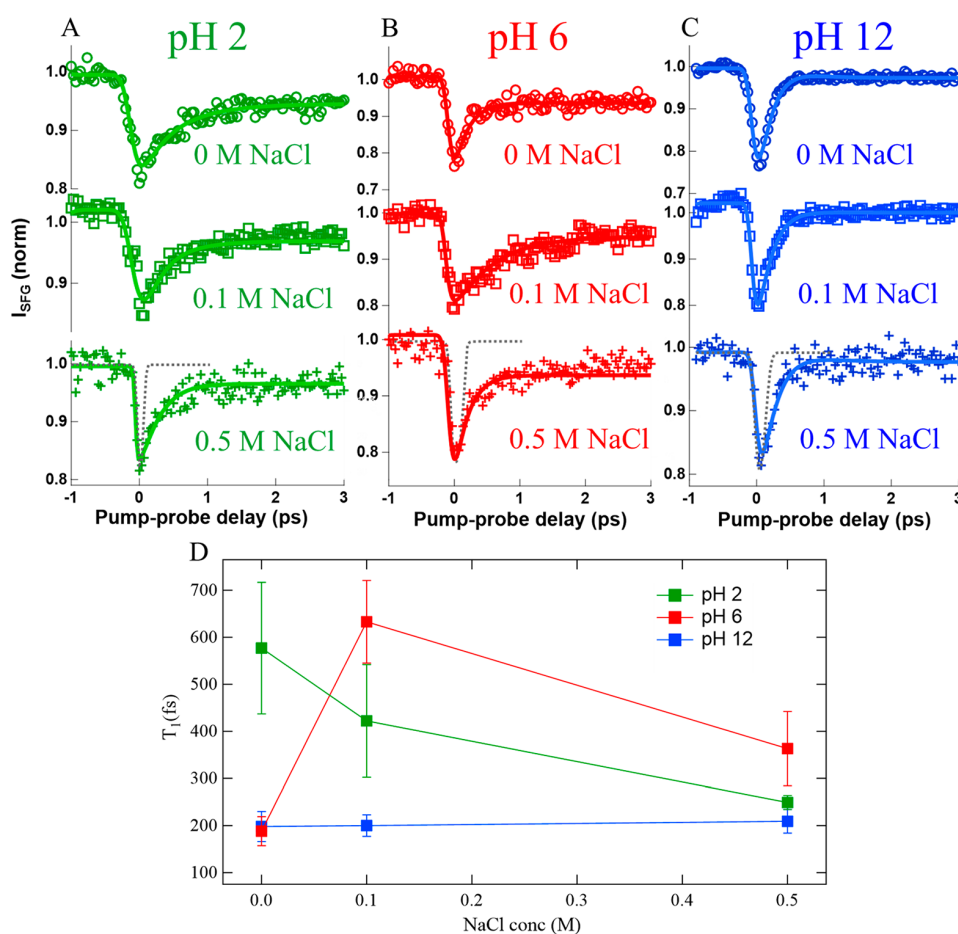


Figure 1. Effect of ions on the vibrational dynamics of the O–H stretch in H_2O at the silica–water interface at (A) pH 2, (B) pH 6, and (C) pH 12. The gray dotted line represents the cross-correlation of the IR pump, IR probe, and visible pulses, i.e., the instrument response function, indicating a fwhm of ~ 120 fs. The solid lines are the best fits with a four-level system, described in the Supporting Information. (D) T_1 (O–H vibrational lifetime) vs NaCl concentration. The T_1 values reported are the average T_1 from separate measurements repeated at least 3 times, and in some cases up to 5 times. The error bars indicate the standard deviation for all the individual T_1 values obtained on different days.

directly sensitive to the competing effects of the surface charge distribution, surface–solvent–ion correlations, and the interfacial hydrogen bonding environment, which are all extremely difficult to probe experimentally. Hence, the detailed understanding of these interfacial properties is not accounted for in the most commonly used Stern–Gouy–Chapman (SGC) model. Therefore, experimental tools that can provide quantitative and molecular understanding of the EDL are key to the development of more sophisticated models that can accurately describe its structure, composition, and energetics.

Vibrational sum frequency generation (vSFG) spectroscopy, a laser-based second-order nonlinear optical technique, has played a key role in the last few decades in advancing our understanding of the EDL structure at the silica–electrolyte interface.^{21,22,24,29–33} In a typical vSFG experiment, an infrared (IR) laser beam which is in resonance with a molecular vibration is temporally and spatially overlapped with a visible laser at an interface of interest, resulting in the generation of sum frequency (SF) photons whose frequency is the sum of the IR and visible frequencies. Within the dipole approximation, only noncentrosymmetric molecules and environments generate a vSFG signal. Centrosymmetry is inherently broken at any interface between two bulk media, thus making vSFG spectroscopy an exclusive probe of molecular vibrations

at the interface and hence an ideal tool for probing the EDL. Moreover, vSFG can be employed in both the frequency domain (steady-state (SS) vSFG) and the time-domain (time-resolved (TR) vSFG) to extract structural and dynamics information on the EDL. Despite a plethora of investigations of the silica–electrolyte interface using SS-vSFG^{31,34–40} and TR-vSFG,^{21,22,41,42} a complete molecular picture of the silica–electrolyte EDL is still lacking. This mainly stems from two critical shortcomings in past vSFG studies.

The first issue is due to the ambiguity of the probing depth of vSFG at charged interfaces (the silica–water interface is habitually charged except at its PZC, around pH 2–4) where the surface electric field can break the centrosymmetry of bulklike water residing further than the first few interfacial layers and hence contributing to, or even dominating, the vSFG signal. This has greatly complicated the interpretation of vSFG studies of silica–water interfaces and has impeded a definitive rationalization of the structure and dynamics of the EDL, since it is unclear which populations (interfacial water or electric field-oriented bulklike water) are probed. However, recent experimental⁴³ and computational⁴⁴ studies have developed methodologies to separate vSFG spectra into contributions originating from the first few layers [binding interfacial layer (BIL)] and from the electric field oriented

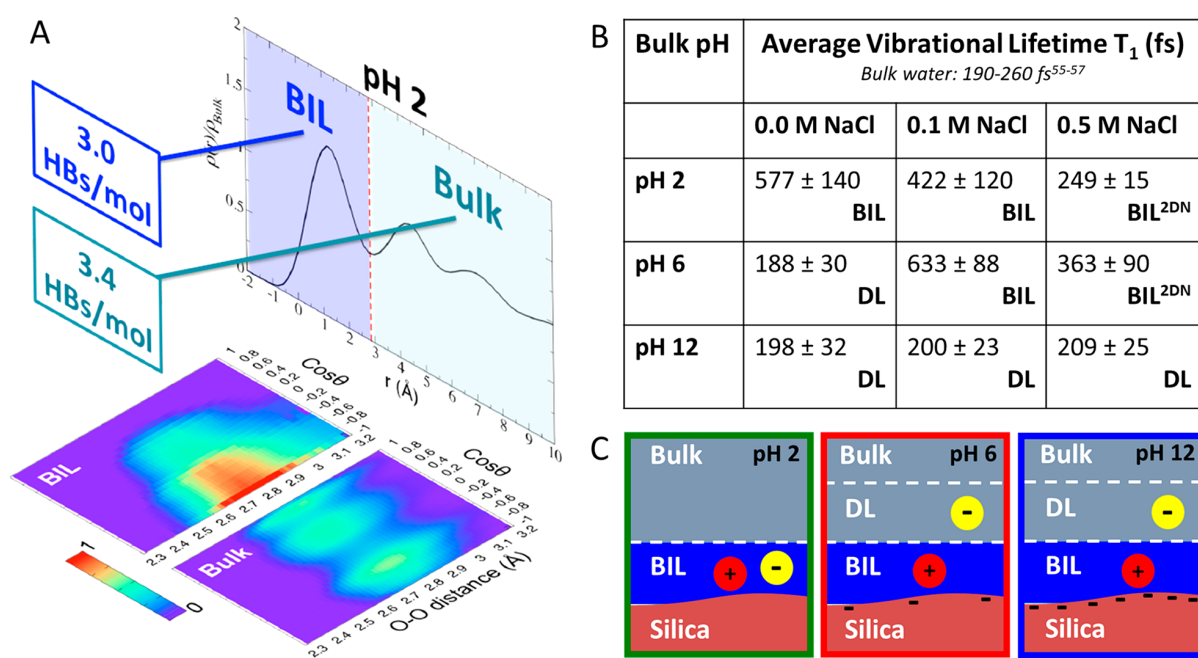


Figure 2. (A) Three descriptors used for characterizing and determining water BIL/DL/Bulk layers at the neat silica–water interface at pH 2. They are (see refs 44, 54, and 55) the water density profile with respect to the distance from the surface (r), the average water coordination (HBs/molecule), and the 3D-plots evaluating the probability for water–water HBs formed in each layer with a given HB (O–O) distance and orientation with respect to the normal to the surface (red regions correspond to the maximum probability to find water with preferential HB distances and orientations; see Section S6 in the SI for details). See all details in Section S5 of the SI. (B) Average vibrational lifetime T_1 at different bulk pH and NaCl concentrations, obtained from 4 level model fits (described in the SI) to TR-vSFG traces. The error bars indicate the standard deviation for all the individual T_1 values obtained on different days. The labels “BIL” (binding interfacial layer), “BIL^{2DN}” (2DN stands for the 2D–H bond-network formed by the BIL water), and “DL” (diffuse layer) refer to the interfacial region that dominates the vSFG response in each aqueous environment, as described in the text. (C) Schemes of the structural organization of water and ions at the 1 M electrolytic amorphous silica–water interface (pH = 2, 6, 12) extracted from the AIMD/DFT-MD simulations. Red/yellow balls with +/- signs represent the cations/anions and their distribution at the interface (BIL vs DL).

bulklike contribution [diffuse layer (DL)]. The BIL water region is analogous to the Stern layer in the double layer theory from the aspect of the spatial distribution of the ions.⁴³ Only recently, this methodology has been applied to vSFG studies of the fused silica–aqueous interface revealing important insight on its chemical and physical properties (for example, microscopic hydrophobicity).^{29,74}

The second shortcoming stems from the lack of understanding of how the presence of ions affects the vSFG signal. Historically, the ion associated attenuation of the vSFG signal at the silica–aqueous interface has been assigned to the Debye screening effect (as predicted by GC theory); i.e., ions reduce the thickness of the non-centrosymmetric diffuse layer probed by vSFG. It is also obvious that ions can rearrange the interfacial hydrogen-bonding environment due to ion–solvent and ion–surface interactions. However, it is unclear how ion-induced screening and ion-induced solvent rearrangement affect the vSFG signal. The need to look beyond the GC/SGC models to understand the silica–electrolyte EDL, in order to disclose the more complex molecular-level rearrangements occurring in the BIL, is the missing ingredient for the development of next-generation models describing ion activity at interfaces. The need for such development was, for instance, recently pointed out in nonlinear spectroscopy studies by Borguet et al.,³⁵ Gibbs et al.,²⁵ and Geiger et al.²³ where they provided evidence for highly pH-dependent specific ion effects, whose understanding is beyond the GC/SGC models. Here, we report a joint effort, combining time-resolved vibrational

sum frequency generation (TR-vSFG) spectroscopy with ab initio DFT-based molecular dynamics simulations (AIMD/DFT-MD), to reveal novel molecular details on how ions change the interfacial water structure in the BIL and consequently affect its ultrafast vibrational dynamics. TR-vSFG spectroscopy, measuring the vibrational relaxation time-scale of the O–H stretching vibrations, provides an excellent quantifiable probe of the hydrogen bonding environments of the silica–electrolyte EDL, allowing us to experimentally detect ion-induced changes in the BIL, which may otherwise be too subtle or nonexistent in the SS-vSFG signal.^{24,35} Complementarily, DFT-MD simulations provide a detailed understanding of the microscopic mechanism(s) resulting in the ion-induced effects on the TR-vSFG measurements. Our results clearly show that the GC/SGC models are insufficient in describing the ion activity at silica surfaces, and the molecular insights provided by this study could be significant in the development of more accurate and sophisticated EDL models that would account for the interface specific chemistry, surface charge and ion distribution, and the resulting hydrogen bonding environment.

RESULTS AND DISCUSSION

Time-Resolved Sum Frequency Generation. The vibrational dynamics of the silica–water interface, measured using TR-vSFG spectroscopy (experimental and sample preparation details are provided in the SI), is clearly a function of both bulk pH and ionic strength (Figures 1 and 2B). More

precisely, the water OH stretch T_1 lifetime is found to strongly depend on the ion concentration at pH 2 and 6, while a constant T_1 of ~ 200 fs is observed for pH 12 in the 0–0.5 M NaCl range. At pH ~ 12 , the silica surface is dehydroxylated by $\sim 25\%$,⁴⁵ inducing a rather high surface charge density of ~ -0.2 C/m², thus resulting in a surface potential of ~ 170 mV, as calculated using the silica deprotonation ratio and the GC model (described in Section S3 of the SI, see also Figures S4 and S5). There is therefore a strong water DL impact to vSFG due to the surface field-oriented bulklike water (see, e.g., refs 21, 22, 44, 46, and 47). Both the BIL and the DL impact the vSFG response, and their relative weighted contributions to the final TR-vSFG measurements can be qualitatively estimated from the surface potential by using the framework described hereafter. See Section S5 in the SI for the BIL/DL definition. The vSFG signal in the DL is due to the potential drop across the DL ($\Delta\varphi_{\text{DL}}$, assumed here as equal to the surface potential; see Table S2 for a comparison with other choices) through $\chi_{\text{DL}}^{(2)}(\omega) = \chi_{\text{bulk}}^{(3)}(\omega) \Delta\varphi_{\text{DL}}$,^{43,44,46} where $\chi_{\text{bulk}}^{(3)}(\omega)$ is the third-order susceptibility of bulk liquid water (this expression is here written without interference contributions^{48,49} which are only important at low ionic strength and hence trivial at pH 12 which has an ionic strength of 10 mM). $\chi_{\text{bulk}}^{(3)}(\omega)$ is known.^{43,44} In the present experiments, $|\chi_{\text{DL}}^{(2)}(\omega)|^2$ signals are measured to deduce T_1 relaxation times; thus, $|\chi_{\text{DL}}^{(2)}(\omega)|^2 = |\chi_{\text{bulk}}^{(3)}(\omega)|^2 (\Delta\varphi_{\text{DL}})^2$. Defining I_{BIL} and I_{DL} as the integral of $\chi_{\text{BIL}}^{(2)}(\omega)$ and $\chi_{\text{DL}}^{(2)}(\omega)$ in the O–H stretching region, one finds that $I_{\text{DL}}/I_{\text{BIL}} \propto (\Delta\varphi_{\text{DL}})^2$, i.e., the ratio of DL/BIL intensities, is proportional to the square of the surface potential. According to previous works on silica–water interfaces,^{44,46} values of $I_{\text{DL}}/I_{\text{BIL}} \sim 10$ were found for $\Delta\varphi_{\text{DL}} \sim 10$ mV. Taking $\Delta\varphi_{\text{DL}} \sim 10$ mV as the reference ($(\Delta\varphi_{\text{DL}}(\text{ref}))$), we can estimate the $I_{\text{DL}}/I_{\text{BIL}}$ ratio at any other $\Delta\varphi_{\text{DL}}$ value as $I_{\text{DL}}/I_{\text{BIL}}(\Delta\varphi_{\text{DL}}) = I_{\text{DL}}/I_{\text{BIL}}(\Delta\varphi_{\text{DL}}(\text{ref})) \times (\Delta\varphi_{\text{DL}}/(\Delta\varphi_{\text{DL}}(\text{ref})))^2 = 10(\Delta\varphi_{\text{DL}}/10 \text{ mV})^2$. See Sections S9 and S10 for more details. Therefore, $I_{\text{DL}}/I_{\text{BIL}} \sim 2960$ is expected here for $\Delta\varphi_{\text{DL}} \sim 172$ mV at pH ~ 12 (see Table S2). The vSFG response at the neat pH ~ 12 silica–water interface is consequently dominated by the water in the DL, i.e., by bulklike oriented liquid, and indeed one measures $T_1 = 198 \pm 32$ fs (Figures 1 and 2B), typical of the 190–260 fs^{50–52} relaxation measured in bulk liquid water. When adding 0.1 and 0.5 M salt, the surface potential is reduced but is still of the order ~ 100 mV (see Table S2), thus giving rise to the same DL-dominated fast interfacial relaxation. These results suggest that higher concentrations than 0.5 M are needed to screen the silica surface potential and hence suppress the DL contribution to vSFG at pH ~ 12 . This is indeed the conclusion of the recent vSFG measurements by Tahara's group,⁴⁰ where 2 M NaCl is needed to measure only the BIL contribution at pH 12.

When lowering the pH to 6, the silica surface is now only $\sim 1\%$ dehydroxylated.⁴⁵ A smaller surface potential (~ 80 mV) is hence created, and in the absence of additional ions, $\Delta\varphi_{\text{DL}} \sim 80$ mV (Figure S5 in the SI). Correcting for interference effects, which now need to be considered for the neat pH 6 condition (where the ionic strength is 10^{-6}), an $I_{\text{DL}}/I_{\text{BIL}}$ ratio of 26 is obtained (see Sections S9 and S10 and Table S2 in the SI), still large enough to conclude that the measured relaxation time is dominated by the DL contribution. Consistently, we measure $T_1 = 188 \pm 30$ fs (Figures 1 and 2B), similar to pH 12 conditions. A recent study from Hore-Tyrodé³² reported a surface potential of ~ 200 mV for the same neat pH 6

conditions (i.e., no excess salt). Taking this larger surface potential value leads to an even larger $I_{\text{DL}}/I_{\text{BIL}}$ ratio, making our conclusion on dominant DL contributions even stronger.

Adding 0.1 or 0.5 M salt at pH ~ 6 results in an accumulation of cations at the negatively charged surface, hence reducing the surface potential by more than 1 order of magnitude (Figure S5 and Table S2, SI). We note here that addition of ions is known to increase the percentage of deprotonated sites.^{32,45,53} Despite the increase in deprotonation, the surface potential is lower than in the case of no salt (Figure S5B), as shown in a recent study.³² This is possibly due to the counterion screening the surface potential by directly interacting with the deprotonated SiO^- sites, as shown by a previous study.⁵³ Moreover, the surface potential is observed to decay exponentially away from the surface when salt is present (Figure S5) so that it is only 4 and 1 mV at 1 nm away from surface for 0.1 and 0.5 M NaCl, respectively. Due to the lower surface potential and rapid decay (see Figure S5 and Table S2 in the SI), the DL contribution to the vSFG signal is largely suppressed at pH 6 when salt is added.

In agreement with these estimates, we find that the presence of 0.1 M NaCl initially slows down T_1 to 633 fs, which is similar to the T_1 at neat pH 2. This means that the 0.1 M NaCl at pH 6 is mainly only responsible for screening surface charge, hence excluding the DL water contribution to T_1 lifetime, as one would expect from the GC model and consistent with a previous study.²² However, when the salt concentration is further increased to 0.5 M, T_1 becomes faster (363 fs), deviating from the behavior expected from GC theory. Since the surface potential is very low at pH 6 with 0.5 M [NaCl], the T_1 decrease has to arise from ion-induced changes in the BIL.

In analogy with the findings at pH 6, a similar BIL-specific effect is also observed for pH 2, point of zero charge (PZC) conditions, where the measured T_1 lifetimes (Figures 1 and 2B) show that the vibrational relaxation of water is accelerated by increasing the bulk ionic concentration. In the absence of salt, the surface potential is close to zero (Figure S5A and Table S2, SI) and we can consequently assume that the silica surface is neutral and that the vSFG probing depth and the T_1 lifetimes reflect the water structure in the BIL alone. When ions are introduced, the T_1 lifetime decreases from 577 fs for the neat interface to 422 fs for 0.1 M [NaCl] and to 249 fs for 0.5 M [NaCl], while the surface potential remains close to zero (Figure S5 and Table S2, SI). The BIL is thus expected to be solely responsible for the measured T_1 lifetime in the entire investigated concentration range at pH = 2, meaning that there is no preferential adsorption of cations over anions or vice versa, and both ionic species have the same probability to populate the BIL layer.

Here, it is important to consider the possibility of cations preferentially accumulating at the neutral silica surface compared to anions (as is known to occur at higher pH values, above PZC), resulting in a slightly positive surface so that the vSFG probes DL (“bulklike”) water via the $\chi^{(3)}$ effect and causing an acceleration of the T_1 . However, this scenario would manifest in a large DL-water contribution to the total SS-vSFG spectra. This was indeed reported in a recent vSFG study²⁴ which showed a significant increase in the vSFG signal at pH 2 when the NaCl concentration was raised from 10 to 100 mM, which was interpreted as an overcharging effect. However, the overcharging effect was mostly apparent for the ssp-vSFG signal and not for the ppp-vSFG signal. We use the

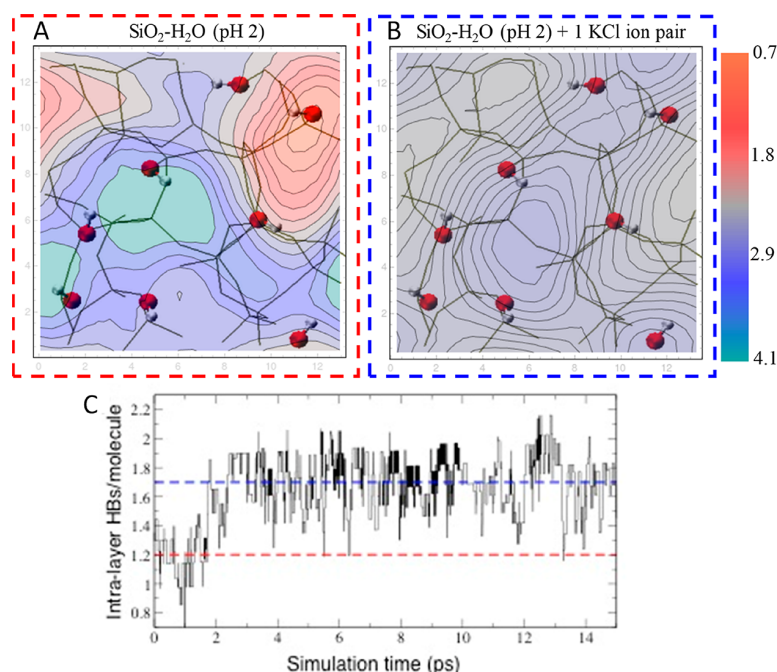


Figure 3. AIMD/DFT-MD simulations of the amorphous silica–water interface at pH \sim 2. Time-averaged coordination number of the water molecules in the BIL spatially resolved along the lateral x – y directions of the silica surface (in Å) for (A) neat aqueous silica interface and (B) aqueous silica interface with one KCl ion pair in the BIL. The water coordination is expressed in terms of the number of HBs (sum of water–water and water–silanol HBs) per water molecule (see Section S6 in the SI for details). The color coding (vertical scale in the plots) goes from light red (0.7 HBs/molecule), dark red (1.8 HBs/molecule), grayish-blue (2.9 HBs/molecule) to greenish-blue (4.1 HBs/molecule). The top view of the interface shows the solid Si–O covalent bonds in gray lines to highlight the solid surface covalent patterns. The surface silanols are marked by the O–H groups in red (O) and white (H) spheres. (C) Time-evolution of the number of intra-BIL HBs formed per water molecule located within the BIL. $t = 0$ is the time when a KCl ion-pair is introduced in the BIL. The red and blue dashed lines indicate the average number of intra-BIL HBs per water molecule for the neat interface (red, 1.2) and for the KCl electrolyte interface (blue, 1.7), respectively.

latter polarization combination in this study. Also, hysteresis has been reported when pH is varied at constant ionic strength, which is how the above-mentioned study was conducted. In our study, we vary the ionic strength at constant pH which avoids the hysteresis issue. We see no significant increase in SS-vSFG signal at pH 2 when NaCl concentration is increased (Figure S6), which is consistent with other past studies of silica–water interfaces at pH \sim 2 conditions³⁵ as well as with the estimated surface potential values (Figure S5A). On the contrary, we notice a small decrease in ppp-vSFG intensity with salt addition, which could also be in principle attributed to the screening effect of the electrolyte (by hypothesizing that a small net surface charge persists at pH 2). However, we also see an acceleration of T_1 when 0.1 M salt is added. Thus, the decrease in ppp-vSFG intensity cannot be entirely due to the screening effect. As we will show later, such a decrease can be explained when the ion-induced changes in the BIL water structure are considered.

In the light of all the above-discussed evidence, the accelerations of T_1 lifetimes at pH \sim 2 conditions and pH 6 with [NaCl] = 0.1–0.5 M are ascribed to ion inducing order and more interconnectivity within the structure of the BIL water, i.e., a kosmotropic effect. A deep understanding of the associated microscopic mechanism, which goes beyond pure electrostatic effects and is almost entirely driven by specific ion-induced changes in water–water and water–surface interactions, is pivotal in order to improve our comprehension and modeling of electrolytic interfaces. We hence now make use of DFT-MD simulations to address this challenge.

DFT Molecular Dynamics. A DFT-MD simulation of the aqueous amorphous silica surface (4.5 SiOH/nm², representative of the silica surfaces in experiments) at pH 2 was performed (see Section S5 in the SI for all computational details). In agreement with the experimental results, the simulation shows that when the surface is neutral (pH \sim 2), only the water in the BIL is noncentrosymmetric and hence vSFG-active. This is summarized in Figure 2A, where water in the BIL is shown to be denser than in the bulk, forming fewer water–water HBs, and with a noncentrosymmetric orientation, while bulklike water coordination, orientation, and density are recovered right beyond the BIL, i.e., further than 3.0 Å from the SiO₂ surface (see also Section S6 of the SI). The absence of a DL confirms that the aqueous silica interface is at the isoelectric point at pH \sim 2.

What the DFT-MD simulation also reveals is that the inhomogeneous spatial distribution of silanols at the amorphous silica surface results in a nonuniform spatial distribution of the coordination number of the water molecules in the BIL (Figure 3A, where the time averaged spatial distribution of the coordination number of water in the BIL is shown in a contour-map). Water coordination results from the sum of water–water and water–silanol HBs, where a standard HB definition is applied (O–O distance <3.2 Å and O(–H)–O angle in 140–220° interval).⁵⁴ If, on average, water is 3-fold coordinated in the BIL, this number is in fact due to two distinct populations: 60% of the water molecules in the BIL are tetrahedrally coordinated (HB/mol \geq 3.1, blue zones in Figure 3A), while the other 40% are undercoordinated (HB/mol <2.2,

red zones). These two water populations are located above silica areas made of high (bottom half of Figure 3A and B) and low (top half of Figure 3A and B) silanol densities, respectively, which we have recently identified as hydrophilic/hydrophobic patches on the macroscopically hydrophilic silica surface.^{29,56}

To reveal how ions affect the BIL water structure and dynamics, eight additional DFT-MD simulations have been performed in the presence of a KCl ion-pair. In AIMD simulations, the Na⁺ cation is known to require much larger plane wave basis sets for its accurate electronic representation than K⁺, hence considerably increasing the computational cost of the AIMD, and, thus, the choice of K⁺ in the present simulations. The results obtained with KCl have been then confirmed with one supplementary MD simulation where one NaCl ion-pair is accommodated at the silica–water interface (see Section S8 in the SI). The similarity between Na⁺/K⁺ behaviors found in the present work is consistent with a previous study.⁵⁷ As already discussed, since the silica surface is at the isoelectric point at pH \sim 2, and no static field is generated by the neutral surface, there is no surface electrostatic driving force to favor cations over anions (and vice versa) to approach closer to the silica surface. Starting from this knowledge, nine distinct initial ion configurations have been prepared for the MD simulations, where both K⁺/Na⁺ and Cl[−] ions were randomly located within the BIL layer (see Sections S4 and S8 of the SI).

We make the choice to discuss hereafter the results from one representative DFT-MD simulation, the results of which have been validated by all the other simulations (the total of nine simulations amounts to 150 ps time-scale), revealing that our findings are independent of the average position and configuration (i.e., contact ion-pair CIP, solvent shared ion-pair SSIP) that ions have in the BIL, as well as on the K⁺/Na⁺ nature of the cation (all detailed in Section S8 of the SI).

The resulting picture obtained from the DFT-MD simulations is the following. The presence of the electrolyte in the BIL leads to the BIL water becoming homogeneously 3-fold coordinated (Figure 3B); i.e., there is one single water population (91% of the water in the BIL), highly interconnected by H-bonds formed within the layer (1.7 intra-BIL HBs on average). This striking change in the water structural organization in the BIL from the neat to the electrolytic SiO₂–water interface is due to two combined factors: by approaching the silica surface, the ions are able to complete their solvation shell with surface silanols on top of BIL water molecules (i.e., ions adsorbed in innerspheres, see Figure 4C), as already shown at the crystalline quartz–water⁵⁸ and alumina–water⁵⁹ interfaces, thereby breaking local water–surface H-bonds that were previously present at the neat aqueous silica interface. Innersphere ions hence locally drive the breaking of water–surface interactions which is characteristic of the hydrophobic patches at the silica surface.^{29,56} They consequently increase the portion of the surface assigned to the hydrophobic domain. Above these ion-induced hydrophobic domains, water adapts to this change by maximizing H-bonds in between interfacial water molecules (intra-BIL HBs), hence increasing the water–water H-bond connectivity within the BIL. As a result of such an ion-catalyzed shift in the balance between water–water and water–surface interactions toward the former, a highly ordered water–water HB-network with HBs parallel to the silica surface plane is formed in the whole BIL, reminiscent of the 2D-HB-network recently revealed at

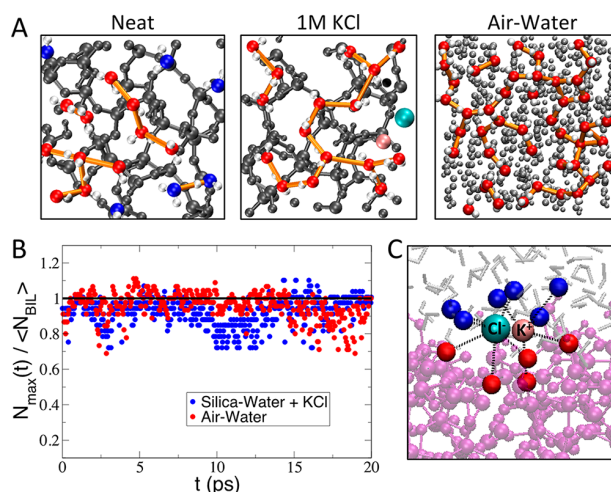


Figure 4. (A) Top views of the BIL water structural arrangement at the neat silica–water (left), the silica–water interface with one KCl ion pair in the BIL (middle), and the canonical hydrophobic air–water interface (right) used here as a reference for the highly interconnected H-bond network (2D-HB-network) formed by the water in the BIL.^{54,55} The silica surface atoms are black balls (left and middle), while the gray balls in the right-hand figure are the water in the bulk liquid. The water molecules in the BIL are color-coded according to their coordination number, i.e., blue if ≤ 2.2 HBs/mol, red if > 2.2 HBs/mol. In the absence of ions, water molecules with lower coordination number (blue) and with higher coordination number (red) are present, connected only by few H-bonds (orange). When KCl is added, blue water molecules disappear, and only red water molecules remain, resembling the canonical air–water interface. The increase in the number of orange connections between BIL water molecules from the neat to the electrolytic interface illustrates how ions increase in-plane H bonding within the BIL. (B) Evolution with time of the number of water molecules (N_{\max}) that are interconnected by intra-BIL HBs into one single 2D-HB-network, normalized by the average number of water in the BIL ($\langle N_{\text{BIL}} \rangle$). Red, reference air–water interface; blue, silica–water + KCl interface. A similar plot is not reported for the neat silica–water interface, as the 2D-HB-network does not exist at that interface. (C) Innersphere adsorption of the KCl ion-pair at the SiO₂–water interface. The ions use silanols (red balls for the oxygens) and water in the BIL (blue balls for the oxygens) in order to achieve an innersphere adsorption.

the canonical hydrophobic air–water interface,⁵⁴ where 1.7 intra-BIL HBs are also found on average.^{55,60} The time-evolution for the formation of the 2D-HB-network at the silica–water interface (Figure 3C) reveals that the number of intra-BIL HB/molecule increases in a few picoseconds, from 1.2 (neat interface, start of the dynamics) to 1.7, by adding one KCl ion-pair in the BIL.

The electrolyte-induced increase in water interconnectivity is further illustrated in Figure 4A where top views of the BIL water molecules (20 on average in these simulation boxes) of the neat SiO₂–water (left), the SiO₂–water+KCl (middle), and the air–water interface (right; taken from refs 54 and 55; be aware of the larger simulation box) are compared. One can immediately observe the 60%/40% ratio between the two water populations discussed above at the neat solution interface (Figure 4A, left), with the isolated blue-waters above the hydrophobic patches (which are too small for water to form a 2D-HB-network) on one hand and the locally interconnected, tetrahedral red-waters above the hydrophilic patches on the other hand. Once the electrolytes are present in

the BIL (pink/green balls in Figure 4A, middle), one immediately observes the disappearance of the blue-undercoordinated water molecules, and the increased HB interconnectivity in between the red-water molecules, now 3-fold coordinated and extended over the whole silica surface. This is similar to the HB interconnectivity at the air–water interface^{54,55} (Figure 4A, right).

To understand the time-dependent behavior of the HB network of the KCl–silica–water interface with respect to the air–water, we further compare in Figure 4B the time-evolution of the 2D-HB-network size (N_{\max}), normalized by the average number of BIL water molecules ($\langle N_{\text{BIL}} \rangle$) ($\langle N_{\text{BIL}} \rangle = 45$ and 20, respectively, at the air–water and silica–water interfaces). One can see that the two interfaces behave similarly over time, with the normalized 2D-HB-network size steadily varying between 0.8 and 1.0 during the whole simulation.

We can hence conclude that innersphere adsorbed ions alter the water organization in the BIL by shifting the balance from dominant water–surface interactions (“out-of-plane ordering”) to in-plane water–water interactions (“in-plane ordering”). Our molecular picture is consistent with previous theoretical studies^{61–63} showing that adsorbed ions can reorder the interfacial H-bonding network at the quartz (101)–water interface by promoting the formation of intrasurface H-bonds and disrupting the surface water H-bonds. This drives an inhomogeneous interfacial water coordination landscape toward a homogeneous, highly interconnected in-plane 2D hydrogen bonding network, reminiscent of the canonical, hydrophobic air–water interface.

Connecting TR-vSFG and AIMD. We now make use of the structural knowledge obtained from the simulations to provide a rationalization for the T_1 lifetime acceleration upon ion addition at pH 2. The MD simulations demonstrated that there is no DL contribution to the vSFG at the fully hydroxylated (pH 2) silica–water interface and hence confirmed that the acceleration of interfacial relaxation dynamics can only be due to the ion-induced changes in the BIL structure, which in turn alter the intermolecular coupling and affect the BIL dynamics. In more details, we have seen that ions change both water–water interactions and SiOH–water interactions. The question remains as to which is responsible for the experimentally measured changes in T_1 . The SiOH vibrations are expected to exhibit slower relaxation dynamics than OH vibrations of water as the former do not have access to Fermi resonance coupling (which is known to be a major OH vibrational relaxation pathway^{51,64–68}) into its SiOH bend overtone due to the large energy mismatch. The SiOH bend mode is at ~ 800 cm^{-1} , and thus, its overtone is at ~ 1600 cm^{-1} , which is far away from the SiOH stretch vibrational modes (>3000 cm^{-1}).⁵⁶ This is consistent with time-resolved measurements done in the 1980s by Cavanagh et al.⁶⁹ which determined the vibrational lifetime for hydroxyls at the silica–vacuum interface as ~ 200 ps, which decreased to ~ 56 ps in the presence of significant amounts of physisorbed water (5 $\text{H}_2\text{O}/100$ \AA^2). In our study, the silica hydroxyls are H-bonded to adjacent water and thus are expected to have a shorter vibrational lifetime than ~ 200 ps, but it is highly unlikely to be anywhere close to the 100s of femtosecond time-scales we measure. Moreover, SiOH–water couplings are weakened by increasing ion concentration due to ion breaking of water–surface HBs (as discussed before). This would reasonably provoke a slowdown in the SiOH relaxation due to reduced connections to the aqueous environment. In light of all of this,

SiOH group dynamics would explain an increase in T_1 , not a decrease (as observed experimentally). Based on this, we can argue that the SiOH–water coupling contribution to the overall relaxation within the BIL is much less important than the one from water–water couplings. This is consistent with the fact that water molecules in the BIL are much more abundant than surface silanols (from MD simulations, we calculate an average of 12.4 BIL waters/ nm^2 vs 4.5 SiOH/ nm^2), as well as with water providing the dominant contribution to the vSFG intensity of silica–water interfaces in the OH-stretching region. From integration of the theoretical vSFG spectra,^{29,47} we find that water contributes 76% of the imaginary $\chi^{(2)}$ vSFG spectra in the 3000–3800 cm^{-1} range, while surface SiOH groups only contribute 24% at frequencies <3300 cm^{-1} . This 24% value is further reduced to $\sim 6\%$ when considering that we are measuring the $|\chi^{(2)}|^2$ signal in this study.

What remain to be evaluated are the ion-induced water–water couplings within the BIL as the reason for the acceleration of T_1 at pH 2 (and 6) when ions are introduced. As mentioned above, Fermi resonance coupling is known to be a major OH vibrational relaxation pathway.^{51,64–68} Since the H_2O bend mode is at ~ 1650 cm^{-1} (and so its overtone is at ~ 3300 cm^{-1} , without accounting for anharmonicity), there is Fermi resonance coupling between the H_2O stretch vibrations and the H_2O bend. Therefore, an ion-induced increase in water–water interactions is expected to lead to efficient coupling thereby accelerating the vibrational energy transfer and causing a decrease in T_1 . Additional evidence comes from comparing the BIL water structure and T_1 lifetimes at the silica–water and the air–water interfaces. As discussed previously, the BIL structure at the air–water interface is dominated by water–water couplings resulting in a 2D-HB-network, and the T_1 for this hydrogen bonded water has been experimentally measured to be 200–300 fs.^{70–73} Similarly, ion-induced water–water coupling resulting in a 2D-HB-network is detected for the silica–water interface, and consequently, T_1 of 250 fs is also measured. This correlation between the BIL structure and the T_1 lifetime at two different interfaces supports our claim that ion-induced water–water coupling is responsible for the reduction of T_1 .

We further suggest that the acceleration of interfacial relaxation processes with increasing NaCl concentration is justified not only by the ion-induced increased HB-connectivity within the BIL (increased water–water couplings) but also by the net reduction in the number of “strongly undercoordinated” water molecules at the interface (blue water in Figure 4), which are expected to have the slowest relaxation due to the reduced connectivity with the environment.

In light of these findings, the slow T_1 lifetime ($T_1 = 577 \pm 140$ fs) measured for the neat interface at pH 2 conditions can be ascribed to the substantial density of undercoordinated water molecules (40%) and weak H-bond interconnectivity within the out-of-plane ordered BIL. The ion-induced in-plane ordering provokes the acceleration in the vibrational relaxation processes within the BIL, from $T_1 \sim 600$ fs, typical of the water out-of-plane ordering, to $T_1 \sim 250$ fs, typical of the water in-plane ordering, that is reminiscent of the fast vibrational relaxation measured for the air–water interface. The same microscopic mechanism revealed for pH 2 also rationalizes the acceleration of T_1 at pH 6 in the presence of high salt concentration. Such an acceleration at pH 6 has been observed previously²² and was hypothesized to be due to ion-induced

interfacial ordering, but in this study, we are able to provide, for the first time, a molecular mechanism that explains the T_1 acceleration at the silica–electrolyte interface. Even though we are mainly probing the BIL water at pH 2 and pH 6 (with salt), it is important to note that the absolute values of T_1 are not strictly identical (Figure 2B), presumably reflecting the structural variations of surface silanol groups at the two pH conditions, including the difference in the ionic species enrichment at the neutral vs charged silica surface (see the scheme in Figure 2).⁷⁵ Nevertheless, the ratio in the T_1 values at the two ionic concentrations is identical: water systematically relaxes 1.7 times faster at the higher 0.5 M ionic concentration due to the highly interconnected 2D-HB-network formed in the BIL.

Finally, the transition from out-of-plane to in-plane ordering of BIL water due to breaking of water–surface HBs (vSFG active since oriented along the normal to the surface) and consequent formation of intra-BIL water–water H-bonds (non-vSFG active due to the orientation parallel to the surface) also explains the microscopic origin of the previously discussed decrease (albeit small) of the SS-vSFG (ppp) signal when ions adsorb at the neutral silica–water interface.³⁵

CONCLUSIONS

In conclusion, the interplay between experimental vibrational dynamics measurements and the interfacial structural characterization by theory provides a compelling combination to reveal the ion adsorption process at silica–water interfaces and its effect on interfacial structure and dynamics, as a function of pH/electrolyte conditions. At highly and moderately charged silica–water interfaces (pH > 6), cations are preferentially adsorbed at the surface, and their major impact on the interfacial arrangement is screening the surface charge, as expected from GC theory. However, more subtle molecular changes in the BIL are hidden below the dominant DL contribution at these high pH conditions. As revealed by both experiments and simulations performed in this work, such changes manifest at low surface charges (pH < 6) and high ionic concentrations, and they cannot be rationalized by pure electrostatic models as they are driven by local chemistry associated with the ion adsorption processes.

We here show, for the first time, that the acceleration of interfacial vibrational energy relaxation is due to the kosmotropic effect of ions that drive in-plane ordering of water within the BIL, the topmost interfacial layer. This deeper understanding of such a phenomenon, which is beyond the existing GC/SGC theories, represents a key ingredient in the development of more accurate models for describing electrolytic interfaces. Ions such as KCl and NaCl are hence shown to be able to form innersphere complexes at the silica surface, even at low pH (i.e., around PZC) conditions. This requires breaking of previously existing water–surface HBs, thereby forming local “hydrophobic” areas on the silica surface, which adds to the already present hydrophobic patches (silanol poor areas) in the BIL. In such ion-induced hydrophobic domains, water rearranges by forming the extended 2D-HB-network, similar to the canonical air–water interface. TR-vSFG experiments, directly probing interfacial vibrational dynamics, are shown to be a powerful tool to reveal such BIL structural transitions, which is modulated by the delicate balance between water–surface and water–water interactions and is marked by the ion-induced acceleration of interfacial vibrational relaxation.

The methodology employed here for aqueous silica interfaces can be broadly applied to reveal the kosmotropic/chaotropic nature of ions at other aqueous interfaces: TR-vSFG experiments provide a direct measure of BIL water ordering/disordering, while DFT-MD simulations unveil the underlying microscopic mechanisms.

ASSOCIATED CONTENT

Supporting Information

The Supporting Information is available free of charge at <https://pubs.acs.org/doi/10.1021/jacs.9b13273>.

Experimental and theoretical methods, additional information on the experimental vSFG setup and sample preparation, the model used to describe vibrational dynamics of O–H in water, calculations of the surface electric potential at the silica–water interface, AIMD/DFT-based molecular dynamics simulations and their interpretation in terms of BIL (binding interfacial layer) and DL (diffuse layer), and the model used to separate BIL/DL contributions to TR-vSFG (PDF)

AUTHOR INFORMATION

Corresponding Authors

Marie-Pierre Gaigeot – LAMBE UMR8587, Université d'Evry val d'Essonne, CNRS, CEA, Université Paris-Saclay, 91025 Evry, France; orcid.org/0000-0002-3409-5824; Email: mgaigeot@univ-evry.fr

Eric Borguet – Department of Chemistry, Temple University, Philadelphia, Pennsylvania 19122, United States; orcid.org/0000-0003-0593-952X; Email: eborguet@temple.edu

Authors

Aashish Tuladhar – Physical Sciences Division, Physical & Computational Sciences Directorate, Pacific Northwest National Laboratory, Richland, Washington 99352, United States; Department of Chemistry, Temple University, Philadelphia, Pennsylvania 19122, United States; orcid.org/0000-0003-2449-4984

Shalaka Dewan – Department of Chemistry, Temple University, Philadelphia, Pennsylvania 19122, United States

Simone Pezzotti – LAMBE UMR8587, Université d'Evry val d'Essonne, CNRS, CEA, Université Paris-Saclay, 91025 Evry, France

Flavio Siro Brigiano – LAMBE UMR8587, Université d'Evry val d'Essonne, CNRS, CEA, Université Paris-Saclay, 91025 Evry, France

Fabrizio Creazzo – LAMBE UMR8587, Université d'Evry val d'Essonne, CNRS, CEA, Université Paris-Saclay, 91025 Evry, France

Complete contact information is available at: <https://pubs.acs.org/10.1021/jacs.9b13273>

Author Contributions

†A.T., S.D., and S.P. contributed equally to this work.

Notes

The authors declare no competing financial interest.

ACKNOWLEDGMENTS

The authors acknowledge the National Science Foundation for supporting this work (NSF Grants CHE 1337880 and MRI 1828421) and thank Dr. Ali Eftekhari-Bafrooei for helpful discussions and Dr. Mark DelloStritto for helping in making

the contour plots. A.T. acknowledges the support provided by the US Department of Energy (DOE), Office of Science, Office of Basic Energy Sciences, Materials Sciences and Engineering Division and Chemical Sciences, Geosciences, and Biosciences Division at The Pacific Northwest National Laboratory, operated by Battelle for the US Department of Energy (DOE) under Contract DE-AC05-76RL01830. HPC resources from GENCI-France Grant 072484 (CINES/IDRIS/TGCC) are acknowledged. S.P., F.S.B., F.C., and M.-P.G. acknowledge that this work was done under funding by ANR DYNAWIN Grant 14-CE35-0011-01 and LABEX CHARMA₃T 11- LABEX-0039/ANR-11-IDEX-0003-02 "Excellence Laboratory" program of the University Paris-Saclay. The authors thank Dr. Daria Ruth Galimberti for discussions and advice.

REFERENCES

- (1) Dessler, A. E.; Sherwood, S. C. A Matter of Humidity. *Science* **2009**, *323*, 1020–1021.
- (2) Jung, M.; Reichstein, M.; Schwalm, C. R.; Huntingford, C.; Sitch, S.; Ahlström, A.; Arneeth, A.; Camps-Valls, G.; Ciais, P.; Friedlingstein, P.; Gans, F.; Ichii, K.; Jain, A. K.; Kato, E.; Papale, D.; Poulter, B.; Raduly, B.; Rödenbeck, C.; Tramontana, G.; Viovy, N.; Wang, Y.-P.; Weber, U.; Zaehle, S.; Zeng, N. Compensatory Water Effects Link Yearly Global Land CO₂ Sink Changes to Temperature. *Nature* **2017**, *541*, 516–520.
- (3) Ball, P. Water is an Active Matrix of Life for Cell and Molecular Biology. *Proc. Natl. Acad. Sci. U. S. A.* **2017**, *114*, 13327–13335.
- (4) Maddox, J. Putting Molecular Biology into Water. *Nature* **1993**, *364*, 669.
- (5) Chaplin, M. Do We Underestimate the Importance of Water in Cell Biology? *Nat. Rev. Mol. Cell Biol.* **2006**, *7*, 861–866.
- (6) Chen, S.; Itoh, Y.; Masuda, T.; Shimizu, S.; Zhao, J.; Ma, J.; Nakamura, S.; Okuro, K.; Noguchi, H.; Uosaki, K.; Aida, T. Subnanoscale Hydrophobic Modulation of Salt Bridges in Aqueous Media. *Science* **2015**, *348*, 555–559.
- (7) Ojha, L.; Wilhelm, M. B.; Murchie, S. L.; McEwen, A. S.; Wray, J. J.; Hanley, J.; Massé, M.; Chojnacki, M. Spectral Evidence for Hydrated Salts in Recurring Slope Lineae on Mars. *Nat. Geosci.* **2015**, *8*, 829–832.
- (8) McEwen, A. S.; Ojha, L.; Dundas, C. M.; Mattson, S. S.; Byrne, S.; Wray, J. J.; Cull, S. C.; Murchie, S. L.; Thomas, N.; Gulick, V. C. Seasonal Flows on Warm Martian Slopes. *Science* **2011**, *333*, 740–743.
- (9) Sposito, G.; Skipper, N. T.; Sutton, R.; Park, S.-h.; Soper, A. K.; Greathouse, J. A. Surface Geochemistry of the Clay Minerals. *Proc. Natl. Acad. Sci. U. S. A.* **1999**, *96*, 3358–3364.
- (10) Pekel, J.-F.; Cottam, A.; Gorelick, N.; Belward, A. S. High-Resolution Mapping of Global Surface Water and its Long-Term Changes. *Nature* **2016**, *540*, 418–422.
- (11) Tunuguntla, R. H.; Henley, R. Y.; Yao, Y.-C.; Pham, T. A.; Wanunu, M.; Noy, A. Enhanced Water Permeability and Tunable Ion Selectivity in Subnanometer Carbon Nanotube Porins. *Science* **2017**, *357*, 792–796.
- (12) Franzese, G.; Bianco, V. Water at Biological and Inorganic Interfaces. *Food Biophys.* **2013**, *8*, 153–169.
- (13) Shelton, D. P. Water-Water Correlations in Electrolyte Solutions Probed by Hyper-Rayleigh Scattering. *J. Chem. Phys.* **2017**, *147*, 214505.
- (14) Chen, Y.; Okur, H. I.; Dupertuis, N.; Dedic, J.; Wilkins, D. M.; Ceriotti, M.; Roke, S. Comment on "Water-Water Correlations in Electrolyte Solutions Probed by Hyper-Rayleigh Scattering" [*J. Chem. Phys.* **147**, 214505 (2017)]. *J. Chem. Phys.* **2018**, *149*, 167101.
- (15) Shelton, D. P. Response to "Comment on 'Water-Water Correlations in Electrolyte Solutions Probed by Hyper-Rayleigh Scattering'" [*J. Chem. Phys.* **149**, 167101 (2018)]. *J. Chem. Phys.* **2018**, *149*, 167102.
- (16) Chan, Y. C.; Wong, K. Y. Study of the Pair Correlations Between P-Nitroaniline Molecules in Solution by Depolarized Hyper-Rayleigh Scattering. *J. Chem. Phys.* **2012**, *136*, 174514.
- (17) O'Brien, J. T.; Williams, E. R. Effects of Ions on Hydrogen-Bonding Water Networks in Large Aqueous Nanodrops. *J. Am. Chem. Soc.* **2012**, *134*, 10228–10236.
- (18) Smith, J. D.; Saykally, R. J.; Geissler, P. L. The Effects of Dissolved Halide Anions on Hydrogen Bonding in Liquid Water. *J. Am. Chem. Soc.* **2007**, *129*, 13847–13856.
- (19) Lin, Y. S.; Auer, B. M.; Skinner, J. L. Water Structure, Dynamics, and Vibrational Spectroscopy in Sodium Bromide Solutions. *J. Chem. Phys.* **2009**, *131*, 144511.
- (20) Omta, A. W.; Kropman, M. F.; Woutersen, S.; Bakker, H. J. Negligible Effect of Ions on the Hydrogen-Bond Structure in Liquid Water. *Science* **2003**, *301*, 347–349.
- (21) Eftekhari-Bafrooei, A.; Borguet, E. Effect of Surface Charge on the Vibrational Dynamics of Interfacial Water. *J. Am. Chem. Soc.* **2009**, *131*, 12034–12035.
- (22) Eftekhari-Bafrooei, A.; Borguet, E. Effect of Electric Fields on the Ultrafast Vibrational Relaxation of Water at a Charged Solid-Liquid Interface as Probed by Vibrational Sum Frequency Generation. *J. Phys. Chem. Lett.* **2011**, *2*, 1353–1358.
- (23) Ohno, P. E.; Chang, H.; Spencer, A. P.; Liu, Y.; Boamah, M. D.; Wang, H.-f.; Geiger, F. M. Beyond the Gouy-Chapman Model with Heterodyne-Detected Second Harmonic Generation. *J. Phys. Chem. Lett.* **2019**, *10*, 2328–2334.
- (24) Darlington, A. M.; Jarisz, T. A.; Dewalt-Kerian, E. L.; Roy, S.; Kim, S.; Azam, M. S.; Hore, D. K.; Gibbs, J. M. Separating the pH-Dependent Behavior of Water in the Stern and Diffuse Layers with Varying Salt Concentration. *J. Phys. Chem. C* **2017**, *121*, 20229–20241.
- (25) DeWalt-Kerian, E. L.; Kim, S.; Azam, M. S.; Zeng, H. B.; Liu, Q. X.; Gibbs, J. M. pH-Dependent Inversion of Hofmeister Trends in the Water Structure of the Electrical Double Layer. *J. Phys. Chem. Lett.* **2017**, *8*, 2855–2861.
- (26) Macias-Romero, C.; Nahalka, I.; Okur, H. I.; Roke, S. Optical Imaging of Surface Chemistry and Dynamics in Confinement. *Science* **2017**, *357*, 784–788.
- (27) Chapman, D. L. A Contribution to the Theory of Electrocapillarity. *Philos. Mag.* **1913**, *25*, 475–481.
- (28) Grahame, D. C. The Electrical Double Layer and the Theory of Electrocapillarity. *Chem. Rev.* **1947**, *41*, 441–501.
- (29) Cyran, J. D.; Donovan, M. A.; Vollmer, D.; Siro Brigiano, F.; Pezzotti, S.; Galimberti, D. R.; Gaigeot, M.-P.; Bonn, M.; Backus, E. H. G. Molecular Hydrophobicity at a Macroscopically Hydrophilic Surface. *Proc. Natl. Acad. Sci. U. S. A.* **2019**, *116*, 1520–1525.
- (30) Covert, P. A.; Jena, K. C.; Hore, D. K. Throwing Salt into the Mix: Altering Interfacial Water Structure by Electrolyte Addition. *J. Phys. Chem. Lett.* **2014**, *5*, 143–148.
- (31) Jena, K. C.; Covert, P. A.; Hore, D. K. The Effect of Salt on the Water Structure at a Charged Solid Surface: Differentiating Second- and Third-order Nonlinear Contributions. *J. Phys. Chem. Lett.* **2011**, *2*, 1056–1061.
- (32) Hore, D. K.; Tyrode, E. Probing Charged Aqueous Interfaces Near Critical Angles: Effect of Varying Coherence Length. *J. Phys. Chem. C* **2019**, *123*, 16911–16920.
- (33) Dalstein, L.; Potapova, E.; Tyrode, E. The Elusive Silica/Water Interface: Isolated Silanols Under Water as Revealed by Vibrational Sum Frequency Spectroscopy. *Phys. Chem. Chem. Phys.* **2017**, *19*, 10343–10349.
- (34) Du, Q.; Freysz, E.; Shen, Y. R. Vibrational Spectra of Water Molecules at Quartz/Water Interfaces. *Phys. Rev. Lett.* **1994**, *72*, 238–241.
- (35) Dewan, S.; Yeganeh, M. S.; Borguet, E. Experimental Correlation Between Interfacial Water Structure and Mineral Reactivity. *J. Phys. Chem. Lett.* **2013**, *4*, 1977–1982.
- (36) Yang, Z.; Li, Q.; Chou, K. C. Structures of Water Molecules at the Interfaces of Aqueous Salt Solutions and Silica: Cation Effects. *J. Phys. Chem. C* **2009**, *113*, 8201–8205.

- (37) Myalitsin, A.; Urashima, S.-h.; Nihonyanagi, S.; Yamaguchi, S.; Tahara, T. Water Structure at the Buried Silica/Aqueous Interface Studied by Heterodyne-Detected Vibrational Sum-Frequency Generation. *J. Phys. Chem. C* **2016**, *120*, 9357–9363.
- (38) Ostroverkhov, V.; Waychunas, G. A.; Shen, Y. R. Vibrational Spectra of Water at Water/ α -Quartz (0001) Interface. *Chem. Phys. Lett.* **2004**, *386*, 144–148.
- (39) Lis, D.; Backus, E. H. G.; Hunger, J.; Parekh, S. H.; Bonn, M. Liquid Flow Along a Solid Surface Reversibly Alters Interfacial Chemistry. *Science* **2014**, *344*, 1138–1142.
- (40) Urashima, S.-h.; Myalitsin, A.; Nihonyanagi, S.; Tahara, T. The Topmost Water Structure at a Charged Silica/Aqueous Interface Revealed by Heterodyne-Detected Vibrational Sum Frequency Generation Spectroscopy. *J. Phys. Chem. Lett.* **2018**, *9*, 4109–4114.
- (41) McGuire, J. A.; Shen, Y. R. Ultrafast Vibrational Dynamics at Water Interfaces. *Science* **2006**, *313*, 1945–1948.
- (42) Eftekhari-Bafrooei, A.; Borguet, E. Effect of Hydrogen-Bond Strength on the Vibrational Relaxation of Interfacial Water. *J. Am. Chem. Soc.* **2010**, *132*, 3756–3761.
- (43) Wen, Y.-C.; Zha, S.; Liu, X.; Yang, S.; Guo, P.; Shi, G.; Fang, H.; Shen, Y. R.; Tian, C. Unveiling Microscopic Structures of Charged Water Interfaces by Surface-Specific Vibrational Spectroscopy. *Phys. Rev. Lett.* **2016**, *116*, 016101.
- (44) Pezzotti, S.; Galimberti, D. R.; Shen, Y. R.; Gaigeot, M.-P. Structural Definition of the BIL and DL: a New Universal Methodology to Rationalize Non-Linear $\chi^{(2)}(\omega)$ SFG Signals at Charged Interfaces, Including $\chi^{(3)}(\omega)$ Contributions. *Phys. Chem. Chem. Phys.* **2018**, *20*, 5190–5199.
- (45) Dove, P. M. The Dissolution Kinetics of Quartz in Sodium Chloride Solutions at 25 Degrees to 300 Degrees C. *Am. J. Sci.* **1994**, *294*, 665–712.
- (46) Pezzotti, S.; Galimberti, D.; Shen, Y.; Gaigeot, M.-P. What the Diffuse Layer (DL) Reveals in Non-Linear SFG Spectroscopy. *Minerals* **2018**, *8*, 305.
- (47) Pezzotti, S.; Galimberti, D. R.; Gaigeot, M.-P. Deconvolution of BIL-SFG and DL-SFG spectroscopic signals reveals order/disorder of water at the elusive aqueous silica interface. *Phys. Chem. Chem. Phys.* **2019**, *21*, 22188–22202.
- (48) Ohno, P. E.; Saslow, S. A.; Wang, H.-f.; Geiger, F. M.; Eienthal, K. B. Phase-Referenced Nonlinear Spectroscopy of the α -Quartz/Water Interface. *Nat. Commun.* **2016**, *7*, 13587.
- (49) Gonella, G.; Lütgebaucks, C.; de Beer, A. G. F.; Roke, S. Second Harmonic and Sum-Frequency Generation from Aqueous Interfaces Is Modulated by Interference. *J. Phys. Chem. C* **2016**, *120*, 9165–9173.
- (50) Fecko, C. J.; Eaves, J. D.; Loparo, J. J.; Tokmakoff, A.; Geissler, P. L. Ultrafast Hydrogen-Bond Dynamics in the Infrared Spectroscopy of Water. *Science* **2003**, *301*, 1698–1702.
- (51) Lock, A. J.; Bakker, H. J. Temperature Dependence of Vibrational Relaxation in Liquid H₂O. *J. Chem. Phys.* **2002**, *117*, 1708–1713.
- (52) Cowan, M. L.; Bruner, B. D.; Huse, N.; Dwyer, J. R.; Chugh, B.; Nibbering, E. T. J.; Elsaesser, T.; Miller, R. J. D. Ultrafast Memory Loss and Energy Redistribution in the Hydrogen Bond Network of Liquid H₂O. *Nature* **2005**, *434*, 199–202.
- (53) Campen, R. K.; Pymer, A. K.; Nihonyanagi, S.; Borguet, E. Linking Surface Potential and Deprotonation in Nanoporous Silica: Second Harmonic Generation and Acid/Base Titration. *J. Phys. Chem. C* **2010**, *114*, 18465–18473.
- (54) Pezzotti, S.; Galimberti, D. R.; Gaigeot, M.-P. 2D H-Bond Network as the Topmost Skin to the Air–Water Interface. *J. Phys. Chem. Lett.* **2017**, *8*, 3133–3141.
- (55) Pezzotti, S.; Serva, A.; Gaigeot, M.-P. 2D-HB-Network at the Air–Water Interface: A Structural and Dynamical Characterization by Means of Ab Initio and Classical Molecular Dynamics Simulations. *J. Chem. Phys.* **2018**, *148*, 174701.
- (56) Isaenko, O.; Borguet, E. Hydrophobicity of Hydroxylated Amorphous Fused Silica Surfaces. *Langmuir* **2013**, *29*, 7885–7895.
- (57) Pfeiffer-Laplaud, M.; Gaigeot, M.-P. Electrolytes at the Hydroxylated (0001) α -Quartz/Water Interface: Location and Structural Effects on Interfacial Silanols by DFT-Based MD. *J. Phys. Chem. C* **2016**, *120*, 14034–14047.
- (58) Pfeiffer-Laplaud, M.; Gaigeot, M.-P. Adsorption of Singly Charged Ions at the Hydroxylated (0001) α -Quartz/Water Interface. *J. Phys. Chem. C* **2016**, *120*, 4866–4880.
- (59) Wang, R.; DelloStritto, M.; Remsing, R. C.; Carnevale, V.; Klein, M. L.; Borguet, E. Sodium Halide Adsorption and Water Structure at the α -Alumina(0001)/Water Interface. *J. Phys. Chem. C* **2019**, *123*, 15618–15628.
- (60) Serva, A.; Pezzotti, S.; Bougueroua, S.; Galimberti, D. R.; Gaigeot, M.-P. Combining Ab-Initio and Classical Molecular Dynamics Simulations to Unravel the Structure of the 2D-HB-Network at the Air–Water Interface. *J. Mol. Struct.* **2018**, *1165*, 71–78.
- (61) Kubicki, J. D.; Sofo, J. O.; Skelton, A. A.; Bandura, A. V. A New Hypothesis for the Dissolution Mechanism of Silicates. *J. Phys. Chem. C* **2012**, *116*, 17479–17491.
- (62) DelloStritto, M. J.; Kubicki, J. D.; Sofo, J. O. Effect of Ions on H-Bond Structure and Dynamics at the Quartz(101)–Water Interface. *Langmuir* **2016**, *32*, 11353–11365.
- (63) DelloStritto, M. J.; Kubicki, J.; Sofo, J. O. Density Functional Theory Simulation of Hydrogen-Bonding Structure and Vibrational Densities of States at the Quartz (1 0 1)-Water Interface and its Relation to Dissolution as a Function of Solution pH and Ionic Strength. *J. Phys.: Condens. Matter* **2014**, *26*, 244101.
- (64) Lindner, J.; Vöhringer, P.; Pshenichnikov, M. S.; Cringus, D.; Wiersma, D. A.; Mostovoy, M. Vibrational Relaxation of Pure Liquid Water. *Chem. Phys. Lett.* **2006**, *421*, 329–333.
- (65) Ashihara, S.; Huse, N.; Espagne, A.; Nibbering, E. T. J.; Elsaesser, T. Ultrafast Structural Dynamics of Water Induced by Dissipation of Vibrational Energy. *J. Phys. Chem. A* **2007**, *111*, 743–746.
- (66) Bakker, H. J.; Skinner, J. L. Vibrational Spectroscopy as a Probe of Structure and Dynamics in Liquid Water. *Chem. Rev.* **2010**, *110*, 1498–1517.
- (67) Lawrence, C. P.; Skinner, J. L. Vibrational Spectroscopy of HOD in Liquid D₂O. VI. Intramolecular and Intermolecular Vibrational Energy Flow. *J. Chem. Phys.* **2003**, *119*, 1623–1633.
- (68) Rey, R.; Hynes, J. T. Vibrational Energy Relaxation of HOD in Liquid D₂O. *J. Chem. Phys.* **1996**, *104*, 2356–2368.
- (69) Heilweil, E. J.; Casassa, M. P.; Cavanagh, R. R.; Stephenson, J. C. Vibrational Deactivation of Surface OH Chemisorbed on SiO₂: Solvent Effects. *J. Chem. Phys.* **1985**, *82*, 5216–5231.
- (70) Inoue, K.-i.; Ishiyama, T.; Nihonyanagi, S.; Yamaguchi, S.; Morita, A.; Tahara, T. Efficient Spectral Diffusion at the Air/Water Interface Revealed by Femtosecond Time-Resolved Heterodyne-Detected Vibrational Sum Frequency Generation Spectroscopy. *J. Phys. Chem. Lett.* **2016**, *7*, 1811–1815.
- (71) Hsieh, C.-S.; Okuno, M.; Hunger, J.; Backus, E. H. G.; Nagata, Y.; Bonn, M. Aqueous Heterogeneity at the Air/Water Interface Revealed by 2D-HD-SFG Spectroscopy. *Angew. Chem., Int. Ed.* **2014**, *53*, 8146–8149.
- (72) Zhang, Z.; Piatkowski, L.; Bakker, H. J.; Bonn, M. Ultrafast Vibrational Energy Transfer at the Water/Air Interface Revealed by Two-Dimensional Surface Vibrational Spectroscopy. *Nat. Chem.* **2011**, *3*, 888–893.
- (73) Van Der Post, S. T.; Hsieh, C.-S.; Okuno, M.; Nagata, Y.; Bakker, H. J.; Bonn, M.; Hunger, J. Strong Frequency Dependence of Vibrational Relaxation in Bulk and Surface Water Reveals Sub-Picosecond Structural Heterogeneity. *Nat. Commun.* **2015**, *6*, 8384.
- (74) Wang, H.; Xu, Q.; Liu, Z.; Tang, Y.; Wei, G.; Shen, Y. R.; Liu, W.-T. Gate-Controlled Sum-Frequency Vibrational Spectroscopy for Probing Charged Oxide/Water Interfaces. *J. Phys. Chem. Lett.* **2019**, *10* (19), 5943–5948.
- (75) Dewan, S.; Carnevale, V.; Bankura, A.; Eftekhari-Bafrooei, A.; Fiorin, G.; Klein, M. L.; Borguet, E. The Structure of Water at Charged Interfaces: A Molecular Dynamics Study. *Langmuir* **2014**, *30* (27), 8056–8065.

Ions Tune Interfacial Water Structure and Modulate Hydrophobic

Interactions at Silica Surfaces

Aashish Tuladhar^{a,†,‡}, Shalaka Dewan^{a,†}, Simone Pezzotti^{a,#}, Flavio Siro Brigiano[#], Fabrizio Creazzo[#], Marie-Pierre Gaijeot^{,#}, and Eric Borguet^{*,†}*

[†]Department of Chemistry, Temple University, 1901 N. 13th St., Philadelphia, PA 19122, USA

[‡] Physical & Computational Sciences Directorate, Pacific Northwest National Laboratory, Richland, WA 99352

[#]LAMBE UMR8587, Université d'Evry val d'Essonne, CNRS, CEA, Université Paris-Saclay, 91025, Evry, France

^a These authors contributed equally to this work.

Corresponding Authors

* Tel.: 33 1-69-47-01-40 E-mail: mgaijeot@univ-evry.fr

* Tel.: 1-215-204-9696. E-mail: eborguet@temple.edu

Supporting Information

S1 - Experimental setup.

Optical Setup. To access the vibrational lifetimes of the interfacial O-H stretch, one-color IR pump – vSFG probe measurements were performed at the silica/water interface using the experimental setup described in previous studies.¹⁻⁵ In brief, a one box Ti:Sapphire oscillator + regenerative amplifier (Coherent, LIBRA –F-1K-110-HE+) produces 5.0 mJ at 800 nm with a pulse duration of 120 fs at a repetition rate of 1 kHz (Figure S1). 90% of the output (4.5 mJ) was used to pump a commercial OPA (Coherent, TOPAS-Prime HE) to produce 1.3 W of signal and idler. The DFG/OPA combination was tuned to generate IR pulses, centered at 3200 cm^{-1} with a typical pulse energy of $20\text{ }\mu\text{J}$ @ $3\text{ }\mu\text{m}$ ($\sim 200\text{ cm}^{-1}$ FWHM), which were then split in a 70%-30% ratio to be used as IR pump and IR probe, respectively. The remaining 5% of the regenerative amplifier output, spectrally narrowed to a FWHM of $\sim 2.5\text{ nm}$ (38 cm^{-1}) using a narrow bandpass filter, was used as the visible light for vSFG measurements. The infrared probe and visible beams that generate the vSFG probe have incident angles of 65° and 70° , respectively, with respect to the surface normal, while the IR pump was incident at an angle of 75° with respect to the surface normal (Figure S2). The incident angles were selected based on the best Fresnel factor enhancement under total internal reflection, similar to previous studies.^{2-3, 6-7} The focal spot diameters of the IR pump, IR probe, and VIS probe were $150\text{ }\mu\text{m}$, $150\text{ }\mu\text{m}$ and $200\text{ }\mu\text{m}$, respectively. All incident beams were p polarized and the vSFG signal was collected in p polarization.

Sample Preparation. IR transmitting amorphous fused SiO_2 triangular roof prisms ($15\text{ x }13\text{ x }13\text{ x }15\text{ mm}$) with the $15\text{ x }15\text{ mm}$ square face (opposite of the roof) were purchased from Team Photon Inc. (San Diego, CA). Before the experiment, the SiO_2 triangular prism was first cleaned with freshly prepared “piranha” solution (1 volume concentration H_2O_2 : 3 volume concentration

H₂SO₄) for ~30 minutes in a Teflon holder. (**CAUTION:** “*piranha*” is a very reactive mixture and must be handled with great care by using protective equipment including appropriate gloves, goggles, and lab coat). This was followed with copious amount of rinsing with deionized water (>18.2 MΩ·cm resistivity, Thermoscientific Barnstead Easypure II purification system with a UV lamp) and then the prism was dried by filtered compressed N₂ gas. The SiO₂ prism was then assembled onto the sample holder and exposed to neat water immediately and allowed to equilibrate in ambient at room temperature before experiments.

The silica/water interface was achieved by pressing the silica prism against a volume of water in a home-built sample cell (Fig. S2). The design of the sample cell allowed for an easy exchange of the aqueous media without moving the prism. This provision prevents any change in the position of the interface.

All solutions were prepared using deionized water, the pH of which was ~6 after equilibration with the laboratory ambient. Solutions of pH 2 and 12 were made by dropwise adding small amounts of concentrated HCl (~12.0 M, Fisher Scientific, analytical grade) and 6 M NaOH (Fluke Analytical, analytical grade), respectively, till the pH of the solution reached the desired level as measured by a pH meter (Oakton). Salt solutions of 0.1 M and 0.5 M were prepared using NaCl (Fisher Scientific, >99.8%), which was baked overnight at 500 °C to remove possible organic impurities.

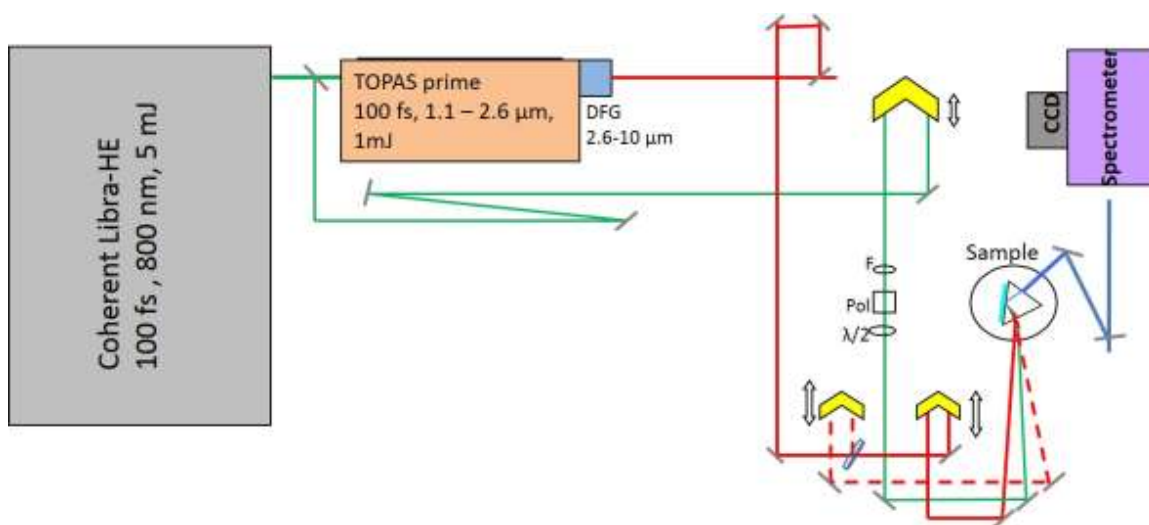


Figure S1: Schematic of the laser system and the experimental set up for frequency SFG measurements with the Libra-HE laser system, used to perform one-color TR-vSFG measurements

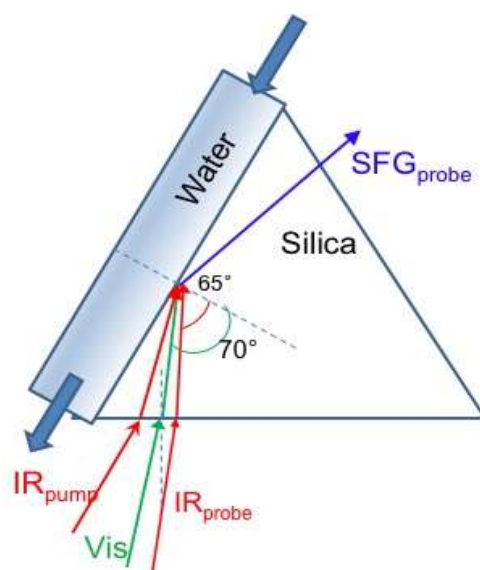


Figure S2: Diagram of the TR-vSFG measurements performed under total internal reflection conditions at the silica/water interface

Experimental Details. Previous TR-vSFG studies have shown that at the silica/H₂O interface, the vibrational dynamics do not exhibit any frequency dependence^{2, 8}. In other words, for one-color TR-vSFG, we expect similar results for strongly and weakly hydrogen bonded water, i.e., the same dynamics for IR frequencies centered at 3200 cm⁻¹ or 3400 cm⁻¹. Owing to better signal to noise of the vSFG spectra obtained at 3200 cm⁻¹ region, all the results discussed here are pumped and probed at 3200 cm⁻¹ region of the O-H stretch, which corresponds to the strongly hydrogen bonded water species. Additionally, it is important to mention that usually the bleach signal can be accompanied by a hot band response. However, due to anharmonicity, the hot band of O-H stretch is 200-400 cm⁻¹ red-shifted from the fundamental O-H stretch and therefore, outside the window of our probe vSFG (3100 to 3300 cm⁻¹). The tail of the hot band might affect the bleach dynamics, but we expect its contribution to be insignificant on the T₁ lifetime, since we are primarily probing the population at the 3200 cm⁻¹ region (ground state OH stretch).

The vibrational relaxation of interfacial water at a silica surface is determined by the recovery of the bleach in the vSFG intensity as a function of the delay between the IR pump and the vSFG probe. The kinetics of vibrational relaxation is modeled using a four level system (Figure S3), already extensively used in previous work to describe the dynamics of bulk water⁹⁻¹¹ as well as water at mineral oxide surfaces^{1-5, 8, 12}.

S2 - Model used to describe vibrational dynamics of O-H in water:

In this model, the vibrational energy of the excited $\nu=1$ state is first transferred to an intermediate state ν^* state, via inter- and intramolecular energy transfer to the overtone of the bend, or via resonant energy transfer to the O-H stretches of other water molecules that may be coupled via hydrogen bonds². This occurs with a relaxation time (T_1), which corresponds to the vibrational lifetime of the first excited state ($\nu=1$) of the O-H oscillator. The relaxation from the intermediate

v^* state to a hot ground state v_0^* occurs via a thermalization process with a time constant of T_{th} . The thermalization step involves the statistical distribution of the remaining vibrational energy to all possible modes, including librations and the hydrogen bond reorganization¹³⁻¹⁴.

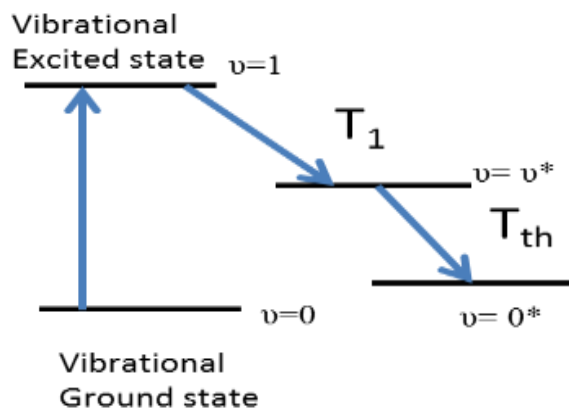


Figure S3: Four level model used to describe vibrational relaxation of water in the bulk and at interfaces.

The time-resolved vSFG data can be fit to the following equation, which describes the kinetics of vibrational relaxation:

$$I_{SFG} = \text{IRF}(t) * [N_0(t) - N_1(t) + C_2 N_2(t) + C_3 N_3(t)]^2 \quad (S1)$$

where N_0 , N_1 , N_2 , and N_3 are the populations of the $v=0$, $v=1$, v^* , and $v^*=0$ states, respectively, and are determined by the solution to the system of coupled differential equations that describe the rates of population change for the four levels. C_2 and C_3 are factors related to the strengths of the vSFG signal from the intermediate and final levels, and $\text{IRF}(t)$ represents the Gaussian profile of the instrument response function (IRF).

Since our experiments were not sensitive to the thermalization effect, the T_{th} value was held constant to a previously reported²⁻³ value of 700 fs while fitting the data. The insensitivity of our data towards the thermalization effect probably stems from the pump IR and probe IR being identical. If we were to pump the strongly hydrogen bonded region and probe the weakly hydrogen bonded region, the thermalization timescale can be more accurately measured. However, this is not the scope of our investigation.

S3 - Calculated surface electric potential

The silica surface charge (σ_0) was calculated at each pH and ionic strength using Equation (S2):

$$\sigma_0 = \sigma_{max} \times (\theta > SiO_{total}) \quad (S2)$$

where σ_{max} (~ 0.72 C/m²) is the maximum surface charge generated by deprotonation of all the silanol groups (4.5 SiOH/nm²) on the silica surface and ($\theta > SiO_{tot}$) is the total number of deprotonated sites (SiO⁻ and SiO⁻Na⁺) obtained from Dove's model¹⁵. The surface potential (ϕ_0) was estimated from the Gouy-Chapman model as¹⁶⁻¹⁷:

$$\phi_0 = \frac{2kT}{ze} \sinh^{-1} \left(\frac{\sigma_0}{\sqrt{8kT\epsilon_0\epsilon N_A I}} \right) \quad (S3)$$

where k , N_A , T , I , and z are Boltzmann's constant, Avogadro's number, the absolute temperature, the ionic strength of the solution, and the electrolyte valence, respectively, and ϵ_0 and ϵ are the permittivity of free space and dielectric constant of the electrolyte. The calculated surface potential (Figure S4) using Equation (S3) at the silica surface with background electrolyte of 0.5 M NaCl is in good agreement with the measured surface potential reported by Eisenthal et al.¹⁸

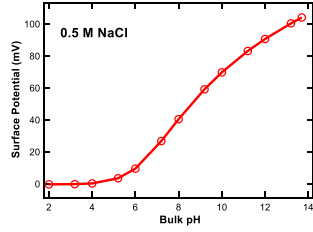


Figure S4: Calculated surface potential using the Gouy-Chapman model (Equation S3) as a function of bulk pH at 0.5 M Na⁺ ionic strength. It is in good agreement with the measured surface potential by Eiseenthal et al.¹⁸

The decay of the potential as a function of distance from the silica surface can be estimated by solving the Poisson-Boltzmann equation as¹⁶⁻¹⁷:

$$\phi(x) = \frac{4kT}{ze} \tanh^{-1} \left\{ \tanh \left(\frac{ze\phi_0}{4kT} \right) e^{-\kappa x} \right\} \quad (S4)$$

where κ is the inverse of the Debye length and can be estimated as¹⁷:

$$\kappa = \sqrt{\frac{2z^2 e^2 N_A I}{\epsilon_0 \epsilon k T}} \quad (S5)$$

The drop of the surface potential at pH 2, 6, and 12 in the presence of 0, 0.1 M, and 0.5 M NaCl is shown in Figure S5.

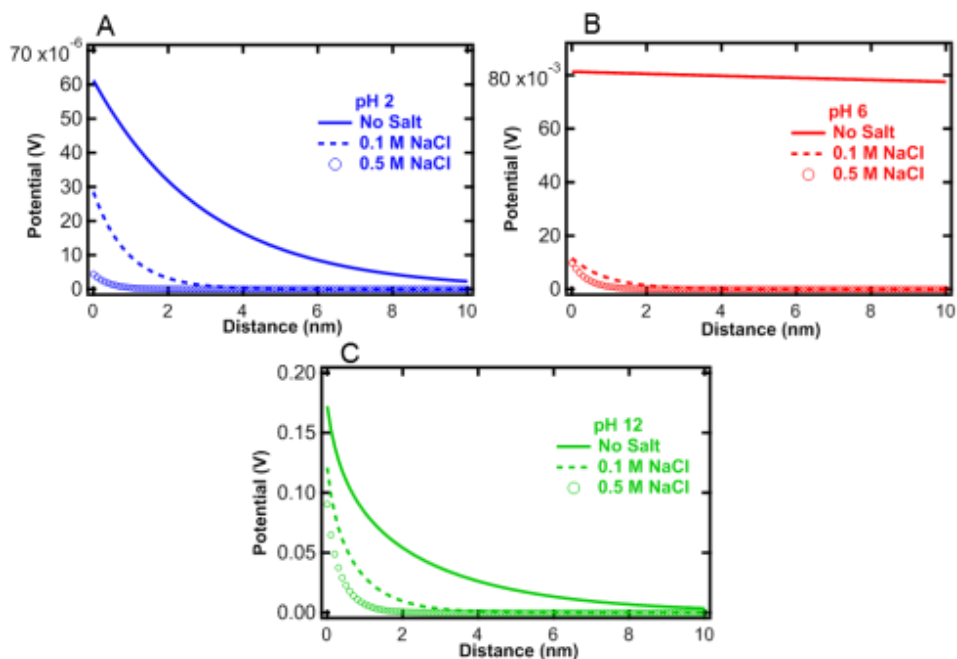


Figure S5: Calculated drop in surface potential as a function of distance using the Poisson-Boltzmann model (Equation S4) at bulk pHs (A) 2, (B) 6, and (C) 12 at varying ionic strength of 0 M, 0.1 M, and 0.5 M NaCl

S4 – SS-vSFG signal counts at pH 2 conditions

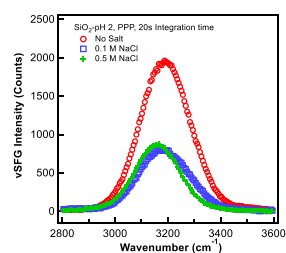


Figure S6: Non-normalized steady-state vSFG signal counts at SiO_2 -pH 2 conditions in the presence of bulk NaCl concentrations of 0 M (red circle), 0.1 M (blue square), and 0.1 M (green plus).

S5 - AIMD/DFT-MD molecular dynamics simulations.

Density Functional Theory-based Molecular Dynamics simulations (DFT-MD or AIMD for Ab Initio MD) have been carried out on amorphous silica-liquid water interfaces. See a snapshot in Figure S7. The amorphous silica model is taken from Ugliengo *et al*¹⁹, with a 4.5 SiOH/nm² silanol coverage of the surface in contact with the air (i.e. eight SiOH groups in our simulation box). Once put in contact with water, the surface is found stable along the simulation length (30 ps). The 4.5 SiOH/nm² silanol coverage is typical of hydrophilic silica surfaces¹⁹ and typical of the experimental conditions close to the PZC potential of zero charge (pH~2-4)¹⁵. The PZC condition also corresponds to the isoelectric point for aqueous amorphous silica. This is shown in section S6 where we define water layers at increasing distance from the surface and water structural properties within each layer are characterized. Our results clearly show that at the amorphous silica/water interface at PZC condition the interfacial layer is solely composed by the BIL, which is directly followed by bulk water. Since no DL is observed at this interface, we can conclude that PZC condition indeed corresponds to the isoelectric point.

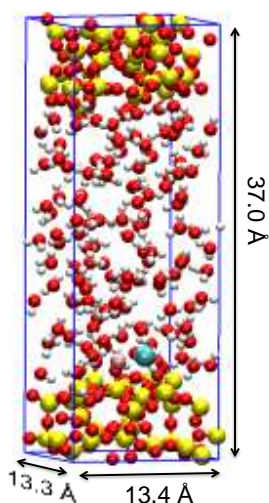


Figure S7. Snapshot of the DFT-MD simulation box, with amorphous silica, water and the KCl ion pair (Contact Ion-Pair in an inner-sphere adsorption).

The DFT-MD simulations were conducted with the CP2K software package²⁰, consisting in Born Oppenheimer MD, BLYP²¹⁻²² electronic representation including Grimme D2 correction for dispersion²³, GTH pseudopotentials²⁴ and a combined plane waves (400 Ry energy cut-off) and SR-DZVP-MOLOPT Gaussian basis set for all atoms. The dimensions of the simulation box are 13.386 Å X 13.286 Å X 37.0 Å, the box is periodically repeated in all directions of space. The silica slab is 15 Å thick, composed of 204 atoms, while the liquid water is modeled with 120 molecules in the box, providing the required 1 g/cm³ liquid density. The amorphous silica slab was re-optimized in the gas phase at the level of theory adopted for the dynamics, then put in contact with bulk water. After an equilibration run of 10 ps (5 ps with possible rescaling of velocities plus 5 ps in the pure NVE ensemble) the dynamics was run in the NVE ensemble for 20 ps with a time step of 0.4 fs, where data are collected and analyzed.

Nine DFT-MD simulations of the amorphous silica-water interface in presence of salt were conducted on the same system, including one NaCl (note KCl is replaced by NaCl in one of the nine simulations) ion-pair in contact with the neat amorphous silica surface. The simulations setup is the same as for the case of the neat silica-water interface. The only exception is the plane wave cutoff used for the simulation with NaCl, which has been enlarged to 1000 Ry in order to properly sample the Na⁺ diffusion. All simulations consists of a 5 ps equilibration run (2.5 ps with possible rescaling of velocities plus 2.5 ps in the pure NVE ensemble) and a subsequent dynamics in the NVE ensemble, with a time step of 0.4 fs and simulations lengths in the 15 ps – 25 ps range for all trajectories, for a total of 150 ps. In these additional simulations, the initial position of the ion pair is randomly varied in the box, to check the dependence of the MD results on the initial configuration, as detailed in section S8 (see also Table S1).

As the silica surface is modelled at the isoelectric point at PZC conditions, there is no surface electrostatic driving force to favor cations over anions (and vice versa) to approach closer to the silica surface when adding electrolytes at the SiO₂/water interface. This is demonstrated in section S6 by showing that there is not a DL layer at the neat silica-water interface, and it is confirmed by the surface potential estimations (Figure S5). Three generic scenarios can hence be envisaged in the relative position of K⁺ and Cl⁻ at SiO₂/water interfaces: 1) the two ions are simultaneously located in the BIL and interact with the silica surface, 2) K⁺(resp. Cl⁻) is in the BIL while Cl⁻(resp. K⁺) is in the DL, 3) both ions are in liquid water (DL or Bulk). Scenario-1 is compatible with the PZC isoelectric conditions at the silica/water interface, while scenario-2 would induce a non-negligible surface potential (incompatible with the estimated close to zero electrostatic potential at the electrolytic interface, see S3-2) and scenario-3 is of no importance for the interfacial properties.

We have therefore chosen to include KCl/NaCl in the BIL-water (i.e. at the direct interface with the surface, see BIL/DL definitions in S5) by adding one ion pair in the simulation box at the SiO₂/water interface.

Both ions remain in the BIL over the total simulation time (see details in section S8), without significant vertical diffusion of the ionic species over this time-scale. Note that we have shown in refs²⁵⁻²⁶ that NaCl and KCl behave identically at silica-water interfaces. We refer to Figure S7 for a snapshot of the system extracted from the simulation. The KCl/NaCl ion-pair is furthermore shown (see main text) to preferentially adsorb in an inner-sphere mode.

S6 – Characterization of BIL and DL water layers in molecular dynamics simulations.

A critical issue in calculating and interpreting vSFG nonlinear spectra (and associated T_1 relaxation times) is a clear and unambiguous definition of the water thickness contributing to the total signal, i.e., the extent of the region where the water is non-centrosymmetric. The pioneering work of Tian *et al.*²⁷ has provided a framework comprised of the two universal water layers, named BIL (Binding Interfacial Layer) and DL (Diffuse Layer), solely responsible for vSFG activity at any interface (only the BIL contributes to the vSFG spectra at neutral/isoelectric interfaces). In refs²⁸⁻³⁰, we have developed, applied and validated a theoretical protocol to unambiguously define these layers from (DFT)-MD simulations on the basis of water structural properties only. Our method uses three structural descriptors: (1) The water density profile as a function of the distance (z) from the surface, which provides the number of water layers and their z -boundaries; (2) The average number of hydrogen bonds formed by the water molecules within the layers found in 1); (3) 3D-plots of the distribution of water-water H-Bond lengths and H-Bond angles (defined with respect to the normal to the surface) that provide the general structural organization of water within the layers defined in 1.

The layers where water has all three descriptors identical to bulk liquid water are termed ‘liquid water’. This is further verified by checking that the associated vSFG spectrum is equal to zero, as it should indeed be for centrosymmetric liquid water. The layers where all descriptors are identical to bulk liquid water except for the orientation of the water-water H-Bonds along one given direction of space are associated to the DL (Diffuse Layer). This DL is indeed bulk water reoriented by the surface charge potential/field, and therefore is not centrosymmetric anymore. The DL can hence be seen as bulk water under the influence of an external field. The layers where all descriptors are different from bulk liquid water are called the BIL. From our previous works²⁸⁻

^{29, 31}, the BIL has been systematically found to be composed of one monolayer of water, within ~ 3 Å thickness. The present work makes no exception to this result.

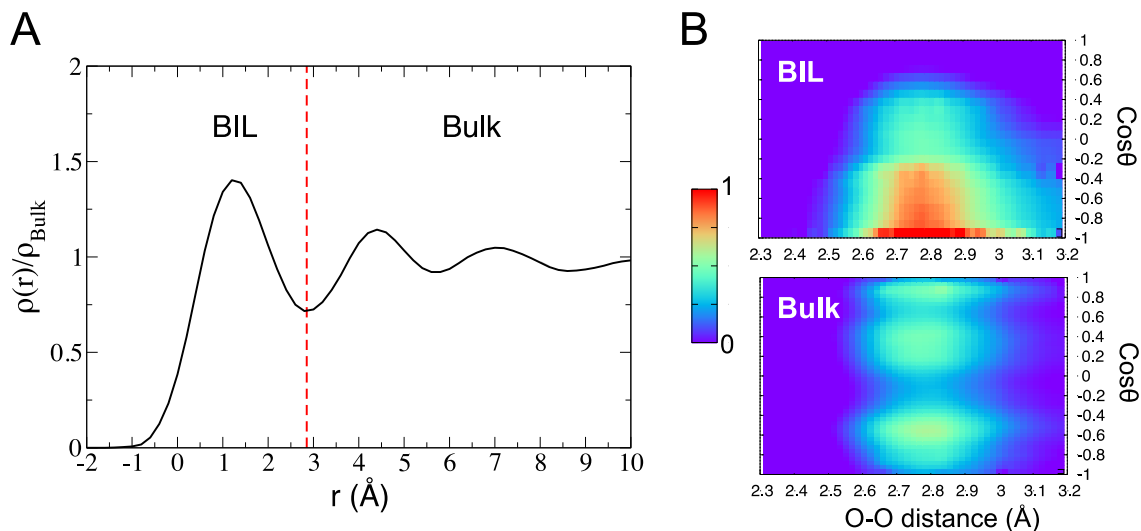


Figure S8. Two of the three descriptors used for characterizing and extracting water layers at neutral and charged interfaces. The third descriptor is the average number of HBs/molecule in each layer and is discussed in the text.

A: Time averaged water density profile (normalized with respect to bulk water density) as a function of the distance from the instantaneous surface for the neat silica-water interface. The boundary between the BIL and the DL is marked with a red dashed line.

B: 3D-plots of the HB patterns formed between the water molecules in the BIL and Bulk layers at the neat silica-water interface. The x-axis reports the O-O distance between two H-Bonded water molecules and the y-axis provides the angle (cosine values) between the O-O vector (from donor to acceptor) and the normal to the surface (oriented from liquid to solid phase). The color represents the probability to find one O-H group in the BIL/Bulk layer forming one HB with a given distance and orientation.

The same methodology has been applied here to the simulated amorphous silica-water interfaces, neat (without electrolytes) and in presence one KCl ion pair (roughly corresponding to 1M concentration in the simulations). The density profile and 3D-plots for the neat silica-water interface are presented in Figure S8, in order to show the layer characterization and definition. The BIL layer corresponds to the first peak in the density profile. It has a higher density than bulk

water. In this layer, water molecules form on average 3.0 HBs/molecule (including water-solid and water-water HBs), less than the value of 3.4 HBs/molecule obtained from a reference simulation of bulk water (with the same computational setup)²⁹. In addition, water molecules in this first layer are not in an isotropic environment, as shown in the 3D-plot (Figure S8 B - BIL), where one can see an inhomogeneous distribution in cosine values (in contrast with the homogeneous distribution in bulk water), as water molecules preferentially form water-water HBs with water located in the subsequent (bulk) layer (thus the red region at negative cosine values). Water in the BIL thus differs from bulk water for all the investigated structural properties. On the contrary, after this first layer, water molecules have an average coordination of 3.4 (equal to the value obtained for bulk water) and spatial orientation isotropy is recovered (homogeneous distribution in cosine values as shown in the 3D-plot). Bulk water is thus recovered after one water monolayer only at the investigated neutral silica-water interface.

In Figure S9 we present a schematic representation of the water layers at the neat (A panel) and 1M-electrolytic (B panel) amorphous silica/water interfaces characterized in the present work by DFT-MD simulations. These schemes are for PZC conditions. Figure 2 in the main text provides the three schemes at pH=2 (PZC), 6, 12 conditions. See text above (and main text) for the justification of why both cations and anions are simultaneously located in the BIL water layer in our simulation at PZC (pH=2) conditions (surface at the isoelectric point).

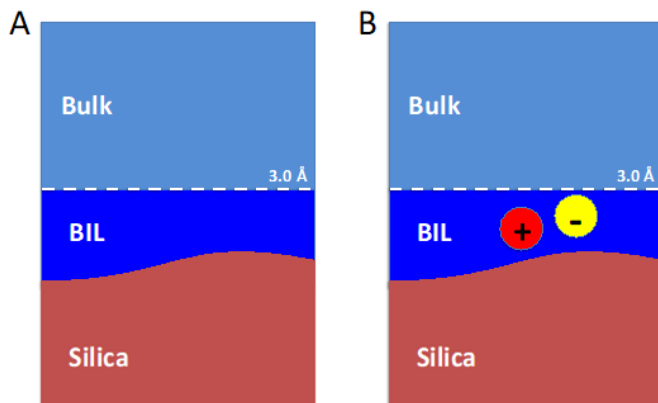


Figure S9. pH=2 (PZC conditions), schematic representations of the water layers (BIL and Bulk) identified for the neat (A) and electrolytic (B) amorphous silica/water interfaces investigated in the two DFT-MD simulations performed in this work. The 3Å thickness of the BIL interfacial region is highlighted in dark blue in the figure. For the electrolytic interface (B) the location of the cation and anion in the BIL is also highlighted. The SI and the main text provide explanations of why the two ions of the electrolyte are simultaneously located in the BIL water layer at PZC conditions.

S7 – Coordination of water mapped in the BIL.

The time averaged spatial distribution of the coordination number of water in the BIL shown in Figures 3A and 3B in the main text is obtained by the following procedure. Two water molecules are considered hydrogen bonded, and therefore coordinated, if the O-O distance is less than 3.2 Å and if the O(-H)-O angle is in the range of 140-220°. This is the standard HB criterion³⁰. The same criterion is applied for water-silanol hydrogen bonds. The coordination numbers in Figures 3A-B (main text) take into account water-water and water-silanol HBs. The coordination number/water molecule is calculated at each time-step of the dynamics and then averaged over the whole trajectory. These coordination numbers have been calculated for each water molecule that belongs to the identified BIL (see section S5), and these coordination numbers have been plotted with respect to the average position of the water molecules along the trajectory, within the x-y lateral directions of the silica surface, resulting in the x-y spatial mapping shown in Figures 3A-B

in the main text. This results in a 3D-map, where the color-coding (scale on the left-hand side of each figure) reports the average coordination number/water molecule. The scaling goes from dark blue zones for coordination numbers < 2.2 to green-red zones for coordination numbers ≥ 3.1 . The reference value is 3.4 in bulk liquid water (obtained from AIMD simulations of bulk liquid water using the same set-up as the one employed here).

S8 – Dependence of the MD results on the limited statistic of DFT-MD simulations.

The rationalization, emerging from the DFT-MD results, for the way ions affect interfacial water structure and dynamics in the BIL is that both anion (Cl^-) and cation (K^+) are able to form inner sphere complexes with the silica surface when located in the BIL, hence completing their coordination shell using both BIL-water and surface SiOH (silanol) terminations. These ion-silanols interactions replace previously existing water-silanols H-Bonds, resulting in the formation of dangling OH-groups which in turn reorient in-plane to form new water-water intra-BIL HBs, leading to the creation of an extended 2D-HB network (2DN) connecting BIL-water molecules via intra-BIL HBs (parallel to the surface). This highly connected 2D-HB-Network is reminiscent of the hydrophobic BIL-water revealed at the air-water interface²⁹⁻³⁰. This ultimately leads to a more homogeneous water coordination landscape above the surface and thus to a strong reduction of the number of under-coordinated water molecules in the BIL, which we propose to be the reason for the ion-induced acceleration of water vibrational relaxation observed at pH=2 & 6. One key point of this interpretation is that the ions (K^+ & Cl^-) form inner sphere complexes with the silica surface when located in the BIL.

Thus, we will first focus on ion configurations within the BIL. Since DFT-MD simulations do not provide enough sampling to correctly characterize the way ions are adsorbed at the silica-water

interface, we show that our conclusion that KCl (NaCl) ions located in the BIL complete their hydration layer using both water and surface SiOH groups remains true also when randomly varying the ion position within the BIL in the total of 9 MD simulations (8 with KCl + 1 with NaCl, for a total of 150ps simulation time) that we have performed.

For each of the 9 simulations, the initial point has been chosen by randomly locating the ions in the simulation box, within a maximum initial distance of 6 Å from the water surface. The ions are hence randomly located either in the BIL or in the first bulk water layer (as defined in section S5). Each simulation has been accumulated for ~15-20 ps after a short equilibration time, for a total of 150 ps.

Averaging over all the 8 simulations with KCl, we first find that K⁺ and Cl⁻ spend the same total amount of time in the BIL, equal to 83% for K⁺ and 81% for Cl⁻. For the remaining 17% / 19% of the time, both ions never reach distances larger than 8 Å from the silica surface. This is in agreement with the DFT-MD simulation of the neat silica-water interface (see section S5) and with the experimental estimation of surface potential (see section S3), both showing that the system is at the isoelectric point, thus without an electrostatic driving force for the preferential adsorption of one ion over the other. The additional simulation with NaCl confirm this result, with both ions remaining for more than 85% of the time within the BIL.

The second and even more important result is that both K⁺/Na⁺ and Cl⁻ are found to systematically form inner sphere complexes when located in the BIL, independent of the kind of surface sites they interact with (i.e. germinal, isolated...), of the kind of ion pair they form (i.e. CIP, SSIP...),

and of where they are located within the BIL. This shows that the conclusion obtained from DFT-MD simulations presented in the main text and in sections S4 & S5 are not an artifact of the limited statistic of DFT-MD and remains valid also when different ion configurations are explored.

In particular, the average (over all the trajectories) composition of the K^+ and Cl^- coordination shells (when the ions are located in the BIL) is the following: 3.9 water + 3.2 silanols for K^+ & 3.6 water + 2.3 silanols for Cl^- . A similar result is obtained from the trajectory with NaCl. See Table S1 for a summary. This shows that NaCl and KCl behave similarly. The total ions coordination resulting from ion-water + ion-silanol interactions is equivalent to the ion coordination in the bulk²⁵. Note also that these results are in agreement with the coordination shell composition calculated for K^+ and Cl^- ions adsorbed at quartz-water interfaces from DFT-MD simulations in ref.²⁵. The trajectory of 20 ps discussed in the main text corresponds to trajectory 1 in the following table.

	K^+ - H₂O	K^+ - SiOH	Cl^- - H₂O	Cl^- - SiOH	Ion pair type
Trajectory 1	4.2	2.0	3.1	3.0	CIP
Trajectory 2	3.6	4.3	4.8	2.0	Far apart
Trajectory 3	4.0	4.0	2.5	2.4	CIP
Trajectory 4	4.4	2.4	2.4	1.2	CIP/SSIP
Trajectory 5	3.9	4.2	4.0	2.2	SSIP
Trajectory 6	4.2	2.7	2.4	2.9	CIP
Trajectory 7	3.3	2.6	2.9	2.3	CIP/SSIP
Trajectory 8	5.0	3.5	4.8	1.6	Far apart
Average	3.9±0.6	3.2±0.8	3.6±1.1	2.3±0.6	/

Traj. NaCl	3.2	2.1	3.5	1.6	CIP
-------------------	-----	-----	-----	-----	-----

Table S1. Coordination shell composition of K^+/Na^+ and Cl^- ions when located in the BIL. For each of the 9 independent simulations performed, the time-averaged K^+/Na^+ -SiOH, K^+/Na^+ -H₂O, Cl^- -SiOH, Cl^- -H₂O coordination numbers are reported, as well as the kind of configuration assumed by the ions during the simulation time, i.e. contact ion pair (CIP), solvent shared ion pair (SSIP, with part of the first hydration layer being shared in between the two ions) and far ions not forming an ion pair (far, with anion-cation distance larger than 6 Å).

Now that preferential absorption of the $Cl^-/Na^+/K^+$ ions in inner-sphere mode has been proved for all trajectories, we present in Figure S10 the corresponding 9 plots for the time averaged spatial distribution of the coordination number of water in the BIL (like the ones shown in Figures 3A and 3B in the main text). These plots allow us to evaluate the ions effect on the BIL-water HB-structure.

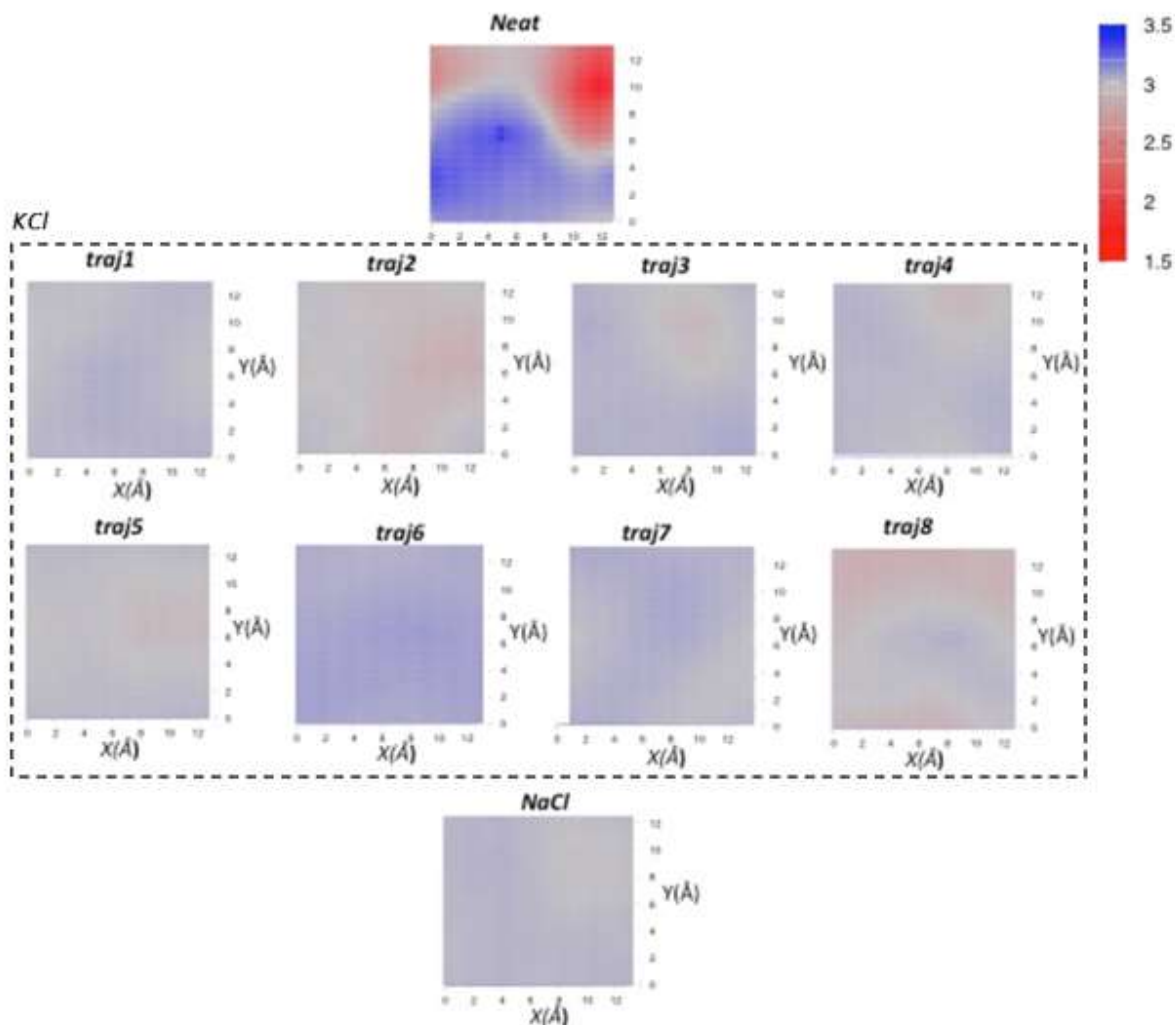


Figure S10. Time averaged coordination number of the water molecules in the BIL spatially resolved along the lateral x - y directions of the silica surface (in \AA) for: Neat aqueous silica interface (top), Each of the 8 trajectories (described in Table S1) with one KCl ion pair in the BIL (inside the dashed box) labeled as “traj1” to “traj8”, Trajectory with one NaCl ion pair in the BIL (bottom). The color coding (vertical scale in the plots) goes from red (1.5 HBs/molecule) to blue (3.5 HBs/molecule). Note that “neat” and “traj1” are the same as the plots shown in the main text, but in a slightly modified scale.

Figure S10 confirms (for all 9 trajectories with ions) the conclusion reached in the main text, i.e. that KCl/NaCl ions are able to order BIL-water molecules by inducing the formation of an air-water like 2D-HB-Network, resulting in a uniform 3-fold coordination for all water molecules in the BIL (vs the inhomogeneous and less connected BIL-water structure above the neat interface). This can be deduced from the homogeneous grey coloring in the plots for all the 9 trajectories with

ions added to the interface vs the inhomogeneous coloring of the plot for the neat silica-water interface. In agreement, we also find that averaging over all the 9 simulations with one ion-pair in the BIL, a value of 1.74 ± 0.09 intra-BIL HBs/molecule (i.e. the in-plane oriented HBs forming the 2D-HB-Network) is obtained, coherent with the value of 1.7 intra-BIL HBs/molecule discussed in the main text.

S9 – Estimation of BIL/DL contributions to TR-SFG based in the surface potential ΔV

As discussed in the main text, the BIL/DL contributions to SS-SFG and TR-SFG (i.e. to the measured T_1 lifetimes) can be qualitatively estimated from the surface potential (ΔV), knowing that relaxation processes from both BIL/DL layers will contribute to the measured T_1 lifetimes for a charged interface. This is because both BIL and DL layers are SFG active ($|\chi^{(2)}(\omega)|^2 = |\chi^{(2)}_{\text{BIL}}(\omega) + \chi^{(2)}_{\text{DL}}(\omega)|^2$), with the DL-SFG signal being proportional to the surface potential drop across DL ($\Delta\phi_{\text{DL}}$) through $|\chi^{(2)}_{\text{DL}}(\omega)|^2 = |\chi^{(3)}_{\text{bulk}}(\omega)|^2 (\Delta\phi_{\text{DL}})^2$. Note that $\Delta\phi_{\text{DL}}$ defines the potential difference across the DL, which can, in first approximation, usually estimated as equal to the surface potential. However, for a quantitative estimation of the DL contribution, one should also consider the potential drop within the BIL layer, so that $\Delta\phi_{\text{DL}} < \Delta V$. The potential drop within the BIL is usually assumed negligible for large Debye lengths, i.e. for slow decaying surface potentials.

To better illustrate the deconvolution of the total SFG signals and T_1 lifetimes into BIL/DL contributions, taking a theoretical point of view, we can consider that the total SFG (ppp) response of any aqueous interface is proportional to the Fourier transform of the sum of correlation functions between the z-component of the dipole moment of each water molecule at time t_1 ($\mu_{z,m}(t_1)$) and

the zz -element of the polarizability tensor of each water molecule at time t_0 ($\alpha_{zz,l}(t_0)$). For a system composed of N water molecules, the water SFG response will depend on $N \times N$ correlation terms (i.e. between all possible pairs of water molecules):

$$\chi_{zzz}^{(2)}(\omega) \propto \sum_{m=1}^N \sum_{l=1}^N \int_{-\infty}^{+\infty} dt e^{i\omega t} \langle \mu_{z,m}(t_1) \alpha_{zz,l}(t_0) \rangle = \langle N N \rangle \quad S(6)$$

In the equation above, we named the sum of these $N \times N$ correlation terms as $\langle N N \rangle$. By considering that both BIL/DL layers are SFG active for a charged interface, we can partition the sum over $m=1$ to N in the equation above into $N_{\text{BIL}} + N_{\text{DL}}$ where N_{BIL} and N_{DL} are the numbers of water molecules within the BIL and DL regions, respectively. We hence obtain $\langle N N \rangle = \langle N_{\text{BIL}} N \rangle + \langle N_{\text{DL}} N \rangle$, where $\langle N_{\text{BIL}} N \rangle$ and $\langle N_{\text{DL}} N \rangle$ are respectively the I_{BIL} and I_{DL} discussed in the text, once integrated in the OH stretching region. By applying the same rationale to the second term in the correlation functions (i.e. to the sum over $l=1$ to N in the equation above), we obtain that $\langle N_{\text{BIL}} N \rangle = \langle N_{\text{BIL}} N_{\text{BIL}} \rangle + \langle N_{\text{BIL}} N_{\text{DL}} \rangle$ and $\langle N_{\text{DL}} N \rangle = \langle N_{\text{DL}} N_{\text{BIL}} \rangle + \langle N_{\text{DL}} N_{\text{DL}} \rangle$, where $\langle N_{\text{BIL}} N_{\text{DL}} \rangle$ and $\langle N_{\text{DL}} N_{\text{BIL}} \rangle$ are the BIL/DL cross-correlation terms.

The partition into I_{BIL} and I_{DL} hence takes into account BIL/DL cross correlation terms, in principle. However, in the present paper, we do not calculate theoretical vSFG spectra for pH 6 and 12 conditions, as the interpretation can be achieved with experiments and potential estimation alone.

To do this, we make use of the relationship $I_{\text{DL}}/I_{\text{BIL}} \propto (\Delta\phi_{\text{DL}})^2$, i.e. the ratio of DL/BIL intensities is proportional to the square of the surface potential.

In order to be able to evaluate the ratio of DL/BIL intensities for any given $\Delta\phi_{\text{DL}}$ value, we need to know the value of $I_{\text{DL}}/I_{\text{BIL}}$ for a reference case, at a given $\Delta\phi_{\text{DL}}$ value which will become our

reference potential $\Delta\phi_{DL}(\text{ref})$. Once a reference is obtained, we can calculate I_{DL}/I_{BIL} at any other $\Delta\phi_{DL}$ value as:

$$I_{DL}/I_{BIL}(\Delta\phi_{DL}) = I_{DL}/I_{BIL}(\Delta\phi_{DL}(\text{ref})) * (\Delta\phi_{DL} / \Delta\phi_{DL}(\text{ref}))^2 \quad (\text{S7})$$

According to our previous works on silica-water interfaces^{28, 31}, a value of $I_{DL}/I_{BIL} \sim 10$ is obtained for $\Delta\phi_{DL} \sim 10$ mV (with both I_{DL}/I_{BIL} and $\Delta\phi_{DL}$ calculated ab initio from DFT-MD, see all details in ref. ^{28, 31}). We hence take $\Delta\phi_{DL}(\text{ref}) = 10$ mV as the reference, with $I_{DL}/I_{BIL}(\Delta\phi_{DL}(\text{ref})) = 10$.

Thus, Equation S7 is used to qualitatively estimate how much BIL and DL contribute to vSFG and hence to T_1 relaxation time by making use of:

1) the theoretically calculated I-BIL/I-DL ratio for a silica-water interface with $(\Delta\phi_{DL}) = 10$ mV (determined from ab-initio).

2) the relationship $I_{DL}/I_{BIL} \propto (\Delta\phi_{DL})^2$, where we assume $\Delta\phi_{DL} = \Delta V$

The total measured T_1 lifetime can be finally estimated as a first simple approximation by considering that the measured relaxation time can be physically interpreted as the weighted average of the relaxation processes involving different BIL/DL populations, so that: $T_1 = T_1(\text{BIL}) \frac{I_{BIL}}{I_{BIL} + T_1(\text{DL}) I_{DL}}$.

Equation S7 leads e.g. to $I_{DL}/I_{BIL}(\Delta\phi_{DL}) = 2958$ for pH 12 and no ions (where $\Delta V = 172$ mV), and to $I_{DL}/I_{BIL}(\Delta\phi_{DL}) = 1464$ for pH 12 + 0.1 M [NaCl] (where $\Delta V = 121$ mV). See Table S2 below.

The ratio is reduced if the $\Delta\phi_{DL}$ is estimated with more accuracy by also accounting for the screening of the potential within the BIL region. In order to show this, we now do not consider anymore $\Delta\phi_{DL}=\Delta V$, but we take the potential values (from Figure S5) at a distance from the surface which correspond to the BIL/DL boundary.

From MD simulations, we know that the BIL/DL boundary is located at 0.3 nm from the instantaneous water surface (see section S6), which corresponds to a distance of 0.7-0.8 nm from the silica surface plane defined by the topmost heavy-atoms. Thus, if we take the ΔV values at 1 nm from the solid surface, close to the BIL/DL boundary, we get $\Delta\phi_{DL} = \sim 80$ mV for pH 12 and no ions (instead of ~ 200 mV) and $\Delta\phi_{DL} = \sim 30$ mV for pH 12 + ions (instead of 100 mV). These values, however, still lead to dominant DL contributions ($I_{DL}/I_{BIL}=690$ and 80, respectively; see Table S2), confirming the conclusion reached with the less accurate surface potential estimation.

We also notice that for pH 6 and no ions, $\Delta\phi_{DL} = 80$ mV for both surface potential estimation methods (due to the slow decay typical of such a low ionic strength, i.e. 10^{-5} - 10^{-7} M), while when ions are added to the system, the $\Delta\phi_{DL}$ value is very low (~ 4 mV) at 1 nm from the surface (Figure S5 & Table S2), and so the DL-SFG contributions are negligible in the latter case.

S10 – Interferences effect on the BIL/DL intensity ratio

In our experiments, the ion concentration for the system with pH 6 and $[\text{NaCl}] = 0$ M is expected to be on the order of 10^{-5} - 10^{-7} M. For these concentration values the “effective” DL intensity which is experimentally measured at the silica-water interface (as well as any other charged aqueous interface), is known to be largely reduced due to destructive interferences^{27, 32-34}. For the silica-

water interface investigated here, such behavior has been previously observed by Bonn et al.³² and Hore-Tyrode³⁴. From these works, it is evident that, depending on the experimental geometry, the DL intensity is decreased up to 20% of its original intensity (i.e. when interferences effect on the DL-SFG intensity are negligible).

In order to correct our estimated I_{DL}/I_{BIL} ratio for interferences, following the derivation detailed in ref.34, we can recast Equation S7 in the form:

$$I_{DL}/I_{BIL}(\Delta\phi_{DL}) = I_{DL}/I_{BIL}(\Delta\phi_{ref}=10\text{mV}) * |\Delta\phi_{DL} f_3(\kappa, \Delta k_z)|^2 / \Delta\phi_{ref}^2 \quad (\text{S8})$$

Where $f_3(\kappa, \Delta k_z)$ is the interference term, with $f_3(\kappa, \Delta k_z) = \kappa / (\kappa - i\Delta k_z)$, $\kappa =$ inverse of the Debye Length and $\Delta k_z =$ wave vector mismatch for SFG photons generated at different probing depths³⁴. The equation is here written by neglecting BIL-DL correlation terms for simplicity. This is possible because for such a large I_{DL} value ($I_{BIL}/I_{DL}=640$ before correcting for interferences, since $\Delta\phi_{DL}=80$ mV) including the cross terms would not alter the results and conclusions reached from the I_{BIL}/I_{DL} estimation (i.e. that DL contributions are dominant for pH 6 and no ions conditions). However, for a quantitative estimation of the BIL/DL contributions to the vSFG (which is out of the scope of the present investigation), the BIL/DL cross correlation terms should be explicitly included in the modeling.

By using Equation S8 to correct the I_{DL}/I_{BIL} ratio for interferences, and knowing that at pH 6 and no ions conditions $\Delta\phi_{DL}=80$ mV (and $|f_3(\kappa, \Delta k_z)|=0.2$), we obtain $I_{DL}/I_{BIL}=26$, i.e. the DL contribution is still dominant also after correcting for interferences.

	ΔV (mV) @ z=0 nm	I_{DL}/I_{BIL}	$\Delta\phi_{DL}$ (mV) @ z = 1 nm	I_{DL}/I_{BIL}	I_{DL}/I_{BIL} (with Interference)	DL or BIL
pH 12	172	2958.4	83	688.9	688.9	DL
pH 12 + 0.1 M NaCl	121	1464.1	29	84.1	84.1	DL
pH 12 + 0.5 M NaCl	90	810	7	4.9	4.9	DL
pH 6	81	656.1	81	656.1	26.2	DL
pH 6 + 0.1 M NaCl	11	12.1	4	1.6	1.6	DL + BIL
pH 6 + 0.5 M NaCl	10	10	1	0.1	0.1	BIL
pH 2	6.0E-02	3.6E-04	4.4E-05	1.9E-10	1.9E-10	BIL
pH 2 + 0.1 M NaCl	3.0E-02	9.0E-05	9.6E-06	9.2E-12	9.2E-12	BIL
pH 2 + 0.5 M NaCl	4.0E-03	1.6E-06	4.2E-07	1.8E-14	1.8E-14	BIL

Table S2: I_{DL}/I_{BIL} ratio calculated for the surface potential at the silica surface (ΔV @ z = 0 nm) and for the surface potential at the BIL-DL interface ($\Delta\phi_{DL}$ @ z = 1 nm). Reduced I_{DL}/I_{BIL} ratio is also calculated for the pH 6 condition where the interference effect is expected, and the last column indicates whether the DL or the BIL dominates based on the I_{DL}/I_{BIL} ratio.

REFERENCES

1. Tuladhar, A.; Piontek, S. M.; Borguet, E. Insights on Interfacial Structure, Dynamics, and Proton Transfer from Ultrafast Vibrational Sum Frequency Generation Spectroscopy of the Alumina (0001)/Water Interface. *J. Phys. Chem. C* **2017**, *121*, 5168-5177.
2. Eftekhari-Bafrooei, A.; Borguet, E. Effect of Surface Charge on the Vibrational Dynamics of Interfacial Water. *J. Am. Chem. Soc.* **2009**, *131*, 12034-12035.
3. Eftekhari-Bafrooei, A.; Borguet, E. Effect of Electric Fields on the Ultrafast Vibrational Relaxation of Water at a Charged Solid-Liquid Interface as Probed by Vibrational Sum Frequency Generation. *J. Phys. Chem. Lett.* **2011**, *2*, 1353-1358.
4. Tuladhar, A.; Dewan, S.; Kubicki, J. D.; Borguet, E. Spectroscopy and Ultrafast Vibrational Dynamics of Strongly Hydrogen Bonded OH Species at the α -Al₂O₃(11 $\bar{2}$ 0)/H₂O Interface. *J. Phys. Chem. C* **2016**, *120*, 16153-16161.
5. Tuladhar, A.; Piontek, S. M.; Frazer, L.; Borguet, E. Effect of Halide Anions on the Structure and Dynamics of Water Next to an Alumina (0001) Surface. *J. Phys. Chem. C* **2018**, *122*, 12819-12830.
6. Dewan, S.; Yeganeh, M. S.; Borguet, E. Experimental Correlation Between Interfacial Water Structure and Mineral Reactivity. *J. Phys. Chem. Lett.* **2013**, *4*, 1977-1982.

7. Eftekhari-Bafrooei, A.; Borguet, E. Effect of Hydrogen-Bond Strength on the Vibrational Relaxation of Interfacial Water. *J. Am. Chem. Soc.* **2010**, *132*, 3756-3761.
8. McGuire, J. A.; Shen, Y. R. Ultrafast Vibrational Dynamics at Water Interfaces. *Science* **2006**, *313*, 1945-1948.
9. Fecko, C. J.; Eaves, J. D.; Loparo, J. J.; Tokmakoff, A.; Geissler, P. L. Ultrafast Hydrogen-Bond Dynamics in the Infrared Spectroscopy of Water. *Science* **2003**, *301*, 1698-1702.
10. Lock, A. J.; Bakker, H. J. Temperature Dependence of Vibrational Relaxation in Liquid H₂O. *J. Chem. Phys.* **2002**, *117*, 1708-1713.
11. Cowan, M. L.; Bruner, B. D.; Huse, N.; Dwyer, J. R.; Chugh, B.; Nibbering, E. T. J.; Elsaesser, T.; Miller, R. J. D. Ultrafast Memory Loss and Energy Redistribution in the Hydrogen Bond Network of Liquid H₂O. *Nature* **2005**, *434*, 199-202.
12. Piontek, S. M.; Tuladhar, A.; Marshall, T.; Borguet, E. Monovalent and Divalent Cations at the alpha-Al₂O₃(0001)/Water Interface: How Cation Identity Affects Interfacial Ordering and Vibrational Dynamics. *J. Phys. Chem. C* **2019**, *123*, 18315-18324.
13. Lock, A. J.; Woutersen, S.; Bakker, H. J. Ultrafast Energy Equilibration in Hydrogen-Bonded Liquids. *J. Phys. Chem. A* **2001**, *105*, 1238-1243.
14. Rey, R.; Møller, K. B.; Hynes, J. T. Ultrafast Vibrational Population Dynamics of Water and Related Systems: A Theoretical Perspective. *Chem. Rev.* **2004**, *104*, 1915-1928.
15. Dove, P. M. The Dissolution Kinetics of Quartz in Sodium Chloride Solutions at 25 Degrees to 300 Degrees C. *Am. J. Sci.* **1994**, *294*, 665-712.
16. Bard, A. J.; Faulkner, L. R. Fundamentals and Applications. *Electrochemical Methods* **2001**, *2*, 482.
17. Bard, A. J.; Faulkner, L. R.; Leddy, J.; Zoski, C. G., *Electrochemical Methods: Fundamentals and Applications*; Vol. 2, Wiley: New York, 1980.
18. Ong, S.; Zhao, X.; Eissenthal, K. B. Polarization of Water Molecules at a Charged Interface: Second Harmonic Studies of the Silica/Water Interface. *Chem. Phys. Lett.* **1992**, *191*, 327-335.
19. Ugliengo, P.; Sodupe, M.; Musso, F.; Bush, I. J.; Orlando, R.; Dovesi, R. Realistic Models of Hydroxylated Amorphous Silica Surfaces and MCM-41 Mesoporous Material Simulated by Large-scale Periodic B3LYP Calculations. *Advanced Materials* **2008**, *20*, 4579-4583.
20. VandeVondele, J.; Krack, M.; Mohamed, F.; Parrinello, M.; Chassaing, T.; Hutter, J. Quickstep: Fast and Accurate Density Functional Calculations Using a Mixed Gaussian and Plane Waves Approach. *Computer Physics Communications* **2005**, *167*, 103-128.
21. Becke, A. D. Density-Functional Exchange-Energy Approximation with Correct Asymptotic Behavior. *Phys. Rev. A* **1988**, *38*, 3098-3100.
22. Lee, C.; Yang, W.; Parr, R. G. Development of the Colle-Salvetti Correlation-Energy Formula into a Functional of the Electron Density. *Phys. Rev. B* **1988**, *37*, 785-789.
23. Stefan, G. Semiempirical GGA-type Density Functional Constructed with a Long-Range Dispersion Correction. *J. Comput. Chem.* **2006**, *27*, 1787-1799.
24. Goedecker, S.; Teter, M.; Hutter, J. Separable Dual-Space Gaussian Pseudopotentials. *Phys. Rev. B* **1996**, *54*, 1703-1710.
25. Pfeiffer-Laplaud, M.; Gaigeot, M.-P. Adsorption of Singly Charged Ions at the Hydroxylated (0001) α -Quartz/Water Interface. *J. Phys. Chem. C* **2016**, *120*, 4866-4880.

26. Pfeiffer-Laplaud, M.; Gaigeot, M.-P. Electrolytes at the Hydroxylated (0001) α -Quartz/Water Interface: Location and Structural Effects on Interfacial Silanols by DFT-Based MD. *J. Phys. Chem. C* **2016**, *120*, 14034-14047.
27. Wen, Y.-C.; Zha, S.; Liu, X.; Yang, S.; Guo, P.; Shi, G.; Fang, H.; Shen, Y. R.; Tian, C. Unveiling Microscopic Structures of Charged Water Interfaces by Surface-Specific Vibrational Spectroscopy. *Phys. Rev. Lett.* **2016**, *116*, 016101.
28. Pezzotti, S.; Galimberti, D. R.; Shen, Y. R.; Gaigeot, M.-P. Structural Definition of the BIL and DL: a New Universal Methodology to Rationalize Non-Linear $\chi^{(2)}(\omega)$ SFG Signals at Charged Interfaces, Including $\chi^{(3)}(\omega)$ Contributions. *Phys. Chem. Chem. Phys.* **2018**, *20*, 5190-5199.
29. Pezzotti, S.; Galimberti, D. R.; Gaigeot, M.-P. 2D H-Bond Network as the Topmost Skin to the Air–Water Interface. *J. Phys. Chem. Lett.* **2017**, *8*, 3133-3141.
30. Pezzotti, S.; Serva, A.; Gaigeot, M.-P. 2D-HB-Network at the Air-Water Interface: A Structural and Dynamical Characterization by Means of Ab Initio and Classical Molecular Dynamics Simulations. *J. Chem. Phys.* **2018**, *148*, 174701.
31. Pezzotti, S.; Galimberti, D.; Shen, Y.; Gaigeot, M.-P. What the Diffuse Layer (DL) Reveals in Non-Linear SFG Spectroscopy. *Minerals* **2018**, *8*, 305.
32. Schaefer, J.; Gonella, G.; Bonn, M.; Backus, E. H. G. Surface-Specific Vibrational Spectroscopy of the Water/Silica Interface: Screening and Interference. *Phys. Chem. Chem. Phys.* **2017**, *19*, 16875-16880.
33. Gonella, G.; Lütgebaucks, C.; de Beer, A. G. F.; Roke, S. Second Harmonic and Sum-Frequency Generation from Aqueous Interfaces Is Modulated by Interference. *J. Phys. Chem. C* **2016**, *120*, 9165-9173.
34. Hore, D. K.; Tyrode, E. Probing Charged Aqueous Interfaces Near Critical Angles: Effect of Varying Coherence Length. *J. Phys. Chem. C* **2019**, *123*, 16911-16920.

5.10 Summary of the chapter

We have provided a microscopical characterization of the amorphous silica-water interface organization in response to the variations in the hydrophilic character of the silica surface at the interface with liquid water (see sections 5.6 and 5.7) and in response to the electrolytes concentration (see section 5.9).

In section 5.6 we have investigated the evolution of silica-water interactions by tuning the degree of hydroxylation of the silica surface and monitoring the outcome on the solid-water SFG signatures assigned to specific water OH populations. We have identified the presence of two interfacial water populations respectively located above the hydrophobic (silanols poor) and hydrophilic (silanols rich) microscopic patches of the amorphous silica surface, each one characterized by a specific solid-water SFG signature. Water molecules above the hydrophobic patches point one of their OH groups toward siloxane bridging oxygen atoms giving rise to a positive SFG band at $\sim 3660\text{ cm}^{-1}$, while water molecules above the hydrophilic patches point one of their OH groups toward an in-plane surface silanol site giving rise to a broad positive SFG band at $\sim 3470\text{ cm}^{-1}$. By monitoring the evolution of the two SFG water-solid marker bands as a function of the spatial extension of hydrophobic and hydrophilic patches over the silica surface we have identified the SFG spectroscopic marker bands for the hydrophobicity of water.

In section 5.7 we have characterized the evolution of the structural arrangements of the interfacial water molecules in response to variations in the silica surface degree of hydroxylation. By tuning the degree of hydroxylation of the amorphous surface model we can play with the patches's size, and hence observe the outcome on the interfacial water organization. We have found the relative dimensions of hydrophilic and hydrophobic silica surface patches to dictate the BIL-water organization. At high and intermediate degree of hydroxylation (7.6 and 4.5 SiOH/nm²), where none of the hydrophobic and hydrophilic patches prevail on the surface, we observe a disordered BIL-water organization characterized by the simultaneous presence of low (above the hydrophobic patches) and high coordinated (above the hydrophilic patches) water molecules. The lowering of the surface degree of hydroxylation (increasing the size of the hydrophobic patches) down to the value of 3.5 SiOH/nm² causes a drastic change in the water organization at the interface with the silica: water molecules maximize water-water interactions formed parallel to the surface (horizontal order) to compensate for the lack of solid-water interactions (vertical order). We observe the transition from the inhomogeneous water BIL structure (found at the 4.5 and 7.6 SiOH/nm² hydroxylated surfaces) to an extended homogeneous 2D H-Bond network, characterized by water molecules with a homogeneous coordination number. This is the same organization that we revealed and fully characterized at the prototypic hydrophobic air-water interface in ref.[103].

We have investigated in section 5.9 how the structure and the SFG response of electrolytic silica-water interfaces is affected by changes in the solution ionic strength (NaCl electrolyte is used). We have revealed that the addition of electrolytes at the 4.5 SiOH/nm^2 hydroxylated silica-water interface produces the same effect as decreasing the surface hydroxylation, thus inducing the transition from the inhomogeneous water-BIL structure obtained at the 4.5 SiOH/nm^2 silica-water interface to an interfacial water that is highly interconnected into a 2D-H-Bond network, reminiscent of the one observed and characterized at the hydrophobic air-water interface[48]. We propose such variation in the microscopic organization of the BIL-water to be at the origin of the decrease in the vibrational life time of vibrationally excited water OH stretching modes measured experimentally when increasing the solution electrolytes concentration.

Chapter 6

The amorphous silica aqueous surface as a function of pH conditions

The results presented in this chapter have been obtained in collaboration with one of our experimental partners: Prof. W. Liu's group at Fudan University in Shanghai, China, in collaboration with Prof. Y.R. Shen at the University of Berkeley, USA

6.1 Generalities

Beyond the interfacial water organization, another important aspect to consider when dealing with aqueous silica interfaces is the silica surface structural organization and ionization state as a function of the solution pH.

The ratio between SiOH/SiO⁻ groups at the aqueous silica surfaces is tuned by the solution pH condition. Another factor that influences the protonation state of the surface, even if less dominant, is the solution ionic strength (see section 5.3 of the previous chapter). The promotion of a negative charge via deprotonation of SiOH groups at the silica surface, in response to an increase in the pH condition, can have an enormous impact on water and biomolecules adsorption on silica[267].

The generation of a negative charge on amorphous silica surfaces has been typically followed by means of surface sensitive spectroscopic techniques[232, 212]. In particular Ong *et al.*[212] have followed the promotion of a negative charge at the aqueous fused silica surface by measuring the SHG (second harmonic generation) response of water molecules in the DL (Diffuse Layer) as a function of the solution pH conditions (see Fig. 6.1). The resulting SHG titration curve is characterized by the presence of two successive jumps divided by 4 pH units that clearly reveal the existence of two silanol surface groups with distinct acidities: 19 % of the silanols exhibit a pKa of 4.5

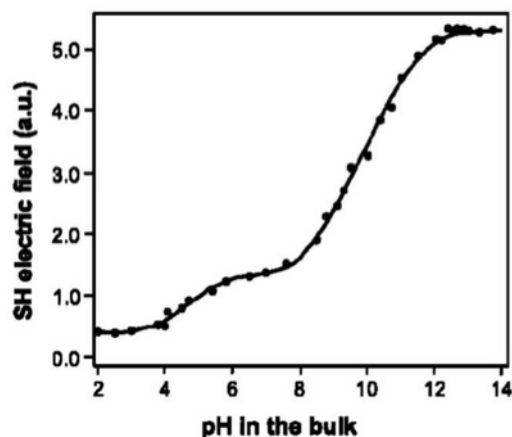


Figure 6.1: Intensity of the SHG (second harmonic generation) electric field (proportional to the surface charge) at the fused silica-water interface as a function of the solution pH. Figure adapted with permission from ref.[212]

(acidic silanols), while the remaining 81% are found with a pKa value of 8.5 (non acidic silanols). Similar results have been obtained by Shen *et al.*[268] on the aqueous (0001) α -quartz surface investigated by means of SFG spectroscopy. Also evanescent wave cavity ring-down spectroscopy experiments based on the adsorption of cationic species on silica as a function of the pH conditions has confirmed the bimodal acidity of silica[267].

Conversely experiments[269] based on acid-base titration do not find any pH jump by measuring the density of negative charge on silica surfaces as a function of pH (see Fig. 6.2). The reason for this discrepancy between the

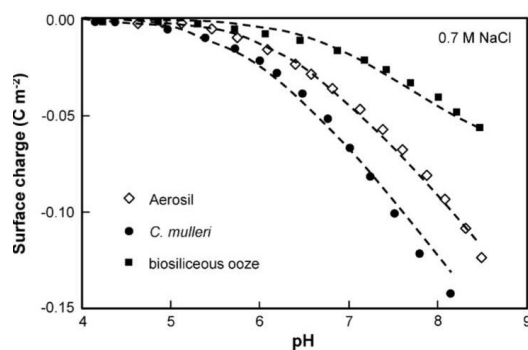


Figure 6.2: Surface charge densities obtained by proton titration for three different silica, one aerosil and two biological silica, as a function of pH. Figure adapted with permission from ref.[269]

data obtained by SHG and SFG measurements with the ones obtained by acid-base titration is still not known.

In the last decade computational works have attempted to microscopically identify the nature of the acidic and non acidic populations of silanols by associating their chemical nature (geminals, isolated and vicinals) and their

H-Bond connectivity with water (silanols H-Bonds acceptor and/or donor with respect to water) with the calculated pKa values[181, 193, 270]. In particular Pfeiffer *et al.*[181], calculating the silanols pKa's at the amorphous silica-water interface by biased DFT-MD techniques, have found the water to play a key role in determining the silanols acidity by varying the stabilization of the silanols conjugate bases as a function of the conjugate bases exposure to water. These authors further excluded a possible role of the nature of the silanols (i.e. geminal, isolated, vicinal) in the silica bimodal acidity.

Rimola *et al.*[184] have explained the silica bimodal acidity by attributing respectively the acidic silanol sites (pKa~4.5) to the terminal SiOH groups involved in a chain of mutually H-Bonded silanols and the non-acidic silanol sites (pKa~8.5) to isolated SiOH groups.

Interestingly the computational work of Leung *et al.*[271] suggests the silanols on strained surface regions with low silanol coverage to be associated to the acidic silanols (pKa~4.5).

An important aspect that has not been considered up to now in the literature when modelling, silanol acidities is the possible direct dependence of the silanol's pKa values to the solution pH condition. For instance all the above mentioned computational works have calculated the acidity of silanol groups without taking into account the possible effects of the silica surface charge (at high pH condition). An isolated species in water has, by definition, a pKa value which is independent from the pH condition of the solution while the pKa value of a surface group at an interface can be affected by the negative surface charge within a certain proximity (i.e. generated by the deprotonation of other silanol groups in the proximity of the first one) that is in turn dependent on the pH condition of the solution. This implies that a dependence of the silanols pKa values on the solution pH condition cannot be *a priori* excluded. This is an issue that we will in part consider in section 6.5 of this chapter. The importance of such aspect, especially at high pH conditions, is also highlighted in the review by Rimola *et al.*[184].

Another aspect that has not been taken into account up to now is how the deprotonation of silanol groups on amorphous silica can lead to species other than silanolate groups. For instance, in section 6.3 we will find that the deprotonation of certain silanol groups does not lead to stable silanolate species. We indeed observe along our DFT-MD simulations the formation of exposed silicium five fold coordinated species (Si5). This will be shown in section 6.3.

As highlighted in the review by Tielens[193] the formation of Si5 species is observed on crystalline silicates compressed at high pressure[272, 273], which is of great interest in the domain of geophysics and geochemistry in the upper and lower mantles of the Earth crust. Si5 species are supposed to have significant influence on wave velocities anomalies, deformation mechanisms and chemical reactivity of silicate rocks[193]. Interestingly, Si5 structures have also been found on the dry (011) α -quartz surface as result of the reconstruction process following the homolytic fracture of α -quartz crystal at room temperature[274]. In these works Si5 structures have been systematically

found to be characterized by a silicon atom penta coordinated by oxygens at the center of trigonal base bipyramidal and/or square pyramidal geometries.

It is clear from the above discussion that a technique able to probe directly the evolution of silica surfaces when exposed to increasing pH conditions is necessary in order to rationalize the acid-base properties of silica. SFG spectroscopy in the phonon frequency region ($800\text{--}1200\text{ cm}^{-1}$) probes the solid surface vibrational modes and the associated surface structures at the interface with water[275, 183, 276, 277, 278, 279]. It thus represents the perfect candidate for such characterization.

The works by Liu *et al.*[183, 275] on aqueous and dry silica surfaces have experimentally identified and characterized the SFG responses of silica surface groups in the phonon frequency region ($800\text{--}1200\text{ cm}^{-1}$). In particular, the phonon ssp SFG spectrum of the neat (0001) α -quartz surface under ambient condition[183] reports two vibrational modes at 880 and 980 cm^{-1} (see Fig. 6.3-A) that have been assigned to the Si-O stretching vibrations respectively of the Si-O-Si and Si-O(H) species at the surface. Liu *et al.*[183] have followed

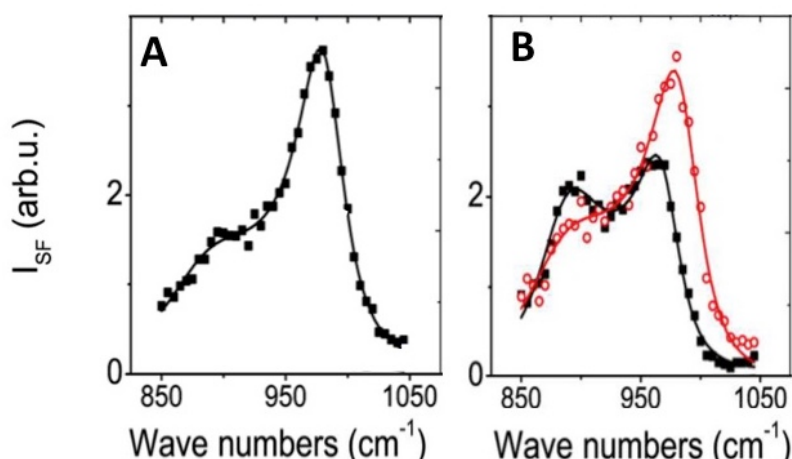


Figure 6.3: SSP-SFG spectra of: **A**) freshly cleaned (0001) α -quartz surface at ambient condition. **B**) (0001) α -quartz surface after being baked at 100°C (black curve with solid squares) and then rehydroxylated (red curve with open circles). Figure adapted with permission from ref.[183]

directly the interconversion process between the Si-O-Si and Si-OH groups by monitoring their associated SFG-marker bands when the surface is exposed to dehydroxylation-hydroxylation cycles. The dehydroxylation of the surface is obtained by heat treating the quartz at high temperature ($2\text{ SiOH} \rightarrow \text{Si-O-Si} + \text{H}_2\text{O}$), while the hydroxylation is obtained by putting the surface in contact with water ($\text{Si-O-Si} + \text{H}_2\text{O} \rightarrow 2\text{ SiOH}$). The heat treatment of the silica surface at 100°C (black curve with solid squares in Fig. 6.3-B) leads to a decrease in intensity of the 980 cm^{-1} peak assigned to Si-OH groups and an increase of the 880 cm^{-1} assigned to Si-O-Si groups. When compared to the

non temperature pretreated quartz SFG spectrum (Fig. 6.3-A) one concludes that there is a conversion of silanol groups Si-OH to siloxane bridges Si-O-Si. The process of dehydroxylation is found to be reversible. Indeed, after rehydroxylating the quartz surface by contact with water ($\text{Si-O-Si} + \text{H}_2\text{O} \rightarrow 2 \text{SiOH}$) the final spectrum is the same one as the one of the non pretreated surface. See red curve with open circles in Fig. 6.3-B.

This work reveals the capability of SFG experiments in the phonon frequency region ($800\text{-}1200 \text{ cm}^{-1}$) to spectroscopically describe changes in the silica surface organization in response to perturbations in its chemical and physical environment.

This is the context of our theoretical work which main objective is to characterize the complex evolution of the silica surface structure and chemical properties in response to variations in the bulk water pH conditions. To that end, we couple experimental SFG phonon spectroscopy with computational techniques.

The direct access to the surface groups chemical nature and structural organizations under different pH conditions offered by phonon SFG experiments, coupled with the molecular rationalization emerging from DFT-MD and enhanced sampling of biased DFT-MD simulations provides a deep insight into the controversial acidity of the silica surface.

In this chapter we first focus on the experimental spectroscopic evidences from the SFG spectra of an amorphous silica-water interface recorded as a function of the pH conditions in the $900\text{-}1150 \text{ cm}^{-1}$ phonon frequency range (section 6.2). The experimental findings show that a molecular picture based only on the balance between Si-OH and Si-O⁻ species at the silica surface is not enough in order to rationalize the trends in the phonon SFG bands in the 4-9 pH range. In particular, the spectroscopic data suggest the appearance of chemical species at the silica-water interface other than silanol or silanolate groups when increasing the solution pH conditions.

We then provide in section 6.3 a theoretical description at the molecular level of the amorphous silica aqueous surface chemistry under various pH conditions by means of DFT-MD and DFT-MD metadynamics simulations. In order to mimic the right deprotonation state of the model silica surface at a given pH condition we have initially characterized the pKa of the various Si-OH surface groups in contact with water. The formation of Si5 species on the silica surface in response to an increase of the solution pH conditions is revealed and characterized as a function of the pKa of the silanols.

Our study continues in section 6.4 where we provide a direct link with experiments by computing the spectroscopic signatures arising from the silica surface models exposed to different pH conditions.

A complete rationalization of the SFG experiments is reached in section 6.5 where the stability of the Si5 species as a function of the pH conditions is found to nicely match the SFG bands trends.

Our results provide a new interesting molecular picture of the silica-water interface at different pH conditions coherent with the surface Si-O SFG ex-

periments on fused silica-water interface from the group of Prof. W. Liu (Fudan University, China).

6.2 Experimental data and opened questions (from Y.R.Shen, W.Liu *et al.*, Fudan University)

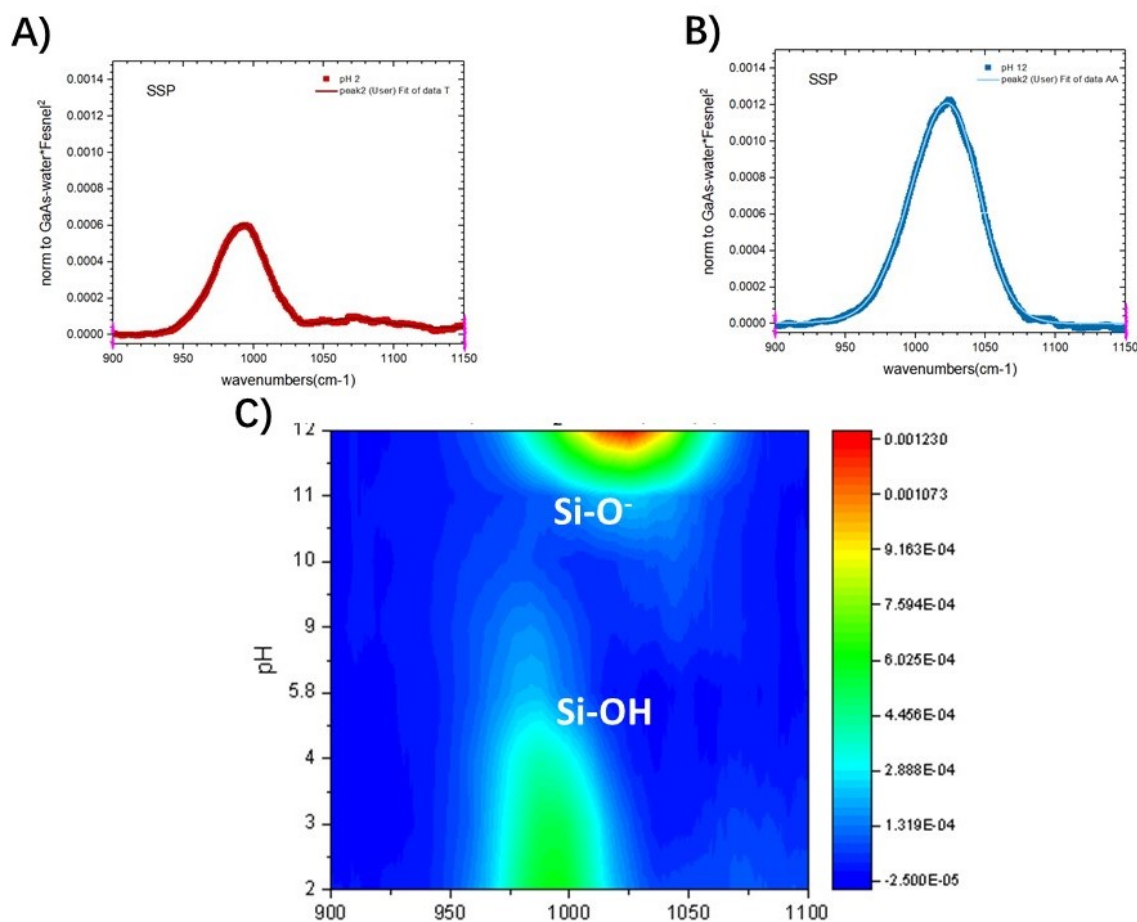


Figure 6.4: Panel A: *ssp* SFG spectrum of the amorphous silica-water interface at $pH=2$, recorded in the phonon frequency region ($900-1150\text{ cm}^{-1}$).

Panel B: *ssp* SFG spectrum of the amorphous silica-water interface at $pH=12$, recorded in the phonon frequency region ($900-1150\text{ cm}^{-1}$).

Panel C: Evolution of the amorphous silica-water interface phonon SFG spectra as a function of the solution pH (pH range 2-12). On the X axis are reported the frequencies (cm^{-1}) and on the Y axis the pH values. The colors represent the SFG intensity in arbitrary units (a.u.). The SFG intensity increases from blue to red. All spectra have been recorded by the group of Prof. Weitao Liu at Fudan University (China).

The SFG spectra of an amorphous silica-water interface have been recorded as a function of pH conditions in the $900-1150\text{ cm}^{-1}$ phonon frequency range, where the Si-O surface modes allow to directly detect the protonation state

of the silanol sites exposed to water. In particular, the specific signatures of Si-O(H) and SiO⁻ terminations can be determined by considering the SFG spectra recorded at extreme pH 2 (Si-OH) and 12 (SiO⁻) conditions.

The main spectral feature at pH 2, is a prominent band centred at 980 cm⁻¹ (Panel A of Fig. 6.4). Since the silica surface is supposed to be on average fully protonated at this specific pH condition[178], the 980 cm⁻¹ band is assigned to the Si-O vibration of Si-OH groups. Note that the IR marker bands of the silica lattice Si-O-Si symmetric and antisymmetric stretches vibrations are respectively at 1107 and 876 cm⁻¹ [280], therefore an overlap in frequency between the Si-O(H) and the Si-O-Si bands can be excluded.

Increasing the pH condition up to 12, where only silanolate groups SiO⁻ are supposed to be present at the silica surface[212], one single band at 1020 cm⁻¹ is recorded (see Panel B Fig. 6.4). The band at 1020 cm⁻¹ is thus assigned as the SFG spectroscopic marker band of SiO⁻ groups. The assignments presented here are in agreement with previous spectroscopic assignments on colloidal silica particles obtained by FTIR and Raman spectroscopies[280].

The evolution of the amorphous silica-water interface SFG spectra in the 800-1150 cm⁻¹ frequency range as a function of the increase of the solution pH (2-12) is now presented in Panel C of Fig. 6.4. The colors represent the SFG intensity in arbitrary units (a.u.). The SFG intensity increases from blue to red.

At low pH conditions (in the range 2-4), the Si-O(H) band at 980 cm⁻¹ is systematically present, with the same intensity between pH 2 and 4. This is the signature of Si-OH groups at the surface, as expected. The surface is fully protonated, without acid-base processes occurring at the silica-water interface. This is coherent both with the experimental value of the Point of Zero Charge (PZC \sim 2-4) measured in ref.[178] and previous silanol groups pKa's measurements[212].

Increasing the pH from 4 to 9, one can see that there is a huge drop in SFG intensity, plus a red shift in frequency by 30 cm⁻¹ when intensity is present. The SFG band amplitude is hence found to decrease by 50 % at pH 5.8, to finally disappear around pH \sim 9.5. There is one striking conclusion that appears from the SFG plot: while the SFG intensity of the 980 cm⁻¹ band (pH=2-4) disappears in between pH \sim 4 and 9.5, there is no simultaneous appearance of any other SFG band in the 900-1100 cm⁻¹ range for this pH interval. Further experiments outside of the 900-1100 cm⁻¹ frequency range have not shown any other spectral band appearing.

It is only in the pH range 9-12 that one can see the appearance of an SFG signal, the one corresponding to SiO⁻ at \sim 1020 cm⁻¹. The SiO⁻ signal appears for the first time around pH \sim 9.5-10.0 and then its intensity increases up to pH 12. Thus the drop of the Si-O(H) SFG signal is not accompanied by the simultaneous appearance of the SiO⁻ marker band, as it should be expected when gradually going from fully protonated silica surface (PZC) towards basic conditions. Notice that the appearance of the SiO⁻ band at pH

10 is in contrast with previous pKa measurements estimating the emergence of the SiO⁻ groups at the silica surface around pH \sim 5-6 [212, 232, 267], i.e. 20 % of the silanol groups are predicted to be already deprotonated around pH \sim 6.

One possible explanation for the trend of the two marker bands could be the reorientation of silanol (Si-OH) and silanolate (SiO⁻) groups in response to the silica surface deprotonation. The Si-O bond reorientation could indeed induce variation in the SFG activity of the surface Si-OH and SiO⁻ groups, explaining the trends in the two associated bands intensity observed in the pH range 4-9. To test such hypothesis, phonon-SFG spectra as a function of pH were recorded with the ppp configuration. The comparison between ssp and ppp SFG spectra in the 800-1200 cm⁻¹ frequency region is reported in Fig.1 of section 6.7.1. The ppp/ssp amplitude ratio of Si-O(H) and SiO⁻ bands changes only slightly with increasing pH, indicating that there is no dramatic orientational change in the Si-O bonds at the surface. For this reason the surface groups re-orientation has to be disregarded as possible cause of the SFG drop in the pH range 4-9.

The spectroscopic data clearly mean that the silanol species that get deprotonated do not lead to stable silanolate groups (SiO⁻) in the pH range 4-9. Therefore, the possible appearance of new chemical species at the silica-water interface due to surface reconstruction(s) in this pH range has to be considered.

It is obvious that a description at the molecular level is required in order to directly characterize the surface chemistry governing the silica-water interface at different pH conditions, that in turn can explain the SFG features.

To that end, we have modelled the silica-water interface under various pH conditions by means of DFT-MD simulations and we have extracted vibrational marker bands from the simulations.

6.3 DFT-MD at aqueous silica and pKa values of silanols. Appearance of Si5 motifs at the surface.

A model of amorphous silica with a degree of surface hydroxylation of 4.5 OH/nm²[31], close to the 5 OH/nm² average degree of hydroxylation found experimentally for a set of about 100 different silica aerogel samples in absence of pretreatment [254, 176, 177], is used in our DFT-MD simulations.

This model surface is 13.386 Å X 13.286 Å X 15.0 Å in the three directions of space and put in contact with water (120 water molecules), hence the z direction of the box being 35 Å. At the surface of this amorphous silica there are 8 Si-OH groups and three exposed Si-O-Si bridges. These two groups form patches of hydrophilic and hydrophobic (less hydrophilic at least) regions, see our ref.[135, 243].

It is therefore relevant to characterize the pKa of the various Si-OH surface groups in contact with water, and thus be able to mimic the right depro-

nation state of the model silica surface at a given pH condition. It is known experimentally [212] that there is a bimodal behaviour of the silica silanols, with one group of acidic character and another group of basic character. Simulations [182, 181, 271] have tried to unveil the microscopic origin of these 2- pK_a behaviours. Here, we want to deprotonate Si-OH groups as a function of increasing pH and characterize the deprotonated surface in terms of structure and SFG fingerprints. It is thus important to deprotonate the right sites at the right pH. Therefore, we have performed DFT-MD simulations in order to calculate the pK_a values of all the 8 Si-OH groups present at the surface of our model aqueous amorphous silica.

To that end, metadynamics DFT-MD are performed (see sections 6.7.2 and 6.7.3 for details). The biased metadynamics are done with the coordination number of the chosen silanol oxygen with respect to all the hydrogen atoms of the system (CN_{Si-O-H}) as reaction coordinate. This allows to model one single silanol deprotonation event at a time, silanol by silanol. Adding the coordination number of the silanol oxygen with respect to all the silicon atoms of the silica ($CN_{Si-O-Si}$) as a second reaction coordinate allows to sample possible surface reconstruction processes. If no surface reconstructions are taking place a reaction path orthogonal to the $CN_{Si-O-Si}$ coordinate would be observed.

The microscopic picture emerging from the metadynamics simulations is that there are two groups of surface silanols, that differ by the subsequent reorganization processes once one Si-OH is deprotonated (Panel A and B of Fig. 6.5):

A) We find that 37.5 % of the silanol groups at the aqueous 4.5 OH/nm² silica surface (three Si-OH groups over eight in our model) are not stable as silanolate species once deprotonated by water.

There is indeed a nucleophilic attack on the first Si neighbour atom (belonging to a SiO₄ tetrahedra) leading to the formation of a new Si-O covalent bond in between this Si and the one that was initially carrying the OH silanol (see Panel A of Fig. 6.5). The reconstruction process results in the formation of an exposed silicium five fold coordinated species (Si5), as illustrated in Panel A of Fig. 6.5, characterized by a base square pyramidal geometry with the five coordinated silicium atom at the center and the oxygen atoms at the edges. The free energy landscape associated to this nucleophilic attack and the subsequent reconstruction, is reported in Panel A-Right. It shows two well defined minima respectively related to the Si-OH (reactant species) and Si5 species (final product species). These minima correspond to the $CN_{Si-O-Si}$ reaction coordinate equal to 1.0 and 1.6 respectively. The surface reconstruction process is found to proceed from the Si-OH minimum to the Si5 stable one through a concerted mechanism characterized by the simultaneous proton transfer from the Si-OH group to water and the formation of a new Si-O-Si bond. The resulting reconstruction process is endoergonic ($\Delta G(G_{SiO^-} - G_{SiOH}) > 0$) with the Si-OH minimum 22.3 kJ/mol more stable with respect to the Si5 one. No minimum is found for the SiO⁻ group,

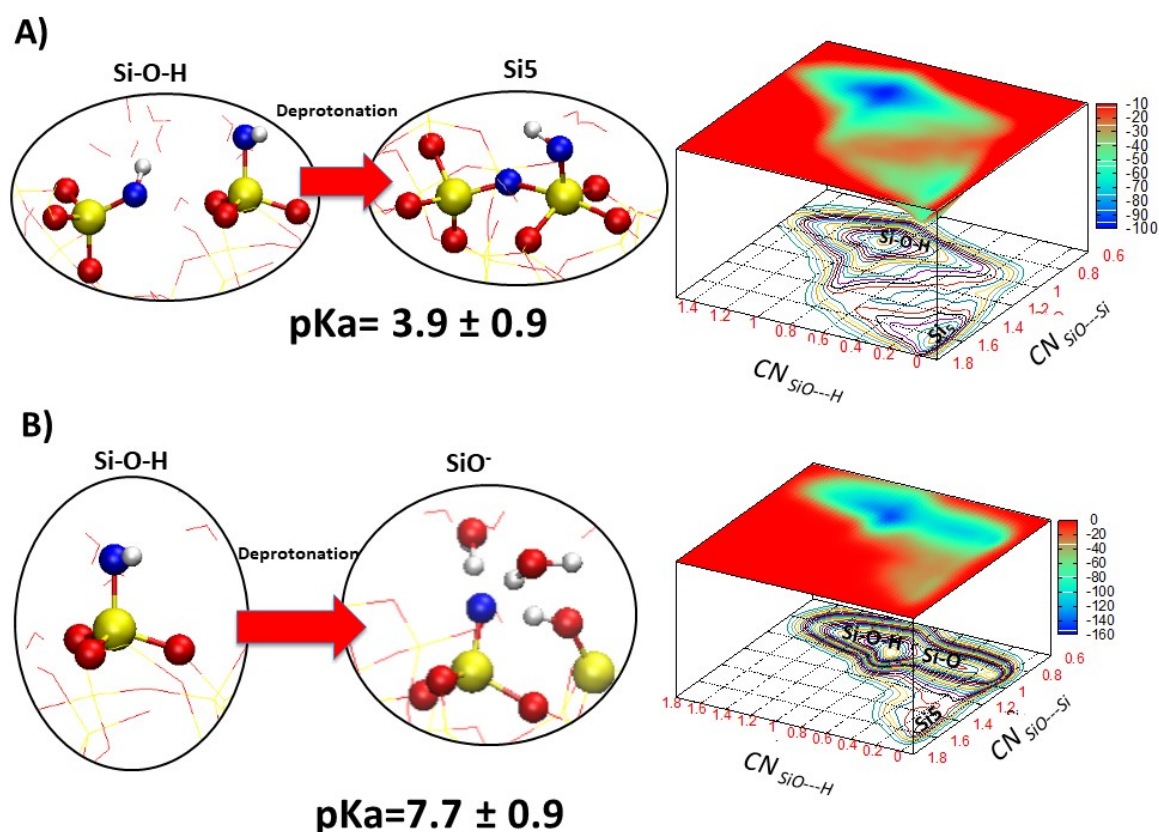


Figure 6.5: Panel A: On the top left, reaction scheme of the silanol deprotonation process leading to Si5 structures at the amorphous silica-water interface. On the top right, the free energy landscape associated with the considered reconstruction process. Two minima associated with the silanol Si-OH and Si5 groups are found as written in the plot. The formation of the Si5 structure occurs through a concerted step-wise mechanism with the simultaneous deprotonation of the Si-OH group by water and the formation of a Si-O-Si covalent bond. At the bottom of Panel A is reported the averaged pKa value of the silanol groups exhibiting such behaviour. Panel B: Reaction scheme and free energy landscapes associated with the silanol deprotonation process leading to the formation of a stable silanolate (SiO⁻) species at the amorphous silica-water interface. Three minima associated with the silanol (Si-OH), silanolate (SiO⁻) and Si5 structures are found, as indicated in the plot. At the bottom of the Panel is reported the average pKa value with its standard deviation of the silanol groups showing such behaviour

indicating that it is not stable at the surface. From this free energy surface we can calculate (see section 6.7.3) the pKa value of the Si-OH site. The pKa calculations reveal an acidic character for two of the three silanols behaving as described above once deprotonated, with an average pKa value of 3.9 ± 0.9 (see bottom of Panel A). It was not possible to calculate the pKa value of one of these silanols because the formation of the covalent Si-O-Si bond induces a chain reaction along the silica surface with the consecutive cleavage and formation of new Si-O-Si bonds, thus preventing the calculation of the pKa value of this Si-OH site.

B) We find that the remaining 62.5 % Si-OH (five Si-OH sites over eight

for our model) of the aqueous 4.5 OH/nm² surface do have the expected behaviour of forming a stable silanolate species once deprotonated by water (see Panel B of Fig. 6.5). The silanolate group is found to form stable H-Bonds with water and/or neighbouring silanol groups of the surface (the oxygen average coordination number is found equal to 3.0). The free energy landscape of the deprotonation process reveals the existence of two stable minima respectively associated with the Si-OH and SiO⁻ groups located respectively at 1.0 and 0.4 along the CN_{Si-O--H} reaction coordinate.

The reaction is found to proceed directly from the "Si-OH minimum" to the "SiO⁻ one" along the CN_{Si-O--H} reaction coordinate. The minimum associated to the Si5 structure (minimum located at around 1.6 for the CN_{Si-O--Si} reaction coordinate), when it is present (one metadynamics over five only), results in an unstable species and the minimum is found flat (~ 5 kJ/mol deep) at a higher energy with respect to the silanol and silanolate ones ($\Delta G(G_{Si5} - G_{SiOH}) = 95$ kJ/mol). The pKa calculations reveal that all these Si-OH groups are basic with an average pKa value of 7.7 ± 0.9 .

Two crucial conclusions are obtained here from the DFT-MD simulations:

1) We find a bimodal acid-base behaviour of the Si-OH groups at the aqueous silica surface, which is compatible with previous experiments[212, 232]. The silanols that lead to the formation of stable Si5 species, once deprotonated, are acidic with an average calculated pKa value of 3.9, while the ones forming stable silanolate SiO⁻ species are found to be about 3.8 pKa units less acidic with an average pKa=7.7. The pKa difference of 3.8 units we have found between the acidic-basic silanol types is in line with the experimental value of 4 pKa units. Note however that our acidic and basic sites are on average slightly more acidic than in the experiments: 3.9 in our DFT-MD *vs* 4.5 in the experiments for the acidic silanol groups and 7.7 in our DFT-MD *vs* 8.5 in the experiments for the less acid ones[212]. Such discrepancy between theoretical and experimental pKa values could arise from the limited number of silanols investigated in the simulations, thus a reduced statistics. Another possible explanation is the chosen DFT set-up here with BLYP functional plus D2 correction. However our results present an excellent agreement with the experimental trend, as highlighted by the good theoretical reproduction of the experimental pKa differences between the acidic and less acidic silanol groups (3.8 *vs* 4.0 pKa units).

2) Our calculations reveal the nature of the silanol conjugate base, i.e. Si5 or SiO⁻, to be an essential factor in determining the amorphous silica surface groups acidity. The relevance of the conjugate base has already been shown in ref.[181]. Our findings are in line with the pKa calculations of Pfeiffer *et al.*[181], showing the silica surface acidity to be essentially determined by the stability of the silanol conjugate base.

In particular, the metadynamics calculations reveal here that the Si5 species at the surface is 22 kJ/mol more stable as silanol conjugate base than

the silanolate species (the Si5 free energy well in Panel A is 22 kJ/mol deeper with respect to the SiO⁻ one in Panel B). This results in a more acidic silanol group, which hence leads to Si5 species, when deprotonated (pKa=3.9).

Now that we have acquired the knowledge and comprehension of the silanols pKa values, we can characterize the evolution of the silica surface in contact with water as a function of the progressive increase in pH by DFT-MD simulations.

6.4 DFT-MD and SFG bands at increasing pH

In our DFT-MD simulations the pH conditions are tuned by playing with the protonation states of the silanol groups. Three surface scenarios, corresponding to the three pH ranges explored in the phonon SFG experiments, have been envisaged. In order to provide a direct link between calculations and experiments, the Si-O VDOS (velocity density of states, see section 6.7.6) signatures (i.e. without the SFG intensity) of the SiO⁻ and Si-OH surface groups have been calculated for each scenario and compared with the experimental SFG bands (for their positions).

The reported SFG experiments (Fig. 6.4) and the microscopic picture arising from the DFT-MD simulations, go hand in hand (see Fig. 6.6), in particular:

1) Region 1, pH~PZC (pH<4): according to our pKa calculations of Si-OH groups and according to experimental pKa measurements[212, 232, 178] the silica surface is fully protonated, and remains fully protonated throughout the 40 ps DFT-MD simulations. As a consequence the VDOS (calculations) and SFG (experiments) spectral signatures are the ones of Si-OH groups, i.e. 920 cm⁻¹ in the DFT-MD/VDOS (Fig. 6.6, top) and 980 cm⁻¹ in the experiments (Fig. 6.4). The main feature of the Si-O VDOS spectrum arising from the Si-OH silica surface groups consists in a single band centred at 920 cm⁻¹ corresponding to the 980 cm⁻¹ experimental band. Note that the small mismatch between theoretical and experimental values can be related to the well known frequency shift due to the BLYP functional.

2) Region 3, pH>9: all the acidic silanol sites (average experimental pKa=4.5, DFT-MD pKa=3.9) are deprotonated while the basic ones (average experimental pKa=8.5, DFT-MD pKa=7.7) are expected to get progressively deprotonated up to pH 12 where all the silica surface will be fully deprotonated [212]. With these elements in hands, we have simulated a high pH scenario (pH 12) by deprotonating all the silanol groups at the 4.5 OH/nm² silica-water interface in our DFT-MD. With such a deprotonation state we find that there

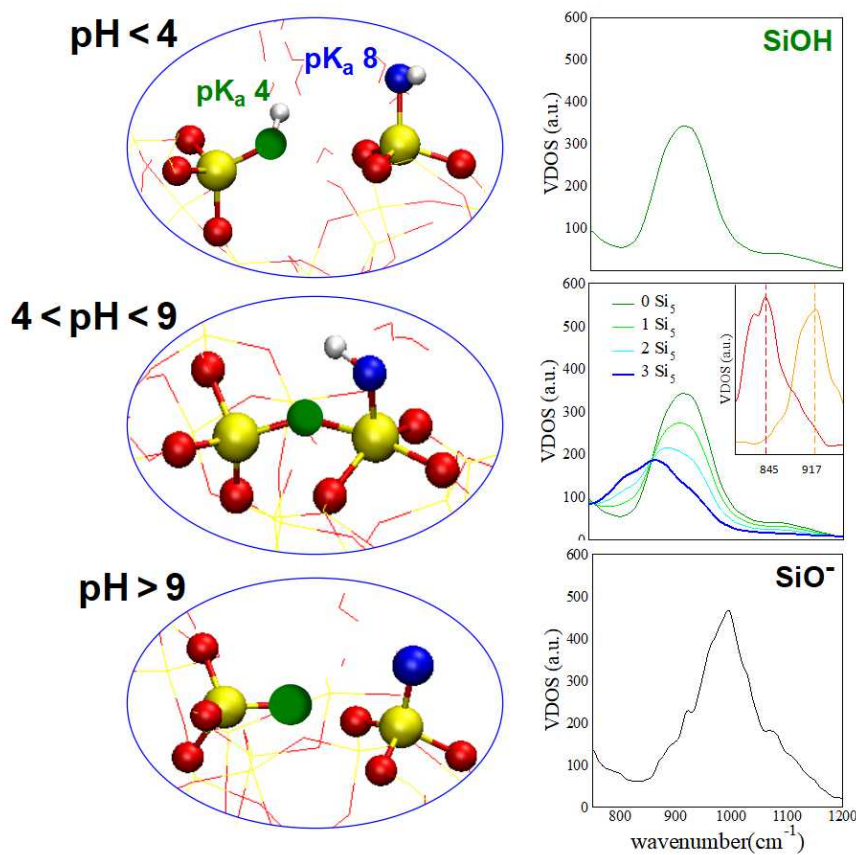


Figure 6.6: *On the left: Schematic illustration of the silanol protonation states considered for each pH range explored. The silanol belonging to the acidic groups has the oxygen atom marked in green, the one belonging to the basic group is marked in blue. On the right: Si-O VDOS (velocity density of states) spectra in the frequency range 800-1200 cm^{-1} arising from the Si-OH and SiO^- surface groups for each pH scenario explored. For the pH range $4 < \text{pH} < 9$ the Si-OH theoretical VDOS signature as a function of a progressive increase of the Si5 structures present on the silica surface is presented. For the same pH range an inset showing the VDOS signatures for the basic Si-OH (blue oxygen) before (orange curve) and after (red curve) the Si5 formation is presented.*

are formations of silanolate SiO^- which are stable for all the DFT-MD simulation time scale (two separate simulations of 30 ps each, were achieved). No Si5 species were detected in this pH condition. As we will demonstrate in the next section by quantifying the stabilities of Si5 species as a function of the pH condition by metadynamics, increasing the pH condition beyond pH 9 leads to a progressive disappearance of the Si5 structures over the silica surface.

To summarize, at high pH condition ($\text{pH} > 9$) our theoretical result predicts the formation of stable silanolate groups and the instability of Si5 structures at the silica surface. The instability of the Si5 species and the stable formation of SiO^- explain the 1020 cm^{-1} (experiments)/ 980 cm^{-1} (VDOS/DFT-MD) band starting at $\text{pH} = 9.5$ in the experiments and its increase in intensity up to pH 12 (see Fig. 6.6, bottom plus Fig. 6.4). Note that we find again

$\sim 50\text{-}60\text{ cm}^{-1}$ redshift in frequency between theory and experiment (see top and bottom of Fig. 6.6).

3) Region 2, $4 < \text{pH} < 9$: according to experimental and calculated pKas, all acidic Si-OHs are deprotonated ($\text{pK}_a = 4.5$ from experiments, 3.8 from DFT-MD). The deprotonation of the most acidic silanols systematically results into Si5 species appearing after few ps of dynamics (seen over the 6 DFT-MD simulations performed), no SiO^- species appear. Our six DFT-MD simulations (length-time of 30 ps each) show the Si5 species to be stable in the 4-9 pH window. This will be further demonstrated in the next section. It is worth mentioning here that SFG spectroscopy is not sensitive to the Si-O stretch related to Si-O-Si structures at the amorphous silica surface for question of symmetry, as reported in ref.[183]. The Si-O-Si bond involved in the Si5 species formation is thus not directly detected by SFG experiments in this spectral range. It follows that the Si5 appearance in the 4-9 pH range can only be probed by SFG spectroscopy in the $900\text{-}1100\text{ cm}^{-1}$ region by the decrease in intensity of the Si-O(H) band, without the appearance of any other band. Si5 species are therefore found here as the microscopical origin of the decrease in intensity and further disappearance of SFG band(s) in the 4-9 pH domain.

However, the Si5 species do not directly explain the red shift of the Si-O(H) band observed experimentally when the pH increases beyond 4. To understand this point we have deconvolved the Si-O(H) VDOS signal arising from the silanols hosting the Si5 species (the oxygen of the silanol group considered is marked in blue in Fig. 6.6) from the signal due to the rest of the silanol groups of the surface. The inset in Fig. 6.6 reports the average VDOS Si-O(H) signature respectively for the silanol groups involved in the Si5 species (red curve, Si5) and the silanol groups not belonging to Si5 species (orange curve, Si4).

When not involved in Si5 species, the Si-OH silanols give rise to a vibrational band centred at 917 cm^{-1} (orange curve of the inset in Fig. 6.6). Conversely when the Si-OHs are involved in Si5 species, their spectroscopic signature (red curve in Fig. 6.6) is redshifted by 70 cm^{-1} , resulting in a band centred at 845 cm^{-1} , with a shoulder located around 830 cm^{-1} .

The flux of electronic negative charge into the central silicium atom that follows the formation of the Si5 species, leads to a weakening of the Si-O(H) bond, which average distance systematically increases by 0.05 \AA along the DFT-MD simulations. As a consequence Si-O(H) vibrational frequency redshifts of 70 cm^{-1} are obtained.

In a second step, we have modelled the evolution of the total Si-O(H) VDOS signal in response to the increase in the number of Si5 species going from pH 4 to 9. The total Si-O(H) signals for four distinct surface scenarios with an increasing number of Si5 species have been obtained by combining the two Si-O(H) VDOS marker bands (Si4 and Si5) weighted by the abundance of their associated silanol species (Fig. 6.6). The progressive increase

of the pH, and thus the growth in the number of Si5 species over the silica surface, leads to an overall red-shift of the Si-O(H) band from 920 cm^{-1} in absence of Si5 species ($\text{pH} < 4$, dark green curve) to 880 cm^{-1} in presence of three Si5 species over the surface ($5 < \text{pH} < 9$, blue curve).

The obtained red shift of 40 cm^{-1} is in good agreement with the 30 cm^{-1} one recorded experimentally in Fig. 6.4 in the 4-9 pH range. The change in the coordination number of the central silicium atom, as it occurs in the Si5 species formation in the 4-9 pH range, induces variations in the spectroscopic signatures of the Si-OH groups involved in the Si5 species, inducing an overall 30 cm^{-1} red shift of the total Si-O(H) SFG band. We can therefore consider the SFG Si-O(H) band red-shift in the pH range 4-9 as a direct spectroscopic evidence of the Si5 formation at the silica-water interface.

We further notice that our simple model can in part explain also the SFG Si-O(H) band strong decrease in intensity recorded in the 4-6 pH range: For each Si5 species formed on the surface, one Si-O(H) signal red-shifts in frequency and one disappears, such phenomenon not only provokes a red-shift of the Si-O(H) signal, but induces also a strong decrease in the Si-O(H) intensity at 970 cm^{-1} as one can see by both the VDOS calculations in the 4-9 pH range (Fig. 6.6) and experiments (Panel C of Fig. 6.4).

To summarize, our results clearly indicate a pH window from 4 to 9 where Si5 species are formed once acidic Si-OH silanol sites get deprotonated. The Si5 species remain stable over the silica surface. The formation of Si5 structures is directly probed by SFG spectroscopy by the red-shift of the Si-O(H) band, and indirectly by the strong decrease in intensity of the Si-O(H) band, without any appearance of SFG signatures for SiO^- species. Our theoretical calculations show that the formation of SiO^- species on the deprotonated silica surface starts when the pH goes above ~ 9 . This is seen in the SFG spectrum with the appearance of the SiO^- band at $\text{pH} \sim 9.5$ and in the progressive increase of the SFG intensity up to pH 12.

In the next section we will further characterize and rationalize the stability of Si5 species as a function of the pH conditions by metadynamics. In particular we will directly simulate the disappearance of Si5 structures at high pH conditions and we will shed light on the microscopic origin of such phenomenon.

6.5 Si5 structures stability as a function of the pH conditions

We have characterized the evolution of the Si5 stability as a function of the progressive increase of the pH. To that end, we have considered one single Si5 species at the aqueous 4.5 OH/nm^2 silica surface and we have simulated its disappearance in response to changes in the pH condition by one metadynamics (see section 6.7.2 for details). The disappearance of the Si5 species is expected to lead to the formation of two Si4 (four fold coordinated silicium

atom) species as schematically presented in Panel A of Fig. 6.7.

The pH condition is directly tuned in the metadynamics simulations by considering as reaction coordinate the protonation states of the two oxygen atoms involved in the formation of the Si5 species considered (identified and characterized along the DFT-MD simulations in the previous section). The two oxygen atoms are the ones, that along the Si5 formation, respectively belong to one basic silanol group (pKa=7.7 from our calculation) hosting the Si5 species (labelled O1 and marked in blue in Panel A of Fig. 6.7) and to one acidic silanol group (pKa 3.9 from our calculation) involved in the nucleophilic attack (labelled O2 and marked in green in Panel A of Fig. 6.7). Note that preliminary metadynamics indicate that the O1 and O2 oxygen atoms involved in the Si5 formation, are also the main actors in the Si5 disappearance.

We have therefore chosen as reaction coordinate the difference between the coordination number of the O2 atom with respect to all the hydrogen atoms of the system and the coordination number of the O1 atom with respect to all the hydrogen atoms of the system (C_{O2-O1} coordination number) in order to take into account the effect of the protonation state of both oxygen atoms. In particular, this reaction coordinate takes the value of -1 if only the acidic silanol (O2, oxygen coloured in green in Fig. 6.7) is deprotonated ($C_{O2-O1}=0-1$), 0 if both considered silanols are protonated ($C_{O2-O1}=1-1$) and a value of +1 if only the basic silanol site (O1, oxygen coloured in blue in Fig. 6.7) is deprotonated ($C_{O2-O1}=1-0$).

We have further chosen a second reaction coordinate which is the coordination number of the O2 oxygen atom with respect to all the Silicium atoms of the system (Si-O-Si coordinates, green arrow in Panel A of Fig. 6.7) in order to sample the presence or not of the Si5 species on the silica surface. In particular, this coordinate takes the value of 1.6, when the Si5 species is stable at the silica surface with the O2 atom bridging two silicium atoms at the base of the Si5 geometry, while it takes a value of 0.9 when the Si5 species evolves into a Si4 species whereby the O2 atom is bonded to only one silicium atom. With the two adopted reaction coordinates we can therefore probe the nature and the stability of the molecular species (Si5 or Si4) residing at the surface over different pH ranges.

In Fig. 6.7 the free energy landscape with the reactive species associated to each of the minima explored along the metadynamics simulation is presented. Minimum 1 has the Si-O1 group that is deprotonated (pKa=4.5) while the Si-O2 group is protonated (pKa=8.3), this situation corresponds to a pH condition roughly in the range 5–9 where only the more acidic silanols get deprotonated on the silica surface. As one can see by the position of the minimum along the Si-O-Si coordinate, the Si5 species is stable at the surface in this pH range.

From structure 1, the Si5 disappears through a concerted mechanism characterized by the simultaneous proton transfer from water to the O2 group and the cleavage of the O2-Si covalent bond. The process terminates with the for-

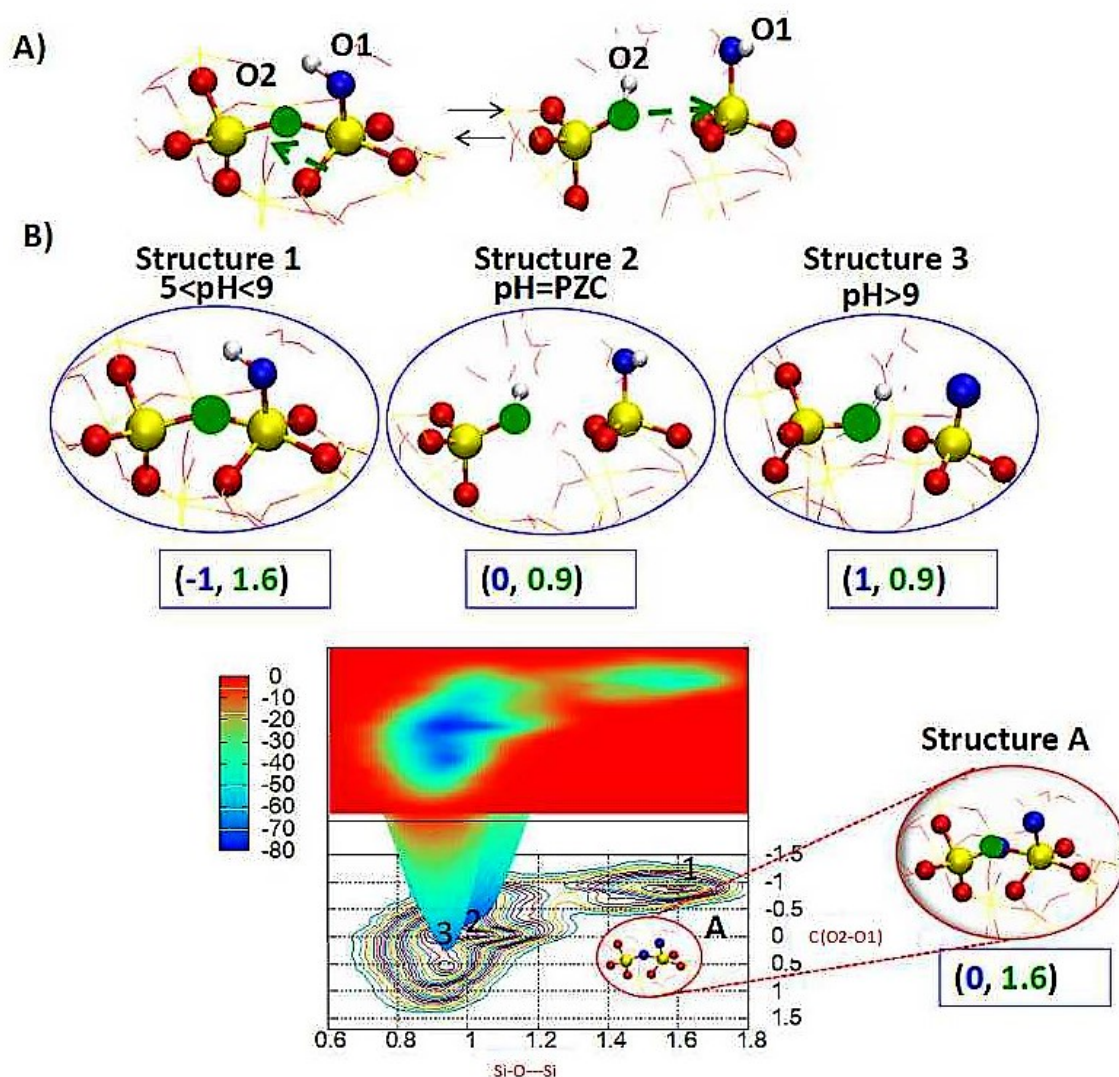


Figure 6.7: Panel A: Schematic illustration of the reaction coordinates adopted along the metadynamics. The difference between the protonation states of the two oxygens marked in blue and in green (C_{O2-O1}) is used as one reaction coordinate. The coordination of the O2 atom with respect to all the silicium atoms of the system is chosen as a second reaction coordinate and it is represented by a green arrow in the figure. Panel B: On the top the chemical structures associated to the minima explored along the metadynamics simulation. The pH range of existence of each structure is also reported. At the bottom the free energy landscape underlying the breaking/formation of Si5 structures reaction is illustrated.

mation of two Si4 species (minimum 2 in Fig. 6.7) on the silica surface. Minimum 2, has both silanols protonated, such surface protonation state corresponds to pH=PZC (pH<4). As one can see by the position of the minimum along the Si-O-Si coordinate, the Si5 species is not present anymore in this pH range.

The minimum associated to the Si5 structure (structure 1) is found with a roughly 35 kJ/mol barrier to overpass for the interconversion reaction to structure 2 to proceed.

No minimum is found either for the Si5 species at $\text{pH} > 9$ where both the silanol groups considered are deprotonated (Structure A in Panel B of Fig. 6.7). This result indicates a high instability of the Si5 species when the pH is increased beyond 9. Along the metadynamics simulation we sample a third minimum associated to structure 3 (Panel B of Fig. 6.7), with the more basic silanol group deprotonated ($\text{pH} > 9$).

In order to further confirm our metadynamics result that Si5 is not stable any more at $\text{pH} > 9$ (where also the most basic sites with $\text{pK}_a > 7.7$ start to be deprotonated), we have run two additional DFT-MD simulations, deprotonating only the two silanol groups involved in the Si5 formation, i.e. the silanol group performing the nucleophilic attack (acidic silanol $\text{pK}_a = 3.9$, green oxygen in Fig. 6.6) and the silanol linked to the Si atom hosting the Si5 species (basic silanol $\text{pK}_a = 7.7$, blue oxygen in Fig. 6.6). The considered microscopic scenario corresponds to a silica surface exposed to solution at high pH conditions ($\text{pH} > 9$) because of the basic character (pK_a value of 7.7) of one of the silanol groups being deprotonated (the blue oxygen in Fig. 6.7). This given deprotonation state leads to the formation of two silanolate groups at the silica-water interface, stable for all the time of the DFT-MD simulations (30 ps), no formation of Si5 species is detected at the silica surface.

These DFT-MD simulations are in line with the metadynamics, and indicate a progressive disappearance of the Si5 structures with the increase of the pH beyond nine, a range where also the most basic sites with $\text{pK}_a > 7.7$ are progressively deprotonated. The straightforward physical rationalization of such phenomenon lies in the deprotonation of the silanol hosting the nucleophilic attack at high pH condition (average pK_a of 7.7) that provokes a flux of negative charge to the silicium at the center of the Si5 geometry, strongly reducing its electrophilic character. This makes the central Si atom less prone to accept the nucleophilic attack from the silanolate group (SiO^-), hampering the Si5 formation to proceed.

6.6 Conclusions

Our work provides an original molecular picture on the acid-base chemistry of amorphous silica surfaces. The direct access to the surface groups nature and organizations under different pH conditions by means of SFG and DFT-MD simulations have allowed identify "in situ" the formation of Si5 species at the silica-water interface.

The Si5 species have been characterized both structurally, spectroscopically (see sections 6.2 and 6.4) and energetically (see section 6.3) and their stability as a function of the pH conditions is assessed (see section 6.5).

The previous molecular picture based on the balance between silanol and silanolate groups at the silica surface as a function of the solution pH conditions is modified. The emergence of a third molecular species, the "Si5", reveals a more complex acid-base surface chemistry of amorphous silica.

We have found in particular the Si5 species formation strongly modulating

the silica surface acidity: the silanols that lead to the formation of stable Si5 species, once deprotonated, are acidic with an average calculated pKa value of 3.9, while the ones forming stable silanolate SiO⁻ species are found to be about 3.8 pKa units less acidic with an average value of pKa=7.7.

Moreover the stability of Si5 species is directly dependent on the pH conditions: Si5 is stable in the pH range 4-9, while it converts into two silanolate groups when increasing the pH above 9. This implies that the surface charge generated at the silica surface by increasing the pH is not only due to the formation of silanolate groups. It arises also from the appearance/disappearance of Si5 species. The emergence of the Si5 species breaks down the biunivocal correspondence between the generation of a surface negative charge on silica and the silanol group deprotonation event. This assumption has been widely used in the past to measure the acidity of aqueous amorphous silica surface[267, 212, 268].

The molecular picture on the amorphous silica surface consisting in 19 % of the silanols exhibiting a pKa of 4.5 (acidic silanols) and 81% a pKa value of 8.5 (non acidic silanols) extrapolated by indirect measurements of the surface charge as a function of pH[212, 268, 267] could be strongly altered when taking into account the formation of Si5 species in the model, as revealed in this work. However, further studies able to deconvolve and quantify the silica surface charges generated from respectively the silanolate and Si5 species are needed in order to provide a direct link between the acid-base chemistry of silica and the experimental evolution of the silica surface charge as a function of pH[212, 268, 267] .

More details on our investigation can be found in the paper reported at the end of the chapter at page 273. It is still a preliminary version of the paper.

6.7 Experimental and computational details

6.7.1 SSP and PPP SFG spectra of the amorphous silica-water interface

The details for the SFG experiments can be found in the paper reported at page 273. Below are reported the experimental SFG spectra of silica-water interfaces as a function of the solution pH condition.

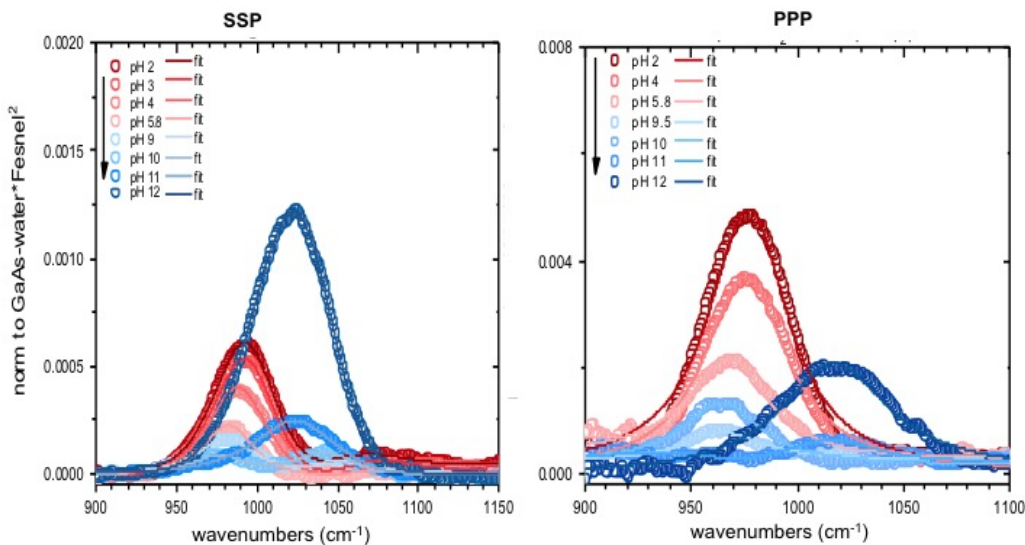


Figure 6.8: On the left are reported the SSP SFG spectra of the amorphous silica-water interface as a function of the solution pH, in the frequency range 900-1150 cm^{-1} . On the right are reported the PPP SFG spectra of the amorphous silica-water interface as a function of the solution pH, in the frequency range 900-1150 cm^{-1} . For both PPP and SSP polarization schemes, the pH is progressively increased from 2 (red curve) to 12 (blue curve). Increasing the pH in the 2-10 range induces a red shift and a progressive loss in intensity of the Si-O(H) SFG band at 980 cm^{-1} , until its complete disappearance at $\text{pH} \sim 9.5$. The SiO^- band at 1020 cm^{-1} appears at $\text{pH} \sim 9.5$ and strongly increases in intensity up to pH 12. The PPP/SSP ratio of the Si-O(H) SFG band amplitude changes only slightly at increasing pH, indicating that there is not a dramatic change in orientation of the Si-O groups.

6.7.2 DFT-MD and metadynamics set up

All the DFT-MD and DFT-MD metadynamics simulations have been carried out using the CP2K package[118] at the BLYP[120][121] level of representation and including Grimme D2[122] correction for van der Waals interactions and a combination of GTH pseudo-potentials[123] and Gaussian Plane Waves basis sets[119]. The DVZP-MOLOPT-SR basis set, augmented with a 400 Ry plane wave basis set have been used. The nuclei displacements have been predicted using the classical Newton's equations of motions integrated through the velocity verlet algorithm.

The DFT-MD simulations employed for the calculations of the VDOS spectra (see section 6.7.6) have been equilibrated for 10 ps in the NVT ensemble with a CSVR thermostat[281] at the target temperature of 300 K and then have been carried on for 50 ps in the pure NVE ensemble. The VDOS were performed over these 50 ps. The rest of the DFT-MD simulations and the DFT-MD metadynamics have been performed in the NVT ensemble with a CSVR thermostat[281] and a target temperature of 300 K.

The 4.5 OH/nm² amorphous silica-water interface is modelled in a box of dimension 13.4 Å X 13.3 Å X 35 Å. There are 8 Si-OH groups at the silica surface and the liquid water is modelled with 120 water molecules.

For the 5.5 and 7.6 OH/nm² amorphous silica-water interfaces, boxes of dimension 9.117 Å X 16.342 Å X 32 Å are used. The surfaces are respectively composed of 8 and 12 SiOH groups and in both cases the liquid water is modelled with 115 water molecules.

The α (0001) quartz/water interface is simulated with a box of dimension 9.82 Å X 8.5 Å X 32 Å. There are 8 Si-OH groups on the quartz surface and the liquid water is modelled with 64 water molecules.

Neutral boxes were employed for all the metadynamics simulations done in this work in order to calculate the silanol pKa values. For the metadynamics testing the Si5 stability as a function of the pH condition presented in section 6.5 of the main text, we have ensured the neutrality of the box by placing one K⁺ cation far from the silica surface (> 8 Å), i.e. located in the bulk of water. For the DFT-MD simulations where the Si-O⁻ or Si5 species are simulated in absence of the H₃O⁺ species, the resulting net negative charge in the box is counterbalanced by an artificial uniform charge background to avoid the divergence of the Ewald summation. The total simulation time amounts to 360 ps for the DFT-MD simulations and to 270 ps for the metadynamics simulations.

6.7.3 Details for the DFT-MD metadynamics

The free energy profiles for the Si-OH acid-base equilibrium at the aqueous silica surface have been obtained by DFT-MD metadynamics simulations as implemented in the CP2K software package[118]. The acid-base behaviour (i.e. protonation/deprotonation of the surface sites) of each silanol over the 4.5 OH/nm² silica surface has been simulated and characterized. Eight metadynamics are performed, one per silanol present at the surface.

Our computational approach for the metadynamics is similar to the one successfully adopted in previous works[62, 20, 126] for the study of reactions at aqueous solid interfaces. The type of reaction coordinate $c(A-B)$ adopted is the coordination number[127] of an atom A with respect to a set of atoms B, defined as:

$$c(A - B) = \sum_{I \in B} \frac{1 - (R_{AI}/R_{AB}^0)^6}{1 - (R_{AI}/R_{AB}^0)^{12}} \quad (6.1)$$

where R_{AI} is the distance between atoms A and I (belonging to the chosen set of B atoms). R_{AB}^0 is a fixed cut-off parameter based on the equilibrium bond distance between A and B atoms. In particular, we have chosen to simulate the silanol acid-base behaviour adopting the following reaction coordinates:

1) The silanol oxygen coordination number with respect to all the hydrogen atoms of the system (CN_{Si-O-H}), going from 1 (SiOH) to 0.5 (SiO⁻). This allows to model silanol deprotonation events.

2) The silanol oxygen coordination number with respect to all the silicium atoms of silica ($CN_{Si-O-Si}$). This allows to sample possible surface reconstruction processes.

The height of the Gaussian hills added along the biased metadynamics are 0.8 kJ/mol. The width of the Gaussian hills function (δ_s) is 0.05. These values have been shown by previous works to provide accurate estimations of the free energy barriers of chemical reactions at solid-water interfaces[20].

In order to avoid the "hill-surfing", as discussed in ref.[43, 62, 20, 126], a Gaussian hill is added every time the dynamics explores a spot on the reaction coordinate space at a distance $3/2\delta_s$ from the spot where the previous Gaussian hill was deposited:

$$|s(t) - s(t_i)| = \frac{3}{2}\delta_s \quad (6.2)$$

where $s(t)$ is the position along the reaction coordinate at a given time t , δ_s is the width of the Gaussian hills, and t_i is the time when the last Gaussian hill was deposited.

The computed free energy is considered at convergence after having observed the double crossing of the energetic barrier forward and backward along the same reaction coordinate. The convergence criterion is on average reached within 20 ps of dynamics for all systems studied here (8 metadynamics, one for each silanol of the surface model used in this investigation).

The pKa value of each silanol is calculated as the free energy difference (ΔG) between the minima of respectively the silanol species (SiOH) and the conjugate base (SiO⁻ or Si5):

$$pKa = \Delta G/2.303RT \quad (6.3)$$

where T is the temperature of the system in Kelvin (imposed by the NVT ensemble) and R ($8.314 \text{ JK}^{-1}\text{mol}^{-1}$) is the ideal gas constant.

6.7.4 Validation of the pKa values

A plethora of computational works have recently shown how the computation of the free energy landscape obtained by the combination of DFT-MD with the metadynamics technique provides accurate estimates of the pKa values for weak acids, amino acids and polyprotic acids in aqueous solutions[282, 283, 284, 285, 286]. In particular, Tummanapelli *et al.*[282, 283, 284] have calculated pKa values by metadynamics for a wide range of acidic and basic species in aqueous solution, reporting an accuracy within 0.1 pKa units with respect to experiments.

However there are not in the literature, according to the best of our knowledge, works reporting the acidity of solid surfaces by metadynamics techniques. We have therefore assessed the reliability of our metadynamics in describing the acid-base behaviour of silica surfaces, by comparing our pKa results on a crystalline silica surface with the one obtained on the same system by the "reversible proton-insertion" method[130]. Developed by Sprik's group, the "reversible proton-insertion" method is a computational technique[130] based on MD simulations that describes the acidity constants of a vast range of oxyde surfaces immersed in liquid water.[182, 181, 271, 180, 287]

In this method the free energy difference between the acidic species and its conjugate base, necessary for the pKa calculation, is obtained by a thermodynamic integration in which the AH species is gradually transformed into the deprotonated base A^- along a fictitious reaction coordinate. The derivative of the free energy at each step of the thermodynamic integration is calculated from the vertical energy gap for the insertion (or removal) of the proton in the system. More information on the "reversible proton-insertion method" can be found in ref.[182, 180, 287].

The acidity calculations done on the (0001) α -quartz surface in contact with water.[182] by the "reversible proton insertion method", have revealed the presence of two silanol groups on the quartz surface, with two distinct acidities. It has been shown in ref.[182] that the in-plane silanols (half of the silanols at the aqueous quartz surface), i.e. pointing their OH group parallel to the silica surface, are found basic with a pKa value of 8.6, while the out-of-plane silanols (half of the silanols at the aqueous quartz surface), i.e. pointing their OH groups toward water, are found acidic with a pKa value of 5.6.

Therefore we have made use of these silanols pKa's estimations as a reference and we have compared their values with the ones calculated for the in-plane and out-of-plane silanols on the same system (same simulation box and DFT set-up as in ref.[182]) by our metadynamics approach.

The acid-base behaviour respectively of the out-of-plane and in-plane silanols over the (0001) α -quartz have been described by adopting the same reaction coordinates as the ones described above (see section 6.7.3), i.e. the coordination number of the silanol oxygen with respect to all the hydrogen atoms of the system (CN_{Si-O-H}) and the coordination number of the silanol

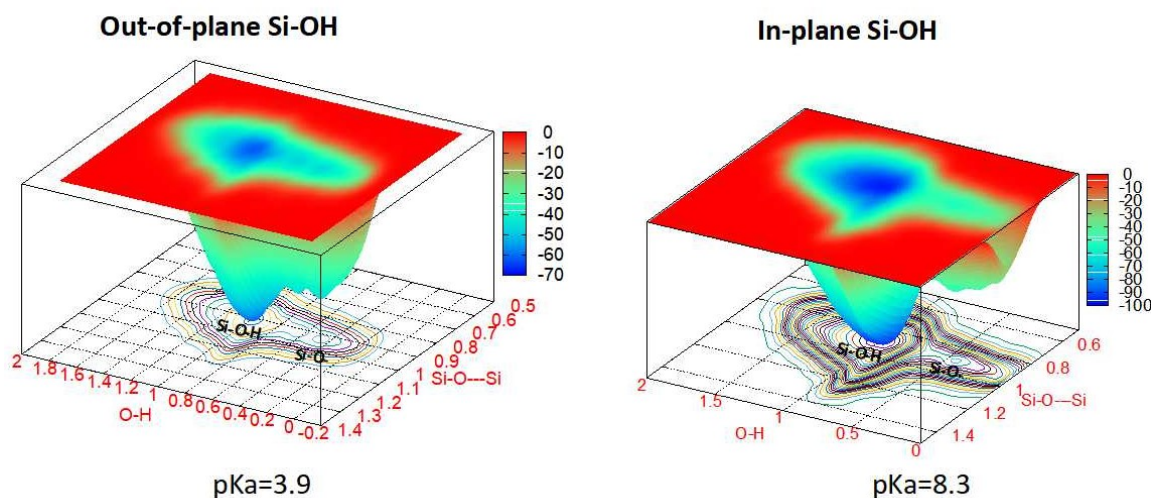


Figure 6.9: *Left: free energy landscape associated with the out-of-plane silanol acid-base behaviour at the aqueous (0001) α -quartz. Two minima associated with the silanol (Si-OH) and silanolate (SiO⁻) groups are found. Right: free energy landscape associated with the out-of-plane silanol acid-base behaviour at the aqueous (0001) α -quartz. Two minima associated with the silanol (Si-OH) and silanolate (SiO⁻) groups are found. At the bottom of the Figure are reported the calculated pKa values for both the in-plane and out-of-plane silanols ($pK_a = \Delta G / 2.303 RT$), to be compared to the values of 8.6 and 5.6 from ref.[182].*

oxygen with respect to all the silicium atoms of the surface ($CN_{Si-O--Si}$). The free energy profiles in Fig. 6.9 show both the in-plane and out-of-plane silanols to have silanolate species (SiO⁻) as conjugate bases, as one can see by the two minima positions along the $CN_{Si-O--H}$ reaction coordinate on the free energy profiles. For both the in-plane and out-of-plane silanol species, the deeper minimum around 1.0 on the $CN_{Si-O--H}$ coordinate corresponds to the undissociated silanol (SiOH) while the minimum at 0.5 corresponds to the silanolate species (SiO⁻).

The microscopic picture arising from the values obtained by metadynamics (Fig. 6.9) is again characterized by two groups of silanols with two distinct acidities : the out-of-plane SiOHs are found acidic with a pKa value of 3.9 while the in-plane SiOHs are found basic with a pKa value of 8.3. The analysis of the free energy profiles indicates that the calculated difference in acidities between the two surface groups is mostly due to the higher stability of the in-plane SiOH free energy minimum ($G_{inplane}^{SiOH} - G_{outofplane}^{SiOH} = 23$ kJ/mol) with respect to the out-of-plane one, as one can see by comparing the free energy values of the Si-OH minima in Fig. 6.9 (~ -100 kJ/mol for the in-plane silanols and ~ -70 kJ/mol for the out-of-plane one). This brings to a higher free energy difference between the SiOH and the SiO⁻ minimum (ΔG used in the pKa calculations) for the in-plane silanols that is in turn reflected by a lower acidity of the in-plane silanols with respect to the out-of-plane ones.

Our metadynamics calculations predict a bimodal acid-base behaviour of the two Si-OH groups at the aqueous (0001) α -quartz surface, which is in

agreement with the previous pKa calculations performed by the "reversible proton-insertion method" [182] on the same system. Note however that our acidic and basic sites are slightly more acidic than the ones calculated by the "reversible proton-insertion method": 3.9 in our work *vs* 5.6 in ref.[182] for the acidic silanol species and 8.3 in our work *vs* 8.5 for the basic silanol species in ref.[182]. Such discrepancy (especially for the acidic silanols) between the two sets of theoretical pKa values can be partly due to the different level of basis sets adopted for the MD-simulations (DZVP in the case of metadynamics and TVZP in the case of the "reversible proton-insertion method"), partly due to the different boundary conditions between the two methods, e.g. imposing constraints in the case of the thermodynamic integration, and partly due to errors associated with the Gaussian hills deposition frequency in the case of the present metadynamics. However the pKa final difference of 4.4 and 3.0 between the in-plane and out-of-plane silanols found respectively by metadynamics and the "reversible proton-insertion method" are far beyond the numerical error of both methods and both methods point to the same acid-base bimodal behaviour at the (0001) α -quartz surface associated to the in-plane *vs* out-of-plane surface silanols.

Our calculations are also in good agreement with the (0001) α -quartz acid-base bimodal behaviour revealed by SFG experiments[268]. The pKa measurements of Ostroverkhov *et al.*[268] by SFG spectroscopy indeed indicate the presence of two distinct silanol populations at the (0001) α -quartz surface characterized by pKa values respectively of 4.5 and 9.5, close to the pKa values of 3.9 and 8.3 here found by our metadynamics simulations of the pKas.

To conclude, the agreement with past pKa calculations[182] on the same system (same simulation box and slightly different DFT set up) and with experiments[268] shows the combination of DFT-MD and metadynamics to be a reliable technique for the pKa calculations of silica surface groups at the interface with liquid water.

Interestingly the formation of Si5 species (see the main text) is neither observed for the in-plane or the out-of-plane silanols at the aqueous (0001) α -quartz surface. The convergence criterion of metadynamics is reached within 20 ps of metadynamics. We have however continued our metadynamics until 90 ps in order to sample higher energy structures. With this much higher energy exploration, no minimum associated to the Si5 has been found. Such results indicate a non existence/high instability of the Si5 species at the (0001) α -quartz aqueous surface.

6.7.5 Structural Characterization of Si5 species

In this section we investigate the microscopic origins of the Si5 species formation at the amorphous silica-water interface. We focus on the specific structural "local" properties of the silica-water interface that can lead to the formation of Si5 species.

A first aspect that we have considered is the possible role of water in the

Si5 formation on the amorphous silica surface (the model used here is with 4.5 SiOH/nm² silanol density). In this regard we have specifically considered the silanols, that once deprotonated in presence of water lead to the formation of Si5 species. We have deprotonated these sites one by one in absence and in presence of water in three distinct simulations, and we have observed their subsequent behaviour at the silica-air surface and at the silica-water surface. We find that the same behaviour whether water is present or not. The same SiOH sites are found to form Si5 species, once deprotonated, with and without liquid water at the interface with silica. Following such results, we have thus disregarded water as playing a role in the Si5 species stabilization on the 4.5 OH/nm² silica surface.

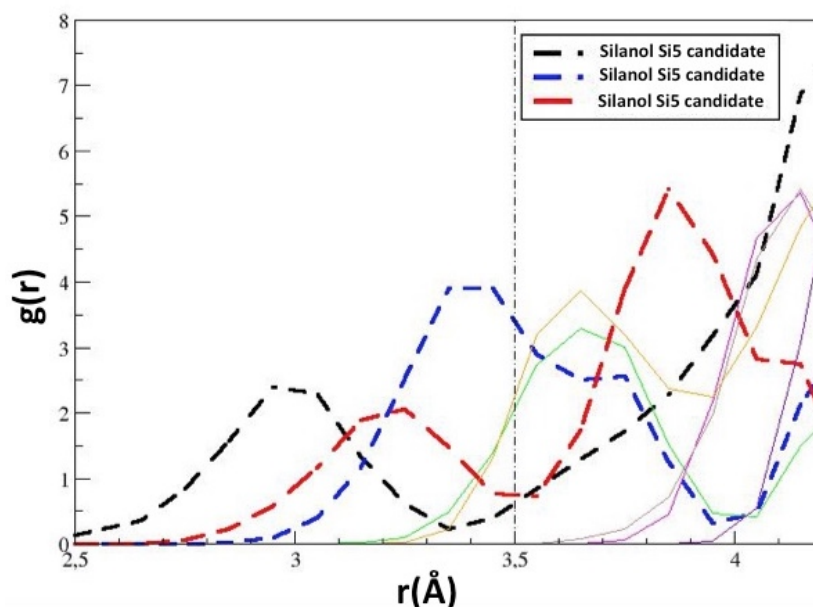


Figure 6.10: Radial distribution functions (RDF) of the silanol group oxygen atoms with respect to all the silicium atoms at the 4.5 OH/nm² silica surface. The red, black and blue dashed curves are associated to the oxygen atoms of the SiOH groups that are found able to form Si5 species, once they are deprotonated.

We have then focused on whether there are specific morphological surface factors for the Si5 formation. We report in Fig. 6.10 the O–Si radial distribution functions for the oxygen atom of each SiOH group at the 4.5 OH/nm² surface with respect to all the Si atoms of the system. The SiOH groups involved in the nucleophilic attack leading to the Si5 formation, once deprotonated (red, blue and black dashed curves in Fig. 6.10), are closer (<3.5 Å) to surface Si atoms than other silanol groups (> 3.5 Å). Such result might suggest that the proximity between a Si–OH group and a surface Si atom could be a mandatory condition for the Si5 formation. However, despite the proximity, steric hindrance between the reactive SiOH site and the SiO groups belonging to the SiO₄ tetrahedra, hosting the nucleophilic attack, could still hamper the Si5 formation.

For this reason the orientation between the reaction partners involved in

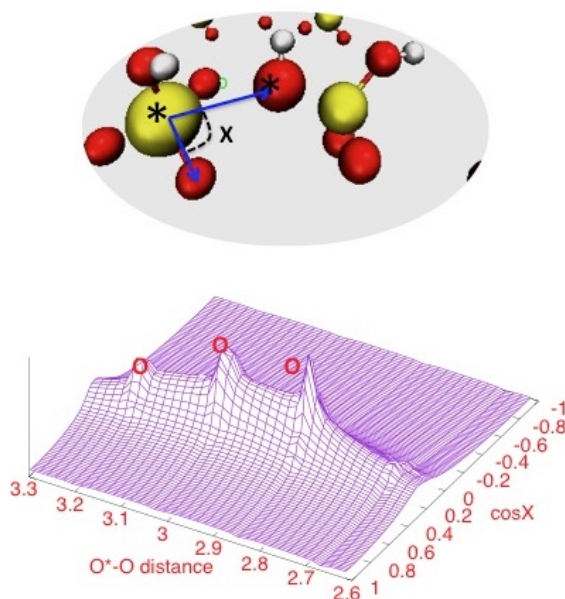


Figure 6.11: *On the top is reported a snapshot from the DFT-MD simulations representing the SiO_4 tetrahedra perfectly oriented with respect to the reactive SiOH for the $\text{Si}5$ formation. The blue arrows correspond to the vectors defining the angle analyzed (x). In yellow the silicium atoms, in red the oxygen atoms and in white the hydrogen atoms. At the bottom are illustrated the angular and distance densities of the SiO groups linked to the central Si atom of SiO_4 building block of bulk silica, hosting the nucleophilic attack, with respect to the reactive SiOH group.*

the $\text{Si}5$ formation has also been analysed. We have studied the orientation of the SiOH groups that lead to the formation of $\text{Si}5$ once deprotonated with respect to the SiO groups belonging to the neighbouring SiO_4 tetrahedra participating in the $\text{Si}5$ formation reaction.

The angle x (top of Fig. 6.11) that describes the orientation of the Si-O belonging to the silanol group performing the nucleophilic attack with respect to the SiO groups linked to the central Si atom, is defined by the two vectors reported on the top of Fig. 6.11 (blue arrows).

At the bottom of Fig. 6.11 is reported the angular ($\cos x$) and distance density distribution of the SiO groups linked to the central Si atom with respect to the reactive SiOH group (that gets deprotonated). The density map has been calculated only for the three SiO groups facing the reactive SiOH species. The maxima positions reveal a preferential orientation of the SiO groups at 90 degrees ($\cos x=0$) with respect to the oxygen atom of the SiOH group. Such conformation is indeed ideal for the $\text{Si}5$ formation since it avoids any steric hindrance between SiO and SiOH groups during the nucleophilic attack (see the snapshot extracted from the MD simulation on the top of Fig. 6.11).

Our structural analysis points to the proximity and good orientation between SiOH groups and SiO_4 tetrahedra as one necessary condition for the

formation of Si5 species.

In order to verify if the results on the silica surface reconstruction as a function of the pH condition obtained here and in the main text for the 4.5 OH/nm² model silica aqueous surface are independent of the silica model used, two additional models of the silica surface with varying degrees of hydroxylation have been investigated, i.e. 7.6 and 5.5 OH/nm² amorphous silica model surfaces[188] put in contact with liquid water.

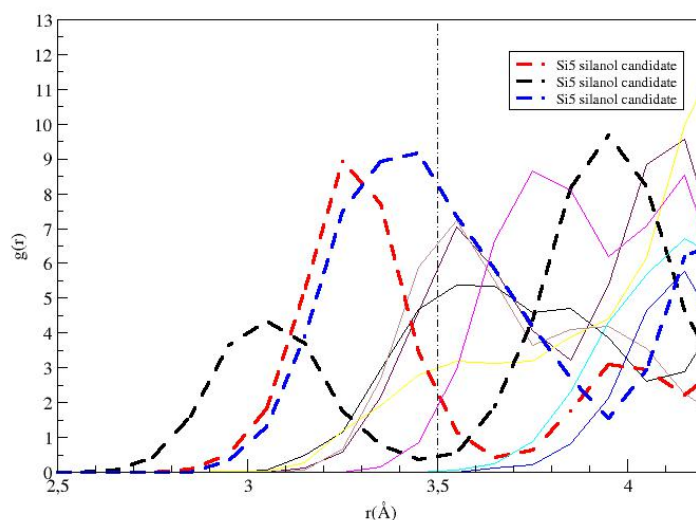


Figure 6.12: Radial distribution functions (RDF) of the silanol group oxygen atoms with respect to all the silicium atoms at the 7.6 OH/nm² silica aqueous surface. The red, black and blue dashed curves are associated to the oxygen atoms of the SiOH groups forming Si5 species, once they are deprotonated.

We have first identified the silanol groups that do have the structural properties (in terms of orientations and proximity) found at the 4.5 OH/nm² surface to be necessary for the Si5 formation, and we have then characterized their chemical behaviour after deprotonation, by DFT-MD simulations. Interestingly three silanols over the 7.6 OH/nm² silica surface are found with the right distance and orientation for the possible formation of the Si5 species (named hereafter silanols Si5 candidates), as can be appreciated in Fig. 6.12 where the O–Si radial distribution functions of the oxygen atom of each SiOH group at the 7.6 OH/nm² surface with respect to all the Si atoms of the system are reported.

However, once the silanols candidates for the Si5 formation are deprotonated, there is no nucleophilic attack occurring on the neighbour Si atom along our 30 ps DFT-MD simulations. The silanols are systematically reprotonated within few ps of dynamics by a silanol group in the proximity

through a proton transfer mechanism mediated by water (see Panel A of Fig. 6.13). Despite the silanol proximity and good orientation toward a surface SiO_4 tetrahedra, the reprotonation of the SiO^- group hinders the possible formation of the Si_5 on the $7.6 \text{ OH}/\text{nm}^2$ amorphous aqueous silica surface.

However the observed intra-silanol proton transfer clearly indicates that

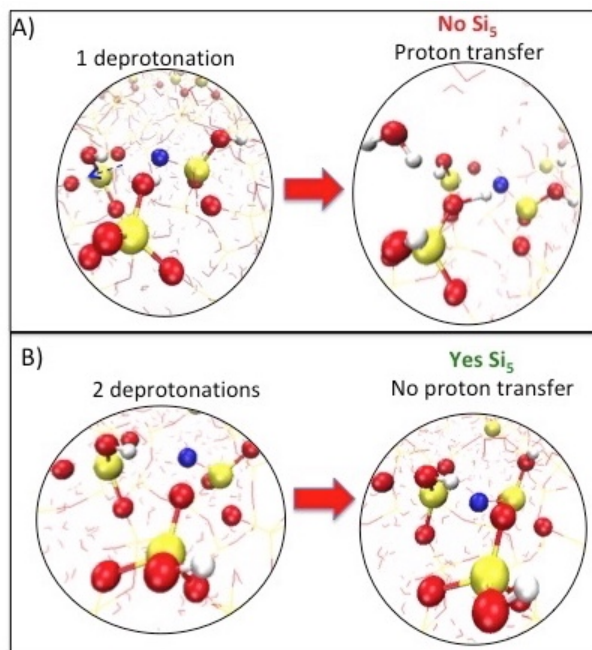


Figure 6.13: *Panel A: illustration of the silanol Si_5 candidate behaviour when deprotonated at the $7.6 \text{ OH}/\text{nm}^2$ amorphous silica surface in contact with water. The reprotonation (few ps of dynamics) by a silanol group located in the proximity through a proton transfer mechanism hampers the Si_5 formation. Panel B: Illustration of the Silanol Si_5 candidate behaviour when deprotonated together with its silanol proton transfer partner at the $7.6 \text{ OH}/\text{nm}^2$ amorphous silica surface in contact with water. As expected, in absence of the intra silanol proton transfer the silanolate group is now free to approach the SiO_4 tetrahedra in the proximity. It can then perform a nucleophilic attack that leads to the formation of one Si_5 species. In both panels the oxygen performing the nucleophilic attack on the other Si atom is marked in blue, the other oxygen atoms are in red, the hydrogens in white and the silicon atoms in yellow.*

the explored microscopic scenario, where the considered silanol Si_5 candidate is deprotonated alone at the silica surface, is in this case physically meaningless. The observed intra-silanol proton transfer reveals a lower acidity of the silanol Si_5 candidates with respect to its proton transfer partner (the one donating the proton), i.e. the silanol donating the proton is more acidic than the silanol Si_5 candidate accepting the proton. Therefore the microscopic scenario that we have explored by deprotonating the Si_5 candidate (less acidic) and leaving protonated its proton transfer silanol partner (more acidic) is not plausible. The deprotonation of the silanol Si_5 candidate at a given intermediate-high pH condition imposes the deprotonation of its proton transfer silanol partner. Thus, if we want to envisage a plausible microscopic scenario where the Si_5 candidate is deprotonated we have to consider its pro-

ton transfer silanol partners deprotonated too.

For such reasons we have decided to explore a microscopic scenario where both the silanol Si5 candidate and its neighbour silanol are simultaneously deprotonated. As expected, in absence of the intra silanol proton transfer (see Panel B Fig. 6.13), the silanolate group is now "free" to approach the SiO₄ tetrahedra and do the expected nucleophilic attack, hence leading to the formation of a Si5 species. For this specific deprotonation condition the Si5 is formed at the 7.6 OH/nm². The same is found at the 4.5 OH/nm² and 5.5 OH/nm² silica surfaces.

Our results indicate that the possibility of Si5 species formation on various silica surfaces that differ from each others by their degree of hydroxylation (here taken as 4.5, 5.5 and 7.6 OH/nm²) depends on the solution pH. In particular, when in contact with water at pH conditions higher than the silica PZC (point of zero charge), the Si5 is formed regardless of the degree of hydroxylation.

6.7.6 Velocity Density of States calculations

The assignment of the vibrational bands in the phonon frequency region (800-1200 cm⁻¹) into the molecular motions of the silica surface groups is achieved in this work by making use of the VDOS (*Velocity Density of States*)[288]. The VDOS are obtained through the Fourier Transform of the atomic velocity autocorrelation function and the VDOS spectrum, denoted here $I_{VDOS}(\omega)$, is calculated as:

$$I_{VDOS}(\omega) = \sum_{i=1}^M \int_{-\infty}^{\infty} \langle \vec{v}_i(t) \cdot \vec{v}_i(0) \rangle \exp(i\omega t) dt \quad (6.4)$$

where i runs over all the M atoms of the investigated system. $\vec{v}_i(t)$ is the velocity vector of atom i at time t . The \sum is over the M atoms of the system. The angular brackets represent a statistical average of the correlation function. The VDOS spectrum provides all vibrational modes of the molecular system whether active in Infrared, Raman or SFG spectroscopies. The expression in eq. 6.4 can also be restrained by replacing M in the summation by a selection of given atoms instead of all atoms. In that case the $I_{VDOS}(\omega)$ gives the signatures of the selected atoms only. In the present work we have selected the atoms belonging respectively to the silanol SiOH, silanolate SiO⁻ and Si5 species in order to identify their VDOS signatures in the phonon frequency region (800-1200 cm⁻¹).

New species identified at the silica water interface

Xiaoqun Li,^{†,1} Flavio S. Brigiano,^{†,2} Simone Pezzotti,^{†,2} Huiling Chen,¹ Ying Li,¹ ... Y. Ron Shen^{*,1,3}, Marie-Pierre Gaigeot^{*,2}, Wei-Tao Liu^{*,1}

¹Physics Department, State Key Laboratory of Surface Physics, Key Laboratory of Micro and Nano Photonic Structures [Ministry of Education (MOE)], Fudan University, Shanghai 200433, China.

²LAMBE UMR8587, Université d'Evry val d'Essonne, CNRS, CEA, Université Paris-Saclay, 91025 Evry, France.

³Department of Physics, University of California at Berkeley, Berkeley, CA 94702, USA.

* Corresponding Authors: yrshen@berkeley.edu, mgaigeot@univ-evry.fr, wliu@fudan.edu.cn

[†] Authors contributed equally to this study.

Abstract

The water interaction with mineral oxides shapes our landscape and determines atmospheric content. Exact knowledge about the structure and composition of these hydrous surfaces is a prerequisite for understanding all underlying mechanisms. Yet even for ubiquitous materials like silicon oxides, there still lacked such knowledge due to limited access to the buried solid surfaces in water. In this study we realize an *in situ* surface-specific spectroscopy of oxide lattices in liquid water. Combined with *ab initio* molecular dynamics simulations, we uncovered a surface reconstruction leading to five-coordinated silicon species upon reacting with water. This newly identified species, rather than conventional silanolates, act as the major deprotonation products of silanol groups in acidic solutions that cause the intriguing bimodal behavior of the interface discovered decades ago. The finding remodels our picture of this classical material system, and provides a new framework for understanding all related phenomena including interfacial water properties.

Introduction

Aqueous interfaces of mineral oxides are ubiquitous, constituting the most abundant solid/liquid interfacial system in nature. They play a crucial role in the Earth ecosystem, hosting a broad spectrum of phenomena in numerous disciplines and fields [1-3]. For example, the protonation and deprotonation of silicate minerals can strongly affect their weathering process at the water interface, as well as their ability to serve as the major carbon dioxide sink in global carbon cycle [4]. At such interfaces, the oxide surface together with vicinal water molecules form a surface-specific bonding network that dominates the functionality and reactivity of the system [5, 6]. Accurate knowledge on its composition and structure is a prerequisite to the fundamental understanding of all aspects of these interfaces. Experimentally, such buried oxide/water interfaces are notoriously difficult to probe [7, 8], and the surface-specific nonlinear optical methods are arguably the most viable among all available tools [9-14]. In 1992, Eiseenthal and coworkers first employed second harmonic generation (SHG) to monitor the acid/base chemistry of the silica (SiO_2)/water interface [15]. They discovered a bimodal titration behavior at the interface that led to the classical two-site model [16-18]. Soon afterwards, Shen and coworkers obtained the first sum-frequency vibrational spectrum (SFVS) of OH bonds at the SiO_2 /water interface and achieved a new level of understanding [18-21]. Since then, SHG and SFVS [22-26], together with the ever-growing capability of theoretical calculation and modeling [References on theory], have made great advances in exploring the mineral aqueous interfaces.

Nonetheless, our understanding is still far from thorough. SHG cannot distinguish between responses originated from either water or oxide, and SFVS in the OH range provides information predominantly about the water. Neither of them could directly monitor the oxide surface, meaning that half of this interfacial system remains in fog. In surface science, probing insulating oxide surfaces has long been a hard nut to crack [8], let alone at the buried aqueous interfaces. Previously, SFVS has successfully discovered lattice vibrational modes from bare surfaces of silica, titania, and alumina [27-31]. Yet the extension to aqueous interfaces was not trivial, because of the strong infrared attenuation in both water and oxides [Ref]. In this study, we realized the first *in situ* sum-frequency vibrational spectroscopy of oxide surface lattices at the water interface, using an oxide thin film on infrared transparent substrate. With optimal geometric parameters, the IR field could not only penetrate the oxide layer, but be strongly and specifically enhanced at the boundary of interest [32]. This enabled our observation of lattice vibrations from silanol (Si-OH) and silonate (Si-O^-) groups at a well-defined, extended

SiO₂/water interface. Surprisingly, at varying pH values, the two surface groups do not interconvert as had always been acquiesced. With *ab initio* molecular dynamic simulations (DFT-MD), we unveiled a novel reconstruction at this aqueous interface: a five-fold coordinated silicon species [Si(5c)] resultant from the deprotonation of SiOH at acidic pH. The Si(5c) species served as the center of surface negative charges, softening the surrounding Si-OH bonds as experimentally detected.

Discovery of the new species answers the long-standing controversy about this interface: what is the microscopic origin of the bimodal behavior of SiOH groups. Since its discovery in 1990s [15, 33], the behavior has remained to be a research focus, with debates on whether it is due to different types of SiOH groups [16, 33-37], or SiOH seeing different bonding environment [17, 18, 38-40]. Now our *in situ* spectroscopy provides direct, unambiguous information about the structure and coverage of surface Si-O species for answering this question. Our *ab initio* simulation reveals that, at low pH, the deprotonation of SiOH leads to the formation of stable Si(5c) species; while at high pH, SiO⁻ groups take over as the stable deprotonation product. The two sequential processes lead to the bimodal deprotonation of SiOH groups. High concentration of cations can reverse the relative stability between Si(5c) and SiO⁻, rendering the latter to show up at less basic pH. This finding could remodel our understanding of this very fundamental mineral surface, as well as that of interacting water molecules with the oxide surface.

The experimental setup of SFVS was described elsewhere [41]. As sketched in Fig. 1a, the infrared beam was sent through the infrared-transparent wafer, overlapping with the near infrared (NIR) beam at the water interface and generated the sum-frequency (SF) signal (see details in Experimental Section and SI). Here, a silicon dioxide (amorphous silica, SiO₂) thin film was deposited on the silicon wafer and in contact with water. As we showed in [32], such a structure could act like an optical cavity and boost up the SF response from selected interface. When the infrared and NIR beams are centered at 1000 cm⁻¹ and 800 nm, respectively, the total local field strength of input/output beams at the SiO₂/water interface reaches a maximum for a ~150 nm-thick SiO₂ film (Fig. 1b) (see details in SI). Meanwhile, the local field strength at the silicon/SiO₂ interface remains low, ensuring the total SF signal to be dominated by that from the

water interface [41]. We thus deposited a 150 nm-thick SiO₂ film on an n-type silicon wafer with PECVD (see details in SI). First we measured the SF spectrum of the thin film at the air interface (Fig. 1c), which exhibited a prominent resonance at ~970 cm⁻¹ due to the Si-O stretching vibration of surface silanol groups (Si-OH). The spectrum agreed nicely with that from the air interface of a typical bulk fused silica sample (Fig. 1c) [28]. We then immersed the thin film sample in water solutions, and took a series of pH dependent SF spectra in the O-H stretching frequency range, which also agreed nicely with those using bulk samples (see details in SI) [11, 20]. These measurements confirmed the surface quality of SiO₂ thin film samples.

We then acquired SiO₂/water interfacial spectra in the Si-O stretching frequency range (800~1100 cm⁻¹) at varying pH values, as presented in Fig. 1d. Sodium chloride (NaCl) buffer solution was used to keep the ion activity a constant [42, 43], and the polarization combination was SSP (S-SF, S-NIR, P-IR) [44]. At pH 2, the SiO₂ surface is essentially all covered by SiOH groups [15, 45]; and close to that at the air interface, the spectrum shows a single resonance due to the Si-OH stretch vibrational mode (ν_{SiOH}) at ~980 cm⁻¹ (Fig. 1d) [46]. When pH increases, SiOH groups are gradually deprotonated, and the ν_{SiOH} mode dropped accordingly, accompanied by a steady frequency redshift [47, 48] to ~940 cm⁻¹ toward pH 10. At that point, the ν_{SiOH} mode nearly disappeared, and a new resonance at ~1020 cm⁻¹ emerged. This mode was not detected at the air interface, but was found in hydrated silica particles and attributed to the stretching vibration mode of deprotonated silanolate groups (Si-O⁻) [47]. Accordingly, the ~1020 cm⁻¹ mode grows stronger with progressive deprotonation at even higher pH values (Fig. 1d). The results are reproducible upon tens of cycles of pH variation (see details in SI). These nice agreements confirmed our successful detection of SiO₂ surface lattice species at the aqueous interface.

Nonetheless, the spectra revealed a highly unexpected relationship between the SiOH and SiO⁻ surface groups. They are believed to have a one-to-one correspondence, converting to each other through $\text{SiOH} + \text{OH}^- \leftrightarrow \text{SiO}^- + \text{H}_2\text{O}$. However, as seen in Fig. 1d, or more clearly from the 2D mapping in Fig. 2a, SiO⁻ started to show up only when SiOH almost disappeared. To check possible effects due to bond re-orientation and ion adsorptions, we also took spectra with different beam polarization combination (PPP) and ion concentrations, as shown in Figs. 2b-2d. In all cases, we saw the absence of both SiOH and SiO⁻ resonances near pH 9~10. Figures 2e and 2f display extracted amplitudes (A) of ν_{SiOH} and ν_{SiO^-} modes versus pH (see details in SI), all

normalized to A_{SiOH} at pH 2 [30]. According to the basic theory of SFG, the mode amplitude is proportional to the surface number density of corresponding species [49-53]. Dashed and dotted curves present the SiOH and SiO⁻ coverages calculated from standard Gouy-Chapman-Stern (GCS) model with a single pKa value at 10 mM and 0.5 M, respectively [Ref] (Figs. 2e and 2f). Though the GCS model can reproduce the contrast between different ion concentrations, quantitatively the calculated coverages vs. pH are both very off from the experimental results. The calculated SiOH coverage dropped at a much slower rate compared to the measured A_{SiOH} . Previous SHG studies have derived the surface coverage of SiO⁻ vs. pH [15], and the result matched with A_{SiO^-} found in our case (Fig. 2f, dashed and cross curve). However, if we assume a one-to-one correspondence between SiOH and SiO⁻ groups, again the derived SiOH coverage was quite off from the measured A_{SiOH} (Fig. 2e, dashed and cross curve).

To understand why SiOH and SiO⁻ signals do not conserve, we consider the following possibilities. First, there might have been other silanol species than the one showing the 970 cm⁻¹ resonance [54]. Yet in the extended Si-O stretch frequency range from ~800 to 1200 cm⁻¹ [27, 28, 47, 54], we did not observe any other mode from this interface (see details in SI). Second, the Si-OH bonds might undergo significant orientational change at varying pH, which could also alter the resonance amplitude [49-51]. For a linear bond on an isotropic surface, SSP spectra probe mostly the out-of-plane dipole moment, and PPP more of the in-plane component [55]. As PPP spectra showed very similar pH dependence to that of SSP (Fig. 2a-2d), the orientation of SiOH and SiO⁻ groups would not have strong dependence on pH. The extracted polar angles of both groups are presented in SI. Overall Si-O⁻ bonds tilt more away from the surface normal than Si-OH bonds, but neither varied much with the pH.

Another possibility is that, as alkaline cations and SiO⁻ can form SiO⁻...R⁺ complexes [56], it might shift the related Si-O⁻ stretch frequencies away from the detectable range. However, even for Na⁺ and K⁺ ions that form inner sphere adsorption with the surface, the distance between cations and Si-O⁻ is over ~2.4 Å [57, 58], unlikely to cause any appreciable frequency change in the latter. Moreover, if the complex formation were important, we would expect A_{SiO^-} to be further suppressed at higher cation concentration. With 0.5 M of Na⁺ or K⁺ added to the electrolyte, on both SSP and PPP spectra (Fig. 2c, 2d, and SI), the A_{SiOH} dropped more rapidly compared to that with 10 mM of cations (Fig. 2f, 2g) at above point-of-zero-charge (pzc) (pH 2), in accordance with previous studies suggesting that alkaline cations facilitate the SiOH

deprotonation [47, 59-61]. However, the Si-O⁻ mode appeared at even lower pH, and grew more rapidly toward the higher pH (Fig. 2c), clearly showing that the complex formation would not suppress the Si-O⁻ resonance. Overall, none of the above could explain the imbalance between SiOH and SiO⁻ groups, and the phenomenon awaits further analysis.

By carefully examine the interface with DFT-MD simulations, we identified a new chemical species from SiOH deprotonation in the range of pH 4~9. Details of the simulation are described elsewhere [57, 58] and provided in SI. Briefly, we started from an amorphous silica model with 4.5 OH/nm² [62], then deprotonated SiOH groups at increasing pH, and characterized the deprotonated surface structure and resultant SFVS spectral features. To model one single SiOH deprotonation event at one time, we chose the reaction coordinates to be the coordination number of one SiOH oxygen with respect to all hydrogen atoms of the system (CN_{SiO-H}), and that with respect to all silicon atoms of the system (CN_{SiO-Si}). A reaction path orthogonal to the latter exclude possible surface reconstructions, and vice versa. At low pH, when the deprotonation rate is less than 40%, the free energy landscape (Fig. 3a) shows a well-defined minimum related to SiOH as the reactant. Yet no minimum is found for the SiO⁻ group, meaning that it is not a stable deprotonation product. Instead, a surface reconstruction was identified, corresponding to a five-fold coordinated silicium species [Si(5c)] (Fig. 3a). The reconstruction proceeds from the SiOH minimum to the Si(5c) stable one through a concerted mechanism: upon the proton transfer from SiOH to water, a simultaneous nucleophilic attack occurs on the neighboring silicon atom and forms a new Si-O-Si covalent bond (Fig. 3b, see details in SI). The metadynamics analysis revealed an acidic character for SiOH groups deprotonated through the above mechanism, with an average pK_a value of 3.9±0.9. The Si(5c) species act as the conjugated base, as well as center of negative charges.

At higher pH, when the surface is more negatively charged, the free energy landscape becomes very different (Fig. 3c). A minimum corresponding to SiO⁻ is now clearly seen, but that for Si(5c) diminishes. So SiO⁻ is energetically more favorable as the reaction product of SiOH deprotonation (Fig. 3d), which proceeded directly from the SiOH minimum to the SiO⁻ minimum along the CN_{SiO-H} reaction coordinate. The metadynamics analysis revealed corresponding SiOH groups to have an average pK_a of 7.7±0.9. Meanwhile, the Si(5c) species disappeared progressively at increasing pH (see details in SI). The physical picture is straightforward: the deprotonation of more basic SiOH provokes a flux of negative charge to the corresponding

silicium, strongly reducing its electrophilic character and less prone to accept the nucleophilic attack. In summary, the simulation reproduces the bimodal acid-base behavior of SiOH groups, with two pKa values at ~ 3.9 and 7.7 , respectively. They are nicely in-line with experimental values of ~ 4 and 9 found by SHG and other methods [15, 63-66]. More importantly, the simulation revealed a novel surface reconstruction upon the deprotonation of low pKa SiOH groups, which leads to the new Si(5c) species at about 22 kJ/mol lower than the commonly assumed SiO⁻.

The calculation results immediately explained the non-conservation between SiOH and SiO⁻ groups we observed experimentally. When pH increases from ~ 2 to 9 , most SiOH groups are deprotonated without producing SiO⁻. Meanwhile, the Si-O-Si bonds involved in Si(5c) formation are randomly oriented across the amorphous silica surface, which are inactive in SFVS and not detectable [28]. Only at higher pH, when the more basic SiOH groups are deprotonated and Si(5c) centers are decomposed, the SiO⁻ groups start to appear in the spectra. Though Si(5c) species do not produce SFG signals by themselves, they lead to spectral changes that are directly observable. We computed the Si-O vibrational density of states (VDOS) signature of both SiOH and SiO⁻ groups. For pH near pzc, the SiO₂ surface is fully protonated, and produces a 920 cm⁻¹ mode in VDOS due to the Si-OH stretching vibrations (Fig. 3e). This is in accordance with the ~ 980 cm⁻¹ mode in SF spectra, with a small mismatch due to the well-known frequency shift from the B3LYP functionals [62, 67, 68]. For $4 < \text{pH} < 9$, all acidic Si-OHs are gradually deprotonated by producing Si(5c) species, without yielding SiO⁻. Among the remaining Si-OH species, those hosting the Si(5c) show a redshift by ~ 70 cm⁻¹ compared to those far away from Si(5c) (inset of Fig. 3f). This is caused by the negative charge centered on Si(5c) that weakens the connected Si-OH bond, with the average bond length elongated by ~ 0.05 Å (see details in SI). Evolution of the total Si-OH VDOS upon deprotonation is presented in Fig. 3f, showing a progressive redshift of the entire SiOH band by ~ 40 cm⁻¹, which agreed very well with the experimental observation. For pH > 9 , the deprotonation of residual SiOH groups and the decomposition of Si(5c) lead to the formation of SiO⁻ groups, and indeed a new mode emerge in VDOS near 1000 cm⁻¹ (Fig. 2g) in accordance with the spectroscopy results.

To conclude, we develop an *in situ* experimental study that can shed light on the buried oxide surfaces in water. With DFT-MD calculations, even for a model system like SiO₂/H₂O, which

has been investigated intensively for nearly a century, we were able to reveal unexpected new aspects on its most prevailing surface reactions. The result provides new insight into the nature of surface hydrous species that determine the surface chemistry, reactivity, and all applications based on them [Ref]. Moreover, our understanding of vicinal water structures was largely built on the conventional picture of silica surfaces. The new knowledge about the oxide now calls for a reinvestigation of such understanding: for example, the Si(5c) and SiO⁻ are likely to interact with water, and affect the water structures in different ways. Our experimental scheme is applicable to all sorts of oxide surfaces with no fundamental limitation. Moreover, the usage of semiconducting substrate makes it ready for electrochemistry studies. Combined with theoretical efforts, as well as spectroscopic information from the water side, we can expect to achieve new perceptiveness and mechanistic understanding on oxide/water interfaces, as one of the most important interfacial systems on our planet.

Figures

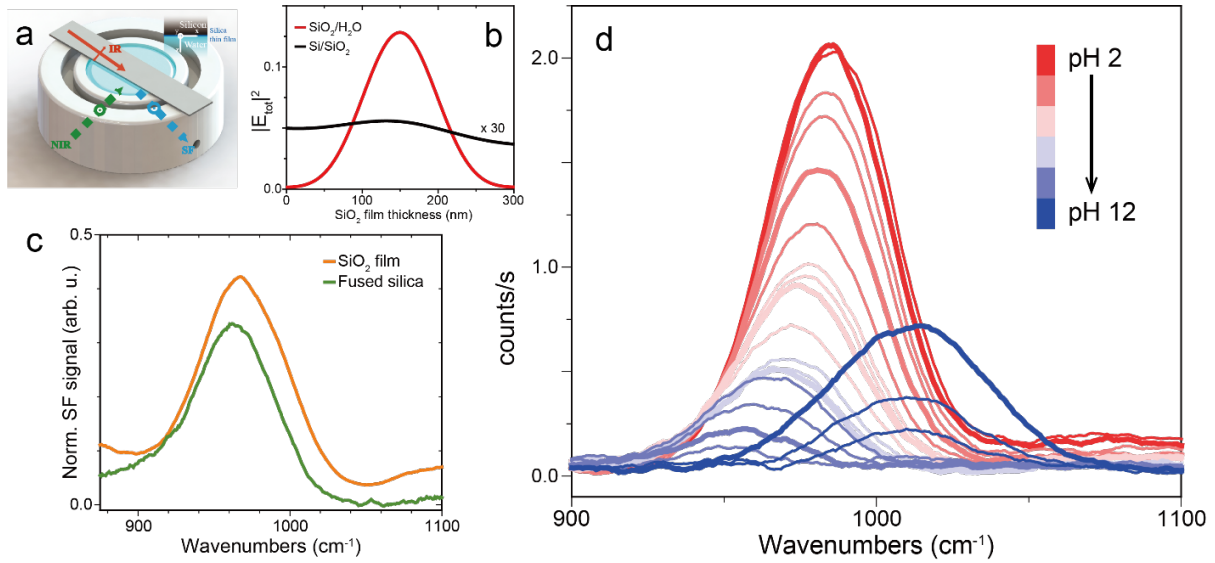


Figure 1. Experimental scheme, the field enhancement and the sum frequency spectra of oxide thin film. **a)** The sample cell and beam geometry. **b)** The calculated local field intensity ($|E_{\text{tot}}|^2$) combining input/output beams at various interfaces in a Si/SiO₂/H₂O junction vs. the SiO₂ thin film thickness. Both Si and H₂O are taken as semi-infinite. The two curves are values at the SiO₂/H₂O and Si/SiO₂ interfaces, respectively, with the latter magnified by 30 times. **c)** The Si-O stretch vibrational SF spectra at the air interface of a 150 nm-thick SiO₂ film grown on Si substrate (orange), and that of a bulk phase fused silica sample (green). Peaks at ~960 cm⁻¹ are due to the stretch vibration of surface Si-OH bonds ($\nu_{\text{Si-OH}}$). Both spectra are normalized to the calculated $|E_{\text{tot}}|^2$ at the two interfaces. **d)** *In situ* SF spectra from the SiO₂/H₂O interface of a Si/SiO₂(150 nm)/H₂O junction with pH increasing from 2 to 12. Spectra at pH 2, 4, 6, 8, 10, and 12 are thickened for clarity. Peaks at 950~980 cm⁻¹ for pH < 10 are due to the $\nu_{\text{Si-OH}}$ mode, and those at ~1020 cm⁻¹ due to the stretch vibration of deprotonated Si-O⁻ mode ($\nu_{\text{Si-O}^-}$). Spectra were taken with the SSP beam polarization combination (S polarized SF, S polarized NIR, and P polarized IR).

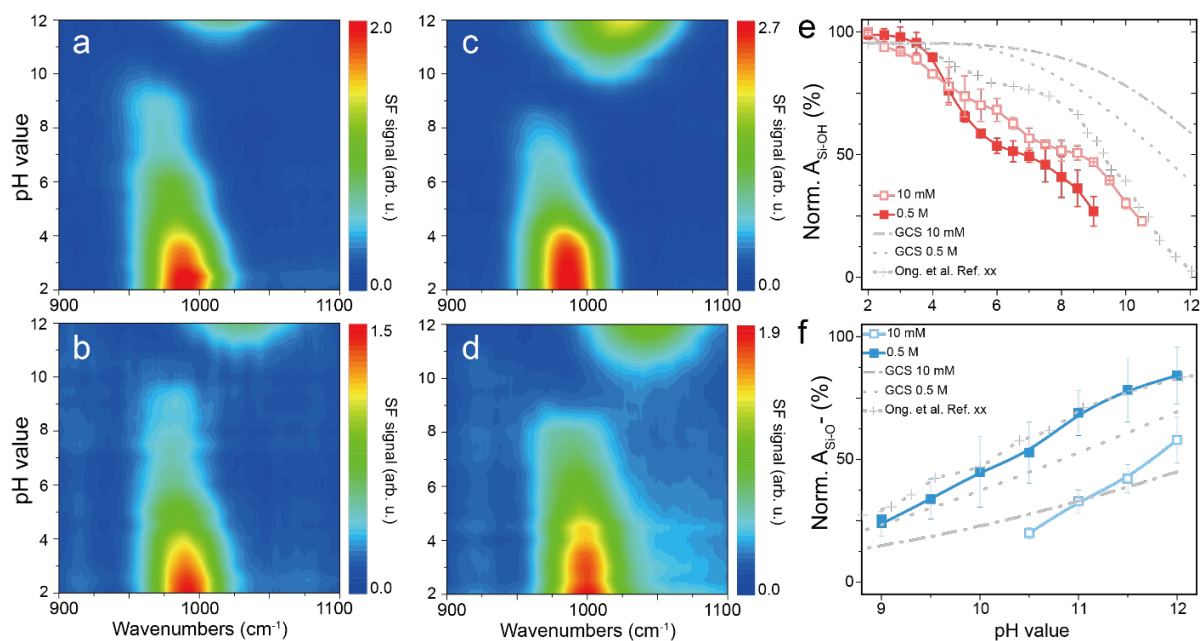


Figure 2. Si-O surface vibration signals at the water interface vs. pH at various conditions. SF spectra with various beam polarization combinations and ion activity (NaCl as the buffer solution): **a)** SSP, 10 mM; **b)** PPP, 10 mM; **c)** SSP, 0.5 M; **d)** PPP, 0.5 M. **e)** Resonant amplitudes of the $\nu_{\text{Si-OH}}$ mode at 10 mM (open square) and 0.5 M (solid square) vs. pH, and calculated SiOH coverage vs. pH from Guoy-Chapman-Stern (GCS) model (dashed and dotted curves) and Ref. xx (cross). All data normalized to that at pH 2. **f)** Resonant amplitudes of the $\nu_{\text{Si-O}^-}$ mode at 10 mM (open square) and 0.5 M (solid square) vs. pH, and calculated SiO⁻ coverage vs. pH from (GCS) model (dashed and dotted curves) and Ref. JCP2005 (cross).

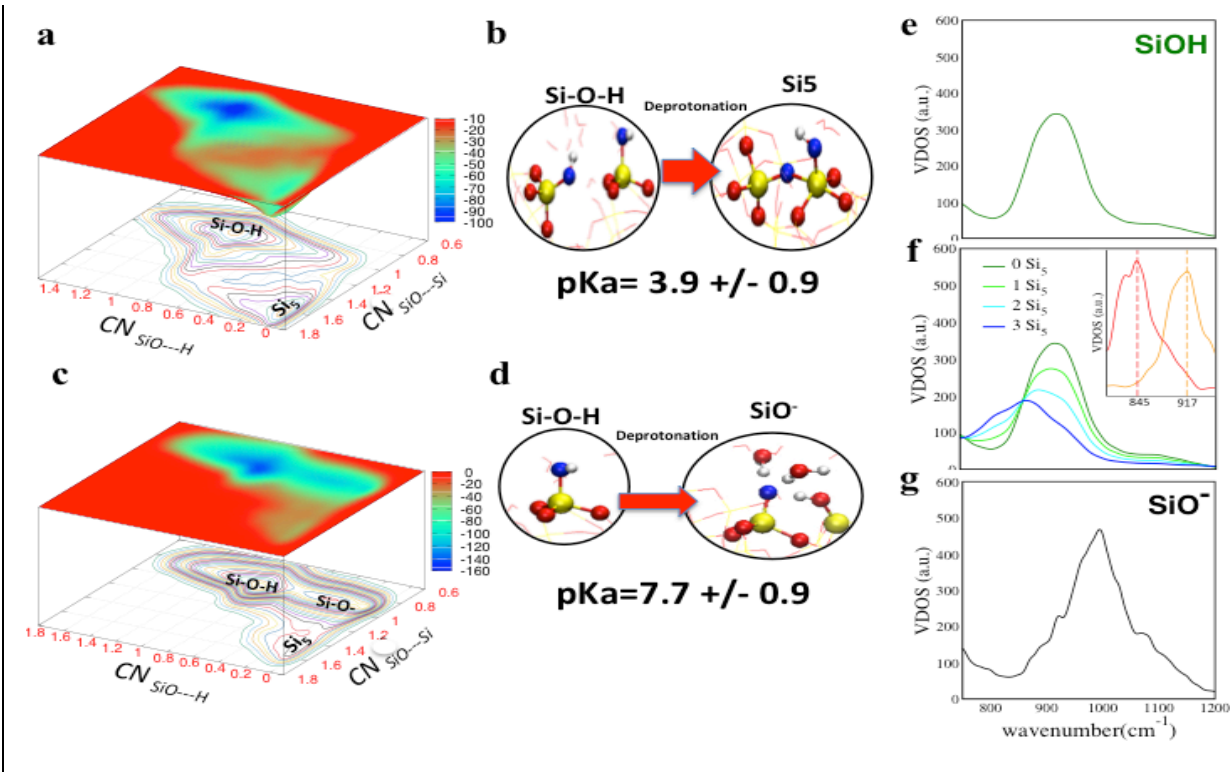


Figure 3. Free energy landscapes, reaction schemes and vibrational density of states (VDOS) spectra of various surface species by the DFT-MD simulation of silica/water interface. a) The free energy landscape associated with SiOH deprotonation process at acidic pH. Two minima associated with SiOH groups and the reconstructed five-fold Si [Si(5c)] species are clearly seen. **b)** Top: reaction scheme of the SiOH deprotonation process leading to Si(5c) structures described by **a)**; bottom: the charge distribution near Si(5c). **c)** The free energy landscape associated with SiOH deprotonation process at more basic pH. The energy minimum associated with Si(5c) species diminishes, and is replaced by a new minimum with SiO⁻ group. **d)** Top: reaction scheme of the SiOH deprotonation process leading to SiO⁻ group described by **c)**; bottom: the charge distribution near SiO⁻. **e)** VDOS spectra arising from SiOH groups at the highest coverage. **f)** Spectra from residual SiOH groups upon the progressive increase of the Si(5c) structures presented on the surface. **Inset:** Spectra from the SiOH group associated with normal four-fold Si species (yellow) and that with Si(5c) species (red). **g)** Spectra from SiO⁻ groups.

References:

- [1]. Brown, G.E., V.E. Henrich, W.H. Casey, D.L. Clark, C. Eggleston, A. Felmy, D.W. Goodman, M. Gratzel, G. Maciel, M.I. McCarthy, K.H. Nealson, D.A. Sverjensky, M.F. Toney, and J.M. Zachara, Metal oxide surfaces and their interactions with aqueous solutions and microbial organisms. *CHEMICAL REVIEWS*, 1999. 99(1): p. 77-174.
- [2]. Henderson, M.A., The interaction of water with solid surfaces: fundamental aspects revisited. *SURFACE SCIENCE REPORTS*, 2002. 46(PII S0167-5729(01)00020-61-8): p. 1-308.
- [3]. Putnis, A., Why Mineral Interfaces Matter. *Science*, 2014. 343(6178): p. 1441-1442.
- [4]. Gin, S., L. Neill, M. Fournier, P. Frugier, T. Ducasse, M. Tribet, A. Abdelouas, B. Parruzot, J. Neeway, and N. Wall, The controversial role of inter-diffusion in glass alteration. *Chemical Geology*, 2016. 440: p. 115-123.
- [5]. Striolo, A., From Interfacial Water to Macroscopic Observables: A Review. *ADSORPTION SCIENCE & TECHNOLOGY*, 2011. 29(3): p. 211-258.
- [6]. Wen, Y., S. Zha, X. Liu, S. Yang, P. Guo, G. Shi, H. Fang, Y.R. Shen, and C. Tian, Unveiling Microscopic Structures of Charged Water Interfaces by Surface-Specific Vibrational Spectroscopy. *Physical Review Letters*, 2016. 116(1): p. 016101.
- [7]. Zaera, F., Probing Liquid/Solid Interfaces at the Molecular Level. *Chemical Reviews*, 2012. 112(5): p. 2920-2986.
- [8]. Darlington, A.M. and J.M. Gibbs-Davis, Bimodal or Trimodal? The Influence of Starting pH on Site Identity and Distribution at the Low Salt Aqueous/Silica Interface. *The Journal of Physical Chemistry C*, 2015. 119(29): p. 16560-16567.
- [9]. Baldelli, S., Interfacial Structure of Room-Temperature Ionic Liquids at the Solid - Liquid Interface as Probed by Sum Frequency Generation Spectroscopy. *The Journal of Physical Chemistry Letters*, 2013. 4(2): p. 244-252.
- [10]. Lis, D., E.H.G. Backus, J. Hunger, S.H. Parekh, and M. Bonn, Liquid flow along a solid surface reversibly alters interfacial chemistry. *Science*, 2014. 344(6188): p. 1138.
- [11]. Waychunas, G.A., Y.R. Shen and V. Ostroverkhov, New Information on Water Interfacial Structure Revealed by Phase-Sensitive Surface Spectroscopy. *Physical Review Letters*, 2005. 94(4): p. 046102.
- [12]. Jubb, A.M., W. Hua and H.C. Allen, Organization of Water and Atmospherically Relevant Ions and Solutes: Vibrational Sum Frequency Spectroscopy at the Vapor/Liquid and Liquid/Solid Interfaces. *Accounts of Chemical Research*, 2012. 45(1): p. 110-119.
- [13]. Sung, J., L. Zhang, C. Tian, G.A. Waychunas, and Y.R. Shen, Surface Structure of Protonated R-Sapphire (1 $\bar{1}$ 02) Studied by Sum-Frequency Vibrational Spectroscopy. *Journal of the American Chemical Society*, 2011. 133(11): p. 3846-3853.
- [14]. Corn, R.M. and D.A. Higgins, Optical second harmonic generation as a probe of surface chemistry. *Chemical Reviews*, 1994. 94(1): p. 107-125.
- [15]. Ong, S., X. Zhao and K.B. Eisenthal, Polarization of water molecules at a charged interface: second harmonic studies of the silica/water interface. *Chemical Physics Letters*, 1992. 191(3): p. 327-335.
- [16]. Fan, H., F. Li, R.N. Zare, and K. Lin, Characterization of Two Types of Silanol Groups on Fused-Silica Surfaces Using Evanescent-Wave Cavity Ring-Down Spectroscopy. *Analytical Chemistry*, 2007. 79(10): p. 3654-3661.
- [17]. Yang, Z., Q. Li and K.C. Chou, Structures of Water Molecules at the Interfaces of Aqueous Salt Solutions and Silica: Cation Effects. *The Journal of Physical Chemistry C*, 2009. 113(19): p. 8201-8205.
- [18]. Ostroverkhov, V., G.A. Waychunas and Y.R. Shen, New information on water interfacial structure revealed by phase-sensitive surface spectroscopy. *PHYSICAL REVIEW LETTERS*, 2005. 94(0461024).
- [19]. Shen, Y.R. and V. Ostroverkhov, Sum-frequency vibrational spectroscopy on water interfaces: Polar orientation of water molecules at interfaces. *CHEMICAL REVIEWS*, 2006. 106(4): p. 1140-1154.
- [20]. Ostroverkhov, V., G.A. Waychunas and Y.R. Shen, Vibrational spectra of water at water/alpha-quartz (0001) interface. *CHEMICAL PHYSICS LETTERS*, 2004. 386(1-3): p. 144-148.
- [21]. DU, Q., E. FREYSZ and Y.R. SHEN, VIBRATIONAL-SPECTRA OF WATER-MOLECULES AT QUARTZ WATER INTERFACES. *PHYSICAL REVIEW LETTERS*, 1994. 72(2): p. 238-241.
- [22]. Li, I., J. Bandara and M.J. Shultz, Time Evolution Studies of the H₂O/Quartz Interface Using Sum Frequency Generation, Atomic Force Microscopy, and Molecular Dynamics. *Langmuir*, 2004. 20(24): p. 10474-10480.

- [23]. Eisenthal, K.B., Liquid Interfaces Probed by Second-Harmonic and Sum-Frequency Spectroscopy. *Chemical Reviews*, 1996. 96(4): p. 1343-1360.
- [24]. Covert, P.A. and D.K. Hore, Geochemical Insight from Nonlinear Optical Studies of Mineral - Water Interfaces. *Annual Review of Physical Chemistry*, 2016. 67(1): p. 233-257.
- [25]. Geiger, F.M., Second Harmonic Generation, Sum Frequency Generation, and $\chi^{(3)}$: Dissecting Environmental Interfaces with a Nonlinear Optical Swiss Army Knife. *Annual Review of Physical Chemistry*, 2009. 60(1): p. 61-83.
- [26]. Backus, E., J. Schaefer and M. Bonn, The mineral/water interface probed with nonlinear optical spectroscopy. *Angew Chem Int Ed Engl*, 2020.
- [27]. Liu, W. and Y.R. Shen, Sum-frequency phonon spectroscopy on alpha-quartz. *PHYSICAL REVIEW B*, 2008. 78(0243022).
- [28]. Liu, W. and Y.R. Shen, Surface vibrational modes of alpha-quartz(0001) probed by sum-frequency spectroscopy. *PHYSICAL REVIEW LETTERS*, 2008. 101(0161011).
- [29]. Liu, X., T. Zhou and W. Liu, Structural variation of anatase (101) under near infrared irradiations monitored by sum-frequency surface phonon spectroscopy. *JOURNAL OF CHEMICAL PHYSICS*, 2019. 150(0847018).
- [30]. Yang, D., Y. Li, X. Liu, Y. Cao, Y. Gao, Y.R. Shen, and W. Liu, Facet-specific interaction between methanol and TiO₂ probed by sum-frequency vibrational spectroscopy. *PROCEEDINGS OF THE NATIONAL ACADEMY OF SCIENCES OF THE UNITED STATES OF AMERICA*, 2018. 115(17): p. E3888-E3894.
- [31]. Tong, Y., J. Wirth, H. Kirsch, M. Wolf, P. Saalfrank, and R.K. Campen, Optically probing Al-O and O-H vibrations to characterize water adsorption and surface reconstruction on alpha-alumina: An experimental and theoretical study. *JOURNAL OF CHEMICAL PHYSICS*, 2015. 142(0547045).
- [32]. Shi, H., Y. Zhang, H. Wang, and W. Liu, Matrix formalism for radiating polarization sheets in multilayer structures of arbitrary composition. *CHINESE OPTICS LETTERS*, 2017. 15(0819018).
- [33]. Dong, Y., S.V. Pappu and Z. Xu, Detection of Local Density Distribution of Isolated Silanol Groups on Planar Silica Surfaces Using Nonlinear Optical Molecular Probes. *Analytical Chemistry*, 1998. 70(22): p. 4730-4735.
- [34]. O'Reilly, J.P., C.P. Butts, I.A. l'Anso, and A.M. Shaw, Interfacial pH at an Isolated Silica-Water Surface. *Journal of the American Chemical Society*, 2005. 127(6): p. 1632-1633.
- [35]. Vance, F.W., B.I. Lemon, J.A. Ekhoﬀ, and J.T. Hupp, Interrogation of Nanoscale Silicon Dioxide/Water Interfaces via Hyper-Rayleigh Scattering. *The Journal of Physical Chemistry B*, 1998. 102(11): p. 1845-1848.
- [36]. Fisk, J.D., R. Batten, G. Jones, J.P. O'Reill, and A.M. Shaw, pH Dependence of the Crystal Violet Adsorption Isotherm at the Silica-Water Interface. *The Journal of Physical Chemistry B*, 2005. 109(30): p. 14475-14480.
- [37]. Rosenholm, J.M., T. Czuryzkiewicz, F. Kleitz, J.B. Rosenholm, and M. Lindén, On the Nature of the Brønsted Acidic Groups on Native and Functionalized Mesoporous Siliceous SBA-15 as Studied by Benzylamine Adsorption from Solution. *Langmuir*, 2007. 23(8): p. 4315-4323.
- [38]. Sulpizi, M., M. Gageot and M. Sprik, The Silica - Water Interface: How the Silanols Determine the Surface Acidity and Modulate the Water Properties. *Journal of Chemical Theory and Computation*, 2012. 8(3): p. 1037-1047.
- [39]. Cimas, Á., F. Tielens, M. Sulpizi, M. Gageot, and D. Costa, The amorphous silica - liquid water interface studied by ab initio molecular dynamics (AIMD): local organization in global disorder. *Journal of Physics: Condensed Matter*, 2014. 26(24): p. 244106.
- [40]. Azam, M.S., C.N. Weeraman and J.M. Gibbs-Davis, Specific Cation Effects on the Bimodal Acid - Base Behavior of the Silica/Water Interface. *The Journal of Physical Chemistry Letters*, 2012. 3(10): p. 1269-1274.
- [41]. Wang, H., Q. Xu, Z. Liu, Y. Tang, G. Wei, Y.R. Shen, and W. Liu, Gate-Controlled Sum-Frequency Vibrational Spectroscopy for Probing Charged Oxide/Water Interfaces. *The Journal of Physical Chemistry Letters*, 2019. 10(19): p. 5943-5948.
- [42]. Urashima, S., A. Myalitsin, S. Nihonyanagi, and T. Tahara, The Topmost Water Structure at a Charged Silica/Aqueous Interface Revealed by Heterodyne-Detected Vibrational Sum Frequency Generation Spectroscopy. *JOURNAL OF PHYSICAL CHEMISTRY LETTERS*, 2018. 9(14): p. 4109-4114.
- [43]. Myalitsin, A., S. Urashima, S. Nihonyanagi, S. Yamaguchi, and T. Tahara, Water Structure at the Buried Silica/Aqueous Interface Studied by Heterodyne-Detected Vibrational Sum-Frequency Generation. *JOURNAL OF PHYSICAL CHEMISTRY C*, 2016. 120(17): p. 9357-9363.
- [44]. Liu, X., D. Yang, Y. Li, Y. Gao, and W. Liu, Anisotropic Adsorption of 2-Phenylethyl Alcohol on a Rutile (110) Surface. *JOURNAL OF PHYSICAL CHEMISTRY C*, 2019. 123(49): p. 29759-29764.

- [45]. Dalstein, L., E. Potapova and E. Tyrode, The elusive silica/water interface: isolated silanols under water as revealed by vibrational sum frequency spectroscopy. *Physical Chemistry Chemical Physics*, 2017. 19(16): p. 10343-10349.
- [46]. Bertoluzza, A., C. Fagnano, M. Antonietta Morelli, V. Gottardi, and M. Guglielmi, Raman and infrared spectra on silica gel evolving toward glass. *Journal of Non-Crystalline Solids*, 1982. 48(1): p. 117-128.
- [47]. Lagström, T., T.A. Gmür, L. Quaroni, A. Goel, and M.A. Brown, Surface Vibrational Structure of Colloidal Silica and Its Direct Correlation with Surface Charge Density. *Langmuir*, 2015. 31(12): p. 3621-3626.
- [48]. Warring, S.L., D.A. Beattie and A.J. McQuillan, Surficial Siloxane-to-Silanol Interconversion during Room-Temperature Hydration/Dehydration of Amorphous Silica Films Observed by ATR-IR and TIR-Raman Spectroscopy. *Langmuir*, 2016. 32(6): p. 1568-1576.
- [49]. Liu, W., L. Zhang and Y.R. Shen, Interfacial layer structure at alcohol/silica interfaces probed by sum-frequency vibrational spectroscopy. *Chemical Physics Letters*, 2005. 412(1): p. 206-209.
- [50]. Richmond, G.L., Molecular Bonding and Interactions at Aqueous Surfaces as Probed by Vibrational Sum Frequency Spectroscopy. *Chemical Reviews*, 2002. 102(8): p. 2693-2724.
- [51]. Shen, Y.R., Surface properties probed by second-harmonic and sum-frequency generation. *Nature*, 1989. 337(6207): p. 519-525.
- [52]. Buck, M. and M. Himmelhaus, Vibrational spectroscopy of interfaces by infrared - visible sum frequency generation. *Journal of Vacuum Science & Technology A*, 2001. 19(6): p. 2717-2736.
- [53]. Vidal, F. and A. Tadjeddine, Sum-frequency generation spectroscopy of interfaces. *Reports on Progress in Physics*, 2005. 68(5): p. 1095-1127.
- [54]. Murashov, V., Ab initio cluster calculations of silica surface sites. *Journal of Molecular Structure*, 2003. 650(1): p. 141-157.
- [55]. Liu, W. and Y.R. Shen, Sum-frequency spectroscopy on bulk and surface phonons of noncentrosymmetric crystals. *ANNALEN DER PHYSIK*, 2011. 523(1-2SI): p. 101-106.
- [56]. Campen, R.K., A.K. Pymmer, S. Nihonyanagi, and E. Borguet, Linking Surface Potential and Deprotonation in Nanoporous Silica: Second Harmonic Generation and Acid/Base Titration. *The Journal of Physical Chemistry C*, 2010. 114(43): p. 18465-18473.
- [57]. Pfeiffer-Laplaud, M., M. Gaigeot and M. Sulpizi, pKa at Quartz/Electrolyte Interfaces. *The Journal of Physical Chemistry Letters*, 2016. 7(16): p. 3229-3234.
- [58]. Pfeiffer-Laplaud, M. and M. Gaigeot, Adsorption of Singly Charged Ions at the Hydroxylated (0001) α -Quartz/Water Interface. *The Journal of Physical Chemistry C*, 2016. 120(9): p. 4866-4880.
- [59]. Dove, P.M. and C.M. Craven, Surface charge density on silica in alkali and alkaline earth chloride electrolyte solutions. *Geochimica et Cosmochimica Acta*, 2005. 69(21): p. 4963-4970.
- [60]. Bolt, G.H., Determination of the Charge Density of Silica Sols. *The Journal of Physical Chemistry*, 1957. 61(9): p. 1166-1169.
- [61]. Sonnefeld, J., A. Göbel and W. Vogelsberger, Surface charge density on spherical silica particles in aqueous alkali chloride solutions. *Colloid and Polymer Science*, 1995. 273(10): p. 926-931.
- [62]. Ugliengo, P., M. Sodupe, F. Musso, I.J. Bush, R. Orlando, and R. Dovesi, Realistic Models of Hydroxylated Amorphous Silica Surfaces and MCM-41 Mesoporous Material Simulated by Large-scale Periodic B3LYP Calculations. *Advanced Materials*, 2008. 20(23): p. 4579-4583.
- [63]. Allen, L.H., E. Matijević and L. Meites, Exchange of Na⁺ for the silanolic protons of silica. *Journal of Inorganic and Nuclear Chemistry*, 1971. 33(5): p. 1293-1299.
- [64]. Leung, K., I.M.B. Nielsen and L.J. Criscenti, Elucidating the Bimodal Acid-Base Behavior of the Water-Silica Interface from First Principles. *Journal of the American Chemical Society*, 2009. 131(51): p. 18358-18365.
- [65]. Darlington, A.M. and J.M. Gibbs-Davis, Bimodal or Trimodal? The Influence of Starting pH on Site Identity and Distribution at the Low Salt Aqueous/Silica Interface. *The Journal of Physical Chemistry C*, 2015. 119(29): p. 16560-16567.
- [66]. Azam, M.S., A. Darlington and J.M. Gibbs-Davis, The influence of concentration on specific ion effects at the silica/water interface. *J Phys Condens Matter*, 2014. 26(24): p. 244107.
- [67]. Becke, A.D., Density - functional thermochemistry. III. The role of exact exchange. *The Journal of Chemical Physics*, 1993. 98(7): p. 5648-5652.
- [68]. Murashov, V.V. and J. Leszczynski, A comparison of the B3LYP and MP2 methods in the calculation of phosphate complexes. *Journal of Molecular Structure: THEOCHEM*, 2000. 529(1): p. 1-14.

Chapter 7

Conclusions and perspectives

Many chemical reactions have been shown strongly accelerated when occurring at aqueous interfaces as compared to bulk water. Such acceleration has been observed on atmospheric aerosols, sprays, water nanodroplets, oil-water emulsions, extended air-water and solid-water interfaces with huge impact in prebiotic, atmospheric, biological and synthetic organic chemistry. A microscopic comprehension of the processes occurring at the boundary between water and other media that govern the enhancement in the reaction rates can open the route for the design of novel and more green chemical processes at industrial scale. However, such understanding is limited by the experimental difficulty in discerning the specific catalytic effects originating from the heterogeneous interfacial water environment.

In this PhD thesis we have provided a molecular description of chosen chemical reactions at aqueous interfaces by means of DFT-MD and enhanced sampling DFT-MD simulations in order to rationalize the catalytic roles of liquid-solid and liquid-vapour interfaces.

The first part of the manuscript (chapters 3 and 4) has been dedicated to the study of the prebiotic peptide bond condensation reaction at the air-water interface. In 2012 Prof. Vaida and collaborators [15] have experimentally observed the formation of polypeptides at room temperature in dilute conditions from amino acid esters and CuCl_2 salt at the air-water interface, suggesting the surface of oceans and marine aerosols as suitable environments for the birth of life on the prebiotic Earth. Understanding the specific role of the air-water interface in the peptide bond condensation reaction and the microscopic reasons for which this reaction occurs at the interface, while it does not occur in bulk water, have been the central objectives of our theoretical investigations.

Our data point to novel catalytic roles of the air-water interface for the peptide bond condensation reaction (see chapter 3) that go beyond the already well-known catalytic interfacial factors, e.g. concentration of reactants, aligning reactants, pKa shifts, partial desolvation of reactants. In particular we have identified how the under-coordinated nature of the interfacial water environment provides specific "reactive" molecular arrangement of the reac-

tants, that is not stable in bulk water. This allows the reaction to proceed at the air-water interface only.

We have further shown the Cl^- in the salt to have a catalytic role at the heart of the peptide bond condensation reaction. The presence of the Cl^- at the interface hence reduces by more than two times the free energy barrier of the reaction rate determining step, by the stabilization of the transition state and by inducing proximity and good orientation of the reactants. These findings can be possibly extended to other water restricted environment processes. For instance, it is interesting to remark that the transition state stabilization and the proximity of reactants, observed along the peptide formation reaction at the air-water interface, are two of the principal catalytic effects that have been ascribed to the Ribosome Active site in the synthesis of polypeptides in biological cells[289].

An intriguing perspective is opened by the catalytic role of the Cl^- revealed in this PhD thesis, that can provide the link between the peptide bond condensation at the air-water interface and the "salt induced peptide formation" (SIPF) reaction known in the literature. The SIPF is a chemical route that produces high yields of polypeptides in simple prebiotic compatible conditions using copper Cu^{2+} and amino acids in a partially dehydrated aqueous environment with high concentration of sodium chloride salt (5M). An essential component of the SIPF reaction is the presence of the Cl^- in the reaction medium[89, 54], i.e. in absence of the Cl^- a dramatic decrease in the polypeptide production is obtained experimentally [91]. In the light of our findings, it would be interesting to provide a molecular insight into the SIPF reaction in order to understand the catalytic roles of the Cl^- along the reaction pathway.

It is also important to know that the same peptide bond reaction as studied in this PhD manuscript leads to high yields of polypeptides in the bulk of ethanol [290]. In such reaction, a reactive complex between the Cu^{2+} , two amino acid leucine-ethyl-esters and one chloride anion Cl^- is formed. The reactive complex in ethanol is found experimentally with a conformation reminiscent of the one observed and characterized for the reactive complex (R) at the air-water interface along our work and in ref.[15]. In the future, it would thus be interesting to investigate the microscopic reasons behind the formation of such reactive complex conformation in liquid ethanol and to compare the results with the ones obtained at the air-water interface in our present work. This could reveal a fascinating similarity between the way air-water interfaces and anhydrous solvents stabilize reactive species along chemical reactions.

Another intriguing aspect is the possible enantio-selectivity (capability of the reaction to form a specific enantiomer) of the peptide bond condensation reaction induced by the air-water interface. It will be interesting in the future to probe the possibility of a preferential formation of L-polypeptides over D-polypeptides at the air-water interface and compare to bulk water conditions. The asymmetric interfacial air-water environment could favour

the condensation of L-amino acids with respect to D-amino acids. This could provide an improvement in the comprehension of the origin of the proteins's homochirality (proteins are composed exclusively by L-amino acids in nature) and could further assess the plausibility of air-water interfaces as source of polypeptides in the primordial Earth.

In the second part of this PhD, we have focused on the characterization of the structure and reactivity of aqueous amorphous silica interfaces by coupling DFT-MD simulations and SFG spectroscopy. The characterization at the molecular level of the structure and reactivity of the amorphous silica-water interface is especially relevant for the development of new technologies in the field of materials design and heterogeneous catalysis.

We have first considered the effect of various interfacial conditions (hydrophilicity, hydrophobicity, pH, electrolytes concentration) on the water organization at the boundary with silica (see chapter 5). We have characterized the water molecular structural arrangements at the interface and their associated SFG signatures as a function of the silica surface degree of hydroxylation and morphology.

Our works reveal how the electrolytes and the surface degree of hydroxylation modulate the water organization at the interface with silica, thereby affecting the interfacial water dynamical, structural and spectroscopic properties. We especially find that lowering the silica surface degree of hydroxylation and increasing the solution electrolytes concentration cause a drastic change in the water organization at the interface with the silica: water molecules maximize water-water interactions formed parallel to the surface (horizontal order) to compensate for the lack of solid-water interactions (vertical order). We observe the transition from a local "quartz-like" inhomogeneous water structure (found at the 4.5 and 7.6 SiOH/nm² hydroxylated surfaces) to an extended homogeneous water 2D-H-Bond network, characterized by water molecules preferentially oriented with their HBonds parallel to the silica surface. This is the same organization that we revealed and fully characterized at the prototypic hydrophobic air-water interface in ref.[103].

The specific SFG signatures of the different water arrangements formed at the interface with silica have been identified and their evolution as a function of interfacial conditions (hydrophilicity, electrolytes concentration) have been characterized. This opens the way for a clear molecular interpretation of debated experimental SFG spectra.

In a second step (chapter 6, we have characterized the silica surface reactivity in contact with liquid water as a function of pH conditions. We have followed the evolution of the silica surface structure and chemistry in response to variations in the water pH conditions by coupling experimental SFG phonon spectroscopy (in collaboration with Prof. Weitao Liu, Fudan University, China) with DFT-MD simulations. The direct access to the chemical nature of the surface groups and their organization under different pH conditions given by phonon SFG experiments, coupled with the molecular

rationalization emerging from the DFT-MD simulations has provided a deep insight into the controversial acid-base behaviour of the silica surface.

Our work shows that a molecular picture based only on the balance between Si-OH (silanol) and Si-O⁻ (silanolate) species at the silica surface is not enough in order to rationalize the trends in the SFG bands as a function of pH. The emergence of a third molecular species, denoted "Si5", reveals a more complex acid-base surface chemistry at aqueous amorphous silica surfaces for the pH values in the range 4-9. The silanols that lead to the formation of stable Si5 species are found to be more acidic (by about 3.8 pKa units) than the ones forming stable silanolate Si-O⁻ species.

Our data provide a new microscopical rationalization of the acid-base bimodal behaviour of the silica surface groups observed experimentally and reveal the Si5 species as an essential key to understand the chemistry at aqueous silica surfaces.

Future works able to deconvolve and quantify the silica surface charges generated from respectively the silanolate and Si5 species are needed in order to provide a direct link between the acid-base chemistry of silica and the experimental evolution of the silica surface charge as a function of pH[212, 268, 267]. The molecular picture of the amorphous silica surface consisting in 19% of the silanols exhibiting a pKa of 4.5 (acidic silanols) and 81% exhibiting a pKa of 8.5 (non acidic silanols) extrapolated by indirect measurements of the surface charge as a function of pH[212, 268, 267] could be altered when taking into account the surface charge generated by the formation of Si5 species in the 4-9 pH range.

Si5 species have been shown to have significant influence on deformation mechanisms and chemical reactivity of silicate rocks[193, 272, 273]. Now that we have revealed their presence at aqueous amorphous silica surfaces it would be interesting to characterize their effects on other chemical and physical properties of silica surfaces. For instance, the presence of Si5 species at silica surfaces present in/on the Earth crust (silica is the most abundant compound on Earth) could alter the adsorption of electrolytes present in natural water and polluting emissions, with an impact in the domains of geochemistry, geophysics and environmental sciences.

The adsorption of ions on silica surfaces is also of extreme importance as it modulates the surface acidity (see sections 5.3 and 6.1). The microscopic reasons behind the dependence of the silica surface acidity on the solution ionic strength are still debated and unclear. In the light of our recent findings on the silica surface acidity (see chapter 6) and on the silica-water interface organization at high ionic strength solution (see section 5.9 and ref.[243]), we could investigate how electrolytes modulate the silica surface acidity by enhanced sampling DFT-MD simulations. We could in particular focus on the effect of the electrolytes on the relative stability of silanols (Si-OH), silanolate (SiO⁻) and Si5 species, as a function of pH, and quantify the ion-induced shifts in the pKas of the surface sites. How high concentrations of cations could affect the relative stability between Si5 and SiO⁻ species at the silica surface and

how this effect could in turn modulate the surface acidity, are also relevant questions for future investigations. Theoretical results could be directly validated against SFG experiments performed in the group of Prof. Weitao Liu at Fudan University in China.

Another perspective is the possible formation of Si5 species on crystalline silica surfaces. Si5 structures have been found on the dry (011) α -quartz surface as the result of the reconstruction process following the homolytic fracture of α -quartz crystal at room temperature[274]. We have investigated the acidity of the aqueous (0001) α -quartz surface in section 6.7.4, finding no formation of Si5 species for both the in-plane and out-of-plane silanols of the particular (0001) facet. In the future we will extend our investigations to other α -quartz crystalline facets. This could assess the possible presence of Si5 species on silicalite rocks in nature, and could provide further microscopic insights into the specific surface morphology necessary for the formation of Si5 species on silica.

Bibliography

- [1] R. M. Bain, C. J. Pulliam, X. Yan, K. F. Moore, T. Muller and R. G. Cooks, *J. Chem. Educ.*, 2014, **91**, 1985–1989.
- [2] J. K. Lee, S. Kim, H. G. Nam and R. N. Zare, *Proc. Natl. Acad. Sci.*, 2015, **112**, 3898–3903.
- [3] J. K. Lee, S. Banerjee, H. G. Nam and R. N. Zare, *Q. Rev. Biophys.*, 2015, **48**, 437–444.
- [4] M. R. Watry and G. L. Richmond, *J. Phys. Chem. B*, 2002, **106**, 12517–12523.
- [5] A. Fallah-Araghi, K. Meguellati, J.-C. Baret, A. El Harrak, T. Mangeat, M. Karplus, S. Ladame, C. M. Marques and A. D. Griffiths, *Phys. Rev. Lett.*, 2014, **112**, 028301.
- [6] S. Vaitheeswaran and D. Thirumalai, *J. Am. Chem. Soc.*, 2006, **128**, 13490–13496.
- [7] J. Pierce, M. Evans, C. Scott, S. D’Andrea, D. Farmer, E. Swietlicki and D. Spracklen, *Atmos. Chem. Phys.*, 2013, **13**, 3163–3176.
- [8] C. Zhu, M. Kumar, J. Zhong, L. Li, J. S. Francisco and X. C. Zeng, *J. Am. Chem. Soc.*, 2016, **138**, 11164–11169.
- [9] J. M. Beames, F. Liu, L. Lu and M. I. Lester, *J. Am. Chem. Soc.*, 2012, **134**, 20045–20048.
- [10] T. R. Lewis, M. A. Blitz, D. E. Heard and P. W. Seakins, *Phys. Chem. Chem. Phys.*, 2015, **17**, 4859–4863.
- [11] J. Zhong, C. Zhu, L. Li, G. L. Richmond, J. S. Francisco and X. C. Zeng, *J. Am. Chem. Soc.*, 2017, **139**, 17168–17174.
- [12] J. Zhong, M. Kumar, C. Q. Zhu, J. S. Francisco and X. C. Zeng, *Angew. Chem. Int.*, 2017, **56**, 7740–7744.
- [13] J. Zhong, M. Kumar, J. S. Francisco and X. C. Zeng, *Acc. Chem. Res.*, 2018, **51**, 1229–1237.
- [14] A. Brack, *Chem. Biodivers.*, 2007, **4**, 665–679.

- [15] E. C. Griffith and V. Vaida, *Proc. Natl. Acad. Sci.*, 2012, **109**, 15697–15701.
- [16] S. Laporte, F. Pietrucci, F. Guyot and A. M. Saitta, *J. Phys. Chem. C*, 2020, **124**, 5125–5131.
- [17] P. A. Zapata, J. Faria, M. P. Ruiz, R. E. Jentoft and D. E. Resasco, *J. Am. Chem. Soc.*, 2012, **134**, 8570–8578.
- [18] L. Zhang, K. Chen, B. Chen, J. L. White and D. E. Resasco, *J. Am. Chem. Soc.*, 2015, **137**, 11810–11819.
- [19] K. Chen, J. Kelsey, J. L. White, L. Zhang and D. Resasco, *ACS Catalysis*, 2015, **5**, 7480–7487.
- [20] E. Schreiner, N. N. Nair, C. Wittekindt and D. Marx, *J. Am. Chem. Soc.*, 2011, **133**, 8216–8226.
- [21] D. T. Bregante, A. M. Johnson, A. Y. Patel, E. Z. Ayla, M. J. Cordon, B. C. Bukowski, J. Greeley, R. Gounder and D. W. Flaherty, *J. Am. Chem. Soc.*, 2019, **141**, 7302–7319.
- [22] C. B. Dartt and M. E. Davis, *Appl. Catal. A*, 1996, **143**, 53–73.
- [23] C. Khouw, C. Dartt, J. Labinger and M. Davis, *J. Catal.*, 1994, **149**, 195–205.
- [24] P. R. Davies, *Top. Catal.*, 2016, **59**, 671–677.
- [25] C.-R. Chang, Z.-Q. Huang and J. Li, *Wiley Interdiscip. Rev. Comput. Mol. Sci.*, 2016, **6**, 679–693.
- [26] H.-Y. Su, M.-M. Yang, X.-H. Bao and W.-X. Li, *J. Phys. Chem. C*, 2008, **112**, 17303–17310.
- [27] M. Haruta, T. Kobayashi, H. Sano and N. Yamada, *Chem. Lett.*, 1987, **16**, 405–408.
- [28] M. Date and M. Haruta, *J. Catal.*, 2001, **201**, 221–224.
- [29] B. R. Goldsmith, T. Hwang, S. Seritan, B. Peters and S. L. Scott, *J. Am. Chem. Soc.*, 2015, **137**, 9604–9616.
- [30] A. Corma, P. Esteve and A. Martinez, *J. Catal.*, 1996, **161**, 11–19.
- [31] P. Ugliengo, M. Sodupe, F. Musso, I. J. Bush, R. Orlando and R. Dovesi, *Adv. Mater.*, 2008, **20**, 4579–4583.
- [32] M. Gierada, I. Petit, J. Handzlik and F. Tielens, *Phys. Chem. Chem. Phys.*, 2016, **18**, 32962–32972.
- [33] K. Stawicka, M. Gierada, J. Gajewska, F. Tielens and M. Ziolek, *Appl. Surf. Sci.*, 2020, **513**, 145802.

- [34] P. Anzenbacher Jr and M. A. Palacios, *Nat. Chem.*, 2009, **1**, 80.
- [35] A. N. Khlobystov, *ACS nano*, 2011, **5**, 9306–9312.
- [36] D. M. Vriezema, M. Comellas Aragonès, J. A. Elemans, J. J. Cornelissen, A. E. Rowan and R. J. Nolte, *Chem. Rev.*, 2005, **105**, 1445–1490.
- [37] A. L. Christensen, C. Lohr, S. M. Christensen and D. Stamou, *Lab on a Chip*, 2013, **13**, 3613–3625.
- [38] S. Ruiz-Barragan, D. Munoz-Santiburcio and D. Marx, *J. Phys. Chem. Lett.*, 2018, **10**, 329–334.
- [39] S. Ruiz-Barragan, D. Muñoz-Santiburcio, S. Körning and D. Marx, *Phys. Chem. Chem. Phys.*, 2020.
- [40] Y. A. P. Sirkin, A. Hassanali and D. A. Scherlis, *J. Phys. Chem. Lett.*, 2018, **9**, 5029–5033.
- [41] L. Rubinovich and M. Polak, *Top. Catal.*, 2018, **61**, 1237–1246.
- [42] D. Muñoz-Santiburcio and D. Marx, *Phys. Rev. Lett.*, 2017, **119**, 056002.
- [43] D. Munoz-Santiburcio and D. Marx, *Chem. Sci.*, 2017, **8**, 3444–3452.
- [44] S. Pantaleone, P. Ugliengo, M. Sodupe and A. Rimola, *CHEM-EUR J.*, 2018, **24**, 16292–16301.
- [45] M. Kumar, J. Zhong, X. C. Zeng and J. S. Francisco, *J. Am. Chem. Soc.*, 2018, **140**, 4913–4921.
- [46] A. Laio and M. Parrinello, *Proc. Natl. Acad. Sci.*, 2002, **99**, 12562–12566.
- [47] M. Sprik and G. Ciccotti, *J. Chem. Phys.*, 1998, **109**, 7737–7744.
- [48] S. Pezzotti, D. R. Galimberti and M.-P. Gaigeot, *J. Phys. Chem. Lett.*, 2017, **8**, 3133–3141.
- [49] S. Pezzotti, D. R. Galimberti and M.-P. Gaigeot, *Phys. Chem. Chem. Phys.*, 2019, **21**, 22188–22202.
- [50] F. S. Brigiano, Y. Jeanvoine, A. Largo and R. Spezia, *A & A*, 2018, **610**, A26.
- [51] T. K. Esser, H. Knorke, F. Siro-Brigiano, D. R. Galimberti, K. R. Asmis, M.-P. Gaigeot and J. M. Lisy, *Phys. Chem. Chem. Phys.*, 2018, **20**, 28476–28486.
- [52] J. W. Schopf, *Science*, 1993, **260**, 640–646.

- [53] J. G. Forsythe, S.-S. Yu, I. Mamajanov, M. A. Grover, R. Krishnamurthy, F. M. Fernández and N. V. Hud, *Angew. Chem. Int.*, 2015, **54**, 9871–9875.
- [54] B. M. Rode, H. L. Son, Y. Suwannachot and J. Bujdak, *Origins Life Evol. B.*, 1999, **29**, 273–286.
- [55] S. L. Miller *et al.*, *Science*, 1953, **117**, 528–529.
- [56] M. H. Engel and B. Nagy, *Nature*, 1982, **296**, 837.
- [57] M. H. Engel, S. Macko and J. Silfer, *Nature*, 1990, **348**, 47.
- [58] M. H. Engel and S. Macko, *Nature*, 1997, **389**, 265.
- [59] J. R. Cronin and S. Chang, in *The chemistry of life's origins*, Springer, 1993, pp. 209–258.
- [60] K. Plankensteiner, H. Reiner, B. Schranz and B. M. Rode, *Angew. Chem. Int.*, 2004, **43**, 1886–1888.
- [61] I. Mamajanov, P. J. MacDonald, J. Ying, D. M. Duncanson, G. R. Dowdy, C. A. Walker, A. E. Engelhart, F. M. Fernandez, M. A. Grover, N. V. Hud *et al.*, *Macromolecules*, 2014, **47**, 1334–1343.
- [62] E. Schreiner, N. N. Nair and D. Marx, *J. Am. Chem. Soc.*, 2008, **130**, 2768–2770.
- [63] J.-F. Lambert, *Origins Life Evol. B.*, 2008, **38**, 211–242.
- [64] M. G. Schwendinger and B. M. Rode, *Inorganica Chim. Acta*, 1991, **186**, 247–251.
- [65] B. M. Rode and M. G. Schwendinger, *Origins Life. Evol. B.*, 1990, **20**, 401–410.
- [66] V. Goldschmidt, *New Biol.*, 1952, **12**, 97–105.
- [67] R. M. Hazen, *Am. Min.*, 2006, **91**, 1715.
- [68] A. CAIRNS-SMITH and H. Hartman, *Cambridge and New York, Cambridge University Press, 1986, 204*, 1986.
- [69] M. Schoonen, A. Smirnov and C. Cohn, *AMBIO: J. Hum. Environ.*, 2004, **33**, 539–552.
- [70] T. Georgelin, M. Jaber, H. Bazzi and J.-F. Lambert, *Origins Life Evol. B.*, 2013, **43**, 429–443.
- [71] J. B. Lambert, S. A. Gurusamy-Thangavelu and K. Ma, *Science*, 2010, **327**, 984–986.

- [72] A. Ricardo, M. Carrigan, A. Olcott and S. Benner, *Science*, 2004, **303**, 196–196.
- [73] K. Von Damm, *Annu. Rev. Earth Pl. Sc.*, 1990, **18**, 173–204.
- [74] K. L. Von Damm, M. Lilley, W. Shanks Iii, M. Brockington, A. Bray, K. O'grady, E. Olson, A. Graham, G. Proskurowski *et al.*, *Earth Planet. Sc. Lett.*, 2003, **206**, 365–378.
- [75] N. G. Holm and J. L. Charlou, *Earth Planet. Sc. Lett.*, 2001, **191**, 1–8.
- [76] J. A. Baross and S. E. Hoffman, *Origins Life Evol. B.*, 1985, **15**, 327–345.
- [77] C. Huber and G. Wächtershäuser, *Science*, 1998, **281**, 670–672.
- [78] C. Huber, W. Eisenreich, S. Hecht and G. Wächtershäuser, *Science*, 2003, **301**, 938–940.
- [79] S. Boudesocque, O. Dargaud, L. Stievano, C. Methivier, J.-F. Lambert, T. Coradin and C.-M. Pradier, *Surf. Interface Anal.*, 2010, **42**, 466.
- [80] A. Rimola, S. Tosoni, M. Sodupe and P. Ugliengo, *ChemPhysChem*, 2006, **7**, 157–163.
- [81] A. Rimola, M. Sodupe and P. Ugliengo, *J. Phys. Chem. C*, 2016, **120**, 24817–24826.
- [82] A. Rimola, M. Fabbiani, M. Sodupe, P. Ugliengo and G. Martra, *ACS Catalysis*, 2018, **8**, 4558–4568.
- [83] R. Saladino, G. Botta, B. M. Bizzarri, E. Di Mauro and J. M. Garcia Ruiz, *Biochem.*, 2016, **55**, 2806–2811.
- [84] M. Signorile, C. Salvini, L. Zamirri, F. Bonino, G. Martra, M. Sodupe and P. Ugliengo, *Life*, 2018, **8**, 42.
- [85] L. Stievano, L. Y. Piao, I. Lopes, M. Meng, D. Costa and J.-F. Lambert, *Eur J Mineral*, 2007, **19**, 321–331.
- [86] V. A. Basiuk, *Surfactant Sci. Ser.*, 1998, 55–88.
- [87] N. Vlasova and L. Golovkova, *Colloid J.*, 2004, **66**, 657–662.
- [88] K. Ruiz-Mirazo, C. Briones and A. de la Escosura, *Chem. Rev.*, 2014, **114**, 285–366.
- [89] B. M. Rode and Y. Suwannachot, *Coord. Chem. Rev.*, 1999, **190**, 1085–1099.
- [90] B. M. Rode, *Peptides*, 1999, **20**, 773–786.
-

- [91] A. H. Eder and B. M. Rode, *J. Chem. Soc., Dalton Trans.*, 1994, 1125–1130.
- [92] F. Li, D. Fitz, D. G. Fraser and B. M. Rode, *Journal of inorganic biochemistry*, 2008, **102**, 1212–1217.
- [93] E. C. Griffith, A. F. Tuck and V. Vaida, *Acc. Chem. Res.*, 2012, **45**, 2106–2113.
- [94] A. D. Anbar, *Science*, 2008, **322**, 1481–1483.
- [95] A. Tuck, *Surv. Geophys.*, 2002, **23**, 379–409.
- [96] C. M. Dobson, G. B. Ellison, A. F. Tuck and V. Vaida, *Proc. Natl. Acad. Sci.*, 2000, **97**, 11864–11868.
- [97] D. Donaldson, H. Tervahattu, A. Tuck and V. Vaida, *Origins Life Evol. B.*, 2004, **34**, 57–67.
- [98] A. Cairns-Smith, *Nature*, 1978, **276**, 807.
- [99] X. Zhao, S. Subrahmanyan and K. B. Eisenthal, *Chem. Phys. Lett.*, 1990, **171**, 558–562.
- [100] R. Bianco, S. Wang and J. T. Hynes, *J. Phys. Chem. A*, 2008, **112**, 9467–9476.
- [101] K. Liao and X. Du, *J. Phys. Chem. B*, 2009, **113**, 1396–1403.
- [102] P. A. Sutton and D. A. Buckingham, *Acc. Chem. Res.*, 1987, **20**, 357–364.
- [103] S. Pezzotti, D. R. Galimberti and M.-P. Gaigeot, *J. Phys. Chem. Lett.*, 2017, **8**, 3133–3141.
- [104] A. Serva, S. Pezzotti, S. Bougueroua, D. R. Galimberti and M.-P. Gaigeot, *J. Mol. Struct.*, 2018, **1165**, 71 – 78.
- [105] S. Pezzotti, A. Serva and M.-P. Gaigeot, *J. Chem. Phys.*, 2018.
- [106] S. Minakata and M. Komatsu, *Chem. Rev.*, 2009, **109**, 711–724.
- [107] K. El Hage, P. K. Gupta, R. Bemish and M. Meuwly, *J. Phys. Chem. Lett.*, 2017, **8**, 4600–4607.
- [108] C. Aerts, E. Verraedt, A. Depla, L. Follens, L. Froyen, J. Van Humbeeck, P. Augustijns, G. Van den Mooter, R. Mellaerts and J. Martens, *Int. J. Pharm.*, 2010, **397**, 84–91.
- [109] M. Delle Piane, S. Vaccari, M. Corno and P. Ugliengo, *J. Phys. Chem. A*, 2014, **118**, 5801–5807.

-
- [110] M. Delle Piane, M. Corno, A. Pedone, R. Dovesi and P. Ugliengo, *J. Phys. Chem. C*, 2014, **118**, 26737–26749.
- [111] F. Tielens, N. Folliet, L. Bondaz, S. Etemovic, F. Babonneau, C. Gervais and T. Azaïs, *J. Phys. Chem. C*, 2017, **121**, 17339–17347.
- [112] F. Tielens, C. Gervais, J. F. Lambert, F. Mauri and D. Costa, *Chem. Mater.*, 2008, **20**, 3336–3344.
- [113] N. Folliet, C. Roiland, S. Bégu, A. Aubert, T. Mineva, A. Goursot, K. Selvaraj, L. Duma, F. Tielens, F. Mauri *et al.*, *J. Am. Chem. Soc.*, 2011, **133**, 16815–16827.
- [114] S. Pezzotti, D. R. Galimberti, Y. R. Shen and M.-P. Gageot, *Phys. Chem. Chem. Phys.*, 2018, **20**, 5190–5199.
- [115] L. Verlet, *Physical review*, 1967, **159**, 98.
- [116] P. Hohenberg and W. Kohn, *Physical review*, 1964, **136**, B864.
- [117] S. Grimme, *J. Comput. Chem.*, 2006, **27**, 1787–1799.
- [118] J. Hutter, M. Iannuzzi, F. Schiffmann and J. VandeVondele, *WIREs Comput Mol Sci*, 2014, **4**, 15–25.
- [119] J. VandeVondele, M. Krack, F. Mohamed, M. Parrinello, T. Chassaing and J. Hutter, *Comp. Phys. Comm.*, 2005, **167**, 103–128.
- [120] A. D. Becke, *Phys. Rev. A*, 1988, **38**, 3098–3100.
- [121] C. Lee, W. Yang and R. G. Parr, *Phys. Rev. B*, 1988, **37**, 785–789.
- [122] S. Grimme, J. Antony, S. Ehrlich and H. Krieg, *J. Chem. Phys.*, 2010, **132**, 154104.
- [123] S. Goedecker, M. Teter and J. Hutter, *Phys. Rev. B.*, 1996, **54**, 1703–1710.
- [124] E. Caldarulo, *Ph.D. thesis*, ETH Zurich, 2017.
- [125] H. Jónsson, G. Mills and K. W. Jacobsen, 1998.
- [126] N. N. Nair, E. Schreiner and D. Marx, *J. Am. Chem. Soc.*, 2008, **130**, 14148–14160.
- [127] M. Sprik, *Chem. Phys.*, 2000, **258**, 139–150.
- [128] P. Raiteri, A. Laio, F. L. Gervasio, C. Micheletti and M. Parrinello, *The journal of physical chemistry B*, 2006, **110**, 3533–3539.
- [129] J. McMurry, Susan McMurry, *Study guide and solutions manual, Fundamentals of organic chemistry, seventh edition*, Thomson, 2011.
-

- [130] M. Sulpizi and M. Sprik, *Phys. Chem. Chem. Phys.*, 2008, **10**, 5238–5249.
- [131] S. Pezzotti, 2019.
- [132] A. Morita and J. T. Hynes, *J. Phys. Chem. B.*, 2002, **106**, 673–685.
- [133] A. Morita and T. Ishiyama, *Phys. Chem. Chem. Phys.*, 2008, **10**, 5801–5816.
- [134] R. Khatib, E. H. G. Backus, M. Bonn, M.-J. Perez-Haro, M.-P. Gaigeot and M. Sulpizi, *Sci. Reports*, 2016, **6**, 24287.
- [135] J. D. Cyran, M. A. Donovan, D. Vollmer, F. Siro Brigiano, S. Pezzotti, D. R. Galimberti, M.-P. Gaigeot, M. Bonn and E. H. G. Backus, *Proc. Natl. Acad. Sci.*, 2019, **116**, 1520–1525.
- [136] Q. Du, E. Freysz and Y. R. Shen, *Phys. Rev. Lett.*, 1993, **70**, 2313–2316.
- [137] N. Ostroverkhov, C. Tian and Y. Shen, *Phys. Rev. Lett.*, 2008, **100**, 096102.
- [138] S. Nihonyanagi, R. Kusaka, K. Inoue, A. Adhikari, S. Yamaguchi and T. Tahara, *J. Chem. Phys.*, 2015, **143**, 124707.
- [139] S. Sun, R. Liang, X. Xu, H. Zhu, Y. R. Shen and C. Tian, *J. Chem. Phys.*, 2016, **144**, 244711.
- [140] P. Miranda, Q. Du and Y. Shen, *Chem. Phys. Lett.*, 1998, **286**, 1–8.
- [141] Y. Rao, M. Subir, E. A. McArthur, N. J. Turro and K. B. Eisenthal, *Chem. Phys. Lett.*, 2009, **477**, 241–244.
- [142] K. Ariga, T. Nakanishi, J. P. Hill, M. Shirai, M. Okuno, T. Abe and J.-i. Kikuchi, *J. Am. Chem. Soc.*, 2005, **127**, 12074–12080.
- [143] S. Strazdaite, K. Meister and H. J. Bakker, *J. Am. Chem. Soc.*, 2017, **139**, 3716–3720.
- [144] M. T. Martins-Costa, F. F. García-Prieto and M. F. Ruiz-López, *Organic & biomolecular chemistry*, 2015, **13**, 1673–1679.
- [145] X. Zhao, S. Subrahmanyam and K. B. Eisenthal, *Chem. Phys. Lett.*, 1990, **171**, 558 – 562.
- [146] E. C. Griffith and V. Vaida, *J. Am. Chem. Soc.*, 2013, **135**, 710–716.
- [147] C. Y. Tang, Z. Huang and H. C. Allen, *J. Phys. Chem. B*, 2010, **114**, 17068–17076.
- [148] M. J. Shultz, T. H. Vu, B. Meyer and P. Bisson, *Acc. Chem. Res.*, 2011, **45**, 15–22.

- [149] P. B. Petersen and R. J. Saykally, *J. Phys. Chem. B*, 2005, **109**, 7976–7980.
- [150] V. Buch, A. Milet, R. Vácha, P. Jungwirth and J. P. Devlin, *Proc. Natl. Acad. Sci.*, 2007, **104**, 7342–7347.
- [151] J. K. Beattie, A. M. Djerdjev and G. G. Warr, *Faraday Discuss.*, 2009, **141**, 31–39.
- [152] P. Creux, J. Lachaise, A. Graciaa, J. K. Beattie and A. M. Djerdjev, *J. Phys. Chem. B*, 2009, **113**, 14146–14150.
- [153] C. J. Mundy, I.-F. W. Kuo, M. E. Tuckerman, H.-S. Lee and D. J. Tobias, *Chem. Phys. Lett.*, 2009, **481**, 2–8.
- [154] L. M. Levering, M. R. Sierra-Hernandez and H. C. Allen, *J. Phys. Chem. C*, 2007, **111**, 8814–8826.
- [155] S. Enami, M. R. Hoffmann and A. J. Colussi, *J. Phys. Chem. Lett.*, 2010, **1**, 1599–1604.
- [156] S. Enami, L. A. Stewart, M. R. Hoffmann and A. J. Colussi, *J. Phys. Chem. Lett.*, 2010, **1**, 3488–3493.
- [157] A. K. Badu-Tawiah, C. Wu and R. G. Cooks, *Anal. Chem.*, 2011, **83**, 2648–2654.
- [158] A. K. Badu-Tawiah, D. I. Campbell and R. G. Cooks, *J. Am. Soc. Mass Spectr.*, 2012, **23**, 1077–1084.
- [159] M. Girod, E. Moyano, D. I. Campbell and R. G. Cooks, *Chem. Sci.*, 2011, **2**, 501–510.
- [160] X. Yan, R. Augusti, X. Li and R. G. Cooks, *ChemPlusChem*, 2013, **78**, 1142–1148.
- [161] X. Yan, R. M. Bain and R. G. Cooks, *Angew. Chem. Int. Ed.*, 2016, **55**, 12960–12972.
- [162] A. Laio, A. Rodriguez-Forteza, F. L. Gervasio, M. Ceccarelli and M. Parrinello, *J. Phys. Chem. B*, 2005, **109**, 6714–6721.
- [163] M. Ferus, F. Pietrucci, A. M. Saitta, A. Knížek, P. Kubelík, O. Ivanek, V. Shestivska and S. Civiš, *Proc. Natl. Acad. Sci.*, 2017, **114**, 4306–4311.
- [164] V. Venkateshwaran, S. Vembanur and S. Garde, *Proc. Natl. Acad. Sci.*, 2014, **111**, 8729–8734.
- [165] E. Knipping, M. Lakin, K. Foster, P. Jungwirth, D. Tobias, R. Gerber, D. Dabdub and B. Finlayson-Pitts, *Science*, 2000, **288**, 301–306.

- [166] E. M. Knipping, M. J. Lakin, K. L. Foster, P. Jungwirth, D. J. Tobias, R. B. Gerber, D. Dabdub and B. J. Finlayson-Pitts, *Science*, 2000, **288**, 301–306.
- [167] J. P. Greenstein, *Chemistry of the amino acids*, 1961.
- [168] K. Chuchev and J. J. BelBruno, *J. Mol. Struct.: Theochem*, 2008, **850**, 111–120.
- [169] R. Bonaccorsi, P. Palla and J. Tomasi, *J. Am. Chem. Soc.*, 1984, **106**, 1945–1950.
- [170] A. K. Ojha, N. Vyas and S. P. Dubey, *Comput. Theor. Chem.*, 2012, **1002**, 16–23.
- [171] J. Almlöf, Å. Kvik and J. Thomas, *J. Chem. Phys.*, 1973, **59**, 3901–3906.
- [172] K. Frimand, H. Bohr, K. J. Jalkanen and S. Suhai, *Chem. Phys.*, 2000, **255**, 165–194.
- [173] A. Willard and D. Chandler, *J. Phys. Chem. B.*, 2010, **114**, 1954–1958.
- [174] J. S. Hub, C. Caleman and D. van der Spoel, *Phys. Chem. Chem. Phys.*, 2012, **14**, 9537–9545.
- [175] A. Habartová, A. Obisesan, B. Minofar and M. Roeselová, *Theor. Chem. Acc.*, 2014, **133**, 1455.
- [176] L. Zhuravlev, *Colloids Surf. A Physicochem. Eng. Asp.*, 1993, **74**, 71–90.
- [177] L. Zhuravlev, *Colloids Surf. A Physicochem. Eng. Asp.*, 2000, **173**, 1–38.
- [178] M. Kosmulski, *J. Colloid Interf. Sci.*, 2002, **253**, 77–87.
- [179] A. A. Hassanali and S. J. Singer, *J. Phys. Chem. B*, 2007, **111**, 11181–11193.
- [180] M.-P. Gageot, M. Sprik and M. Sulpizi, *J. Phys-Condens. Mat.*, 2012, **24**, 124106.
- [181] M. Pfeiffer-Laplaud, D. Costa, F. Tielens, M.-P. Gageot and M. Sulpizi, *J. Phys. Chem. C*, 2015, **119**, 27354–27362.
- [182] M. Sulpizi, M.-P. Gageot and M. Sprik, *J. Chem. Theory Comput.*, 2012, **8**, 1037–1047.
- [183] W.-T. Liu and Y. R. Shen, *Phys. Rev. Lett.*, 2008, **101**, 016101.
- [184] A. Rimola, D. Costa, M. Sodupe, J.-F. Lambert and P. Ugliengo, *Chem. Rev.*, 2013, **113**, 4216–4313.

- [185] E. P. Laetitia Dalstein and E. Tyrode, *Phys.Chem.Chem.Phys.*, 2017, **19**, 10343–10349.
- [186] G. Engelhardt and D. Michel, 1987.
- [187] R. N. Lamb and D. N. Furlong, *J. Chem. Soc., Faraday Trans.1*, 1982, **78**, 61–73.
- [188] S. Iarlori, D. Ceresoli, M. Bernasconi, D. Donadio and M. Parrinello, *J. Phys. Chem. B*, 2001, **105**, 8007–8013.
- [189] F. Tielens, C. Gervais, J. F. Lambert, F. Mauri and D. Costa, *Chem. Mater.*, 2008, **20**, 3336–3344.
- [190] A. Ö. Yazaydın and R. W. Thompson, *Micropor. mesopor. mat.*, 2009, **123**, 169–176.
- [191] S. Bordiga, P. Ugliengo, A. Damin, C. Lamberti, G. Spoto, A. Zecchina, G. Spano, R. Buzzoni, L. Dalloro and F. Rivetti, *Top. Catal.*, 2001, **15**, 43–52.
- [192] M. Trzpit, M. Soulard, J. Patarin, N. Desbiens, F. Cailliez, A. Boutin, I. Demachy and A. Fuchs, *Langmuir*, 2007, **23**, 10131–10139.
- [193] F. Tielens, M. Gierada, J. Handzlik and M. Calatayud, *Catal. Today*, 2019.
- [194] G. G. Y. Oumi, *Impact of Zeolites and other Porous Materials on the New Technologies at the Beginning of the New Millennium, Proceedings of the 2nd International FEZA Conference, Taormina, Italy*, Elsevier, 2002.
- [195] A. M. Schrader, J. I. Monroe, R. Sheil, H. A. Dobbs, T. J. Keller, Y. Li, S. Jain, M. S. Shell, J. N. Israelachvili and S. Han, *Proc. Natl. Acad. Sci.*, 2018, **115**, 2890–2895.
- [196] R. K. Iler, *The chemistry of silica*, 1979.
- [197] P. M. Dove and C. M. Craven, *Geochim. Cosmochim. Acta*, 2005, **69**, 4963–4970.
- [198] B. Carroll and E. Freeman, *J. Phys. Chem.*, 1954, **58**, 335–338.
- [199] R. Abendroth, *J. Colloid Inter. Sci.*, 1970, **34**, 591–596.
- [200] J. Sonnefeld, *Colloid Polym. Sci.*, 1995, **273**, 932–938.
- [201] J. Lyklema, *Mol. Phys.*, 2002, **100**, 3177–3185.
- [202] D. Sverjensky, *Geochim. and Cosmochim. Acta*, 1994, **58**, 3123.
- [203] D. Sverjensky and N. Sahai, *Geochim. and Cosmochim. Acta*, 1996, **60**, 3773.

- [204] F. Bellucci, S. S. Lee, J. D. Kubicki, A. Bandura, Z. Zhang, D. J. Wesolowski and P. Fenter, *J. Phys. Chem. C*, 2015, **119**, 4778–4788.
- [205] M. Pfeiffer-Laplaud and M. Gaigeot, *J. Phys. Chem. C*, 2016, 4866–4880.
- [206] P. M. Dove and D. A. Crerar, *Geochim. Cosmochim. Acta*, 1990, **54**, 955–969.
- [207] P. M. Dove and S. F. Elston, *Geochim. Cosmochim. Acta*, 1992, **56**, 4147–4156.
- [208] P. M. Dove, *Am. J. Sci.*, 1994, **294**, 665–712.
- [209] P. M. Dove and C. J. Nix, *Geochim. Cosmochim. Acta*, 1997, **61**, 3329–3340.
- [210] P. M. Dove, *Geochim. Cosmochim. Acta*, 1999, **63**, 3715–3727.
- [211] A. F. Wallace, G. Gibbs and P. M. Dove, *J. Phys. Chem. A*, 2010, **114**, 2534–2542.
- [212] S. Ong, X. Zhao and K. B. Eisenthal, *Chem. Phys. Lett.*, 1992, **191**, 327–335.
- [213] F. Geiger, *Annu. Rev. Phys. Chem.*, 2009, **60**, 61.
- [214] Y. Shen, *Annu. Rev. Phys. Chem.*, 2013, **64**, 129.
- [215] C. Tian and Y. R. Shen, *Surf. Sci. Reports*, 2014, **69**, 105–131.
- [216] A. Jubb, W. Hua and H. Allen, *Annu. Rev. Phys. Chem.*, 2012, **63**, 107.
- [217] P. Covert and D. Hore, *Annu. Rev. Phys. Chem.*, 2016, **67**, 233.
- [218] V. Ostroverkhov, G. A. Waychunas and Y. R. Shen, *Phys. Rev. Lett.*, 2005, **94**, 046102.
- [219] D. Lis, E. H. G. Backus, J. Hunger, S. H. Parekh and M. Bonn, *Science*, 2014, **344**, 1138–1142.
- [220] D. E. Gragson, B. M. McCarty and G. L. Richmond, *J. Am. Chem. Soc.*, 1997, **119**, 6144–6152.
- [221] S. Nihonyanagi, S. Yamaguchi and T. Tahara, *J. Am. Chem. Soc.*, 2014, **136**, 6155–6158.
- [222] C. S. Tian and Y. R. Shen.
- [223] J. A. Mondal, S. Nihonyanagi, S. Yamaguchi and T. Tahara, *J. Am. Chem. Soc.*, 2012, **134**, 7842–7850.

- [224] K. C. Jena, P. A. Covert and D. K. Hore, *J. Phys. Chem. Lett.*, 2011, **2**, 1056.
- [225] S. Nihonyanagi, S. Yamaguchi and T. Tahara, *Chem. Rev.*, 2017, **117**, 10665–10693.
- [226] C.-S. Hsieh, M. Okuno, J. Hunger, E. H. G. Backus, Y. Nagata and M. Bonn, *Angew. Chem.*, 2014, **53**, 8146–8149.
- [227] S. Yamamoto, A. Ghosh, H.-K. Nienhuys and M. Bonn, *Phys.Chem.Chem.Phys.*, 2010, **12**, 12909.
- [228] H. Arnolds and M. Bonn, *Surf. Sci. Rep.*, 2010, **65**, 45.
- [229] M. Bonn, H. J. Bakker, A. Ghosh, S. Yamamoto, M. Sovago and R. K. Campen, *J. Am. Chem. Soc.*, 2010, **132**, 14971.
- [230] A. Eftekhari-Bafrooei and E. Borguet, *J. Am. Chem. Soc.*, 2009, **131**, 12034.
- [231] A. Eftekhari-Bafrooei and E. Borguet, *J. Am. Chem. Soc.*, 2010, **132**, 3756.
- [232] Q. Du, E. Freysz and Y. R. Shen, *Phys. Rev. Lett.*, 1994, **72**, 238.
- [233] J. A. McGuire and Y. R. Shen, *Science*, 2006, **313**, 1945.
- [234] A. Myalitsin, S.-h. Urashima, S. Nihonyanagi, S. Yamaguchi and T. Tahara, *J. Phys. Chem. C*, 2016, **120**, 9357–9363.
- [235] P. E. Ohno, S. A. Saslow, H. fei Wang, F. M. Geiger and K. B. Eisenthal, *Nat. Commun.*, 2016, **7**, 13587–13591.
- [236] O. Isaienko and E. Borguet, *Langmuir*, 2013, **29**, 7885–7895.
- [237] H. Wang, Q. Xu, Z. Liu, Y. Tang, G. Wei, Y. R. Shen and W.-T. Liu, *J. Phys. Chem. Lett.*, 2019, **10**, 5943–5948.
- [238] N. Ji, V. Ostroverkhov, C.-Y. Chen and Y.-R. Shen, *J. Am. Chem. Soc.*, 2007, **129**, 10056–10057.
- [239] Y. R. Shen and V. Ostroverkhov, *Chem. Rev.*, 2006, **106**, 1140–1154.
- [240] Y.-C. Wen, S. Zha, X. Liu, S. Yang, P. Guo, G. Shi, H. Fang, Y. R. Shen and C. Tian, *Phys. Rev. Lett.*, 2016, **116**, 016101.
- [241] S.-h. Urashima, A. Myalitsin, S. Nihonyanagi and T. Tahara, *J. Phys. Chem. Lett.*, 2018, **9**, 4109–4114.
- [242] B. Ellen, S. Jan and B. Mischa, *Angewandte Chemie (International ed. in English)*.

- [243] A. Tuladhar, S. Dewan, S. Pezzotti, F. S. Brigiano, F. Creazzo, M.-P. Gaigeot and E. Borguet, *J. Am. Chem. Soc.*, 2020, **142**, 6991–7000.
- [244] S. Dewand, M. Yeganeh and E. Borguet, *J. Phys. Chem. Lett.*, 2013, **4**, 1977.
- [245] Z. Yang, Q. Li and K. C. Chou, *J. Phys. Chem. C*, 2009, **113**, 8201–8205.
- [246] M. Bouhadja and A. Skelton, *J. Phys. Chem. C*, 2018, **122**, 1535–1546.
- [247] A. M. Darlington, T. A. Jarisz, E. L. DeWalt-Kerian, S. Roy, S. Kim, M. S. Azam, D. K. Hore and J. M. Gibbs, *J. Phys. Chem. C*, 2017, **121**, 20229–20241.
- [248] H. Zhang, A. A. Hassanali, Y. K. Shin, C. Knight and S. J. Singer, *J. Chem. Phys.*, 2011, **134**, 024705.
- [249] S. Dewan, V. Carnevale, A. Bankura, A. Eftekhari-Bafrooei, G. Fiorin, M. L. Klein and E. Borguet, *Langmuir*, 2014, **30**, 8056–8065.
- [250] D. E. Yates and T. W. Healy, *J. Colloid Inter. Sci.*, 1976, **55**, 9–19.
- [251] P. E. Ohno, H.-f. Wang and F. M. Geiger, *Nat. Commun.*, 2017, **8**, 1032.
- [252] A. M. Darlington and J. M. Gibbs-Davis, *J. Phys. Chem. C*, 2015, **119**, 16560–16567.
- [253] P. E. Ohno, S. A. Saslow, H.-f. Wang, F. M. Geiger and K. B. Eisenthal, *Nat. Commun.*, 2016, **7**, 13587.
- [254] L. Zhuravlev, *Langmuir*, 1987, **3**, 316–318.
- [255] V. Bolis, B. Fubini, L. Marchese, G. Martra and D. Costa, *J. Chem. Soc., Faraday Trans.*, 1991, **87**, 497–505.
- [256] R. West, L. S. Whatley and K. J. Lake, *J. Am. Chem. Soc.*, 1961, **83**, 761–764.
- [257] M.-P. Gaigeot, M. Sprik and M. Sulpizi, *J. Phys: Cond. Matt.*, 2012, **24**, 124106.
- [258] M. Sulpizi, M.-P. Gaigeot and M. Sprik, *J. Chem. Theory Comput.*, 2012, **8**, 1037–1047.
- [259] P. Masini and M. Bernasconi, *J. Phys. Condens. Matter*, 2002, **14**, 4133.
- [260] A. Cimas, F. Tielens, M. Sulpizi, M.-P. Gaigeot and D. Costa, *J. Phys.: Cond. Matt.*, 2014, **26**, 244106.
- [261] J. Dedecek, S. Sklenak, C. Li, F. Gao, J. Brus, Q. Zhu and T. Tatsumi, *J. Phys. Chem. C*, 2009, **113**, 14454–14466.

- [262] T. Kawai and K. Tsutsumi, *J. Coll. Int. Science*, 1999, **212**, 310 – 316.
- [263] V. Bolis, C. Busco, S. Bordiga, P. Ugliengo, C. Lamberti and A. Zecchina, *Appl. Sur. Sci.*, 2002, **196**, 56–70.
- [264] M. Pfeiffer-Laplaud and M.-P. Gageot, *J. Phys. Chem. C*, 2016, **120**, 14034–14047.
- [265] Z. Zhang, L. Piatkowski, H. Bakker and M. Bonn, *Nat. Chem.*, 2011, **3**, 888–893.
- [266] K. Inoue, T. Ishiyama, S. Nihonyanagi, S. Yamaguchi, A. Morita and T. Tahara, *J. Phys. Chem. Lett.*, 2016, **7**, 1811–1815.
- [267] J. D. Fisk, R. Batten, G. Jones, J. P. O'Reill and A. M. Shaw, *J. Phys. Chem. B*, 2005, **109**, 14475–14480.
- [268] V. Ostroverkhov, G. A. Waychunas and Y. Shen, *Phys. Rev. Lett.*, 2005, **94**, 046102.
- [269] S. Dixit and P. Van Cappellen, *Geochim. Cosmochim. Acta*, 2002, **66**, 2559–2568.
- [270] M. Gierada, F. De Proft, M. Sulpizi and F. Tielens, *J. Phys. Chem. C*, 2019, **123**, 17343–17352.
- [271] K. Leung, I. M. Nielsen and L. J. Criscenti, *J. Am. Chem. Soc.*, 2009, **131**, 18358–18365.
- [272] Y. Hu, B. Kiefer and P. Dera, AGU Fall Meeting Abstracts, 2016.
- [273] Y. Hu, B. Kiefer, C. R. Bina, D. Zhang and P. K. Dera, *Geophys. Res. Lett.*, 2017, **44**, 11–340.
- [274] P. E. Lopes, E. Demchuk and A. D. Mackerell Jr, *Int. J. Quantum Chem.*, 2009, **109**, 50–64.
- [275] W.-T. Liu and Y. Shen, *Phys. Rev. B*, 2008, **78**, 024302.
- [276] Y. Tong, J. Wirth, H. Kirsch, M. Wolf, P. Saalfrank and R. K. Campen, *J. Chem. Phys.*, 2015, **142**, 054704.
- [277] W.-T. Liu and Y. Shen, *Annalen der Physik*, 2011, **523**, 101–106.
- [278] C. Humbert, O. Pluchery, E. Lacaze, A. Tadjeddine and B. Busson, *Phys. Chem. Chem. Phys.*, 2012, **14**, 280–289.
- [279] C. J. Winta, S. Gewinner, W. Schöllkopf, M. Wolf and A. Paarmann, *Phys. Rev. B*, 2018, **97**, 094108.
- [280] S. L. Warring, D. A. Beattie and A. J. McQuillan, *Langmuir*, 2016, **32**, 1568–1576.

BIBLIOGRAPHY

- [281] G. Bussi, D. Donadio and M. Parrinello, *J. Chem. Phys.*, 2007, **126**, 014101.
- [282] A. K. Tummanapelli and S. Vasudevan, *J. Phys. Chem. B*, 2014, **118**, 13651–13657.
- [283] A. K. Tummanapelli and S. Vasudevan, *J. Phys. Chem. B*, 2015, **119**, 12249–12255.
- [284] A. K. Tummanapelli and S. Vasudevan, *Phys. Chem. Chem. Phys.*, 2015, **17**, 6383–6388.
- [285] A. W. Sakti, Y. Nishimura and H. Nakai, *J. Chem Theory Comput.*, 2018, **14**, 351–356.
- [286] J.-G. Lee, E. Ascitutto, V. Babin, C. Sagui, T. Darden and C. Roland, *J. Phys. Chem. B*, 2006, **110**, 2325–2331.
- [287] S. Tazi, B. Rotenberg, M. Salanne, M. Sprik and M. Sulpizi, *Geochim. Cosmochim. Acta*, 2012, **94**, 1–11.
- [288] M.-P. Gaigeot, *Phys. Chem. Chem. Phys.*, 2010, **12**, 3336–3359.
- [289] P. Nissen, J. Hansen, N. Ban, P. B. Moore and T. A. Steitz, *Science*, 2000, **289**, 920–930.
- [290] M. Wagatsuma, S. Terashima and S. Yamada, *Tetrahedron*, 1973, **29**, 1497–1502.

Appendix A

The formation of urea in space

In the first 8 months of my PhD thesis I have investigated the possible chemical routes leading to the formation of urea in the interstellar medium (ISM) [50]. This work has been obtained under the supervision of my previous thesis director Dr. R. Spezia (now at Sorbonne University, Paris) and in collaboration with Prof A. Largo in Spain. We report hereafter the work that has been published.

The formation of urea in space-I. Ion-molecule, neutral-neutral, and radical gas-phase reactions

Flavio Siro Brigiano, Yannick Jeanvoine, Antonio Largo, Riccardo Spezia
A&A, **610**, A26, (2018).

The formation of urea in space

I. Ion-molecule, neutral-neutral, and radical gas-phase reactions

Flavio Siro Brigiano¹, Yannick Jeanvoine¹, Antonio Largo², and Riccardo Spezia^{1,*}

¹ LAMBE, Univ. Evry, CNRS, CEA, Université Paris-Saclay, 91025 Evry, France
e-mail: riccardo.spezia@univ-evry.fr

² Computational Chemistry Group, Departamento de Química Física, Facultad de Ciencias, Universidad de Valladolid, 47002 Valladolid, Spain

Received 21 July 2017 / Accepted 1 November 2017

ABSTRACT

Context. Many organic molecules have been observed in the interstellar medium thanks to advances in radioastronomy, and very recently the presence of urea was also suggested. While those molecules were observed, it is not clear what the mechanisms responsible to their formation are. In fact, if gas-phase reactions are responsible, they should occur through barrierless mechanisms (or with very low barriers). In the past, mechanisms for the formation of different organic molecules were studied, providing only in a few cases energetic conditions favorable to a synthesis at very low temperature. A particularly intriguing class of such molecules are those containing one N–C–O peptide bond, which could be a building block for the formation of biological molecules. Urea is a particular case because two nitrogen atoms are linked to the C–O moiety. Thus, motivated also by the recent tentative observation of urea, we have considered the synthetic pathways responsible to its formation.

Aims. We have studied the possibility of forming urea in the gas phase via different kinds of bi-molecular reactions: ion-molecule, neutral, and radical. In particular we have focused on the activation energy of these reactions in order to find possible reactants that could be responsible for to barrierless (or very low energy) pathways.

Methods. We have used very accurate, highly correlated quantum chemistry calculations to locate and characterize the reaction pathways in terms of minima and transition states connecting reactants to products.

Results. Most of the reactions considered have an activation energy that is too high; but the ion-molecule reaction between NH_2OH_2^+ and formamide is not too high. These reactants could be responsible not only for the formation of urea but also of isocyanic acid, which is an organic molecule also observed in the interstellar medium.

Key words. astrochemistry – astrobiology – methods: numerical – ISM: molecules – ISM: kinematics and dynamics

1. Introduction

In recent years a growing number of organic molecules have been detected in space, in particular in the interstellar medium (ISM) thanks to advances in radioastronomy, and in comets (e.g., the recent mission on the P67/Churyumov-Gerasimenko comet) already reported the presence of some interesting molecules like methyl isocyanate, acetone, acetamide, propionaldehyde, and glycine (Goesmann et al. 2015; Altwegg et al. 2016) and more are expected in the near future). A particularly interesting class of organic molecules is that containing N–C single bonds, since these molecules can be the precursors for direct formation of peptides without passing from the single amino acids, as was initially suggested by Rubin et al. (1971) together with formamide (H_2NCHO) observation in the ISM. After formamide, other molecules containing N–C bonds were found in the ISM, like cyanamide (H_2NCN , Turner et al. 1975), H_3CNC (Cernicharo et al. 1988; Gratier et al. 2013), acetamide (H_2NCOCH_3 , Hollis et al. 2006), cyanoformaldehyde (CNCHO , Remijan et al. 2008), H_2NCO^+ (Gupta et al. 2013), methylamine (H_3CNH_2 , Kaifu et al. 1974; Fourikis et al. 1974),

aminoacetonitrile ($\text{H}_2\text{NCH}_2\text{CN}$, Belloche et al. 2008), and, very recently, urea ($(\text{H}_2\text{N})_2\text{CO}$, Remijan et al. 2014) and N-methylformamide (H_3CNHCHO , Belloche et al. 2017). Urea has the peculiarity of containing two N–C bonds and it is considered to be very important for the formation of life, since it can be a precursor for the synthesis of cytosine and uracil (Kolb 2014). A tentative detection of urea in Sgr B2 molecular cloud was reported by collecting data from four independent astronomical instrumentations (Remijan et al. 2014). Extraterrestrial urea was observed previously in the Murchinson C2 chondrite (Hayats et al. 1975) and its presence was suggested on grain mantles (Raunier et al. 2004).

From the point of view of astrochemistry, the question that arises, related to the observation of these organic molecules, concerns the mechanisms that can be responsible for their synthesis. In general, low temperature environments promote only barrierless reaction pathways. Following this hypothesis, quantum chemistry calculations reported that while some possible mechanisms for the formation of formamide (Redondo et al. 2014b) and glycine (Barrientos et al. 2012) should be discarded due to high reaction barriers, others are possible, like the formation of acetamide through $\text{H}_2\text{NCHO} + \text{CH}_5^+$ reaction (Redondo et al. 2014a) or formamide through a radical mechanism (Barone et al. 2015). Ion-molecule collisions

* Present address: Sorbonne Universités, UPMC Univ. Paris 06, UMR – CNRS 7616, Laboratoire de Chimie Théorique, 75252 Paris, France.

were suggested as a possible mechanism in both experimental (Geppert & Larsson 2013; Larsson et al. 2012; Blagojevic et al. 2003; Petrie & Bohme 2007; Snow et al. 2007) and theoretical studies (Spezia et al. 2016). In this case even reactions with (small) activation barriers are possible thanks to the transformation in the collision of some of the translational energy into internal energy. Also gas-phase neutral-neutral reactions are a possible source of synthesis of carbon-bearing molecules (Kaiser 2012).

Another suggested way for the synthesis of these molecules is that they were formed on interstellar grains surface. One particularly studied case is ice, which can decrease the activation energy. For example, the formation of glycine (Holtom et al. 2005), amino acids (Elsila et al. 2007), dipeptides (Kaiser et al. 2013), hydroxyacetonitrile, aminomethanol and polyoxymethylene (Danger et al. 2012, 2014), glycolaldehyde and glyceraldehyde (de Marcellus et al. 2015), or alpha-aminoethanol (Duvernay et al. 2010) in ice was reported experimentally. Recently, Forstel et al. (2016) have synthesized urea in cometary model ices thanks to the irradiation of inorganic ice (which contains CO and NH₃), proposing a mechanism in which NH₂[·] is added to hydrogenated CO.

In many cases, calculations have shown that the activation energies are reduced by the presence of water molecules (Woon 1999, 2001, 2002; Koch et al. 2008; Chen & Woon 2011; Rimola et al. 2012). Even if the activation barriers were reduced, they are still generally too high to allow a thermal reaction at low temperature conditions; however, in some cases they are compatible with the observed abundances in low-mass protostars and dark cores (Rimola et al. 2014).

In the present work, we have studied, by highly correlated quantum chemistry calculations, the possibility of forming urea by three classes of gas-phase reactions: ion-molecule, neutral-neutral, and radical. In the case of ion-molecule reaction, one tempting reactant to check is neutral and protonated hydroxylamine (NH₂OH). In particular, the protonated form was suggested to be a possible precursor for the formation of glycine and formamide by ion-molecule collisions (Snow et al. 2007; Spezia et al. 2016), but the potential energy surfaces always have an activation barrier (Barrientos et al. 2012; Redondo et al. 2014b). Despite the neutral form not being observed in the ISM, its protonated species could be formed and just not detected, as suggested by Pulliam et al. (2012), who provided a clear picture of the non-detection of the neutral species suggesting the possibility of the existence of the protonated one. Our calculations have found that the NH₂OH₂⁺ + H₂NCHO (formamide) reaction proceeds via a barrierless pathway, such that this is a plausible route for its synthesis under ISM conditions. We should note that NH₂OH₂⁺ is the high energy form of protonated hydroxylamine: calculations by Boulet et al. (1999) have shown that protonation of neutral NH₂OH could provide both isomers (NH₃OH⁺ and NH₂OH₂⁺), whose interconversion barrier is too high to be passed, so that the more reactive NH₂OH₂⁺ species can exist. Other reactions involving species observed in the ISM are also investigated but reactions proceed through non-negligible energy barriers. Finally we have studied the neutral-neutral reaction and the radical-molecule reaction. Both have reaction barriers that are too high.

The remainder of the article is as follows. The methods used are described in Sect. 2, results are then presented first in terms of the thermodynamics of the reactions investigated (Sect. 3.1) and then we detail the reaction pathways in terms of minima and transition states connecting reactants to products (Sects. 3.2, 3.3, and 3.4). Section 4 concludes.

2. Computational details

All structures (minima and transition states, TSs) were first optimized at the B3LYP/6-311++G(d, p) level of theory (Becke 1993; Lee et al. 1988), then, using these structures as starting points, we located minima and TSs using the Møller-Plesset level of theory (MP2) with aug-cc-pVTZ basis set (Dunning Jr. 1989; Davidson 1996). Finally, the electronic energies were calculated using the highly correlated coupled cluster method, CCSD(T) (Purvis III & Bartlett 1982; Pople et al. 1987), with the same basis set. Energies are thus reported using the CCSD(T)/aug-cc-pVTZ electronic energy on the MP2/aug-cc-pVTZ minima and TSs. Zero point energy (ZPE) is calculated at the same MP2 level of theory. These results are thus labeled as CCSD(T)/aug-cc-pVTZ//MP2/aug-cc-pVTZ in the following. With structures of reactants and products, we calculated the energy differences taking into account the ZPE corrections and the Gibbs free energy differences at 15 K using standard thermochemistry and the harmonic frequencies (McQuarrie 1973).

To verify that the TSs correctly connect the minima identified in the potential energy surface (PES), we performed intrinsic reaction coordinate (IRC) calculations (Fukui 1981). All results show that the TSs correspond to the saddle point in the minimum energy path between two given minima (reactants, products and intermediates).

In the case of radical reactions, we considered the doublet spin multiplicity and verified that there is no spin contamination. We obtained $\langle S \rangle^2$ values very close to the theoretical one (0.75) and, for two transition states that have values about 10% higher than the theoretical value, T1 diagnostics (Lee & Taylor 1989) on CCSD(T) calculations were performed, providing very small values, thus strengthening our confidence in the calculation results.

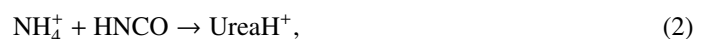
Spontaneous emission rate constants were calculated using frequencies and Einstein coefficients obtained by ab initio calculations and using the method reported by Herbst (1982) with our in-house code. All quantum chemistry and thermochemistry calculations were performed using Gaussian 09 software (Frisch et al. 2009).

3. Results

3.1. Thermodynamics

We first considered the energetics in terms of ΔE including the ZPE effects and gas phase ΔG at 15 K of possible reactions leading to urea. In particular we took into account three classes of reactions, ion-molecule, neutral-neutral, and radical reactions. Results are summarized in Table 1. In Fig. 1 we show the structures of reactants and products considered here (we omitted simple products like H, H₂, H₂O, and CH₄).

First, let us consider ion-molecule reactions. The most simple ones would be



which correspond to the condensation of NH₃ with CONH₂⁺ or NH₄⁺ with HNCO, both being exothermic. However, the urea eventually formed needs an environment to keep the excess energy or, alternatively, can be stabilized by spontaneous emission of a photon (corresponding to a radiative association reaction). In the gas phase, there is no environment to take the energy of the formed protonated urea, so there are two competing routes: (i) unimolecular dissociation and (ii) radiative decay.

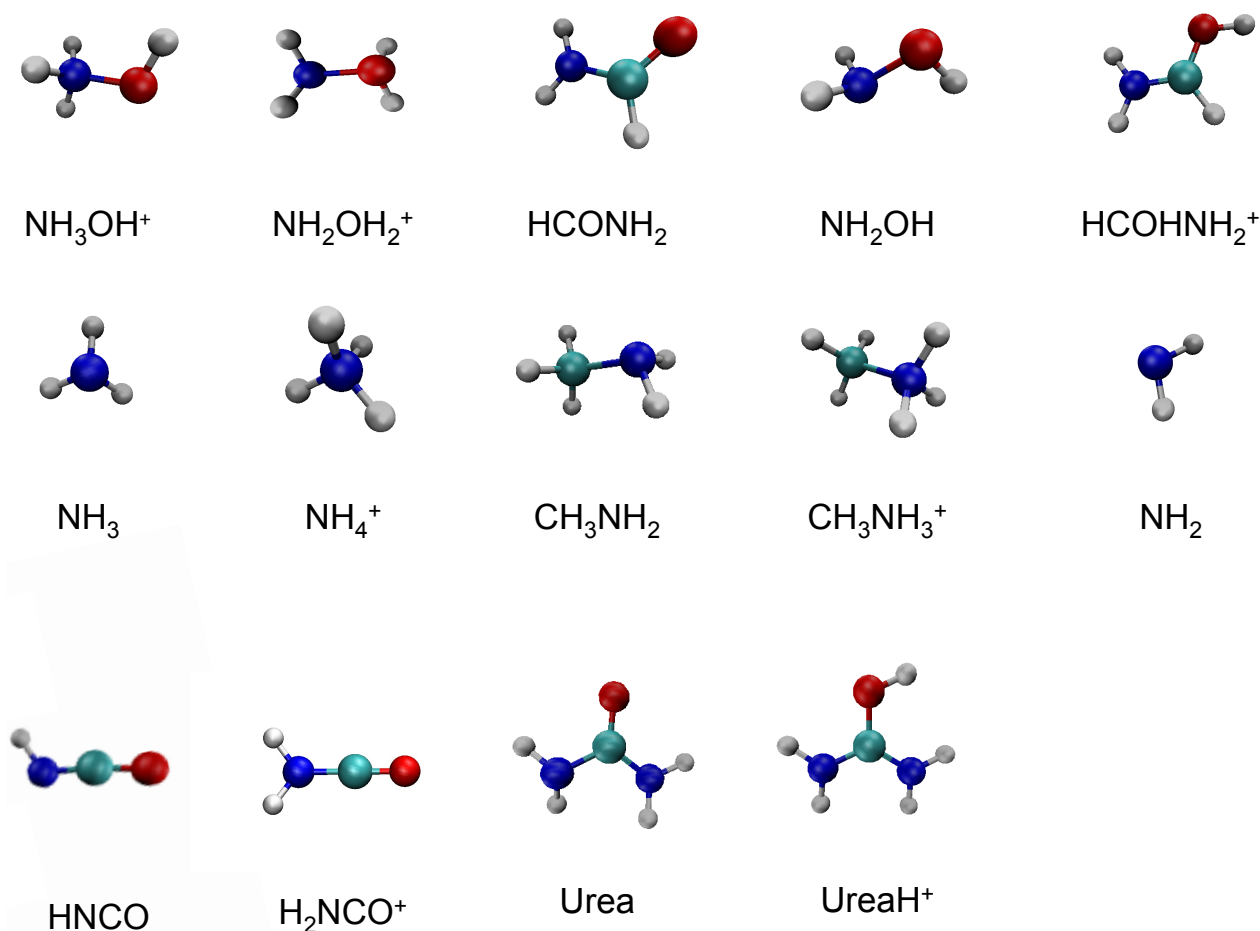


Fig. 1. Structures of reactants and products considered (simple products like H[·], H₂, H₂O, and CH₄ are omitted). Oxygen atoms are in red, nitrogen in blue, carbon in cyan, and hydrogen in white.

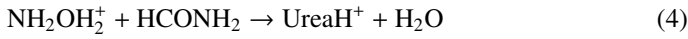
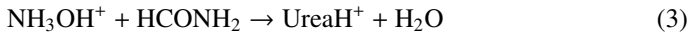
Table 1. Energetics: ΔE with ZPE correction and ΔG calculated at 15 K as obtained from MP2/aug-cc-pVTZ//CCSD(T)/aug-cc-pVTZ calculations.

Reaction	ΔE (kcal/mol)	ΔG (kcal/mol)	E^a (kcal/mol)
Ion-molecule			
(1) $\text{NH}_3 + \text{CONH}_2^+ \rightarrow \text{UreaH}^+$	-50.48	-50.30	(-7.82) ^a
(2) $\text{NH}_4^+ + \text{HNCO} \rightarrow \text{UreaH}^+$	-20.31	-20.14	(23.15) ^a
(3) $\text{NH}_3\text{OH}^+ + \text{HCONH}_2 \rightarrow \text{UreaH}^+ + \text{H}_2\text{O}$	-71.60	-70.10	17.60
(4) $\text{NH}_2\text{OH}_2^+ + \text{HCONH}_2 \rightarrow \text{UreaH}^+ + \text{H}_2\text{O}$	-97.40	-97.30	-8.04
(5) $\text{NH}_2\text{OH} + \text{HCOHNH}_2^+ \rightarrow \text{UreaH}^+ + \text{H}_2\text{O}$	-70.49	-70.40	18.80
(6) $\text{NH}_4^+ + \text{HCONH}_2 \rightarrow \text{UreaH}^+ + \text{H}_2$	-4.89	-4.73	85.18
(7) $\text{NH}_3 + \text{HCOHNH}_2^+ \rightarrow \text{UreaH}^+ + \text{H}_2$	-12.41	-12.26	77.66
(8) $\text{CH}_3\text{NH}_2 + \text{HCOHNH}_2^+ \rightarrow \text{UreaH}^+ + \text{CH}_4$	-35.47	-35.44	70.58
(9) $\text{CH}_3\text{NH}_3^+ + \text{HCONH}_2 \rightarrow \text{UreaH}^+ + \text{CH}_4$	-16.94	-16.89	89.13
Neutral-neutral			
(10) $\text{NH}_3 + \text{HNCO} \rightarrow \text{Urea}$	-14.78	-14.64	-
(11) $\text{NH}_2\text{OH} + \text{HCONH}_2 \rightarrow \text{Urea} + \text{H}_2\text{O}$	-57.46	-57.38	60.26
(12) $\text{NH}_3 + \text{HCONH}_2 \rightarrow \text{Urea} + \text{H}_2$	0.61	0.75	-
(13) $\text{CH}_3\text{NH}_2 + \text{HCONH}_2 \rightarrow \text{Urea} + \text{CH}_4$	-22.44	-22.79	-
Radical			
(14) $\text{NH}_2\cdot + \text{HCONH}_2 \rightarrow \text{Urea} + \text{H}\cdot$	-1.84	-1.65	16.22
(15) $\text{NH}_3 + \text{HCONH}\cdot \rightarrow \text{Urea} + \text{H}\cdot$	-11.76	-11.65	6.18

Notes. Activation energies, E^a (with ZPE correction), as obtained at the same level of theory for the different path investigated are shown. When a pathway was not characterized (see text) it is marked with -. For UreaH⁺ we report the energy formation for the most stable isomer. ^(a) Values as from Spezia et al. (2009).

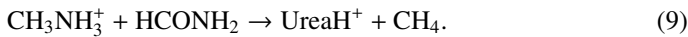
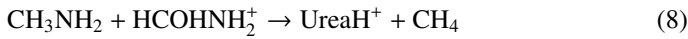
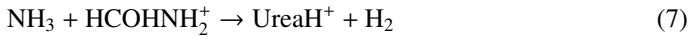
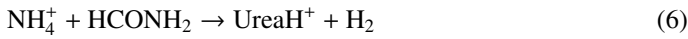
The rate constants for the unimolecular dissociation of protonated urea were previously reported by [Spezia et al. \(2009\)](#) and they are, for energies in 40–300 kcal/mol range, in the ps-ns timescale. Spontaneous emission rate constants are an order of magnitude larger (between 40 and 650 s⁻¹ in the same energy range), suggesting that it is unlikely that the urea would be stabilized in this way. We should note that this same previous work reported that the NH₃ + CONH₂⁺ reaction channel would be barrierless (the original study focused on the unimolecular decomposition of protonated urea).

We now consider ion-molecule reactions, which produce two products, such that the final relative translational energy can take the excess energy and stabilize the products. First, in analogy with reactions proposed for the gas-phase bimolecular synthesis of formamide ([Redondo et al. 2014b](#)) and glycine ([Barrientos et al. 2012](#)), we have considered the following reactions



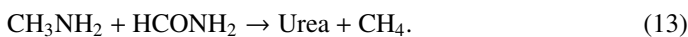
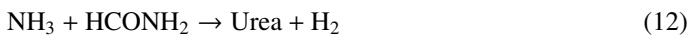
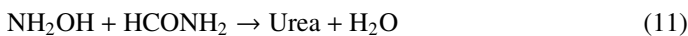
All of them are strongly exothermic and exergonic, so we better investigated the corresponding PES to obtain information on the barrier energies. These PESs are reported in Sect. 3.2.

We have also considered reactions between NH₃, HCONH₂, and CH₃NH₂, considering in each case a neutral and a protonated species:



NH₃ (ammonia), HCONH₂ (formamide), and CH₃NH₂ (methylamine) were observed in the ISM by [Cheung et al. \(1968\)](#), [Rubin et al. \(1971\)](#), [Kaifu et al. \(1974\)](#); [Fourikis et al. \(1974\)](#), respectively, so they should be considered as possible reactants. Protonated ammonia, NH₄⁺, cannot be observed for symmetry reasons, but recently the observation of the NH₃D⁺ isotope was reported by [Cernicharo et al. \(2013\)](#), strengthening the possibilities of the existence of NH₄⁺ in the ISM. Also in this case, all the corresponding reactions are exothermic and exergonic, while the energy and free energy differences are smaller than for reactions 3–5. It is worth investigating the PES also for those reactions in order to localize the barrier energies.

We then considered the following neutral-neutral reactions:



Reaction 10 is exothermic and exergonic, but in the gas phase it also has the problem of stabilization by radiative emission. The radiative emission rate constant is in the 40–350 s⁻¹ range for energies in the 40–300 kcal/mol range, similar to protonated urea values, suggesting that it would be easier to dissociate back to reactants than to stabilize the products by emitting infra-red light. We thus do not follow this reaction. Reaction 12 is slightly

endothermic and endergonic and thus the barrier will also be positive, and thus we did not study the details of the corresponding PES. Finally, reactions 11 and 13 are exothermic and exergonic, even if, as expected, less so than corresponding ion-molecule reactions. Generally, barriers for neutral-neutral reactions are higher (and positive) than corresponding ion-molecule reactions, because in the latter the electrostatic barrier corresponding to the approaching of the reactants is lowered by ion-dipole attraction, while in neutral-neutral, weaker dipole-dipole interactions have a negative contribution to the interaction ([Levine 2005](#)). We will show the PES of the most exothermic and exergonic reaction 11 in order to have information on the barrier in Sect. 3.3.

Finally, inspired by the recent work by [Barone et al. \(2015\)](#) on formamide, we studied two simple radical reactions:



Also in this case the reactions are exothermic and exergonic, while values are smaller than ion-molecule reactions 3–5, but also smaller than the neutral-neutral reaction 11. We will study the PES associated to these radical reaction in Sect. 3.4.

To conclude, almost all the reactions reported have a favorable thermochemistry, such that it will be worth investigating for most of them the details of the PES in order to locate the corresponding barriers. We should note that in both ion-molecule and neutral-neutral reactions, the ones in which a water molecule is formed have the most negative energy and free energy, similarly to what has been reported in previous studies of formamide ([Redondo et al. 2014b](#)) and glycine ([Snow et al. 2007](#); [Barrientos et al. 2012](#)).

3.2. Mechanisms for ion-molecule reactions

We now report the PES in terms of connected minima and TSs for the ion-molecule reactions considered previously. First, we start with reactions 3–5, which are responsible for the formation of protonated urea and neutral water, reaction 4 being in particular the most thermodynamically favored among all the reactions considered in the present work. As we will see, it transpires that this last has a reaction channel leading to the formation of protonated urea (and not only), which is barrierless. The reaction pathway diagram is shown in Fig. 2. Investigating in more detail this pathway, we can observe that the interaction between NH₂OH₂⁺ with HCONH₂ leads to the formation of the complex I3A, which shows a hydrogen bond between the carbonyl oxygen of formamide and the hydrogen atom of the amine group of protonated hydroxylamine. This complex I3A can then evolve to the I4A intermediate through the transition state TS3A that represents the highest energy barrier (–8.04 kcal/mol with respect to reactants) of this reaction pathway. The mechanism that leads to I4A implies the electrophilic attack of the amino group of hydroxylamine to the amino group of formamide. This results in a simultaneous formation of a N–N bond and in the cleavage of the N–O bond with consequent formation of a water molecule. We should note that to form I4A, the system has to pass the TS3A barrier, which is higher in energy than the exit channel leading to NH₃OH⁺ + HCONH₂ and NH₂OH + HCOHNH₂⁺ products, shown as asymptotic lines in Fig. 2. The system has thus different possibilities and the branching ratio will depend on the dynamical evolution of I3A. If a purely statistical kinetic regime will hold, then the exit channels will be likely favored, but a fraction of trajectories would be able to pass the TS3A, forming I4A.

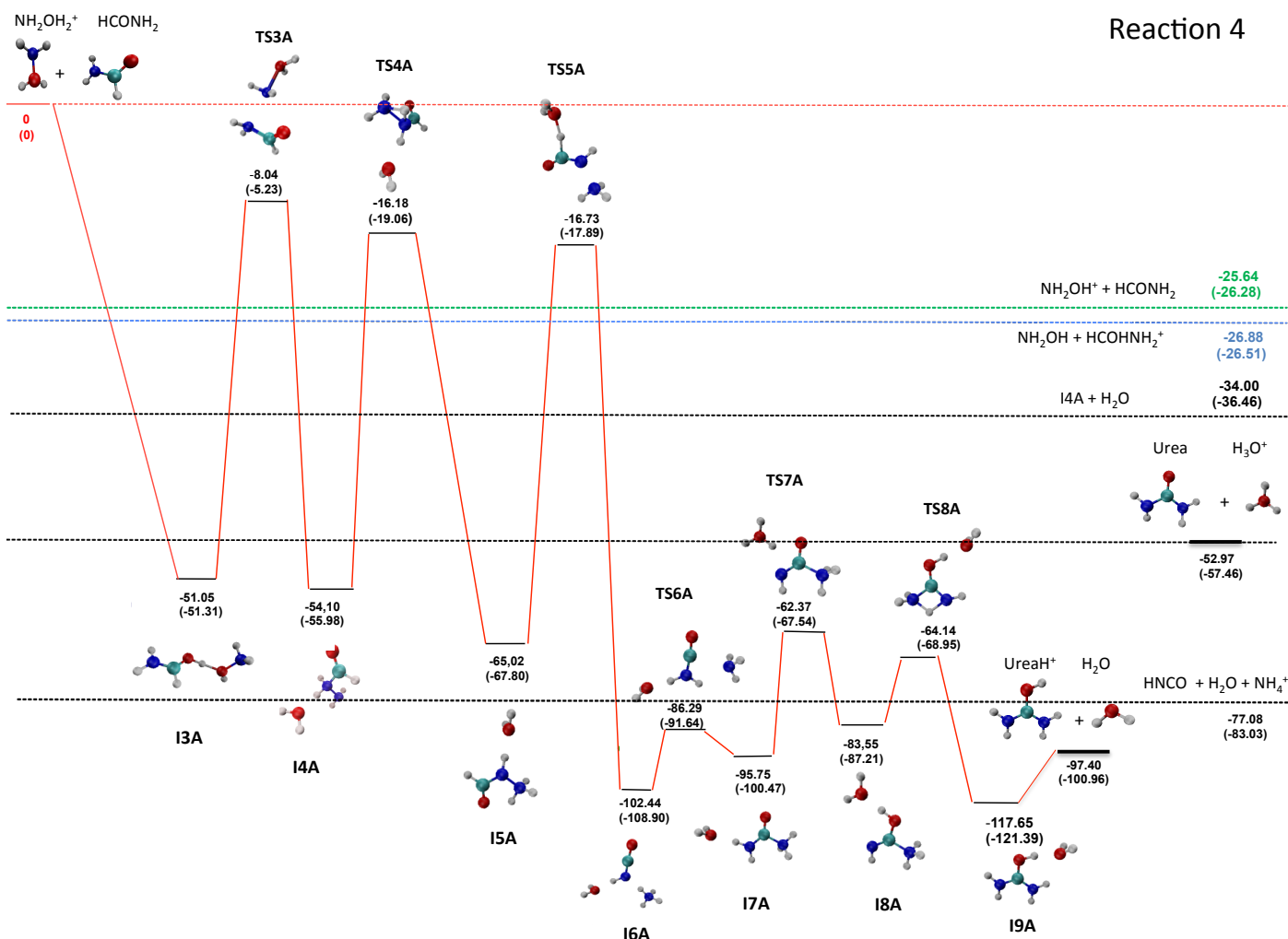


Fig. 2. Energy profiles, in kcal/mol, for the ion-molecule reaction $\text{NH}_2\text{OH}_2^+ + \text{HCONH}_2$, as obtained by CCSD(T)/aug-cc-pVTZ//MP2-aug-cc-pVTZ and MP2/aug-cc-pVTZ (in parenthesis) calculations. These values contain zero-point energies (ZPE). In the final step we report the energy of the cluster, the final product energy being reported in Table 1.

Dynamical calculations will be useful in the future to better understand this aspect.

If I4A intermediate is obtained then it can evolve to I5A through hydrogen migration from the secondary to the primary amino group, through TS4A. The barrier of this and the following TSs is lower than the previous one (TS3A). The concerted mechanism, responsible for the formation of I6A through TS5A, involves the hydrogen abstraction reaction of the C atom by the water molecule and the simultaneous cleavage of the N–N bond. This mechanism leads to the formation of I6A, a cluster made by isocyanic acid, protonated ammonia, and water. We should note that all these three species have been detected in the Sgr B2 cloud (Cheung et al. 1969; Snyder & Buhl 1972); in the case of ammonium, the isotope NH_3D^+ was detected by Cernicharo et al. (2013). It is thus possible that this cluster breaks into its constituents, being a possible barrierless pathway also for the formation of neutral isocyanic acid. In fact, the energy of the three separated species is -77.08 kcal/mol with respect to reactants (see the asymptotic line in Fig. 2), such that the I6A needs only 25.36 kcal/mol to break into these pieces, which is comparable with the energy needed to pass the TSs and obtain protonated urea + H_2O .

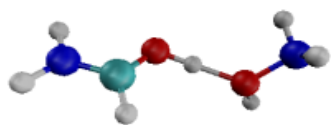
From I6A the formation of the more stable isomer of protonated urea takes place through a three-step mechanism. In the

first step, the hydrogen abstraction reaction of the ammonium ion by the imino group of the isocyanic acid induces the nucleophilic attack of the ammonia to the isocyanic carbon atom, leading to the formation of N-protonated urea through TS6A. In the second step, the hydrogen migration, assisted by water which becomes hydronium ion, H_3O^+ , in the transition state TS7A from the amino-group of N-protonated urea to its oxygen atom, produces I8A. In the third step, the more stable isomer of protonated urea is produced from I8A through the transition state TS8A, where a hydrogen migration takes place.

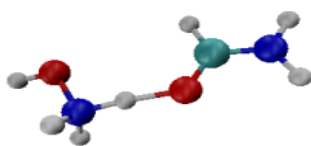
We should note that TS7A is actually a cluster composed of H_3O^+ and an isomer of neutral urea. The products urea + H_3O^+ are 52.97 kcal/mol more stable than $\text{NH}_2\text{OH}_2^+ + \text{HCONH}_2$ reactants (see the corresponding asymptotic line in Fig. 2) and the system has thus enough energy to take a different path instead of the minimum energy path connecting TS7A to I8A (and then to $\text{UreaH}^+ + \text{H}_2\text{O}$), thus forming neutral urea. However, when optimizing the neutral HNCONH_3 species of TS7A, we obtained spontaneously isocyanic acid (HNCO) and ammonia. The structures of relevant intermediates and transition states along this pathway are reported in Fig. 3.

The PESs for reactions 3 and 5 show a positive and high activation energy and the corresponding diagrams are reported in Fig. A.1 as Path A and B, respectively. The corresponding

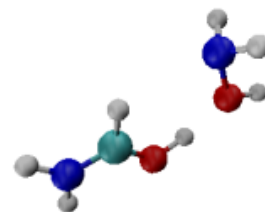
Intermediates



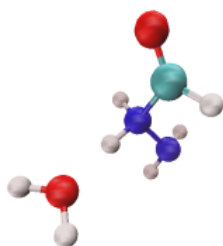
I3A



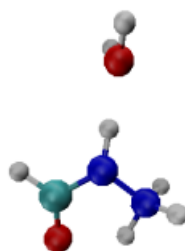
I1A



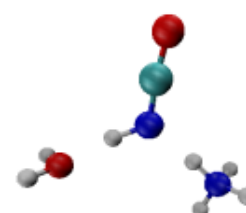
I2A



I4A

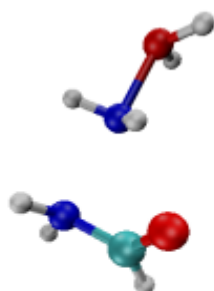


I5A

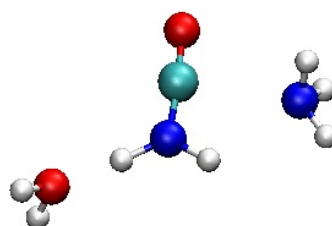


I6A

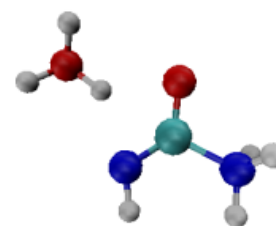
Transition states



TS3A



TS6A



TS7A

Fig. 3. Structures of most relevant intermediates and transition states as obtained from reactions 3, 4, and 5. Oxygen atoms are in red, nitrogen in blue, carbon in cyan, and hydrogen in white.

barriers of 17.6 and 18.8 kcal/mol for Path A and B, respectively, make the two reactions impossible under low temperature conditions. Details are given in Appendix A.1.

The results of our PES analysis show that only the reaction involving the less stable isomer of protonated hydroxylamine, NH_2OH_2^+ , with neutral formamide, HCONH_2 , leads to urea through a barrierless pathway. This same pathway can be responsible for the formation of isocyanic acid, which was found as an intermediate of the full pathway. Of course, once the I3A complex is formed from a $\text{NH}_2\text{OH}_2^+ + \text{HCONH}_2$ reaction, it can evolve, forming protonated urea via TS3A or isomerizing into I2A and I1A, in this case reacting back and forming $\text{NH}_3\text{OH}^+ + \text{HCONH}_2$ or $\text{NH}_2\text{OH} + \text{HCOH}\text{NH}_2^+$.

An estimate of the ratio of the two reaction channels can be obtained from the RRKM rate constant to pass the TS3A (k^{TS3A}) versus TS2A (k^{TS2A}) transition states, as shown in Fig. 4. The evolution of the rate constant ratio as a function of internal energy shows that, while for low energy values the pathway initiated by the TS2A isomer is dominant, the other pathway becomes increasingly important as the internal energy of the intermediate increases, with a ratio close to one at higher

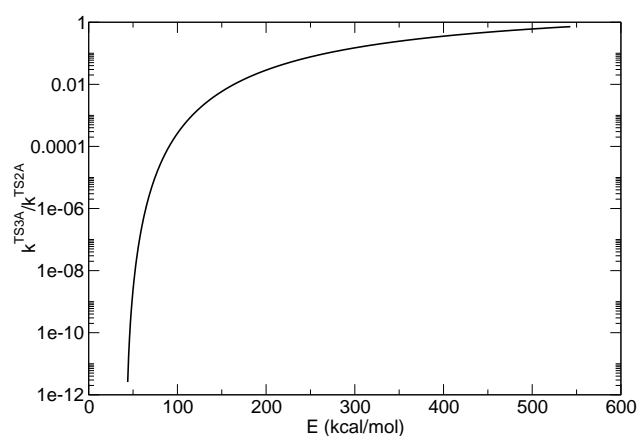


Fig. 4. Ratio between k^{TS3A} and k^{TS2A} rate constants corresponding to the activation of I3A complex as function of its internal energy (E).

energies. Of course, this is a simple picture that does not take into account the dynamical effect related to the collision between

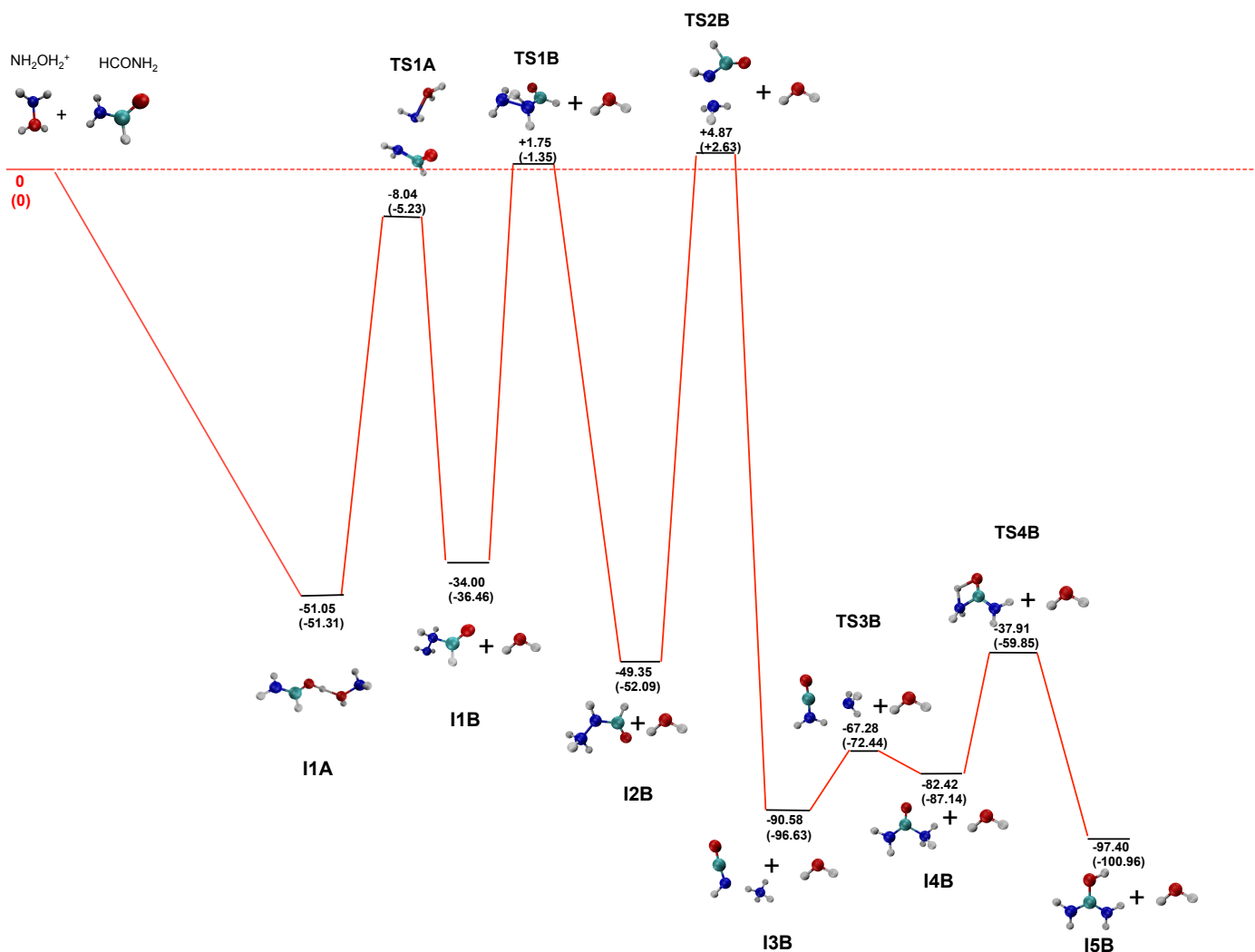


Fig. 5. Energy profile, in kcal/mol, for ion-molecule reaction $\text{NH}_2\text{OH}_2^+ + \text{HCONH}_2$ in which water molecule was separated from ion once formed, as obtained by CCSD(T)/aug-cc-pVTZ//MP2-aug-cc-pVTZ (in parenthesis) calculations. These values contain zero-point energies (ZPE).

NH_2OH_2^+ and HCONH_2 , and a more detailed study of such reactive scattering events would shed more light on the competition between the different pathways. In conclusion, both neutral isocyanic acid and protonated urea can be formed from a $\text{NH}_2\text{OH}_2^+ + \text{HCONH}_2$ reaction under the ISM conditions, even if their formation will be in competition with the formation of $\text{NH}_3\text{OH}^+ + \text{HCONH}_2$ and $\text{NH}_2\text{OH} + \text{HCOH}\text{NH}_2^+$ products.

Finally, we investigated the key role of the water molecule in the previously discussed pathway. To this end, we calculated minima and TSs removing the H_2O (i.e., calculating separately the energies of the ions and the neutral water molecule) following its formation from intermediate I2B (before the mechanism is by definition the same) up to the final products. Results are shown in Fig. 5. In the absence of the water molecule, the energy of minima and (more importantly) TSs increases, such that the reaction has a net activation barrier of 4.87 kcal/mol. The stability of ion-water clusters during the reaction path is thus crucial, the water molecule acting somehow as a catalyzer in the reaction.

We now consider reactions 6 and 7, involving formamide and ammonia (neutral and protonated). The PES leading to the formation of protonated urea and H_2 is shown in Fig. A.2. The two paths identified have a positive barrier of 85.18 and 77.66 kcal/mol, respectively, and thus they can be disregarded

as possible pathways for the formation of urea in the ISM. Details are given in Appendix A.1.

We finally move to ion-molecule reactions 8 and 9 involving methylamine and formamide. These reactions are also potentially very interesting since the neutral species of both reactants and products were all detected in the ISM (Kaifu et al. 1974; Remijan et al. 2014; Rubin et al. 1971; Lacy et al. 1991). In Fig. A.3 we report the PES of the two pathways, which have positive barriers of 70.58 and 89.13 kcal/mol, respectively. Thus, despite the high exothermicity of reaction 8 ($\Delta E = -35.47$ kcal/mol), it is not likely to occur in the ISM due to the high activation energy barrier. We discuss details of these pathways in Appendix A.1.

To summarize, the only ion-molecule reaction that shows a barrierless pathway for the synthesis of protonated urea is reaction 4, which has as reactant the high energy protonated hydroxyl amine (NH_2OH_2^+). The same reaction can also lead to neutral isocyanic acid.

3.3. Mechanisms for neutral-neutral reactions

We now consider the PES connecting reactants and products for neutral-neutral reaction 11, which is the most exothermic

and exergonic reaction. In this case, we found two different pathways, shown in Fig. A.4, whose energetic is very similar, both with a positive barrier (61.59 and 60.26 kcal/mol for Path A and B, respectively). These barriers make the reaction unlikely under ISM conditions and details are thus discussed in Appendix A.2.

3.4. Mechanisms for radical reactions

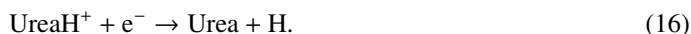
Finally, we consider the PES of the two radical reactions 14 and 15, which are shown in Fig. A.5 (Path A and B, respectively). Both reactions occur on a doublet potential energy surface, which is conserved through the reaction. The resulting activation energies are of 16.22 and 6.18 kcal/mol, being too high for thermal reactivity in the ISM. Details of the PES of these reactions are thus reported in Appendix A.3.

4. Conclusions and outlooks

In this work we have investigated, by highly correlated quantum chemistry calculations, the thermodynamic and kinetic possibility of forming urea in ISM conditions through ion-molecule, neutral-neutral, and radical reactions. Recently a tentative detection of urea in the ISM was reported by Remijan et al. (2014) and this is the first quantum chemistry study devoted to understanding possible gas-phase reactions concerning the formation of this molecule, while a recent theoretical chemistry study relevant to the astrophysical presence of urea considered the stability of different urea isomers, concluding that the $(\text{NH}_2)_2\text{CO}$ form is the one likely to be observed in the ISM (Fouurré et al. 2016).

We have summarized in Table 1 the activation energies, E^a , of the different pathways chosen on the basis of our calculations – here we consider as E^a the energy difference between the reactants and the transition state highest in energy along the given pathway. Only the reaction between NH_2OH_2^+ (the high energy tautomer of protonated hydroxylamine) and formamide is possible through a barrierless mechanism, suggesting the possibility of this happening in the ISM. The NH_2OH_2^+ reactant, thus, seems to be a key species, since it was also suggested to be a reactant for the formation of formamide in a recent ion-molecule collisional study (Spezia et al. 2016). In line with what has been suggested by Pulliam et al. (2012), who reported the non-observation of neutral hydroxylamine, it is possible that the protonated species is present in the ISM.

Protonated urea can give neutral urea via a typical dissociative recombination reaction:



Of course, the addition of one electron to protonated urea can lead also to different fragmentation products of the neutral radical species formed. This structure, however, is a (local) minimum, as reported by MP2 geometry optimization, and to further react, losing H· or other species, it will need energy and thus it will depend on the internal energy of the molecules.

Another way of forming neutral urea would be by proton exchange with a species, X, with higher proton affinity (PA):



The PA of urea was determined experimentally by Zheng & Cooks (2002) to be 868.4 ± 2.5 kJ/mol, and our calculations report a value of 868.4 kJ/mol at 15 K and 862.5 kJ/mol at 298 K, which is in good agreement with the experimental determination. This value of PA is relatively

high with respect to values known for molecules present in Sgr B2 (data are summarized in Table B.1), so that only few species, like cyclopropenylidene (PA = 915.1 kJ/mol), iron oxide (PA = 907 kJ/mol), methylamine (PA = 899 kJ/mol), ethanimine (PA = 884.6 kJ/mol), and C_2S (PA = 869.6 kJ/mol) are compatible with a proton transfer reaction from protonated urea.

Furthermore, we have pointed out that the barrierless mechanism needs the H_2O water molecule, once formed before the ion isomerizes to the urea structure, to stay close to this ion in order to decrease the proton transfer barriers. While the present calculations are done in the gas phase, this result could be a suggestion to study the role of catalytic ice on these reactions, which could largely favor the reactivity, as pointed out from calculations studying the synthesis of other species (Woon 1999, 2001, 2002; Koch et al. 2008; Chen & Woon 2011; Rimola et al. 2012, 2014). Finally, we should note that the same reaction pathway responsible for the formation of protonated urea can also lead to isocyanic acid (here directly the neutral form), which was also observed in the ISM (Snyder & Buhl 1972); structures of this part of the PES can also lead to H_3O^+ and neutral urea, while the isomer is not stable and, in our static calculations, spontaneously formed isocyanic acid and ammonia.

Dynamical-based calculations would be interesting for future works to better elucidate some possible competing reaction pathways, in particular for the $\text{NH}_2\text{OH}_2^+ + \text{HCONH}_2$ reaction in which the barrierless formation of protonated urea is in competition with simple proton transfers forming $\text{NH}_2\text{OH} + \text{HCOH}_2\text{NH}_2^+$ or $\text{NH}_3\text{OH}^+ + \text{HCONH}_2$. Other reactions show a too high energy barrier such that they should be disregarded. In conclusion, quantum chemistry calculations show that it would be possible that protonated urea is formed via an ion-molecule reaction under ISM conditions; then the neutral form can be finally obtained via a typical dissociative recombination reaction or from proton transfer to a molecule with higher proton affinity.

Acknowledgements. R.S. and Y.J. thank ANR DynBioReact (Grant No. ANR-14-CE06-0029-01) for support and CNRS program INFINITI (project ASTROCOL) for partial support. R.S. thanks Universidad de Valladolid for an invited professor fellowship.

References

- Altwegg, K., Balsiger, H., Bar-Nun, A., et al. 2016, *Science Adv.*, 2
 Barone, V., Latouche, C., Skouteris, D., et al. 2015, *MNRAS*, 453, L31
 Barrientos, C., Redondo, P., Largo, L., Rayon, V. M., & Largo, A. 2012, *ApJ*, 748, 99
 Becke, A. D. 1993, *J. Chem. Phys.*, 98, 5648
 Belloche, A., Menten, K. M., Comito, C., et al. 2008, *A&A*, 482, 179
 Belloche, A., Meshcheryakov, A. A., Garrod, R. T., et al. 2017, *A&A*, 601, A49
 Blagojevic, V., Petrie, S., & Bohme, D. K. 2003, *MNRAS*, 339, L7
 Boulet, P., Gilardoni, F., Weber, J., Chermette, H., & Ellinger, Y. 1999, *Chem. Phys.*, 244, 163
 Cernicharo, J., Kahane, C., Guelin, M., & Gomez-Gonzalez, J. 1988, *A&A*, 189, L1
 Cernicharo, J., Tercero, B., Fuente, A., et al. 2013, *ApJ*, 771, L10
 Chen, L., & Woon, D. E. 2011, *J. Phys. Chem. A*, 115, 5166
 Cheung, A. C., Rank, D. M., Townes, C. H., Thornton, D. D., & Welch, W. J. 1968, *Phys. Rev. Lett.*, 21, 1701
 Cheung, A., Rank, D. M., Townes, C., Thornton, D. D., & Welch, W. 1969, *Nature*, 221, 626
 Danger, G., Duvernay, F., P., T., Borget, F., & Chiavassa, T. 2012, *ApJ*, 756, 11
 Danger, G., Rimola, A., Mrad, N. A., et al. 2014, *Phys. Chem. Chem. Phys.*, 16, 3360
 Davidson, E. R. 1996, *Chem. Phys. Lett.*, 260, 514
 de Marcellus, P., Meinert, C., Myrgorodska, I., et al. 2015, *PNAS*, 112, 965
 Dunning Jr., T. H. 1989, *J. Chem. Phys.*, 90, 1007
 Duvernay, F., Dufauert, V., Danger, G., et al. 2010, *A&A*, 523, A79
 Elsila, J. A., Dworkin, J. P., Bernstein, M. P., Martin, M. P., & Sandford, S. A. 2007, *ApJ*, 660, 911

- Forstel, A., Maksytenko, P., Jones, B. M., et al. 2016, *Chem. Commun.*, **52**, 741
- Fourikis, N., Takagi, K., & Morimoto, M. 1974, *ApJ*, **191**, L139
- Fourré, I., Rosset, L., Chevreau, H., & Y. Ellinger, Y. 2016, *A&A*, **589**, A18
- Frisch, M. J., Trucks, G. W., Schlegel, H. B., et al. 2009, Gaussian 09, Revision D.01
- Fukui, K. 1981, *Acc. Chem. Res.*, **81**, 363
- Geppert, W. D., & Larsson, M. 2013, *Chem. Rev.*, **113**, 8872
- Goesmann, F., Rosenbauer, H., Bredehöft, J. H., et al. 2015, *Science*, **349**, aab0689
- Gratier, P., Pety, J., Guzmán, V., et al. 2013, *A&A*, **557**, A101
- Gupta, H., Gottlieb, C. A., Lattanzi, V., Pearson, J. C., & McCarthy, M. C. 2013, *ApJ*, **778**, L1
- Hayats, R., Studier, M. H., Moore, L. P., & Anders, E. 1975, *Geochim. Cosmochim. Acta*, **39**, 471
- Herbst, E. 1982, *Chem. Phys.*, **65**, 185
- Hollis, J. M., Lovas, F. J., Remijan, A. J., et al. 2006, *ApJ*, **643**, L25
- Holtom, P. D., Bennet, C. J., Osamura, Y., Mason, N. J., & Kaiser, R. I. 2005, *ApJ*, **626**, 940
- Hunter, E. P., & Lias, S. G. 1998, *J. Phys. Chem. Ref. Data*, **27**, 413
- Kaifu, N., Morimoto, M., Nagane, K., et al. 1974, *ApJ*, **191**, L135
- Kaiser, R. I. 2012, *Chem. Rev.*, **102**, 1309
- Kaiser, R. I., Stockton, A. M., Kim, Y. S., Jensen, E. C., & Mathies, R. A. 2013, *ApJ*, **765**, 111
- Koch, D. M., Toubin, C., Peslherbe, G. H., & Hynes, J. T. 2008, *J. Phys. Chem. C*, **112**, 2972
- Kolb, V. M. 2014, *Astrobiology: An Evolutionary Approach* (CRC Press)
- Lacy, J., Carr, J., Evans, N. J., et al. 1991, *ApJ*, **376**, 556
- Larsson, M., Geppert, W. D., & Nyman, G. 2012, *Rep. Prog. Phys.*, **75**, 066901
- Lee, T. J., & Taylor, P. R. 1989, *Int. J. Quantum Chem., Quant. Chem. Symp.*, **S23**, 199
- Lee, C., Yang, W., & Parr, R. G. 1988, *Phys. Rev. B*, **88**, 785
- Levine, R. D. 2005, *Molecular Reaction Dynamics* (Cambridge University Press)
- McQuarrie, D. A. 1973, *Statistical Thermodynamics* (Harper and Row), 4
- Petrie, S., & Bohme, D. K. 2007, *Mass Spec. Rev.*, **26**, 258
- Pople, J. A., Head-Gordon, M., & Raghavachari, K. 1987, *J. Chem. Phys.*, **87**, 5968
- Pulliam, R. L., McGuire, B. A., & Remijan, A. J. 2012, *ApJ*, **751**, 1
- Purvis III, G. D., & Bartlett, R. J. 1982, *J. Chem. Phys.*, **76**, 1910
- Raunier, S., Chiavassa, T., Duvernay, F., et al. 2004, *A&A*, **416**, 165
- Redondo, P., Barrientos, C., & Largo, A. 2014a, *ApJ*, **793**, 32
- Redondo, P., Barrientos, C., & Largo, A. 2014b, *ApJ*, **780**, 181
- Remijan, A. J., Hollis, J. M., Lovas, F. J., et al. 2008, *ApJ*, **675**, L85
- Remijan, A. J., Snyder, L. E., McGuire, B. A., et al. 2014, *ApJ*, **783**, 77
- Rimola, A., Sodupe, M., & Ugliengo, P. 2012, *ApJ*, **754**, 24
- Rimola, A., Taquet, V., Ugliengo, P., Balucani, N., & Ceccarelli, C. 2014, *A&A*, **572**, A70
- Rubin, R., Swenson Jr, G., Benson, R., Tigelaar, H., & Flygare, W. 1971, *ApJ*, **169**, L39
- Snow, J. L., Orlova, G., Blagojevic, V., & Bohme, D. K. 2007, *J. Am. Chem. Soc.*, **129**, 9910
- Snyder, L. E., & Buhl, D. 1972, *ApJ*, **177**, 619
- Spezia, R., Salpin, J.-Y., Gaigeot, M.-P., Hase, W. L., & K., S. 2009, *J. Phys. Chem. A*, **113**, 13853
- Spezia, R., Jeanvoine, Y., Hase, W. L., Song, K., & Largo, A. 2016, *ApJ*, **826**, 107
- Turner, B. E., Liszt, H. S., Kaifu, N., & Kisliakov, A. G. 1975, *ApJ*, **201**, L149
- Woon, D. E. 1999, *Icarus*, **142**, 550
- Woon, D. E. 2001, *Icarus*, **149**, 277
- Woon, D. E. 2002, *ApJ*, **571**, L177
- Zheng, X., & Cooks, R. G. 2002, *J. Phys. Chem. A*, **106**, 9939

Reactions 3 and 5

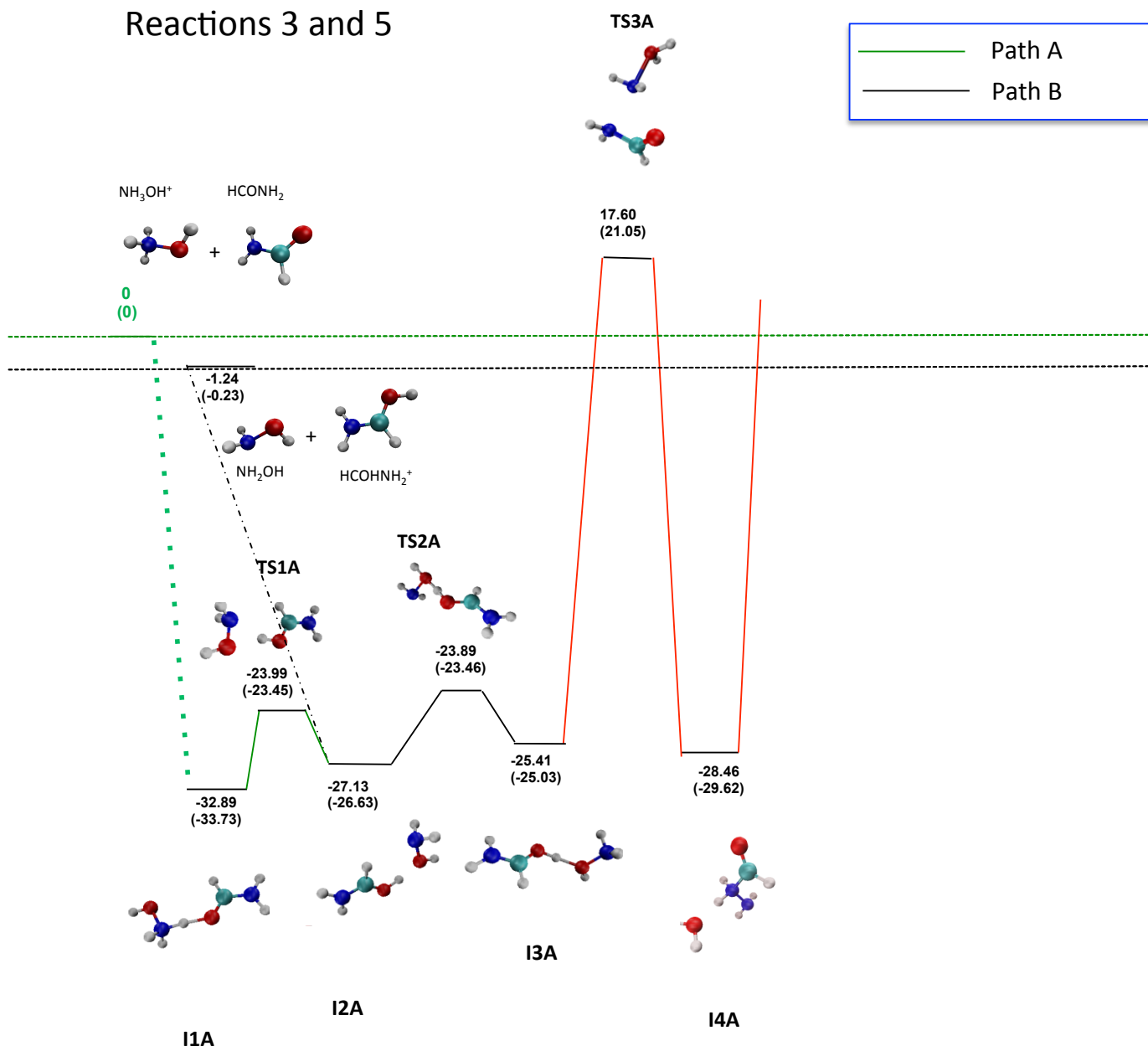


Fig. A.1. Energy profiles, in kcal/mol, for ion-molecule reactions $\text{NH}_3^+\text{OH} + \text{HCONH}_2$ (Path A) and $\text{NH}_2\text{OH} + \text{HCOH}\text{NH}_2^+$ (Path B), as obtained by CCSD(T)/aug-cc-pVTZ//MP2-aug-cc-pVTZ and MP2/aug-cc-pVTZ (in parenthesis) calculations. These values contain zero-point energies (ZPE). The diagram stops at I4A structure since afterwards it would be the same as Fig. 2.

Appendix A: Complementary reaction diagrams

Here we report the energy profiles of the reaction pathways, which show activation energy barriers that are too high. Details on the neutral-neutral reaction pathways are given in the following.

A.1. Ion-molecule reactions

Here we detail the PES for ion-molecule reactions with energy barriers that are too high, so that these reactions are not doable under low temperature conditions. First we discuss reactions 3 and 5, reported in Fig. A.1 as Path A and B, respectively.

The electrostatic interaction between NH_3OH^+ and the neutral formamide (reaction 3) leads to the formation of the

complex I1A. Then, the complex I1A evolves to I2A through a hydrogen migration from the nitrogen to the oxygen atom, involving TS1A. The transition state TS2A connects the two intermediates I2A and I3A, implying the rotation around the torsional angle O-H-O-N. The structures of I1A and I2A are also reported in Fig. 3. From I3A, the formation of the more stable isomer of protonated urea takes place as described previously. In this case, however, since the reactants are lower in energy, the pathway has a barrier of 17.6 kcal/mol, making this process not possible under low temperature conditions.

The ion-molecule interaction between neutral hydroxylamine with protonated formamide forms the complex I2A (Path B of Fig. A.1). From I2A, the reaction mechanism for the synthesis of protonated urea is the one already described, with a net activation barrier of 18.8 kcal/mol.

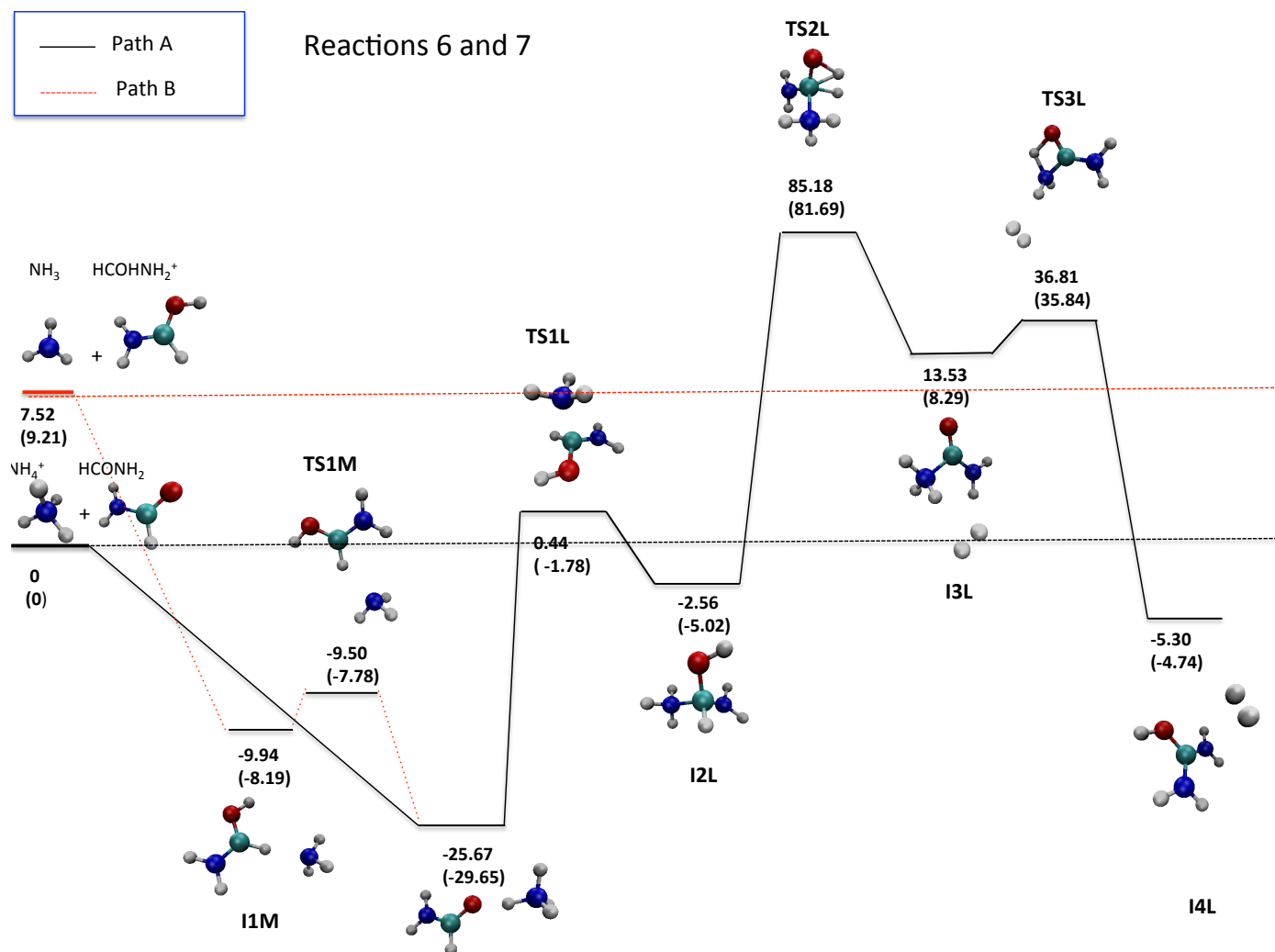


Fig. A.2. Energy profiles, in kcal/mol, for ion-molecule reactions $\text{NH}_4^+ + \text{HCONH}_2$ (Path A) and $\text{NH}_3 + \text{HCOH}_2\text{NH}_2^+$ (Path B), as obtained by CCSD(T)/aug-cc-pVTZ//MP2-aug-cc-pVTZ and MP2/aug-cc-pVTZ (in parenthesis) calculations. These values contain zero-point energies (ZPE). In the final step we report the energy of the cluster, the final product energy being reported in Table 1.

We now consider reactions 6 and 7, involving formamide and ammonia (neutral and protonated), whose PES leading to the formation of protonated urea and H_2 , is shown in Fig. A.2. As we can notice from Path A (corresponding to $\text{NH}_4^+ + \text{HCONH}_2$ reactants), the electrostatic interaction between formamide and ammonium ion results in the formation of the complex I1L, where a hydrogen bond interaction between the carbonyl oxygen of formamide and ammonium ion takes place.

The reaction proceeds through TS1L, where the deprotonation of the ammonium ion induces a nucleophilic attack on the carbon atom by the nitrogen atom of ammonia, leading to the formation of I2L. From the tetrahedral intermediate I2L, the reaction evolves to I3L by removing molecular hydrogen through TS2L. This is the rate determinant step of this reaction since it corresponds to the high energy barrier. Then a proton transfer leads to the final products via TS3L transition state. A similar route, in which only the initial steps are different, corresponds to $\text{NH}_3 + \text{HCOH}_2\text{NH}_2^+$ reaction (Path B in Fig. A.2). In both cases the pathways connecting these reactants to exothermic products have a highly positive barrier, 85.18 and 77.66 kcal/mol for Path A and B, respectively, and they can be disregarded as possible pathways for the formation of urea in the ISM.

Finally, we discuss the PES of reactions 8 and 9 involving methylamine and formamide, which are reported in Fig. A.3.

The reaction between CH_3NH_2 and $\text{HCOH}_2\text{NH}_2^+$ (Path A in Fig. A.3) is somehow particular, showing a feature that can arise when localizing minima and TSs on the Born-Oppenheimer surface and then adding ZPE correction (as always in theoretical chemistry). I1G, the complex between the two reactants, and I2G, an intermediate, are connected via a TS, TS1G. Considering only electronic energy (shown in red in Fig. A.3), the TS is higher in energy than the intermediate I2G, while adding the ZPE on reactants, TSs, and products; now the TS is lower in energy than its corresponding product. We note that the IRC calculation connecting, via the minimum energy path, the TS with the products (in this case I1G and I2G) is done on the Born-Oppenheimer surface, which does not contain ZPE correction. This means that dynamically, even at 0 K, the I1G to I2G isomerization is barrierless. We will not go more in detail on this aspect since we are interested in the highest energy barrier on each pathway, which in the present case does not correspond to this peculiar TS. In fact, from I2G the system needs to pass through TS2G, where the simultaneous cleavage of the C–N bond of methylamine and the formation of a new C–N bond occur. TS2G is the highest energy TS of this reaction pathway with an energy barrier of 70.58 kcal/mol. The other pathway shown in Fig. A.3 (Path B) differs from Path A by the initial steps. First the complex I1H is formed, then leading to the complex I1G, in which

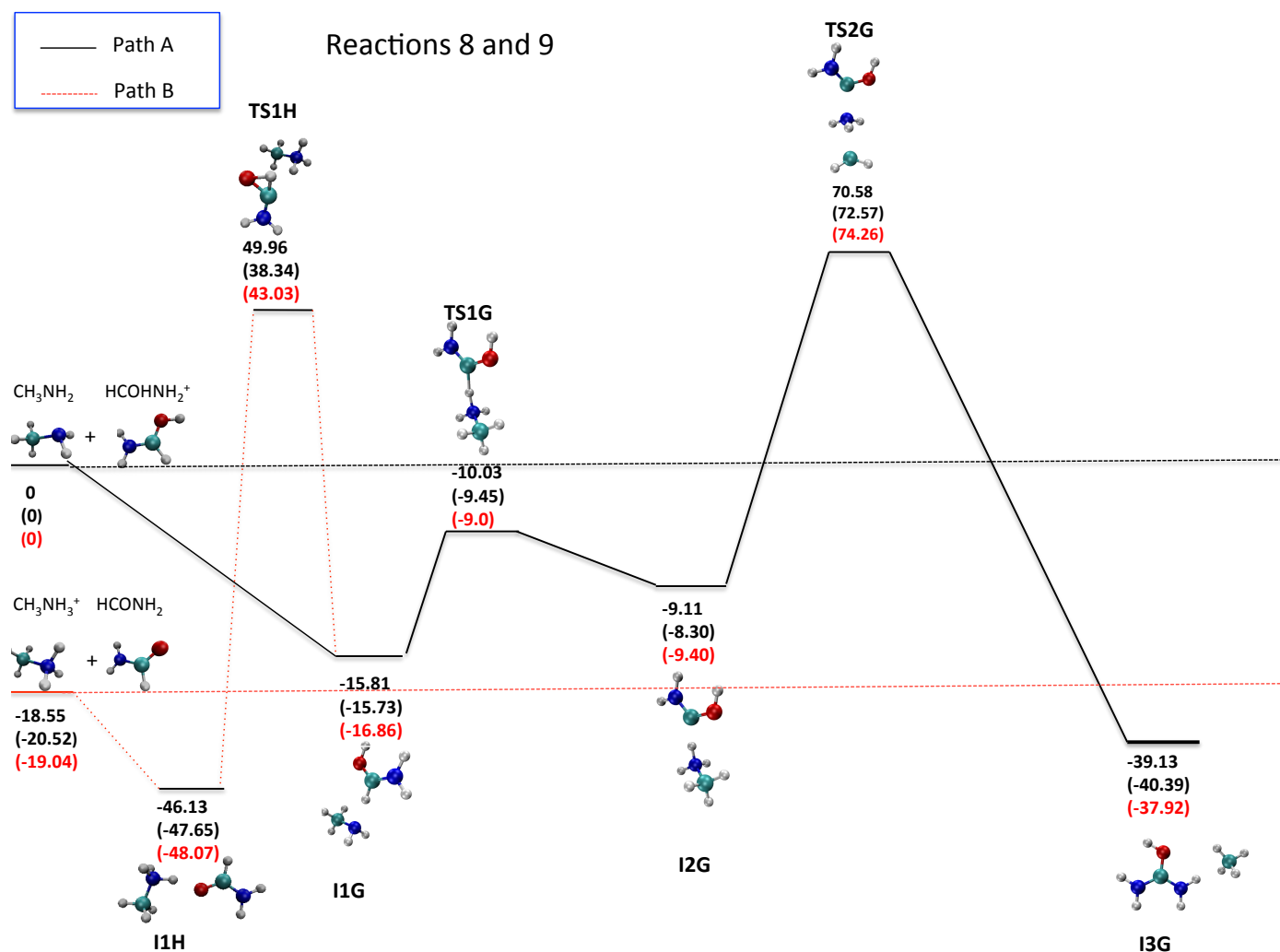


Fig. A.3. Energy profiles, in kcal/mol, for ion-molecule reactions $\text{CH}_3\text{NH}_2 + \text{HCOHNH}_2^+$ and $\text{CH}_3\text{NH}_3^+ + \text{HCONH}_2$ as obtained by CCSD(T)/aug-cc-pVTZ//MP2-aug-cc-pVTZ and MP2/aug-cc-pVTZ (in parenthesis) calculations. These values contain zero-point energies (ZPE). In red we report values concerning only electronic energies, which show that I2G is lower in energy than the TS1G transition state for electronic energies, while ZPE inverts the order (see text for more details). In the final step we report the energy of the cluster, the final product energy being reported in Table 1.

the formamide is now protonated. TS1H is the only structure with a saddle point topology found, since when we try to transfer a proton from the NH₃ group of protonated methylamine to the oxygen atom of formaldehyde, the system always come back to structure I1H. However, the rate determining step is the TS2G, which is in common between the two pathways. In fact, once I1G is obtained then the reaction proceeds as for Path A.

A.2. Neutral-neutral reactions

In Fig. A.4 we show the PES corresponding to the neutral-neutral reactions. Two pathways were identified, Path A and Path B, and they both show positive barriers such that they cannot be considered as likely to occur under ISM conditions. One pathway, Path A in Fig. A.4, is the neutral-neutral analog of the one between protonated hydroxylamine and neutral formamide. The first step of this process is the formation of the complex I1C, resulting in a hydrogen bond interaction between the amine group of the formamide and the amino group of hydroxylamine. The 1, 2-hydrogen shift from the nitrogen atom to the oxygen atom in the hydroxylamine and the successive formation of a

new N–O bond leads to the intermediate I2C, through the transition state TS1C. This transition state is 61.59 kcal/mol higher than the reactants and represents the highest energy barrier of this reaction path. The reaction advances through the hydrogen migration from the secondary to the primary amine of I2C and leads to the formation of the intermediate I3C, involving TS2C. The I3C evolves to the I4C through the TS4C, where a rotation of the aldehyde group around the C–N bond occurs. The I4C progresses through TS5C, where a hydrogen migration from the secondary amino group of I4C to its primary amino group leads to the intermediate I5C. From I5C the reaction reaches I6C through a concerted mechanism, via TS5C: a hydrogen atom migration from the carbon atom to the nitrogen atom of the secondary amino group, which induces the N–N bond cleavage and the consequent formation of ammonia. The intermediate I6C is a cluster formed by isocyanic acid, water, and ammonia, similar to what is obtained in the pathway of reaction 4, here of course all species being neutral. From I6C the reaction progresses to I7C through the TS6C, which implies a proton transfer, assisted by water, from the nitrogen atom of the ammonia molecule to the carbonyl oxygen of the isocyanic acid. This proton transfer favors the nucleophilic attack by the nitrogen atom on the carbonyl

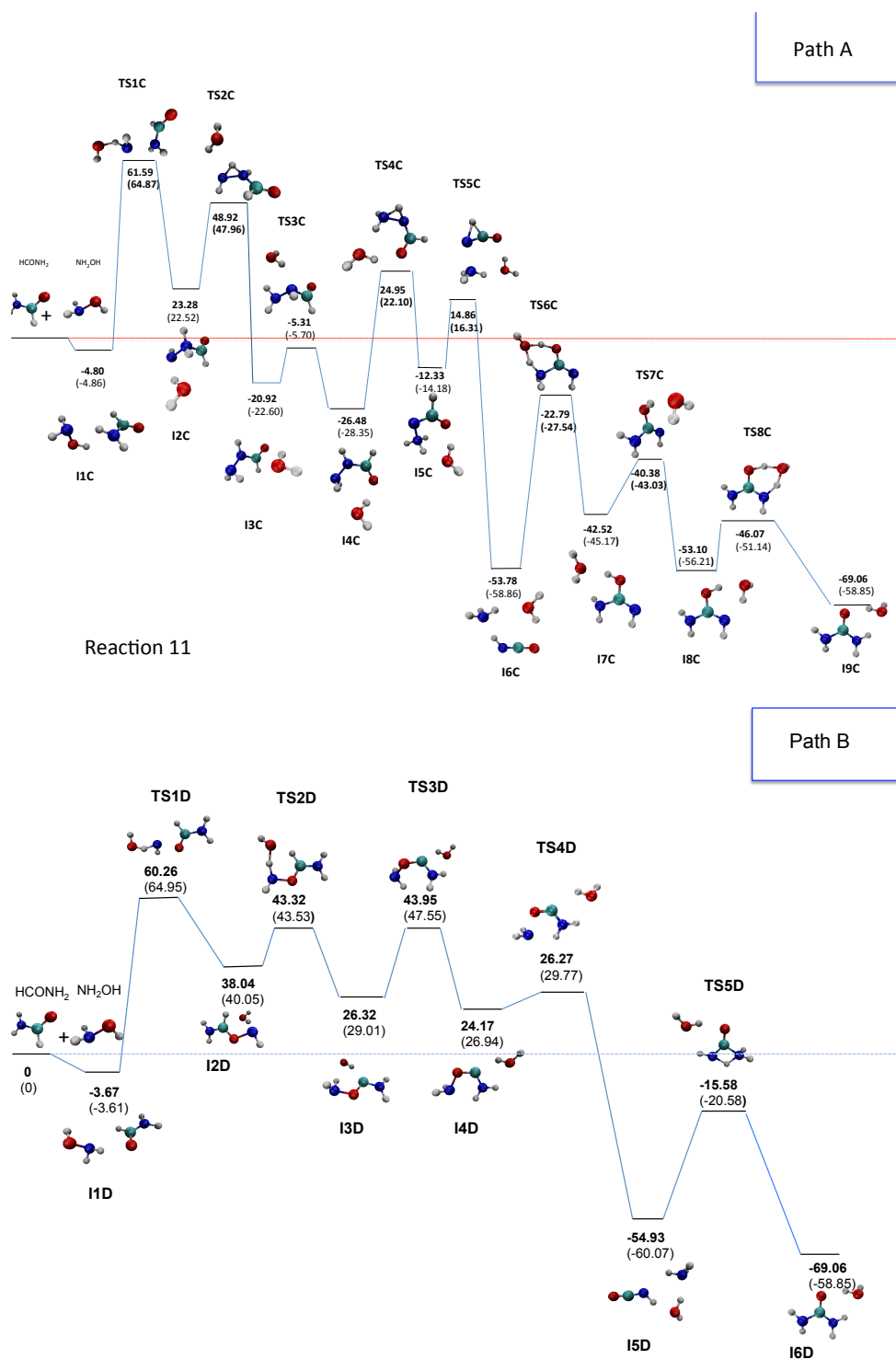


Fig. A.4. Energy profiles, in kcal/mol, for two pathways of neutral-neutral reaction $\text{NH}_2\text{OH} + \text{HCONH}_2$ as obtained by CCSD(T)/aug-cc-pVTZ//MP2-aug-cc-pVTZ and MP2/aug-cc-pVTZ (in parenthesis) calculations. These values contain zero-point energies (ZPE). In the final step we report the energy of the cluster, the final product energy being reported in Table 1. *Upper panel:* Path A; *lower panel:* Path B.

carbon atom. Then, the rotation of the alcoholic hydrogen around the C–O bond takes place in TS7C and leads to I8C. From I8C the urea is produced through TS8C, where a proton transfer, assisted by water, takes place from the oxygen atom to the nitrogen atom.

Path B is shown in Fig. A.4. In this case, the reaction begins with the formation of the complex I1D, which implies a hydrogen bond interaction between the oxygen of formamide and the hydrogen of the amino group of hydroxylamine, and which

is slightly less stable than the complex I1C of Path A. The reaction mechanism, which leads from I1D to I2D, then consists in a 1, 2 hydrogen shift from the nitrogen atom to the oxygen atom of the hydroxylamine, with consequent cleavage of the N–O bond. The highest barrier for this path is TS1D and it is located 60.26 kcal/mol above the energy of the reactants. A proton transfer, assisted by water, from the carbon atom to the nitrogen atom leads to the formation of I3D, through TS2D. Then, I3D evolves to I4D via TS3D, where a rotation of the torsional

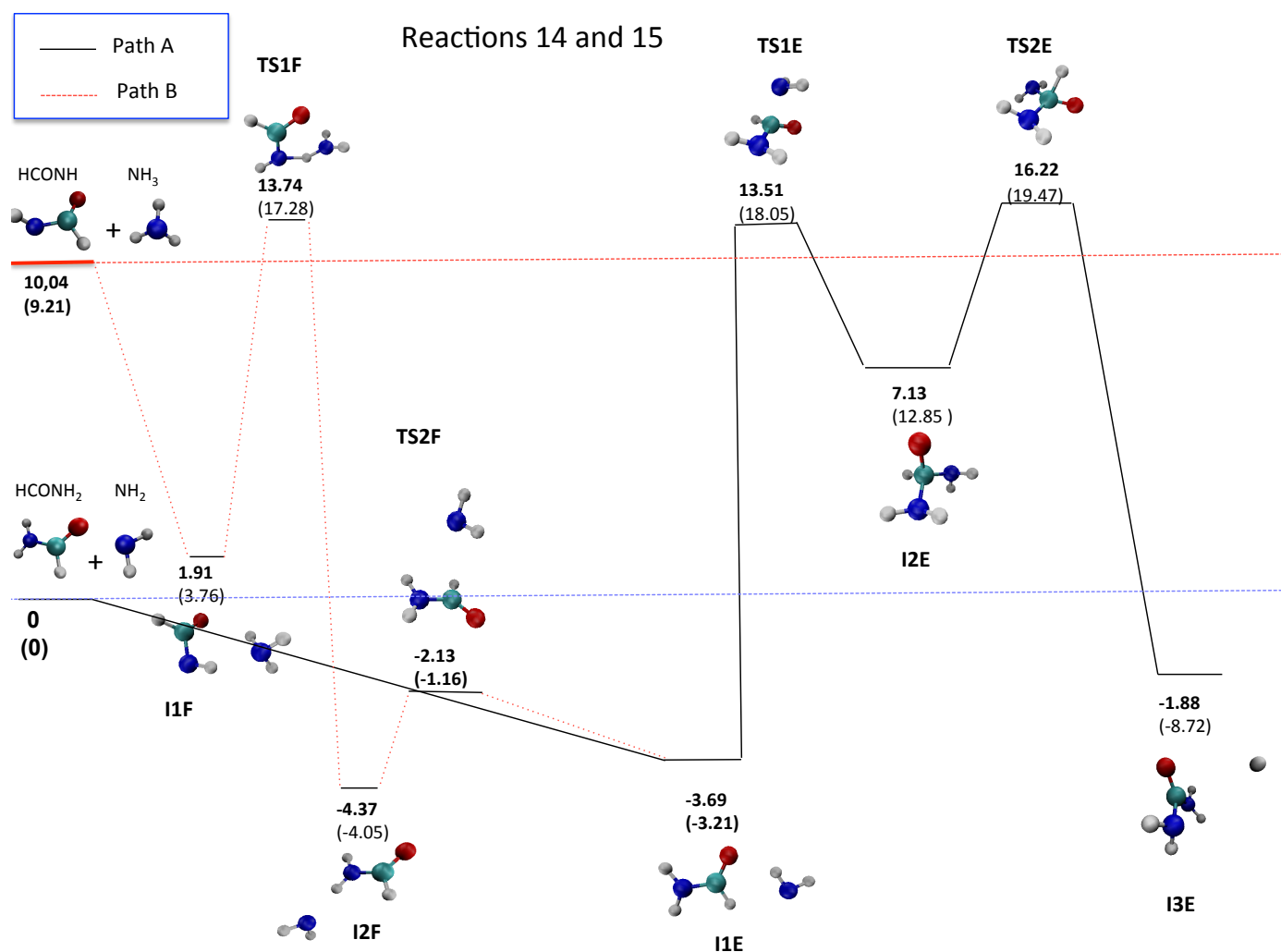


Fig. A.5. Energy profiles, in kcal/mol, for radical reactions $\text{NH}_2 + \text{HCONH}_2$ (black path) and $\text{HCONH} + \text{NH}_3$ (red path) at the CCSD(T)/aug-cc-pVTZ//MP2/aug-cc-pVTZ and MP2/aug-cc-pVTZ (in parentheses) levels. Zero-point vibrational energy differences are included.

angle N-O-C-N takes place. The hydrogen abstraction reaction of the amino group by the NH_2 group through TS4D leads to the formation of I5D, which is (again) a neutral cluster composed by isocyanic acid, ammonia, and water. From I5D, the hydrogen migration from the nitrogen atom of ammonia to the nitrogen atom of the amino group induces a nitrogen nucleophilic attack on the carbonyl C atom, leading to I6D, via structure TS5D.

A.3. Radical reactions

The PESs corresponding to $\text{NH}_2\cdot + \text{HCONH}_2$ and $\text{NH}_3 + \text{HCONH}\cdot$ are shown in Fig. A.5 as Path A and B, respectively. In both cases the activation energy is positive. In the case of Path A, the reaction starts with the formation of the complex I1E, in which the amino radical interacts with the carbonyl group of neutral formamide. The complex I1E progresses to the tetrahedral intermediate I2E through the TS1E structure, which implies

the nucleophilic attack of the nitrogen atom on the carbonyl C atom. The I2E evolves to the urea through the TS2E, where the homolytic cleavage of the C-H bond occurs. Even if this radical reaction is exothermic (-1.84 kcal/mol), the net activation barrier is 16.22 kcal/mol, making this process unlikely for ISM conditions. The PES profile for Path B, corresponding to the most exothermic and exergonic reaction, is also reported in Fig. A.5. At the beginning the electrostatic interaction between the ammonia and the radical, formamide is responsible for the formation of the complex I1F. Then, the hydrogen abstraction reaction of the ammonia by the nitrogen atom of radical formamide leads from I1F to I2F, through TS1F. The I2F evolves to I1E through the re-orientation of the amino radical around the formamide molecule. From I1E the system progresses to the products with the same reaction mechanism described previously for Path A. In this case, the activation barrier of the process is smaller than for Path A but still positive (6.18 kcal/mol), thus making it unlikely for the ISM.

Appendix B: Proton affinity

Here we report the proton affinities of molecules observed or for which tentative observations are reported in the Sgr B2 cloud from data listed in the National Institute of Standards and Technology (NIST) web-book. For urea we report also the values obtained from our calculations at 15 and 298 K, and for hydroxylamine (not present in the experimental data-base) we report calculated values at the same temperatures.

Table B.1. Experimental values of available proton affinities (PA) of neutral molecules suggested to be present in the Sgr B2 cloud.

Molecule	PA (kJ/mol)	Source	Reference
Urea	868.4 ± 2.5	NIST	Zheng & Cooks (2002)
	868.432	calculations at $T = 15$ K	This work
	862.549	calculations at $T = 298$ K	This work
Cyclopropenylidene	951.1	NIST	Hunter & Lias (1998)
Iron oxide	907	NIST	Hunter & Lias (1998)
Methylamine	899.0	NIST	Hunter & Lias (1998)
Ethanimine	885.1	NIST	Hunter & Lias (1998)
C ₂ S	869.6	NIST	Hunter & Lias (1998)
Acetamide	863.6	NIST	Hunter & Lias (1998)
N-methylformamide	851.3	NIST	Hunter & Lias (1998)
Methyl isocyanide	839.1	NIST	Hunter & Lias (1998)
Ketene	825.3	NIST	Hunter & Lias (1998)
Aminoacetonitrile	824.9	NIST	Hunter & Lias (1998)
Formamide	822.2	NIST	Hunter & Lias (1998)
Methyl acetate	821.6	NIST	Hunter & Lias (1998)
Phenol	817.3	NIST	Hunter & Lias (1998)
Ethylene glycol	815.9	NIST	Hunter & Lias (1998)
Acetone	812	NIST	Hunter & Lias (1998)
Cyanamide	805.6	NIST	Hunter & Lias (1998)
Isopropyl cyanide	803.6	NIST	Hunter & Lias (1998)
Propylene oxide	803.3	NIST	Hunter & Lias (1998)
Ethyl formate	799.4	NIST	Hunter & Lias (1998)
Propyl cyanide	798.4	NIST	Hunter & Lias (1998)
Propenal	797	NIST	Hunter & Lias (1998)
Ethylcyanide	794.1	NIST	Hunter & Lias (1998)
Phosphorus mononitride	789.4	NIST	Hunter & Lias (1998)
Propanal	786	NIST	Hunter & Lias (1998)
Vinylcyanide	784.7	NIST	Hunter & Lias (1998)
Acetic acid	783.7	NIST	Hunter & Lias (1998)
Methyl formate	782.5	NIST	Hunter & Lias (1998)
Methyl cyanide	779.2	NIST	Hunter & Lias (1998)
Silicon monoxide	777.8	NIST	Hunter & Lias (1998)
Ethanol	776.4	NIST	Hunter & Lias (1998)
Methyl mercaptan	773.4	NIST	Hunter & Lias (1998)
Amino radical	773.4	NIST	Hunter & Lias (1998)
Hydrogen isocyanide	772.3	NIST	Hunter & Lias (1998)
Methyl isocyanate	764.4	NIST	Hunter & Lias (1998)
Acetaldehyde	768.5	NIST	Hunter & Lias (1998)
Thioformaldehyde	759.7	NIST	Hunter & Lias (1998)
Methanol	754.3	NIST	Hunter & Lias (1998)
Isocyanic acid	753	NIST	Hunter & Lias (1998)
Cyanoacetylene	751.2	NIST	Hunter & Lias (1998)
Methyl-acetylene	748	NIST	Hunter & Lias (1998)
Formic acid	742.0	NIST	Hunter & Lias (1998)
Water	691	NIST	Hunter & Lias (1998)
Carbonyl sulfide	628.5	NIST	Hunter & Lias (1998)
N ₂ O	575.2	NIST	Hunter & Lias (1998)
Nitric oxide	531.8	NIST	Hunter & Lias (1998)
Hydrogen fluoride	484	NIST	Hunter & Lias (1998)

Appendix B

Influence of argon and D₂ tagging on the hydrogen bond network in Cs⁺(H₂O)₃; kinetic trapping below 40 K

On top of all the works presented in this thesis, another investigation has been performed in this PhD work in collaboration with the experimental group of Prof J.M. Lisy in the USA and with the experimental group of Prof K. Asmis in Germany. I have conducted the theory part in collaboration with Dr. D.R. Galimberti, Post-Doc in the Gaiqeot group. We report hereafter the work that has been published.

Influence of argon and D₂ tagging on the hydrogen bond network in Cs⁺(H₂O)₃; kinetic trapping below 40 K

Tim K Esser, Harald Knorke, Flavio Siro Brigiano, Daria Ruth Galimberti, Knut R Asmis, Marie-Pierre Gaiqeot, James M Lisy
Phys. Chem. Chem. Phys., **20** 28476-28486, (2018).



Cite this: *Phys. Chem. Chem. Phys.*,
2018, 20, 28476

Influence of argon and D₂ tagging on the hydrogen bond network in Cs⁺(H₂O)₃; kinetic trapping below 40 K[†]

Tim K. Esser,^a Harald Knorke,^a Flavio Siro-Brigiano,^b Daria Ruth Galimberti,^b Knut R. Asmis,^{a*} Marie-Pierre Gaigeot^{b*} and James M. Lisy^{c*}

The influence of enthalpic and entropic effects as well as of kinetic trapping processes on the structure of Ar/D₂-tagged Cs⁺(H₂O)₃ clusters is studied by temperature-dependent infrared photodissociation spectroscopy combined with harmonic vibrational spectra calculations and anharmonic free energy profiles from finite temperature metadynamics molecular dynamics simulations. Each tag favors a different hydrogen bond network of water molecules, with Ar-tagging (vs. D₂-tagging) of Cs⁺(H₂O)₃ leading to the lower energy conformation. The relative population of these conformers can be tuned over a temperature range of 12 to 21 K. The formation mechanisms of these tagged clusters can be deduced from the free energy profiles. This investigation demonstrates that a variety of factors, both thermodynamic and kinetic, play a role in the structure of flexible molecular species, even at cryogenic temperatures.

Received 25th September 2018,
Accepted 29th October 2018

DOI: 10.1039/c8cp06020g

rsc.li/pccp

Introduction

Strong intermolecular (ion-neutral) interactions play key roles in impacting solution,^{1,2} atmospheric,^{3,4} and biological chemistry,^{5–8} by adjusting the orientation of precursors, the acceleration of reaction rates, and the configuration of macro-molecules, respectively. These chemical processes occur at or near room temperature (~250–310 K), where slight changes can alter the balance between competing forces such as ion-molecule and hydrogen bond interactions. At lower temperatures, two additional factors can play a role. The first is the competition between enthalpic and entropic effects,^{9–14} with the former more dominant as temperatures reach cryogenic regimes (10–80 K). The second is kinetic trapping,^{15–19} when the energy barriers are large compared to thermal energies, preventing the system of interest from reaching its ground (lowest energy) state.²⁰ Such effects have even been observed for weakly bound neutral species.^{21,22} Understanding these effects involves a combination of experimental and theoretical

approaches. From an experimental perspective, the vibrational spectroscopy of cluster ions has been particularly useful, as molecular vibrations, both intramolecular and intermolecular, are particularly sensitive to intermolecular interactions and conformer structure.^{23–25} By utilizing the charged nature of the clusters, mass spectrometric methods enable these systems to be studied as a function of ion-type, neutral binding partner(s), and cluster size/composition.^{26,27} The addition of weakly-bound neutral “messenger” species, such as He, Ne, Ar, H₂ and D₂, facilitates single photon infrared photodissociation (IRPD) in the linear spectroscopy regime, typically with minor perturbation to the cluster ion of interest.^{27–33} Computation studies, using traditional electronic structure calculations (*ab initio* and density functional) providing structures and scaled infrared frequencies,^{34–36} or Born–Oppenheimer Molecular Dynamics (BOMD) that directly give anharmonic vibrational frequencies and intensities,³⁷ are often used to compare with the experimental observations. The experimental and theoretical data are essentially independent of one another and have been combined synergistically in collaborative studies by a large number of research groups.^{4,11,38–47}

The competition between enthalpic- and entropic-favored structures of cluster ions has been carefully examined by recent IRPD studies using temperature-controlled ion traps. Two examples involve the partial breaking of hydrogen bonds, NO₃[−](H₂O) and I[−](H₂O)₂.^{11,39} As NO₃[−](H₂O) was heated from 50 to 350 K, the entropically-favored structure with a single hydrogen bond could be observed at temperatures above 200 K.

^a Wilhelm-Ostwald-Institut für Physikalische und Theoretische Chemie, Universität Leipzig, Linnéstrasse 2, D-04103 Leipzig, Germany. E-mail: knut.asmis@uni-leipzig.de

^b LAMBE UMR8587, Univ Evry, Université d'Evry Val d'Essonne, CNRS, CEA, Université Paris-Saclay, 91025 Evry, France. E-mail: mpgaigeot@univ-evry.fr

^c Department of Chemistry, University of Illinois at Urbana-Champaign, Urbana, Illinois 61801, USA. E-mail: j-lisy@illinois.edu

[†] Electronic supplementary information (ESI) available. See DOI: 10.1039/c8cp06020g

Only the enthalpically-favored structure with bidentate hydrogen bonding was seen spectroscopically below this temperature. With $\text{I}^-(\text{H}_2\text{O})_2$, the water–water hydrogen bond began to break at temperatures above 70 K, and the dissociation energy was determined to be 4.6 (4) kJ mol^{-1} , approximately 1/3 of the gas-phase dissociation energy of the water dimer.¹¹

Mapping out the potential energy landscape for hydrogen-bonded clusters is particularly challenging as the relative differences in conformer energies, and barrier heights can be small, on the order of a few kJ mol^{-1} . These energies are close to the limit of predictive reliability of computational methods. In a previous study of $\text{Li}^+(\text{H}_2\text{O})_4$,¹⁶ it was observed that the presence of one argon atom messenger led to two distinct conformers with different hydrogen-bonded configurations. Neither of these represented the lowest energy configuration, where the four waters are configured in a tetrahedral arrangement about the lithium ion with no water–water hydrogen bonds. Subsequent BOMD simulations of the cluster ion formation at ~ 75 K revealed the barrier to breaking pre-existing hydrogen bonds was greater than the thermal energy.⁴⁸ This resulted in kinetic trapping of the higher energy conformers, a process that did not occur at higher temperatures ~ 300 – 400 K. The height of the barriers to rearrangement was due to the strong electrostatic influence of the lithium ion. Its significant ability to polarize the water molecule and strengthen the hydrogen bonds between water molecules in the first and second hydration layers was the determining factor at these temperatures.

There has been a long-standing concern over the role that messengers can play in influencing the structure of hydrated cations. This has been a major issue in protonated water²⁷ and methanol⁴⁹ cluster ions. From the earliest use of messengers in H_7O_3^+ and H_9O_4^+ ,²⁸ there was the potential that even the attachment of H_2 was sufficient to perturb the system. This has been verified by studies from the Johnson group.^{11,29} For protonated methanol, the binding energy of various messengers has been exploited to influence the effective temperature of the cluster ions.⁴⁹ This has been used to influence the balance between enthalpically- and entropically-favored structures. In both of these protonated systems, the mobility of the excess proton and the variety of chain and ring structures are

particularly susceptible to the presence of a messenger, with differences even noted between Ar, Ne, H_2 and He.^{49–51} Differences between argon-tagged protonated and deuterated systems have been observed as well, with the argon preferentially binding to the OD group in $\text{Ar-H}_4\text{DO}_2^+$.⁴

While it has generally been assumed that H_2 or D_2 tagging has a minimal effect on the structure of cluster ions, there have been some subtle effects noted in earlier studies. In protonated glycine, both He and H_2 tags bind at the protonation site, but there is evidence that with three H_2 molecules, at least one H_2 molecule binds to the uncharged carboxylic acid.⁵² In this study, we report argon and D_2 tagging to $\text{Cs}^+(\text{H}_2\text{O})_3$, where two structures with different hydrogen-bond networks are present for both tagging species. Amazingly, each tag has its own preferred hydrogen-bond network; argon-tagging is associated with the most stable conformer with two hydrogen bonds, while D_2 -tagging favors a higher-energy conformer with a single, weaker hydrogen bond. The relative population of these two conformers can be changed over a temperature range of 12 to 21 K. In the case of argon, the higher energy conformer is only observable at temperatures less than 40 K. The role that D_2 plays as both buffer gas and tag is largely responsible for the formation of this higher energy conformer. Metadynamics analysis provides a solid interpretation for this effect, consistent with the experimental observations.

Experimental details

Infrared photodissociation (IRPD) experiments were carried out using the Leipzig 6 K ring-electrode ion trap triple mass spectrometer.⁵³ Neutral $(\text{H}_2\text{O})_n\text{Ar}_m$ clusters were produced using a pulsed Amsterdam piezo valve (MassSpecpecD BV)⁵⁴ by expanding a water vapor/argon mixture at 3 bar through a 200 μm nozzle at 700 Hz. $\text{Cs}^+(\text{H}_2\text{O})_n\text{Ar}_m$ ions were formed by evaporative cooling after collisions with cesium cations, produced ~ 3 cm downstream from the nozzle by an axial molecular beam ionizer (Extrel CMS), which is schematically shown in Fig. 1. The two main components are the filament and cylindrical grid, indicated by spirals and dashed lines in the figure. The filament was coated with a CsCl-containing molecular sieve

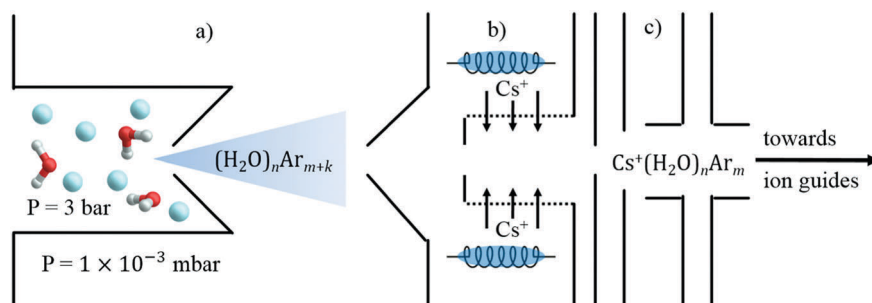


Fig. 1 (a) Neutral $(\text{H}_2\text{O})_n\text{Ar}_m$ clusters were produced using a pulsed piezo valve by expanding a water vapor/argon mixture at 3 bar through a 200 μm nozzle at 700 Hz. (b) Thermionically-emitted cesium ions, provided by an axial molecular beam ionizer (Extrel CMS) with a CsCl containing molecular sieve paste coated filament held at +18.7 V, collided with the neutral species ~ 3 cm downstream from the nozzle, forming (evaporatively cooled) $\text{Cs}^+(\text{H}_2\text{O})_n\text{Ar}_m$ ions. (c) The ions are then extracted from the formation region using a stack of DC lenses.

paste and thermionically emitted cesium cations when heated. The latter were directed towards the neutral beam by a potential difference between the filament and grid, held at +18.7 V and +14.4 V respectively. When a similar ion source was used at Illinois,⁵⁵ $\text{Cs}^+(\text{H}_2\text{O})_n\text{Ar}_m$ ions were extracted from the ionization region perpendicular to the neutral cluster beam, while they were extracted along the axis of the molecular beam in Leipzig, as shown in Fig. 1. The ion cluster beam was collimated in two He-filled radio frequency (RF) octupole ion guides where collisions with the buffer gas reduced the ion beam kinetic energy. The cluster ions were not thermalized to room temperature by these collisions as $\text{Cs}^+(\text{H}_2\text{O})_n$ cluster ions with multiple argon atoms were detected upon exiting the ion guides. Ions of interest were mass-selected in a quadrupole mass-filter, deflected by 90°, and focused into a RF ring-electrode ion-trap. To allow for continuous ion loading and thermalization close to the ion trap temperature, the trap was continuously filled with He or D₂ gas. The latter was used to form $\text{Cs}^+(\text{H}_2\text{O})_n(\text{D}_2)_z$ complexes by three-body collisions in the ion trap.³⁰ Note, under such experimental conditions some ions will not be fully thermalized. However, these “hot” ions will also not tag efficiently and hence their effect on the IRPD measurements is small and negligible, for the present purpose.

Every 100 ms, all ions are extracted and focused both temporally and spatially into the center of the extraction region of an orthogonally mounted reflectron time-of-flight (TOF) tandem photofragmentation mass spectrometer. The reflectron was used to select complexes with single D₂ molecules. Thereafter, the ion packet is irradiated with the tunable infrared radiation in the spectral range from 1500 to 3900 cm⁻¹ supplied by an optical parametric oscillator/amplifier (LaserVision) laser system⁵⁶ operated at 10 Hz with a bandwidth of ~3 cm⁻¹ and a pulse energy of 1–10 mJ, adequately attenuated to avoid saturation.

All parent and photofragment ions are then accelerated toward an MCP detector. An IRPD spectrum is measured by continuously scanning the laser wavelength, which is monitored online using a HighFinesse WS6-600 wavelength meter, with a scan speed such that an averaged TOF mass spectrum (over 100 laser shots) is obtained every 2 cm⁻¹. Typically, at least two scans are measured and averaged and the photodissociation cross section, σ_{IRPD} , was determined as described previously.^{53,57}

Computational details

Untagged and Ar-/D₂-tagged structures of $\text{Cs}^+(\text{H}_2\text{O})_3$ clusters have been optimized at the MP2 and DFT-B3LYP-D3BJ levels of electronic representation, with the Gaussian09 package.⁵⁸ See ESI† for all details. In the following, only the DFT calculations will be used. Table 1 is reporting rankings in energies. Optimized geometries are reported in Fig. 2, for untagged and Ar/D₂-tagged $\text{Cs}^+(\text{H}_2\text{O})_3$ clusters. The labeling is with a Roman numeral-number coding I to IV for untagged (by increasing order of energy), the additional number is for tagged clusters, e.g. I-2, III-1, etc. (see ESI† for more details). The reference of energy is the I-conformer for untagged clusters, and it is the I-1 conformer for tagged clusters. For the four untagged clusters, we have reported rankings in electronic energies, in the vibrational zero-point energy (ZPE), and in free energies calculated at 20 K, i.e. E , E^{ZPE} , and $\Delta G_{20\text{K}}$, respectively in Fig. 2. Table 1 also reports these values for the untagged clusters, with a comparison and validation to MP2 and CCSD(T) calculations.

The ‘OP’ sign in Fig. 2 refers to the position of the Ar/D₂ tag being located out-of-the plane formed by the oxygen atoms of the water molecules. The reliability of the B3LYP-D3 electronic representation has been tested on MP2 and CCSD(T) calculations, with a good agreement in terms of geometries, energy ranking and binding energies. All calculations are performed with the Los Alamos double-zeta basis set⁵⁹ with an effective core potential for Cs, and the correlated all-electron basis set aug-cc-pVDZ⁶⁰ for all other atoms. Harmonic frequencies have been systematically calculated in order to check for minima on the potential energy surface, and are further used for harmonic vibrational spectra in order to interpret and assign the experimental IRPD spectra. To that end, harmonic frequencies are scaled by a 0.9686 factor,⁶¹ very close to the 0.97 scaling factor used in previous work by the Lisy group⁹ and found by the systematic alignment of the O–H stretching band position between calculation and experiment for the $\text{Cs}^+(\text{H}_2\text{O})_2$ cluster.⁶²

To estimate the role of entropy on the relative stability of the conformers at finite temperatures, free energy profiles have been calculated for the untagged I–IV interconversion and for the III cluster stability at three temperatures (10 K, 20 K, 50 K). This is done through biased metadynamics DFT-BLYP-D3 based molecular dynamics simulations using the CP2K code.^{37,63} See ESI† for details. Metadynamics are performed with a time step of 0.4 fs, the bias has been chosen along the O–O distance between the oxygens of the two H-bonded water molecules.

Table 1 Ranking of electronic and ZPE corrected energies for $\text{Cs}^+(\text{H}_2\text{O})_3$ I–IV clusters. Energies are in kJ mol⁻¹. Structures are presented in Fig. 2. Conformer I is the lower in energy and its energy is set to zero; conformer II–IV energies are given with respect to this reference (ΔE , ΔE^{ZPE}). MP2 versus B3LYP-D3 electronic representations, geometry optimizations using the aug-cc-pVDZ Gaussian basis set. CCSD(T) calculations (basis set aug-cc-pVDZ for O, H, D and Ar atoms, Los Alamos double zeta for the Cs) are single points on the MP2 optimized structures, the ZPE is the one obtained at the MP2 level of representation

	MP2	B3LYP-D3	CCSD(T)//MP2	MP2 ZPE corrected	B3LYP-D3 ZPE corrected	CCSD(T)//MP2 ZPE corrected
I	0.00	0.00	0.00	0.00	0.00	0.00
II	-3.77	-0.75	-4.2	5.52	2.13	4.7
III	26.02	17.53	25.3	13.10	7.15	12.5
IV	13.89	13.26	13.1	9.25	7.87	8.5

	Untagged	Tagged					
		1	2	3	4	5	6
I	$\Delta G_{20K}=0.0$ $\Delta E^{ZPE}=0.0$ $\Delta E=0.0$	 OP Ar: 0.0 D ₂ : 0.0	 Ar: +0.7 D ₂ : +1.3	 Ar: -1.3 D ₂ : +0.4	 OP Ar: +0.8 D ₂ : +0.6	 Ar: 0.0 D ₂ : -	 OP Ar: +0.8 D ₂ : +0.8
II	$\Delta G_{20K}=+2.2$ $\Delta E^{ZPE}=+2.1$ $\Delta E=-0.8$	 Ar: +2.5 D ₂ : +2.8			 OP Ar: +1.3 D ₂ : +3.2		
III	$\Delta G_{20K}=+6.8$ $\Delta E^{ZPE}=+7.2$ $\Delta E=+17.5$	 Ar: +5.8 D ₂ : +9.2	 Ar: +5.8 D ₂ : +8.4				
IV	$\Delta G_{20K}=+7.8$ $\Delta E^{ZPE}=+7.9$ $\Delta E=+13.2$	 Ar: +8.9 D ₂ : +9.1	 OP Ar: +8.7 D ₂ : +8.3	 Ar: +8.74 D ₂ : +9.2	 OP Ar: +6.2 D ₂ : +8.4	 Ar: +7.2 D ₂ : -	 Ar: - D ₂ : +9.0

Fig. 2 Optimized structures of untagged $\text{Cs}^+(\text{H}_2\text{O})_3$ and Ar/D₂ tagged $\text{Cs}^+(\text{H}_2\text{O})_3$ clusters from B3LYP-D3/aug-cc-pVDZ electronic representation. Energies are given in units of kJ mol^{-1} . Untagged structures: the zero of energy is taken for the I-1 conformer. Tagged clusters: the zero of energy is taken for the I-1 conformer. 'OP' refers to the tag atom/molecule located out-of-the plane formed by the oxygen atoms of the water molecules. Cs^+ is represented in blue, Ar is in pink, D₂ is in light grey. H-bonds are represented by red dashed lines. Relative energy rankings: E stands for electronic energy, E^{ZPE} accounts for ZPE corrections, ΔG_{20K} free energy calculated at 20 K. Tagged structures are presented with the Ar-tag for I–III conformers, and presented with the D₂-tag for the IV-conformer (at the exception of structure IV-5 that can be optimized only with Ar). Whenever '-' is written, the associated conformer does not exist (*i.e.* IV-5 exists only for Ar-tagged, IV-6 exists only for D₂-tagged).

Results

The IRPD spectra were recorded in both the OH stretching region, from 3500 to 3800 cm^{-1} , and the H₂O bending region, from 1500 to 1700 cm^{-1} . These are presented in Fig. 3, with trap temperatures of 7 K for $\text{Cs}^+(\text{H}_2\text{O})_3\text{Ar}$, and 12 K for $\text{Cs}^+(\text{H}_2\text{O})_3\text{D}_2$, the latter spectra were obtained under two different cluster ion preparation methods. The individual spectral features are labeled a_1 to a_{13} . Assignments of these features (as discussed below) are given in Table 2. The temperature dependence for both tagged species were also obtained over a range of 7 to 40 K for $\text{Cs}^+(\text{H}_2\text{O})_3\text{Ar}$, and 12 to 21 for $\text{Cs}^+(\text{H}_2\text{O})_3\text{D}_2$, as shown in Fig. S1 (ESI[†]). The temperature range for D₂ is reduced, as at temperatures below 12 K D₂ condenses on the ion trap, and the weak binding of D₂ to $\text{Cs}^+(\text{H}_2\text{O})_3$ leads to loss of the D₂ tag at temperatures above 25 K.

H₂O bending region

Calculations revealed that the addition of either argon or D₂ to the $\text{Cs}^+(\text{H}_2\text{O})_3$ conformers I–IV has a negligible impact on the water bending vibrational frequency. As a result the bending frequencies of the untagged conformers were used for comparison with the

experimental data and to make structural assignments for $\text{Cs}^+(\text{H}_2\text{O})_3\text{Ar}$, and $\text{Cs}^+(\text{H}_2\text{O})_3\text{D}_2$, verified further in the O–H stretching region.

When formed with argon as $\text{Cs}^+(\text{H}_2\text{O})_3\text{Ar}_1$, there is a dyad with peaks at 1617 and 1648 cm^{-1} (a_{12} and a_{10} , in Fig. 3a) with apparent shoulders on either side of the 1617 cm^{-1} peak that fade with increasing trap temperature (from 7 to 40 K). This dyad is consistent with the computed spectrum of the lower energy conformer I, with a calculated splitting of 32 cm^{-1} , nearly identical to the observed splitting of 31 cm^{-1} , as shown in Fig. 4. The computed harmonic frequencies are however lower than the experimental values by $\sim 35 \text{ cm}^{-1}$.

When formed as $\text{Cs}^+(\text{H}_2\text{O})_3$ and trapped at 12 K with D₂ as $\text{Cs}^+(\text{H}_2\text{O})_3\text{D}_2$, there is a dyad with peaks at 1604 and 1630 cm^{-1} (a_{13} and a_{11} in Fig. 3c). These bands match closely to the shoulders observed on either side of the 1617 cm^{-1} band of $\text{Cs}^+(\text{H}_2\text{O})_3\text{Ar}_1$. This new dyad, with an observed splitting of 24 cm^{-1} , is shifted to lower frequency ($\sim 13 \text{ cm}^{-1}$ for the low frequency component of each dyad) relative to that observed for $\text{Cs}^+(\text{H}_2\text{O})_3\text{Ar}_1$. Of the three other conformers, only conformer IV has a dyad with a shift to lower frequency (14 cm^{-1}),

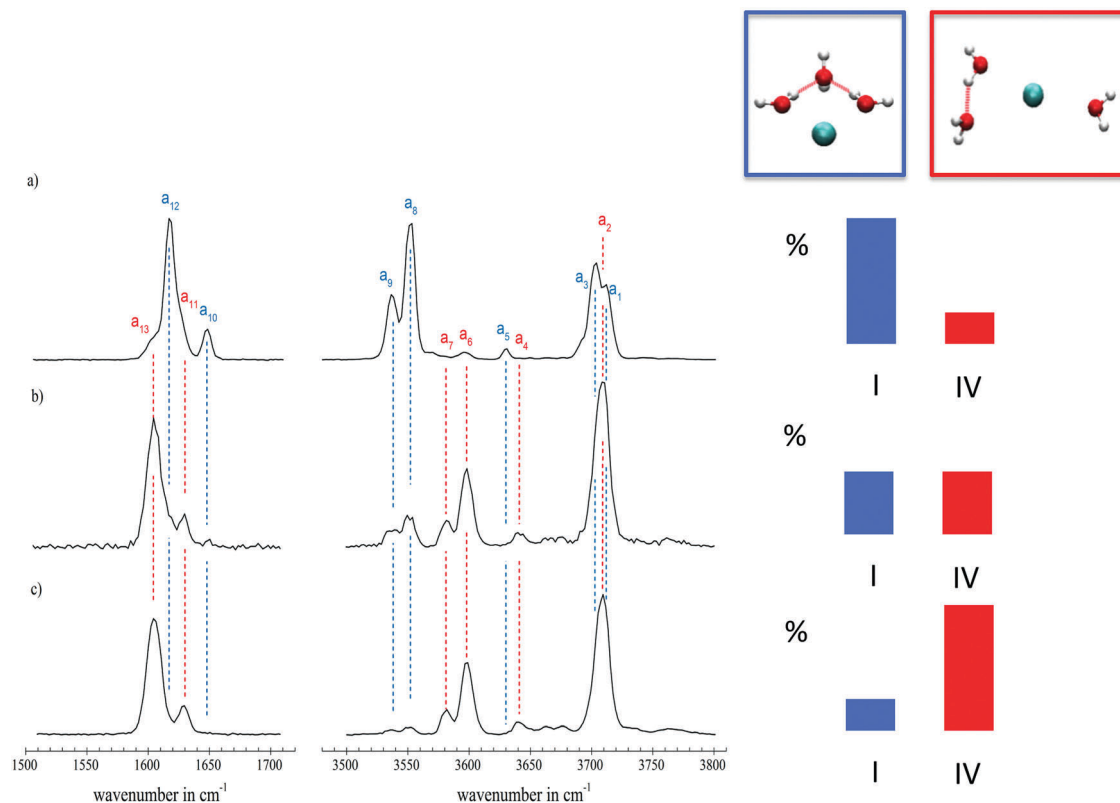


Fig. 3 IRPD spectra of (a) $\text{Cs}^+(\text{H}_2\text{O})_3\text{-Ar}$ at nominal ion trap temperature of 7 K, (b) $\text{Cs}^+(\text{H}_2\text{O})_3\text{D}_2$ where $\text{Cs}^+(\text{H}_2\text{O})_3\text{Ar}$ was mass selected in the quadrupole mass filter and Ar was replaced by D_2 in the ion trap at 12 K and (c) $\text{Cs}^+(\text{H}_2\text{O})_3\text{D}_2$ where $\text{Cs}^+(\text{H}_2\text{O})_3$ was mass selected and the complex was formed at 12 K. Assignment of the conformers (I & IV) responsible for the IRPD features on the left side: the red and blue bars illustrate an estimate of the relative contribution of the two isomers to the spectra. See main text for all details.

Table 2 Experimental IRPD band positions (in cm^{-1}), computed vibrational frequencies (in cm^{-1}) and assignments for bands of $\text{Cs}^+(\text{H}_2\text{O})_3\text{Ar}$ and $\text{Cs}^+(\text{H}_2\text{O})_3\text{D}_2$. The calculated frequencies are scaled by the factor 0.9686

Label	IRPD ^a	Theory	Assignment
a ₁	3712	3748	Free OH stretch I-conformer
a ₂	3709	3753	Free OH stretch IV-conformer
a ₃	3703	3740	Free OH stretch I-conformer
a ₄	3641	3668	Symmetric H ₂ O OH stretch IV-conformer
a ₅	3630	3653	Symmetric H ₂ O OH stretch I-conformer
a ₆	3598	3572	H-bonded OH stretch IV-conformer
a ₇	3581	—	H-bonded OH stretch IV-conformer
a ₈	3552	3550	H-bonded OH stretch I-conformer
a ₉	3538	3525	H-bonded OH stretch I-conformer
a ₁₀	1648	1616	H ₂ O bend I-conformer
a ₁₁	1630	1592	H ₂ O bend IV-conformer
a ₁₂	1617	1575	H ₂ O bend I-conformer
a ₁₃	1604	1561	H ₂ O bend IV-conformer

^a Band position are given with an error of 5 cm^{-1} .

and a splitting (29 cm^{-1}) that is consistent with experiment (Fig. 4).

A second method of forming $\text{Cs}^+(\text{H}_2\text{O})_3\text{D}_2$ was also examined (Fig. 3b). Here $\text{Cs}^+(\text{H}_2\text{O})_3\text{Ar}$ is selected from the source and trapped at 12 K with D_2 . Following collisional loss of Ar in the trap, $\text{Cs}^+(\text{H}_2\text{O})_3$ is tagged with D_2 , and spectroscopy is performed on $\text{Cs}^+(\text{H}_2\text{O})_3\text{D}_2$. Under these conditions, the 1604 and 1630 cm^{-1}

bands are dominant, but some signal is also observed at 1648 cm^{-1} (a₁₀). This suggests that both I and IV conformers may be present under these conditions. Although the presence of conformers II and III cannot be entirely ruled out (Fig. 4a), as the single OH bending IR band calculated for these conformers systematically overlaps with one of the dyads of conformers I or IV, the more direct assignment of the two experimental dyads is through conformers I and IV.

OH stretching region

When formed with argon as $\text{Cs}^+(\text{H}_2\text{O})_3\text{Ar}$, the spectrum recorded in Leipzig is similar to that reported in previous work from Illinois^{9,64} as shown in Fig. S2 (ESI[†]). The assignment of the dominant bands follows from the previous work. The 3538 (a₉) and 3552 (a₈) cm^{-1} bands correspond to hydrogen-bonded OH stretches, from the symmetric and antisymmetric combinations respectively, of the two equivalent hydrogen-bonded OH groups in conformer I. A small peak at 3630 cm^{-1} (a₅) has been assigned to the symmetric stretch of the second shell water of the I-conformer and the doublet at 3703 and 3712 cm^{-1} (a₃, a₁) to the remaining free OH stretching modes. These five features are consistent with the calculated spectral features for the I-conformer, as seen in Fig. 4b, and assigned as such in Table 2 in accord with previous investigations.^{9,65} A weaker band at 3598 cm^{-1} (a₆) is also present and will be discussed later.

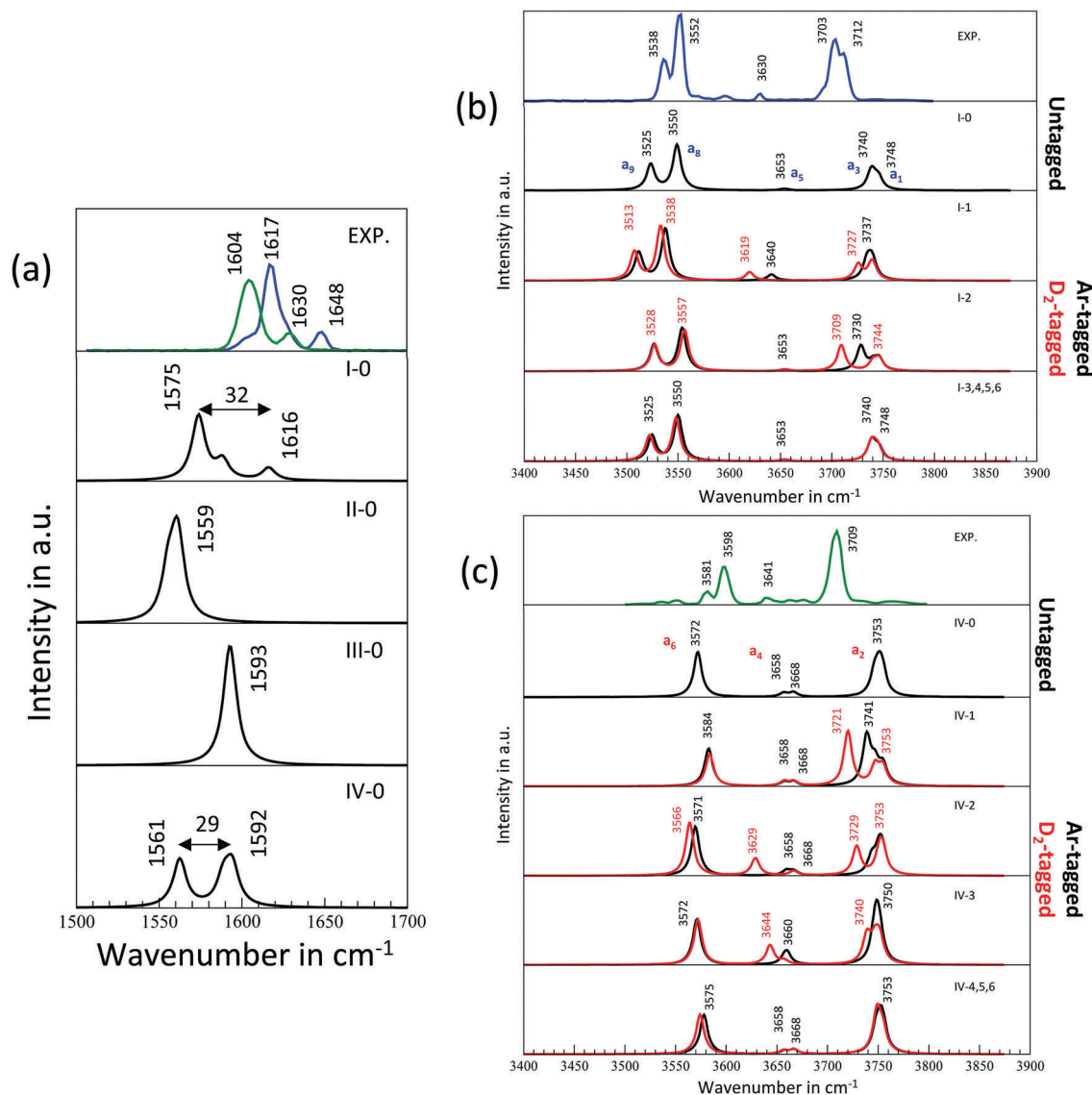


Fig. 4 (a) Calculated harmonic vibrational spectra for untagged conformers I–IV in the H₂O bending region. Note that only conformers I and IV have a doublet structure, with the IV-conformer shifted 14 cm⁻¹ to lower frequency. (b) Calculated harmonic spectra in the O–H stretching region of the I-conformer, both untagged and tagged, and (c) of the IV-conformer, both untagged and tagged. Scaled frequencies (0.9686). The labels ‘a_n’ refer to the same band labeling as in the IRPD experiments; see Fig. 3.

Attempts to more precisely specify the position of the argon atom should be viewed with caution. It is clear that there are only small energy differences between the six conformers, I-1 to I-6, as given in Fig. 2, and minor variations of the OH stretching frequencies in the computed spectra as shown in Fig. 4b. However, the lack of a large splitting in the free OH stretching region suggests that conformer I-2 is not present. Of the other five conformers, I-1 is the only one that shows a small, but noticeable shift for the symmetric OH stretch (a₅) of about 10 cm⁻¹ to lower frequency. This conformer is the only one where the argon interacts directly with the second shell water molecule. Conformers I-4 to I-6, where the Ar interacts with the cation, and conformer I-3 where the out-of-plane Ar interacts with the three water molecules also have the free O–H and H-bonded stretches that match the a₃–a₁ and a₉–a₈ experimental bands and could be present as well.

When formed as Cs⁺(H₂O)₃ and trapped at 12 K with D₂ as Cs⁺(H₂O)₃D₂, the 3538 and 3552 cm⁻¹ a₉–a₈ bands, associated with the I-conformer are barely observed, while the a₇–a₆ bands at 3581 and 3598 cm⁻¹ are dominant (Fig. 3c). A small peak at 3641 cm⁻¹ (a₄) and single free O–H peak at 3709 cm⁻¹ (a₂) are present. The free OH stretch is narrower than in the argon case.

It is clear that the dominant structure for the D₂-tagged species has a weaker hydrogen-bond network than the Ar-tagged species. Among the four conformers identified in the computational study, I, II, and IV possess hydrogen bonds (Fig. 2), however, only conformer IV has a substantially weaker hydrogen bond, based on the present calculations. The computed spectra associated with the untagged and tagged IV-conformers are shown in Fig. 4c. Previous computational work on Cs⁺(H₂O)₃ did not suggest that the IV conformer (a single water and a water

dimer subunit structure) had all three water molecules interacting with the cesium ion, which would weaken further the water–water hydrogen bond in the dimer subunit.^{10,62,65} However, the current computational analysis with a larger basis set indicates that this structure is indeed stable and relatively low-lying in energy with respect to the most stable I conformer (~ 8 kJ mol⁻¹, Fig. 2). A recent study by Paesani and co-workers has not only identified this IV conformer, but has also confirmed the other three structures, I, II and III within ~ 5 kJ mol⁻¹ of each other (ZPE-corrected).⁶⁶

There is less than 1 kJ mol⁻¹ difference in energy between the five D₂-tagged IV-conformers. In addition, it should be noted that the D₂ binding energy is substantially less than that for argon; the D₂-tagged clusters are not observed for trap temperatures above 25 K. It is possible that D₂ may freely “roam” about Cs⁺(H₂O)₃, and with the vibrational spectrum of Cs⁺(H₂O)₃D₂ represented by a combination of conformers.

None of the D₂-tagged IV-conformers have an IR-active doublet similar to the experimental 17 cm⁻¹ split a₇–a₆ dyad, but instead display one single H-bonded stretching band. The calculated frequency for this band is located at 3572 cm⁻¹ for the untagged IV-conformer. It shifts to higher or lower frequency depending on the location of the D₂ tag. Once all five conformers are taken into account, a dyad would be expected in this region, with a splitting of 10 to 20 cm⁻¹, as in the a₆–a₇ dyad. Moving up in frequency, the experimental a₄ band, at 3641 cm⁻¹, assigned to the symmetric O–H stretching of the water, is 11 cm⁻¹ higher in frequency than that observed (a₅) for Cs⁺(H₂O)₃Ar. This shift is consistent with the calculated results, with the symmetric stretch for the IV-conformer, 13 cm⁻¹ higher in frequency. Of the D₂-tagged IV-conformers, IV-1, IV-4, and IV-6, have symmetric stretches at the same frequency as the untagged IV-conformer. While not ruling out the presence of conformers IV-2 and IV-3, the other binding locations for D₂ may be preferentially populated. Turning to the free OH stretching region, the experimental spectrum has a single feature at 3709 cm⁻¹ (a₂), which is narrower than the doublet observed for Cs⁺(H₂O)₃Ar. This suggests that D₂ does not bind directly to an OH group as depicted by conformer IV-1, with a calculated splitting of 22 cm⁻¹. Of the three conformers that are consistent with the experimental a₄ band, conformers IV-4 and IV-6 have single free OH stretches. It is worth noting that both of these conformers have the D₂ binding to Cs⁺, either in the plane of the heavy (oxygen and cesium) atoms or out-of-plane. Only these two D₂-tagged IV conformers have calculated spectra that are consistent with all of the experimental OH stretching bands.

As mentioned earlier, Cs⁺(H₂O)₃Ar has a small band (a₆) at 3598 cm⁻¹. This can now be assigned to the presence of a minor population of the IV-conformer.

Using the second method of forming Cs⁺(H₂O)₃D₂ by selecting Cs⁺(H₂O)₃Ar from the source and trapping at 12 K with D₂, the collisional/exchange process, as can be seen in Fig. 3, substantially reduces the population of the I-conformer in favor of the IV-conformer. Thus it seems that with the loss of argon, sufficient energy is imparted to nascent Cs⁺(H₂O)₃ to rupture (partially or completely) the hydrogen bond network of the I-conformer. This in turn leads to the formation of the

IV-conformer as the nascent Cs⁺(H₂O)₃ is converted to Cs⁺(H₂O)₃D₂, through 3-body collisions with cold D₂. The 3538 and 3552 cm⁻¹ a₉–a₈ bands associated with the I-conformer have $\sim 1/3$ the intensity of the a₇–a₆ bands at 3581 and 3598 cm⁻¹. The remaining features at 3641 cm⁻¹ and 3709 cm⁻¹ reflect the dominance of the IV-conformer. At this point, it is unclear whether the presence of the I-conformer is due to (1) retention of a fraction of the I-conformer population following the loss of argon, (2) reformation of I-conformer from the IV-conformer, or (3) the formation of both conformers from the III-conformer that has no hydrogen bonds. We will return to collisional exchange process of D₂ for argon in the discussion below.

Temperature dependence

The 3-body collisional generation of the I- and IV-conformers indicated that a low barrier may exist between the two conformers that enables kinetic trapping of the IV-conformer. As a result, we examined the temperature dependence of the IR spectra of these species over a trap temperature range of 12 to 21 K, for Cs⁺(H₂O)₃D₂, and 7–40 K, for Cs⁺(H₂O)₃Ar, with the results shown in Fig. S3 (ESI[†]). The dependence on temperature is clearly seen for Cs⁺(H₂O)₃D₂, but somewhat less apparent for Cs⁺(H₂O)₃Ar. Difference spectra, generated by subtracting the lowest temperature spectra (7 K for argon, 12 K for D₂) from those taken at higher temperatures, indicate the growth or reduction of individual spectral features. These are presented in Fig. 5.

As seen in Fig. 5 and Fig. S3 (ESI[†]) for Cs⁺(H₂O)₃D₂, an increase in temperature enables the bands associated with the I-conformer in the H₂O bending region (a₁₀ and a₁₂) and the OH stretching region (a₈ and a₉) to gain intensity. Conversely, bands associated with the IV-conformer, a₁₃ in the bend, and in the stretch, a₆, a₇, and a₂, lose intensity. Thus, there is strong evidence that increasing the ion trap temperature by 8 K is sufficient to alter the relative contributions of conformers I and IV to the ensemble of Cs⁺(H₂O)₃D₂ cluster ions. The temperature dependence of the Cs⁺(H₂O)₃Ar spectrum depicts slight changes in the relative intensity of the I-conformer bands. For spectral regions associated with the IV-conformer (~ 1603 cm⁻¹ for a₁₃, and 3598 cm⁻¹ for a₆), there is a clear loss of intensity with increasing temperature. So for both Cs⁺(H₂O)₃D₂ and Cs⁺(H₂O)₃Ar, an increase in temperature leads to a reduction in the population of the higher energy IV-conformer.

To consider the relative stability of these two conformers as a function of temperature, metadynamics calculations were performed at three temperatures: 10, 20 and 50 K. Three free energy profiles are presented in Fig. 6a, depicting the inter-conversions between the Cs⁺(H₂O)₃ I and IV conformers. Entropic effects are clearly seen in these two profiles. While conformer I is favored by free energy at all three temperatures, the barrier to reach the IV-conformer is substantially reduced at 50 K (20 kJ mol⁻¹ at 10 K vs. 5 kJ mol⁻¹ at 50 K). Conversely, the barrier to reach the I-conformer from the IV-conformer is reduced from 5 kJ mol⁻¹ at 10 K to less than 2 kJ mol⁻¹ at 50 K. Furthermore, the free energy well of the IV-conformer is rather flat at 50 K, so the effective population of this conformer will be small to

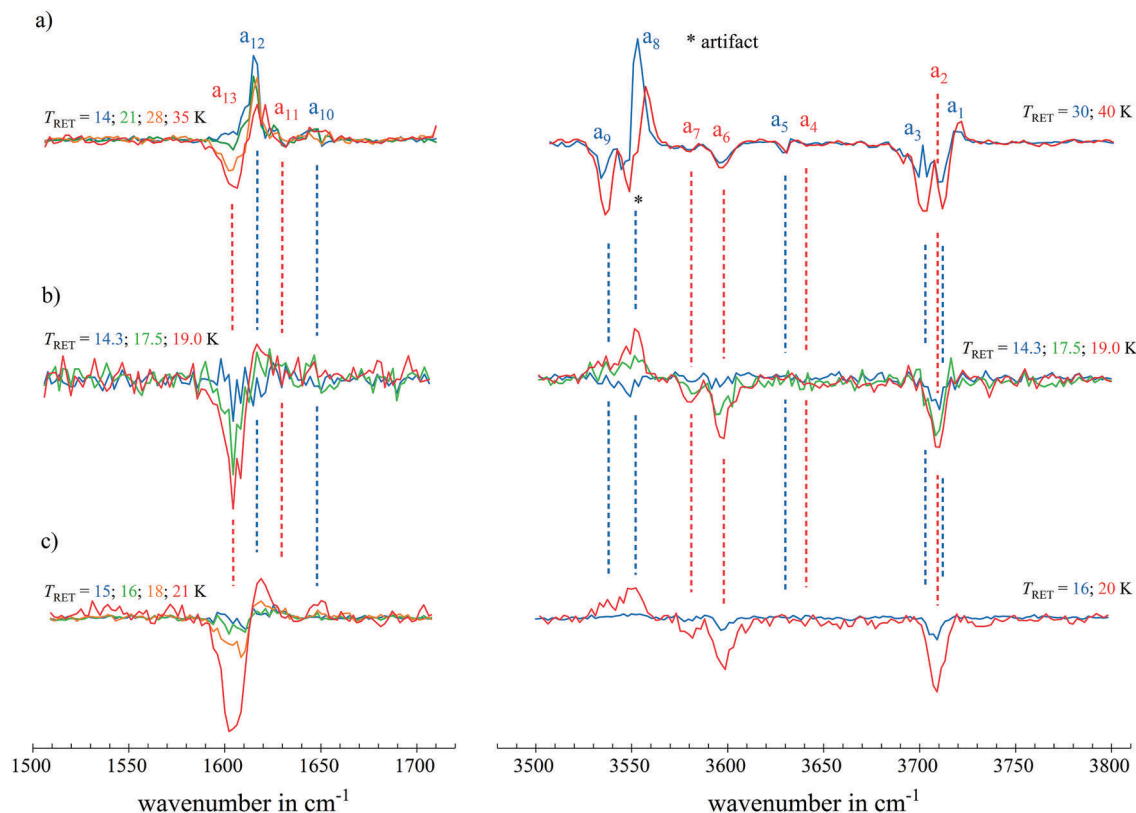


Fig. 5 Difference IRPD spectra of: (a) $\text{Cs}^+(\text{H}_2\text{O})_3\text{Ar}$ between 7 K and given temperature; (b) $\text{Cs}^+(\text{H}_2\text{O})_3\text{D}_2$ (formed by collisional loss of argon in the trap) between 12 K and given temperature; (c) $\text{Cs}^+(\text{H}_2\text{O})_3\text{D}_2$ (formed from $\text{Cs}^+(\text{H}_2\text{O})_3$ and tagged with D_2) between 12 K and given temperature. Negative deviations indicate loss of intensity. Positive deviations indicate gain of intensity. * This feature is due to slightly different peak shapes in the original 7 and 40 K spectra (see Fig. S1, ESI[†]) and does not represent an IR absorption.

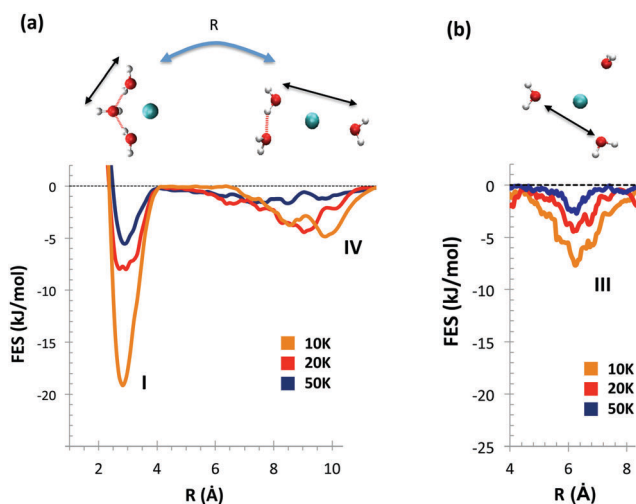


Fig. 6 Free energy profiles from the finite temperatures metadynamics MD simulations (including anharmonicities and entropic effects): (a) the interconversion between the I and IV conformers. R measures the distance between the oxygens of the middle and top water molecules in the I-conformer, (b) the stability of the conformer III. R measures the distance between the oxygens of two water molecules in this conformer.

non-existent. Thus, the metadynamics calculations are consistent with the experimental temperature dependence of the

$\text{Cs}^+(\text{H}_2\text{O})_3\text{D}_2$ and $\text{Cs}^+(\text{H}_2\text{O})_3\text{Ar}$ spectra recorded under all three experimental conditions (a through c in Fig. 3). An increase in temperature for either tagged species will tend to favor the I-conformer over the IV-conformer, as the IV-conformer becomes unstable.

Mechanisms of formation of the tagged clusters and final conclusions

In these experiments, either $\text{Cs}^+(\text{H}_2\text{O})_3\text{Ar}$ or $\text{Cs}^+(\text{H}_2\text{O})_3$ are generated by evaporative cooling of nascent cluster ions formed when cesium ions collide with neutral clusters of $(\text{H}_2\text{O})_m\text{Ar}_n$ in the source region. From previous studies by the Illinois group, estimates for the effective temperature for these clusters depend on the binding of the most labile constituent of the cluster ion. $\text{Cs}^+(\text{H}_2\text{O})_3\text{Ar}$ is formed by evaporative cooling of argon, and has an effective temperature of 80 to 100 K. $\text{Cs}^+(\text{H}_2\text{O})_3$ is formed by evaporative cooling of water, which binds more strongly to the ion, and results in a higher effective temperature of approximately 300 K.¹⁰ After a small number of collisions with He in the RF octopole ion guides, mass selection and focusing into a RF ring-electrode ion-trap, the cluster ions undergo a significant number of collisions with either He or D_2 at trap temperatures ranging from 7 to 40 K, and 12 to 21 K, respectively.

The spectrum for $\text{Cs}^+(\text{H}_2\text{O})_3\text{Ar}$ in the OH stretching region at 7 K in this study, and the previously published spectrum of

$\text{Cs}^+(\text{H}_2\text{O})_3\text{Ar}$ by Ke and co-workers⁶⁵ formed by evaporative cooling of argon are similar as mentioned earlier (Fig. S2, ESI[†]). The 7 K spectrum resulting from collisions with cold helium gas in this report has sharper, narrower features that would be expected in comparison to the warmer spectrum with a temperature established by evaporative cooling of argon. As noted above, the dominant conformer is structure I, which is also the minimum energy structure, with a small contribution from conformer IV. Analysis of the computed spectra suggests that the argon is likely located near the second shell water molecule, conformer I-1. These spectra demonstrate that a few collisions with He, which do not dislodge the argon atom from $\text{Cs}^+(\text{H}_2\text{O})_3\text{Ar}$, do not impart sufficient energy to affect the ensemble generated by evaporative cooling of argon.

The $\text{Cs}^+(\text{H}_2\text{O})_3\text{D}_2$ spectra, formed from either $\text{Cs}^+(\text{H}_2\text{O})_3\text{Ar}$ or $\text{Cs}^+(\text{H}_2\text{O})_3$ via the 3-body collisions with cryogenic D_2 , are very different from the $\text{Cs}^+(\text{H}_2\text{O})_3\text{Ar}$ spectrum. The dominant conformer in both cases is structure IV, with a single hydrogen bond. The location of the D_2 is unclear. While conformers IV-4 and IV-6 have computed bands consistent with all of the experimental features, the small differences in binding energy would allow contributions from other conformers as well. As $\text{Cs}^+(\text{H}_2\text{O})_3\text{D}_2$ was generated in two ways, first consider the formation from the $\text{Cs}^+(\text{H}_2\text{O})_3$ precursor. The nascent cluster ion, as it enters the RF ring-electrode ion-trap, has an effective temperature of 300 K based on earlier work.¹⁰ Under these conditions, the dominant conformer with the lowest free energy is structure III (no hydrogen bonds, see Fig. S3, ESI[†] for temperature-dependent free energies), with small contributions from conformers I and IV.⁹ However based on the free energy analysis, the most stable conformer at or below 80 K is the I-conformer with two hydrogen bonds. Collisions with cryogenic D_2 at temperatures of 12–20 K, rapidly quenching a warm cluster ensemble of $\text{Cs}^+(\text{H}_2\text{O})_3$ and rapid cooling of conformer III would follow a pathway leading to the IV-conformer with a single hydrogen bond, and then to the more stable I-conformer with 2 hydrogen bonds. From the metadynamics analysis, kinetic trapping of the IV-conformer is possible as the temperature drops below 50 K, as seen in Fig. 6a, with a substantial barrier to a path leading to the I-conformer. The barrier decreases with increasing temperature, enabling a portion of the IV-conformer to convert to the I-conformer. Fig. 6b reveals a decrease in stability for the III-conformer from 10 K to 50 K, with a barrier of $\sim 2 \text{ kJ mol}^{-1}$ from another free energy well at 50 K. The free energy minimum of III-conformer is also shrinking in width, showing large entropic effects. If there were vibrational signatures for the III-conformer, they would only appear for temperatures below 50 K.

The other production route involves collisional loss of Ar from $\text{Cs}^+(\text{H}_2\text{O})_3\text{Ar}$ in the ion trap, followed by collisional cooling with D_2 , and its subsequent attachment via three-body collisions. The collisional loss of Ar clearly increases the internal energy of the $\text{Cs}^+(\text{H}_2\text{O})_3$ product by an amount sufficient to induce a change in the distribution of conformers from the initial $\text{Cs}^+(\text{H}_2\text{O})_3\text{Ar}$ cluster ion distribution. Since conformer IV is dominant when $\text{Cs}^+(\text{H}_2\text{O})_3\text{D}_2$ is formed directly from

$\text{Cs}^+(\text{H}_2\text{O})_3$, it appears that the collisional process involving $\text{Cs}^+(\text{H}_2\text{O})_3\text{Ar}$ generates an ensemble with an effective temperature range, based on the argon binding energy of 80 to 120 K,⁹ where both conformers I and III have comparable free energies (Fig. S3, ESI[†]). Additional collisions with cryogenic D_2 to temperatures of 12–20 K preserved both IV and I conformers with the same temperature dependence as observed when $\text{Cs}^+(\text{H}_2\text{O})_3$ was the precursor. Thus the same arguments provided for the direct cryogenic cooling of $\text{Cs}^+(\text{H}_2\text{O})_3$ leading to a temperature dependence of the relative contributions of the IV- and I-conformers, as described in the preceding paragraph, apply here as well. The only difference is due to the initial distribution of III and I conformers between nascent $\text{Cs}^+(\text{H}_2\text{O})_3$ as opposed to $\text{Cs}^+(\text{H}_2\text{O})_3$ formed by collisional loss of argon in the trap.

The combined experimental (Ar/ D_2 tagging IRPD spectroscopy and temperature dependence) and theoretical (harmonic vibrational spectra and free energy profiles from finite temperature metadynamics MD simulations) strategies can be generalized to any cluster. Even at cryogenic temperatures, conformers can display a preference depending on the tagging species, and a measurable temperature dependence over a range of $\sim 30 \text{ K}$. The experimental methods of cluster ion formation and cooling, and the topology of the potential energy surface, suggest that kinetic trapping can have a considerable effect on the conformer distribution.

Conflicts of interest

There are no conflicts of interest to declare.

Acknowledgements

JML gratefully acknowledges support from the Alexander von Humboldt Foundation for a research award, and that this material is based on work done while serving at the U.S. National Science Foundation during 2016–7. This work was performed using HPC resources from GENCI-France Grant 072484 (CINES/IDRIS/TGCC). DRG and MPG acknowledges ANR-14-CE35-0011-01 for funding. KRA acknowledges funding by the Deutsche Forschungsgemeinschaft within the Collaborative Research Center 1109, “Metal Oxide/Water Systems”. The authors wish to acknowledge Dr John T. Kelly for his helpful comments and assistance in the installation of the ion source in the apparatus.

References

- 1 R. Cabot and C. A. Hunter, *Chem. Soc. Rev.*, 2012, **41**, 3485–3492.
- 2 C. A. Hunter, *Angew. Chem., Int. Ed.*, 2004, **43**, 5310–5324.
- 3 V. Vaida, H. G. Kjaergaard and K. J. Feierabend, *Int. Rev. Phys. Chem.*, 2003, **22**, 203–219.
- 4 L. R. McCunn, J. R. Roscioli, B. M. Elliott, M. A. Johnson and A. B. McCoy, *J. Phys. Chem. A*, 2008, **112**, 6074–6078.

- 5 S. I. Stupp and L. C. Palmer, *Chem. Mater.*, 2014, **26**, 507–518.
- 6 N. Veljkovic, S. Glisic, V. Perovic and V. Veljkovic, *Expert Opin. Drug Discovery*, 2011, **6**, 1263–1270.
- 7 A. M. van Oijen, *Curr. Opin. Biotechnol.*, 2011, **22**, 75–80.
- 8 A. B. Wolk, C. M. Leavitt, E. Garand and M. A. Johnson, *Acc. Chem. Res.*, 2014, **47**, 202–210.
- 9 D. J. Miller and J. M. Lisy, *J. Am. Chem. Soc.*, 2008, **130**, 15381–15392.
- 10 D. J. Miller and J. M. Lisy, *J. Am. Chem. Soc.*, 2008, **130**, 15393–15404.
- 11 C. T. Wolke, F. S. Menges, N. Tötsch, O. Gorlova, J. A. Fournier, G. H. Weddle, M. A. Johnson, N. Heine, T. K. Esser, H. Knorke, K. R. Asmis, A. B. McCoy, D. J. Arismendi-Arrieta, R. Prosmitti and F. Paesani, *J. Phys. Chem. A*, 2015, **119**, 1859–1866.
- 12 B. Bandyopadhyay, K. N. Reishus and M. A. Duncan, *J. Phys. Chem. A*, 2013, **117**, 7794–7803.
- 13 L. Voronina and T. R. Rizzo, *Phys. Chem. Chem. Phys.*, 2015, **17**, 25828–25836.
- 14 J. S. Prell, T. C. Corraera, T. M. Chang, J. A. Biles and E. R. Williams, *J. Am. Chem. Soc.*, 2010, **132**, 14733–14735.
- 15 V. Brites, A. Cimas, R. Spezia, N. Sieffert, J. M. Lisy and M. P. Gaigeot, *J. Chem. Theory Comput.*, 2015, **11**, 871–883.
- 16 O. Rodriguez and J. M. Lisy, *J. Phys. Chem. Lett.*, 2011, **2**, 1444–1448.
- 17 J. D. Rodriguez and J. M. Lisy, *Int. J. Mass Spectrom.*, 2009, **283**, 135–139.
- 18 N. Khanal, C. Masellis, M. Z. Kamrath, D. E. Clemmer and T. R. Rizzo, *Anal. Chem.*, 2017, **89**, 7601–7606.
- 19 J. S. Prell, T. M. Chang, J. A. Biles, G. Berden, J. Oomens and E. R. Williams, *J. Phys. Chem. A*, 2011, **115**, 2745–2751.
- 20 J. A. Silveira, K. L. Fort, D. Kim, K. A. Servage, N. A. Pierson, D. E. Clemmer and D. H. Russell, *J. Am. Chem. Soc.*, 2013, **135**, 19147–19153.
- 21 R. M. Forck, J. M. Dieterich, C. C. Pradzynski, A. L. Huchting, R. A. Mata and T. Zeuch, *Phys. Chem. Chem. Phys.*, 2012, **14**, 9054–9057.
- 22 C. W. Dierking, F. Zurheide, T. Zeuch, J. Med, S. Parez and P. Slaviček, *J. Chem. Phys.*, 2017, 146.
- 23 J. M. Lisy, *Int. Rev. Phys. Chem.*, 1997, **16**, 267–289.
- 24 T. Ebata, A. Fujii and N. Mikami, *Int. Rev. Phys. Chem.*, 1998, **17**, 331–361.
- 25 E. J. Bieske and O. Dopfer, *Chem. Rev.*, 2000, **100**, 3963–3998.
- 26 O. Dopfer, *Z. Phys. Chem.*, 2005, **219**, 125–168.
- 27 K. Mizuse and A. Fujii, *Phys. Chem. Chem. Phys.*, 2011, **13**, 7129–7135.
- 28 M. Okumura, L. I. Yeh, J. D. Myers and Y. T. Lee, *J. Chem. Phys.*, 1986, **85**, 2328–2329.
- 29 C. J. Johnson, A. B. Wolk, J. A. Fournier, E. N. Sullivan, G. H. Weddle and M. A. Johnson, *J. Chem. Phys.*, 2014, 140.
- 30 M. Brümmer, C. Kaposta, G. Santambrogio and K. R. Asmis, *J. Chem. Phys.*, 2003, **119**, 12700–12703.
- 31 E. Garand, *J. Phys. Chem. A*, 2018, **122**, 6479–6490.
- 32 J. M. Voss, K. C. Fischer and E. Garand, *J. Phys. Chem. Lett.*, 2018, **9**, 2246–2250.
- 33 J. M. Voss, S. J. Kregel, K. C. Fischer and E. Garand, *J. Am. Soc. Mass Spectrom.*, 2018, **29**, 42–50.
- 34 C. W. Liu and Y. Q. Gao, *Int. J. Quantum Chem.*, 2015, **115**, 541–544.
- 35 Y. Wang and J. M. Bowman, *J. Chem. Phys.*, 2012, 136.
- 36 K. Szalewicz, *Int. Rev. Phys. Chem.*, 2008, **27**, 273–316.
- 37 J. Hutter, M. Iannuzzi, F. Schiffmann and J. Vandevondele, *Wiley Interdiscip. Rev.: Comput. Mol. Sci.*, 2014, **4**, 15–25.
- 38 C. T. Wolke, J. A. Fournier, L. C. Dzugan, M. R. Fagiani, T. T. Odbadrakh, H. Knorke, K. D. Jordan, A. B. McCoy, K. R. Asmis and M. A. Johnson, *Science*, 2016, **354**, 1131–1135.
- 39 N. Heine, E. G. Kratz, R. Bergmann, D. P. Schofield, K. R. Asmis, K. D. Jordan and A. B. McCoy, *J. Phys. Chem. A*, 2014, **118**, 8188–8197.
- 40 V. Brites, A. L. Nicely, N. Sieffert, M. P. Gaigeot and J. M. Lisy, *Phys. Chem. Chem. Phys.*, 2014, **16**, 13086–13095.
- 41 J. P. Beck, A. Cimas, J. M. Lisy and M. P. Gaigeot, *Spectrochim. Acta, Part A*, 2014, **119**, 12–17.
- 42 J. P. Beck, M. P. Gaigeot and J. M. Lisy, *Phys. Chem. Chem. Phys.*, 2013, **15**, 16736–16745.
- 43 N. Yang, C. H. Duong, P. J. Kelleher, M. A. Johnson and A. B. McCoy, *Chem. Phys. Lett.*, 2017, **690**, 159–171.
- 44 G. E. Doublerly, R. S. Walters, J. Cui, K. D. Jordan and M. A. Duncan, *J. Phys. Chem. A*, 2010, **114**, 4570–4579.
- 45 B. M. Elliott, R. A. Relph, J. R. Roscioli, J. C. Bopp, G. H. Gardenier, T. L. Guasco and M. A. Johnson, *J. Chem. Phys.*, 2008, 129.
- 46 B. M. Marsh, J. M. Voss, J. Zhou and E. Garand, *Phys. Chem. Chem. Phys.*, 2015, **17**, 23195–23206.
- 47 X. Lei, X. Kong, B. Zhang, Z. Zhao, D. Dai, X. Yang and L. Jiang, *J. Phys. Chem. A*, 2018, **122**, 8054–8057.
- 48 V. Brites, J. M. Lisy and M. P. Gaigeot, *J. Phys. Chem. A*, 2015, **119**, 2468–2474.
- 49 T. Shimamori, J. L. Kuo and A. Fujii, *J. Phys. Chem. A*, 2016, **120**, 9203–9208.
- 50 Y. C. Li, T. Hamashima, R. Yamazaki, T. Kobayashi, Y. Suzuki, K. Mizuse, A. Fujii and J. L. Kuo, *Phys. Chem. Chem. Phys.*, 2015, **17**, 22042–22053.
- 51 T. Hamashima, Y. C. Li, M. C. H. Wu, K. Mizuse, T. Kobayashi, A. Fujii and J. L. Kuo, *J. Phys. Chem. A*, 2013, **117**, 101–107.
- 52 A. Masson, E. R. Williams and T. R. Rizzo, *J. Chem. Phys.*, 2015, 143.
- 53 N. Heine and K. R. Asmis, *Int. Rev. Phys. Chem.*, 2015, **34**, 1–34.
- 54 D. Irimia, D. Dobrikov, R. Kortekaas and H. Voet, D. A. Van Den Ende, W. A. Groen and M. H. M. Janssen, *Rev. Sci. Instrum.*, 2009, 80.
- 55 O. M. Cabarcos, C. J. Weinheimer, T. J. Martínez and J. M. Lisy, *J. Chem. Phys.*, 1999, **110**, 9516–9526.
- 56 W. R. Bosenberg and D. R. Guyer, *J. Opt. Soc. Am. B*, 1993, **10**, 1716–1722.
- 57 N. Heine and K. R. Asmis, *Int. Rev. Phys. Chem.*, 2016, **35**, 507.
- 58 G. W. T. M. J. Frisch, H. B. Schlegel, G. E. Scuseria, M. A. Robb, J. R. Cheeseman, G. Scalmani, V. Barone, G. A. Petersson, H. Nakatsuji, X. Li, M. Caricato, A. V. Marenich, J. Bloino, B. G. Janesko, R. Gomperts, B. Mennucci, H. P. Hratchian,

- J. V. Ortiz, A. F. Izmaylov, J. L. Sonnenberg, D. Williams-Young, F. Ding, F. Lipparini, F. Egidi, J. Goings, B. Peng, A. Petrone, T. Henderson, D. Ranasinghe, V. G. Zakrzewski, J. Gao, N. Rega, G. Zheng, W. Liang, M. Hada, M. Ehara, K. Toyota, R. Fukuda, J. Hasegawa, M. Ishida, T. Nakajima, Y. Honda, O. Kitao, H. Nakai, T. Vreven, K. Throssell, J. A. Montgomery, Jr., J. E. Peralta, F. Ogliaro, M. J. Bearpark, J. J. Heyd, E. N. Brothers, K. N. Kudin, V. N. Staroverov, T. A. Keith, R. Kobayashi, J. Normand, K. Raghavachari, A. P. Rendell, J. C. Burant, S. S. Iyengar, J. Tomasi, M. Cossi, J. M. Millam, M. Klene, C. Adamo, R. Cammi, J. W. Ochterski, R. L. Martin, K. Morokuma, O. Farkas, J. B. Foresman and D. J. Fox, *Gaussian 09, Revision C.01*, Gaussian, Inc., Wallingford CT, 2009.
- 59 T. H. Dunning Jr. and J. P. Hay, in *Modern Theoretical Chemistry*, ed. H. F. S. Plenum III, New York, 1977, vol. 3, pp. 1–28.
- 60 R. A. Kendall, T. H. Dunning Jr and R. J. Harrison, *J. Chem. Phys.*, 1992, **96**, 6796–6806.
- 61 J. P. Merrick, D. Moran and L. Radom, *J. Phys. Chem. A*, 2007, **111**, 11683–11700.
- 62 M. Kołaski, H. M. Lee, Y. C. Choi, K. S. Kim, P. Tarakeshwar, D. J. Miller and J. M. Lisy, *J. Chem. Phys.*, 2007, 126.
- 63 J. Vandevondele, M. Krack, F. Mohamed, M. Parrinello, T. Chassaing and J. Hutter, *Comput. Phys. Commun.*, 2005, **167**, 103–128.
- 64 H. Ke, C. Van Der Linde and J. M. Lisy, *J. Phys. Chem. A*, 2014, **118**, 1363–1373.
- 65 H. Ke, C. Van Der Linde and J. M. Lisy, *J. Phys. Chem. A*, 2015, **119**, 2037–2051.
- 66 M. Riera, S. E. Brown and F. Paesani, *J. Phys. Chem. A*, 2018, **122**, 5811–5821.

Titre : Réactivités aux interfaces aqueuses par simulations DFT-MD

Mots clés : interfaces aqueuses, réactivités, chimie prébiotique, silice, simulation DFT-MD

Résumé : La compréhension microscopique des réactions chimiques qui se produisent à l'interface entre l'eau et d'autres milieux représente une étape essentielle de la chimie pour l'élaboration des réactions à haut rendement. Cependant, la difficulté expérimentale pour discerner l'effet catalytique provenant spécifiquement de l'environnement de l'eau interfaciale rend le rôle de l'interface au cours de la réaction encore incompris.

L'objectif principal de cette thèse de doctorat a été de fournir une description moléculaire de réactions chimiques aux interfaces aqueuses par simulations de dynamique moléculaire basées sur la théorie de la fonctionnelle de la densité (DFT-MD / AIMD) afin de rationaliser les rôles catalytiques des interfaces.

La première partie du manuscrit porte sur l'étude des réactions chimiques dans la chimie prébiotique, où de nombreuses réactions aux interfaces aqueuses ont été envisagées dans la littérature pour rationaliser l'origine des premiers biopolymères sur la Terre primordiale. En particulier, la première réaction de condensation d'une liaison peptidique est un sujet controversé. La condensation des acides aminés en oligopeptides en l'absence d'enzymes est connue pour être entravée par des raisons à la fois thermodynamiques et cinétiques dans l'eau liquide. Par contre, l'équipe de la Prof. Vaida a observé expérimentalement la formation de polypeptides à partir d'esters d'acides aminés et du sel CuCl_2 à l'interface air-eau. Cela suggère que la surface des océans est un environnement approprié pour la naissance de la vie sur la Terre. Cependant, le rôle de l'interface air-eau lors de la formation des liaisons peptidiques et les raisons pour lesquelles cette réaction se produit à l'interface et non dans l'eau liquide n'est pas clair.

Nous fournissons une compréhension à l'échelle microscopique de la réaction à l'interface air-eau par simulations DFT-MD. La caractérisation de la structure de l'eau interfaciale, couplée à la comparaison entre les mécanismes et les énergies de réactions observées à l'interface air-eau versus l'eau liquide nous permet de révéler les facteurs clés qui mènent à la formation de polypeptides.

Nos données montrent de nouveaux rôles catalytiques de l'interface air-eau qui sont essentiels pour que la réaction se produise. Nous identifions notamment pourquoi les propriétés de solvation des espèces réactives et la présence du Cl^- à l'interface sont d'importance pour catalyser la réaction.

Dans la deuxième partie de cette thèse de doctorat, nous nous sommes concentrés sur la caractérisation de la structure et de la réactivité d'interfaces de silices amorphes aqueuses en couplant des simulations DFT-MD et des calculs de spectroscopie SFG (Sum Frequency Génération). L'objectif principal de notre étude est la compréhension de la réactivité de la surface de la silice au contact de l'eau liquide en fonction des conditions du pH. Nous avons suivi l'évolution de la structure et de la surface de silice en réponse à la variation des conditions du pH de la solution en couplant simulations DFT-MD et spectroscopie SFG (en collaboration avec la Prof. Wei-Tao Liu, Chine). Nos travaux apportent une compréhension du comportement acido-basique controversé de la surface de silice, montrant qu'une image moléculaire basée uniquement sur l'équilibre entre Si-OH (silanol) et Si-O⁻ (silanolate) à la surface de la silice n'est pas suffisante pour rationaliser les spectres SFG en fonction du pH. L'émergence d'une troisième espèce moléculaire, notée «Si5», révèle une chimie acide-base de la surface plus complexe. Nos données apportent une nouvelle rationalisation microscopique du comportement acido-basique bimodal des groupes de la surface de silice observés expérimentalement et révèle l'espèce Si5 comme une clé pour comprendre la chimie des surfaces de silices aqueuses.

Title : Reactivity at aqueous interfaces by DFT-MD simulations

Keywords : aqueous interfaces, reactivity, prebiotic chemistry, silica, DFT-MD simulation

Abstract : The microscopic comprehension of chemical reactions that occur at the boundary between water and other media represents an essential step in chemical science for the development of high yield chemical reactions. However the experimental difficulty in discerning the specific catalytic effect originating from the specific interfacial water environment makes the role of the interface along the reaction pathways still far to be understood.

The main objective of this PhD thesis has been to provide a molecular description of chemical reactions at aqueous interfaces by Density Functional Theory-based Molecular Dynamics simulation techniques (DFT-MD/AIMD) in order to rationalize the catalytic roles of interfaces, especially from the structural point of view.

The first part of the manuscript is dedicated to the study of chemical reactions of relevance in prebiotic chemistry, where many routes at aqueous interfaces have been envisaged in the literature in order to rationalize the origin of the first biopolymers on the primordial Earth. In

We especially identify why the solvation properties of the reactive species and the presence of Cl^- anions at the interface are of utmost importance in catalyzing the peptide bond condensation reaction.

In the second part of this PhD, we have focused on the characterization of the structure and reactivity of aqueous amorphous silica interfaces by coupling DFT-MD and SFG (Sum Frequency Generation) spectroscopy. This is especially relevant for the development of new technologies in the field of materials design and heterogeneous catalysis. The main targets of our investigation is the comprehension of the silica surface reactivity in contact with liquid water as a function of pH conditions. We have followed the evolution of the silica surface structure and chemistry in response to the variation in the water pH conditions by coupling experimental SFG spectroscopy (in collaboration with Prof. Wei-Tao Liu, China) with DFT-MD simulations. Our work provides a deep insight into the controversial acid-base behaviour of the silica surface, showing that a molecular picture based only on the balance between silanol SiOH

particular the first peptide bond condensation reaction is a highly debated topic. The condensation of amino acids into oligopeptides in absence of enzymes is known to be hindered by both thermodynamic and kinetic reasons in bulk water at ambient conditions. By contrast, Prof. Vaida group has experimentally observed the formation of polypeptides at room temperature in dilute conditions from amino acid esters and CuCl_2 salt at the air-water interface, suggesting the surface of oceans as a suitable environment for the birth of life on the prebiotic Earth. However the specific role of the air-water interface during the peptide bond formation and the reasons for which this reaction occurs at the interface and not in bulk water are still unclear.

We provide a microscopical insight into the peptide bond formation reaction at the air-water interface by DFT-MD simulations. The characterization of the interfacial water network, coupled with the comparison between energetics and reaction mechanisms observed at the air-water interface versus bulk water allows us to reveal the key factors that promote the polypeptides formation in such heterogeneous conditions.

Our data point to novel catalytic roles of the air-water interface which are essential in making the reaction occur.

and silanolate SiO^- species at the silica surface is not enough to rationalize the trends in the SFG bands as a function of pH. The emergence of a third molecular species, denoted "Si5", reveals a more complex acid-base surface chemistry, and strongly modulates the silica surface acidity. Our data provide a new microscopical rationalization of the acid-base bimodal behaviour of the silica surface groups observed experimentally and reveal the Si5 species as an essential key to understand the chemistry at aqueous silica surfaces.